密级:_____

中国科学院大学
University of Chinese Academy of Sciences

博士学位论文

银河系分子云与恒星形成

作者姓名: 闫庆增

指导教师: 唐正宏、徐烨、张波 研究员

中国科学院上海天文台、紫金山天文台

国外导师: **Dr. J. P. Macquart A. J. Walsh P. J. Hancock**

ICRAR/Curtin University

学位类别: 理学博士

学科专业: 天体测量与天体力学

研 究 所: 中国科学院上海天文台

2018 年 **03** 月

Molecular Clouds and Star Formation in The Milky Way

by

Qingzeng Yan

A dissertation submitted to
The University of Chinese Academy of Sciences
in partial fulfillment of the requirements
for the degree of
Doctor of Radio Astronomy

Shanghai Astronomical Observatory, Chinese Academy of Sciences

March, 2018

中国科学院大学

研究生学位论文原创性声明

本人郑重声明：我所呈交的学位论文是本人在导师指导下进行的研究工作及所取得的研究成果。尽我所知，除了文中已经标注引用的内容外，本论文中不含其他个人或集体已经发表或撰写过的研究成果。对本文的研究做出贡献的个人和集体，均已在文中作了明确的说明或致谢。

作者签名：_____

日　　期：_____

中国科学院大学

学位论文授权使用声明

本人完全了解并同意遵守中国科学院有关保存和使用学位论文的规定，即中国科学院有权保留送交学位论文的副本，允许该论文被查阅，可以公布该论文的全部或部分内容，可以采用影印、缩印或其他复制手段保存、汇编本学位论文。

（涉密的学位论文在解密后适用本声明）

作者签名：_____　　导师签名：_____

日　　期：_____　　日　　期：_____

摘　要

恒星的形成与演化是一直是天文学研究的难点和热点，而作为诞生恒星的地方，分子云本身的形成和演化同样是天文学的难点问题。本论文通过观测和研究银河系中三个典型区域，来试图获得关于恒星和分子云形成与演化的线索。

为了研究触发恒星形成过程，我们用紫金山天文台青海观测站的 13.7 米毫米波射电望远镜观测了银道面上的 13 个大质量恒星形成区的五条分子谱线，^{12}CO ($J = 1 \rightarrow 0$)、^{13}CO ($J = 1 \rightarrow 0$)、C^{18}O ($J = 1 \rightarrow 0$)、HCN ($J = 1 \rightarrow 0$) 和 HCO^{+} ($J = 1 \rightarrow 0$)。通过分析和证认，我们在四个红外 Bubble 附近，找到四个外向分子流。我们认为H II 区在膨胀过程中，会堆积分子云，进而会加速或者触发周围的恒星形成活动。

为了获得银河系内更加完备的大质量恒星形成区样本，我们利用 *WISE* H II 区星表和先进的机器学习算法，从 IRAS 星表中筛选H II 区候选体。我们首先从 IRAS 中抽取部分已知H II 区和非H II 区的样本：H II 区样本通过匹配 *WISE* H II 区星表和 IRAS 星表获得；非H II 区样本通过从 IRAS 星表中选取高银纬的源来构建。利用监督式机器学习中的 SVM 算法，我们在双色图上确定H II 区和非H II 区的分割线，也就是H II 区候选体选择判据。我们得到的最优判据的不等式形式为 $\log(F_{60}/F_{12}) \geqslant (-0.30 \times \log(F_{100}/F_{25}) + 1.53)$，另外我们要求源在 60 μm 和 100 μm 波段有信号。利用这个判据，我们从 IRAS 星表中选出 2962 个H II 区，并得出银河系内总的H II 区数目的下限为 9900。

银河系中心附近的分子云的物理性质和环境跟银盘上的分子云有较大差别，所以是检验恒星形成理论的良好场所。但是，银心附近分子云的三维结构长期处于模糊状态，限制了银心分子云的价值。为了理清银河系中心分子云的三维结构，我们提出了一个可以精确计算 OH 基态柱密度、激发温度和光深的方法。利用 CfA1.2 米望远镜观测的 CO 发射线和 Parkes 64 米射电望远镜观测的 OH 吸收线，我们推导出了银心分子云的三维结构。计算表明，在银心附近，分子云也有棒旋结构，倾角为 $67.5 \pm 2.1°$。但是，我们的结果受限与数据的空间分辨率。

高银纬分子云观测对研究分子云的形成和演化有重要价值。我们利用青海站 13.7 米望远镜观测了大熊座分子云的三条 CO 同位素谱线，^{12}CO ($J = 1 \rightarrow 0$)、^{13}CO ($J = 1 \rightarrow 0$) 和 C^{18}O ($J = 1 \rightarrow 0$)。C^{18}O ($J = 1 \rightarrow 0$) 辐射低于青海站望远镜的探测灵敏度，而 ^{12}CO ($J = 1 \rightarrow 0$) 和 ^{13}CO ($J = 1 \rightarrow 0$) 则显示了高银纬弥散分子云的众多细节。我们发现，基于高银纬弥散分子云，在更完备的分子核统计样

本上，分子核质量函数 (CMF) 的形状仍然跟初始质量函数 (IMF) 形状类似。

关键词：分子云，分子核，分子团块，大质量恒星形成，银河系中心，红外 Bubble，外向分子流，星际介质，分子谱线，H II 区，高银纬，大熊座分子云，CO，OH，IRAS

ABSTRACT

We present a study of the molecular clouds and star formation in the Milky Way. This PhD thesis is composed of four parts, with respect to three typical regions: the Galactic plane, the Galactic Centre, and high Galactic latitudes.

In the first part, we investigated H II regions and star formation processes around them. We performed observations of 13 galactic infrared bubble fields containing 18 bubbles. Five molecular lines, ^{12}CO ($J = 1 \rightarrow 0$), ^{13}CO ($J = 1 \rightarrow 0$), C^{18}O ($J = 1 \rightarrow 0$), HCN ($J = 1 \rightarrow 0$), and HCO$^+$ ($J = 1 \rightarrow 0$), were observed, and several publicly available surveys, GLIMPSE, MIPSGAL, ATLASGAL, BGPS, VGPS, MAGPIS, and NVSS, were used for comparison. We find that these bubbles are generally connected with molecular clouds, most of which are giant. Several bubble regions display velocity gradients and broad shifted profiles, which could be due to the expansion of bubbles. The masses of molecular clouds within bubbles range from 100 to 19,000 $M_{\odot}$, and their dynamic ages are about 0.3-3.7 Myr, which takes into account the internal turbulence pressure of surrounding molecular clouds. Clumps are found in the vicinity of all 18 bubbles, and molecular clouds near four of these bubbles with larger angular sizes show shell-like morphologies, indicating that either collect-and-collapse or radiation-driven implosion processes may have occurred. Due to the contamination of adjacent molecular clouds, only six bubble regions are appropriate to search for outflows, and we find that four of them have outflow activities. Three bubbles display ultra-compact H II regions at their borders, and one of them is probably responsible for its outflow. In total, only six bubbles show star formation activities in the vicinity, and we suggest that star formation processes might have been triggered.

In the second part, in order to obtain a more complete census of high-mass star forming regions in the Milky Way, we refined the criteria of selecting H II regions from IRAS sources with a newly produced H II region catalog from *WISE* data. The criteria are defined by the linear decision boundary of two samples: IRAS point sources associated with H II regions, which serve as the H II region sample, and IRAS point sources at high Galactic latitudes, which serve as the non-H II region sample. A machine learning classifier, specifically a support vector machine (SVM), is used to determine the decision boundary. We investigate all combinations of four IRAS bands and suggest that the optimal criterion

is $\log(F_{60}/F_{12}) \geqslant -0.30 \times \log(F_{100}/F_{25}) + 1.53$, with detections at 60 and 100 μm. This identifies 2962 H II region candidates in the Milky Way. We find that IRAS H II region candidates show evidence for evolution on the two-color diagram. Merging the *WISE* H II catalog with IRAS H II regions candidates, we find that the total number of H II regions forming high-mass stars in the Milky Way is approximately 9900.

In the third part, we examined the three-dimensional structure of the molecular clouds in the Galactic Centre (GC) using CO emission and OH absorption lines. Two CO isotopologue lines, ^{12}CO ($J = 1 \rightarrow 0$) and ^{13}CO ($J = 1 \rightarrow 0$), and four OH ground-state transitions, surveyed by the Southern Parkes Large-Area Survey in Hydroxyl (SPLASH), contribute to the study of the GC. We develop a novel method to calculate the OH column density, excitation temperature, and optical depth precisely using all four OH lines and employ it to derive a three-dimensional model for the distribution of molecular clouds in the GC for six slices in Galactic latitude. The angular resolution of the data is 15.5′, which at the distance of the GC (8.34 kpc) is equivalent to 38 pc. We find that the total mass of OH in the GC is in the range 2400-5100 $M_{\odot}$. The face-on view at a Galactic latitude of $b = 0^{\circ}$ displays a bar-like structure with an inclination angle of $67.5 \pm 2.1^{\circ}$ with respect to the line of sight. No ring-like structure in the GC is evident in our data, likely due to the low spatial resolution of the CO and OH maps

In the fourth part, we studied diffuse molecular clouds at high Galactic latitudes , which are valuable to the study of the formation and evolution of molecular clouds. We performed a deep CO survey towards the Ursa Major Clouds, costing ∼1400 hours and covering an area of approximately 27 degree^2. The signal of C^{18}O ($J = 1 \rightarrow 0$) is found below 0.1 K, but ^{12}CO ($J = 1 \rightarrow 0$) and ^{13}CO ($J = 1 \rightarrow 0$) have revealed many details of the diffuse molecular clouds at high Galactic latitudes. Under a more complete census, we found that the shape of the core mass function (CMF) in the Ursa Major Clouds resembles the shape of the IMF.

Key Words: molecular clouds, molecular cores, molecular clumps, high-mass star formation, the central melecular zone, infrared bubbles, molecular outflow, ISM, molecular lines, H II region, high galactic latitudes, the Ursa Major Clouds, CO, OH, IRAS

目　录

摘　要 ..... **vii**

ABSTRACT ..... **ix**

目　录 ..... **xi**

图形列表 ..... **xvii**

表格列表 ..... **xxi**

符号列表 ..... **xxiii**

第一章　引言 **1**

1.1　恒星 2

1.1.1　恒星的结构 3

1.1.2　恒星的形成 4

1.2　星际介质 5

1.2.1　分子云 6

1.2.1.1　分子云的物理和化学性质 8

1.2.1.2　分子云纤维结构 10

1.2.2　H II 区 11

第二章　大质量恒星触发恒星形成 **13**

2.1　红外 Bubble 15

2.2　观测和数据处理 19

2.2.1　德令哈 CO 观测 20

2.3　红外 Bubble 的分子谱线 21

2.3.1　红外 Bubble 分子云的物理性质 21

2.3.2　分子团块 25

2.3.3　H II区的膨胀 28

2.3.4　13 个红外 Bubble 天区 28

2.3.4.1　N4 28

2.3.4.2 N14 ····· 32
2.3.4.3 N37 ····· 33
2.3.4.4 N44 ····· 35
2.3.4.5 N49 ····· 36
2.3.4.6 N55 ····· 40
2.3.4.7 N75 和 N74 ····· 43
2.3.4.8 N82 ····· 46
2.3.4.9 N89 和 N90 ····· 48
2.3.4.10 N95 ····· 50
2.3.4.11 N105 ····· 52
2.3.4.12 N123 ····· 53
2.3.4.13 N133 ····· 55
2.4 外向分子流 ····· 56
2.4.1 外向分子流 N14 ····· 59
2.4.2 外向分子流 N55 ····· 61
2.4.3 外向分子流 N105 ····· 62
2.4.4 外向分子流 N133 ····· 63
2.5 红外 Bubble 结果分析 ····· 63
2.5.1 分子云和分子团块 ····· 63
2.5.2 外向分子流和恒星形成 ····· 64
2.5.3 跟其他红外 Bubble 的研究比较 ····· 65
2.6 红外 Bubble 研究总结 ····· 65

第三章 新的H II 区候选体判据 ····· 67

3.1 数据分析 ····· 69
3.1.1 星表 ····· 69
3.1.2 支持向量机 ····· 70
3.1.3 确定H II 区候选体判据 ····· 71
3.1.4 SVM 算法和 LDA 算法对比 ····· 77
3.2 IRAS 星表中的H II 区 ····· 77
3.2.1 H II 区分布 ····· 77

3.2.2 银河系H II 区总数 ····· 79
3.2.3 H II 区在双色图上的演化。 ····· 79
3.3 IRAS H II 区候选体讨论 ····· 80
3.3.1 行星状星云 ····· 80
3.3.2 H II 区的演化 ····· 81
3.3.3 跟 WC89 和 HM89 结果比较 ····· 81
3.4 IARS H II 区判据研究总结 ····· 81

第四章 银河系中心的分子云 ····· **83**
4.1 OH 分子谱线 ····· 84
4.1.1 OH 分子 ····· 84
4.1.2 OH 谱线巡天 ····· 85
4.1.2.1 OH 主线观测 ····· 85
4.1.2.2 OH 次线观测 ····· 88
4.2 CMZ ····· 88
4.2.1 气体和尘埃的温度 ····· 90
4.2.2 湍动 ····· 91
4.2.3 Mopra 观测 ····· 93
4.2.4 三维模型 ····· 93
4.2.5 恒星形成 ····· 94
4.3 数据观测和处理 ····· 95
4.3.1 CO 数据 ····· 95
4.3.2 OH 数据 ····· 96
4.3.3 连续谱 ····· 98
4.4 计算模型和假设 ····· 98
4.5 解算 OH 激发温度 ····· 100
4.5.1 背景连续谱稳定已知 ····· 100
4.5.2 解算 CMZ ····· 103
4.5.3 方程组形式 ····· 105
4.5.4 数值求解方程组 ····· 107
4.6 银心分子云的三维结构 ····· 108

4.6.1 连续谱高斯拟合 ····· 108
4.6.2 CO 和 OH 柱密度比 ····· 110
4.6.3 OH 主线激发温度相等假设 ····· 111
4.6.4 模型检验 ····· 111
4.6.5 CMZ 分子三维结构 ····· 115
4.7 CMZ 分子云三维结构分析 ····· 119
4.7.1 OH 分子基态激发温度 ····· 119
4.7.2 低分辨率影响 ····· 121
4.7.3 连续谱辐射超出 ····· 122
4.7.4 跟其他模型的比较 ····· 122
4.8 CMZ 分子云三维结构总结 ····· 125

第五章 大熊座分子云 CO 巡天 ····· 127
5.1 大熊座分子云 ····· 129
5.2 数据观测和处理 ····· 129
5.3 大熊座分子云 CO 观测结果和初步分析 ····· 132
5.3.1 ^{12}CO 和 ^{13}CO 积分强度分布 ····· 132
5.3.2 H I、^{12}CO、IRAS 100 μm 分布对比 ····· 133
5.3.3 分子核 ····· 133
5.3.4 分子核质量函数 ····· 133
5.4 大熊座分子云 CO 观测总结 ····· 137

第六章 研究总结与展望 ····· 139

附录 A Summary in English ····· 141
A.1 Triggered Star Formation ····· 141
A.1.1 Scenarios of Triggered Star Formation ····· 141
A.1.2 Observations of five molecular lines ····· 143
A.1.3 Molecular Clouds Near H II Regions ····· 144
A.1.4 Summary of Infrared Bubble Research ····· 146
A.2 New Criteria For H II Regions ····· 147
A.2.1 High-mass Stars and H II Regions ····· 147

A.2.2 Determining the Criteria 149
A.2.3 The properties of H II Regions in IRAS PSC 152
A.2.4 Summary of the H II Region Research 155
A.3 The Galactic Centre 155
A.3.1 The CMZ 156
A.3.2 CO and OH observations 157
A.3.3 The Model 158
A.3.4 Solving OH Column Densities 160
A.3.5 The distribution of the molecular clouds in the GC 161
A.3.6 Summary of our work on the GC 162
A.4 The Ursa Major Clouds 163
A.4.1 Observations 164
A.4.2 Preliminary Results 164
A.5 Summary 165

参考文献 167

作者简历 191

致 谢 193

图形列表

1.1 银河系 360° 全景图 ····· 2
1.2 太阳内部结构示意图 ····· 3
1.3 中小质量恒星形成的四个阶段 ····· 5
1.4 大质量恒星形成区外流示例 ····· 6
1.5 原子气体和分子气体跟恒星形成率面密度的关系 ····· 7
1.6 银河系 CO 巡天 ····· 8
1.7 金牛座分子云 ^{12}CO 观测 ····· 10
1.8 礁湖星云光学波段观测 ····· 12

2.1 分子云堆积并塌缩模型示意图 ····· 13
2.2 四种不同的触发恒星形成过程示意图 ····· 14
2.3 红外 Bubble S1 和 S7 的 8 μm 图像 ····· 16
2.4 红外 Bubble 在 8 μm、24 μm 和 20 cm 波段的辐射分布 ····· 17
2.5 18 个红外 Bubble 的平均分子谱线 ····· 22
2.6 红外 Bubble 区域 ^{12}CO ($J = 1 \rightarrow 0$) 的平均速度分布 ····· 27
2.7 红外 Bubble N4 图像 ····· 29
2.8 红外 Bubble N4 ^{13}CO 谱线速度通道图 ····· 30
2.9 红外 Bubble N14 图像 ····· 31
2.10 红外 Bubble N14 ^{13}CO 谱线速度通道图 ····· 32
2.11 红外 Bubble N37 图像 ····· 34
2.12 红外 Bubble N37 ^{13}CO 谱线速度通道图 ····· 35
2.13 红外 Bubble N44 图像 ····· 36
2.14 红外 Bubble N44 ^{13}CO 谱线速度通道图 ····· 37
2.15 红外 Bubble N49 图像 ····· 38
2.16 红外 Bubble N49 ^{13}CO 谱线速度通道图 ····· 39
2.17 红外 Bubble N55 图像 ····· 40
2.18 红外 Bubble N55 ^{13}CO 谱线速度通道图 ····· 41
2.19 红外 Bubble N75 和 N74 图像 ····· 42

2.20 红外 Bubble N75 和 N74 ^{13}CO 谱线速度通道图 ····· 43
2.21 红外 Bubble N82 图像 ····· 44
2.22 红外 Bubble N82 ^{13}CO 谱线速度通道图 ····· 45
2.23 红外 Bubble N89 和 N90 的图像 ····· 46
2.24 红外 Bubble N89 和 N90 ^{13}CO 谱线速度通道图 ····· 47
2.25 红外 Bubble N95 的图像 ····· 48
2.26 红外 Bubble N95 ^{13}CO 谱线速度通道图 ····· 49
2.27 红外 Bubble N105 的图像 ····· 50
2.28 红外 Bubble N105 ^{13}CO 谱线速度通道图 ····· 51
2.29 红外 Bubble N123 的图像 ····· 52
2.30 红外 Bubble N123 ^{13}CO 谱线速度通道图 ····· 53
2.31 红外 Bubble N133 的图像 ····· 54
2.32 红外 Bubble N133 ^{13}CO 谱线速度通道图 ····· 55
2.33 外向分子流 N14 的图像 ····· 59
2.34 外向分子流 N55 的图像 ····· 60
2.35 外向分子流 N105 的图像 ····· 61
2.36 外向分子流 N133 的图像 ····· 62

3.1 六个判据的详细结果 ····· 74
3.2 六个判据的样本点相对于分割线的概率密度分布 ····· 75
3.3 LAD 算法给出的分割线 ····· 76
3.4 3061 个H II 区候选体的全天分布 ····· 78
3.5 H II 区候选体沿银纬和银经的分布 ····· 78
3.6 H II 区在双色图上的演化 ····· 79

4.1 OH 分子基态能级 ····· 85
4.2 CMZ 在 0.87 毫米和 8 μm 波段图像 ····· 89
4.3 CMZ24 μm 波段子区域示意图 ····· 90
4.4 CMZ 尘埃的温度分布 ····· 92
4.5 三维模型计算原理示意图 ····· 99
4.6 SPLASH 先导区域谱线 ····· 102

4.7 检测 ^{12}CO ($J = 1 \rightarrow 0$) 光学厚的区域 ····· 104
4.8 CMZ 连续谱高斯拟合 ····· 109
4.9 确定 OH 柱密度和 CO 亮温度比 ····· 110
4.10 检验 OH 主线激发温度相等假设 ····· 112
4.11 计算参数在 L-V 图上的分布 ····· 113
4.12 模型预测谱线跟观测谱线比较 ····· 114
4.13 CMZ 分子云三维结构——$b = -0.375°$ ····· 116
4.14 CMZ 分子云三维结构——$b = -0.25°$ ····· 117
4.15 CMZ 分子云三维结构——$b = -0.125°$ ····· 117
4.16 CMZ 分子云三维结构——$b = 0°$ ····· 118
4.17 CMZ 分子云三维结构——$b = 0.125°$ ····· 118
4.18 CMZ 分子云三维结构——$b = 0.25°$ ····· 119
4.19 CMZ 分子云正向积分强度图 ····· 120
4.20 OH 主线激发温度分布图 ····· 121
4.21 CMZ 中子区域的位置 ····· 124

5.1 古德带示意图 ····· 128
5.2 大熊座分子云位置图 ····· 128
5.3 大熊座分子云 CfA 1.2 米观测 ····· 129
5.4 大熊座分子云 ^{12}CO 积分强度图 ····· 130
5.5 大熊座分子云 ^{13}CO 积分强度图 ····· 131
5.6 大熊座分子气体、原子气体和尘埃分布图 ····· 132
5.7 大熊座分子核分布 ····· 135
5.8 大熊座分子云 CMF 形式 ····· 136

表格列表

1.1 暗云、分子团块和分子核的定义划分 ····· 9

2.1 18 个红外 Bubble 的物理参数 ····· 18
2.2 一些巡天的参数 ····· 19
2.3 五条分子谱线的观测参数 ····· 20
2.4 红外 Bubble 周围分子云的物理参数 ····· 24
2.5 分子团块的物理参数 ····· 26
2.6 分子外向流物理参数。 ····· 63

3.1 使用的星表的观测参数 ····· 70
3.2 所有可能的 15 个H II 区双色图判据 ····· 73

4.1 最近的 OH 巡天 ····· 86
4.2 最近的一些 CMZ 巡天 ····· 87
4.3 OH 四条基态跃迁的参数 ····· 106
4.4 CMZ 中五个子区域的参数 ····· 123

5.1 Duchamp 证认分子核参数设置 ····· 134

符号列表

公式符号

符号	描述	单位
h	普朗克常数	$6.626 \times 10^{-34}\ \mathrm{m^2 \cdot kg \cdot s^{-1}}$
k	玻尔兹曼常数	$1.38 \times 10^{-23}\ \mathrm{m^2 \cdot kg \cdot s^2 \cdot K^{-1}}$
A_{ul}	爱因斯坦 A 系数	$\mathrm{s^{-1}}$
g_{u}	上能级统计权重	
g_{l}	下能级统计权重	
N_{u}	上能级柱密度	
N_{l}	下能级柱密度	

缩写

缩写名	全称
20MC	the 20 km $\mathrm{s^{-1}}$ molecular cloud
50MC	the 50 km $\mathrm{s^{-1}}$ molecular cloud
APEX	the Atacama Pathfinder Experiment
ASKAP	the Australian Square Kilometre Array Pathfinder telescope
ATCA	the Australia Telescope Compact Array
ATNF	the Australia Telescope National Facility
BGPS	the Bolocam Galactic Plane Survey
CfA	the Harvard-Smithsonian Center for Astrophysics
CMB	the Cosmic Microwave Background
CMF	the core mass function
CMZ	the Central Molecular Zone
CSO	Caltech Submillimeter Observatory，加州理工学院亚毫米天文台
EGOs	Extended Green Objects
ESO	European Southern Observatory，欧南天文台

FITS	Flexible Image Transport System
FN	false negatives
GBT	Green Bank Telescope
GLIMPSE	the Galactic Legacy Infrared Mid-Plane Survey Extraordinaire
GRS	the Galactic Ring Survey
HIPASS	the HI Parkes All-Sky Survey
HOPS	H_2O southern Galactic Plane Survey
IGM	the intergalactic medium，星系际介质
IMF	the initial mass function，初始质量函数
IRAS	the Infrared Astronomical Satellite
JVLA	the Karl G. Jansky Very Large Array
LDA	linear discriminant analysis，线性判别分析
LVG	the Large Velocity Gradient，大速度梯度
MAGPIS	the Multi-Array Galactic Plane Imaging Survey
MGPS-2	the second epoch Molonglo Galactic Plane Survey
MIPSGAL	the Multiband Infrared Photometer for *Spitzer* Galactic Plane Survey
NRAO	National Radio Astronomy Observatory，美国国家天文台
NVSS	the NRAO VLA Sky Survey
PCA	principal component analysis，主成分分析
PSC	Point Source Catalog，点源星表
SCUBA	the Submillimeter Common-User Bolometer Array
SED	spectral energy distribution
SPLASH	the Southern Parkes Large-Area Survey in Hydroxyl
SUMSS	the Sydney University Molonglo Sky Survey
SVM	support vector machine，支持向量机
TP	true positives
UC	ultracompact
VLBI	very long baseline interferometry
WISE	*Wide-field Infrared Survey Explorer*
YSOs	Young Stellar Objects，初期恒星体

第一章　引言

飞流直下三千尺，疑是银河落九天。

— 李白

李白的诗虽然意在赞美瀑布，但是九天之上的银河自然是比瀑布更蔚为壮观。在远离城市灯光的郊区，如恰逢新月且万里无云，天空中最亮丽的风景莫过于一条由无数恒星描绘的恒星带——银河。恒星对于天文学而言，就如同银河衍生的神话传说对于人类文化一样，意义深远。作为浩瀚宇宙的重要组成成分，恒星也是天文学研究主要的对象和工具。从搭建宇宙距离阶梯的变星和超新星，到描绘星系旋臂结构的大质量恒星，再到酝酿生命的小质量恒星，恒星一直是我们认识和研究宇宙极其重要的窗口。

威廉·赫歇尔 (F. W. Herschel) 在用他自制的望远镜观测天空的时候，发现有一些天区没有恒星，还有一些天区的恒星的数目比其他区域少很多 (例如图1.1中心区域附近的黑色暗带)。然而赫歇尔并没有意识到导致恒星数目偏少的源头正是恒星形成的场所——分子云。分子云是星际介质的主要组成部分，其主要成分是氢分子和尘埃。分子云的尘埃体密度虽然很低，但是分子云巨大的体积产生的累积效应，足以让尘埃遮挡其背后的星光，形成赫歇尔观测到的空洞。除了氢分子，分子云中还存有很多其他分子，例如一氧化碳 (CO)、福尔马林 (H_2CO) 和水分子 (H_2O) 等。不同的分子存在的物理和化学环境亦有差别，所以分子云中的分子可以提供分子云物理和化学性质信息。因此，恒星形成的研究在很大程度上基于分子云的观测，主要的观测窗口是分子谱线和尘埃连续谱。

尽管恒星在天文学研究中占据重要位置，恒星的形成与演化仍然有很多问题处于争论状态。例如在恒星形成的过程中，大质量恒星在到达主序之前就已经开始进行氢燃烧，在这种情况下，大质量恒星是如何克服强大的辐射压力继续累积质量的呢？目前主流的看法有两种：一种认为大质量恒星跟小质量恒星一样，都是通过吸积盘逐渐累积质量的；另外一种看法认为，由于大质量恒星一般处于星团之中，大质量恒星可能是通过中小质量并和产生的。另外一个悬而未决的问题是，大质量恒星在演化过程中产生的星风，是把周围的星际介质吹散并降低恒星形成效率，还是压缩周围气体并触发下一代的恒星形成？这些问题的解决需要高灵敏度和高分辨率的观测。

本篇论文主要研究银河系中的分子云和其中的恒星形成过程。我们对银河系中三个代表性的区域的一小部分天区进行了分子谱线观测，它们分别位于银盘，银

图 1.1: 银河系 360° 全景图。**版权：ESO**。

Figure 1.1. The 360° panoramic image of the Milky Way. **Image courtesy of ESO.**

心和高银纬区域。这个三个区域截然不同的分子云性质和及其伴随的恒星形成过程可以让我们更全面的认识分子云的性质对恒星形成的影响。

这一章主要介绍对理解本篇论文必需的一些关于恒星和分子云的基本知识，并在最后简要介绍整篇论文的结构。

1.1 恒星

恒星是一类由等离子体构成，并且靠自身引力聚合成球形的发光天体。银河系中恒星的总数目大约为 $1-4\times10^{11}$，其中肉眼可见的大约为 6000 个。在古代，由于天空没有光污染和大气污染，恒星的观测非常容易，所以恒星有非常悠久的观测历史。

不论是在中国还是西方社会，关于恒星的神话传说皆深植于人类的文明史。仅从中国对恒星的命名就可以看出古人对恒星的研究是极为细致和执着的。他们给每一个恒星命名，例如其中较系统的命名系统有二十八星宿，还有一些根据传说命名的恒星，例如织女星 (天琴座 α) 和牛郎星 (天鹰座 α)。中国古人把天空中最亮的星命名为天狼星 (大犬座 α)，虽然天狼星最亮，古人却认为天狼星是一个颗恶星。

中国有二十八星宿，西方有黄道十二宫，也就是我们所说的十二星座。黄道十二宫虽然起源于占星术，但是现代天文文献依然采用这种星座记法。银心方向属于人马座 (又称射手座，Sagittarius)，所以银心区域很多源的名字都以 Sgr 开头，例如银河系中心的大质量黑洞被命名为 Sgr A*。

本节主要介绍恒星结构及其形成过程。关于天文学史的记载，读者可以参考相关文献，本论文不做进一步阐述。

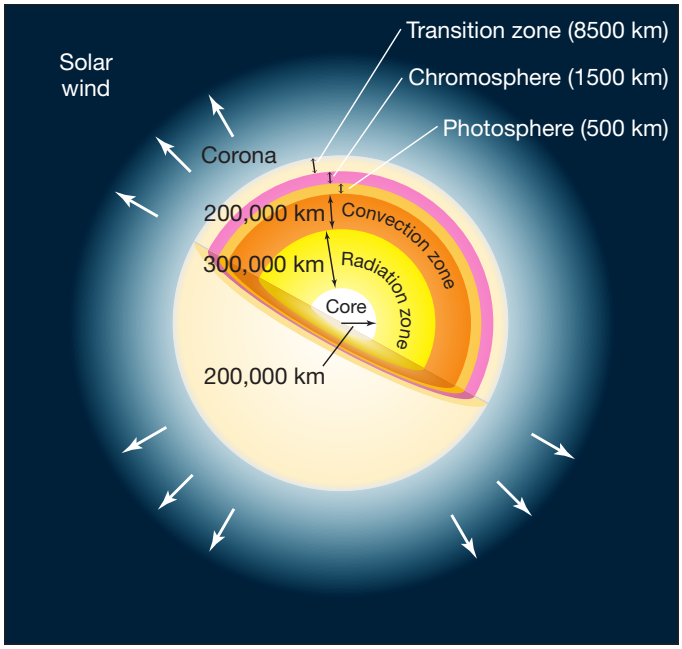

图 1.2: 太阳内部结构示意图 (Chaisson et al., 2005)。

Figure 1.2. The inner structure of the Sun (Chaisson et al., 2005).

1.1.1 恒星的结构

恒星的主要成分是氢和氦：大约 70% 的质量是氢元素，大约 25%-30% 的质量是氦元素。除了氢和氦之外，还有一些重元素，例如氧、碳和氮。

星际介质经过塌缩，将自身引力势能转化为热能，直到把自身内部的氢点燃 (核聚变)，形成恒星。进入主序之后，恒星的演化进入稳定期，此时恒星处于动力学平衡状态——主要是辐射、热运动和引力之间处于平衡，这三者的平衡决定了恒星的结构和演化过程。恒星的结构会随着质量和年龄变化，本节主要介绍恒星在主序时期的结构。恒星主序后的结构变化请读者参考关于恒星演化的文献，本论文不做进一步阐述。

首先，我们来看小质量恒星的结构。作为小质量恒星的典型代表，一个质量小于 $0.35M_{\odot}$ 的恒星 (红矮星)，会处于完全对流状态 (Reiners et al., 2009)，其内部的核燃烧形式主要是质子-质子链反应。由于这些小质量恒星内部的核反应率很低，其内部的温度也很低。低的温度导致了其内部的密度比较大，造成了不透明度 (光

深) 也很大，因此辐射传输率很低。低辐射传输率产生的温度梯度使得这些小质量恒星出现整体的对流。

其次，我们来看具有典型质量恒星的结构。典型太阳质量的恒星 ($0.35M_{\odot} < M < 1.5M_{\odot}$) 内部的核燃烧形式也主要是质子-质子链反应。质子-质子链核反应产生的温度梯度在中小质量恒星内部不足以形成对流，所以这类恒星在内部有一个辐射占主导的辐射区。如所示意图1.2所示，一个典型的类太阳质量的恒星内部从聚变反应核心 (Core) 往外，依次是辐射区 (Radiation zone)、对流区 (Convection zone)、光球层 (Photosphere)、色球层 (Chromosphere)、过渡层 (Transition zone) 和日冕层 (Solar wind)。其中，光球层是太阳可见部分的表面。

最后，我们来看质量比较大的恒星的结构。大质量恒星 ($M > 1.5M_{\odot}$) 内部的氢燃烧形式主要是碳氮氧循环 (CNO cycle)。因为碳氮氧循环反应需要得温度比质子-质子链反应高，所以碳氮氧循环具有更高的能量输出率。由此产生的大的温度梯度，使得大质量恒星内部大部分区域都以对流形式传输能量 (包括核心区域)。在大质量恒星的外围，温度梯度降低，所以仍然有一个辐射占主导的表层。

1.1.2 恒星的形成

恒星形成是星系中最基本的活动之一，研究证实，恒星诞生于分子云 (molecular clouds) 中。由于分子云中的尘埃在光学波段的消光作用，恒星形成区在光学波段不可见，需要长波段的观测。所以，恒星形成的研究一直到射电和红外天文技术有了长足的进步后，才比较大的进展。

总的来说，由于自身引力或者外部作用，分子云中的部分气体和尘埃在克服分子云自身内部的湍动 (turbulence)、磁场 (magnetic field) 和热压力 (thermal pressure) 后，塌缩并形成恒星。中小质量恒星的形成过程比较简单，但是大质量恒星形成过程中的很多问题依然处于争论状态。

小质量恒星的形成过程主要有四个阶段 (Shu et al., 1987)。如图1.3所示，在第一个阶段，由于双极扩散 (ambipolar diffusion)，分子云中的磁场和湍动支撑被转移，分子核开始形成。在第二阶段，原恒星形成，与此同时，由于分子云的塌缩，吸积盘开始形成。在第三阶段，由于强烈的星风，在吸积盘的旋转轴方向上会出现双极外流 (bipolar ouflow) 现象。在第四阶段，吸积停止，恒星诞生。

不同于中小质量恒星的形成，大质量恒星的形成的研究存在很多困难。从观测上讲，大质量恒星的演化时标短 (可供观测样本少)，而且大部分距离太阳很远 (需要高分辨率)。从理论上讲，由于大质量恒星在吸积阶段就已经点燃氢，强烈的辐射压可能会导致吸积反转，造成质量累积停止，所以解释大质量恒星的持续吸积，

存在困难。

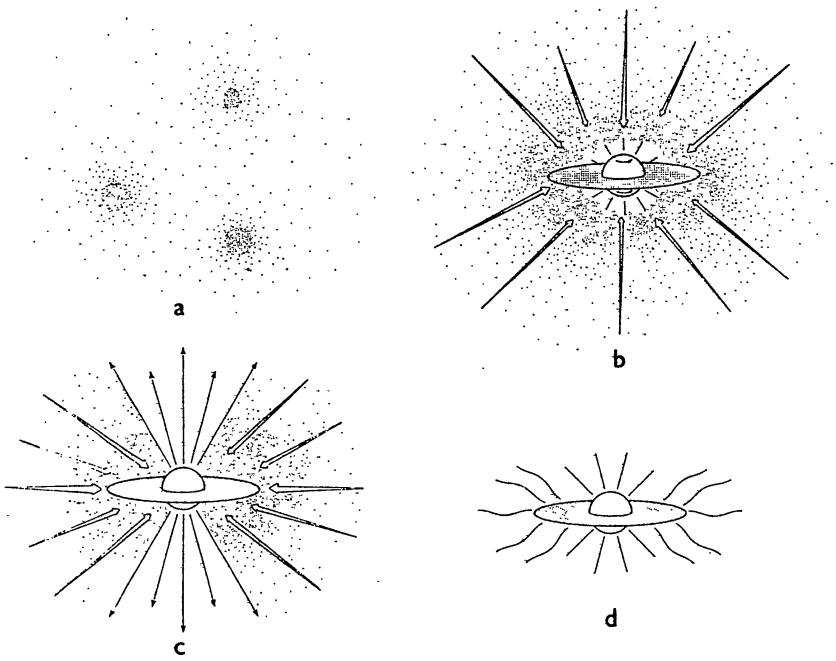

图 1.3: 中小质量恒星形成的四个阶段 (Shu et al., 1987)。a) 分子核形成阶段。b) 吸积盘形成阶段。c) 双极外流形成阶段。d) 恒星诞生，进入主序。

Figure 1.3. Four stages of low-mass star formation (Shu et al., 1987). a) Molecular cores form. b) Acceration disks form. c) Bipolar outflows form. d) Stars enter the main sequence.

最近 Li et al. (2016) 研究了 100 大质量恒星区的外流，他们发现 73% 的大质量恒星区跟外流成协，倾向于支持第二种观点。图1.4展示Li et al. (2016) 证认的一个大质量恒星形成区的外流。不论是从理论上还是观测上来讲，大质量恒星形成仍然是天文学领域的热点问题。

1.2 星际介质

星际介质 (Interstellar Medium) 是指恒星之间的物质，包括等离子体、尘埃、原子气体、分子气体、电磁辐射、磁场和宇宙射线。根据银河系内的研究，星际介质包含的主要元素是氢，其次是氦，氦只占氢元素数目 (非质量) 的 10% 左右 (Herbst, 1995)。一些重元素 (除了氢和氦之外的元素)，例如碳、氮和氧相对于氢的丰度比 (按数目) 分别为 4×10^{-4}、9×10^{-5} 和 7×10^{-4} (Herbst, 1995)。星际介质中以气体

形式存在的物质约占星际介质总质量的 99%，尘埃约占 1% 。按质量来说，这些气体中氢占 70%，氦占 28%，还有大约 1.5% 是其他重元素。星际介质的密度和温度跨度范围都很大。如图1.5所示，恒星形成率的分布跟分子气体的分布一致，所以恒星主要形成于分子云中。在本论文中，我们只简要回顾一下分子云的一些性质。

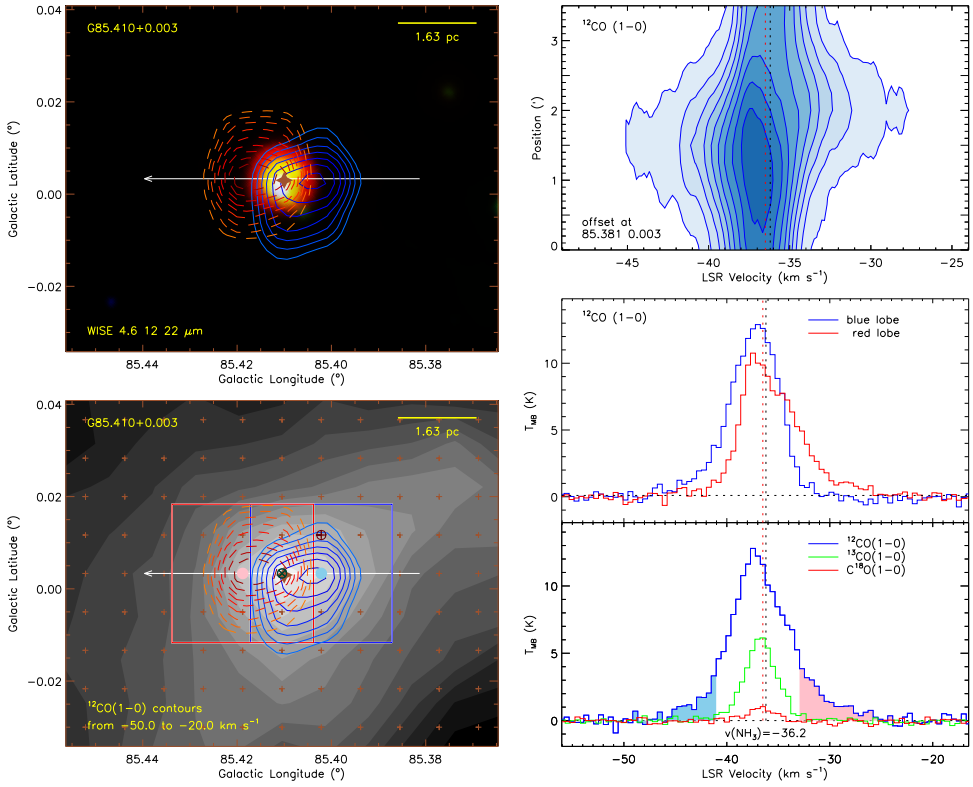

图 1.4: Li et al. (2016) 证认的一个大质量恒星形成区的外流。

Figure 1.4. A moelcular outflow (Li et al., 2016) in a high-mass star-forming region.

1.2.1 分子云

分子云的主要成分是分子气体和尘埃，是星际介质中最冷和最致密的成分，也是恒星诞生的地方 (Bergin et al., 2007; Fukui et al., 2010; Snow et al., 2006)。分子云气体的主要组成部分是分子氢 (H_2)、一氧化碳 (CO) 和其他一些比较复杂的有机和无机分子。虽然分子氢是分子云中的主要成分，但由于其质量小并且是对称的双原子分子 (没有永久偶极距)，氢分子基态的激发需要比较高的温度，而且分子云的温度一般比较低 (小于 100K)，所以分子氢在射电和红外波段不可见——至少对银河系内的分子云来说。

一般情况下，我们用 CO 分子作为氢分子的示踪分子，所以关于分子云和恒星形成的研究工作，有很大一部分是用 CO 分子完成的。CO 分子示踪的分子云的典

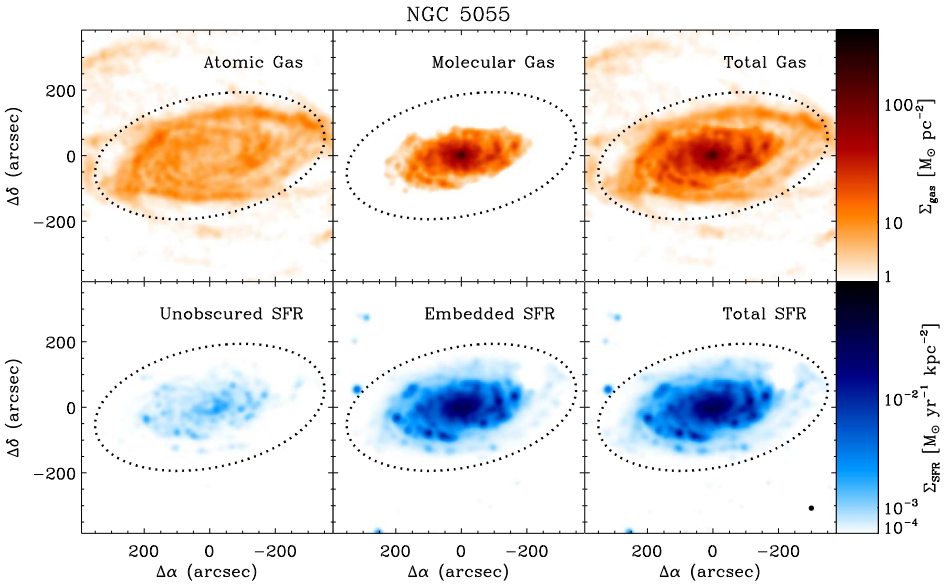

图 1.5: 星系 NGC5055 (M63) 中原子气体和分子气体跟恒星形成率面密度的关系 (Leroy et al., 2008)。

Figure 1.5. The relationship between atomic and molecular gas and the surface density of star formation rate towards NGC5055 (M63) (Leroy et al., 2008).

型温度和临界密度 (^{12}CO ($J = 1 \rightarrow 0$)) 分别为 10 K 和 10^3 cm^{-3} (Evans, 1999)。由于较低的激发温度和临界密度，CO 分子很容易被激发，并且其低转动能级跃迁的波长在毫米和亚毫米波段，此波段非常适合用地面望远镜观测 (Heyer et al., 2015)。除了分子谱线观测，分子云中的尘埃的热连续谱辐射可以在远红外波段被探测到，所以分子谱线和红外辐射是研究分子云和恒星形成的重要工具。

自从星际介质中探测到有 CO 分子 (Wilson et al., 1970) 以来，CO 谱线在分子云、恒星形成和银河系结构中一直起着重要作用。最近，Heyer et al. (2015) 在对分子云研究的综述中，回顾了以前的一些 CO 巡天，其中Dame et al. (2001) 的 CO 银道面巡天是迄今覆盖银河系面积最广的巡天。Dame et al. (2001) 利用 CfA (the Harvard-Smithsonian Center for Astrophysics) 1.2 米望远镜进行的 CO 巡天覆盖整个银道面和部分高银纬区域，空间分辨率为 0.125°，总共获取 488000 条谱线。

他们给出的 CO 在银河系内的分布如图1.6所示。他们发现由 CO 积分强度计算 H_2 柱密度的转换因子 $X \equiv N_{H_2}/W_{CO}$ 在银河系不同区域有一定变化，其平均值约为 1.8×10^{20} cm^{-2} K^{-1} km^{-1}，对 $|b| > 5°$ 的区域，X 因子略大。他们还发现由远红外辐射导出的总的气体柱密度跟 CO 辐射十分吻合，说明远红外辐射也可以很好地示踪分子云。此 CO 巡天揭示的银河系整体的运动和 CO 分子分布为以后分子云和恒星形成的研究及后续巡天的开展奠定了观测基础。

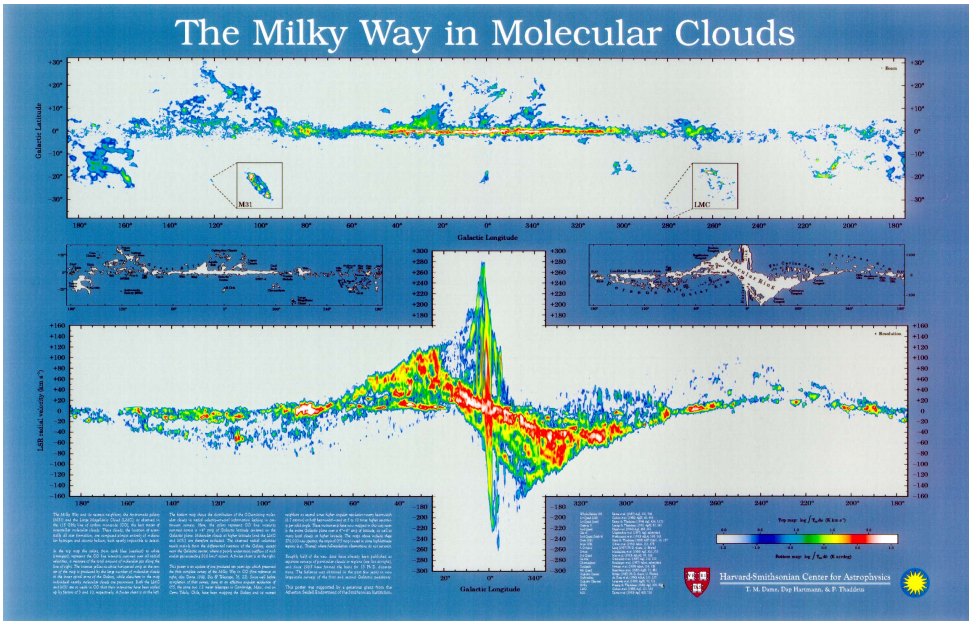

图 1.6: 银河系 CO 巡天 (Dame et al., 2001)。上图是银河系 CO 辐射积分强度图，下图是银河系分子云沿银经的速度分布图 (L-V diagram)。**版权：CfA**。

Figure 1.6. A complete CO survey of the Milky Way (Dame et al., 2001). The upper panel displays the distribution of the integral intensity of CO, while the lower panel illustrates the distirbution of molecular clouds in the Longitude-Velocity (L-V) diagram. **Image courtesy of CfA.**

随着红外天文技术的发展，一些高灵敏度和高分辨率的红外巡天正逐步引领分子云和恒星形成的研究，例如 *Spitzer*、*WISE* 和 *Herschel* 巡天等。尽管这些红外巡天缺乏视向速度信息，但是他们对分子云和恒星形成研究的推动依然十分可观。例如利用内银河的 24 和 70 μm 巡天 (the 24 and 70 Micron Survey of the Inner Galactic Disk with MIPS, MIPSGAL) 和 Hα 谱线观测，我们可以更好的估计恒星形成率 (star formation rate) (Calzetti et al., 2010; Kennicutt et al., 2007)。

恒星形成的研究和进展跟分子云的研究密不可分。但是分子云本身的一些形成和演化问题还没有研究透彻。在下面两小节，我们简要回顾一下分子云的物理、化学和结构性质。

1.2.1.1 分子云的物理和化学性质

分子云是星际介质中最致密的成份，占总星际介质体积不到 1%，其典型的温度和数密度范围分别为 10-20 K 和 $10^2 - 10^6 \mathrm{cm}^{-3}$。由于光学波段星际消光严重，分子云的观测一般采用射电和红外观测窗口。

表 1.1: 暗云、分子团块和分子核的物理性质 (Bergin et al., 2007)。

Table 1.1. Properties of Dark Clouds, Clumps, and Cores (Bergin et al., 2007).

	Clouds	Clumps	Cores
Mass ($M_\odot$)	10^3–10^4	50–500	0.5–5
Size (pc)	2–15	0.3–3	0.03–0.2
Mean density (cm^{-3})	50–500	10^3–10^4	10^4–10^5
Velocity extent (km s^{-1})	2–5	0.3–3	0.1–0.3
Crossing time (Myr)	2–4	≈ 1	0.5–1
Gas temperature (K)	≈ 10	10–20	8–12
Examples	Taurus, Oph, Musca	B213, L1709	L1544, L1498, B68

Bergin et al. (2007) 对分子暗云的研究进行了综述并澄清了关于分子团块和分子核的一些概念，如表1.1所示。分子云 (molecular clouds) 的典型尺度和质量范围分别为 $2-15$ pc 和 $50-500\ M_\odot$，而分子团块 (molecular clumps) 的典型尺度和质量范围分别为 $0.3-3$ pc 和 $0.5-5\ M_\odot$。作为分子云中最致密的成分，分子核 (molecular cores) 的典型尺度和质量分别为 $0.03-0.2$ pc 和 $0.5-5\ M_\odot$。

有些分子云的体积和质量都很大，这类分子云被称为巨分子云 (Giant Molecualr Clouds, GMCs)。巨分子云是银河系内体积最大的天体之一，并且结构十分复杂，其典型尺度和质量分别为 $5-200$ pc (Murray, 2011) 和 $10^5 M_\odot$ (Murray, 2011)。大质量恒星一般诞生于巨分子云中。

分子云内部的湍动可能会主导分子云的一些物理和化学性质。分子云内部湍动的证据之一是Larson (1981) 发现的拉松关系 (Larson's laws)，他们发现分子云内部的速度弥散 (σ)、分子云尺度 (L) 和分子云质量 (M) 之间有很好的相关性，跟柯尔莫夫定律 (Kolmogorov's law) 一致，说明分子云内部是湍动主导的。他们给出分子云内部速度弥散和尺度的关系为 $\sigma \propto L^{0.38}$。近年来有研究证据表明，分子云内部的湍动跟初始质量函数 (initial mass fucntion, IMF) 很可能有内在的联系。

分子云的化学演化还处于研究的初级阶段。因为分子云内部的温度、密度和压强都很低，所以分子云的一些化学性质跟地球上气体的化学性质有较大差别。分子云中一些典型的分子有 H_2、CO、NH_3、HCO^+ 和 HCN。一些研究表明，分子云中的尘埃对分子云的化学演化有重要影响。关于分子云的化学性质的综述见Herbst (1995)。

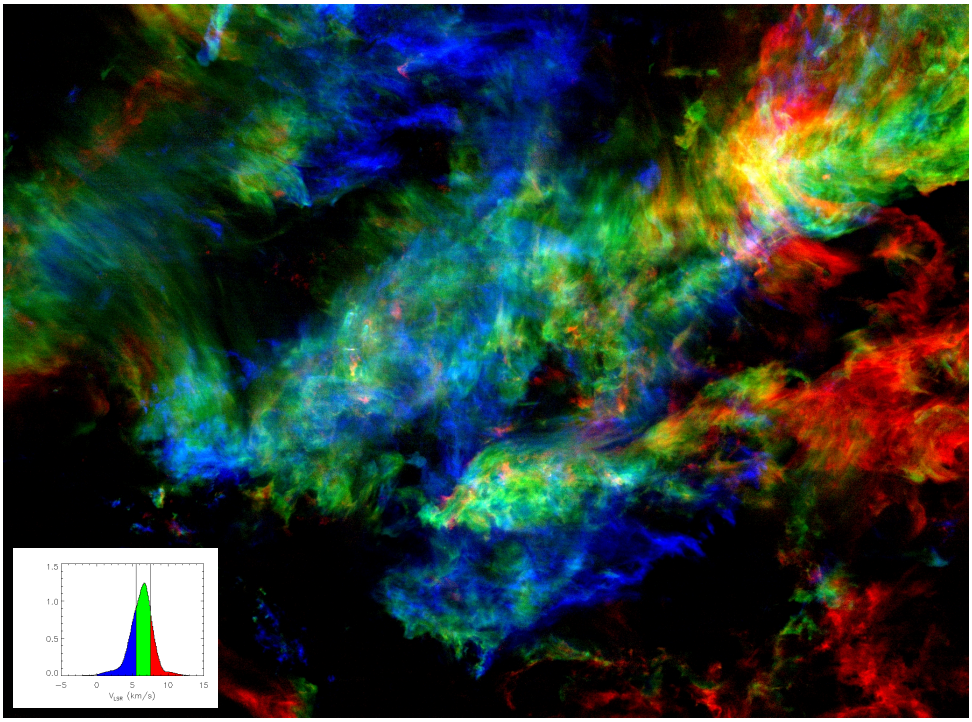

图 1.7: 金牛座分子云 ^{12}CO ($J = 1 \rightarrow 0$) 观测 (Narayanan et al., 2008)，使用位于 FCRAO (the Five College Radio Astronomy Observatory) 的 14 米毫米波射电望远镜。**图片版权：Mark Krumholz (PPVI)。**

Figure 1.7. A ^{12}CO ($J = 1 \rightarrow 0$) survey of the Taurus Molecular Cloud with the Five College Radio Astronomy Observatory (FCRAO) 14 m millimeter-wavelength radio telescope (Narayanan et al., 2008). **Image courtesy of Mark Krumholz (PPVI).**

1.2.1.2 分子云纤维结构

纤维结构 (filaments) 是分子云中比较明显的子结构 (André et al., 2010; Arzoumanian et al., 2011; Molinari et al., 2010a; Schneider et al., 2012)。分子云中的纤维结构是分子云中比较致密且狭长部分。不论分子云中是否有恒星形成活动，分子云都倾向于形成纤维结构。有研究表明，纤维结构可能是分子云发生自引力塌缩的地方。

André et al. (2010) 根据 *Herschel* 对古德带 (Gould Belt Survey, GBS) 的观测，提出纤维结构很可能是由湍动产生的，分子云中的分子团块和分子核形成于纤维结构中。一些研究表明，磁场在纤维结构的形成过程中起着重要作用 (Padoan et al., 2011)。

因为纤维结构很可能会跟初始质量函数有密切关系，所以纤维结构是目前恒星形成研究的热点问题。Hacar et al. (2013) 观测了 L1495/B213 天区的三条分子谱

线——$C^{18}O$ ($J = 1 \rightarrow 0$)、N_2H^+ ($1 - 0$) 和 SO ($J_N = 3_2 - 2_1$)，他们证认出 35 个纤维结构。这些纤维结构的典型长度为 0.5 pc，他们认为这些纤维结构有层次结构。首先，分子云碎裂为大小为 1pc 尺度左右的小块；然后，这些小块进一步碎裂为纤维结构；最后纤维结构自引力塌缩，形成分子核。Battersby et al. (2014) 利用 JVLA (the Karl G. Jansky Very Large Array) 观测了 G32.02+0.06 天区的氨分子辐射，他们观测的空间分辨率达 0.1 pc。他们发现纤维结构中的分子核的质量大约为 10 - 100 $M_\odot$，其中大多数处于引力不稳定状态。

正确的分子云形成和演化的理论模型需要可以预测和解释典型的分子云性质，不论是其内部的物理和化学性质，还是其外在的形态。

作为分子云的示例，我们在图 1.7 展示了 Narayanan et al. (2008) 对金牛座分子云 (the Taurus Molecular Cloud) 的 CO 巡天结果。他们观测了 ^{12}CO ($J = 1 \rightarrow 0$) 和 ^{13}CO ($J = 1 \rightarrow 0$) 两条同位素谱线，这里只展示了前者。图片所示的总巡天面积有 98 平方度。显然，分子云有非常复杂的动力学结构。

1.2.2 H II 区

1939 年丹麦天文学家本特 · 斯特龙根 (Bengt Strömgren) 发现弥散的星际气体主要有两种：一种是由完全中性的氢原子，称为中性氢区；另外一种气体的主要成分是电离氢，称为H II 区。H II 区的电离源主要是大质量恒星和宇宙射线。质量大于八个太阳质量的恒星会辐射很强的 UV 辐射 (大于 13.6 eV)，从而电离其周围的气体，形成H II 区。所以H II 区是研究大质量恒星的重要工具。

作为H II 区的示例，我们在图1.8中展示了著名的礁湖星云 (The Lagoon Nebula、M8、NGC 6523)。这个H II 区距离太阳约 1.3 kpc (Prisinzano et al., 2005)，是距离太阳比较近的大质量恒星形成区之一，关于礁湖星云的综述见 Tothill et al. (2008)。从图1.8上可以看出，大质量恒星在电离周围的气体的时候，会对周围星际介质的形状、气体成分、尘埃温度、气体温度、压强和湍动等产生影响 (feedback)，进而影响下一代的恒星形成。

H II 区形成之后，由于其内部的压强和温度都很高，H II 区会膨胀。随着H II 区膨胀，其边缘的光强度 (intensity) 逐渐降低，一旦光强度不足以补充氢的复合率，H II 区的区域就会宣告终结。所以H II 区是有边界的，这种现象称为 Strömgren 球 (Strömgren sphere)，球的半径称为 Strömgren 半径 (Strömgren radius)。

图 1.8: 礁湖星云 (The Lagoon Nebula、M8、NGC 6523)VLT 光学波段观测 (**版权: ESO/VPHAS+ team**)。

Figure 1.8. The Lagoon Nebula in optical band. **Image courtesy of ESO/VPHAS+ team.**

H II 区的密度跨度范围比较大，从致密H II 区 (离子数密度 $10^3 - 10^4$ cm^{-3})，到数密度只有 10 cm^{-3} 的弥散H II 区，横跨了多个数量级。H II 区在光学波段的谱线主要是氢和氦的复合线 (Recombination lines) 以及一些离子的禁线 (forbidden lines)，例如 [OII]、[OIII] 和 [NII]。在射电波段，除了复合线，H II 区还会辐射离子产生的热辐射 (thermal radio emission)，因为离子在作用前后都处于自由态，所以这种辐射称为自由-自由辐射 (free-free emission)。

H II 区由于其对大质量恒星研究的重要性，一直是研究的重点。我们会在本论文第二章研究H II 区膨胀对周围分子云内部恒星形成的影响，并在第三章利用 IRAS 星表和 *WISE* H II 区星表研究在双色图上证认H II 区的判据。在论文的第四章和第五章，我们分别研究银河系中心和高银纬的分子云。

第二章　大质量恒星触发恒星形成

We find that none of the observational markers improve the chances of correctly identifying a given star as triggered by more than factors of 2 at most. This limits the fidelity of these techniques in interpreting star formation histories. We therefore urge caution in interpreting observations of star formation near feedback-driven structures in terms of triggering.

— J. E. Dale, T. J. Haworth, and E. Bressert

关于H II 区在膨胀过程中触发恒星形成的模型，目前主要有两种：分子云堆积并塌缩模型 (collect-and-collapse, CAC) 和辐射驱动分子云爆缩模型 (radiation-driven implosion, RDI)。前者因为需要分子云的堆积，所以相互作用的空间尺度比较大 (∼10 pc)，作用时间也比较长 (数百万年)；相反，后者的作用空间尺度比较小，大约为 1 pc，作用时间也不到百万年。RDI 模型需要有分子核的前身，也就是说这些分子核在H II 区膨胀前就已经存在了，H II 区只是加速了分子核形成恒星的过程，而 CAC 模型则不需要前身分子核。

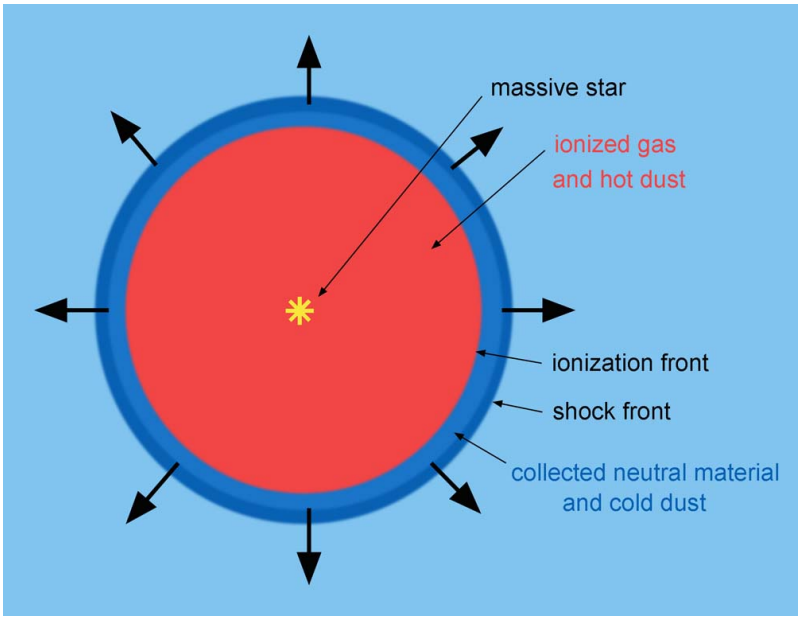

图 2.1: 分子云堆积并塌缩模型示意图 (Deharveng et al., 2010)。

Figure 2.1. A schematic diagram of collect and collapse model (Deharveng et al., 2010)。

早在 CAC 模型提出之前，Blaauw (1964) 就已经注意到有些 OB 星协 (OB associations) 含有一些恒星簇，这些恒星簇的空间分布具有年龄梯度特征。基于这样的

事实，Elmegreen et al. (1977) 提出了触发恒星形成的模型假设。如图 2.1 所示，膨胀的H II 区会在电离前端 (ionization front, IF) 和激波前端 (shock front, SF) 中间堆积致密分子云，一旦这些分子云变得引力不稳定 (gravitationally unstable)，就会形成下一代恒星。

近期的研究结果 (Hosokawa et al., 2005, 2006) 表明，电离前端和激波前端中间堆积的分子云的密度会比周围的气体高一到两个数量级，堆积的分子云质量大约为 $\sim 10^4 M_\odot$，并在H II 区膨胀 ~0.7 Myr 的时候开始表现出引力不稳定性。

实际上，从逻辑上证明H II 区附近的分子核或者恒星过程是触发形成的而不是自发形成的是比较困难的，但是可以通过对H II 区周围分子云的统计研究来说明触发恒星形成过程的可能性。从最新一些对H II 区研究的结果 (Deharveng et al., 2005, 2006, 2008; Pomarès et al., 2009; Zavagno et al., 2006) 来看，堆积塌缩过程在H II 区附近是非常普遍的现象。

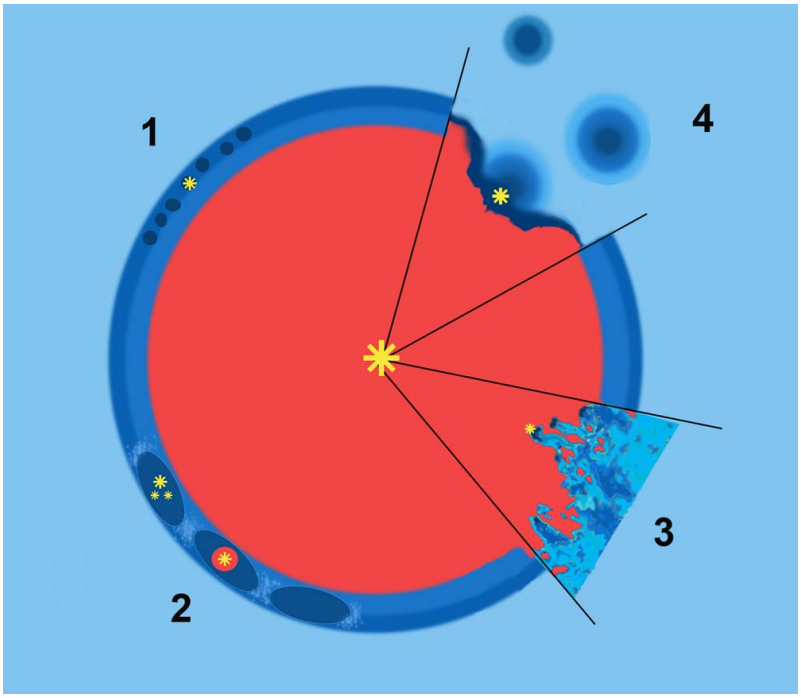

图 2.2: 四种不同的触发恒星形成过程示意图 (Deharveng et al., 2010)。1) 小尺度的引力不稳定性。2) 大尺度的引力不稳定性。3) 电离辐射作用在湍动较强的分子云上。4)RDI 模型，即辐射压加速前身分子核塌缩。

Figure 2.2. Four different models of triggered star formation (Deharveng et al., 2010). 1) Gravitational instabilities occur in small scales. 2) Gravitaional instabilities occur in large scales. 3) High-mass stars impose radiation on a turbulent medium. 4) RDI model.

不同于 CAC 模型，RDI 需要有前身分子核，H II 区的作用只是加速分子核的塌缩。因此，RDI 触发恒星形成的很多研究是基于H II 区附近的红外暗云，这些暗云 (bright-rimmed clouds, BRCs) 通常有明亮的边缘。RDI 模型的证据通常来自 BRCs 中的恒星形成的研究。

Wootten et al. (1983) 利用 CO 分子研究了五个 BRCs 中的恒星形成过程：NGC 1977、IC 1396、IC 1848A、B35 和 NGC 7822。他们虽然确认了一些恒星形成过程，但没有发现这些恒星形成过程跟H II 区之间有明显关系。Sugitani et al. (1994, 1991) 在南天和北天总共证认出 89 个与 IRAS 点源成协的 BRCs。这些 BRCs 的尺度小于 1 pc，与之成协的 IRAS 点源有比较高的光度，说明 BRCs 里面有恒星形成过程，这是 RDI 模型比较可信的证据。

图2.2中对四种可能的触发恒星形成模式进行了总结。在不同的分子云环境下，可能会出现不同的恒星触发模式。为了研究大质量恒星的形成和演化对周围分子云以及下一代恒星形成的影响，我们利用青海站的 13.7 米射电望远镜，观测了 13 个大质量恒星区中的五条分子谱线：^{12}CO $(J = 1 \rightarrow 0)$、^{13}CO $(J = 1 \rightarrow 0)$、C^{18}O $(J = 1 \rightarrow 0)$、HCO$^+$ $(J = 1 \rightarrow 0)$ 和 HCN $(J = 1 \rightarrow 0)$。我们分析了这 13 个天区的分子云的性质并找寻H II 区边缘可能的恒星形成现象，例如超致密H II区和外向分子流。

2.1 红外 Bubble

红外 Bubble 绝大部分是H II 区。红外 Bubble (infrared bubbles) 的概念起源于 *spitzer* 的 GLIMPSE (Galactic Legacy Infrared Mid-Plane Survey Extraordinaire) 巡天 (Benjamin et al., 2003; Churchwell et al., 2009)。GLIMPSE 巡天覆盖天区 $10^\circ \leqslant |l| \leqslant 65^\circ$ 和 $|b| \leqslant 1^\circ$，总覆盖面积大约为 220 平方度，共观测了四个红外波段——3.6、4.5、5.8 和 8.0 μm，空间分辨率约为 2″。

在 3.3、6.2、7.7、8.6 和 11.3 μm 波段，多环芳香烃 (Polycyclic Aromatic Hydrocarbons, PAH) 分子的辐射贡献占主导 (Peeters et al., 2004)。这些 PAH 分子经由紫外辐射 (far-ultraviolet, FUV) 抽运 (pump)，并在红外波段辐射荧光 (infrared fluorescence)。因为大质量恒星 ($\geqslant 8\ M_\odot$) 是星系中主要的 FUV 辐射源，所以 PAH 辐射可以示踪部分恒星形成率 (对 B 型星更敏感)(Peeters et al., 2004)。

GLIMPSE 巡天的 8 μm 波段包含的 PAH 辐射可以示踪H II 区。Churchwell et al. (2006) 利用 8 μm 波段图像证认出了 322 个红外 Bubble (8 μm 波段的环形结构)。如图 2.3所示，这些红外 Bubble 在 8 μm 波段有规则的环形结构，是H II 区边缘的

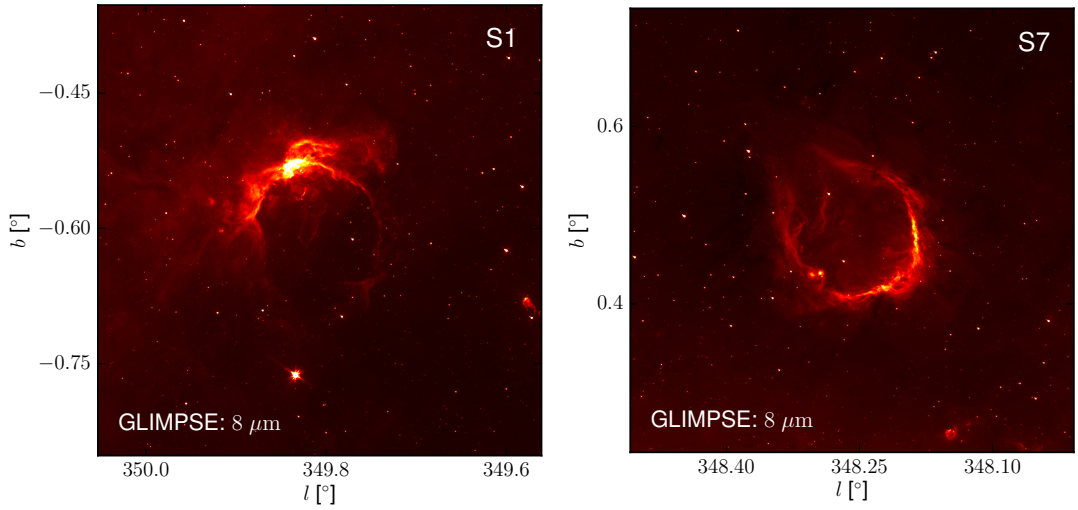

图 2.3: Churchwell et al. (2006) 证认的红外 Bubble 中的 S1 和 S7 的 8 μm 图像。

Figure 2.3. 8 μm image of bubble S1 and S7 identified by Churchwell et al. (2006)。

PAH 辐射。如图 2.4 所示，在红外 Bubble 中心，24 μm 波段的连续谱辐射占主导，也可以由射电波段的由自由-自由辐射示踪。24 μm 波段的连续谱辐射源是被H II 区加热的尘埃，而射电波段的连续谱辐射的辐射源是内部离子的自由-自由辐射。Deharveng et al. (2010) 研究了 102 个红外 Bubble 后得出，Churchwell et al. (2006) 提供的红外 Bubble 星表中有 87% 是跟射电连续源成协的。

由于证认红外 Bubble 人为因素影响比较大且耗时废力，Simpson et al. (2012) 将 GLIMPSE 的数据公开，让网络上的一些志愿者来一起帮忙证认，这个项目被称为银河系项目 (the Milky Way Project, MWP)。最后Simpson et al. (2012) 证认出 5106 个红外 Bubble。由于 GLIMPSE 巡天在银纬方向的限制 ($|b| \leqslant 1°$)，Simpson et al. (2012) 提供的星表并不完备。Anderson et al. (2014) 利用 *WISE* 数据将银河系内红外 Bubble 的数目扩增至 8399 个，这是目前最全的银河系H II 区星表。

目前红外 Bubble 的研究，主要针对红外 Bubble 的结构及其周围的恒星形成过程。Beaumont et al. (2010) 利用 JCMT (James Clerk Maxwell Telescope) 观测了 ^{12}CO ($J = 3 \rightarrow 2$) 和 HCO^+ ($J = 4 \rightarrow 3$)，他们研究了 43 个红外 Bubble 的三维结构并在 Bubble 边缘证认出了 12 个外向分子流。此外，Anderson et al. (2012b) 利用 *Herschel* 数据探测到了红外 Bubble 膨胀的近端 (near-side) 和远端 (far-side)，他们的结果支持红外 Bubble 的三维膨胀模型。

利用 CO 分子研究红外 Bubble 的工作也有很多，例如其中一些 (Hou et al., 2014; Petriella et al., 2010; Sidorin et al., 2014; Xu et al., 2014) 基于银河系的 GRS (the Galactic Ring Survey) ^{13}CO (Jackson et al., 2006) 巡天数据。一些高密度气体探针，例

如 HCN ($J = 1 \rightarrow 0$) 和 HCO^+ ($J = 1 \rightarrow 0$) (Christopher et al., 2005; Wu et al., 2010)，也被用来研究红外 Bubble (Beaumont et al., 2010; Kendrew et al., 2012)，其中不乏对 HCO^+ 和 ^{12}CO ($J = 1 \rightarrow 0$) 外向分子流的研究。因为外向分子流是恒星形成的直接证据 (Rawlings et al., 2004; Zhang et al., 2001)，所以一直是研究的重点。

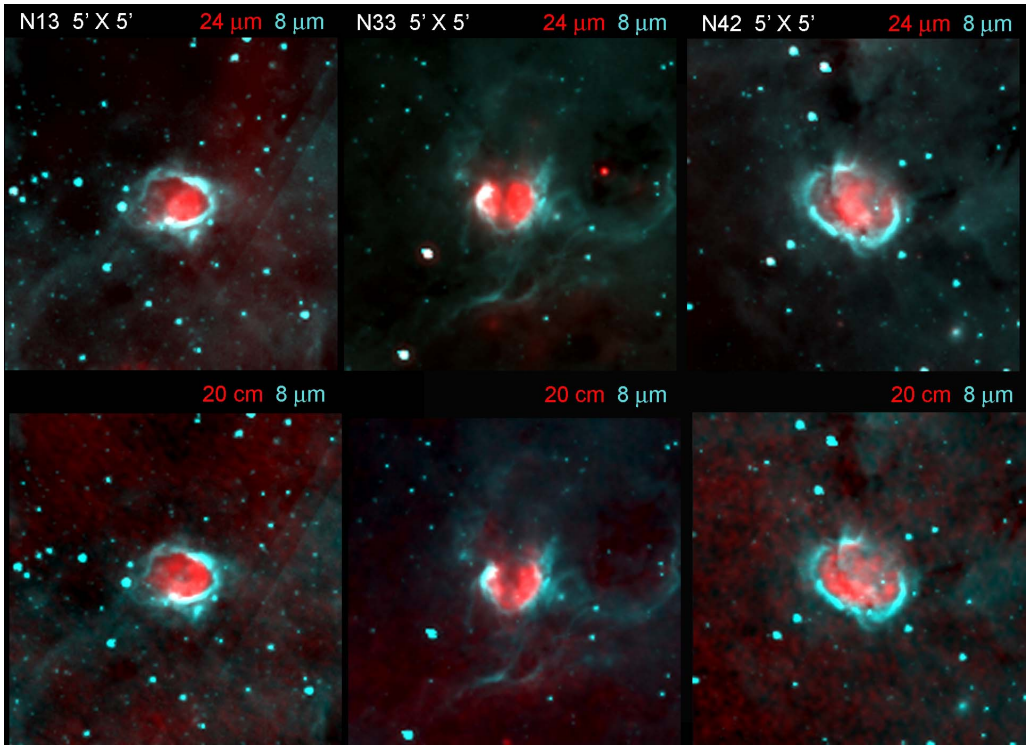

图 2.4: 三个红外 Bubble 在 8 μm、24 μm 和 20 cm 波段的辐射分布 (Deharveng et al., 2010)。从左到右，三个红外 Bubble 分别为 N13、N33 和 N42，红外 Bubble 的星表编号源自Churchwell et al. (2006)，名称中的 N 代表北天。

Figure 2.4. Infrared and radio images of three infrared bubbles (Deharveng et al., 2010).

除了利用分子谱线，很多红外 Bubble 的研究基于边缘初期恒星体 (young stellar objects，YSOs) 的统计分析 (Watson et al., 2008, 2009, 2010)，YSOs 可以根据谱能量分布 (spectral energy distribution, SED) 的特征来证认。Kendrew et al. (2012) 发现大质量 YSOs 的位置分布跟H II 区有很强的相关性。Thompson et al. (2012) 研究了 322 个红外 Bubble 天区的 YSOs，他们也发现在红外 Bubble 边缘 YSOs 的数目明显增多。虽然这些研究都支持H II 区可以有效的触发下一代恒星形成，但是 YSOs 的年龄、质量和距离等参数的不确定性很大，导致他们的结论的不确定性也很大。

但是，也有人分析认为目前对H II 区触发恒星形成的研究过于乐观。Anderson et al. (2012b) 研究认为，红外 Bubble 附近的冷气体的环状是二维结构并非三维结构。在这种情况下，膨胀的激波前不能有效的压缩分子云，反而会导致恒星

形成活动被抑制。Dale et al. (2015) 回顾了 67 篇研究论文和触发恒星形成的研究方法。他们指出，目前这些方法给出的结论的不确定性很大，盲目地把H II 区附近的恒星形成解释为触发恒星形成过程，缺乏有效论证。

表 2.1: 18 个红外 Bubble 的物理参数。

Table 2.1. Parameters of the observed bubbles.

Name [a]	l[b] (deg)	b[b] (deg)	iXdiam[b] (arcmin)	iYdiam[b] (arcmin)	oXdiam[b] (arcmin)	PA[b] °	V_{ion}[h] (km s^{-1})	$S_{1.4GHz}$ (mJy)	Distance[c] (kpc)
N4	11.895	+0.751	3.5	3.3	5.8	7	25.1	2109.9	3.2
N14	13.992	-0.129	2.7	2.6	4.3	38	36	1462.6	3.7
N37	25.291	+0.294	2.7	3.4	4.0	13	39.6	222.4	12.6
N44	26.822	+0.383	1.8	1.9	2.8	48	82.0	58.4	5.0/10.1
N49	28.828	-0.228	2.3	2.3	3.6	30	90.6	642.7	5.5
MWP1G032057+000783[b]	32.057	+0.078	1.2	1.1	1.9	8	96.3	100.0	8.4
N55	32.099	+0.092	1.0	1.1	1.5	59	93.0	43.4	8.4
MWP1G032158+001306[b]	32.158	+0.131	1.1	1.2	1.8	16	95.0	653.3	8.4
N74	38.907	-0.439	2.4	2.1	3.9	49	42.1	7.3	2.8/10.4
N75	38.928	-0.386	1.2	1.3	2.0	25	42.1	6.2	2.8/10.4
N82	42.104	-0.623	2.7	2.6	4.7	10	66.0	786.4	4.3[d]
N89	43.734	+0.117	1.8	2.0	2.8	15	73.1	14.1	6.1
N90	43.775	+0.061	2.5	2.5	3.9	9	70.5	168.3	6.1
N95	45.387	-0.715	2.8	2.8	4.0	27	52.5	315.6	8.0
N105	50.078	+0.570	1.3	1.3	2.4	8	-1.1[g]	101.2	11.2[i]
N123	57.544	-0.282	2.1	2.0	3.3	37	2.0[e]	787.6	8.6[e]
N132	63.121	+0.386	...	...	0.3	...	16.4	9.6	2.1[f]
N133	63.163	+0.441	3.9	3.7	6.8	22	16.4	2900.4	2.1[f]

(1) 从左到右，表格依次列出红外 Bubble 的编号，银经，银纬，内 X 直径，内 Y 直径，外 X 直径，位置偏转角度 (距离 Y 轴)，H II 区视向速度，1.4 GHz 波段流量和距离。表格中的大括号表示红外 Bubble 在同一个天区。

The columns are, from left to right, the bubble identity, galactic longitude, galactic latitude, inner X diameter, inner Y diameter, outer X diameter, ellipse position angle (from the Y axis), velocity of H II region, flux at 1.4 GHz, and distance. Bubbles in the same region are marked with brackets.

(2) 引用文献：a Churchwell et al. (2006); b Simpson et al. (2012); c Deharveng et al. (2010); d Stead et al. (2010); e Watson et al. (2003); f Watson et al. (2010); g Anderson et al. (2011); h Anderson et al. (2014); i Anderson et al. (2012a)。当远近动力学距离无法区时，采用近距离。

References: a Churchwell et al. (2006); b Simpson et al. (2012); c Deharveng et al. (2010); d Stead et al. (2010); e Watson et al. (2003); f Watson et al. (2010); g Anderson et al. (2011); h Anderson et al. (2014); i Anderson et al. (2012a). The near distance is adopted when the kinematic distance is ambiguous.

如果红外 Bubble 真的可以触发恒星形成，那么一些恒星形成的直接证据一定可以在红外 Bubble 周围发现，例如分子云的内落、外向分子流和脉泽等。虽然这些现象并非触发恒星形成所特有，但是我们可以从统计上研究这些现象在红外 Bubble 附近的分布，来研究触发恒星形成过程。相比于内落现象来说，脉泽和外向

分子流比较容易观测。一些脉泽可以有效确认恒星形成过程的存在性，例如 OH、H_2O 和 II 型 CH_3OH (Caswell et al., 1995)。研究发现，在一些红外 Bubble 边缘有 EGOs (Extend Green Objects)，这些 EGOs 可能示踪大质量恒星形成过程中伴随的外向分子流。Cyganowski et al. (2009) 对大约 20 个 EGOs 进行了 I 型和 II 型甲醇脉泽观测，他们发现有有力证据支持这些 EGOs 是大质量恒星形成区的外向分子流。关于红外 Bubble 外向分子流的工作也有但并不多，例如Beaumont et al. (2010) 用眼睛证认出 12 个外向分子流候选体，但是这些外向分子流需要更多的观测来证实。本章节的研究便是针对红外 Bubble 周围可能存在的外向分子流。

2.2 观测和数据处理

我们从 Churchwell et al. (2006) 提供的星表中挑选出角尺度比较大并且分布在北天的 13 个红外 Bubble，并利用紫金山天文台青海观测站 13.7 米毫米波射电望远镜观测五条分子谱线。这 13 个天区中包含 18 个红外 Bubble (见表 2.1)——有的天区含有多个红外 Bubble，观测的五条谱线有 ^{12}CO ($J = 1 \rightarrow 0$)、^{13}CO ($J = 1 \rightarrow 0$)、C^{18}O ($J = 1 \rightarrow 0$)、HCN ($J = 1 \rightarrow 0$) 和 HCO^+ ($J = 1 \rightarrow 0$)。除了这五条分子谱线，我们还利用了一些已经公开的数据，主要是射电和红外巡天数据。研究中用到的巡天有 GLIMPSE 巡天 (Benjamin et al., 2003; Churchwell et al., 2009)，MIPSGAL (the Multiband Infrared Photometer for *Spitzer* (MIPS) Galactic Plane Survey) 巡天 (Carey et al., 2009; Gutermuth et al., 2015)，BGPS (Bolocam Galactic Plane Survey) 巡天 (Aguirre et al., 2011; Rosolowsky et al., 2010)，MAGPIS (the Multi-Array Galactic Plane Imaging Survey) 巡天 (Helfand et al., 2006) 和 NVSS (NRAO VLA Sky Survey) 巡天 (Condon et al., 1998)。这些巡天的具体参数见表2.2。基于这些数据，我们研究了红外 Bubble 附近分子云的性质和其内部的恒星形成活动。

表 2.2: 一些巡天的参数。

Table 2.2. Observation parameters of surveys.

Survey	Wavelengths	Resolutions	Facilities	References
GLIMPSE	3.6, 4.5, 5.8, 8.0 μm	$\sim 2''$	*Spitzer*	Benjamin et al. (2003); Churchwell et al. (2009)
MIPSGAL	24 μm	$6''$	*Spitzer*	Carey et al. (2009); Gutermuth et al. (2015)
BGPS	1.1 mm	$33''$	Bolocam	Aguirre et al. (2011); Rosolowsky et al. (2010)
MAGPIS	20 cm	$6''$	VLA	Helfand et al. (2006)
NVSS	20 cm	$45''$	VLA	Condon et al. (1998)

2.2.1 德令哈 CO 观测

我们用紫金山天文台青海观测站 13.7 米毫米波射电望远镜观测了表2.1列出的 18 个红外 Bubble。青海观测站位于青海省德令哈市，冬季干燥少雨，水汽干扰很少，非常适合毫米波观测。青海站望远镜位于北纬 37°22′.4，其主波束在 110 GHz 大约为 50″。望远镜的接收机使用了上下边带分离的多波束 (3×3) 超导频谱阵列 (a superconducting array receiver, SSAR) (Shan et al., 2012)。后端频谱仪通道数有 16,384 个，带宽 1 GHz，采用快速傅里叶变换频谱仪器 (the fast Fourier transform spectrometer, FFTS)。CO 观测的谱分辨率大约为 0.16 km s^{-1}。关于望远镜的具体参数，请参考青海站望远镜的状态报告[1]。

表 2.3: 五条分子谱线的观测参数。

Table 2.3. Observational parameters of the molecular lines.

Molecular line (J=(1-0))	Rest frequency (GHz)	Critical density[a] (10^3 cm^{-3})	HPBW (″)	$T_{\rm sys}$ (K)	$\eta_{\rm mb}$	δv (km s^{-1})	rms noise (k)
^{12}CO	115.271204	0.0067-0.64[b]	49	220-300	45.9%	0.16	0.5
^{13}CO	110.201353	0.38-1.9[b]	51	140 -190	51.1%	0.17	0.2
C^{18}O	109.782183	1.6-1.9[b]	50	140 -190	54.6%	0.17	0.2
HCN	88.6318473	68[c]	56	140 -190	55.0%	0.18	0.07
HCO$^+$	89.1885260	470[c]	58	140 -190	55.7%	0.18	0.07

[a] 在动力学温度 10 K 下的计算结果。
Under the kinematic temperature of 10 K.

[b] Yoshida et al. (2010)

[c] Shirley (2015)

红外 Bubble 的观测是在 2013 年 5 月到 12 月之间完成的。我们总共观测了五条分子谱线：^{12}CO ($J = 1 \rightarrow 0$)、^{13}CO ($J = 1 \rightarrow 0$)、C^{18}O ($J = 1 \rightarrow 0$)、HCN ($J = 1 \rightarrow 0$) 和 HCO$^+$ ($J = 1 \rightarrow 0$)。望远镜可以同时记录 CO 分子的三条同位素谱线，但是需要额外的时间观测 HCO$^+$ 和 HCN，后面两条谱线虽然可以同时观测，但是不能跟 CO 分子同时观测。望远镜的半功率波束宽度 (the half power beamwidth, HPBW) 在 110.2 GHz 为 52″，跟踪精度大约为 5″，主波束效率为 46% (^{12}CO)、51% (^{13}CO)、55% (C^{18}O、HCN 和 HCO$^+$)，系统温度为 280 K (^{12}CO)、185 K (^{13}CO 和 C^{18}O) 和 140 K (HCN 和 HCO$^+$)。观测采用 OTF (on-the-fly) 扫描成图模式，扫描速率为 50″ s^{-1}，扫描间隔为 15″。对每个红外 Bubble，我们用大约用 2 个

[1] http://www.radioast.nsdc.cn/zhuangtaibaogao.php

小时观测 CO，5 个小时观测 HCN 和 HCO^+。我们对信号比较弱的天区增加了额外的积分时间，以增强信噪比 (signal-to-noise ratio, SNR)。

每个观测天区的大小约为 $10' \times 10'$。我们用GILDAS (the Grenoble Image and Line Data Analysis Software) 软件包对观测数据进行了处理，最后把谱线数据采样为 $30'' \times 30''$ 的网格并保存为 FITS (Flexible Image Transport System) 文件格式。^{12}CO 谱线在 0.16 km s^{-1} 分辨率下的 RMS (root mean squre) 为 0.45 K，^{13}CO 和 $C^{18}O$ 谱线在 0.17 km s^{-1} 分辨率下为的 RMS 为 0.20 K，HCN 和 HCO^+ 在 0.18 km s^{-1} 分辨率下的 RMS 为 0.07 K。

五条分子谱线的具体参数见表2.3。从左到右，表2.3依次列出谱线名称、静止频率、临界密度 (在温度为 10 K 时的值)、HPBW、系统温度、主波束效率、速度分辨率和噪声温度 (RMS)。

2.3 红外 Bubble 的分子谱线

在本小节，我们给出分子谱线的观测结果以及根据分子谱线计算出的红外 Bubble 的物理参数。除了在 N89 和 N90 方向没有观测到 $C^{18}O$ 外 (该天区另外四条谱线均观测到信号)，其他所有的红外 Bubble 均探测到五条分子谱线，其中 N44 和 N123 天区谱线的信噪比略低。$C^{18}O$ 的信噪比普遍低于其他四条分子谱线，这是因为 $C^{18}O$ 的谱线亮温度跟 HCN 和 HCO^+ 一样低，但其积分时间却跟 ^{12}CO 和 ^{13}CO 相同。

我们根据 CO 分子的三条同位素谱线计算了跟红外 Bubble 成协的分子云和分子核的物理参数。分子云的速度参数是根据电离气体的速度信息 (Anderson et al., 2014; Lockman, 1989)，CO 谱线的速度信息 (Beaumont et al., 2010) 和 ^{13}CO 的积分强度分布来共同确定的。另外，根据 ^{12}CO 和 HCO^+ 的谱线特征，我们搜寻了 13 个红外 Bubble 天区中的外向分子流。

2.3.1 红外 Bubble 分子云的物理性质

为了从整体上把握红外 Bubble 附近分子云的性质，我们对红外 Bubble 区域的分子谱线进行了平均。红外 Bubble 的平均分子谱线见图2.5。谱线的平均区域是以 Bubble 为中心的正方形 (边长沿银经和银纬方向)，正方形的边长等于红外 Bubble 的外边界主轴 (Simpson et al., 2012)。从图2.5可以看出，沿红外 Bubble 的视线方向，分子云成分复杂。我们用 ^{12}CO 的谱线作了高斯曲线拟合，发现有一半左右的红外 Bubble 的谱线偏离高斯曲线，说明红外 Bubble 附近的动力学性质比较复杂。

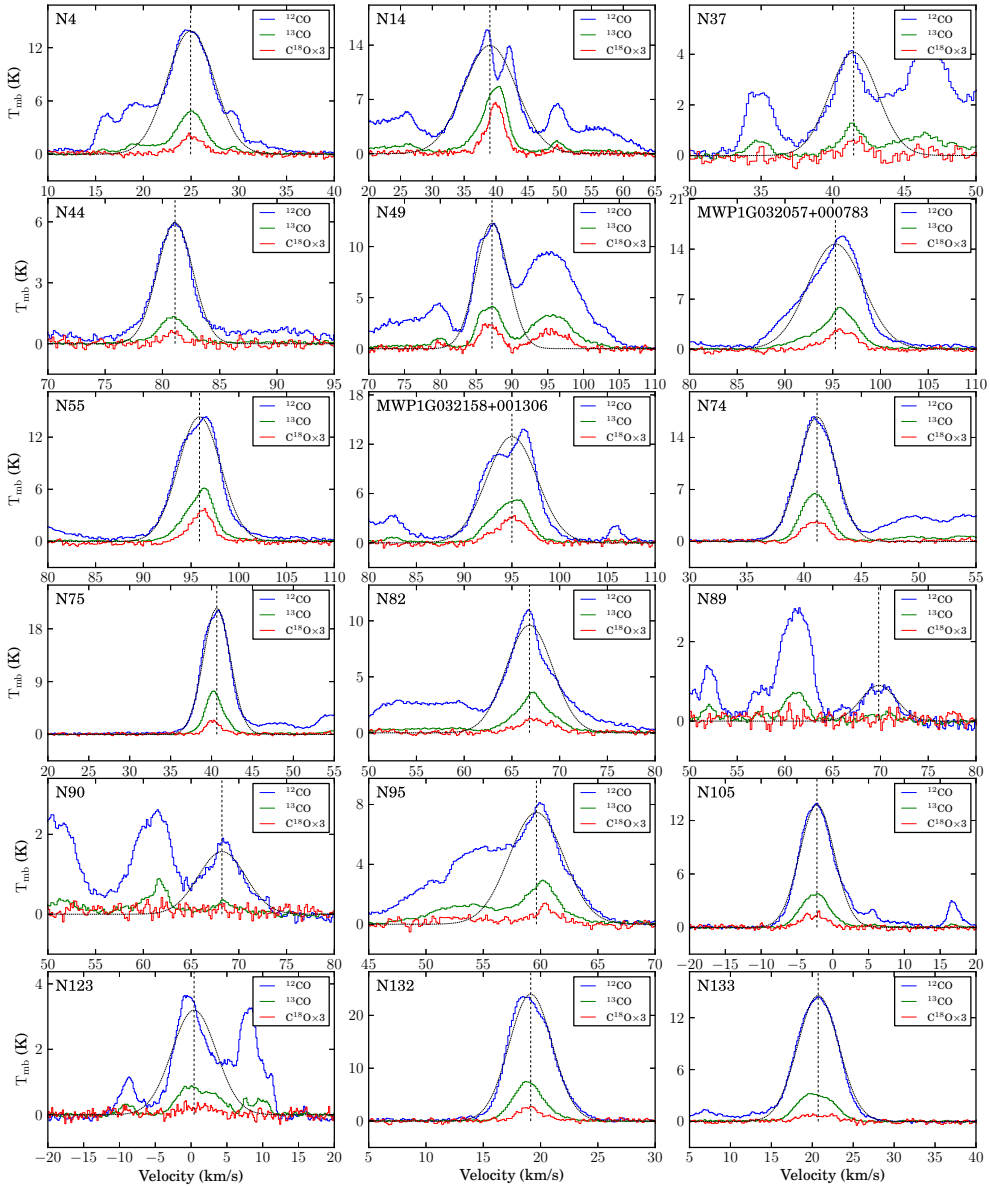

图 2.5: 18 个红外 Bubble 的平均分子谱线。为了清晰起见，$C^{18}O$ 已被放大三倍。黑色点线是用 ^{12}CO 拟合的高斯曲线，高斯曲线的中心速度用垂直的虚线标出。

Figure 2.5. Average spectra for all observed bubbles. The $C^{18}O$ lines are amplified by a factor of 3 for clarity. The black dotted lines delineate the fitted Gaussian curves of ^{12}CO, and the dashed vertical lines mark the center velocities of these Gaussian curves.

我们用 CO 分子的两条同位素谱线，$^{12}CO\ (J = 1 \rightarrow 0)$ 和 $^{13}CO\ (J = 1 \rightarrow 0)$，来计算分子云的物理性质。我们假设分子云处于局部热力学平衡 (local thermodynamic equilibrium, LTE) 状态，并进一步假设 $^{12}CO\ (J = 1 \rightarrow 0)$ 是光学厚 (optically thick) 的，$^{13}CO\ (J = 1 \rightarrow 0)$ 是光学薄的 (optically thin)。光学厚的 $^{12}CO\ (J = 1 \rightarrow$

0) 可以用来计算激发温度 (the excitation temperature, T_{ex})，进而可以用光学薄的 ^{13}CO $(J = 1 \rightarrow 0)$ 来计算光深 (optical depth, τ) 和柱密度 (column density) (Li et al., 2013; Nagahama et al., 1998)。

计算 CO 分子激发温度的公式如下：

$$T_{\rm ex} = 5.53\{\ln[1 + \frac{5.53}{T_R^*(^{12}{\rm CO}) + 0.819}]\}^{-1}, \tag{2.1}$$

其中，$T_R^*(^{12}CO)$ 是 ^{12}CO $(J = 1 \rightarrow 0)$ 的主波束温度。

根据公式 2.1计算出的激发温度，我们可以计算 ^{13}CO $(J = 1 \rightarrow 0)$ 的光深，公式如下：

$$\tau({\rm C}^{13}{\rm O}) = -\ln(1 - \frac{T_R^*(^{13}{\rm CO})}{\frac{5.29}{\exp(5.29/T_{\rm ex}-1)} - 0.89}), \tag{2.2}$$

其中，$T_R^*(^{13}CO)$ 是 ^{13}CO $(J = 1 \rightarrow 0)$ 的主波束温度，T_{ex} 是由公式2.1 计算的 CO 分子激发温度。根据我们的计算，^{13}CO $(J = 1 \rightarrow 0)$ 的光深大部分低于 0.5，说明 ^{13}CO $(J = 1 \rightarrow 0)$ 的光学薄假设基本正确。

除了谱线的激发温度和光深，我们还计算了分子云的尺度。分子云的角尺度可以根据 Simpson et al. (2012) 提供的 Bubble 参数来确定。根据红外 Bubble 的面积 A (即图2.5中平均谱线的天区面积)，计算分子云直径的公式如下：

$$l = D\sqrt{4A/\pi - \theta_{\rm MB}^2}, \tag{2.3}$$

其中，D 是红外 Bubble 到太阳的距离，θ_{MB} 是望远镜的主波束大小。公式2.3其实是在去掉望远镜波束跟分子云角尺度的卷积。

在计算分子云的质量之前，我们先计算了红外 Bubble 区域分子云的平均柱密度。我们用平均过的 ^{12}CO $(J = 1 \rightarrow 0)$ 和 ^{13}CO $(J = 1 \rightarrow 0)$ 谱线计算 H_2 平均柱密度 (Nagahama et al., 1998) 的公式如下：

$$N({\rm H_2}) = 1.49 \times 10^{20}[1 - \exp(\frac{-5.29}{T_{\rm ex}})]^{-1} \times [\frac{\int T_R^*(^{13}{\rm CO})dV}{1{\rm K\ kms^{-1}}}]\ {\rm cm^{-2}}, \tag{2.4}$$

其中，$\int T_R^*(^{13}CO)dV$ 是用 ^{13}CO $(J = 1 \rightarrow 0)$ 拟合的高斯曲线跟 X 轴围成的区域面积。H_2 和 ^{13}CO 的柱密度之比采用Frerking et al. (1982) 给出的 7×10^5。

表 2.4: 红外 Bubble 周围分子云的物理参数。

Table 2.4. Physical parameters of the molecular clouds.

Name	$^{12}CO_v$	$^{12}CO_{peak}$	$^{12}CO_{\Delta V}$	$^{13}CO_v$	$^{13}CO_{peak}$	$^{13}CO_{\Delta V}$	N_{H_2}	Area[a]	M_{LTE}	Age[b]
	(km s^{-1})	(K)	(km s^{-1})	(km s^{-1})	(K)	(km s^{-1})	(10^{21}cm^{-2})	pc^2	$10^3 M_\odot$	(Myr)
N4	24.9	13.9	5.8	25.0	4.6	3.8	10.1	35	7.7	0.8
N14	39.0	14.0	9.8	39.9	8.4	4.7	22.6	23	11.2	0.6
N37	41.5	4.1	3.9	41.6	1.2	2.3	0.8	406	7.3	3.7
N44	81.1	6.0	3.6	81.0	1.3	2.9	1.3	26	0.8	1.7
N49	87.2	12.3	5.3	87.1	4.3	4.0	8.9	46	8.8	1.2
Name[c]	95.3	14.7	6.9	95.7	5.2	4.9	15.0	37	12.1	1.2
N55	95.9	14.3	5.3	96.1	5.7	3.6	12.0	30	7.7	1.7
Name[d]	95.0	12.9	6.2	95.0	5.2	4.5	12.7	37	10.3	0.6
N74	41.1	16.8	3.9	41.0	6.5	2.8	11.9	13	3.5	0.8
N75	40.6	21.5	3.9	40.4	7.1	2.7	14.8	5	1.6	0.3
N82	66.8	9.6	5.7	67.3	3.2	4.5	6.4	43	6.0	0.9
N89	69.8	0.9	4.4	70.3	0.2	3.4	0.1	39	0.1	1.8
N90	68.2	1.6	5.8	68.4	0.2	4.6	0.2	64	0.3	2.2
N95	59.6	7.5	5.6	60.0	2.7	4.0	4.1	110	9.8	2.9
N105	-2.2	13.8	5.7	-2.4	3.8	4.6	9.9	96	24.4	1.6
N123	0.4	3.2	7.3	1.0	0.8	6.7	1.5	107	3.4	1.4
N132	19.1	24.0	4.4	19.0	7.3	3.2	19.6	1	0.2	0.3
N133	20.7	14.6	5.9	20.5	3.3	5.1	9.9	30	6.4	0.4

[a] 红外 bubble 的面积是根据Simpson et al. (2012) 提供的参数确定。

The areas are determined using the parameters of bubbles given by Simpson et al. (2012).

[b] 年龄是根据Tremblin et al. (2014a) 提供的数值模拟结果计算的。

The method of estimating ages are following Tremblin et al. (2014a).

[c] MWP1G032057+000783.

[d] MWP1G032158+001306.

最后，我们根据 $N(H_2)$ 计算分子云质量，公式为

$$M = \mu m_{H_2} N(H_2) \pi l^2 / 4, \tag{2.5}$$

其中，m_{H_2} (3.32×10^{-27} kg) 是单个氢分子的质量，μ 是分子云中气体的氢分子的质量丰度，其值为 1.36 (Hildebrand, 1983)。

Tremblin et al. (2014a) 模拟了银河系内的H II 区在湍动分子云中的三维膨胀，并给出了膨胀的半径、中心天体的光度和H II 区年龄的对应关系。根据Tremblin et al. (2014a) 提供的结果以及 NVSS 巡天中给出的 1.4GHz 射电连续源流量信息，我们计算了每个红外 Bubble 的年龄，具体结果见表2.1。

表2.4中列出了根据上述公式导出的红外 Bubble 周围分子云的物理参数。表格中，^{12}CO 和 ^{13}CO 谱线高斯拟合参数包括中心速度、峰值亮温度和谱线的半峰全宽 (full width at half maximum, FWHM)。除了高斯曲线参数，我们还列出了分子云的平均柱密度、面积、LTE 假设下的质量和红外 Bubble 的年龄。需要强调的是，这里计算分子云的质量只包含了红外 Bubble 附近的小区域，并非跟红外 Bubble 相连的整个分子云的质量，因为我们只对红外 Bubble 堆积的分子云质量感兴趣。

表2.4中的结果显示，红外 Bubble 堆积的分子云质量大约为 $100-19000\ M_{\odot}$，红外 Bubble 的年龄范围为 $0.3-3.7$ Myr。

2.3.2 分子团块

本论文中，我们采用Bergin et al. (2007) 和 Heyer et al. (2015) 给出的分子团块和分子核的定义，认为分子团块和分子核是分子云的子结构，他们的尺度范围分别为 $0.3-3$ pc 和 $0.03-0.2$ pc。青海站望远镜的分辨率在 2.1 kpc 的距离上只有 0.5 pc，无法分辨出分子核，所以我们证认的分子云致密成分为分子团块。

虽然 HCO^+ 和 HCN 两条谱线也都是致密分子云探针，但是这两条谱线非常容易光学厚；为了能准确界定分子团块的中心位置，我们采用光学薄的 $C^{18}O$，$C^{18}O$ 通常示踪柱密度比较大的区域。我们先用 $C^{18}O$ 找寻分子团块，再用较高信噪比的 ^{13}CO 来确认。

在 18 个红外 Bubble 周围，我们总共证认出 23 个分子团块，每个红外 Bubble 边缘至少有一个分子团块。由于 ^{13}CO 在分子云致密区域的光深不确定较大，我们改用 ^{12}CO 和 $C^{18}O$ 谱线计算分子团块的质量。光学厚的 ^{12}CO 可以用来计算激发温度，进而用光学薄的 $C^{18}O$ 估计柱密度。由于 N89 和 N90 天区的 $C^{18}O$ 的信噪比太低，对这两个天区，我们仍然使用 ^{13}CO。

计算 $C^{18}O$ ($J=1\rightarrow 0$) 的光深的公式 (Liu et al., 2014; Scoville et al., 1986) 如下：

$$\tau(C^{18}O)=-\ln(1-\frac{T_R^*(C^{18}O)}{\frac{5.27}{\exp(5.27/T_{ex})}-0.89}), \tag{2.6}$$

其中，$T_R^*(C^{18}O)$ 是 $C^{18}O$ 谱线的亮温度，T_{ex} 是用公式2.1计算的激发温度。有了光深，我们进而可以估算 $C^{18}O$ ($J=1\rightarrow 0$) 的柱密度：

$$\frac{N(\mathrm{C^{18}O})}{\mathrm{cm^{-2}}} = 4.77\times10^{13}\frac{T_{\rm ex}+0.88}{\exp(-5.27/T_{\rm ex})}\frac{\tau(\mathrm{C^{18}O})}{1-\exp(-\tau(\mathrm{C^{18}O}))}\frac{\int T_{\rm mb}{\rm d}v}{\mathrm{K\ km\ s^{-1}}}, \quad (2.7)$$

其中，$\int T_{\rm mb}{\rm d}v$ 是用 $\mathrm{C^{18}O}$ $(J=1\rightarrow0)$ 拟合的高斯曲线跟 X 轴围成的区域的面积。$\mathrm{C^{18}O}$ 跟氢分子的柱密度比 $(\mathrm{C^{18}O/H_2})$ 大约为 1.7×10^{-7} (Frerking et al., 1982)。

表 2.5: 分子团块的物理参数。

Table 2.5. Table Physical parameters of the molecular clumps.

Clumps	Peak position	$V_{\rm range}$[a]	$V_{\rm center}$	ΔV	Tex	τ	Column density	Area	$M_{\rm LTE}$	$M_{\rm vir}$	Lines	Outflow[b]
	(l,b)	(km s^{-1})	(km s^{-1})	(km s^{-1})	(k)		10^{15}cm^{-2}	pc^2	$10^3M_\odot$	$10^3M_\odot$		
N4A	(11.836, 0.742)	20.1 - 29.3	24.7	2.7	25.0	0.08	7.4	4.2	4.1	1.8	$\mathrm{C^{18}O}$	
N4B	(11.903, 0.717)	21.1 - 28.7	24.9	2.2	29.5	0.09	9.6	2.7	3.5	1.0	$\mathrm{C^{18}O}$	
N14A	(14.009, -0.179)	35.4 - 45.7	40.5	3.0	24.5	0.20	20.7	5.3	14.7	2.5	$\mathrm{C^{18}O}$	Y
N37A	(25.320, 0.276)	39.1 - 44.9	42.0	1.7	25.1	0.06	3.6	26.3	12.7	1.8	$\mathrm{C^{18}O}$	
N44A	(26.844, 0.371)	77.7 - 83.7	80.7	1.7	16.6	0.08	2.4	2.5	0.8	0.6	$\mathrm{C^{18}O}$	
N49A	(28.834, -0.253)	82.5 - 91.5	87.0	2.6	21.4	0.19	13.1	7.6	13.3	2.3	$\mathrm{C^{18}O}$	
N49B	(28.842, -0.212)	82.2 - 89.9	86.0	2.3	22.9	0.11	7.3	5.0	4.9	1.4	$\mathrm{C^{18}O}$	
Name[c]	(32.016, 0.063)	89.5 - 105.6	97.5	4.7	21.7	0.12	15.6	26.6	55.4	13.7	$\mathrm{C^{18}O}$	
Name[d]	(32.149, 0.138)	88.4 - 102.4	95.4	4.1	19.5	0.13	11.4	11.7	17.7	6.9	$\mathrm{C^{18}O}$	
N55A	(32.116, 0.088)	92.0 - 101.0	96.5	2.6	24.3	0.13	11.1	14.7	21.8	3.2	$\mathrm{C^{18}O}$	Y
N75A	(38.925, -0.353)	34.4 - 43.6	39.0	2.7	32.3	0.06	9.0	2.5	2.9	1.4	$\mathrm{C^{18}O}$	
N74A	(38.950, -0.462)	37.8 - 45.9	41.9	2.4	23.7	0.15	11.4	3.3	5.0	1.2	$\mathrm{C^{18}O}$	
N74B	(38.925, -0.420)	37.0 - 44.4	40.7	2.2	25.5	0.09	6.9	3.1	2.9	1.0	$\mathrm{C^{18}O}$	
N82A	(42.120, -0.595)	63.2 - 72.9	68.0	2.8	21.1	0.09	6.6	5.8	5.1	2.3	$\mathrm{C^{18}O}$	
N90A	(43.798, 0.051)	64.6 - 72.2	68.4	2.3	12.9	0.31	5.1	6.2	0.5	1.5	$\mathrm{^{13}CO}$	
N89A	(43.723, 0.143)	68.2 - 73.3	70.7	1.5	10.9	0.32	2.4	7.7	0.3	0.7	$\mathrm{^{13}CO}$	
N95A	(45.389, -0.747)	55.2 - 65.5	60.4	3.0	18.3	0.07	4.2	17.4	9.8	4.5	$\mathrm{C^{18}O}$	
N105A	(50.077, 0.561)	-8.9 - 1.6	-3.6	3.1	21.9	0.06	4.9	24.2	16.0	5.7	$\mathrm{C^{18}O}$	
N105B	(50.077, 0.594)	-8.4 - 4.8	-1.8	3.9	18.6	0.04	3.2	46.4	19.8	12.1	$\mathrm{C^{18}O}$	Y
N123A	(57.571, -0.288)	-7.7 - 6.4	-0.6	4.1	14.4	0.04	2.0	19.8	5.3	9.0	$\mathrm{C^{18}O}$	
N133A	(63.115, 0.406)	15.8 - 22.9	19.4	2.1	24.7	0.09	6.9	1.6	1.4	0.7	$\mathrm{C^{18}O}$	
N133B	(63.140, 0.439)	17.1 - 28.0	22.5	3.2	35.3	0.03	7.1	2.1	2.0	1.8	$\mathrm{C^{18}O}$	Y
N133C	(63.248, 0.431)	13.8 - 27.3	20.5	4.0	14.7	0.07	3.6	1.0	0.5	1.9	$\mathrm{C^{18}O}$	

[a] 此速度区间之间的谱线用来拟合高斯曲线并用来确定分子团块中心位置和分子团块的面积 (通过积分强度图，这个速度区间也是积分强度图的积分区间)。

The velocity ranges are the spectral line ranges which are used to fit Gaussian curve and create integral maps which are used to determine the areas of clumps.

[b] 我们用 Y 表示分子团块有外向分子流 (molecular outflow) 特征。

The clumps that are marked by Y are associated with molecular outflow candidates.

[c] MWP1G032057+000783A.

[d] MWP1G032158+001306A.

每个分子团块的角尺度由积分强度半峰值等高线围成的面积确定——速度积

分区间见表2.5。根据这个面积，$A_{1/2}$，计算分子团块直径的公式如下：

$$l_{\rm clump} = D\sqrt{4A_{1/2}/\pi - \theta^2_{\rm MB}}, \tag{2.8}$$

其中，D 是红外 Bubble 到太阳的距离，$\theta_{\rm MB}$ 是望远镜的主波束大小。得到分子团块的直径后，可以根据公式2.5，计算分子团块的质量。

利用分子团块的参数，我们计算了分子团块的位力质量，公式 (MacLaren et al., 1988) 为：

$$\frac{M}{(M_\odot)} = k_2 \frac{l_{\rm clump}/2}{({\rm pc})}\left(\frac{\Delta V}{({\rm km\ s^{-1}})}\right)^2 \tag{2.9}$$

其中，k_2 的值为 210 (假设 $\rho(r)$ 为常数)，ΔV 是根据 $C^{18}O$ ($J = 1 \rightarrow 0$) 拟合的高斯谱线的半峰全宽。我们假定分子核在分子团块中均匀分布，所以我们认为 $\rho(r)$ 假设比较合理。对单个分子核来说，$\rho(r) = 1/r$ 的假设，相对来说，比较准确。

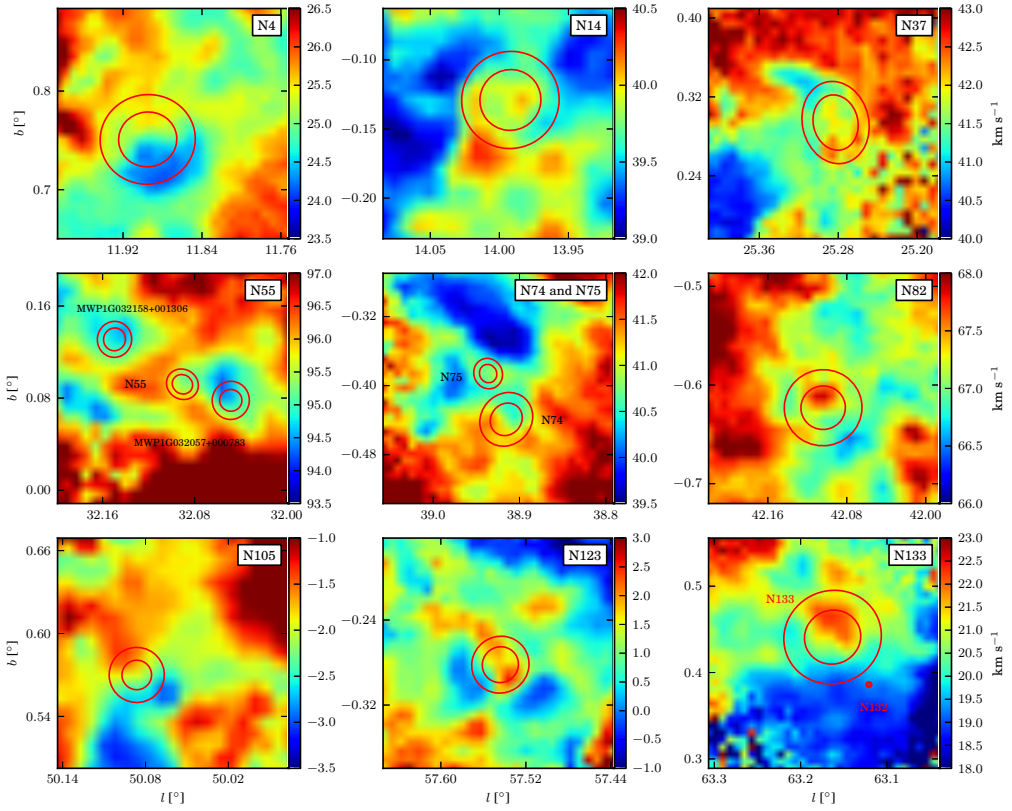

图 2.6: 9 个红外 Bubble 区域 ^{12}CO ($J = 1 \rightarrow 0$) 的平均速度 (权重按亮温度计算) 分布。

Figure 2.6. Intensity weighted velocity distribution of ^{12}CO ($J = 1 \rightarrow 0$) for 9 bubble regions.

表2.5从左到右依次列出分子团块名称，积分强度图的峰值位置，积分速度区间，高斯曲线的中心速度，速度弥散 (高斯曲线的标准差)，高斯曲线峰值，光深，柱密度，分子团块尺度，分子团块质量，位力质量，导出参数用的曲线和外向分子流标记。跟外向分子流成协的分子团块我们用 Y 标记，关于外向分子流的详细结果见 §2.4。分子团块在 §2.3.4中的积分图和通道图上分别用紫色和绿色加号标记。

2.3.3 H II区的膨胀

我们用 ^{12}CO ($J = 1 \rightarrow 0$) 来探测 Bubble 周围的速度分布，因为 ^{12}CO ($J = 1 \rightarrow 0$) 信噪比最高且对速度比较敏感。我们对每一个像素以亮温度为权重计算平均速度。我们发现，有 9 个红外 Bubble 边缘的速度分布梯度比较明显，见图2.6。我们还发现 N14、N74 和 N133 边缘的速度分布有弧形结构，这很有可能是由H II膨胀导致的。这些特征跟Yuan et al. (2014) 研究过的红外 Bubble N6 附近分子云的一些性质相似，较大的区别在于 N6 区域的速度弥散更大一些；除此之外，我们观测的红外 Bubble 的速度弥散跟Ji et al. (2012) 给出的 N22 区域的值一致。

更详细的分子云速度结构见 §2.3.4中的速度通道图。我们发现一些红外 Bubble 边缘的分子云具有弧形结构，例如 N4、N14、N49 和 N133。例如在 N49 附近，有一个非常明显的壳层结构 (速度区间在 79 - 81 km s^{-1})，这极有可能是H II 区膨胀导致的。我们的观测表明红外 Bubble 跟周围分子云是有相互作用的，这也可以从图2.5的 CO 谱线中得到佐证。如图2.5所示，一些 CO 谱线偏离高斯曲线很多，说明红外 Bubble 已经影响了其周围分子云的动力学特征。

2.3.4 13 个红外 Bubble 天区

在这一节，我们详细介绍 13 个红外 Bubble 天区的观测结果，并跟前人的研究结果进行对比。

2.3.4.1 N4

N4 在 8 μm 波段呈现一个清晰且十分规则的环形结构，中间的 20 cm 射电辐射充满 Bubble 的中心区域，见图2.7左上角小图。这是一个非常典型且规则的红外 Bubble。这个天区的射电复合线 (the radio recombination line, RRL) 观测表明 N4 的视向速度为 25.1 km s^{-1} (Anderson et al., 2014; Lockman, 1989)，而个 CO 谱线给出的视向速度为 24.9 km s^{-1} (Deharveng et al., 2010; Li et al., 2013)，两个速度值非常一致。N4 到太阳的距离我们采用Deharveng et al. (2010) 给出的 3.15 kpc。

在我们之前，Li et al. (2013) 也用青海站望远镜观测了 N4 区域的三条 CO 同位素谱线，但他们并未观测 HCN ($J = 1 \rightarrow 0$) 和 HCO^+ ($J = 1 \rightarrow 0$)。他们发现，CO 辐射分布跟 8 μm 结构一致，并认为这个结构更像是一个倾斜的环而不是通常认为的膨胀球壳。Li et al. (2013) 计算出 N4 的激发源是一个质量约为 15 $M_\odot$，年龄约为 1 Myr 的 B 型星。他们还发现在 N4 边缘可能有分子云内落的证据，说明认为在 N4 边缘存在触发恒星形成过程。

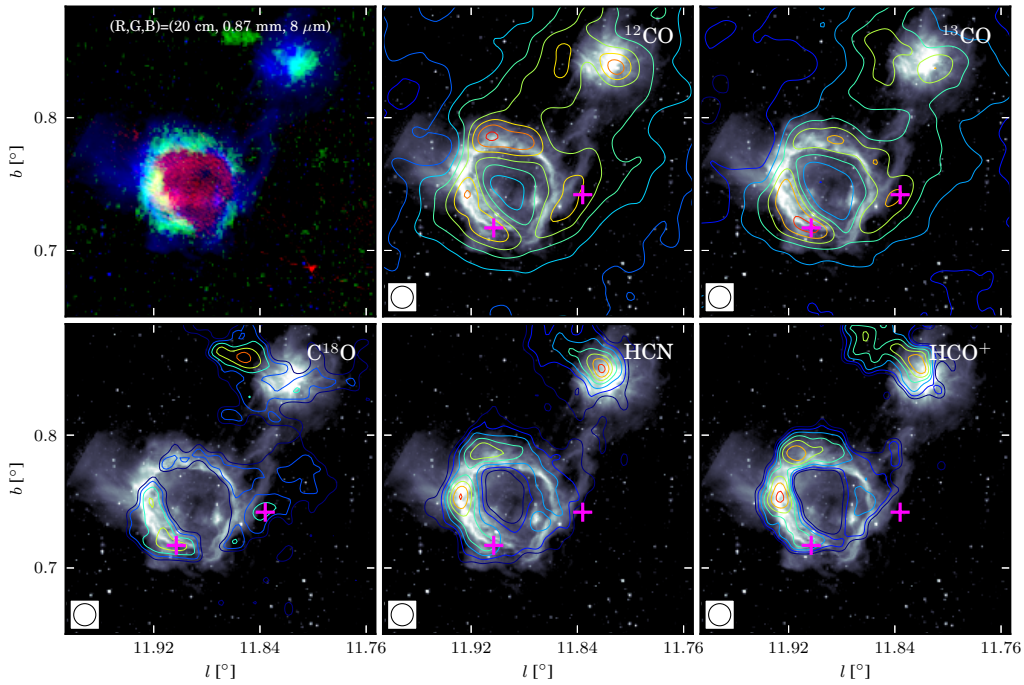

图 2.7: 红外 Bubble N4 图像。左上角是三色图，其中红、绿和蓝色分别代表 20 厘米、0.87 毫米和 8 μm 辐射。其他五图是五条谱线的积分强度轮廓图，背景为 8 μm 中红外辐射，分子团块的位置用紫色加号标记。轮廓图积分区间为 [21.0, 29.0] km s^{-1}。^{12}CO、^{13}CO、C^{18}O、HCN 和 HCO^+ 五条谱线的积分强度图噪声 (σ) 分别为 0.54、0.26、0.26、0.08、和 0.09 K km s^{-1}。五条谱线积分强度轮廓图的等值线都从 8σ 开始，间隔分别为 29、21、4、5 和 3σ。

Figure 2.7. Images of N4. The upper left panel is a three color image with 20 cm in red, 0.87 mm in green, and 8 μm in blue. The other five panels are contours of five spectral line integral intensity maps superimposed on the 8 μm image. The contour maps integrate from 21.0 km s^{-1} to 29.0 km s^{-1}. The rms (σ) of the five line maps, ^{12}CO, ^{13}CO, C^{18}O, HCN, and HCO^+, are 0.54, 0.26, 0.26, 0.08, and 0.09 K km s^{-1}, respectively, and these contours all begin at the 8σ level, spacing with 29, 21, 4, 5, and 3σ, respectively.

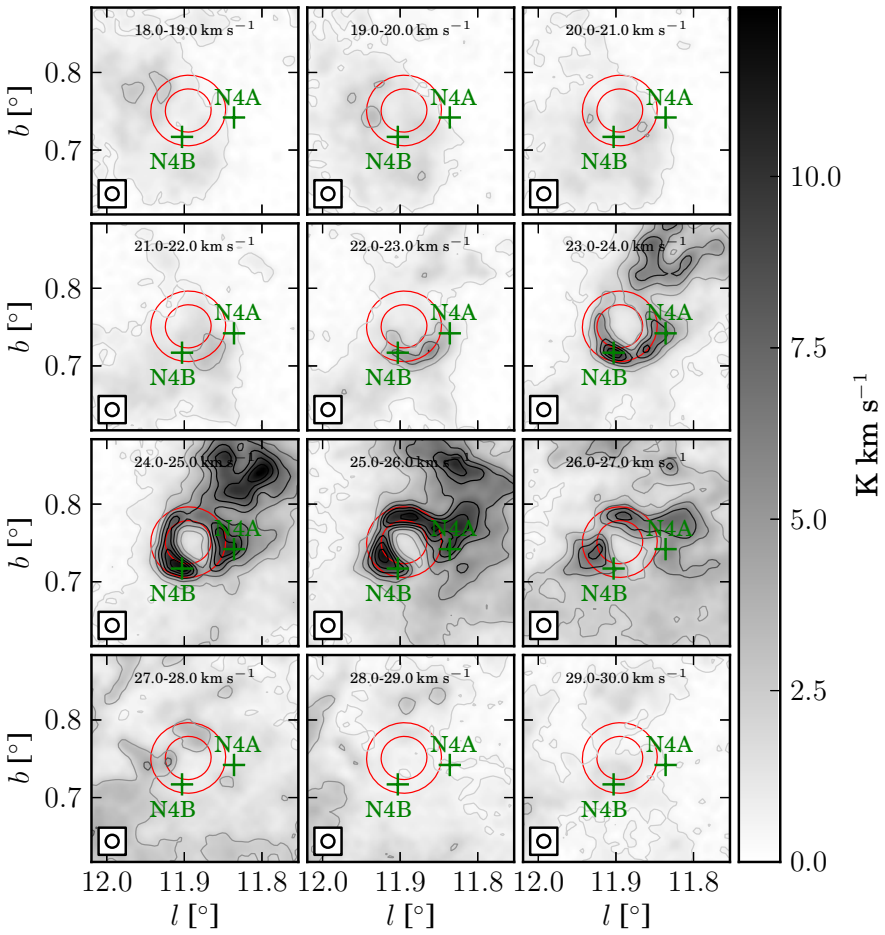

图 2.8: 红外 Bubble N4 ^{13}CO 谱线速度通道图，积分区间从 18.0 km s^{-1} 到 30.0 km s^{-1}，每 1.0 km s^{-1} 积分一次。红色圆圈标记了 N4 的位置，参数见Simpson et al. (2012)，绿色加号标记分子团块的位置。图像背景噪声 (σ) 为 0.09 K km s^{-1}。轮廓等值线从 8.0σ 开始，间隔为 18.1σ。

Figure 2.8. Channel map of ^{13}CO for bubble N4 from 18.0 km s^{-1} to 30.0 km s^{-1} with 1.0 km s^{-1} intervals. The red circles mark the position of N4 from Simpson et al. (2012), and the green crosses mark the peak positions of clumps. The rms (σ) of the image background is about 0.09 K km s^{-1}. The contour levels space linearly from 8.0σ to the peak with a step of 18.1σ.

我们的 CO 观测结果跟Li et al. (2013) 的结果基本一致。在 N4 边缘，C^{18}O 谱线显示有两个分子团块，分别为 N4A 和 N4B，如图2.8所示。图2.7展示了五条谱线的积分强度轮廓图，五条谱线的观测参数见表2.3。我们计算的 N4 区域分子云质量约为 7.7×10$^3 M_\odot$，这个结果跟Li et al. (2013) 给出的 7 × 10$^3 M_\odot$ 非常接近。HCN 和 HCO$^+$ 示踪的致密分子的分布跟 8 μm 结构也非常一致，说明分子云堆积并塌缩过

程在 N4 区域确实存在，但是我们在Li et al. (2013) 证认的内落位置并没有发现蓝不对称 (blue asymmetry) 谱线特征。由于此区域的谱线在红移端和蓝移端都有其他成分干扰，我们无法用 CO 谱线证认外向分子流。

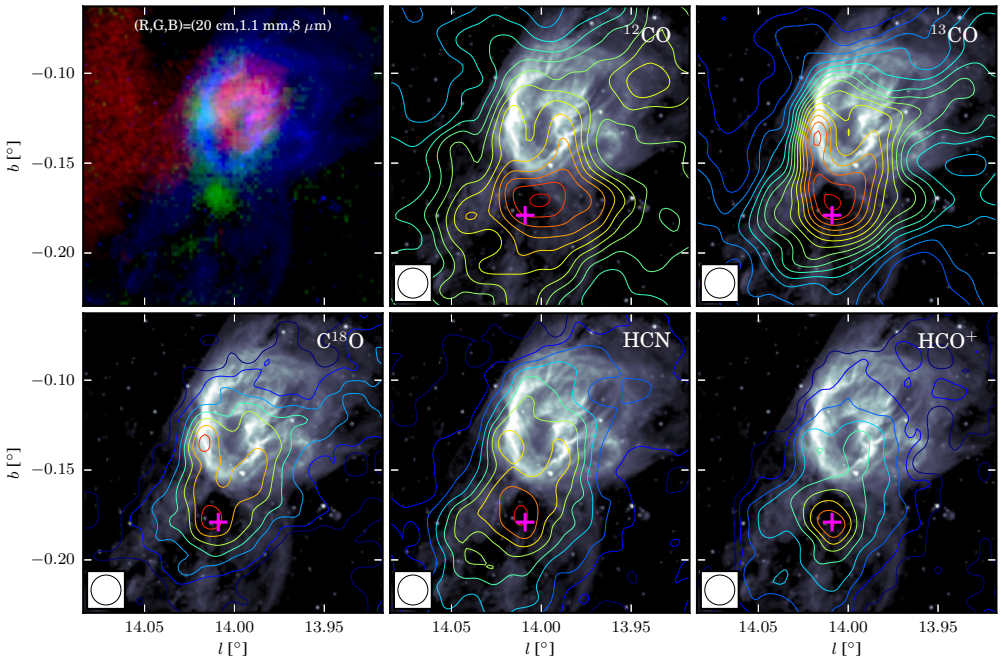

图 2.9: 红外 Bubble N14 图像。左上角是三色图，其中红、绿和蓝色分别代表 20 厘米、1.1 毫米和 8 μm 辐射。其他五图是五条谱线的积分强度轮廓图，背景为 8 μm 中红外辐射，分子团块的位置用紫色加号标记。轮廓图积分区间为 [36.0, 44.0] km s^{-1}。^{12}CO、^{13}CO、C^{18}O、HCN 和 HCO$^+$ 五条谱线的积分强度图噪声 (σ) 分别为 0.57、0.32、0.28、0.07、和 0.08 K km s^{-1}。五条谱线积分强度轮廓图的等值线都从 8σ 开始，间隔分别为 14、11、6、6 和 5σ。

Figure 2.9. Images of N14. The upper left panel is a three color image with 20 cm in red, 1.1 mm in green, and 8 μm in blue. The other five panels are contours of five spectral line integrated intensity maps superimposed on the 8 μm image with positions of clumps marked by purple crosses. The contour maps integrate from 36.0 km s^{-1} to 44.0 km s^{-1}. The rms (σ) of the five line maps, ^{12}CO, ^{13}CO, C^{18}O, HCN, and HCO$^+$, are 0.57, 0.32, 0.28, 0.07, and 0.08 K km s^{-1}, respectively, and these contours all begin at 8σ, spacing with 14, 11, 6, 6, and 5σ, respectively.

2.3.4.2 N14

N14 的角尺度比较大，8 μm 辐射分布在 20 厘米连续谱辐射周围。在 N14 附近有一块红外暗云，其位置跟 1.1 毫米辐射示踪的分子云位置重合。射电复合线的观测给出 N14 的视向速度大约为 36.0 km s^{-1} (Anderson et al., 2014; Lockman, 1989)，此值跟 CO 分子视向速度 (36.0 km s^{-1}, Beaumont et al. (2010)) 一致。因为 N14 的红外和 Hα 辐射都很强，所以我们采用其近运动学距离 3.7 kpc，这跟Deharveng et al. (2010) 建议的值一致。

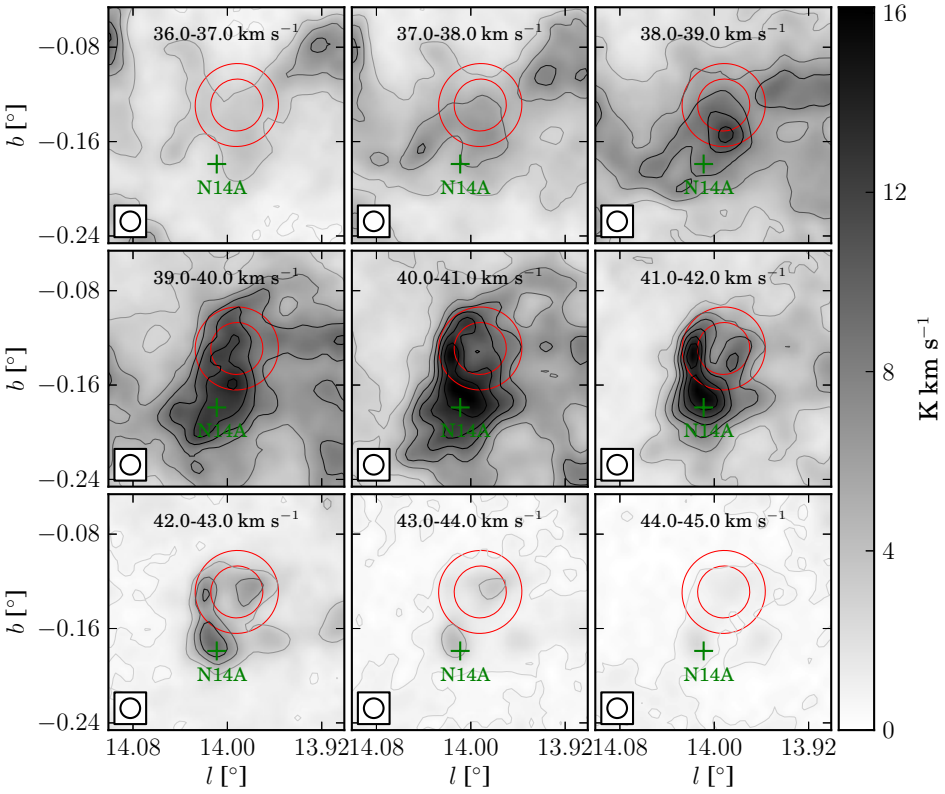

图 2.10: 红外 Bubble N14 ^{13}CO 谱线速度通道图，积分区间从 36.0 km s^{-1} 到 45.0 km s^{-1}，每 1.0 km s^{-1} 积分一次。红色圆圈标记了 N14 的位置，参数见Simpson et al. (2012)，绿色加号标记分子团块的位置。图像背景噪声 (σ) 为 0.11 K km s^{-1}。轮廓等值线从 8.0σ 开始，间隔为 19.1σ。

Figure 2.10. Channel map of ^{13}CO for bubble N14 from 36.0 km s^{-1} to 45.0 km s^{-1} with 1.0 km s^{-1} intervals. The red circles mark the position of N14 (Simpson et al., 2012), and the green cross marks the peak position of the clump. The RMS (σ) of the image background is about 0.11 K km s^{-1}. The contour levels space linearly from 8σ to the peak with step 19.1σ.

Sherman (2012) 观测了 N14 区域的 3 毫米射电连续谱和 7 条分子谱线。他们的 N_2H^+ 谱线观测表明，N14 周围的分子云并非均匀分布。对照 3 毫米连续谱数据，他们在 N14 附近证认了 10 个致密尘埃核。尽管没有在 N14 周围发现明显速度梯度，他们仍然认为触发恒星形成确实存在，只是触发机制可能跟传统的分子云堆积塌索过程不同。

Dewangan et al. (2013) 利用多波段的数据研究了红外 Bubble N14。根据观测，他们认为H II区的膨胀确实会在壳层堆积分子云。但是基于H II区的年龄跟分子云的碎裂时间之间的差异，他们认为这些分子团块的形成过程可能是由于激波压缩或者堆积的分子云在小范围内的金斯不稳定性造成的。根据 YSOs 的面密度，他们发现了一个 I 型初期恒星体星团，这说明H II区很可能已经开始触发恒星形成。

如图2.9所示，我们观测的五条分子谱线辐射跟 N14 的 8 μm 结构一致，具体观测参数见表2.3。在 N14 周围有一个非常明显的分子团块——见图2.10，此团块跟红外暗云应对应同一个天体。虽然 CO 谱线在此团块区域非常复杂，但是 HCO^+ 谱线的红移端谱线显示在此分子团块中心附近有一个外向分子流。在此外向分子流附近有一个 24 μm 红外源，这极有可能示踪外向分子流的激发源。关于此外向分子流的详细参数和讨论，见 §2.4。

2.3.4.3 N37

如图2.11所示，N37 在 8 μm 波段呈现半开结构，内部有弱 20 厘米射电辐射。五条分子谱线的观测参数见表2.3。该区域的电离气体的速度为 39.6 km s^{-1} (Anderson et al., 2014; Lockman, 1989)，跟Beaumont et al. (2010) 给出的 CO 谱线速度 (40.0 km s^{-1}) 一致。虽然Watson et al. (2010) 采用了近距离 3.3 kpc，但是我们选择使用Anderson et al. (2009) 建议的远距离 12.6 kpc。因为，Anderson et al. (2009) 通过分析 H I 的吸收辐射比例 (H I emission/absorption，H I E/A) 和 H I 的自吸收 (H I self-absorption, H I SA) 后认为此 N37 应处于动力学远距离，此结果跟Deharveng et al. (2010) 采用的距离一致。

Beaumont et al. (2010) 用眼睛根据 CO ($J = 3 \rightarrow 2$) 谱线证认了一个外向分子流，位于 $(l, b) = (25.285°, 0.266°)$，但是我们观测的 ^{12}CO 数据并未显示明显的外向分子流证据。他们认为这个区域外向分子流的高速和低速成分分别在 30 和 40 km s^{-1}，但是 ^{12}CO 辐射在这个速度区间比较弱且比较复杂，所以我们认为这个速度区间跟 Bubble 很可能不成协。我们在 N37 边缘证认了一个分子团块，见图2.12。相对来说，分子谱线在 N37 的开放区域信号较弱。

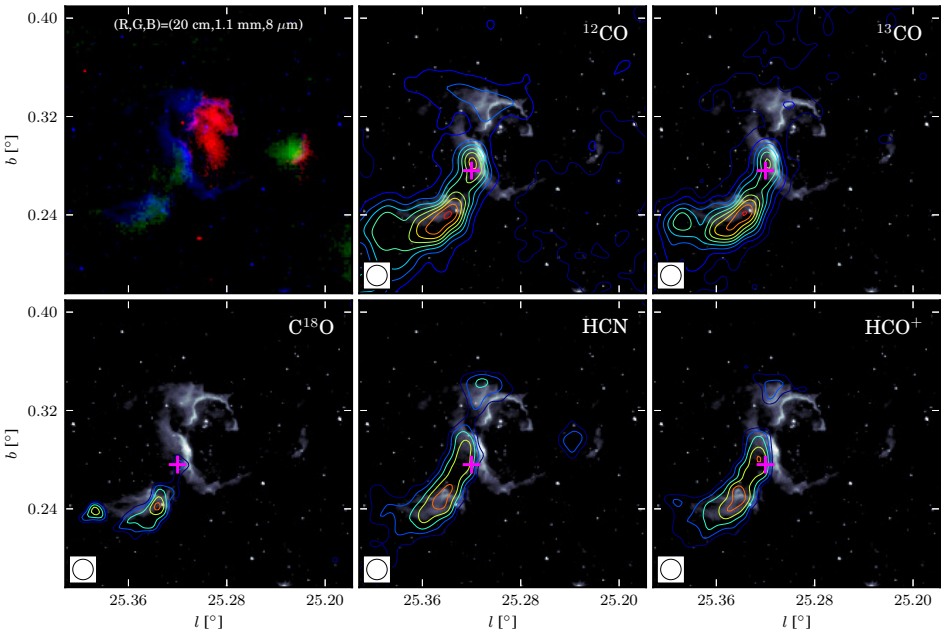

图 2.11: 红外 Bubble N37 图像。左上角是三色图，其中红、绿和蓝色分别代表 20 厘米、1.1 毫米和 8 μm 辐射。其他五图是五条谱线的积分强度轮廓图，背景为 8 μm 中红外辐射，分子团块的位置用紫色加号标记。轮廓图积分区间为 [39.0, 44.0] km s^{-1}。^{12}CO、^{13}CO、C^{18}O、HCN 和 HCO$^+$ 五条谱线的积分强度图噪声 (σ) 分别为 0.36、0.21、0.19、0.05、和 0.05 K km s^{-1}。五条谱线积分强度轮廓图的等值线都从 8σ 开始，间隔分别为 24、12、3、7 和 5σ。

Figure 2.11. Images of N37. The upper left panel is a three color image with 20 cm in red, 1.1 mm in green, and 8 μm in blue. The other five panels are contours of five spectral line integrated intensity maps superimposed on the 8 μm image with positions of clumps marked by purple crosses. The contour maps integrate the intensity from 39.0 km s^{-1} to 44.0 km s^{-1}. The rms (σ) of the five line maps, ^{12}CO, ^{13}CO, C^{18}O, HCN, and HCO$^+$, are 0.36, 0.21, 0.19, 0.05, and 0.05 K km s^{-1}, respectively, and these contours all begin at 8σ, spacing with 24, 12, 3, 7, and 5σ, respectively.

虽然 ^{13}CO 和 HCO$^+$ 显示谱线蓝翼部分有展宽，但是对应的红翼成分却没有展宽，在 C^{18}O 的峰值位置也没有 24 μm 源相对应。因此，我们认为这个比较宽的蓝翼成分可能是由H II 区的膨胀或者其他成分的干扰导致的。我们认为在 N37 区域没有外向分子流，但是考虑到青海站望远镜的分辨率以及 ^{12}CO ($J = 1 \rightarrow 0$) 示踪环境的局限性，在排除 (Beaumont et al., 2010) 证认的外向分子流之前，我们需要更多的观测。

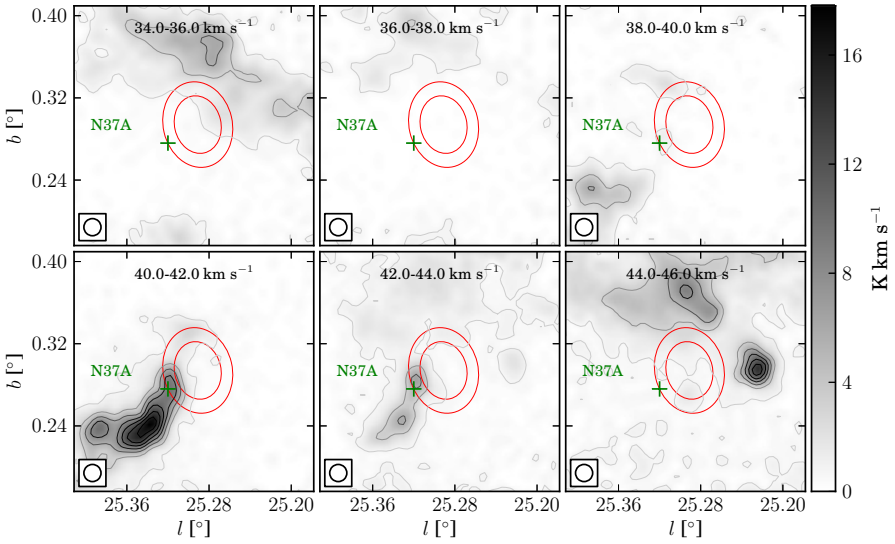

图 2.12: 红外 Bubble N37 ^{13}CO 谱线速度通道图，积分区间从 34.0 km s^{-1} 到 46.0 km s^{-1}，每 2.0 km s^{-1} 积分一次。红色圆圈标记了 N37 的位置，参数见Simpson et al. (2012)，绿色加号标记分子团块的位置。图像背景噪声 (σ) 为 0.13 K km s^{-1}。轮廓等值线从 5.0σ 开始，间隔为 18.3σ。

Figure 2.12. Channel map of ^{13}CO for bubble N37 from 34.0 km s^{-1} to 46.0 km s^{-1} with 2.0 km s^{-1} intervals. The red circles mark the position of N37 (Simpson et al., 2012), and the green cross marks the peak position of the clump. The rms (σ) of the image background is about 0.13 K km s^{-1}, and the contour levels space linearly from 5σ to the peak with step 18.3σ.

2.3.4.4 N44

红外 Bubble N44 的角尺度比较小，形状比较规则，其内部 20 厘米射电辐射比较微弱。N44 天区电离气体的速度为 82 km s^{-1} (Anderson et al., 2014)，与Beaumont et al. (2010) 给出的 CO 速度 (81.1 km s^{-1}) 相吻合。由于 N44 的远近运动学距离没有分辨出，我们简单采用 N44 的近运动学距离——5 kpc。

Deharveng et al. (2010) 在 N44 附近发现了两个致密成分。这两个成分是 N44 天区主要的 CO 辐射源，见图2.13所示五条分子谱线的积分强度图，谱线的观测参数见表2.3。本文我们只研究在 N44 附近的分子团块，其位置已在通道图2.14中，用绿色十字标出。该区域的 CO 线翼被其他成分干扰，所以无法用谱线证认外向分子流。

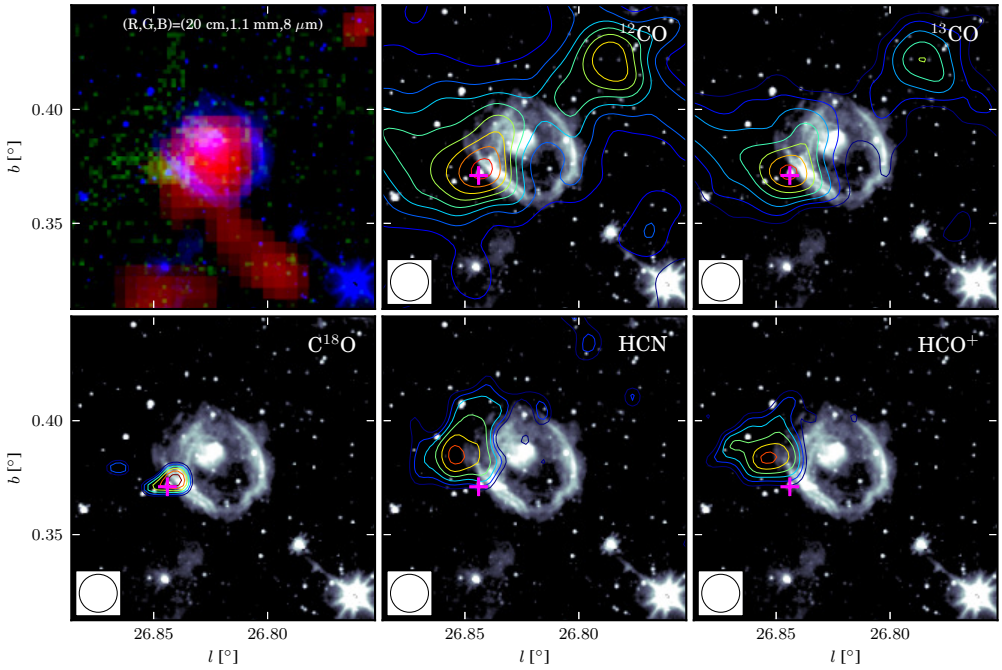

图 2.13: 红外 Bubble N44 图像。左上角是三色图，其中红、绿和蓝色分别代表 20 厘米、1.1 毫米和 8 μm 辐射。其他五图是五条谱线的积分强度轮廓图，背景为 8 μm 中红外辐射，分子团块的位置用紫色加号标记。轮廓图积分区间为 [78.0, 84.0] km s^{-1}。^{12}CO、^{13}CO、C^{18}O、HCN 和 HCO$^+$ 五条谱线的积分强度图噪声 (σ) 分别为 0.31、0.25、0.16、0.05、和 0.05 K km s^{-1}。五条谱线积分强度轮廓图的等值线都从 8σ 开始，间隔分别为 20、7、1、3 和 3σ。

Figure 2.13. Images of N44. The upper left panel is a three color image with 20 cm in red, 1.1 mm in green, and 8 μm in blue. The other five panels are contours of five spectral line integrated intensity maps superimposed on the 8 μm image with positions of clumps marked by purple crosses. The contour maps integrate the intensity from 78.0 km s^{-1} to 84.0 km s^{-1}. The background rms (σ) of the five line maps, ^{12}CO, ^{13}CO, C^{18}O, HCN, and HCO$^+$, are 0.31, 0.25, 0.16, 0.05, and 0.05 K km s^{-1}, respectively, and these contours all begin at 8σ, with 20, 7, 1, 3, and 3σ spacing, respectively.

2.3.4.5 N49

N49 是一个典型的红外 Bubble，由于其典型性，关于 N49 和其周围分子云的研究工作有很多，例如Cyganowski et al. (2009); Watson et al. (2008); Zavagno et al. (2010)。如图2.15所示，N49 的 8 μm 波段环状结构规则，其内部的 20 厘米射电辐射也很强。图2.15中五条分子谱线的详细参数见2.3。在 N49 边缘有一个超致

密H II 区(ultra-compact H II region)，位于 1.1 毫米示踪的分子团块边缘。N49 的电离气体速度大约为 90.6 km s^{-1} (Anderson et al., 2014; Lockman, 1989)，到太阳的距离大约为 5.5 kpc Deharveng et al. (2010)。

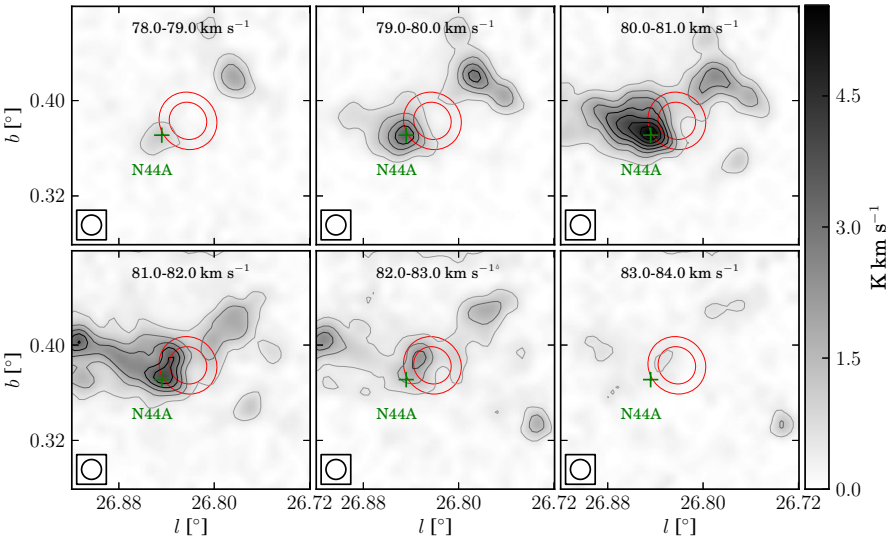

图 2.14: 红外 Bubble N44 ^{13}CO 谱线速度通道图，积分区间从 78.0 km s^{-1} 到 84.0 km s^{-1}，每 1.0 km s^{-1} 积分一次。红色圆圈标记了 N37 的位置，参数见Simpson et al. (2012)，绿色加号标记分子团块的位置。图像背景噪声 (σ) 为 0.13 K km s^{-1}。轮廓等值线从 5.0σ 开始，间隔为 6.9σ。

Figure 2.14. Channel map of ^{13}CO for bubble N44 from 78.0 km s^{-1} to 84.0 km s^{-1} with 1.0 km s^{-1} intervals. The two red circles mark the position of N44 (Simpson et al., 2012), and the green cross marks the peak position of the clump. The rms (σ) of the image background is about 0.13 K km s^{-1}, and the contour levels space linearly from 5σ to the peak with step 6.9σ.

根据 SED 拟合参数，Watson et al. (2008) 在 N49 天区证认出 7 个 YSOs 候选体，其中质量最大的两个候选体在 N49 边缘附近。他们认为 N49 的激发源是一个年龄大于 10^5 yr 的 O5 V 型星，而 N49 周围的 YSOs 是H II 区触发形成的。

Cyganowski et al. (2009) 用 VLA 探测了大约 20 个 EGOs 区域的 I 型和 II 型甲醇脉泽，其中两个 EGOs 在 N49 附近，这两个 EGOs 跟Watson et al. (2008) 证认的两个 YSOs 成协。在 N49 区域，Cyganowski et al. (2009) 探测到了 I 型和 II 型甲醇脉泽信号。其中，II 型 6.7 GHz CH_3OH 甲醇脉泽的存在，说明这里至少有一个大质量恒星正在形成。

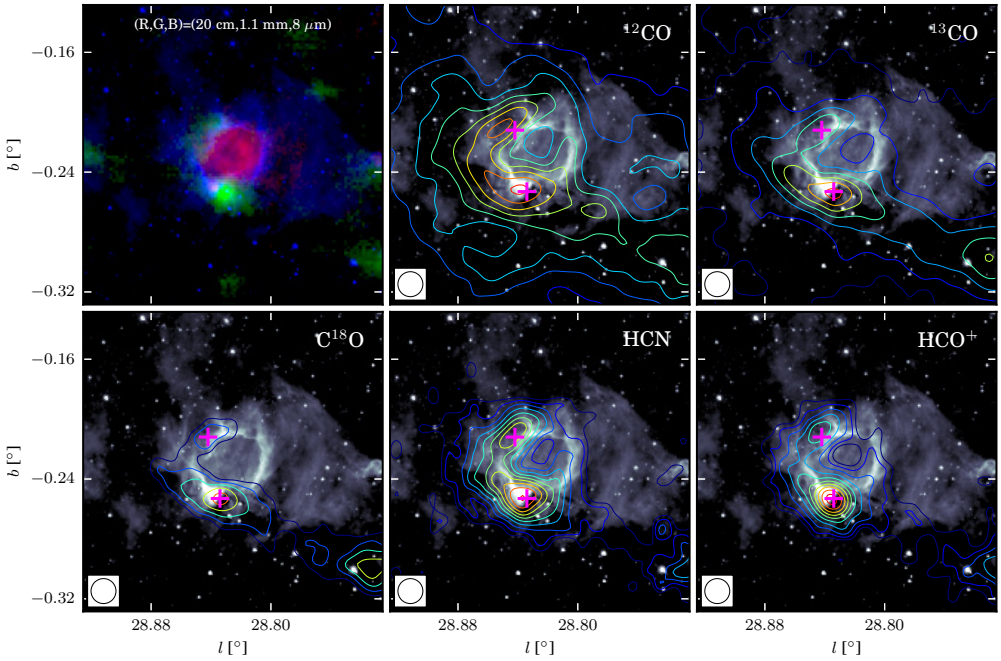

图 2.15: 红外 Bubble N49 图像。左上角是三色图，其中红、绿和蓝色分别代表 20 厘米、1.1 毫米和 8 μm 辐射。其他五图是五条谱线的积分强度轮廓图，背景为 8 μm 中红外辐射，分子团块的位置用紫色加号标记。轮廓图积分区间为 [83.0, 90.0] km s^{-1}。^{12}CO、^{13}CO、C^{18}O、HCN 和 HCO$^+$ 五条谱线的积分强度图噪声 (σ) 分别为 0.44、0.31、0.24、0.06、和 0.07 K km s^{-1}。五条谱线积分强度轮廓图的等值线都从 8σ 开始，间隔分别为 25、19、7、4 和 5σ。

Figure 2.15. Images of N49. The upper left panel is a three color image with 20 cm in red, 1.1 mm in green, and 8 μm in blue. The other five panels are contours of five spectral line integrated intensity maps superimposed on the 8 μm image with positions of clumps marked by purple crosses. The contour maps integrate the intensity from 83.0 km s^{-1} to 90.0 km s^{-1}. The rms (σ) of five line maps, ^{12}CO, ^{13}CO, C^{18}O, HCN, and HCO$^+$, are 0.44, 0.31, 0.24, 0.06, and 0.07 K km s^{-1}, respectively, and these contours all begin at 8σ, spacing with 25, 19, 7, 4, and 5 σ, respectively.

Cyganowski et al. (2009) 利用 JCMT (James Clerk Maxwell Telescope) 观测了 HCO$^+$($J = 3 \rightarrow 2$) 辐射，其速度区间跟 6.7 GHz 甲醇脉泽一致。Cyganowski et al. (2013) 用 45 米望远镜 (Nobeyama Radio Observatory) 观测了 N49 区域，但未探测到水脉泽信号。

Zavagno et al. (2010) 用 *Herschel* 观测的红外巡天数据 (the *Herschel* infrared survey of the Galactic plane, Hi-GAL) 研究了 N49 周围的触发恒星形成过程，他们发

现了一批埋藏得比较深的年轻星，并发现此区域有五个大质量恒星形成区。他们认为 N49 区域的高大质量恒星形成效率可能跟H II 区的膨胀有关。

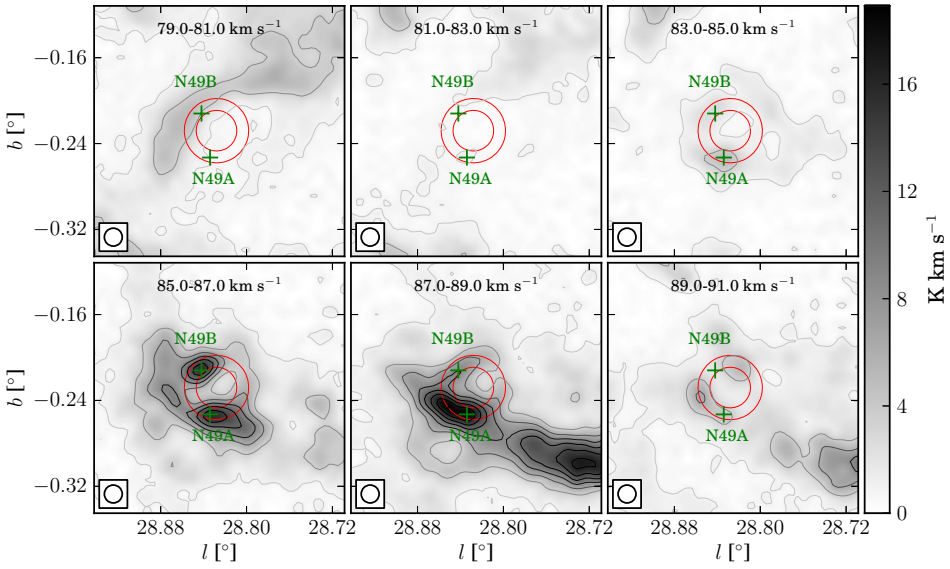

图 2.16: 红外 Bubble N49 ^{13}CO 谱线速度通道图，积分区间从 79.0 km s^{-1} 到 91.0 km s^{-1}，每 2.0 km s^{-1} 积分一次。红色圆圈标记了 N37 的位置，参数见Simpson et al. (2012)，绿色加号标记分子团块的位置。图像背景噪声 (σ) 为 0.17 K km s^{-1}。轮廓等值线从 5.0σ 开始，间隔为 15.5σ。

Figure 2.16. Channel map of ^{13}CO for bubble N49 from 79.0 km s^{-1} to 91.0 km s^{-1} with 2.0 km s^{-1} intervals. The red circles mark the position of N49 (Simpson et al., 2012), and the green crosses mark the peak positions of clumps. The rms (σ) of the image background is about 0.17 K km s^{-1}, and the contour levels space linearly from 5σ to the peak with step 15.5σ.

我们的观测显示，五条分子谱线的辐射主要分布在 N49 周围，跟 8 μm 波段示踪的 PDR 成协。HCO$^+$ 和 HCN 示踪的致密气体呈弧形结构分布，说明这些气体很可能已受H II 区膨胀影响。我们在 N49 周围证认出了两个分子团块，分别为 N49A 和 N48B，如图2.16所示。在图2.16左上角，对应于速度区间 85-87 km s^{-1}，^{13}CO 有非常明显的弧形结构，这个结构很可能是 N49 膨胀形成的。由于在视线方向上有其他成分干扰，我们无法用 CO 和 HCO$^+$ 谱线确认Beaumont et al. (2010) 给出的该区域的外向分子流候选体。

2.3.4.6 N55

N55 的视向速度和到太阳的距离分别为 93 km s^{-1} 和 8.4 kpc (Deharveng et al., 2010)。Rahman et al. (2010) 认为这个区域有很多大质量恒星恒星正在形成，是一个恒星形成复合体 (star forming complex, SFC)。我们观测的五条分子谱线的分布见图2.17，详细的观测参数见表2.3。

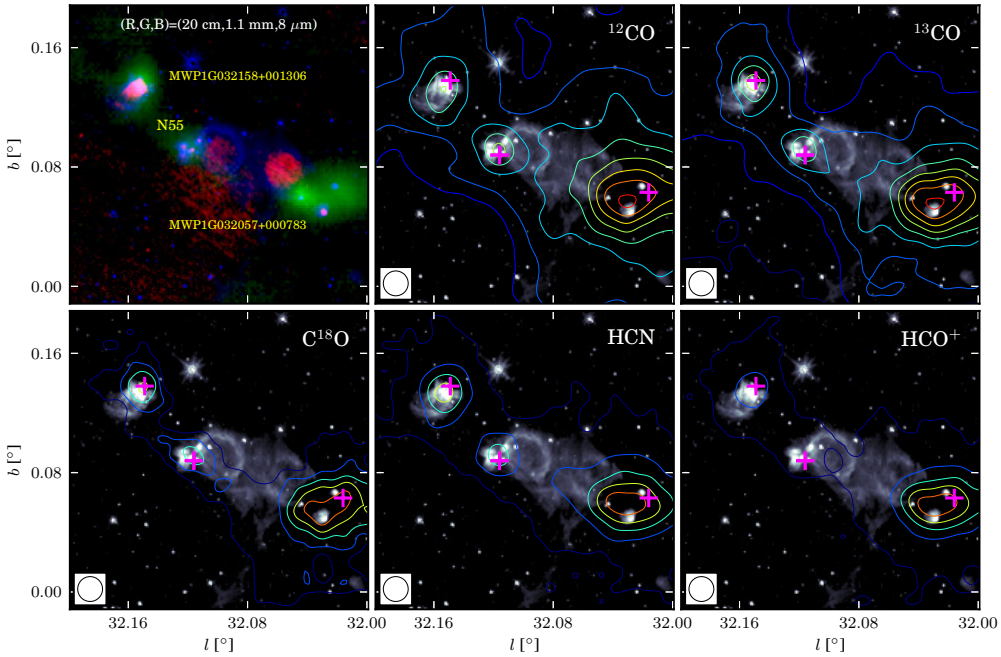

图 2.17: 红外 Bubble N55 图像。左上角是三色图，其中红、绿和蓝色分别代表 20 厘米、1.1 毫米和 8 μm 辐射。其他五图是五条谱线的积分强度轮廓图，背景为 8 μm 中红外辐射，分子团块的位置用紫色加号标记。轮廓图积分区间为 [89.0, 103.0] km s^{-1}。^{12}CO、^{13}CO、C^{18}O、HCN 和 HCO^+ 五条谱线的积分强度图噪声 (σ) 分别为 0.49、0.26、0.27、0.10、和 0.10 K km s^{-1}。五条谱线积分强度轮廓图的等值线都从 8σ 开始，间隔分别为 47、29、7、19 和 26σ。

Figure 2.17. Images of N55. The upper left panel is a three color image with 20 cm in red, 1.1 mm in green, and 8 μm in blue. The other five panels are contours of five spectral line integrated intensity maps superimposed on the 8 μm image with positions of clumps marked by purple crosses. The contour maps integrate the intensity from 89.0 km s^{-1} to 103.0 km s^{-1}. The rms (σ) of five line maps, ^{12}CO, ^{13}CO, C^{18}O, HCN, and HCO^+, are 0.49, 0.26, 0.27, 0.10, and 0.10 K km s^{-1}, respectively, and these contours all begin at 8σ, spacing with 47, 29, 7, 19, and 26σ, respectively.

如图2.17所示，在 N55 附近还有一些致密的H II 区，其中有两个角尺度比较大，分别为 MWPIG032057+000783 和 MWPIG032158+001306 (Simpson et al., 2012)。N55 内部的 20 厘米自由-自由辐射比较弥散，但是 MWPIG032057+000783 和 MWPIG032158+001306 内部的自由-自由辐射较强。20 厘米连续谱辐射还显示，在红外 Bubble N55 附近至少有三个超致密H II 区，说明 N55 附近可能有一个年轻的大质量恒星星团。

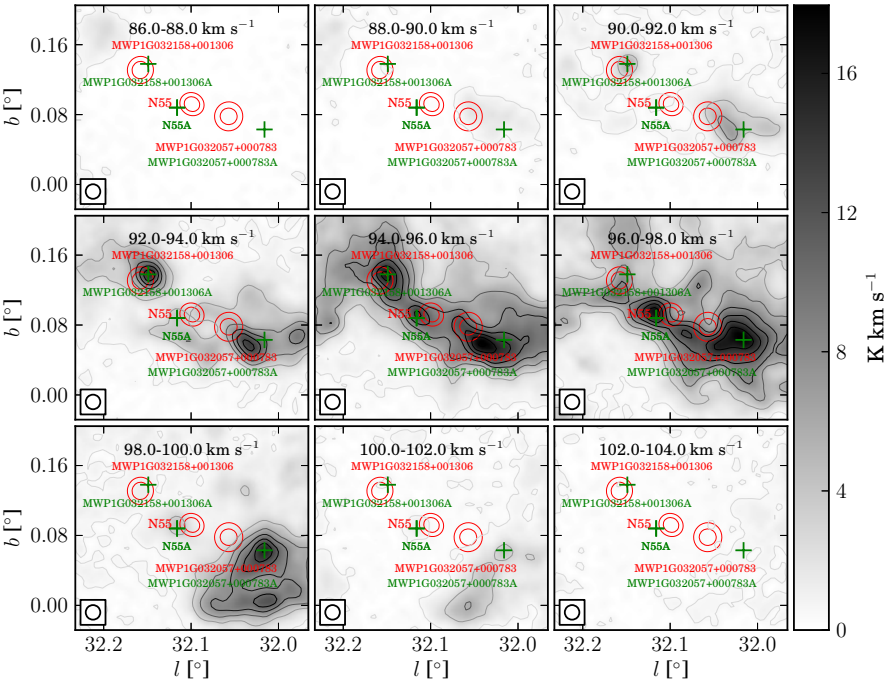

图 2.18: 红外 Bubble N55 ^{13}CO 谱线速度通道图，积分区间从 86.0 km s^{-1} 到 104.0 km s^{-1}，每 2.0 km s^{-1} 积分一次。红色圆圈标记了 N55 的位置，参数见Simpson et al. (2012)，绿色加号标记分子团块的位置。图像背景噪声 (σ) 为 0.10 K km s^{-1}。轮廓等值线从 5.0σ 开始，间隔为 25.3σ。

Figure 2.18. Channel map of ^{13}CO for bubble N55 from 86.0 km s^{-1} to 104.0 km s^{-1} with 2.0 km s^{-1} intervals. The red circles delineate the position of N55 from Simpson et al. (2012), and the green crosses mark the peak position of clumps. The rms (σ) of the image background is about 0.10 K km s^{-1}, and the contour levels space linearly from 5σ to the peak with step 25.3σ.

我们在这个区域总共证认出三个分子团块，他们的位置在图2.17和图2.18中分别用紫色和绿色加号标出。如图2.17所示，这些分子团块跟 1.1 毫米连续谱成协。

在分子团块 N55A 附近，CO 谱线的线翼 (包括红翼和蓝翼) 很宽，说明 N55A

内部可能有外向分子流活动。20 厘米射电连续谱显示这个区域至少有三个超致密H II 区，因此分子团块内部的外向分子流可能不止一个。但是以青海站望远镜的分辨率，我们无法确定外向分子流跟超致密H II 区的对应关系。因此，在计算外向分子流参数的时候，我们暂时把这里的外向分子流当作一个来处理。由于红翼和蓝翼峰值的空间位置是重合的，我们无法估计这个外向分子流的空间尺度和年龄。MWP1G032158+001306A 和 MWP1G032057+000783A 的 CO 和 HCO^+ 谱线在视线方向上已被其他成分干扰，以青海站望远镜的空间分辨率，我们无法用分子谱线探测外向分子流。

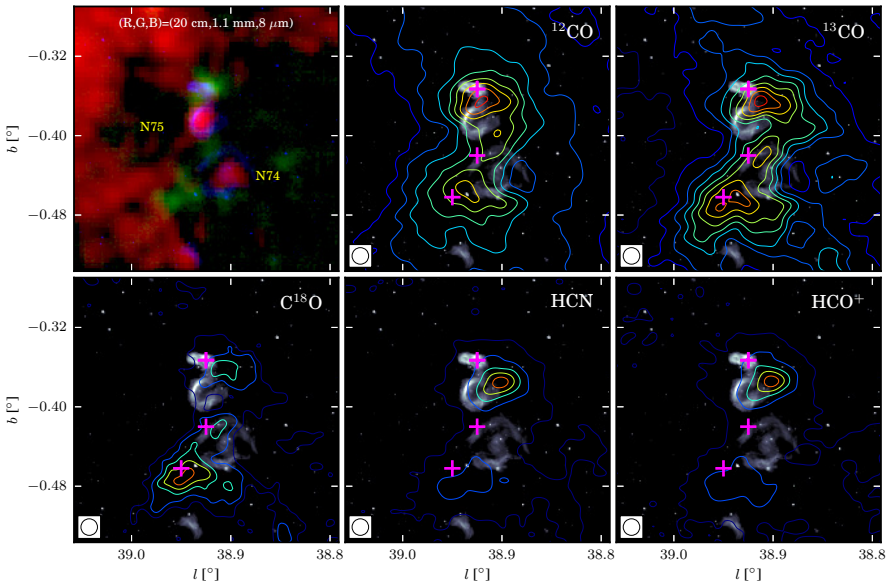

图 2.19: 红外 Bubble N75 和 N74 图像。左上角是三色图，其中红、绿和蓝色分别代表 20 厘米、1.1 毫米和 8 μm 辐射。其他五图是五条谱线的积分强度轮廓图，背景为 8 μm 中红外辐射，分子团块的位置用紫色加号标记。轮廓图积分区间为 [37.0, 44.0] km s^{-1}。^{12}CO、^{13}CO、$C^{18}O$、HCN 和 HCO^+ 五条谱线的积分强度图噪声 (σ) 分别为 0.32、0.18、0.18、0.06,、和 0.06, K km s^{-1}。五条谱线积分强度轮廓图的等值线都从 8σ 开始，间隔分别为 50、26、7、21 和 24σ。

Figure 2.19. Images of N75 and N74. The upper left panel is a three color image with 20 cm in red, 1.1 mm in green, and 8 μm in blue. The other five panels are contours of five spectral line integrated intensity maps superimposed on the 8 μm image with positions of clumps marked by purple crosses. The contour maps integrate the intensity from 37.0 km s^{-1} to 44.0 km s^{-1}. The rms (σ) of five line maps, ^{12}CO, ^{13}CO, $C^{18}O$, HCN, and HCO^+, are 0.32, 0.18, 0.18, 0.06, and 0.06 K km s^{-1}, respectively, and these contours all begin at 8σ, spacing with 50, 26, 7, 21, and 24σ, respectively.

2.3.4.7 N75 和 N74

N74 和 N75 是大质量恒星形成区 G38.9-0.40 (Alexander et al., 2013) 中两个比较明显的红外 Bubble。如图2.19所示，N75 在 8 μm 波段的结构虽然不闭合，但其形状十分规则且边界清晰；相比而言，N74 的形状略显不规则，8 μm 波段辐射也较弱。这两个红外 Bubble 的 20 厘米射电连续辐射都比较弱。图2.19还展示了五条分子谱线的辐射分布，谱线的详细观测参数见表2.3。

根据氢射电复合线观测 (Anderson et al., 2014)，N74 和 N75 的视向速度为 42.1 km s^{-1}，这个碳射电复合线的速度一致 (39.2 km s^{-1}) (Wenger et al., 2013)。因为这两个H II 区的运动学远近距离未分辨出，所以我们简单采用近运动学距离——2.8 kpc。

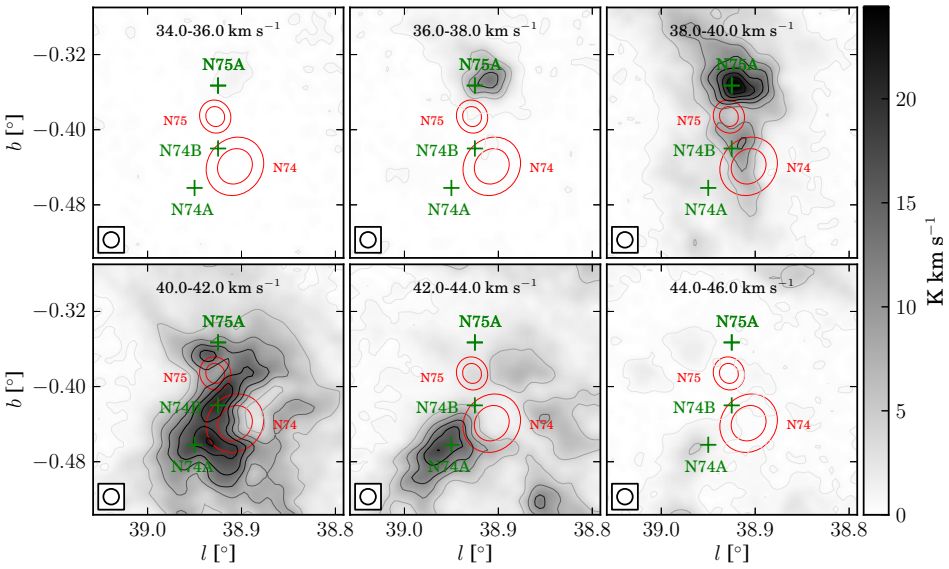

图 2.20: 红外 Bubble N75 和 N74 ^{13}CO 谱线速度通道图，积分区间从 34.0 km s^{-1} 到 46.0 km s^{-1}，每 2.0 km s^{-1} 积分一次。红色圆圈标记了 N75 和 N74 的位置，参数见Simpson et al. (2012)，绿色加号标记分子团块的位置。图像背景噪声 (σ) 为 0.10 K km s^{-1}。轮廓等值线从 5.0σ 开始，间隔为 36σ。

Figure 2.20. Channel map of ^{13}CO for bubble N75 from 34.0 km s^{-1} to 46.0 km s^{-1} with 2.0 km s^{-1} intervals. The two red circles delineate the position of N75 (Simpson et al., 2012), and the green crosses mark the peak position of clumps. The rms (σ) of the image background is about 0.10 K km s^{-1}, and the contour levels space linearly from 5σ to the peak with step 36σ.

Sherman (2012) 用 CARMA (Combined Array for Research in Millimeter-wave As-

trnomy) 研究了 N74 区域的四条分子谱线，HCN、HCO^+、N_2H^+ 和 CS，以及 3.3 毫米射电连续谱辐射。他们发现有迹象表明 N74 边缘的分子云的碎裂程度比一般的暗云大，所以在 N74 区域存在触发恒星形成过程，但是这里的触发恒星形成过程跟经典的分子云堆积塌缩模型并不一致。

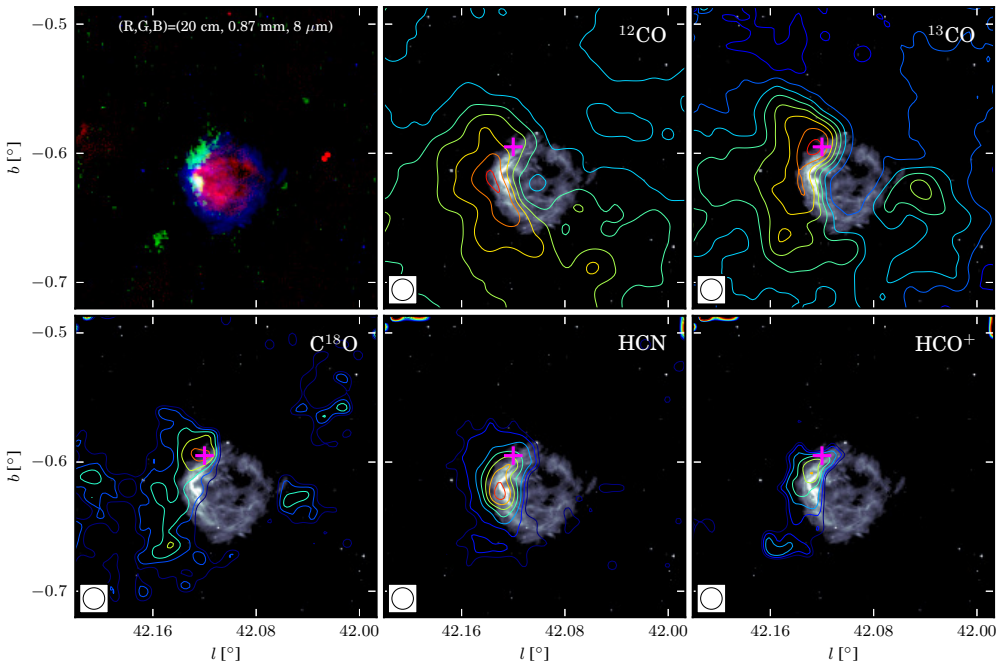

图 2.21: 红外 Bubble N82 图像。左上角是三色图，其中红、绿和蓝色分别代表 20 厘米、1.1 毫米和 8 μm 辐射。其他五图是五条谱线的积分强度轮廓图，背景为 8 μm 中红外辐射，分子团块的位置用紫色加号标记。轮廓图积分区间为 [63.0, 72.0] km s^{-1}。^{12}CO、^{13}CO、$C^{18}O$、HCN 和 HCO^+ 五条谱线的积分强度图噪声 (σ) 分别为 0.38、0.21、0.21、0.08,、和 0.08, K km s^{-1}。五条谱线积分强度轮廓图的等值线都从 8σ 开始，间隔分别为 28、17、3、4 和 2σ。

Figure 2.21. Images of N82. The upper left panel is a three color image with 20 cm in red, 0.87 mm in green, and 8 μm in blue. The other five panels are contours of five spectral line integrated intensity maps superimposed on the 8 μm image with positions of clumps marked by purple crosses. The contour maps integrate the intensity from 63.0 km s^{-1} to 72.0 km s^{-1}. The rms (σ) of five line maps, ^{12}CO, ^{13}CO, $C^{18}O$, HCN, and HCO^+, are 0.38, 0.21, 0.21, 0.08, and 0.08 K km s^{-1}, respectively, and these contours all begin at 8 σ, spacing with 28, 17, 3, 4, and 2σ, respectively.

Alexander et al. (2013) 利用多波段的数据研究了 N74 和 N75 区域的恒星形成过程。他们认为这两个红外 Bubble 的驱动源都为光谱型 O9.5V 的大质量恒星，其

周围还伴有一些星团。虽然他们证认出 162 个年轻星候选体，但是他们认为这个天区并没有触发恒星形成的直接证据，可能是由于这两个红外 Bubble 还处于早期阶段，还没来得及触发恒星形成。他们发现在此区域 YSOs 的质量密度跟气体质量密度之间仍然有很强的相关性，说明影响气体密度对恒星形成的影响比附近恒星形成活动的反馈更重要。

如图2.19所示，CO 辐射跟 8 μm 波段辐射分布一致。我们在这个天区共证认出三个分子团块，见图2.19和图2.20中的紫色和绿色加号。在此区域的视线方向上由于其他成分的干扰，我们无法在这三个分子团块中搜索外向分子流，也无法确认Beaumont et al. (2010) 给出的外向分子流候选体。

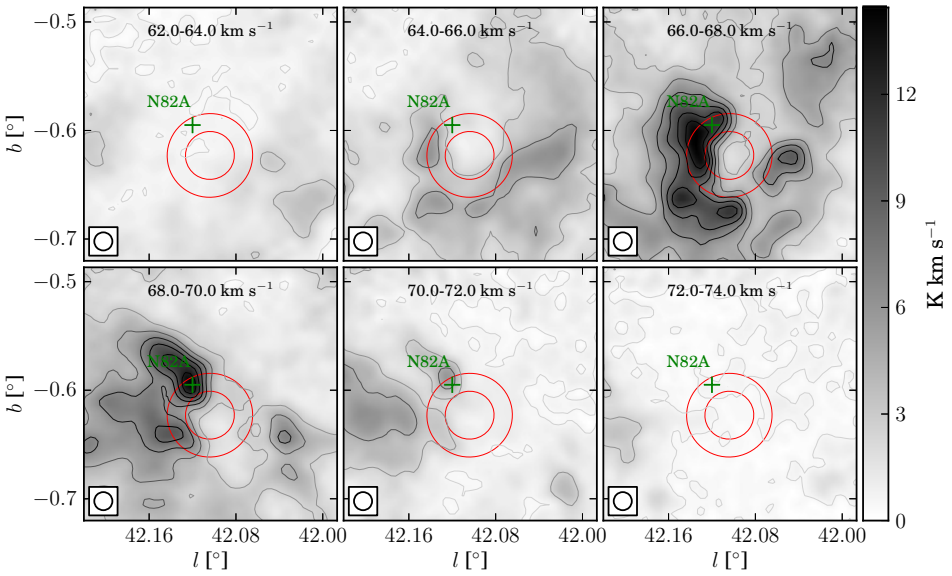

图 2.22: 红外 Bubble N82 ^{13}CO 谱线速度通道图，积分区间从 62.0 km s^{-1} 到 74.0 km s^{-1}，每 2.0 km s^{-1} 积分一次。红色圆圈标记了 N82 的位置，参数见Simpson et al. (2012)，绿色加号标记分子团块的位置。图像背景噪声 (σ) 为 0.10 K km s^{-1}。轮廓等值线从 3.0σ 开始，间隔为 20.6σ。

Figure 2.22. Channel map of ^{13}CO for bubble N82 from 62.0 km s^{-1} to 74.0 km s^{-1} with 2.0 km s^{-1} intervals. The red circles delineate the position of N82 provided by Simpson et al. (2012), and the green cross marks the peak position of the clump. The rms (σ) of the image background is about 0.10 K km s^{-1}, and the contour levels space linearly from 3σ to the peak with step 20.6σ.

2.3.4.8 N82

如图2.21所示，红外 Bubble N82 形状比较规则，其内部的 20 厘米连续谱辐射也比较强，图中五条分子谱线的观测参数见表2.3。从分子辐射的分布上可以明显看出，分子云主要分布在 N82 的一侧，而等高线的轮廓表明 N82 附近的分子云有被挤压的迹象。

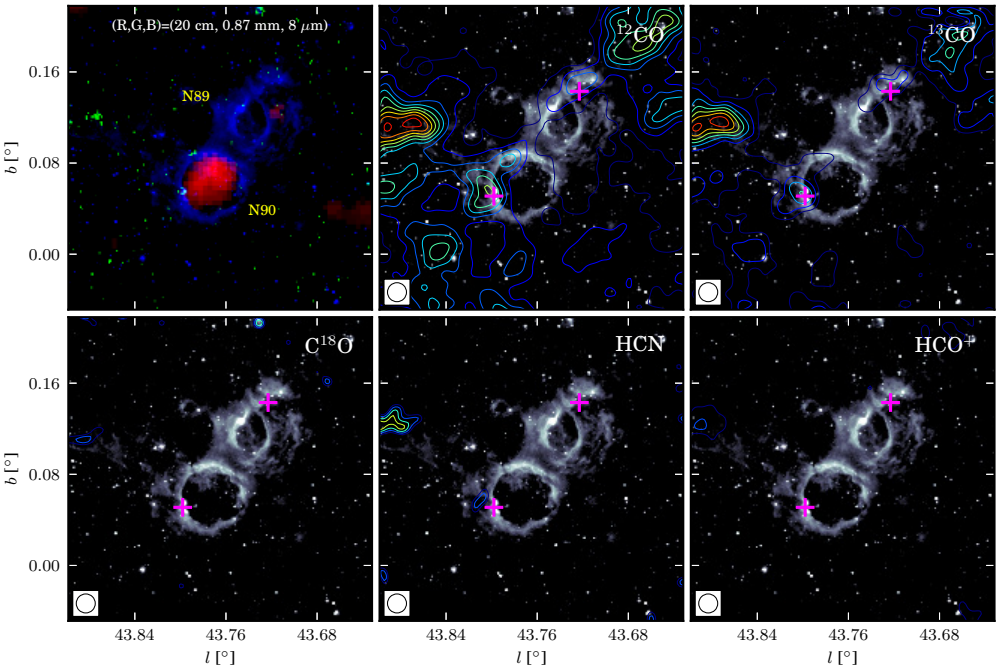

图 2.23: 红外 Bubble N89 和 N90 的图像。左上角是三色图，其中红、绿和蓝色分别代表 20 厘米、1.1 毫米和 8 μm 辐射。其他五图是五条谱线的积分强度轮廓图，背景为 8 μm 中红外辐射，分子团块的位置用紫色加号标记。轮廓图积分区间为 [64.0, 75.0] km s^{-1}。^{12}CO、^{13}CO、C^{18}O、HCN 和 HCO$^+$ 五条谱线的积分强度图噪声 (σ) 分别为 0.37、0.18、0.18、0.06,、和 0.07, K km s^{-1}。五条谱线积分强度轮廓图的等值线都从 8σ 开始，间隔分别为 15、10、3、2 和 5σ。

Figure 2.23. Images of N89 and N90. The upper left panel is a three color image with 20 cm in red, 0.87 mm in green, and 8 μm in blue. The other five panels are contours of five spectral line integrated intensity maps superimposed on the 8 μm image with positions of clumps marked by purple crosses. The contour maps integrate the intensity from 64.0 km s^{-1} to 75.0 km s^{-1}. The rms (σ) of five line maps, ^{12}CO, ^{13}CO, C^{18}O, HCN, and HCO$^+$, are 0.37, 0.18, 0.18, 0.06, and 0.07 K km s^{-1}, respectively, and these contours all begin at 8σ, spacing with 15, 10, 3, 2, and 5σ, respectively.

Lockman (1989) 根据 Hα 给出 N82 区域的视向速度为 66.4 km s^{-1}，这个速度跟Beaumont et al. (2010) 利用 CO ($J = 3 \rightarrow 2$) 得到的视向速度，66.5 km s^{-1}，一致。根据Stead et al. (2010) 和Roman-Duval et al. (2009) 给出的研究结果，我们采用 N82 的近运动学距离——4.3 kpc，而暂不采用Deharveng et al. (2010) 建议的远运动学距离。

Watson et al. (2010) 在 N82 的分子云壳层中证认出 6 个 YSOs，他们发现 YSOs 的面密度在 8 μm 的峰值地方有显著的增加，说明 N82 区域存在触发恒星形成现象。利用新的蒙特卡洛方法 (Monte Carlo method)，Stead et al. (2011) 推测 N82 附近星团的年龄为 1.8 Myr。

青海站望远镜的观测显示，N82 区域分子云主要分布在其周围，说明 N82 的驱动源正在压缩分子云。我们在 N82 附近证认出一个分子团块，见图2.22。由于多个成分的干扰，此区域在青海望远镜的分辨率下，无法用分子谱线证认外向分子流。

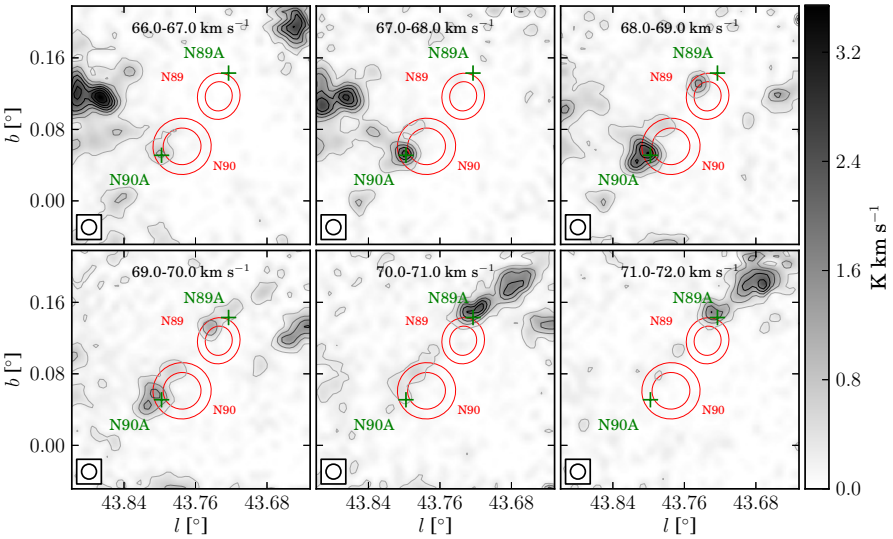

图 2.24: 红外 Bubble N89 和 N90 ^{13}CO 谱线速度通道图，积分区间从 66.0 km s^{-1} 到 72.0 km s^{-1}，每 1.0 km s^{-1} 积分一次。红色圆圈标记了 N8 和 N90 的位置，参数见Simpson et al. (2012)，绿色加号标记分子团块的位置。图像背景噪声 (σ) 为 0.05 K km s^{-1}。轮廓等值线从 5.0σ 开始，间隔为 8.6σ。

Figure 2.24. Channel map of ^{13}CO for bubble N89 and N90 from 66.0 km s^{-1} to 72.0 km s^{-1} with 1.0 km s^{-1} intervals. The red circles delineate the position of N89 and N90 (Simpson et al., 2012), and the green crosses mark the peak position of clumps. The rms (σ) of the image background is about 0.05 K km s^{-1}, and the contour levels space linearly from 5σ to the peak with step 8.6σ.

2.3.4.9 N89 和 N90

N89 和 N90 两个红外 Bubble 的角尺度都比较大，且 8 μm 信号都比较微弱。N90 形状比较规则，其内部有弱的 20 cm 射电连续谱辐射，相比之下，N89 形状不规则，内部也没有发现射电连续谱辐射。这个天区电离气体的速度为 70.5 km s^{-1} (Anderson et al., 2014)。Bania et al. (2012) 利用 Arecibo 观测的射电复合线数据表明，N89 和 N90 的速度分别为 73.1 km s^{-1} 和 70.5 km s^{-1}。N89 和 N90 到太阳的距离约为 6.1 kpc (Deharveng et al., 2010)。

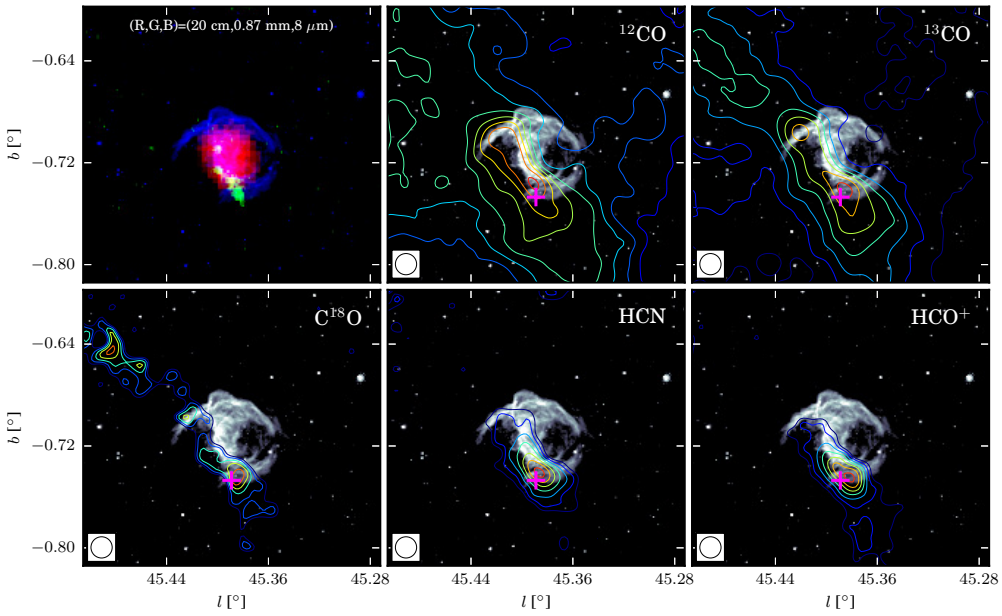

图 2.25: 红外 Bubble N95 的图像。左上角是三色图，其中红、绿和蓝色分别代表 20 厘米、0.87 毫米和 8 μm 辐射。其他五图是五条谱线的积分强度轮廓图，背景为 8 μm 中红外辐射，分子团块的位置用紫色加号标记。轮廓图积分区间为 [57.0, 63.0] km s^{-1}。^{12}CO、^{13}CO、C^{18}O、HCN 和 HCO$^+$ 五条谱线的积分强度图噪声 (σ) 分别为 0.32、0.19、0.19、0.05、和 0.05 K km s^{-1}。五条谱线积分强度轮廓图的等值线都从 8σ 开始，间隔分别为 22、18、2、5 和 4σ。

Figure 2.25. Images of N95. The upper left panel is a three color image with 20 cm in red, 0.87 mm in green, and 8 μm in blue. The other five panels are contours of five spectral line integrated intensity maps superimposed on the 8 μm image with positions of clumps marked by purple crosses. The contour maps integrate the intensity from 57.0 km s^{-1} to 63.0 km s^{-1}. The rms (σ) of five line maps, ^{12}CO, ^{13}CO, C^{18}O, HCN, and HCO$^+$, are 0.32, 0.19, 0.19, 0.05, and 0.05 K km s^{-1}, respectively, and these contours all begin at 8σ, spacing with 22, 18, 2, 5, and 4σ, respectively.

图2.5中 N89 和 N90 的平均 CO 谱线表明，在 $\sim 60-62$ km s^{-1} 速度区间有比较强的 CO 辐射，这个速度成分其实是人马臂 (Sagittarius Arm) 的一部分 (Sawada et al., 2012)。但是这个速度没有对应的 Hα 发射，并且这个速度的积分强度跟 N89 和 N90 在空间位置上并不相关。所以我们认为 $\sim 60-62$ km s^{-1} 速度区间的分子云跟 N89 和 N90 不成协。

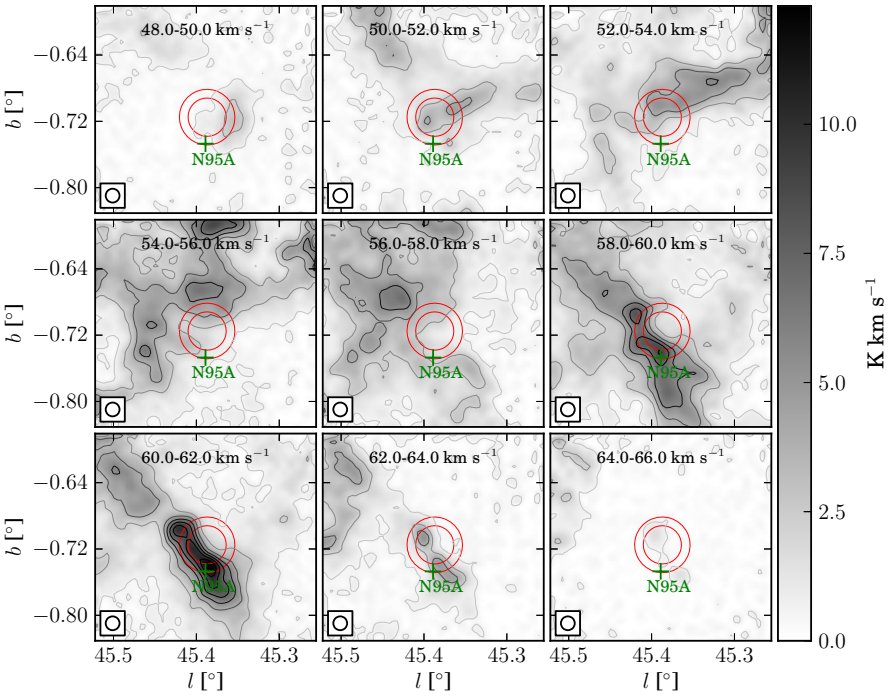

图 2.26: 红外 Bubble N95 ^{13}CO 谱线速度通道图，积分区间从 48.0 km s^{-1} 到 66.0 km s^{-1}，每 2.0 km s^{-1} 积分一次。红色圆圈标记了 N8 和 N95 的位置，参数见Simpson et al. (2012)，绿色加号标记分子团块的位置。图像背景噪声 (σ) 为 0.11 K km s^{-1}。轮廓等值线从 5.0σ 开始，间隔为 14.9σ。

Figure 2.26. Channel map of ^{13}CO for bubble N95 from 48.0 km s^{-1} to 66.0 km s^{-1} with 2.0 km s^{-1} intervals. The red circles delineate the the position of N95 given by Simpson et al. (2012), and the green cross marks the peak position of the clump. The rms (σ) of the image background is about 0.11 K km s^{-1}, and the contour levels space linearly from 5σ to the peak with step 14.9σ.

如图2.23所示，CO 谱线在 70.3 和 68.4 km s^{-1} 速度上的成分跟 N89 和 N90 有很好的相关性，谱线的详细观测参数见表2.3。在这两个红外 Bubble 附近没有探测到 C^{18}O 辐射，HCO$^+$ 和 HCN 的辐射也非常微弱。由于没有探测到 C^{18}O 辐射，我们改用 ^{13}CO 来证认分子团块，所以这个区域的分子团块有一定的不确定性。我们

证认的两个分子团块已经在图2.24中用绿色加号标出。N89 和 N90 在视线方向上有其他速度成分干扰，所以用分子谱线无法证认外向分子流。

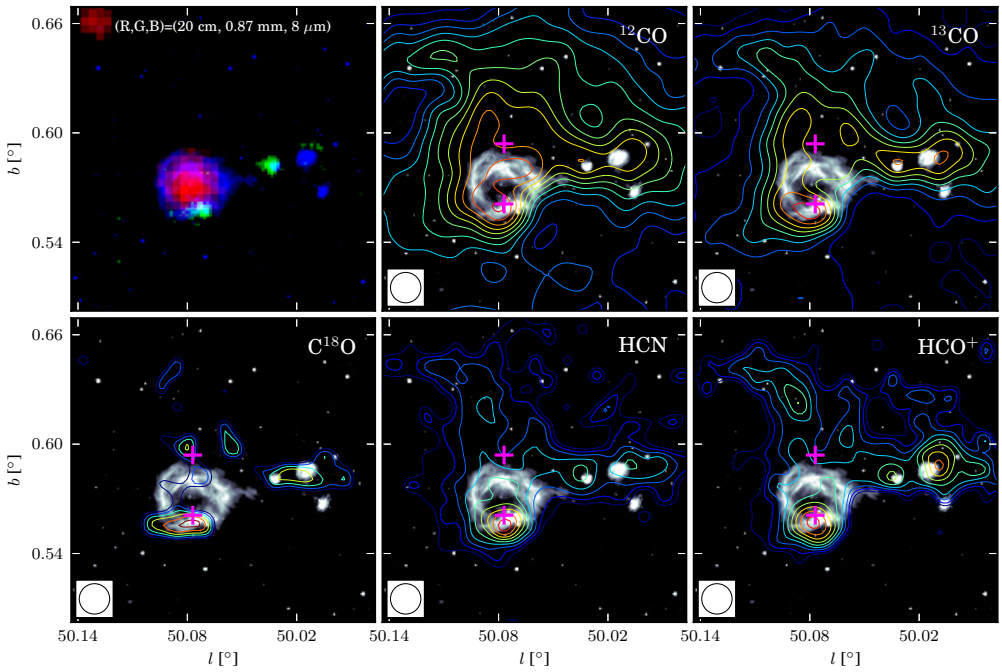

图 2.27: 红外 Bubble N105 的图像。左上角是三色图，其中红、绿和蓝色分别代表 20 厘米、0.87 毫米和 8 μm 辐射。其他五图是五条谱线的积分强度轮廓图，背景为 8 μm 中红外辐射，分子团块的位置用紫色加号标记。轮廓图积分区间为 [-6.0, 2.0] km s^{-1}。^{12}CO、^{13}CO、C^{18}O、HCN 和 HCO$^+$ 五条谱线的积分强度图噪声 (σ) 分别为 0.40、0.22、0.22、0.06、和 0.06 K km s^{-1}。五条谱线积分强度轮廓图的等值线都从 8σ 开始，间隔分别为 21、14、2、3 和 3σ。

Figure 2.27. Images of N105. The upper left panel is a three color image with 20 cm in red, 0.87 mm in green, and 8 μm in blue. The other five panels are contours of five spectral line integrated intensity maps superimposed on the 8 μm image with positions of clumps marked by purple crosses. The contour maps integrate the intensity from -6.0 km s^{-1} to 2.0 km s^{-1}. The rms (σ) of five line maps, ^{12}CO, ^{13}CO, C^{18}O, HCN, and HCO$^+$, are 0.40, 0.22, 0.22, 0.06, and 0.06 K km s^{-1}, respectively, and these contours all begin at 8σ level, spacing with 21, 14, 2, 3, and 3σ, respectively.

2.3.4.10 N95

如图2.25 所示，红外 Bubble N95 的 8 μm 波段环形结构不封闭，但是其边缘形状比较规则且其内部的 20 厘米连续谱线辐射很强。图2.25 中五条分子谱线的观测

参数见表2.3。根据 Deharveng et al. (2010) 给出的结果，N95 的视向速度和距离分别为 52.5 km s^{-1} 和 8.0 kpc。

五条分子谱线的空间分布表明，N95 天区的分子云主要沿着 8 μm 波段的弧形结构分布。从 C^{18}O ($J = 1 \rightarrow 0$) 谱线的积分强度图上可以看出，N95 附近的分子云是一个大的纤维结构 (filament) 的一部分，而H II 区的膨胀已经对其附近分子云造成了挤压。我们在 N95 附近发现一个分子团块——N95A，团块的位置在图2.25和图2.26中已分别用紫色和绿色加号标出。如图2.5中的分子谱线所示，N95 天区视线方向成分复杂，以青海站望远镜的分辨率，我们无法探测 N95A 内部的外向分子流。

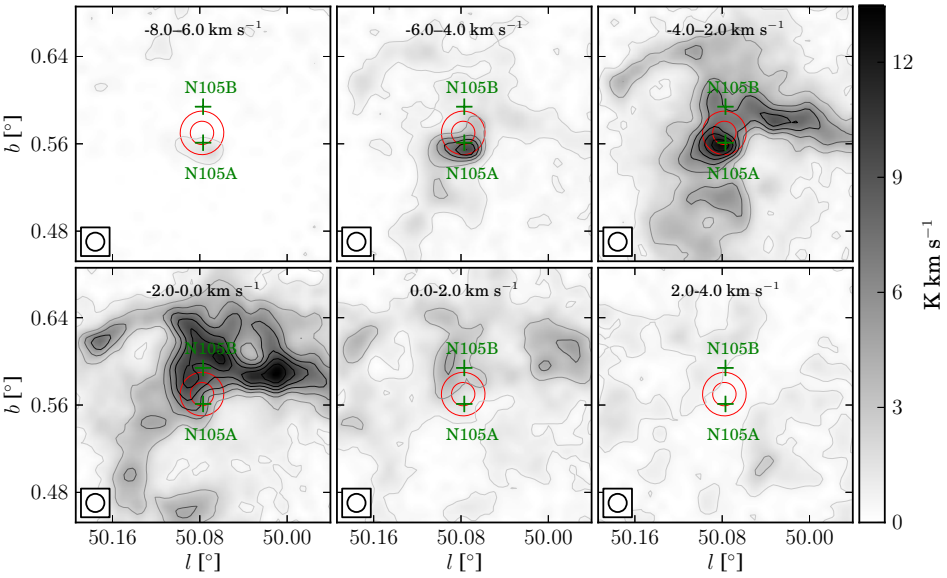

图 2.28: 红外 Bubble N105 ^{13}CO 谱线速度通道图，积分区间从 -8.0 km s^{-1} 到 4.0 km s^{-1}，每 2.0 km s^{-1} 积分一次。红色圆圈标记了 N105 的位置，参数见Simpson et al. (2012)，绿色加号标记分子团块的位置。图像背景噪声 (σ) 为 0.11 K km s^{-1}。轮廓等值线从 5σ 开始，间隔为 17σ。

Figure 2.28. Channel map of ^{13}CO for bubble N105 from -8.0 km s^{-1} to 4.0 km s^{-1} with 2.0 km s^{-1} intervals. The red circles delineate the position of N105 provided by Simpson et al. (2012), and the green crosses mark the peak position of clumps. The rms (σ) of the image background is about 0.11 K km s^{-1}, and the contour levels space linearly from 5σ to the peak with step 17σ.

2.3.4.11 N105

红外 Bubble N105 的角尺度比较小，其内部的 20 厘米连续谱辐射比较弱。图2.27中展示了 N105 的 RGB 三色图——20 厘米连续谱 (红色)、0.87 mm 连续谱 (绿色) 和 8 μm 辐射 (蓝色)——和五条分子谱线的积分强度分布图，谱线的具体观测参数见表2.3。根据Anderson et al. (2012a) 的观测结果，N105 到太阳的距离和视向速度分别为 11.2 kpc 和 -1.1 km s^{-1}。

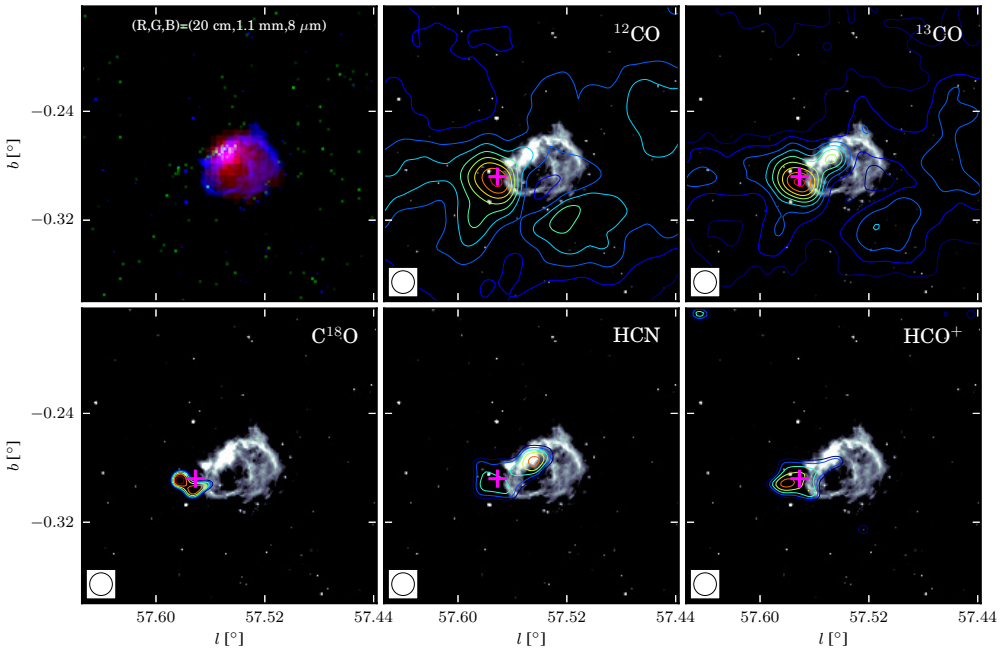

图 2.29: 红外 Bubble N123 的图像。左上角是三色图，其中红、绿和蓝色分别代表 20 厘米、1.1 毫米和 8 μm 辐射。其他五图是五条谱线的积分强度轮廓图，背景为 8 μm 中红外辐射，分子团块的位置用紫色加号标记。轮廓图积分区间为 [-4.0, 6.0] km s^{-1}。^{12}CO、^{13}CO、C^{18}O、HCN 和 HCO$^+$ 五条谱线的积分强度图噪声 (σ) 分别为 0.26、0.17、0.16、0.05、和 0.06 K km s^{-1}。五条谱线积分强度轮廓图的等值线都从 8σ 开始，间隔分别为 27、13、1、3 和 3σ。

Figure 2.29. Images of N123. The upper left panel is a three color image with 20 cm in red, 1.1 mm in green, and 8 μm in blue. The other five panels are contours of five spectral line integrated intensity maps superimposed on 8 μm image with positions of clumps marked by purple crosses. The contour maps integrate the intensity from -4.0 km s^{-1} to 6.0 km s^{-1}. The rms (σ) of five line maps, ^{12}CO, ^{13}CO, C^{18}O, HCN, and HCO$^+$, are 0.26, 0.17, 0.16, 0.05, and 0.06 K km s^{-1}, respectively, and these contours all begin at 8σ, spacing with 27, 13, 1, 3, and 3σ, respectively.

根据青海站的观测，我们在 N105 边缘发现有两个分子团块——N105A 和 N105B，分子团块的位置已在图2.27和图2.28中分别用紫色和绿色加号标出。N105A 区域的谱线线翼并没有明显的展宽，但是 N105B 区域的谱线表明这个区域很可能有一个外向分子流。团块 N105B 分子谱线的蓝翼非常清晰，但是红翼有其他成分干扰。关于此外向分子流的详细结果，见 §2.4。

2.3.4.12 N123

红外 Bubble N123 角尺度比较小，N123 的 RGB 三色图和五条分子谱线的积分强图分布见图2.29，具体的观测参数见表2.3。N123 天区 20 厘米和 6 厘米射电连续谱辐射 (White et al., 2005) 显示，在 N123 边缘很可能有一个超致密H II 区，且此超致密H II 区的 24 μm 辐射 (Carey et al., 2009; Gutermuth et al., 2015) 很强。这个H II 区示踪的大质量恒星位于 N123 边缘位置，所以我们认为它很可能是在 N123 膨胀过程中触发形成的。

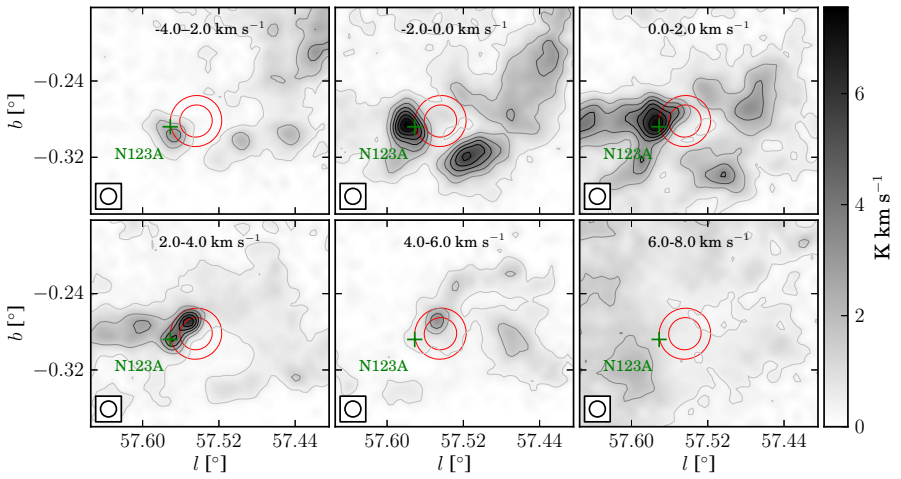

图 2.30: 红外 Bubble N123 ^{13}CO 谱线速度通道图，积分区间从 -4.0 km s^{-1} 到 8.0 km s^{-1}，每 2.0 km s^{-1} 积分一次。红色圆圈标记了 N123 的位置，参数见Simpson et al. (2012)，绿色加号标记分子团块的位置。图像背景噪声 (σ) 为 0.11 K km s^{-1}。轮廓等值线从 5σ 开始，间隔为 13.7σ。

Figure 2.30. Channel map of ^{13}CO for bubble N123 from -4.0 km s^{-1} to 8.0 km s^{-1} with 2.0 km s^{-1} intervals. The red circles delineate the position of N123 provided by Simpson et al. (2012), and the green cross marks the peak position of the clump. The rms (σ) of the image background is about 0.11 K km s^{-1}, and the contour levels space linearly from 5σ to the peak with step 13.7σ.

虽然 Watson et al. (2010) 建议 N123 的视向速度为 25 km s^{-1}，但是在这个速度区间上，CO 辐射的空间分布跟 8 μm 波段并不成协。Watson et al. (2003) 的观测显示，此天区 H110α 和 H_2CO 的视向速度分别为 6.3 和 2.0 km s^{-1}，所以我们认为这个速度区间跟 N123 是成协的。Watson et al. (2003) 给出 N123 的距离为 8.6 kpc。

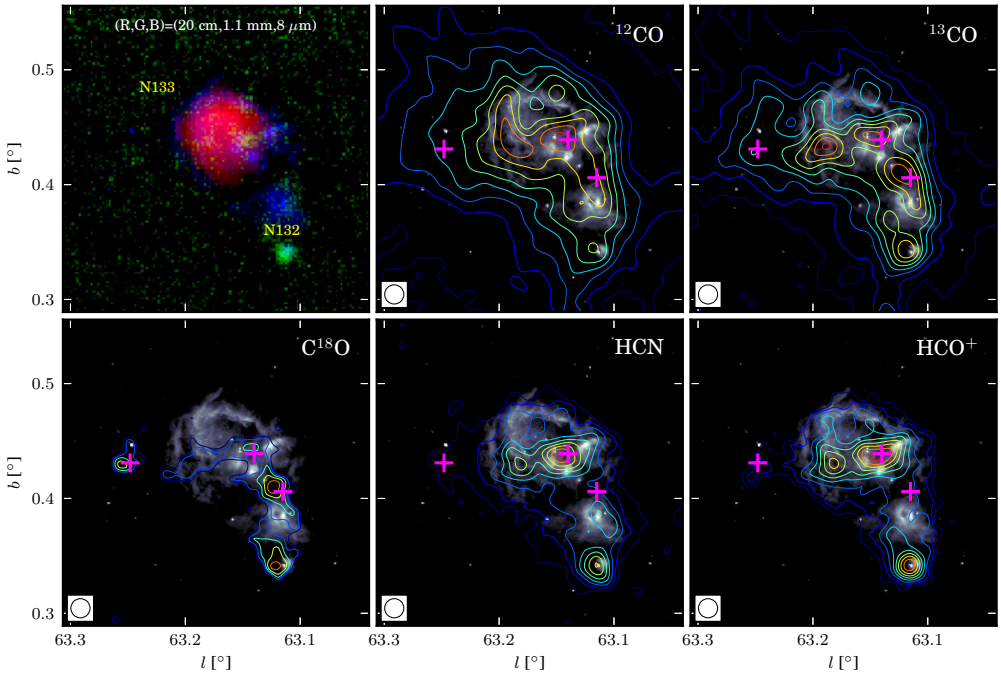

图 2.31: 红外 Bubble N133 的图像。左上角是三色图，其中红、绿和蓝色分别代表 20 厘米、1.1 毫米和 8 μm 辐射。其他五图是五条谱线的积分强度轮廓图，背景为 8 μm 中红外辐射，分子团块的位置用紫色加号标记。轮廓图积分区间为 [15.0, 25.0] km s^{-1}。^{12}CO、^{13}CO、C^{18}O、HCN 和 HCO$^+$ 五条谱线的积分强度图噪声 (σ) 分别为 0.46、0.25、0.24、0.07、和 0.08 K km s^{-1}。五条谱线积分强度轮廓图的等值线都从 8σ 开始，间隔分别为 40、19、3、7 和 5σ。

Figure 2.31. Images of N133. The upper left panel is a three color image with 20 cm in red, 1.1 mm in green, and 8 μm in blue. The other five panels are contours of five spectral line integrated intensity maps superimposed on the 8 μm image with positions of clumps marked by purple crosses. The contour maps integrate from 15.0 km s^{-1} to 25.0 km s^{-1}. The rms (σ) of five line maps, ^{12}CO, ^{13}CO, C^{18}O, HCN, and HCO$^+$, are 0.46, 0.25, 0.24, 0.07, and 0.08 K km s^{-1}, respectively, and these contours all begin at 8σ, spacing with 40, 19, 3, 7, and 5σ, respectively.

根据青海站的观测结果，我们发现 CO 分子在 2 km s^{-1} 左右的辐射跟 N123 成

协，而 HCN 和 HCO^+ 示踪的致密气体分布在 N123 的边缘。在 N123 边缘我们探测到一个分子核，并在图2.29和图2.30中用紫色和绿色加号标出。如图2.5所示，N123 的谱线在线翼上有其他成分干扰，导致我们无法用分子谱线探测外向分子流。

2.3.4.13 N133

N133 是我们观测的样本中唯一个光学可见的H II 区。在 N133 附近，还有一个比较小的红外 Bubble——N132。由于 N132 的角尺度很小，青海站的望远镜无法分辨出 N132，所以本文重点研究角尺度比较大的 N133。如图 2.31所示，N133 内部 20 厘米射电连续谱辐射很强，但是 N132 内部的射电辐射比较微弱。五条分子谱线——详细的观测参数见表2.3——的分布跟 N133 的 8 μm 波段辐射吻合。Watson et al. (2010) 给的出 N133 的视向速度和距离分别为 21.4 km s^{-1} 和 2.1 kpc。

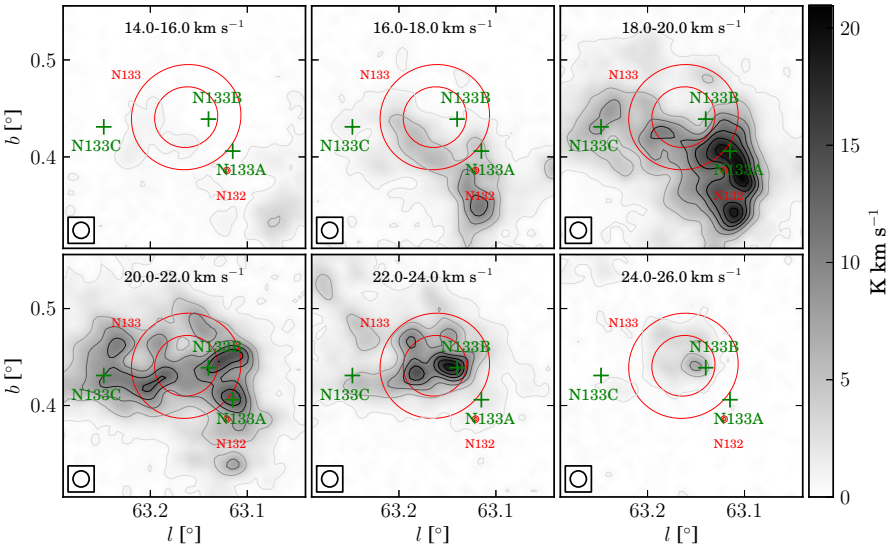

图 2.32: 红外 Bubble N133 ^{13}CO 谱线速度通道图，积分区间从 14.0 km s^{-1} 到 26.0 km s^{-1}，每 2.0 km s^{-1} 积分一次。红色圆圈标记了 N133 的位置，参数见Simpson et al. (2012)，绿色加号标记分子团块的位置。图像背景噪声 (σ) 为 0.11 K km s^{-1}。轮廓等值线从 5σ 开始，间隔为 26.3σ。

Figure 2.32. Channel map of ^{13}CO for bubble N133 from 14.0 km s^{-1} to 26.0 km s^{-1} with 2.0 km s^{-1} intervals. The red circles delineate the position of N133 offered by Simpson et al. (2012), and the green crosses mark the peak position of clumps. The rms (σ) of the image background is about 0.11 K km s^{-1}, and the contour levels space linearly from 5σ to the peak with step 26.3σ.

利用中红外的测光数据，Watson et al. (2010) 在 N133 天区证认出 6 个 YSOs，

但是这 6 个 YSOs 位置分布跟 8 μm 的峰值位置并不一致。Samal et al. (2014) 利用多波段观测数据研究了跟 N133 成协的一个H II 区复合体——Sh2-90。他们在 N133 周围发现了 129 个低质量的 YSOs，并且确认了这个H II 区的激发源是一个光谱型为 O8-O9 V 的大质量恒星，跟Lafon et al. (1983) 的计算结果一致。Samal et al. (2014) 认为在 Sh2-90 内部存在不同时期的恒星形成活动，说明这个区域中的很多恒星是触发形成的。

我们观测的五条分子谱线的空间分布跟 8 μm 波段辐射一致。我们在 N133 附近探测到 3 个分子团块，其位置在图2.31和图2.32已用紫色和绿色加号标出。虽然 N133 天区谱线的红翼被附近的成分干扰，但是蓝翼并未受到影响。我们在 N133 附近证认出一个外向分子流，位于分子团块 N133B，关于此外向分子流的详细结果，见 §2.4。

2.4 外向分子流

外向分子流是恒星形成活动最直接的证据之一。尽管H II 区附近分子云环境复杂，导致探测外向分子流比较困难，我们还是利用分子谱线对H II 区附近可能存在的外向分子流进行了搜寻。

我们探测外向分子流的工具有：分子谱线形状、积分强度图和位置速度 (P-V) 分布图。在 P-V 图上，外向分子流会表现为凸起结构 (Beuther et al., 2004; Smith et al., 1997)，所以 P-V 图是证认外向分子流的重要工具。因为在H II 区附近，分子云受H II 区膨胀影响比较大，所以我们在证认外向分子流的时候要十分小心，以避免将H II 区膨胀引起的谱线变化当作外向分子流。因为H II 区膨胀速度相比于外向分子流来说比较小，所以我们要求外向分子流的分子谱线有较大展宽并且外向分子流的红移瓣或者蓝移瓣的积分强度分布图要跟其他背景成分明显区分开。

探测外向分子流的具体步骤如下：

1. 利用 $C^{18}O$ 谱线估计外向分子流驱动源的中心位置和中心速度。对于表2.5中的每一个分子团块，我们沿速度区间积分 $C^{18}O$ 谱线——包括线翼和线心成分，获取 $C^{18}O$ 积分强度图的峰值点，做为候选驱动源的中心位置。利用候选驱动源所在位置及其附近 1′ 内区域的平均 $C^{18}O$ 谱线作高斯曲线拟合，可以获得候选驱动源的中心速度。

2. 平滑 CO 和 HCO^+ 谱线到 0.8 km s^{-1} 分辨率，以提高谱线线翼的信噪比。Zhang et al. (2005) 把 CO 谱线平滑到 1 km s^{-1} 分辨率，这跟我们平滑后的谱线分辨率基本一致。

3. 根据 ^{12}CO 和 HCO^+ 谱线确定红翼和蓝翼的速度区间。在确定速度区间的时候，红翼和蓝翼速度区间的内边界跟驱动源中心速度之间的间隔是相等的。如果外边界未受其他成分干扰，则速度区间外边界——线翼方向的截止速度——定义为谱线线翼方向的第一零点位置。在确定内边界的时候，我们从零开始逐渐增大线翼速度区间跟中心速度的间隔，也就是说逐渐去掉背景分子云成分，直到至少一个线翼的积分强度图跟背景成分明显区分开。

4. 画出 P-V 图和 24 μm 红外背景图来确定外向分子流线翼和中心驱动源。因为 24 μm 波段红外辐射可以示踪尘埃的热辐射 (Carey et al., 2009; Gutermuth et al., 2015)，所以除了 CO 和 HCO^+ 谱线，我们还利用了 24 μm 红外数据来辅助确认外向分子流驱动源的位置。

在证认外向分子流之前，我们先排除无法探测外向分子流的红外 Bubble。如果红外 Bubble 谱线的蓝翼和红翼都有相近速度成分污染，则此红外 Bubble 会被排除。如果蓝翼和红翼中至少一个未受影响，则此红外 Bubble 适合寻找外向分子流。我们总共发现有 7 个红外 Bubble——N14、N37、N55、N74、N105 和 N133——适合探测外向分子流。虽然图2.5中所示的 N37 和 N14 的 CO 谱线比较复杂，但是这两个红外 Bubble 天区的 HCO^+ 辐射比较强且未受影响，因此我们仍然把他们列为适合找寻外向分子流的红外 Bubble。

在这 7 个红外 Bubble 样本中，我们发现有四个红外 Bubble——N14、N55、N105 和 N133——的边缘有外向分子流迹象。在这四个外向分子流候选体中，只有 N55 天区的外向分子流有明显的双极结构，另外三个外向分子流则由于谱线的线翼干扰，只能确认其单个线翼成分。

在Beaumont et al. (2010) 根据 ^{12}CO ($J = 3 \rightarrow 2$) 用眼睛证认出的 12 个外向分子流候选体中，有三个包含在我们的观测样本中，分别为 N37、N49 和 N74。Beaumont et al. (2010) 给出得 N37 外向分子流的速度区间为 [30, 40] km s^{-1}，但是在此区间内 ^{12}CO 谱线比较复杂，HCO^+ 也没有显示明显的速度展宽，而且在 N37 的外向分子流候选体附近也没有发现亮的 24 μm 辐射源，所以我们认为 N37 的外向分子流候选体的存在性有待进一步确认。N49 区域的 CO 和 HCO^+ 谱线被视线方向的其他成分严重干扰，所以我们无法用青海站观测数据来确认 N49 天区的外向分子流候选体。但是 N49 边缘存在两个超致密的H II 区，所以 N49 附近存在外向分子流的可能性很大。Beaumont et al. (2010) 给出的 N74 附近的外向分子流候选体其实是跟 N75 成协，但是由于其他速度成分干扰，我们无法用谱线确认 N75 区域的外向分子流候选体。

利用Snell et al. (1984) 提供的方法，我们计算了外向分子流气体的一些物理参数，包括质量、动量和能量等。由于外向分子流倾角的不确定性，我们未对参数作任何倾角改正。我们采用 LTE 假设，并进一步假设 ^{12}CO ($J = 1 \rightarrow 0$) 谱线在线翼上是光学薄的。根据这些假设，我们计算了 ^{12}CO 的柱密度，公式如下：

$$N_{^{12}\mathrm{CO}} = \frac{4.2 \times 10^{13} T_{\mathrm{ex}} \int T_R(^{12}\mathrm{CO})\mathrm{d}V}{\exp(-5.5/T_{\mathrm{ex}})}\ \mathrm{cm}^{-2}, \tag{2.10}$$

其中，T_{ex} 是 ^{12}CO ($J = 1 \rightarrow 0$) 的激发温度 (根据线心的亮温度计算，见公式2.1)，$\int T_R(^{12}\mathrm{CO})\mathrm{d}V$ 是 ^{12}CO ($J = 1 \rightarrow 0$) 的积分强度，速度积分区间见表2.6。我们用 ^{12}CO ($J = 1 \rightarrow 0$) 的平均谱线来计算参数，平均区域是红翼或者蓝翼瓣的半峰值等高线围成的区域，这个区域也就是外向分子流瓣的分布区域。我们采用Snell et al. (1984) 给出的 ^{12}CO ($J = 1 \rightarrow 0$) 和 $\mathrm{H_2}$ 的柱密度比 ($N(\mathrm{H_2})/N(^{12}\mathrm{CO})$) 来计算 $\mathrm{H_2}$ 的柱密度，比值约为 1×10^4。

外向分子流动量和能量的计算公式为：

$$\begin{cases} P = & \Sigma \int T_R(^{12}\mathrm{CO}) V \mathrm{d}V \\ E = & \Sigma \int T_R(^{12}\mathrm{CO}) V^2 \mathrm{d}V \end{cases} \tag{2.11}$$

其中，V 是外向分子流中的气体相对于驱动源的速度，公式中的积分区间见表2.6。红移瓣或者蓝移瓣的大小定义为他们的积分强度峰值位置到驱动源中心位置的距离。外向分子流的动力学年龄的计算公式 (Cabrit et al., 1990) 为

$$t_{\mathrm{dyn}} = P/M \tag{2.12}$$

其中，M 是外向分子流单瓣的质量，可由公式2.10计算的平均柱密度给出。根据外向分子流的动力学年龄，可以计算出外向分子流的质量损失率、驱动力和光度，他们的计算公式分别为：

$$\begin{cases} \dot{M} = & M/t_{\mathrm{dyn}} \\ F_{\mathrm{outflow}} = & P/t_{\mathrm{dyn}} \\ L_{\mathrm{outflow}} = & E/t_{\mathrm{dyn}} \end{cases} \tag{2.13}$$

关于外向分子流参数的计算，具体可参考Shepherd et al. (1996); Zhang et al. (2005)，我们在表2.6中列出了详细的外向分子流参数。下面我们对证认出的 4 个外向分子流做进一步分析。

2.4.1 外向分子流 N14

由于 N14 天区在视线方向上成分复杂，CO 谱线提供的关于外向分子流的信息有限，但是因为 HCO^+ 只示踪比较致密的成分，所以可以清晰地看到外向分子流的红移线翼。外向分子流 N14 的谱线和图像见图2.33。

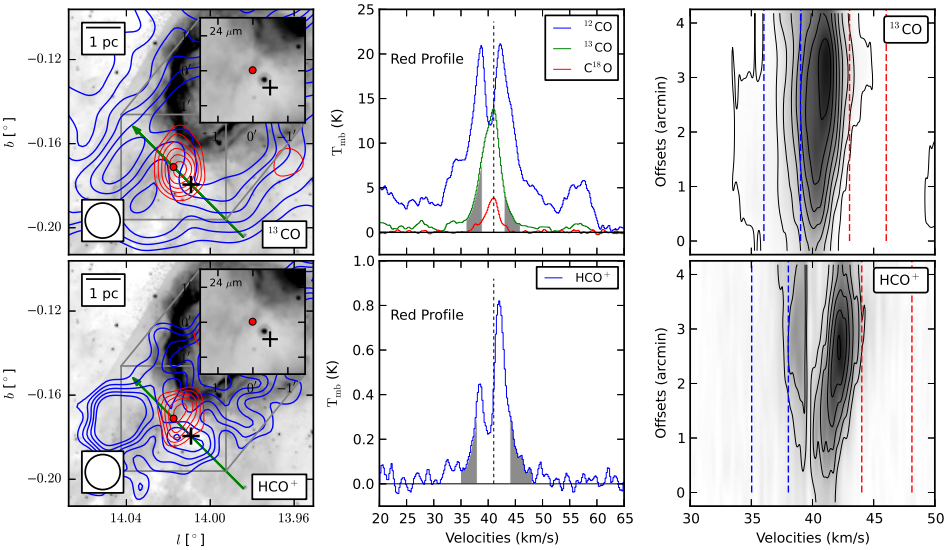

图 2.33: 外向分子流 N14 的图像。图中共有二行三列六个图。第一行从左到右显示的是 ^{13}CO ($J = 1 \rightarrow 0$) 红移瓣和蓝移瓣的积分强度图，CO 分子的三条谱线和 ^{13}CO ($J = 1 \rightarrow 0$) 谱线 P-V 图。第二行从左到右显示的是 HCO^+ ($J = 1 \rightarrow 0$) 红移瓣和蓝移瓣的积分强度图，HCO^+ 的谱线和 HCO^+ 谱线 P-V 图。积分强度图的背景是中红外 8 μm 辐射，为了探测中心驱动源，我们画出了 24 μm 图像。积分强度图中的黑色十字标记出 C^{18}O ($J = 1 \rightarrow 0$) 积分强度图的峰值位置，绿色箭头标记 P-V 图的位置分布和方向。^{13}CO 的等高线图从峰值 50% 开始，间隔为峰值的 10%；HCO^+ 等高线从峰值 60% 开始，间隔为峰值的 10%。

Figure 2.33. Outflow map of N14. The left map shows the 8 μm background image with the ^{13}CO ($J = 1 \rightarrow 0$) integrated intensity contour map superimposed on it. The inset shows a close section of the MIPSGAL 24 μm image. The integrating ranges for the blue and red lobes are shown in the line profiles and position velocity (P-V) slice maps. The black cross marks the peak position of C^{18}O integrated intensity map. The green arrow delineates the origin and direction of the P-V diagram. The ^{12}CO contours start at the 50% level and increase by 10% of the peak value, while the HCO^+ contours start at the 60% level and increase by 10% of the peak value.

在分子团块 N14A 内部，我们发现有一个 24 μm 波段点源，这很可能是外向分子流中心驱动源的准确位置。如图2.33所示，^{13}CO 谱线相对比较简单，在 P-V 图上能清晰地看到一个凸起结构。因为 ^{12}CO ($J = 1 \rightarrow 0$) 谱线被其他成分严重影响，我们无法计算此外向分子流的物理参数，仅能用 HCO$^+$ 谱线证明其存在性。

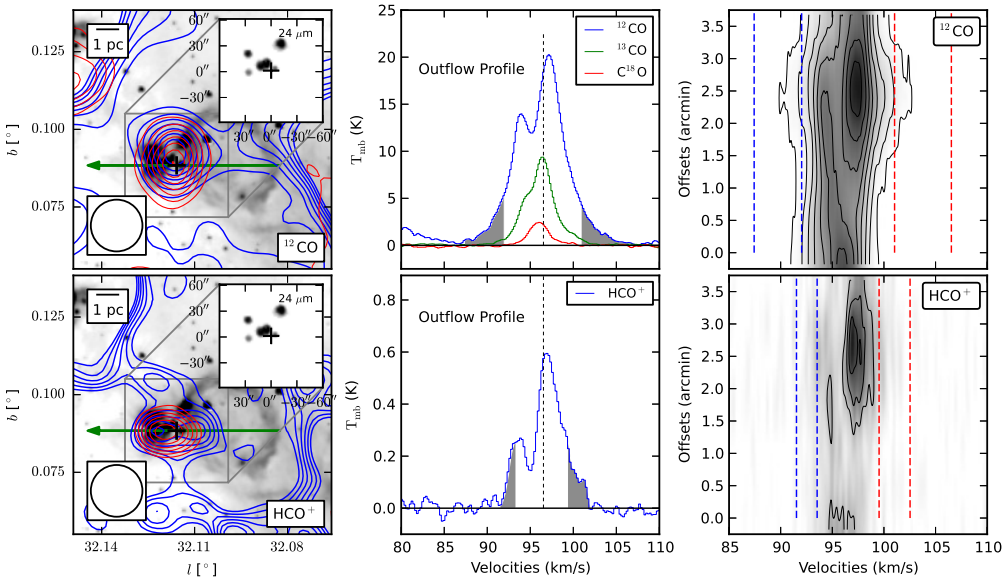

图 2.34: 外向分子流 N55 的图像。图中共有二行三列六个图。第一行从左到右显示的是 ^{12}CO ($J = 1 \rightarrow 0$) 红移瓣和蓝移瓣的积分强度图，CO 分子的三条谱线和 ^{13}CO ($J = 1 \rightarrow 0$) 谱线 P-V 图。第二行从左到右显示的是 HCO$^+$ ($J = 1 \rightarrow 0$) 红移瓣和蓝移瓣的积分强度图，HCO$^+$ 的谱线和 HCO$^+$ 谱线 P-V 图。积分强度图的背景是中红外 8 μm 辐射，为了探测中心驱动源，我们画出了 24 μm 图像。积分强度图中的黑色十字标记出 C^{18}O ($J = 1 \rightarrow 0$) 积分强度图的峰值位置，绿色箭头标记 P-V 图的位置分布和方向。^{12}CO 的等高线图从峰值 40% 开始，间隔为峰值的 10%；HCO$^+$ 等高线从峰值 50% 开始，间隔为峰值的 10%。

Figure 2.34. Outflow maps of N55. The left map shows the 8 μm background image with ^{12}CO ($J = 1 \rightarrow 0$) integrated intensity contour map superimposed on it. The inset shows a close section of the MIPSGAL 24 μm emissions. The integrating ranges for the blue and red lobes are shown in the line profiles and position velocity (P-V) slice maps. The black cross marks the peak position of C^{18}O integrated intensity map. The green arrow delineates the origin and direction of the P-V diagram. The ^{12}CO contours start at the 40% level and increase by 10% of the peak, while the HCO$^+$ contours start at the 50% and increase by 10% of the peak value.

2.4.2 外向分子流 N55

外向分子流 N55 是我们证认出的唯一一个偶极外向流 (bipolar outflow)，这个外向分子流的红移线翼和蓝移线翼都很宽，具体的图像和谱线见图2.34。在分子团块 N55A 区域中，有至少三个超致密H II 区，而以青海站望远镜的分辨率，我们无法区分哪个超致密H II 区是这个偶极外向流的驱动源。更可能的情况是，可能不止一个超致密H II 区有外向分子流现象。在计算外向分子流物理参数的时候，我们暂时把外向分子流 N55 当作一个外向分子流来处理。因为此偶极外向流的红移瓣和蓝移瓣重合在一起，所以我们无法估计外向分子流 N55 的尺度，进而无法计算其年龄，因此我们无法给出跟时间相关的参数。

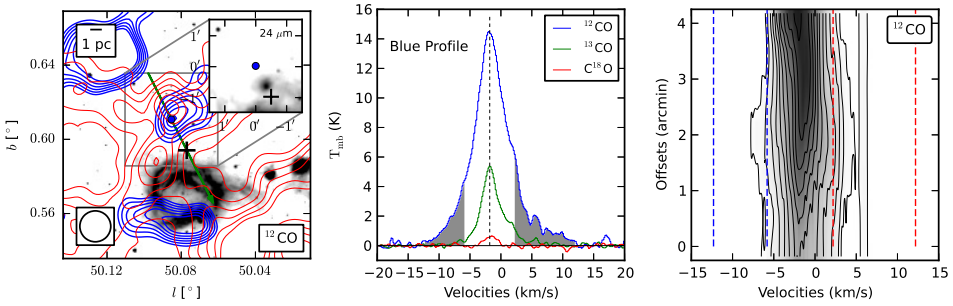

图 2.35: 外向分子流 N105 的图像。图中从左到右显示的是 ^{13}CO ($J = 1 \rightarrow 0$) 红移瓣和蓝移瓣的积分强度图，CO 分子的三条谱线和 ^{12}CO ($J = 1 \rightarrow 0$) 谱线 P-V 图。积分强度图的背景是中红外 8 μm 辐射，为了探测中心驱动源，我们画出了 24 μm 图像。积分强度图中的黑色十字标记出 C^{18}O ($J = 1 \rightarrow 0$) 积分强度图的峰值位置，绿色箭头标记 P-V 图的位置分布和方向。^{12}CO 的等高线图从峰值 50% 开始，间隔为峰值的 10%。

Figure 2.35. Outflow maps of N105. The left map shows the 8 μm background image with ^{12}CO ($J = 1 \rightarrow 0$) integrated intensity contour map superimposed on it. The inset shows a close section of the MIPSGAL 24 μm background. The integrating ranges for the blue and red lobes are shown in the line profiles and position velocity (P-V) slice map. The black cross marks the peak position of C^{18}O integrated intensity map. The green arrow delineates the origin and direction of the P-V diagram. The ^{12}CO contour levels start at 50%, and increase by 10% of the peakvalue.

2.4.3 外向分子流 N105

外向分子流 N105 是一个单极外向分子流，位于分子团块 N105B。如图2.35所示，^{12}CO ($J = 1 \rightarrow 0$) 谱线的蓝翼非常清晰，但红翼部分有其他成分干扰。在 C^{18}O 积分强度图的峰值附近有一个 24 μm 波段点源，我们认为这很可能是外向分子流的激发源。由于 HCO$^+$ 谱线的信噪比很低，我们并未画出 HCO$^+$ 谱线。在 ^{12}CO ($J = 1 \rightarrow 0$) 的 P-V 图上，我们可以清晰地看到蓝翼的凸起结构。

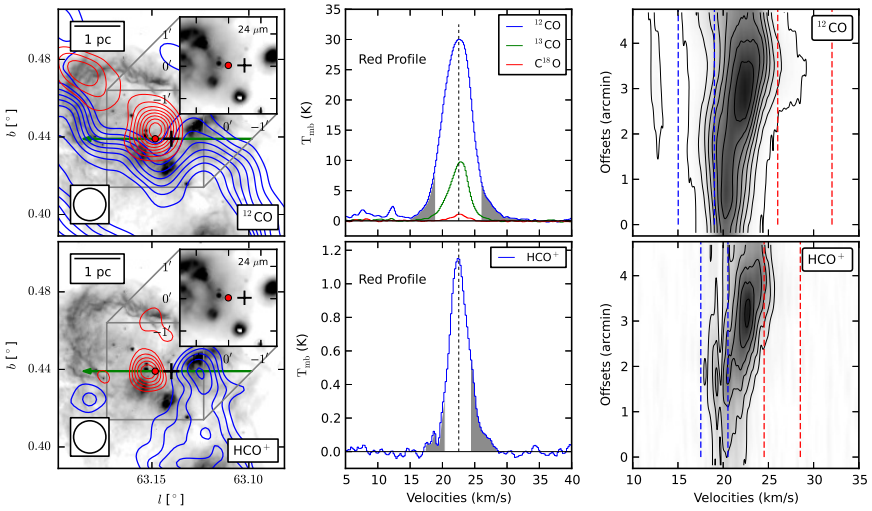

图 2.36: 外向分子流 N133 的图像。图中共有二行三列六个图。第一行从左到右显示的是 ^{12}CO ($J = 1 \rightarrow 0$) 红移瓣和蓝移瓣的积分强度图，CO 分子的三条谱线和 ^{13}CO ($J = 1 \rightarrow 0$) 谱线 P-V 图。第二行从左到右显示的是 HCO$^+$ ($J = 1 \rightarrow 0$) 红移瓣和蓝移瓣的积分强度图，HCO$^+$ 的谱线和 HCO$^+$ 谱线 P-V 图。积分强度图的背景是中红外 8 μm 辐射，为了探测中心驱动源，我们同时画出了 24 μm 图像。积分强度图中的黑色十字标记出 C^{18}O ($J = 1 \rightarrow 0$) 积分强度图的峰值位置，绿色箭头标记 P-V 图的位置分布。^{12}CO 的等高线图从峰值 30% 开始，间隔为峰值的 10%；HCO$^+$ 等高线从峰值 50% 开始，间隔为峰值的 10%。

Figure 2.36. Outflow maps of N133. The left map shows the 8 μm background image with ^{12}CO ($J = 1 \rightarrow 0$) integrated intensity contour map superimposed on it. The inset shows a close section of the MIPSGAL 24 μm background. The integrating ranges for the blue and red lobes are shown in the line profiles and position velocity (P-V) slice maps. The black cross marks the peak position of C^{18}O integrated intensity map. The green arrow delineates the origin and direction of the P-V diagram. The ^{12}CO contours start at 30% and increase by 10% of the peak while the HCO$^+$ contours start at 50% and increase by 10% of the peak.

2.4.4 外向分子流 N133

N133 天区 CO 谱线的蓝移端被另外一个成分严重干扰，但是如图2.36所示，^{12}CO、^{13}CO 和 HCO$^+$ 谱线的红移端未受干扰。我们在分子团块 N133B 中证认出一个外向分子流。在 C^{18}O ($J = 1 \rightarrow 0$) 峰值的地方有多个 24 μm 电源，以青海站望远镜的分辨率，我们无法确定哪一个是外向分子流的驱动源。

表 2.6: 分子外向流物理参数。

Table 2.6. Outflow parameters.

Name	Distance	Lobe	Peak	Velocity Range	Mass	Momentum	Energy	$\bar{v}$	Scale	t_{dyn}	$\dot{M}$	$F_{outflow}$	$L_{outflow}$
							(10^{45})			(10^4)	(10^{-4})	(10^{-3})	
	(kpc)		(°, °)	(km s^{-1})	($M_\odot$)	($M_\odot$ km s^{-1})	(ergs)	(km s^{-1})	(pc)	(yr)	($M_\odot/yr$)	($M_\odot$ km s$^{-1}yr^{-1}$)	$L_\odot$
N14	3.6	Red	(14.018, -0.171)	44.0 - 47.0	...	...	...	...	...	...	...	...	...
N55	8.4	Red	(32.116, 0.088)	101.0 - 106.5	17	103	6.7	...	...	...	...	...	...
N55	8.4	Blue	(32.116, 0.088)	87.4 - 92.0	24	144	8.8	...	...	...	...	...	...
N105	11.2	Blue	(50.085, 0.611)	-12.3 - -5.8	40.4	231.4	14.0	5.7	2.4	40.6	1.00	0.57	0.28
N133	2.5	Red	(63.148, 0.439)	26.0 - 32.0	1.4	6.8	0.3	4.9	0.4	7.3	0.19	0.09	0.04

2.5 红外 Bubble 结果分析

2.5.1 分子云和分子团块

我们的观测结果显示，所有的红外 Bubble 都跟分子云成协，这些分子云大部分是巨分子云并且伴有复杂的谱线。除了 N89 和 N90 没有探测到 C^{18}O 谱线并且 HCO$^+$ 相对较弱之外，其他所有的红外 Bubble 均探测到五条分子谱线。红外 Bubble 都伴有分子团块，并且其中四个红外 Bubble 附近的分子云有弧形结构。如图2.5所示，一些红外 Bubble 附近分子云的谱线比较宽，例如 MWP1G032057+000783、N82 和 N95。这些谱线偏离高斯谱线，并且形状跟一些超新星遗迹天区的谱线 (Su et al., 2014; Zhou et al., 2014) 形状类似，说明附近的分子云环境已经受到H II 区的膨胀影响。我们注意到分子云内部的运动或者整体的旋转也可能导致谱线变宽，但是因为分子云位于H II 区边缘，所以我们认为分子云跟H II 区的相互作用是最可能的原因。

基于 LTE 假设，我们用 CO 的三条同位素谱线计算了分子云和分子团块的物理参数。在计算质量参数的时候我们用的是平均谱线，我们发现 ^{13}CO 的光深大部分都小于 0.5，说明 ^{13}CO 的光学薄假设基本正确。红外 Bubble 堆积分子云的质量大约为 $10^3 - 10^4$ $M_\odot$，此值跟Hosokawa et al. (2005) 研究过的一个大质量恒星形成

区 (~1 Myr) 内堆积的质量 (~$10^4 M_\odot$) 一致。根据我们的计算，分子团块的质量大约在 $10^3 M_\odot$，$C^{18}O$ 的线宽大约为 2 km s^{-1}。我们计算的质量应为分子团块的质量上限，因为我们会不可避免的把分子团块周围的一些分子云一起计算在内。我们还发现在 32 个分子团块中，有 12 个分子团块的位力质量明显小于 LTE 质量，说明这些分子团块是自引力束缚的 (gravitationally bound)。

2.5.2 外向分子流和恒星形成

前人对红外 Bubble 周围恒星形成的研究主要集中在证认 YSOs 上，但是 YSOs 的的一些物理参数比较难确定，例如质量、视向速度和年龄等，而且 YSOs 的证认不确定性也较大。相比之下，外向分子流是直接的恒星形成证据，而且外向分子流的一些参数可以用分子谱线来估计，因此是研究恒星形成的重要工具。

因为大质量恒星形成区内部的动力学过程复杂，所以大部分的红外 Bubble 的分子谱线的形状也十分不规则。另外，大质量恒星形成区大多位于银道面，所以在视线方向上很容易被其他成分干扰，造成利用谱线在H II 区附近寻找外向分子流十分困难。我们发现只有 6 个红外 Bubble 的天区适合用来寻找外向分子流，也就说这些天区谱线的红移端和蓝移端中，至少有一个未受其他成分干扰。我们总共找到四个外向分子流，分别位于 N14、N55、N105 和 N133 附近。在这四个外向分子流中，只有 N55 天区的外向分子流是偶极外向分子流，由于其他成分干扰，其他的三个外向分子流仅探测到一个瓣。

我们在 6 个适合探测外向分子流的红外 Bubble 附近，探测到 4 个外向分子流，所以外向分子流的探测率大约为 67%。作为恒星形成的直接证据之一，外向分子流的存在直接证明恒星形成在膨胀的H II 区周围确实存在。外向分子流 N105 和 N133 的年龄分别为 0.4 和 0.07 Myr，而 N105 和 N133 的年龄分别为 1.6 和 0.4 Myr，所以红外 Bubble 的年龄明显大于其周围恒星形成活动的年龄。这些结果说明，H II 区周围的恒星活动有可能是触发形成的，但是我们需要更高分辨率的观测来进一步确认外向分子流跟红外 Bubble 的关系。

Zhang et al. (2005) 利用 CO ($J = 2 \rightarrow 1$) 谱线研究了 69 个大质量 IRAS 源中的外向分子流，利用美国国家射电天文台 (National Radio Astronomy Observatory, NRAO) 12 米和加州理工学院亚毫米天文台 (Caltech Submillimeter Observatory, CSO) 10.4 米射电望远镜，空间分辨率大约为 29″。他们发现这些大质量恒星形成区的外向分子流的典型能量为 1×10^{46} ergs。根据我们的计算，外向分子流 N55 的蓝移瓣和红移瓣的能量总和为 1.6×10^{46} ergs，而外向分子流 N105 仅蓝移瓣的能量就已达 1.3×10^{46} ergs，所以我们认为这两个外向分子流示踪的可能是大质量恒

星形成过程。按照Cyganowski et al. (2008) 提供的方法，我们搜索了跟外向分子流相关的分子团块区域，并未发现有 EGOs (Extended Green Objects) 天体。我们认为可能的原因有两点，一是这些外向分子流的驱动源只是中小质量恒星，并非 EGOs 示踪的大质量恒星；第二点，这些外向分子流可能太年轻，还没来得及激发 4.5 μm 波段激波气体辐射。

除了外向分子流，我们在 N55、N49 和 N123 边缘发现有超致密H II 区，这些超致密H II 区在 20 或者 6 厘米波段辐射很强。我们认为红外 Bubble 边缘的超致密H II 区也极有可能是红外 Bubble 触发形成的。

2.5.3 跟其他红外 Bubble 的研究比较

我们跟前人对红外 Bubble 的研究进行了对比。一些基于 GRS ^{13}CO ($J = 1 \rightarrow 0$) 数据的研究也发现在红外 Bubble 附近有分子团块。例如Petriella et al. (2010) 研究了红外 Bubble N65，他们发现 N65 周围的分子团块是由原来的分子云碎裂产生的，他们认为在 N65 附近发生过堆积塌缩过程，这跟我们的研究结果一致。他们还在 N65 周围的分子云壳层结构中，发现了一个 EGO 天体，这个 EGO 天体的质量跟我们证认出的分子团块的质量相近。他们在 N65 附近还证认出 22 个 YSOs，根据这些 YSOs 的谱能量分布，他们认为此区域第二代的恒星已经开始形成。前人对红外 Bubble N107 (Sidorin et al., 2014) 和 N115(Xu et al., 2014) 的研究也给出相同的结果。N107 和 N115 的年龄分别为 2 和 1.5 Myr，N107 附近的分子云质量大约为 $4.0 \times 10^4 M_{\odot}$，这些结果跟我们计算的红外 Bubble 的物理参数一致。

Hou et al. (2014) 利用 GRS ^{13}CO ($J = 1 \rightarrow 0$) 数据对红外 Bubble 进行了统计研究。他们发现，在 309 个红外 bubble 中，有大约 60% 跟分子团块成协。基于红外 Bubble 的形状和其周围分子气体分布的相关性，他们认为红外 Bubble 附近的一些分子团块的形成跟H II 区的膨胀有关。

根据前人和我们的研究结果，可以肯定的是大部分红外 Bubble 跟分子团块成协。红外 Bubble 的典型年龄为 1 Myr，其附近堆积的分子云质量大约为 $1 \times 10^4\ M_{\odot}$。

2.6 红外 Bubble 研究总结

我们利用青海站 13.7 米毫米波射电望远镜研究了 13 个天区的 18 个红外 Bubble。对每一个天区，我们观测了五条分子谱线，包括 CO 的三条同位素谱线 (^{12}CO、^{13}CO 和 C^{18}O) 和两条高密度谱线 (HCO$^+$ 和 HCN)。红外 Bubble 周围的 CO 分子谱线的形状、积分强度分布和速度梯度都显示红外 Bubble 跟周围的分子云有相互

作用。HCO^+ 和 HCN 数据证实大部分红外 Bubble 周围都有致密气体分布。根据 $C^{18}O$，我们在 18 个红外 Bubble 附近证认出 24 个分子团块，这些分子团块大部分都处于自引力束缚状态。这些结果表明H II 区对其周围的恒星形成有一定的促进作用，但是由于受到青海站望远镜的空间分辨率限制，我们无法对 CAC 和 RDI 模型做出区分。

我们在 4 个红外 Bubble——N14、N37、N55 和 N133——附近探测到外向分子流，探测率约为 67%，其中只有在 N55 天区的外向分子流有双极结构，其他的红外 Bubble 由于视线方向上其他成分的干扰，我们只能探测到外向分子流的单个瓣。根据我们计算的外向分子流参数，其中一些外向分子流可能示踪大质量恒星形成过程。外向分子流的存在证明在红外 Bubble 附近确实有恒星形成活动，而且除了外向分子流，我们还发现在 N55、N49 和 N123 边缘有致密H II 区，这是红外 Bubble 附近大质量恒星形成的证据。所以总的来说，我们观测的 18 个红外 Bubble 中有 6 个跟恒星形成活动相关，这些恒星形成活动包括外向分子流和致密H II 区，比例约为 33%。我们认为红外 Bubble 附近的恒星活动可能是触发形成的，但是我们需要更高空间分辨率的观测来进一步确认这些恒星形成活动跟他们附近红外 Bubble 的关系。

第三章　新的H II 区候选体判据

I can tell you we never intended to find exact criteria, we did not think that was possible at the time. Besides, we always knew we had contaminating sources, e.g. PNs, SNRs, extragalactic sources, etc.

— In correspondence with Gordon C. MacLeod

大质量恒星是指质量超过 8 $M_{\odot}$ (Zinnecker et al., 2007) 的 OB 星，这些 OB 星的 UV 辐射可以电离其周围的原子和分子气体形成H II 区。因此，通过H II 区的观测我们可以研究大质量恒星的形成、分布和演化。虽然其他一些天体或者天体活动也可以电离氢，例如超新型爆发，星际物质抛射和宇宙线等，但是大质量恒星产生的H II 区在形态和性质上跟其他类型的H II 区有一定差别。通过银河系H II 区的研究，我们可以获取更完备的大质量恒星形成区样本，所以H II 区一直是天文学研究的热点问题。

虽然H II 区的总数目是银河系演化的重要参数，但是银河系内H II 区总数目的不确定性依然很大，原因是H II 区一般距离太阳系比较远且演化速度快 (Zinnecker et al., 2007)。在早期阶段，H II 区非常致密，大质量恒星嵌埋得很深，周围分子云的温度很低，大约为 30 K (Garay et al., 1999; Wolfire et al., 1994)，这些分子云中的尘埃可以在远红外波段探测到，例如在 60 μm 和 100 μm 波段。由于尘埃消光，此时大质量恒星在光学波段不可见，但是在红外和射电波段可见。H II 区边缘的光致离解区在红外 8 μm 波段有较强的辐射，而在内部，被电离氢加热的尘埃可以在 24 μm 辐射热的连续谱 (Churchwell, 2002; Garay et al., 1999)。H II 区内部除了尘埃的热辐射，还有自由离子相互作用产生的自由-自由辐射 (Kurtz et al., 1994; Walsh et al., 1998)。H II 区在不同阶段会在红外波段有不同表现形式，而自由-自由辐射在早期的时候容易在低频波段光学厚 (Kurtz et al., 1994)，导致观测困难。所以要在银河系内证认出全部的由大质量恒星产生的H II 区，我们需要用到多波段的观测数据。

Wood et al. (1989a, 简称 WC89) 利用 IRAS (the all-sky Infrared Astronomical Satellite) 点源星表 (Point Source Catalog, PSC) (Helou et al., 1988; Neugebauer et al., 1984) 搜索了银河系内的超致密 (ultracompact, UC) H II 区。他们在由 IRAS 观测的四个波段构成的双色图上，根据已知的一些超致密H II 区在双色图上的位置，确定了H II 区的分布区域，并以此分布区域在 IRAS 点源星表内筛选超致密H II 区。他们确定的超致密H II 区在双色图上的区域为 $\log(F_{60}/F_{12}) \geqslant 1.30$ 和 $\log(F_{25}/F_{12}) \geqslant$

0.57，其中 F_{12}、F_{25} 和 F_{60} 分别代表 12 μm、25 和 60 μm 波段的流量，并且进一步剔除在 25 和 60 μm 波段没有信号的源。用这个判据，他们从 IRAS PSC 证认出 1717 个超致密H II 区，但是由于 WC89 在确定判据的时候已确认得超致密H II 区样本不全，并且他们只针对超致密H II 区，所以他们可能漏掉了一些演化比较后期的H II 区。

利用已知的H II 区样本，Hughes et al. (1989, 简称 HM89) 研究了 IRAS PSC 内的H II 区候选体。HM89 也是使用的双色图，但是跟 WC89 不同的是，HM89 致力于筛选所有的H II 区候选体，其中包括超致密和一些演化比较后期的H II 区。他们给出的H II 区分布区域为 $\log(F_{25}/F_{12}) \geqslant 0$ 和 $\log(F_{60}/F_{25}) \geqslant 0$。他们还对 F_{100} 波段和银纬进行了限制。HM89 证认出的H II 区数目为 2298。但是由于他们使用的已知H II 区样本也不全，所以我们认为 HM89 的边界并不准确。

最近，Anderson et al. (2014) 利用 *WISE* (*Wide-field Infrared Survey Explorer*) 观测的 12 和 24 μm 波段巡天数据对H II 区进行了人工搜索。在 12 μm 波段，H II 区边缘的多环芳烃 (polycyclic aromatic hydrocarbon, PAH) 辐射占主导，而在 24 μm 波段，H II 区内部的尘埃热辐射占主导。他们根据H II 区在 12 和 24 μm 波段的形态 (Churchwell et al., 2006)，利用眼睛寻找和确认H II 区。这个星表是目前银河系内最完备的H II 区星表，利用这个星表可以大大提高从 IRAS 点源星表筛选H II 区的精确度和完备性。虽然Simpson et al. (2012) 根据 GLIMPSE 巡天数据 (Benjamin et al., 2003) 也提供了类似的H II 区星表，但是Anderson et al. (2014) 星表的完备性和准确性都好于Simpson et al. (2012) 提供的星表。

由于是基于人工操作，我们认为Anderson et al. (2014) 可能漏掉了一些角尺度比较小的H II 区，因为这些H II 区不容易用眼睛发现。在本章节，我们用 IRAS 点源星表来补足 *WISE* 星表，进而估算银河系内的H II 区总数目。我们还参考了一些公开的红外和射电数据，并采用了机器学习算法来提高我们结果的准确性。

从 IRAS 点源星表中筛选H II 区候选体的判据是根据 IRAS 星表中的两类源确定的：H II 区和非H II 区。H II 区可以用 *WISE* H II 区星表跟 IRAS 点源星表来匹配获得，而非H II 区则可以用高银纬的源来构建。有了这两个样本，我们就可以用监督式机器学习里面的支持向量机 (support vector machine, SVM) 算法来确定他们在双色图上的分割线。而这个分割线，就是我们筛选H II 区候选体的判据。利用Tremblin et al. (2014a) 对H II 区在周围介质 (考虑湍动) 中三维膨胀的数值模拟结果，我们还计算了H II 区的年龄，并以此为依据研究了H II 区在双色图上的演化。

3.1 数据分析

在本小节，我们详细描述根据 IRAS 星表和 *WISE* H II 区星表确定H II 区候选体判据的方法。方法的核心在于从 IRAS 星表中先精确的筛选出一部分H II 区和非H II 区样本，因为这是制定判据的基础。用 IRAS 星表匹配 *WISE* H II 区星表可以获得H II 区样本；抽取高银纬 ($|b| > 8°$) 的 IRAS 源可以获取非H II 区的样本，因为在高银纬除了几个明显的大质量恒星形成区之外，H II 区非常稀少。有了这两个样本，我们就可以用 SVM 算法确定他们的边界，并根据边界划分从 IRAS PSC 中证认H II 区。

3.1.1 星表

我们的分析基于 IRAS PSC (Helou et al., 1988), *WISE* H II 区星表 (Anderson et al., 2014) 和三个射电源 (连续谱) 星表 (Condon et al., 1998; Mauch et al., 2003; Murphy et al., 2007)。

IRAS PSC (版本 2.1) 包含四个波段的观测——12、25、60 和 100 μm，空间分辨率从 45″ 到 3′。我们用符号 F_{12}、F_{25}、F_{60} 和 F_{100} 分别表示这四个波段的流量，并用 Q_{12}、Q_{25}、Q_{60} 和 Q_{100} 表示这四个波段流量的数据质量。数据质量有三个值——1、2 和 3, 分别代表上限 (即在 IRAS 灵敏度下，无信号)、中等质量和高质量。在进行后续数据处理之前，我们剔除了由Fullmer et al. (1989) 证认出的河外星系，并进一步剔除跟近邻星系 (Bai et al., 2015; Karachentsev et al., 2013; Kraan-Korteweg, 1986) 和 VLBI (very long baseline interferometry) (Immer et al., 2011; Xu et al., 2006) 校准源相匹配的源 (匹配半径 1′)。剔除这些河外源后，共剩余 234261 个 IRAS PSC 点源。

Anderson et al. (2014) 一共证认出 8399 个H II 区，银纬覆盖 $|b| \leqslant 8°$ 及高银纬的五个大质量恒星形成区。在 *WISE* H II 区星表中，Anderson et al. (2014) 给出了 1413 个H II 区的距离估计，有了距离信息，我们就可以计算光度等参数，并可以用Tremblin et al. (2014a) 的数值模拟结果来估计年龄。

Anderson et al. (2014) 发现跟射电源成协的H II 区的可信度高达 95%。根据这个结果，我们引入一些射电巡天观测来提高H II 区判据的准确性。我们总共使用了三个射电源星表——NVSS (the NRAO VLA Sky Survey) 星表 (Condon et al., 1998)，SUMSS (the Sydney University Molonglo Sky Survey) 星表 (Bock et al., 1999; Mauch et al., 2003) 和 MGPS-2 (the second epoch Molonglo Galactic Plane Survey) 星表 (Murphy et al., 2007)。这三个星表有相似的灵敏度和空间分辨率，并且可以全天覆盖。虽然超致密H II 区的自由-自由辐射在低频 (8-15 GHz) 容易光学厚 (Kurtz et al.,

表 3.1: 我们使用的五个星表的观测参数。

Table 3.1. Catalogs of IRAS point sources, H II regions, and three radio continuum surveys.

Catalog	Telescope	Band	Resolution	Coverage	Reference
IRAS v2.1	IRAS	12, 25, 60, and 100 μm	$45'' - 3'$	all-sky	Helou et al. (1988); Neugebauer et al. (1984)
H II regions	*WISE*	12 and 22 μm	6.5 and 12″	$\|b\| \leqslant 8°$	Anderson et al. (2014)
NVSS	VLA	1.4 GHz	45″	$\delta > -40°$	Condon et al. (1998)
SUMSS	Molonglo	843 MHz	∼45″	$\delta < -30°(\|b\| > 10°)$	Bock et al. (1999); Mauch et al. (2003)
MGPS-2	Molonglo	843 MHz	∼45″	$245° < l < 365°$,$\|b\| < 10°$	Murphy et al. (2007)

1994; Protheroe et al., 2008)，但是跟射电源的相关比例仍然是判断H II 区判据优劣的一个重要指标。

在表3.1中，我们总结了这些星表的参数。表3.1从左到右依次列出星表的名称、望远镜、观测波段、空间分辨率、覆盖面积和相关参考文献。

3.1.2 支持向量机

我们用机器学习里面的 SVM 算法来确定H II 区和非H II 区的边界。SVM 算法是由 Vladimir Vapnik (Vapnik, 1995) 提出的，被广泛用于监督式学习 (supervised machine learning) 中的分类和回归分析上。如果两组点可以用一条直线来划分，那么 SVM 算法给出的线性分割线可以使得这两组点的间隔 (gap) 最大化，换句话说就是在最大程度上对这两组点进行分离。如果两组点不能线性分离，例如一组点被围在另外一个组点中间，这时候 SVM 可以通过一个特殊的映射把这些点投影到更高维度的空间，然后在高维度空间对这些点进行线性分离。

因为在双色图上，H II 区和非H II 区的重合区域不大，可以线性分离，所以我们采用 SVM 里面的线性分离算法。我们使用 *Python* 语言的 *sklearn* 软件包执行 SVM 算法，需要注意的是，在计算过程中，有一个比较重要的参数 C——惩罚因子。这个惩罚因子实际上是分类误差的倍数，高的惩罚因子意味着期望较少的错误分类，在这个情况下 SVM 可能会牺牲间隔来降低误差。对于我们的工作来说，我们不需要高的惩罚因子，因为H II 区在边界处不确定性较大，所以高的惩罚因子并无意义。我们允许一小部分误差，但是误差又不能太小。经过测试，我们发现 $C = 1$ 是比较适合的值，小的 C 值偏离，对结果影响甚微。

3.1.3 确定H II 区候选体判据

HM89 对H II 区在双色图上判据的研究基于一个非常不完备的已知H II 区，而在本小节，我们将使用最新的H II 区星表来对H II 区在 IRAS 双色图上的分布进行更精确的分析。确定H II 区候选体判据的过程主要分为五步，具体如下

1. 匹配 IRAS PSC 和 *WISE* H II 区星表，获得 IRAS PSC 中的H II 区样本。
2. 筛选 IRAS PSC 在高银纬的源，获取 IRAS PSC 中的非H II 区样本。
3. 用 SVM 算法确定H II 区样本和H II 区样本在所有可能的双色图 (共 15 种) 上的边界，获得所有可能的判据。
4. 应用判据到所有 IRAS 源，选出H II 区候选体。
5. 根据H II 区候选体的性质和判据的分类情况确定最佳判据。

在第一步中，我们依据Anderson et al. (2014) 给出的方法来匹配 IRAS PSC 跟 *WISE* H II 区星表。匹配前，为了保证匹配的准确度和 IRAS H II 区样本的纯净，我们剔除了 *WISE* H II 区星表中半径大于 $4'$ 以及与射电连续辐射不成协的H II 区。最后，我们确认有 1773 IRAS 源跟 *WISE* H II 区成协，这些 IRAS 源就是我们寻找的 IRAS 中的H II 区候选体样本。由于H II 区在四个波段的数据观测质量不尽相同，对于某个特定的双色组合，这些 IRAS H II 区样本会根据某些波段的观测质量做进一步筛选。

在第二步中，我们用高银纬的源来构建非H II 区样本。高银纬的大质量恒星形成区很少，因为大质量恒星形成区距离太阳比较远且大部分分布在银盘上 (Zinnecker et al., 2007)。根据Rice et al. (2016) 证认的巨分子云的分布，除了已知的几个比较著名的大质量恒星形成区，例如猎户座星云，在 $|b| > 8°$ 区域没有巨分子云分布，所以高银纬的 IRAS 源一般都是小质量恒星或者河外星系。虽然河外星系中也还有H II 区，但是由于星系际介质 (the intergalactic medium, IGM) 的消光作用 (Assef et al., 2013; Wright, 1981)，我们预期这些河外星系在双色图上的分布跟H II 区重合的区域不大。

因为 *WISE* H II 区星表中H II 区的最大银纬值为 8°，所以我们选择 IRAS PSC 中银纬绝对值大于 8° ($|b| > 8°$) 的源来作为非H II 区样本。我们进一步剔除掉高银纬三个区域的源——猎户座星云、大麦哲伦星系 (the Large Magellanic Cloud, LMC) 和小麦哲伦星系 (the Small Magellanic Cloud, SMC)，其他区域由于H II 区并不集中，我们不再进行剔除操作。根据Wilson et al. (2005) 的 CO 观测，猎户座星云的银经和

银纬范围分别为 [200°, 220°] 和 [-22°, -8°]。由Cook et al. (2014) 提供的星系位置和大小，我们得到 LMC 的银经和银纬范围分别为 [275°, 286°] 和 [300°, 305.5°]，LMC 的银经和银纬范围分别为 [-38.5°, -27.5°] 和 [-47°, -41.5°]。我们用 WC89 和 HM89 的H II 区候选体判据来进一步确认我们非H II 区样本的正确性。在 6204 个可以用判据不等式检验的源中，有 121 个 (2%) 源符合这两个判据。剔除掉这 121 源后，我们得到的非H II 区样本的数目为 100614。尽管 WC89 和 HM89 判据并不完备，我们仍然相信在这 100614 个高银纬 IRAS 源中，H II 区占的比例低于 2%。

在第三步中，我们在由 IRAS 观测波段组成的所有可能的双色图上，对H II 区和非H II 区进行了划分。每个双色图至少要包含三个观测波段，我们要求每个颜色的短波长波段为分母，这样H II 区就会在分界线的上方 (只有一个双色图例外，见表3.2)。对 IRAS 源来说，如果短波长数据质量为 1，那么实际的短波值低于探测极限，这种情况下，H II 区在双色图上的真实位置会在观测位置的右上方，不会影响其划分。相反，如果长波长数据质量为 1，则H II 区候选体在双色图上的真实位置会在观测位置的左下方，这样情况下，我们无法确定这个源是否真的是H II 区。因此，我们要求长波长的数据质量要大于 1。IRAS 四个波段的双色组合总共有 15 种可能，对每一个双色组合，我们都用 SVM 算法确定一个H II 区判据。惩罚因子 C 的值我们设置为 1，我们发现在 $0.5 < C < 1.5$ 范围内，分割线的斜率和截距的变化大多低于 1%。

在进行第四步之前，我们先计算了每个判据 (也就是H II 区和非H II 区的边界线) 的一些统计指标，包括灵敏度 (sensitivity)，精确度 (precision) 和 F_1 值。这些值的定义如下：

$$\begin{aligned} \text{sensitivity} &= \frac{TP}{(TP+FN)}, \\ \text{precision} &= \frac{TP}{(TP+FP)}, \\ F_1 &= \frac{2}{(1/\text{sensitivity}+1/\text{precision})}, \end{aligned} \tag{3.1}$$

其中，TP (true positives) 是H II 区候选体中符合判据的点源数目，FN (false negatives) 是H II 区候选体中不符合判据的点源数目，TN 是非H II 区样本中不符合判据的点源数目，FP 是非H II 区样本中符合判据的点源数目。灵敏度也叫召回率 (recall) 或者真阳性率 (true positive rate, TPR)，精确度也叫正预测值 (positive predictive value, PPV)，而 F_1 是灵敏度和精确度的调和平均 (harmonic mean)。下面我们会修改 F_1 的定义，把H II 区候选体跟射电源的成协比例也考虑在内，修改后的 F_1 值就是我们选择最佳判据的依据。

在第四步中，我们把第三步得出的判据应用到 234261 个 IRAS 点源上，以此筛选H II 区候选体。我们先检查波段数据的观测质量，然后选择位于分割线右上方

的源，并以 1′ 作为匹配半径 (Walsh et al., 1997)，检验筛选出的H II 区候选体的射电源成协比例，具体的射电源成协比例见表3.2。

因为跟射电源成协比例是一个重要的参数，所以为了将这个因素考虑在内，我们对 F_1 值的定义进行了修改，新的形式为：

$$\mathrm{score} = \frac{3}{(1/\mathrm{sensitivity} + 1/\mathrm{precision} + 1/\mathrm{radio\,association})}, \tag{3.2}$$

其中，右边的形式依然为调和平均，只是增加了射电源成协比例 (radio association)。

表 3.2: 所有可能的 15 个H II 区双色图判据参数。

Table 3.2. All possible two-color criteria for selecting H II regions from the IRAS PSC.

Identity	Criterion[c]	Candidates	Association[d] (Radio)	Sensitivity[e]	Precision[f]	Tested[g]	Score[h]
1[a]	$\log\left(\frac{F_{60}}{F_{12}}\right) > \left(-0.18 \times \log\left(\frac{F_{100}}{F_{25}}\right) + 1.51\right), Q_{60}\ \&\ Q_{100} > 1$	3061	32.44%	90.68%	93.13%	24441	0.5704
2	$\log\left(\frac{F_{100}}{F_{60}}\right) > \left(-3.43 \times \log\left(\frac{F_{60}}{F_{12}}\right) + 4.71\right), Q_{60}\ \&\ Q_{100} > 1$	3129	31.86%	90.78%	93.72%	24441	0.5653
3	$\log\left(\frac{F_{60}}{F_{100}}\right) > \left(-1.47 \times \log\left(\frac{F_{100}}{F_{12}}\right) + 2.04\right), Q_{60}\ \&\ Q_{100} > 1$	3147	31.49%	90.48%	93.51%	24441	0.5607
4[b]	$\log\left(\frac{F_{60}}{F_{12}}\right) > \left(-0.45 \times \log\left(\frac{F_{100}}{F_{12}}\right) + 2.00\right), Q_{60}\ \&\ Q_{100} > 1$	3155	31.44%	90.78%	93.53%	24441	0.5606
5	$\log\left(\frac{F_{60}}{F_{12}}\right) > \left(0.18 \times \log\left(\frac{F_{25}}{F_{12}}\right) + 1.18\right), Q_{25}\ \&\ Q_{60} > 1$	4551	30.04%	89.32%	92.72%	24941	0.5428
6	$\log\left(\frac{F_{25}}{F_{12}}\right) > \left(-1.24 \times \log\left(\frac{F_{60}}{F_{25}}\right) + 1.45\right), Q_{25}\ \&\ Q_{60} > 1$	4583	29.91%	89.24%	92.49%	24941	0.5411
7	$\log\left(\frac{F_{60}}{F_{25}}\right) > \left(-5.90 \times \log\left(\frac{F_{60}}{F_{12}}\right) + 8.35\right), Q_{60} > 1$	4883	29.22%	86.25%	92.94%	60315	0.5303
8	$\log\left(\frac{F_{100}}{F_{12}}\right) > \left(0.41 \times \log\left(\frac{F_{100}}{F_{25}}\right) + 1.17\right), Q_{100} > 1$	3781	27.06%	80.48%	91.48%	60349	0.4974
9	$\log\left(\frac{F_{100}}{F_{60}}\right) > \left(-1.49 \times \log\left(\frac{F_{25}}{F_{12}}\right) + 0.86\right), Q_{25}\ \&\ Q_{100} > 1$	3637	28.49%	78.02%	79.69%	10714	0.4961
10	$\log\left(\frac{F_{100}}{F_{12}}\right) > \left(-0.32 \times \log\left(\frac{F_{25}}{F_{12}}\right) + 1.66\right), Q_{25}\ \&\ Q_{100} > 1$	4463	25.21%	92.81%	92.07%	10714	0.4893
11	$\log\left(\frac{F_{100}}{F_{25}}\right) > \left(-1.29 \times \log\left(\frac{F_{25}}{F_{12}}\right) + 1.64\right), Q_{25}\ \&\ Q_{100} > 1$	4513	25.02%	93.11%	91.82%	10714	0.4870
12	$\log\left(\frac{F_{60}}{F_{25}}\right) > \left(-1.83 \times \log\left(\frac{F_{100}}{F_{12}}\right) + 4.00\right), Q_{60}\ \&\ Q_{100} > 1$	4122	22.68%	85.51%	88.47%	24441	0.4472
13	$\log\left(\frac{F_{60}}{F_{25}}\right) > \left(-0.02 \times \log\left(\frac{F_{100}}{F_{60}}\right) + 1.02\right), Q_{60}\ \&\ Q_{100} > 1$	3096	25.39%	60.08%	79.17%	24441	0.4369
14	$\log\left(\frac{F_{60}}{F_{25}}\right) > \left(-0.03 \times \log\left(\frac{F_{100}}{F_{25}}\right) + 1.06\right), Q_{60}\ \&\ Q_{100} > 1$	3104	25.23%	59.98%	79.36%	24441	0.4353
15	$\log\left(\frac{F_{100}}{F_{25}}\right) > \left(0.96 \times \log\left(\frac{F_{100}}{F_{60}}\right) + 1.05\right), Q_{100} > 1$	4621	19.63%	58.19%	78.23%	60349	0.3708

[a] 判据 1 是最佳判据。

Criterion 1 is the optimal criterion.

[b] 为了保证H II 区在右上方，对判据 4，我们用 F_{60}/F_{100} 代替 F_{100}/F_{60}。

In order to make sure H II regions are above the decision boundary, we use F_{60}/F_{100} instead of F_{100}/F_{60} for criterion 4.

[c] 斜率和截距的值已经四舍五入，舍入误差对结果的影响可以忽略。

The slopes and intercepts have been rounded up, the error caused by which is not significant.

[d] 跟射电源成协的H II 区候选体比例。

The proportion of candidates having radio counterparts (radio association).

[e] 灵敏度的定义见公式A.1。

The sensitivity is defined in Equation A.1.

[f] 精确率的定义见公式A.1。

The precision is defined in Equation A.1.

[g] 可用于测试不等式的 IRAS 源的数目，也就是数据质量符合判据要求的点源数目。

The number of IRAS sources tested by the inequality of criteria.

[g] 分数值的定义式见公式A.2。

The score is defined by equation A.2.

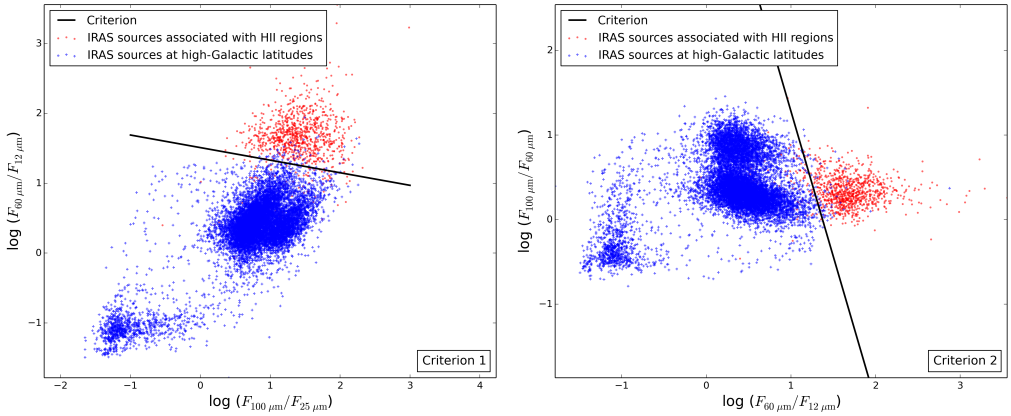

(a) 判据 1

(b) 判据 2

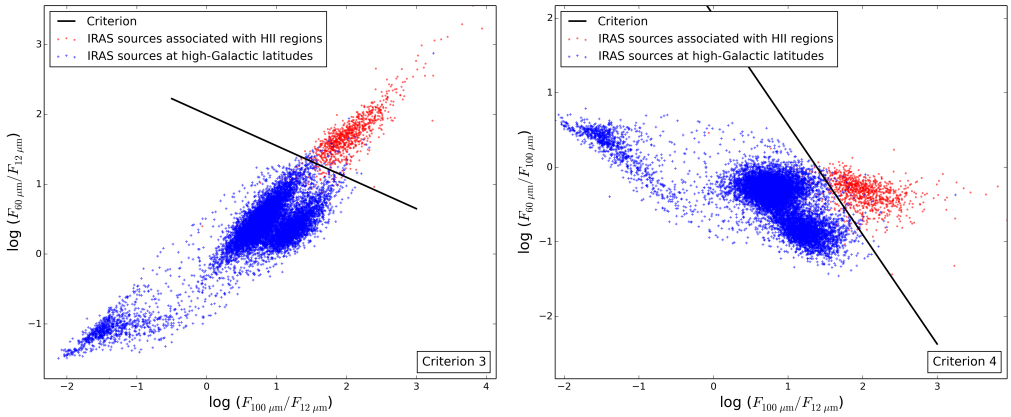

(c) 判据 3

(d) 判据 4

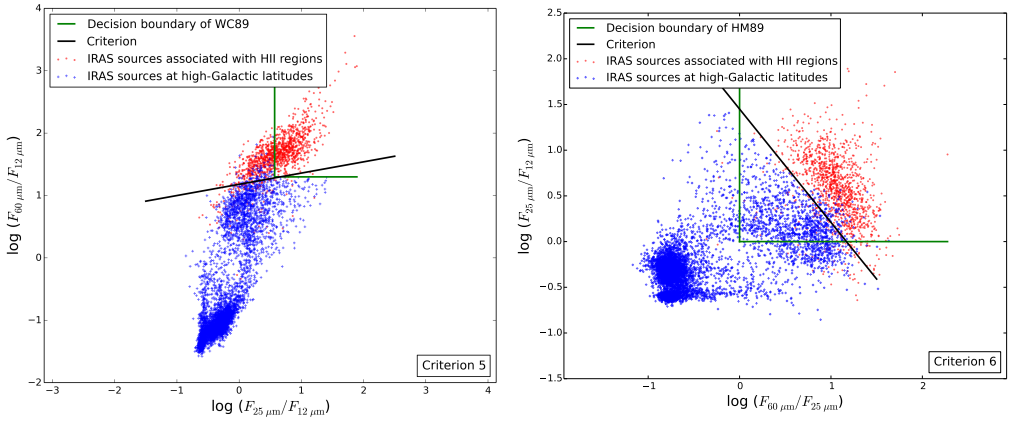

(e) 判据 5

(f) 判据 6

图 3.1: 表3.2中前六个判据的详细结果。图中红色和蓝色点分别表示H II 区和非H II 区样本。黑色实线是用 SVM 算法确定的两个样本的边界，也就是分割线。判据 5 和 6 中的绿色线分别是 WC89 和 HM89 给出的H II 区边界。

Figure 3.1. Top six criteria of Table 3.2. The criteria are criterion (a) 1, (b) 2, (c) 3, (d) 4, (e) 5, and (f) 6. The red and blue markers represent H II regions and non-H II regions, respectively. The black lines denote the decision boundary (given by SVMs) of two groups of points. The green lines in criterion 5 & 6 delineate the decision boundary of WC89 and HM89.

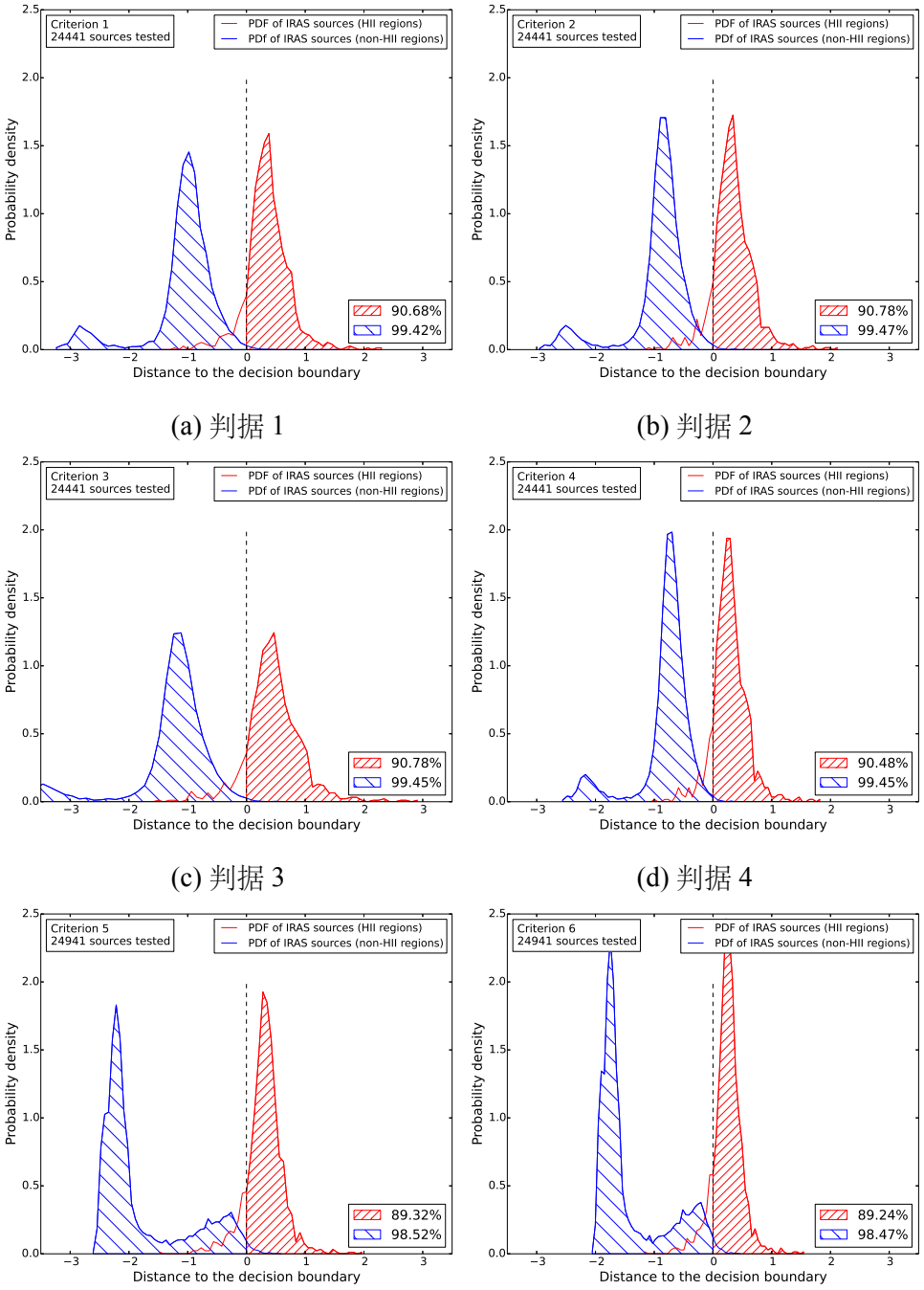

(a) 判据 1 (b) 判据 2

(c) 判据 3 (d) 判据 4

(e) 判据 5 (f) 判据 6

图 3.2: 表3.2中前六个判据的样本点 (training set, 训练集) 相对于分割线的概率密度分布。图中红色和蓝色线分别表示H II 区和非H II 区样本。负值表示样本点位于分割线以下——被判定为非H II 区。红色和蓝色阴影区分别表示判据的灵敏度 (见定义A.1) 和特异性 (specificity, $TN/(TN+FP)$)。

Figure 3.2. PDFs of the top six criteria in Table 3.2. The red (H II regions) and blue (non-H II regions) lines represent the probability density of IRAS sources with respect to the distance to the decision boundaries. Negative distances mean that IRAS sources disagree with the criteria. The red and blue shadowed areas represent the sensitivity (see Equation A.1) and specificity ($TN/(TN+FP)$) of criteria, respectively.

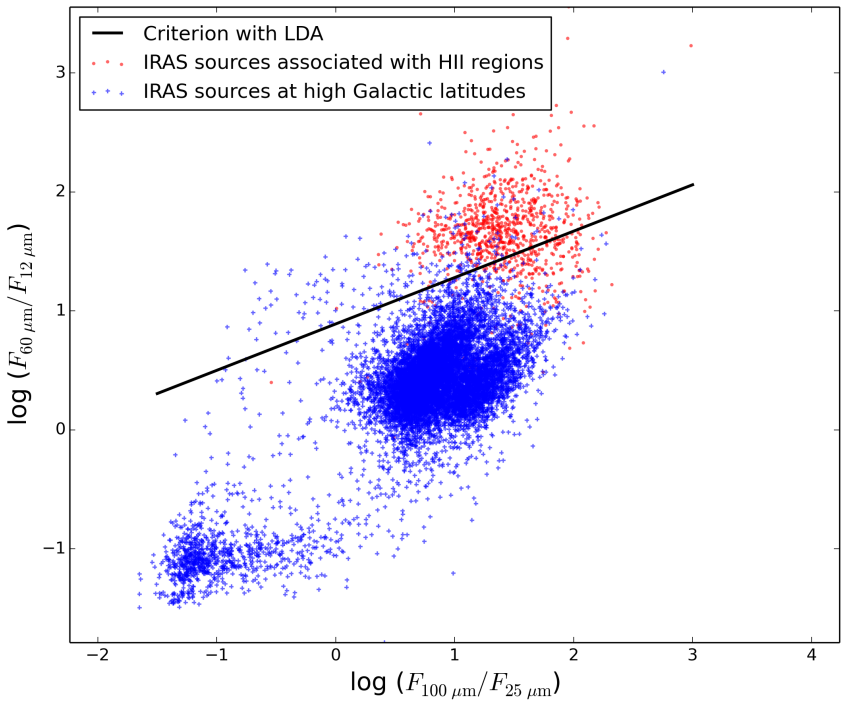

图 3.3: LAD 算法给出的分割线。图中红色和蓝色点分别表示 H II 区和非H II 区样本集。

Figure 3.3. Decision boundary determined by LDA. The red and blue markers represent H II regions and non-H II regions, respectively.

在表3.2中，我们从左到右依次列出判据名称、判据不等式和数据质量要求、总共选出的H II 区候选体数目、跟射电源成协比例、灵敏度、准确率、符合数据质量要求的 IRAS 源和判据打分。对判据进行打分的根据是定义A.2。图3.1中展示了表3.2中前六个判据的详细结果，图3.2中画出H II 区样本和非H II 区样本相对于分割线的概率密度分布。在图3.1中，我们用绿色线表示 HM89 和 WC89 给出的H II 区判据边界。

在第五步中，我们根据 F_1 的值来确定最优判据。根据表3.2，我们得到的最优判据为判据 1。判据 1 的灵敏度 (sensitivity) 表明，大约 87 % 的H II 区已经被选出，其精确度 (precision) 表明H II 区候选体的可信度为 93%。判据 1 选出的H II 区候选体跟射电连续谱源成协比例为 32%，而整个 *WISE* H II 区星表跟射电源的成协比例为 29%，所以我们认为判据 1 选出的H II 区是可靠的。

3.1.4 SVM 算法和 LDA 算法对比

由于在两维空间 (双色图) 确定两组点的分割线的算法不止 SVM 一种，还有一种比较有效的算法是线性判别分析 (linear discriminant analysis, LDA)。LDA 算法确定的分割线会使得两组样本点在分割线上投影的平均位置点距离间隔最大，同时使得两组样本点分布弥散 (方差) 最小。相比较而言，LDA 算法比较注重两组点的整体分布，而 SVM 算法则更注重两组点靠近边界的点的分布情况。

跟 SVM 算法同样，我们用 *sklearn* 软件包对H II 区和非H II 区样本进行 LDA 分析，分析结果见图3.3。因为判据 1 是最佳判据，所以我们只检验了判据 1 的双色图。在图3.3中，LDA 给出的分割线切掉了很大一部分H II 区候选体，所以我们认为 SVM 算法更加适合用来判别H II 区候选体。

3.2 IRAS 星表中的H II 区

在这一小节，我们给出判据 1(见表3.2) 在双色图上筛选出的H II 区候选体的一些结果。我们主要给出这些H II 区候选体在银河系中的分布和银河系中总的H II 区的数目。另外，我们还研究了 H II 区在双色图上的演化。

3.2.1 H II 区分布

判据 1 给出的H II 区候选体 (共 3061 个) 的全天分布见图3.4。图3.4显示，绝大多数H II 区候选体分布在银道面上，高银纬的候选体非常稀少，这些离散的高银纬源主要是一些跟H II 区颜色相近的河外天体。在图3.4中，LMC、SMC 和猎户座星云的的位置非常明显。

在图3.5中，我们画出了H II 区候选体在银经和银纬方向的分布。沿银纬方向的数据统计的分辨率 (bin size) 为 1°，如图3.6a所示，忽略高银纬的 LMC、SMC 和猎户座星云，H II 区在银纬方向近似为高斯分布。沿银经方向的数据统计的分辨率为 2°，图3.6a显示，在 80° 和 280 ° 方向上有峰值。这两个位置分别对应银河系旋臂中的本地臂 (Local Arm) 和人马臂 (Carina Arm)，这跟前人给出的结果 (Avedisova, 1985; Hughes et al., 1989; Xu et al., 2013) 是一致的。

扣除掉 LMC 和 SMC 区域的源，我们总共证认出 2962 个H II 区候选体。这些候选体大约有 67% 分布在第一和第二象限，有 46% 分布在银心 60° 以内。而在 *WISE* H II 区星表中，85% 的源分布在第一和第二象限，77% 的源分布在银心 60° 以内。*WISE* H II 区星表的比例偏高是由于其高空间分辨率可以分辨出一些小的或者比较远的H II 区。我们发现 IRAS 中的H II 区候选体相对于银道面也是不对称的

——有 53% 的候选体分布在负银纬一侧，这跟 *WISE* H II 区的分布 (56%) 是一致的。

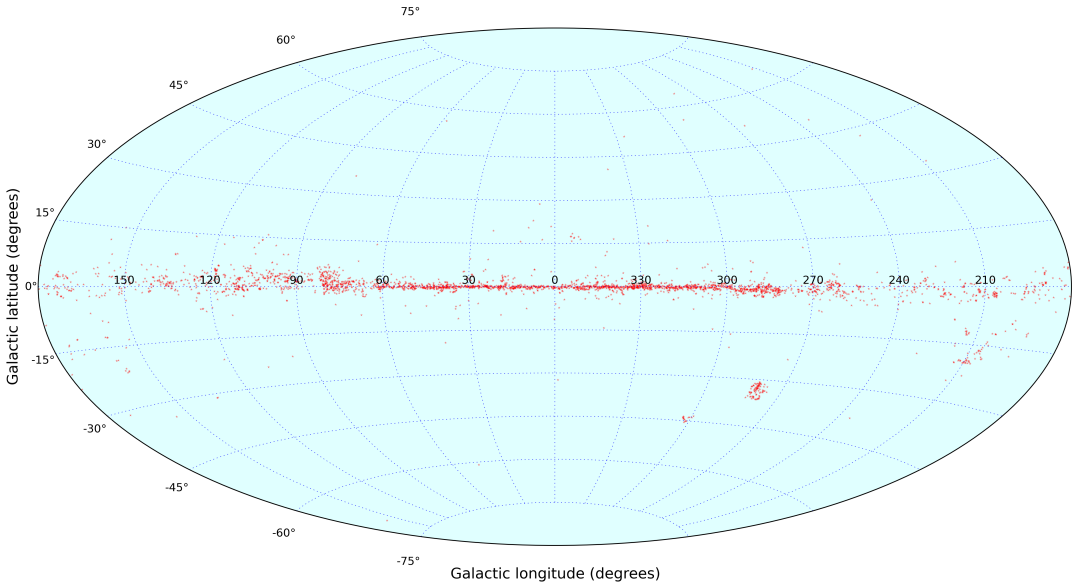

图 3.4: 判据 1 给出的 3061 个H II 区候选体的全天分布。

Figure 3.4. All-sky distribution of 3061 IRAS sources selected by criterion 1.

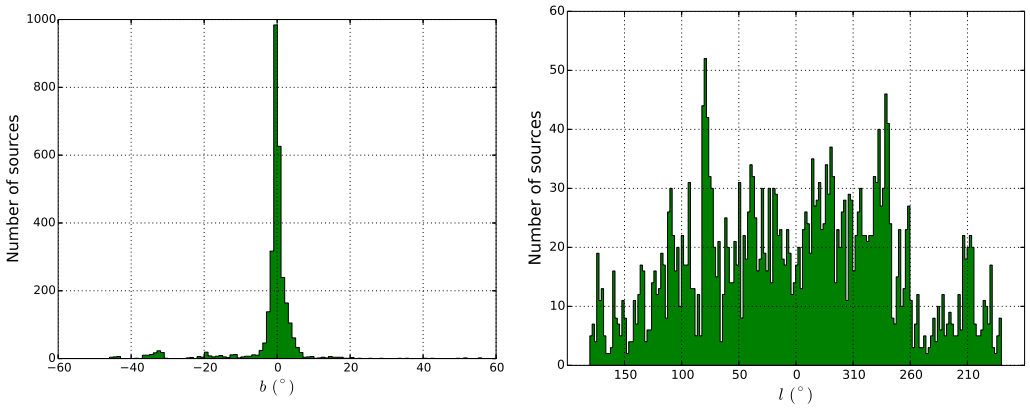

(a) 银纬分布　　(b) 银经分布

图 3.5: H II 区候选体沿银纬 (左) 和银经 (右) 的分布，分布统计分辨率分别为 1° 和 2°。

Figure 3.5. Histograms of Galactic latitude (left) and longitude (right) distribution of H II regions identified by criterion 1, the bin sizes of which are 1° and 2°, respectively.

3.2.2 银河系H II 区总数

根据判据 1 从 IRAS PSC 中选出的H II 区候选体，加上 *WISE* H II 区星表，我们估计了银河系中红外数据示踪的H II 区的总数目。跟据 1′ 匹配半径，我们发现 2962 个H II 区候选体中有 1450 个跟 *WISE* H II 区重叠，所以银河系中红外数据示踪的H II 区数目大约为 2962+8399-1450=9911 个。由于 IRAS 的分辨率偏低 (大约 2′)，一些 IRAS H II 区可能包含多个，加上 IRAS 的灵敏度也比较低，所以这个数目应该是下限。从 IRAS 和 *WISE* 中选出的H II 区候选体的中红外和远红外的辐射都比较强，在这个时期，H II 区中心的大质量 ($> 8M_{\odot}$) 恒星还处于形成时期，所这个数目也是银河系中大质量恒星形成区的数目。

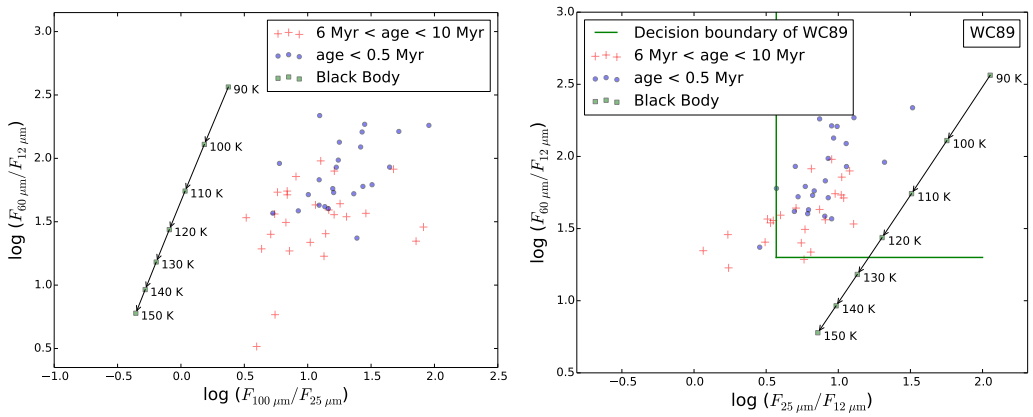

(a) 判据 1 双色图　　(b) WC89 双色图

图 3.6: H II 区在双色图上的演化。H II 区年龄根据Tremblin et al. (2014a) 给出的数值模拟结果估计，蓝色和红色点分别代表年轻和年老的H II 区样本。图中绿色实心正方型表示不同温度的黑体在双色图上的位置。

Figure 3.6. The evolution of H II regions on two-color diagrams. The color combinations of left and right panels correspond to criterion 1 and WC89, respectively. The blue points and red crosses represent young and old samples of IRAS sources, respectively. The age is estimated according to a 3D simulation for the expansion of H II regions (Tremblin et al., 2014a). The positions of blackbodies possessing different temperatures are marked with solid green squares.

3.2.3 H II 区在双色图上的演化。

在本小节，我们研究H II 区在双色图上的演化。H II 区年龄是根据 Tremblin et al. (2014a) 对H II 区三维膨胀的数值模拟结果来估计的。Tremblin et al. (2014a) 的数值

模拟结果考虑了周围气体内部的湍动，我们认为他们给出的是比较准确的。

年龄的计算需要用到H II 区射电连续谱辐射的流量和到太阳的距离信息。Anderson et al. (2014) 在 *WISE* H II 区星表中给出了 1413 个H II 区的距离，其中 627 个与 IRAS 源和射电源同时成协，为了保证源的可靠性，我们剔除数据质量差的源——保证所有的源在四个 IRAS 波段都有观测信号。最后，我们给出了 305 个H II 区的年龄估计。

虽然大质量恒星的嵌埋时标一般来说不大于 5 Myr (Churchwell, 2002; Zinnecker et al., 2007)，我们只剔除了年龄大于 10 Myr 的H II 区，原因是数值模拟只是基于均匀介质而且H II 区距离误差也比较大，所以我们认为嵌埋大质量恒星的计算年龄在 10 Myr 是有可能的。为了比较年轻和演化比较后期的H II 区在双色图上的分布，我们选择年龄小于 0.5 Myr 的 IRAS 源为年轻星样本，选择年龄大于 6 Myr 的 IRAS 为演化比较后期的样本，这两个样本的数目分别为 25 和 26 个。

如图3.6所示，在双色图上，随着大质量恒星的演化，H II 区的颜色会变蓝——向左下方演化。作为对比，在图3.6我们画出了黑体在双色图上的位置和H II 区在 WC89 使用的双色图 (右图) 上的演化。显然，H II 区的红外辐射不能简单用黑体来表示，这跟Walsh et al. (1999) 的结果一致。原因可能是H II 区内部的尘埃颗粒分布导致H II 区呈现双温度结构。颗粒大的尘埃运动比较慢，温度较低，颗粒小的由于加热速度比较快，温度高一些。虽然H II 区的能谱跟黑体辐射有较大差别，但是他们的演化方向基本一致。

3.3 IRAS H II 区候选体讨论

3.3.1 行星状星云

行星状星云中的H II 区来自晚期红巨星的物质抛射，这些电离气体本来是在红巨星内部。同样是电离气体，行星状星云在双色图上可能跟H II 区有重叠区域。为了检验判据 1 是否能排除行星状星云，我们把H II 区候选体跟Frew et al. (2013) 提供的行星状星云星表 (共 1258 个源) 进行匹配——匹配半径 1′，我们发现只有 22 个H II 区在位置上跟行星状星云接近。所以，不到 1% 的H II 区跟行星状星云成协，说明判据 1 可以把H II 区跟行星状星云很好地区分开。这 22 个H II 区依然保留在我们最后的结果中，因为单凭他们在天球上的投影位置靠近行星状星云，并不能排除它们是H II 区。

3.3.2 H II 区的演化

我们得出的H II 区的演化结果跟Xu et al. (2003) 给出的结果一致。Xu et al. (2003) 研究了 482 个 6.7 GHz 甲醇脉泽，其中 361 个跟 IRAS 源成协。他们发现在双色图上，这些 IRAS 源分布在一个较小的区域：$0.57 < \log(F_{60}/F_{12}) < 1.30$, $1.30 < \log(F_{60}/F_{12}) < 2.5$。Xu et al. (2003) 发现超致密H II 区会随着演化温度升高，颜色变蓝，这跟我们得到的结果一致。

3.3.3 跟 WC89 和 HM89 结果比较

由于 WC89 的工作主要针对超致密H II 区，所以他们的判据可能会遗漏一些演化比较后期的H II 区。如图3.1e和图3.6b所示，WC89 的区域的H II 区比较年轻，此时H II 区大多还嵌埋在厚厚的分子云中。

如图3.1f所示，HM89 给出的边界包含了一大片非H II 区区域，说明 HM89 的边界是不准确的。HM89 划定的H II 区区域为 $F_{60}/F_{25} > 0$ 和 $F_{25}/F_{12} > 0$。虽然他们在 F_{100} 和银纬上做了限制，但是我们认为 HM89 的判据可能会错误的选择一些H II 区。

3.4 IARS H II 区判据研究总结

我们通过分析 IRAS 点源星表和 *WISE* H II 区星表，给出了从 IRAS 点源星表中筛选H II 区候选体的新判据。我们用监督式机器学习中的 SVM 算法确定已知的 IRAS 中的H II 区和非H II 区样本的分割线，并以此作为判据，从 IRAS 点源星表中选择H II 区候选体。H II 区样本是由 IRAS 点源星表和 *WISE* H II 区星表匹配 (半径 1′) 产生的，而非H II 区样本则由高银纬 ($|b| > 8°$) 的 IRAS 源构成。

我们确定的最优判据包括三个条件：$\log(F_{60}/F_{12}) \geqslant -0.30 \times \log(F_{100}/F_{25}) + 1.53$, $Q_{60} > 1$ 和 $Q_{100} > 1$，共选出 3061 个 IRAS H II 区候选体，扣除 LMC 和 SMC 后剩余 2962 个。我们的结果跟 HM89 给出的判据相比，有很大改进。有大约 32% 的H II 区候选体跟射电源成协，说明我们的判据是可靠的。合并 (匹配半径 1′)IRAS H II 区候选体和 *WISE* H II 区星表后，我们发现银河系内H II 区的数量下限约为 9900，这也是大质量恒星形成区的数目下限。

根据Tremblin et al. (2014a) 的数值模拟结果，我们计算了一些有距离信息并跟 IRAS 和射电源成协的H II 区的年龄。我们在双色图上发现，H II 区在演化过程中，它们的远红外波段的颜色会变蓝。

监督式机器学习中的 SVM 算法是从星表中辨别特定天体的有效方法，我们期望可以用更高灵敏度和分辨率的数据，例如 *Herschel* 空间望远镜的巡天数据，来提高H II 区候选体样本的准确性和完备性。

第四章　银河系中心的分子云

From our perspective within the Galaxy, it is difficult to establish absolute, spatial relationships of CO emission with other structural features, such as spiral arms or the stellar bar.

— Mark Heyer and T. M. Dame

银河系中心附近大约 500 pc 半径内的区域，称为银心分子云区 (the Central Molecular Zone)，简称 CMZ (Morris et al., 1996)，这是银河系中一个非常特别的区域。CMZ 虽然覆盖区域不大，银经范围大约为 $-1^\circ < l < +1.5^\circ$，但是 CMZ 区域总的分子云质量达 $5.3 \times 10^7 M_\odot$ (Pierce-Price et al., 2000)，而银河系总的分子云质量大约为 $1 \times 10^9 M_\odot$(Heyer et al., 2015)。CMZ 中分子云的密度 (Jones et al., 2012, 2013; Longmore et al., 2013)、温度 (Ao et al., 2013; Ginsburg et al., 2016; Mills et al., 2013) 和压强 (Oka et al., 2001; Shetty et al., 2012) 大多都高于银盘上的分子云。CMZ 区域中发现的星际分子种类繁多，且分子云内部的恒星形成活动也多种多样 (Corby et al., 2015; Kruijssen et al., 2014; Lu et al., 2015; Walsh et al., 2011; Yusef-Zadeh et al., 2009)，所以 CMZ 对分子云和恒星形成的研究有非常重要的价值。

由于太阳系在银河系的银盘上，我们只能从侧向 (edge-on view) 研究 CMZ，而对 CMZ 中分子云的三维结构知之甚少。Molinari et al. (2011) 利用 *Herschel* 的红外巡天 (the Hi-GAL survey) 数据 (Molinari et al., 2010b)，研究发现 CMZ 中可能有一个半径大约为 100 pc 左右的环形结构，其中包含的分子云质量大约为 $\sim 3\times10^7 M_\odot$。他们认为这个环形结构可能位于银河系中心附近比较稳定的 x_2 轨道上 (Binney et al., 1991; Contopoulos et al., 1980)，但是最新的研究表明 CMZ 中分子云的运行轨道可能并不闭合 (Kruijssen et al., 2015)。

为了研究 CMZ 中分子云的正向 (face-on) 结构，Sawada et al. (2004) 提出了一个可以估算分子云在 CMZ 中相对位置的方法。他们提出可以用 CO 发射线和 OH 吸收线来计算分子云相对于银心的位置。跟以前的研究 (Binney et al., 1991; Kruijssen et al., 2015) 不同的是，这个方法不依赖于动力学模型。他们假设 CMZ 中的射电连续谱辐射是轴对称的，并根据 OH 1667 MHz 线的吸收深度来估算分子云视线背后的连续谱辐射温度。虽然他们的结果显示 CMZ 中的分子云有棒结构，但是在计算中，他们假设 OH 的激发温度是常数，并且认为 CO 亮温度跟 OH 光深成正比。我们认为这两个假设是非常不准确的，而且这两个参数直接关系到分子云的相对位置计算的准确性。他们采用的 CO 谱线是 ^{12}CO $(J = 1 \rightarrow 0)$，这条谱

线非常容易光学厚，虽然 CMZ 大的速度梯度可以削弱光学厚效应，但是直接用 ^{12}CO ($J = 1 \rightarrow 0$) 亮温度来限制 OH 的光深会导致比较大的误差。

Dawson et al. (2014) 利用澳大利亚 64 米 Parkes 射电望远镜对 CMZ 进行了 OH 四条谱线的巡天 (the Southern Parkes Large-Area Survey in Hydroxyl, SPLASH)。SPLASH 观测的 OH 谱线包括 1665 和 1667 MHz 的两条主线 (main lines) 以及 1612 和 1720 MHz 的两条次线 (satellite lines)。利用这四条谱线，我们可以改进Sawada et al. (2004) 提出的模型。

为了确认Kruijssen et al. (2015) 提出的轨道模型，在本章，我们利用 SPLASH 观测的四条谱线，CfA 1.2 米望远镜观测的 ^{12}CO 谱线 (Dame et al., 2001) 和 Mopra 22 米望远镜观测的 ^{13}CO ($J = 1 \rightarrow 0$) 数据来改进Sawada et al. (2004) 提出的模型。

4.1 OH 分子谱线

由于我们的研究重点是 OH 分子，所以在介绍 CMZ 和我们的工作之前，我们先回顾一下 OH 分子的研究历史和一些重要的 OH 分子巡天。

4.1.1 OH 分子

在 1963 年，Weinreb et al. (1963) 第一次以吸收线 (1667 MHz 线) 的形式观测到 OH 分子 (hydroxyl radical，羟基)。两年之后，天文学家通过 OH 分子第一次观测到天体脉泽 (maser) 现象。从这以后，OH 分子一直是天文学家研究星际介质和恒星形成的重要工具。

如图4.1所示，由于 Λ 双重分裂 (Λ doubling) 效应 (Barrett, 1964)，OH 分子基态能级 $^2\Pi_{3/2}, J = 3/2$ 分裂成上下两组，紧接着由于原子核和电子的自旋作用 (Dawson et al., 2014; Robinson et al., 1967)，上下两组再次各自分裂，所以 OH 基态总共有四个能级。

OH 分子是研究星际介质和和磁场的重要工具 (Crutcher, 2012)。OH 分子跟天文上很多重要的现象有关联，例如，OH 分子可以示踪大质量恒星形成区 (Argon et al., 2000; Fish et al., 2003)，致密H II 区 (Wynn-Williams et al., 1974)，弥散气体 (Dawson et al., 2014) 和 AGB (Asymptotic Giant Branch) 星 (Wood et al., 1992) 等。

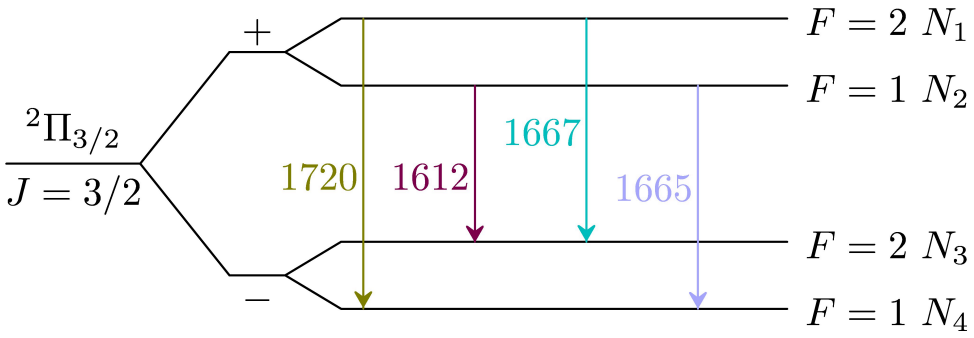

图 4.1: OH 分子基态能级 (Dawson et al., 2014, Figure 1)。N_1、N_2、N_3 和 N_4 分别代表四个能级的柱密度，F 代表总角动量。

Figure 4.1. OH ground-state energy levels, reproduced from Dawson et al. (2014, Figure 1). N_1, N_2, N_3, and N_4 denote the column densities of their corresponding states, and F represents the total angular momentum.

4.1.2 OH 谱线巡天

我们在表4.1中总结了一些 OH 分子的巡天观测。表4.1从左到右依次列出观测用的望远镜，观测谱线，观测区域和相关的参考文献。

近期完成的 SPLASH OH 巡天观测的灵敏度比较高，而且采样率和观测谱线也很完备。SPLASH 观测了 OH 基态在 18 厘米波段的 4 条谱线，还包括观测天区的连续谱。SPLASH 极大的增加了已知 OH 分子脉泽的样本。SPLASH 先导区域的观测范围为 $334° < l < 344°$, $|b| < 2°$，谱线的速度和空间分辨率分别为 0.18 km s^{-1} 和 15.5′，灵敏度为 65 mJy (Dawson et al., 2014)。对于弥散的 OH 辐射，Dawson et al. (2014) 把速度分辨率降低为 0.7 km s^{-1}，以提高探测灵敏度 (16 mJy)。他们发现，背景连续谱的强弱可以显著地影响 OH 分子谱线。如果 OH 分子的激发温度和背景连续谱相近，则 OH 分子谱线亮温度会趋向于低于 Parkes 探测灵敏度。Dawson et al. (2014) 证认的脉泽和脉泽候选体中有大约 50% 属于新样本，其中大部分是 1612 MHz 谱线脉泽。

4.1.2.1 OH 主线观测

Caswell et al. (1983, 1987, 1980) 利用 Parkes 64 米望远镜对 OH 主线——1665 和 1667 MHz 谱线——进行了比较系统行的观测研究。Caswell et al. (1980) 观测的银经覆盖范围为 $326° < l < 340°$，空间分辨率为 12′，系统温度约为 80 K。Caswell et al. (1980) 探测到 40 个主线脉泽，其中 27 个属于新探测源，他们认为这些主线脉泽

表 4.1: 最近的 OH 巡天。

Table 4.1. Recent OH surveys.

Telescope	covered lines	covered Area	Reference
ATCA	Four lines, Masers	$334° < l < 344°$, $\|b\| < 1°$	Qiao et al. (2016)
Parkes 64-m, spatial resolution 12′	Four lines	$334° < l < 344°$, $\|b\| < 1°$	SPLASH, Dawson et al. (2014)
Parkes 64-m	1720 maser	200 southern sites of 1665 and 6035 MHz OH masers	Caswell (2004)
ATCA, VLA	1612	$\|l\| < 44°$, $\|b\| < 3°$	Sevenster et al. (1997a,b, 2001)
VLA	Four lines	91 sources with brightness larger than 1 Jy.	Argon et al. (2000)
VLA	1720 maser	Sgr A and circumnulear disk	Yusef-Zadeh et al. (1999)
76-m Lovell, 10 ″	1665, 1667 MHz	$354° \leq l \leq 8.6°$, $\|b\| \leq 1°$	Boyce et al. (1994)
Parkes 64-m, Effelsberg 100-m, Dwingeloo 25-m	1612 maser	2703 IRAS sources	te Lintel Hekkert et al. (1991)
VLA	1665 MHz	91 sources with brightness larger than 1 Jy.	Forster et al. (1989)

可能跟H II 区成协。Caswell et al. (1983) 观测的银经覆盖范围为 $340° < l < +2°$，他们探测到 49 个 OH 主线脉泽，其中大部分跟恒星形成区成协。这些结果跟后来Caswell et al. (1987) 观测的 $233° < l < 326°$ 区域给出的结果一致。

高空间分辨率的观测 (Caswell, 1998) 显示，有些 OH 主线脉泽确实跟恒星形成活动有关。Caswell (1998) 还发现有一些 OH 主线脉泽可能跟 6.7 GHz 甲醇脉泽 (methanol masers) (Menten, 1991; Szymczak et al., 2002) 成协，说明 OH 主线脉泽也可能会在大质量恒星形成过程中被激发。除了 6.7 GHz 甲醇脉泽，OH 主线脉泽还跟其他一些天体成协，比如红外源和超致密H II 区。

Allen et al. (2012, 2013) 利用 Onsala 空间天文台的 25 米射电望远镜观测了位于 $(l,\ b) \approx (108°,\ 5°)$ 方向比较弱的 1667 MHz 谱线，空间分辨率为 $27' \times 31'$。他们发现弥散 OH 的空间分布跟H I相近，只有不到 10% 的 OH 辐射跟 ^{12}CO ($J = 1 \rightarrow 0$) 成协。有意思的是，Allen et al. (2015) 根据天区 $(l,\ b) \approx (105°,\ 1°)$ 的观测结果得出了类似的结论。Allen et al. (2015) 观测用的望远镜是绿岸望远镜 (Green Bank Telescope, GBT)，总共观测了三条谱线——1665、1667 和 1720 MHz 谱线。他们发现 OH 分子的两条主线处于 LTE 状态，一些没有 CO 辐射的分子云会有 OH 辐射，所以得出 OH 分子是探测这些分子云的重要工具。

表 4.2: 最近的一些 CMZ 巡天。

Table 4.2. Recent surveys towards the CMZ.

Survey	Telescope	covered lines	covered Area	Reference
SPLASH	Parkes 64-m, spatial resolution 12′	Four OH ground-state transitions	CMZ	Dawson et al. (2014)
	22-m Mopra, 60 ″	7-mm band	$-0.72° \leq l \leq 1.80°, -0.3° \leq b \leq +0.22°$	Jones et al. (2013)
MIPSGAL	Spitzer, 3′	3.6, 4.5, 6, 8, 24	$-62° \leq l \leq 63°$, $\|b\| \leq 1°$	Benjamin et al. (2013, 2003); Carey et al. (2009)
	22-m Mopra, 35 ″	3-mm band	$-0.72° \leq l \leq 1.80°, -0.3° \leq b \leq +0.22°$	Jones et al. (2012)
	ATCA , 2′	atomic hydrogen	$-5° \leq l \leq 5°$, $5° \leq b \leq 5°$	McClure-Griffiths et al. (2012)
Hi-GAL	Herschel, 25″ for 350 μm	70, 160, 250, 350, and 500 μm	$359.3° \leq l \leq 0.8°$, $\|b\| \leq 0.5°$	Molinari et al. (2011)
HOPS	22-m Mopra, 125″	12 mm band including H_2O, NH_3, H62α, H69α, HCCCN (3-2)	$290° \leq l \leq 360°, 0° \leq l \leq 30°, -0.5° \leq b \leq +0.5°$	Walsh et al. (2010)
WISE	WISE, 12″ for 22 μm	3.4, 4.6, 12 and 22 μm	All sky	Wright et al. (2010)
BGPS	Bolocam , about 33″	1.1 mm and 0.35 mm	covered the CMZ	Bally et al. (2010)
ATLASGAL	APEX , 19.2″	870 μm	$+15° \leq l \leq 21°$ $-30° \leq l \leq +11.5°, 1° \leq b \leq 1°$	Schuller et al. (2009)
	100-m GBT,	2.5 (1.5′), 6 (2.5′), 20 (9.0′), 90 (138.8′) cm	$-2° < l < 5°$, $\|b\| < 40'$	Law et al. (2008)
	VLA, the resolution of l is 30″, and for b is 10 ″	20 cm continuum	$-2° < l < 5°$, $\|b\| < 40'$	Yusef-Zadeh et al. (2004)
	AST/RO 1.2 m (Antarctic) , 2′	CO (J=4-3), CO (J=7-6), [C1] $^3P_1 - ^3P_0$	$-1.3° < l < 2°$, $0.3° \leq b \leq 0.2°$	Martin et al. (2004)
	SCUBA, JCMT 15-m, 8″ (450 μm), 15″ (850 μm)	continuum	Galactic Centre,	Pierce-Price et al. (2000)
	45-m NRO, 34″ at 49 GHz	CS (1-0)	$-1° \leq l \leq 1.6°$, $\|b\| \leq 0.25°$	Tsuboi et al. (1999)
	45-m Nobeyama Radio Observatory, 34″	^{12}CO ($J = 1 \rightarrow 0$), ^{13}CO ($J = 1 \rightarrow 0$)	$-1.5° \leq l \leq 3.4°$, $0.6° \leq b \leq 0.6°$	Oka et al. (1998)
	1.2 m Southern Millimeter-Wave Telescope (SMWT)	C^{18}O ($J = 1 \rightarrow 0$), HCNO	$-1.05° \leq l \leq +3.6°, -0.9° \leq b \leq +0.75°$	Dahmen et al. (1997)
	10-m Leighton telescope, CSO	800 μm, 30″	$\sim 1.5° \times 0.2°$	Lis et al. (1994)
IRAS	IRAS, 3-5′	12, 25, 60 and 100 microns	96% of the sky	Neugebauer et al. (1984)

4.1.2.2 OH 次线观测

Elitzur et al. (1976) 研究了 1612 MHz 脉泽的抽运模型，认为 1612 MHz 脉泽的抽运机制是 OH 先吸收 35 μm 波段辐射，从能级 $^2\Pi_{3/2}, J = 3/2$ 跃迁到 $^2\Pi_{1/2}, J = 5/2$，然后再跃回 $^2\Pi_{3/2}, J = 3/2$ 能级。相比之下，1720 MHz 谱线的能级反转主要是依靠碰撞抽运 (Elitzur, 1976)。

为了探测 OH/IR 星 (晚期 AGB 星)，te Lintel Hekkert et al. (1991) 观测了 2703 个 IRAS 点源的 1612 MHz 脉泽辐射。这些 IRAS 电源符合 $\log(f_{25\ \mu m}/f_{12\ \mu m}) > -0.2$，$\log(f_{60\ \mu m}/f_{12\ \mu m}) < 0.5$ 和 $f_{12\ \mu m} > 3$ Jy。他们总共找到 738 个 OH/IR 星，其中 579 个属于新探测到的源。这些源的 OH 谱线大部分为双角形状 (double horn structures)，这种谱线特征示踪膨胀的壳层结构 (Eder et al., 1988)。

Haynes et al. (1977) 用 Parkes 望远镜观测了 $326° < l < 340°$ 区域的 1720 MHz 谱线，观测空间分辨率约为 11.8′。他们发现 1612 MHz 和 1720 MHz 谱线大部分情况下处于反对称状态：如果其中一条谱线处于吸收线状态，则另外一条会表现为发射线。Dawson et al. (2014) 在对 SPLASH 先导区域的研究中也发现类似现象。

1612 MHz 次线大多跟晚型星成协 (Sevenster et al., 1997a,b)，而 1720 MHz 次线大多跟超新星遗迹成协 (Green et al., 1997)，也有观测表明部分 OH 次线脉泽跟恒星形成区成协 (Caswell, 1999)。Sevenster et al. (1997a) 利用澳大利亚的 ATCA(the Australia Telescope Compact Array) 干涉阵对天区 $|l| <= 10°, |b| <= 3°$ 进行了 OH 1612 MHz 谱线巡天。他们发现，在 307 个 OH 1612 脉泽中，有 245 个有双角形状，说明这些 OH 脉泽大多跟晚型星成协。Green et al. (1997) 观测了 67 个超新型遗迹，发现有 33 个跟 1720 MHz 脉泽成协。Caswell (1999) 观测了南天的 200 多个恒星形成区，发现其中一些有 1720 MHz 或者 1612 MHz 谱线辐射，说明 OH 次线也会在恒星形成过程中被激发。

这些巡天结果表明，OH 分子谱线是研究分子云、恒星形成和恒星演化的重要工具。目前中国正在建造的 FAST 500 米口径望远镜将在 OH 分子研究领域起重要作用。

4.2 CMZ

由于其对分子云和恒星形成的重要性，针对 CMZ 的研究众多。在本小节，我们简要回顾一下 CMZ 内分子云的一些物理和化学性质及其内部的恒星形成活动。

多个研究工作证实，CMZ 中的分子云质量约占银河系总分子云的 10%。Dahmen et al. (1997) 观测银心附近 $C^{18}O$ $(J = 1 \rightarrow 0)$ 辐射，覆盖天区 $-1.05° \leq l \leq$

$+3.6°, -0.9° \leq b \leq +0.75°$，其空间和速度分辨率分别为 9′ 和 2.93 km s^{-1}。他们发现光学薄的 C^{18}O ($J = 1 \rightarrow 0$) 和光学厚的 ^{12}CO ($J = 1 \rightarrow 0$) 在空间分布上差别很大。根据大速度梯度模型 (the Large Velocity Gradient，LVG)，他们得出银心的分子云总质量约为 $3 \times 10^7 M_\odot$。Pierce-Price et al. (2000) 利用 JCMT 望远镜上的 SCUBA (the Submillimeter Common-User Bolometer Array) 观测了 CMZ 的 850 和 450 μm 的辐射，其空间分辨率分别为 8″ 和 15″，观测覆盖天区范围为 $-1° < l < 1.8°$，$|b| < 0.25°$。根据他们的计算，CMZ 中分子云总质量为 $(5.3 \pm 1.0) \times 10^7 M_\odot$，这跟Dahmen et al. (1997) 得出的结论相吻合。一些致密分子探针的观测 (Jones et al., 2012, 2013) 表明，CMZ 中气体的密度大多高于 10^4 cm^{-3}，但是 H_3^+ 的存在说明 CMZ 也中存在热的弥散气体 (Oka et al., 2005)。

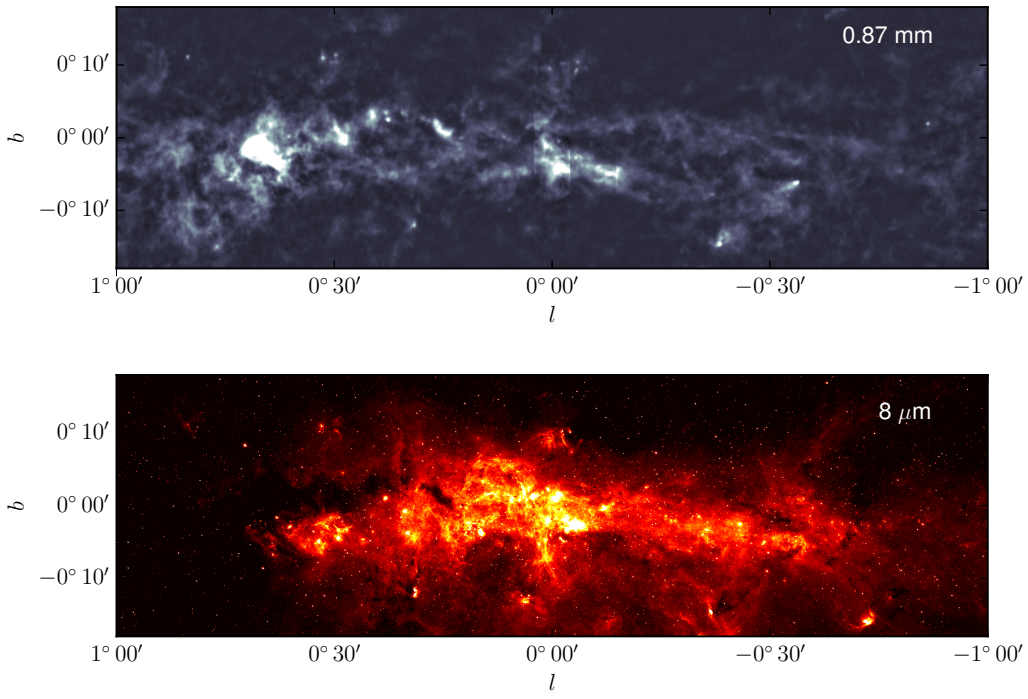

图 4.2: CMZ 在 0.87 毫米和 8 μm 波段图像。上图显示 0.87 毫米 (Schuller et al., 2009), 下图显示 8 μm 图像 (Benjamin et al., 2003; Churchwell et al., 2009)。在 0.87 mm 图像中我们可以清晰的看到Molinari et al. (2011) 证认的环形结构。

Figure 4.2. Images of the CMZ at 0.87 mm and 8 μm. The upper panel displays the image at 0.87 mm from Schuller et al. (2009), in which the twisted ring structure (Molinari et al., 2011) is evidently shown. The lower panel present the *spitzer* 8 μm band emission (Benjamin et al., 2003; Churchwell et al., 2009), which mainly traces H II regions.

CMZ 中的恒星形成活动多种多样，是验证恒星形成理论的绝佳区域。例如大

质量恒星形成区 Sgr B2 区域的恒星形成率极高，呈现星暴特征；也有区域的恒星形成率很低，例如 G0.25-0.01 (Lis et al., 1994, 1998)。图4.3中标注了 G0.25+0.01 和其他一些比较著名的天区的位置。(Yusef-Zadeh et al., 2009) 利用中红外数据研究了 CMZ 中的 YSOs，他们发现跟分子云一样，YSOs 沿这银经的分布也是不对称的。形成这种不对称分布的原因目前还没有研究清楚。

虽然 CMZ 一直是天文学的研究的热点区域，CMZ 分子云的三维结构却一直没有研究清楚。一方面是因为 CMZ 距离太阳比较远 (~8.5 kpc)，另一方面由于靠近银心的黑洞，CMZ 内分子云的运动非常复杂。为了研究银心分子云的正向 (face-on view) 结构并解释一些侧向观测 (见图4.2)，Sawada et al. (2004) 提出可以用 CO 发射线和 OH 吸收线来计算分子云的每个速度成分在 CMZ 的相对位置，他们确认了银心分子云的棒旋结构。Kruijssen et al. (2015) 分析认为 CMZ 内的巨分子云的轨道可能是开放的。然而，CMZ 内分子云的结构需要进一步的理论研究和观测证实。

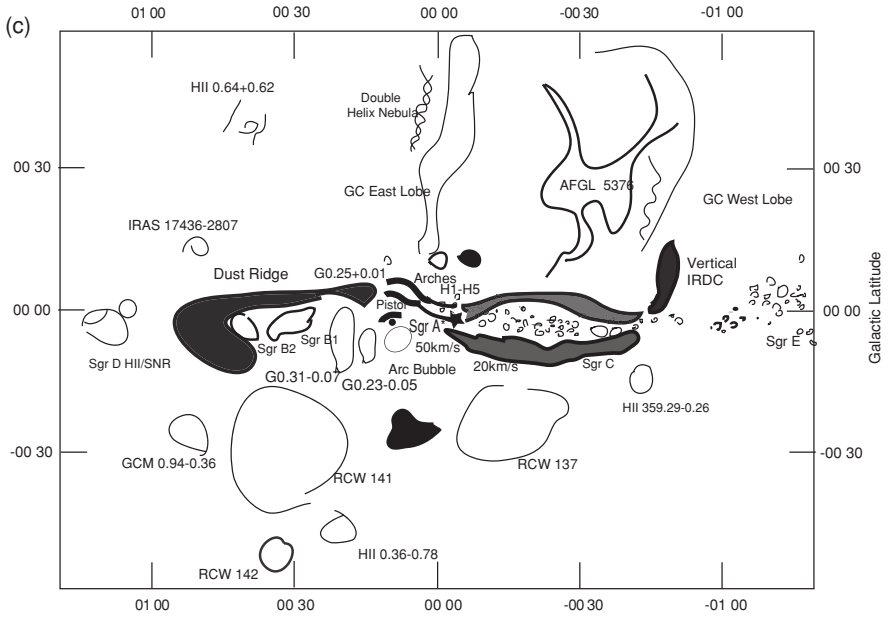

图 4.3: CMZ24 μm 波段子区域示意图 (Yusef-Zadeh et al., 2009)。

Figure 4.3. A schematic diagram of the GC, with prominent features detected at 24 μm. This picture is part of Figure 1 of Yusef-Zadeh et al. (2009).

4.2.1 气体和尘埃的温度

尘埃的温度可以用中远红外辐射来计算，而气体温度则需要用一些对温度敏感的分子进行探测，例如氨分子——NH_3。NH_3 是对称陀螺分子 (symmetric top

molecule)，对温度比较敏感，所以可以用做致密分子云的温度探针 (Danby et al., 1988; Walmsley et al., 1983)。

Ott et al. (2014) 利用 ATCA 观测了 NH_3 的 $(1,1)$ 和 $(2,2)$ 反演线，观测区域为 Sgr A* 和 Sgr B2 之间的致密分子团块。他们的测量对温度范围 10-80 K 比较敏感，他们发现这部分区域的温度分布峰值在 38 K 左右。他们还发现大的分子团块比小的分子团块温度高，沿着 Sgr B2 有明显的速度梯度。Ott et al. (2014) 认为分子云的加热源来自分子云内部的活动。

Mills et al. (2013) 利用 GBT 研究了 CMZ 的 NH_3 的七条亚稳态跃迁，观测模式为单点观测，总共观测 17 个点。他们发现 Sgr A 天区内一些 NH_3 的动力学温度可达 350 到 450 K，而在 Sgr B 天区内，动力学温度可达 600 K。他们认为沿视线方向，有大约 10% 的 NH_3 处于较高的动力学温度状态。

Ginsburg et al. (2016) 在Ao et al. (2013) 工作的基础上，用 p-$H_2CO(J = 3 \rightarrow 2)$ 跃迁研究了 CMZ 气体的温度。p-$H_2CO(J = 3 \rightarrow 2)$ 可以示踪数密度为 $10^4 - 10^5$ cm^{-3} 的致密分子气体。他们观测用的望远镜是 APEX (the Atacama Pathfinder Experiment)，空间和速度分辨率分别为 45″ 和 0.1 km s^{-1}。他们发现致密气体的温度范围为 30-100 K，而且气体温度高于尘埃温度，说明尘埃可能是致密气体冷却的重要途径。Ginsburg et al. (2016) 认为湍动是气体加热的主要机制。

Sodroski et al. (1994) 用 *COBE* DIRBE 观测的 140 和 240 μm 数据研究了 CMZ 尘埃的温度。沿着银经和银纬方向，他们发现 CMZ 有大尺度上的温度梯度——随着远离银心，温度逐渐降低。他们的计算表明，跟中性氢气体成协的冷尘埃 (17-22 K) 对远红外辐射的贡献可达 60%-75%，剩下的有 15%-30% 来自跟分子气体成协的冷尘埃 (大约 19 K)，还有不到 10% 来自比较延展的低密度H II 区中的热尘埃 (大约 29 K)。

Molinari et al. (2011) 利用高分辨率和高灵敏度的 *Herschel* 远红外数据计算了 CMZ 中尘埃的温度，他们发现尘埃温度范围在 15-40 K。如图4.4所示，低温尘埃呈现半径为 100 pc 左右的环形结构。

这些观测和研究表明 CMZ 中的分子云并不处于热动平衡状态，甚至可能会偏离局部热动平衡 (LTE)。

4.2.2 湍动

湍动是分子云基本性质之一，关于分子云湍动的综述见Elmegreen et al. (2004) 和Scalo et al. (2004)。由于其基本性，湍动可能跟分子云几乎所有性质都有关系，例如温度、密度和恒星形成等。

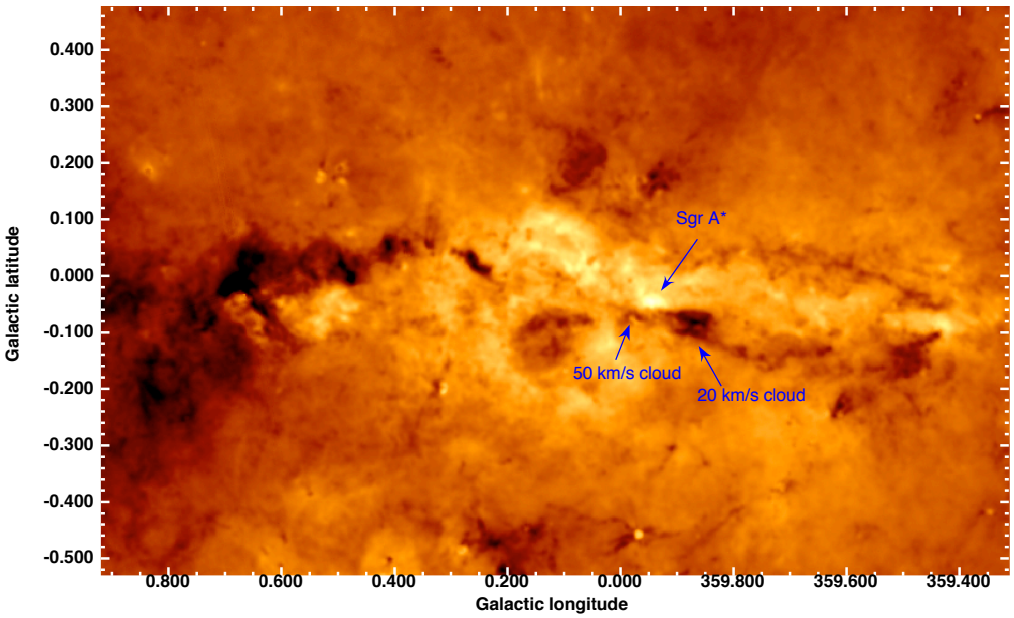

图 4.4: CMZ 尘埃的温度分布 (Molinari et al., 2011)。

Figure 4.4. The temperature of the dust in the CMZ (Molinari et al., 2011).

因为 CMZ 分子云的性质跟银盘上的分子云性质颇为不同，所以研究 CMZ 区域分子云拉松关系 (the Larson scaling relationship) 是有意义的，相关工作见Miyazaki et al. (2000) 和Oka et al. (1998, 2001)。Miyazaki et al. (2000) 观测了 49 GHz 波段的 $C^{32}S(J = 1 \rightarrow 0)$ 跃迁，并证认出 159 个分子团块。他们发现这些分子团块的速度弥散是银盘分子团块速度弥散的 5 倍左右，并给出的线宽-尺度 (line width-radius) 关系：

$$\frac{\Delta V}{\mathrm{km\ s^{-1}}} = (11.7 \pm 1.4)(\frac{R}{\mathrm{pc}})^{0.60\pm0.08}, \tag{4.1}$$

其中，ΔV 是线宽，R 是分子团块的尺度。这个关系跟Larson (1981) 给出的结果差别很大，Larson (1981) 给出的指数值为 0.38。

利用 ^{12}CO $(J = 1 \rightarrow 0)$ 数据，Oka et al. (2001) 推导出 CMZ 分子云尺度线宽关系式指数为 0.5，而关系式系数比从银盘分子云推导出的系数大 3.8 倍。

Shetty et al. (2012) 利用高密度气体分子探针，N_2H^+、HCN、$H^{13}CN$ 和 HCO^+，研究 CMZ 分子云的线宽-尺度关系。他们发现这四个高密度气体分子探针给出的关系的指数分别为 0.67、0.46、0.78 和 0.64，系数分别为 2.6、3.8、2.6 和 2.2。这说明 CMZ 分子云跟英仙座 (Perseus) 中的分子云性质略有不同，但是 CMZ 分子云的性质仍然跟湍动有关。最近的研究 (Kauffmann et al., 2017) 给出类似的结果。

CMZ 中比较低的恒星形成率可能跟其内部湍动强度有很大关系，强的湍动可能会抑制恒星形成。

4.2.3 Mopra 观测

澳大利亚 22 米 Mopra 射电望远镜对 CMZ 进行过一系列的谱线巡天。其中，Jones et al. (2012) 的 3 毫米巡天覆盖区域为 $-0.72^\circ \leq l \leq 1.80^\circ, -0.3^\circ \leq b \leq +0.22^\circ$。他们在 85.3 GHz 到 93.3 GHz 之间探测到 16 条分子谱线——c-C_3H_2、CH_3CCH、$HOCO^+$、SO、$H^{13}CN$、$H^{13}CO^+$、SO、$H^{13}NC$、C_2H、HNCO、HCN, HCO^+、HNC、HC_3N、^{13}CS 和 N_2H^+。在 3 毫米波段，Mopra 的空间和谱线分辨率分别为 40″ 和 2 km s^{-1}。Jones et al. (2012) 对这些谱线中 8 个比较强的谱线进行了主成分分析 (principal component analysis, PCA)，结果表明在大尺度上这些谱线的空间分布基本一致。

根据同样的方法Jones et al. (2013) 研究了 7 毫米波段 (42 - 50 GHzs) 的观测数据，总共观测到 24 条分子谱线，观测到的分子有 CS、CH_3OH、HC_3N、SiO、HNCO、$HOCO^+$、NH_2CHO、OCS、HCS^+、CCS、$C^{34}S$、^{13}CS、^{29}SiO、$H^{13}CCCN$、$HCC^{13}CN$ 和 HC_5N，外加三条氢复合线。他们巡天覆盖 $-0.72^\circ \leq l \leq 1.80^\circ, -0.3^\circ \leq b \leq +0.22^\circ$，谱线空间和速度分辨率分别为 65″ 和 1.8 km s^{-1}。这些分子示踪的气体的典型密度为 10^4 cm^{-3}。

Mopra 在 12 毫米波段的观测 (Walsh et al., 2011) 主要包括 H_2O 脉泽、NH_3、HCCCN 和 CH_3OH，以及一些射电复合线。此波段的巡天简称为 HOPS (H_2O southern Galactic Plane Survey)[1]，HOPS 其他的观测和数据分析见Purcell et al. (2012)，Walsh et al. (2014) 和Longmore et al. (2017)。

Mopra 的观测表明，CMZ 中的气体密度比较高，且其中的环境有利于星际分子的形成。

4.2.4 三维模型

分子气体的结构对银心分子云的研究至关重要，但是要从侧向观测中推测正向结构十分困难。虽然有很多研究致力于此，但是这个问题仍然没有解决。

比较有代表性的是Binney et al. (1991) 提出的一个三维模型。他们用这个模型解释观测到的三条分子谱线H I、CO 和 CS，他们的观测覆盖区域为 $|l| < 10^\circ, |b| < 2^\circ$。他们的模型显示，CMZ 中的分子气体呈现棒结构，这些气体在 x_1 和 x_2 两种轨道上运动。H I气体主要在 x_1 轨道上运动，但是在这些原子气体在接近银心的时候会产生激波，进而会形成 CO 等分子气体。他们的模型可以很好地解释 CO 辐射在 (l, v) 图上的分布以及 CS 辐射在天球投影上的空间分布。

[1] https://research.science.mq.edu.au/hops/public/index.php

为了验证前人提出的一些动力学模型，Sawada et al. (2004) 提出了可以用 CO 发射线和 OH 吸收线来计算分子云沿视线方向的相对位置，这个方法的优点是不依赖于动力学模型。由于我们的研究是基于这个方法，所以在本小节我们对此方法做比较详细地介绍。

Sawada et al. (2004) 提出的计算分子云相对位置的方法基于四个假设。首先，他们假设在视线方向上不同的速度成分的位置是不一样的；其次，他们假设 CO 亮温度问分子气体的数量进而跟 OH 的光深成正比。再次，他们假设 OH 的激发温度是常数。最后，他们假设 CMZ 的 18 cm 波段射电连续谱辐射是轴对称的，并在此基础上对射电连续谱辐射进行建模。我们认为Sawada et al. (2004) 关于 OH 激发温度和光深的假设是不准确的，并将在我们的工作中改进这两个假设。

Sawada et al. (2004) 用来计算分子云位置的方程为：

$$\tau_{\rm app} = \frac{f[1-\exp(-\tau_{\rm OH})][\int_{-\infty}^{s_0} j(r){\rm d}s - T_{\rm ex}({\rm OH})]}{\int_{-\infty}^{s_\odot} j(r){\rm d}s}, \tag{4.2}$$

其中，s_0 是分子云在视线方向的位置，$j(r)$ 是连续谱的发射率 (emissivity)，$T_{\rm ex}({\rm OH})$ 是 OH 的激发温度，$\tau_{\rm OH} = Z \times T_{\rm CO}$ 是 OH 的光深，f 是波束填充因子，$\int_{-\infty}^{s_0} j(r){\rm d}s$ 是连续谱从无穷远到分子云处的积分值，$\int_{-\infty}^{s_\odot} j(r){\rm d}s$ 连续谱从无穷远到太阳的积分值 (可观测)，τ_{app} 是 OH 谱线的相对吸收值 (apparent opacity，可观测)。他们假设 $T_{\rm ex}({\rm OH}) = 4$ K，$Z = 0.15$ K^{-1}，进而可以解算分子云的相对位置。虽然他们的假设中有两个不是很准确，但是他们的结果仍然有一定的意义。

Karlsson et al. (2015) 利用 VLA 观测并分析了距离银心半径 10 pc 内的 OH 分子流，谱线空间和速度分辨率分别为 $7'' \times 5''$ 和 8 km s^{-1}。他们观测了 OH 四条基态跃迁，研究发现银心的黑洞和星团的引力对 OH 分子流有较大影响。

Henshaw et al. (2016) 对银心分子云的三维结构做了一些回顾和总结。Henshaw et al. (2016) 利用三个致密气体分子探针——HNCO、N_2H^+ 和 HNC——对 CMZ 的致密气体进行了研究。利用 Mopra 的 CMZ 数据 (Jones et al., 2012) 和新开发的 IDL 程序，他们分析认为 CMZ 的双旋臂模型 (Sawada et al., 2004; Sofue, 1995) 虽然可以很好的拟合数据，但缺乏合适的物理解释；Molinari et al. (2011) 给出的闭合轨道模型预测跟观测的气体分布有冲突；相比之下，Kruijssen et al. (2015) 提出的开放轨道模型跟观测数据更加吻合，但是需要进一步的观测来证实。

4.2.5 恒星形成

恒星形成是星系中的最基本活动之一，恒星形成过程直接影响星系的形态，并对星系演化有深远的意义，所以理解恒星过程是天文学最基本的课题之一。但是

关于恒星形成仍然有很多问题没有解决，尤其是大质量恒星形成。由于分子云的物理和化学性质及其附近的引力场的特殊性，CMZ 提供了一个可以很好地验证和研究恒星形成理论的场所，因此 CMZ 一直是恒星形成研究的热点区域。

总的来说，虽然 CMZ 中有大量的高密度气体，其内部的恒星形成率却大大低于预期值，所以 CMZ 中的恒星形成处于被抑制状态 (Kauffmann et al., 2017)。除了几个区域有比较明显的恒星形成区，例如 Sgr B2，CMZ 中大部分区域的恒星形成率都很低，例如红外暗云 G0.253+0.016 (the Brick)。Sgr B2 中的恒星形成活动呈星爆状态 (对星爆星系的研究极具参照价值)，而有恒星形成率很低的 G0.253+0.016 则被认为可能是大质量星团的前身。所以，CMZ 对恒星形成的研究有重要意义。

最近Yusef-Zadeh et al. (2009) 利用 MIPS 24 和 70 μm 巡天数据研究了银心半径 400 pc 以内的恒星形成活动。利用双色图和谱能量分布，他们研究了 CMZ 区域内的 YSOs 后发现，YSOs 倾向于分布在负银经一侧，而分子云则大约有 2/3 分布在正银经一侧。他们给出的 CMZ 内的恒星形成率为 0.14 $M_\odot$ yr^{-1}。因为大部分 YSOs 处于 Stage I，他们认为在大约 10^5 年前，CMZ 爆发过恒星形成活动 (burst of star formation)。他们还发现 CMZ 中的恒星形成活动符合施密特-肯尼科特定律 (Schmidt-Kennicutt law)，说明 CMZ 中的物理环境对 CMZ 中的恒星形成影响不大。

An et al. (2011) 给出的 CMZ 中的恒星形成率为 0.07 $M_\odot$ yr $^{-1}$，这个值比Yusef-Zadeh et al. (2009) 给出的还低，而造成这种现象的原因很可能是 CMZ 内强的湍动 (Kruijssen et al., 2014)。Longmore et al. (2013) 和Rathborne et al. (2014) 也认为恒星形成率不只跟柱密度或者数密度有关，湍动对 CMZ 中的低恒星形成率有重要影响。

4.3 数据观测和处理

4.3.1 CO 数据

我们使用两条 CO 同位素谱线，^{12}CO ($J = 1 \rightarrow 0$) 和 ^{13}CO ($J = 1 \rightarrow 0$)，计算 CMZ 中分子云的相对位置，其中 ^{12}CO ($J = 1 \rightarrow 0$) 数据取自Dame et al. (2001) 的 CO 银道面巡天，巡天使用得是在 CfA 和智力 (Cerro Tololo Inter-American Observatorys) 的两台 1.2 米望远镜。银心数据的观测是由后者完成的，空间和谱线分辨率分别为 8.8′ 和 1.3 km s^{-1} (Bitran et al., 1997)，相应的灵敏度为 0.10 K。为了跟 OH 数据匹配，我们对 ^{12}CO ($J = 1 \rightarrow 0$) 数据进行了平滑 (平滑高斯核的 FWHM 为 12.8′)，平滑后 ^{12}CO ($J = 1 \rightarrow 0$) 的空间分辨率为 15.5′。

^{13}CO ($J = 1 \rightarrow 0$) 数据是用澳大利亚 22 米 Mopra 射电望远镜观测的，具体观测参数见Burton et al. (2013)。^{13}CO ($J = 1 \rightarrow 0$) 的数据精确校准还没完成，本

文用的数据是由合作者 R. Blackwell、M. G. Burton 和 G. P. Rowell 提供的初步处理数据，除了部分天区的基线不平外，大部分数据质量良好。Mopra CO 巡天覆盖 $-1.5^\circ \leqslant l \leqslant 3.5^\circ$ 和 $-0.5^\circ \leqslant b \leqslant 1.0^\circ$，总共观测三条 CO 同位素谱线——^{12}CO、^{13}CO 和 C^{18}O。Mopra 观测模式为 OTF 成图，原始数据的空间和速度分辨率分别为 0.6′ 和 0.1 km s^{-1}。

^{13}CO ($J = 1 \rightarrow 0$) 数据观测处理的方法在Burton et al. (2013) 中有详细描述，但是由于 CMZ 的速度弥散很大，为了能更好的获取基线，数据需要做特殊处理。而且 CMZ 观测中参考点也可能存在残余辐射，需要做进一步改正。完整的 CO 数据将在 R. Blackwell 及其合作者以后的文章中做详细描述。R. Blackwell 及其合作者提供的 Mopra CO 巡天的早期数据的空间和速度分辨率分别为 3.0′ 和 2 km s^{-1}。我们用一个高斯核 (FWHM 为 15.2′) 把数据平滑为 15.5′，然后网格化为 7.5′。

4.3.2 OH 数据

我们 CMZ 的数据是 SPLASH 巡天的一部分，关于 SPLASH 详细的观测参数和数据处理见Dawson et al. (2014)。SPLASH 对 OH 分子谱线的观测覆盖整个 CMZ，包括四条 18 厘米基态跃迁——1612、1665、1667 和 1720 MHz。在这一小节，我们对 CMZ 区域 OH 数据处理做简要介绍。

SPLASH 的观测使用的是 64 米 Parkes 射电望远镜 (隶属于 ATNF——the Australia Telescope National Facility)，观测模式为 OTF 成图。Parkes 每次观测 CMZ 中的一块 ($2^\circ \times 2^\circ$)，每块总共观测 10 次，扫描行间隔为 4.2′。相比于 Parkes 的波束 (在 1720 MHz 大约为 ∼12.2′) 来说，扫描过采样——有利于获得高的信噪比和完整的谱线。SPLASH 的 CMZ 巡天覆盖 $-6^\circ \leqslant l \leqslant 6^\circ$ 和 $-2^\circ \leqslant b \leqslant 2^\circ$。

我们用Dawson et al. (2014) 提供的方法做带通校准 (bandpass calibration) 后，用ASAP[2]软件包分离分子谱线和连续谱。对观测信号做带通校准后，我们对积分时间为 4 秒的谱线 (此时包含分子谱线和连续谱信号) 做基线拟合。拟合的方法是，我们先屏蔽 OH 分子有信号的区间，然后根据信号区间外的谱线值做线性插值——以此估计信号区间的基线。如果信号区间不是很宽，这个方法是比较有效的，但在银心信号速度弥散很宽的地方，这个方法给出的基线并不准确。为了获取准确的基线，我们对 CMZ 的谱线做了递归处理。我们对数据一共处理了三次。除了第一次，后面二次我们都会根据上一次处理分理出的分子谱线结果 (只含 OH 信号，没有连续谱) 改进信号屏蔽区间 (mask)。

[2] http://svn.atnf.csiro.au/trac/asap

第一次粗处理时，因为没有分子谱线信息，我们利用ASAP 程序包里的LINEFINDER 任务来自动识别 OH 信号，以此确认信号屏蔽区间。把信号区间屏蔽并做线性插值后，我们对谱线做大尺度平滑 (高斯核 $\sigma = 45$ km s^{-1}) 来获取基线，用原始谱线减去基线，就得到 OH 分子谱线，分子谱线以 FITS (Flexible Image Transport System) 形式保存。

第二次处理的时候，我们利用第一步给出的分子谱线 FITS 文件，做准确的信号区间识别。信号区间识别是用DUCHAMP (Whiting, 2012) 软件包完成的，这是一个三维信号源识别软件，可以在三维 (银经、银纬和速度) 空间给出信号的范围。我们发现，相比于次线来说，OH 两条主线的信号区间识别不准，原因是 OH 两条主线频率靠得太近，银心附近的速度弥散又很大，导致信号屏蔽区间范围很宽。因此，我们利用 OH 次线给出的信号区间来处理 OH 主线，原因是他们的速度区间是基本一致的。

虽然第二步给出得分子谱线 FITS 已经比较准确，但是我们发现有的 OH 吸收区间的亮温度是正的 (应该是负的)，这说明由于两条 OH 主线信号接轨，信号区间过长，进而导致线性插值的基线不准。虽然不依靠模型计算，我们无法获取获取这些区域的准确基线，但是我们可以至少让假的 OH 发射线 (实际上是吸收线) 降低到零附近，这样虽然给出的 OH 分子谱线依然不是准确值，但至少会更接近准确值。在第三步中，我们对每一条谱线用眼睛判别假的 OH 发射线，并取消此区间的屏蔽，也就是说把此区间当基线处理，这样假的发射线就会被压低到零点附近。虽然这样给出的 OH 分子谱线依然不准，但是接下来的处理已经是模型依赖了，所以我们的数据处理到此为止。

在 Sgr A* 附近的连续谱辐射亮温度很高，可能会导致 Parkes 在观测的时候信号饱和。为了检查信号是否饱和，我们调整参数并观测了银心附近的小区域。调整参数后望远镜对接受信号做了更多的衰减处理，这样望远镜就不会处于饱和状态。我们发现在银心的一个波束范围内，Parkes 确实已经饱和，所以我们用调整参数后的观测替换掉了原来的饱和信号。

利用 ATNF 标准源 PKS B1934-638，我们对分子谱线和连续谱做了主波束效率改正，所以我们得到谱线温度都是主波束亮温度。

我们用GRIDZILLA[3]软件包从处理后的 Parkes 文件中提取 OH 分子谱线和连续谱并保存为 FITS 文件格式。提取过程中，我们利用 FWHM 为 20′ 的高斯核 (切断半径为 10′) 做平滑，最终 FITS 的像素大小为 3′，对应的有效空间分辨率为 15.5′，谱线分辨率为 0.18 km s^{-1}。最后的谱线噪声水平大约为 0.1 K。因为平滑后的 CO

[3] http://www.atnf.csiro.au/computing/software/livedata/

谱线分辨率跟 OH 已经十分接近，我们直接利用MIRIAD 软件包 (Sault et al., 1995)，按照 CO FITS 的像素大小 (7.5′) 对 OH FITS 做重采样。

4.3.3 连续谱

因为 SPLASH 只能测量 ON 点和 OFF 点的连续谱差值，我们需要把 OFF 点的连续谱值加到最后的连续谱上，以此获取完整的连续谱值。我们利用 HIPASS (the HI Parkes All-Sky Survey) 巡天 (Calabretta et al., 2014) 给出的 1.4 GHz 连续谱值来估算 OFF 点在四条谱线波段的连续谱值。

在 1.4 GHz，OFF 点的连续谱大约为 8 K，扣掉 CMB (the Cosmic Microwave Background) 后，大约为 5.27 K。根据Platania et al. (2003) 给出的连续谱在此波段的谱指数 (−2.7)，我们估计出 1612、1665、1667 和 1720 MHz 四条谱线在 OFF 点的连续谱值 (不包含 CMB) 分别为 3.7、3.4、3.4 和 3.1 K。通过比较 SPLASH 在不同时间段观测的连续谱值，我们发现连续谱辐射的观测相对误差小于 10%。

4.4 计算模型和假设

我们先简要回顾一下Sawada et al. (2004) 提出的计算分子云相对位置的模型。他们的计算基于 CO 发射线、OH 吸收线和四条假设。首先，他们假设 CO 发射线和 OH 吸收线在同一个速度上对应视线方向的同一个位置。其次，他们假设 OH 光深跟 CO 亮温度成正比。再次，他们假设 OH 激发温度 (1667 MHz) 在整个 CMZ 内是常数。组后，他们假设 CMZ 内的连续谱辐射是光学薄且轴对称的，并且可以分解为三个高斯成分。

计算分子云相对银心位置的原理见图4.5。OH 吸收线的深度取决于 OH 激发温度，光深以及 OH 分子云背后的连续谱温度。如图4.5所示，如果把一个分子云从远到近 (距离太阳) 移动，由于是发射线 (该波段没有射电连续谱辐射)，CO 的亮温度不会有变化，但是由于 OH 背后的连续谱辐射有变化，OH 的吸收线会加深。

关于 OH 吸收线的辐射转移方程在下文有详细描述。除了背景连续谱温度，OH 的光深也会对 OH 谱线有影响。所以一般情况下，我们无法区分这两种影响。因此要计算 OH 的相对位置，我们首先得分离这两种效应。而且根据辐射转移公式，OH 的激发温度和背景连续谱温度耦合在一起，所以我们还要分离激发温度跟背景连续谱温度。

Sawada et al. (2004) 假设 OH 1667 MHz 线的激发温度为 4 K 并认为 OH 的光深跟 CO 亮温度成正比，进而估计 OH 分子云背后的连续谱温度。实际上，这里的 4

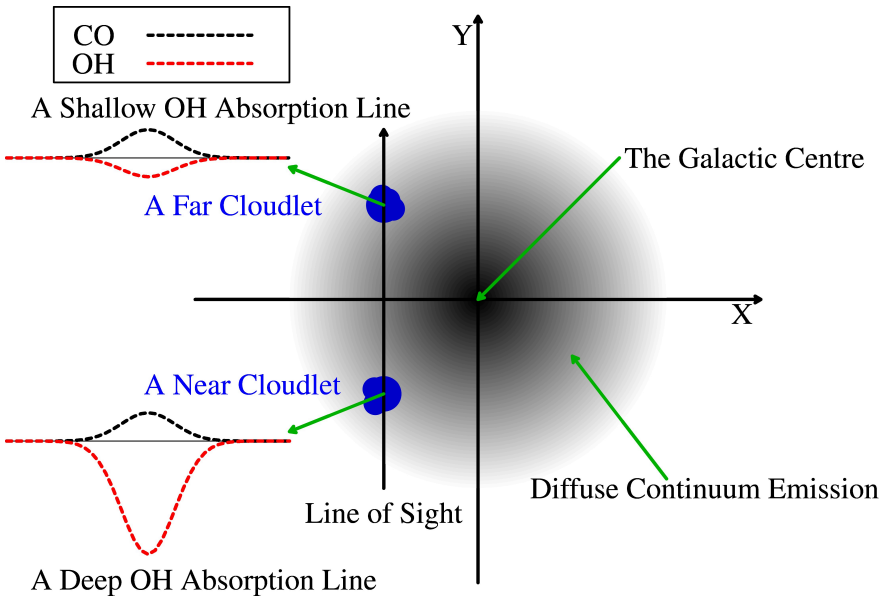

图 4.5: 计算分子云相对银心的位置原理示意图 (Sawada et al., 2004, 图 3)。图中的黑色和红色点线分别表示 CO 发射线和 OH 吸收线。

Figure 4.5. Principles of deriving the relative positions of molecular clouds, which is reproduced from Sawada et al. (2004, Figure 3). The black dashed lines and red lines represent CO emission and OH absorption lines, respectively.

K 是扣掉 CMB 后的激发温度，原来的激发温度值约为 6.7 K。虽然这个激发温度值是合理值 (Crutcher, 1977; Li et al., 2003)，但是假设 OH 激发温度是常数是不准确的。他们采用的 OH 光深跟 ^{12}CO ($J = 1 \rightarrow 0$) 的亮温度的比例为 0.15 K^{-1}，由于 ^{12}CO ($J = 1 \rightarrow 0$) 有时候会变光学厚，这个假设也不准确。

我们利用 SPLASH 观测的四条谱线和 Mopra 观测的 ^{13}CO ($J = 1 \rightarrow 0$) 谱线改进了Sawada et al. (2004) 提出的方法。利用 SPLASH 观测的四条谱线，我们可以更加准确的解算 OH 激发温度和光深，从而减小计算误差。

我们保留了Sawada et al. (2004) 假设中的第一条和第二条，而对另外两条做了修改。在第二条中，我们不直接限制 OH 光深，而选择限制 OH 柱密度，即假设 OH 柱密度跟 CO 亮温度成正比。这个假设在 CO 光学薄的情况下是基本合理的，为了保证 CO 光学薄，我们用 ^{13}CO ($J = 1 \rightarrow 0$) 对 ^{12}CO ($J = 1 \rightarrow 0$) 做了部分改正。在第三条中，我们不认为 OH 的激发温度一直是常数，我们只假设 OH 两条主线的温度相等。对 OH 两条次线，我们不做任何限制。

我们的四条假设总结如下：

1. CO 发射和 OH 吸收成分出自同一个分子云，并且对应于视线方向上同一个

位置。

2. OH 总基态柱密度没，$N(\mathrm{OH})$，跟 $^{12}\mathrm{CO}$ $(J = 1 \to 0)$ 亮温度成正比，也就是说 $N(\mathrm{OH}) = f \times T_{\mathrm{CO}}$，其中 f 是比例系数。

3. OH 两条主线的激发温度相等。

4. CMZ 内的连续谱辐射光学薄且轴对称，并且可以分解为三个高斯成分。

4.5 解算 OH 激发温度

我们找到了一个可以精确解算 OH 激发温度、光深和柱密度的方法——不适应于脉泽，利用这个方法我们极大的改进了Sawada et al. (2004) 的模型。这个方法的核心思想在于，激发温度和光深可以表示为柱密度的函数，并且可以用 OH 基态四条发射线精确解算。

为了清楚阐述我们的方法，我们分两种情况来介绍。有时背景连续谱温度是已知的，这种情况下，OH 的柱密度可以直接用四条 OH 谱线解算。对 CMZ 中的分子云来说，背景连续谱温度未知，且两条主线的信号有可能会混在一起，所以我们需要利用 §A.3.3 中第二条和第三条假设提供的方程作为补充，把背景连续谱温度求出。根据解算的背景连续谱温度和 CMZ 中连续谱辐射分布，我们可以计算分子云的相对位置，进而求得分子云的三维结构。我们将分开描述这两种情况。

4.5.1 背景连续谱稳定已知

在这种情况下，因为背景连续谱可观测，我们不需要额外引入未知量，所以这种情况比较简单。分子谱线的辐射转移方程为：

$$T_{\mathrm{b}}\left(\mathrm{v}\right) = \left(T_{\mathrm{ex}} - T_{\mathrm{c}} - T_{\mathrm{cmb}}\right)\left(1 - \mathrm{e}^{-\tau_{\mathrm{v}}}\right), \tag{4.3}$$

其中，T_{c} 是背景连续谱辐射，T_{cmb} 是 CMB (2.73 K)，T_{ex} 和 τ_{v} 分别是 OH 分在速度 v 附近的激发温度和光深。这个公式对吸收线和发射线都适用，如果 $T_{\mathrm{ex}} < (T_{\mathrm{cmb}} + T_{\mathrm{c}})$，我们观测到的将会是吸收线 $(T_{\mathrm{b}} < 0)$。

如果 T_{c} 已知，方程4.3中的未知量只有 T_{ex} 和 τ_{v}。我们总共观测了四条谱线，每条谱线有两个未知数，所以总共有八个未知数。显然，八个未知数无法用四个方程解算。

我们发现 $T_{\rm ex}$ 和 $\tau_{\rm v}$ 都是柱密度的函数，而 OH 基态只有四个能级，所以我们可以用四个柱密度可以把上述八个未知数全部表示出来。换句话说，我们把求八个柱密度和光深降低为求四个柱密度。如图4.1所示，我们用 N_1、N_2、N_3 和 N_4 表示四个能级的柱密度。

激发温度，$T_{\rm ex}$，的定义式为：

$$\frac{n_{\rm u}}{n_{\rm l}} = \frac{g_{\rm u}}{g_{\rm l}} \exp\left(-\frac{h\nu_0}{kT_{\rm ex}}\right), \tag{4.4}$$

其中，$n_{\rm u}$ 和 $n_{\rm l}$ 分别是谱线上下能级的数密度，$g_{\rm u}$ 和 $g_{\rm l}$ 分别是上下能级的统计权重，h 是普朗克常数，k 是玻尔兹曼常数，ν_0 是谱线的静止频率。激发温度的概念比较容易误解，本质上来说激发温度只是上下能级数密度比的另外一种表示，目的是为了简化辐射转移方程 (Emerson, 1996; Rybicki et al., 1986)。如果各个能级处于 LTE 状态，则激发温度跟动力学温度相等；其他情况下的意义仅为上下能级数密度之比。另外一个理解激发温度的方式是，可以认为谱线的行为跟上下能级处于热平衡状态时的行为一致，但是不同的谱线有不同的激发温度。LTE 假设下，所有谱线的激发温度相等，所以 LTE 假设对 OH 基态来说一般并不成立，我们只假设 OH 两条主线的激发温度近似相等。

改写 $T_{\rm ex}$ 的定义式，并替换数密度为柱密度，可得：

$$T_{\rm ex} = \frac{h\nu_0/k}{\ln\left(N_{\rm l}g_{\rm u}\right) - \ln\left(N_{\rm u}g_{\rm l}\right)}, \tag{4.5}$$

其中，$N_{\rm u}$ 和 $N_{\rm l}$ 分别代表上下能级的柱密度，见图4.1。因此 OH 基态跃迁的激发温度可以用四个柱密度表示。

OH 光深，$\tau_{\rm v}$，的计算公式为：

$$\tau_{\rm v} = \frac{c^3}{8\pi\nu_0^3}\frac{g_{\rm u}}{g_{\rm l}}N_{\rm l}A_{\rm ul}\left(1-{\rm e}^{-\frac{h\nu_0}{kT_{\rm ex}}}\right)\phi_{\rm v}, \tag{4.6}$$

其中，$N_{\rm l}$ 是跃迁下能级的柱密度，$A_{\rm ul}$ 是爱因斯坦系数 (系数 A)，$\phi_{\rm v}$ 是归一化的谱线形状。将方程4.5带入方程4.6，我们有：

$$\tau_{\rm v} = \frac{c^3}{8\pi\nu_0^3}A_{\rm ul}\left(\frac{g_{\rm u}}{g_{\rm l}}N_{\rm l} - N_{\rm u}\right)\phi_{\rm v}. \tag{4.7}$$

显然，光深也是柱密度的函数，所以 OH 基态跃迁的光深也可以用四个柱密度表示。因此，八个激发温度和光深可以转化为四个柱密度。这种从 ($T_{\rm ex}$, $\tau_{\rm v}$) 到 ($N_{\rm l}$, $N_{\rm u}$) 的转换类似于数学中的坐标变换，但是一条谱线来说，这种变换只会增加计算复杂度。将方程4.5和4.7带入方程4.3，我们可以得到只用柱密度表示的辐射转

移方程。所以，用四个柱密度可以表示出四条分子谱线，利用这四个分子谱线组成的方程组，我们可以把四个柱密度解算出来。

这个方法的物理基础在于 OH 基态跃迁相互之间并不独立，因为他们只牵扯到四个能级。有了柱密度，激发温度和光深的计算就很容易了。显然，这四个方程是非线性的，如果观测精度和空间分辨率不够高，可能会导致方程无解。

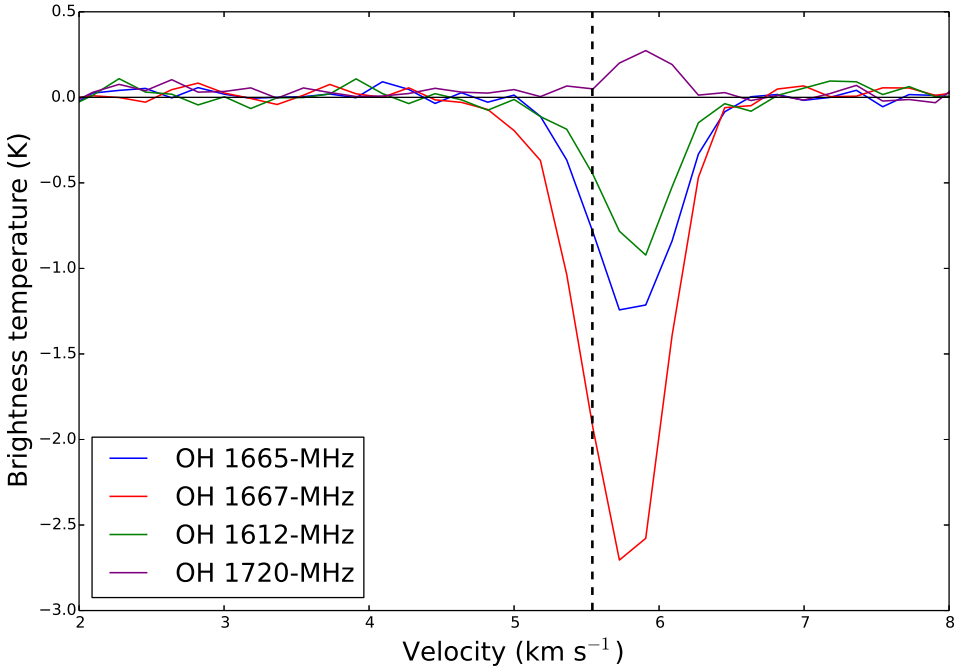

图 4.6: 我们用来验证 OH 基态跃迁方程组的谱线，谱线来自 SPLASH 先导区域 (Dawson et al., 2014)。谱线位置为 $(l,\ b) = (343.5°, -0.05°)$。垂直黑色虚线表示速度 5.54 km s^{-1}。

Figure 4.6. OH ground-state spectral lines at $(l,\ b) = (343.5°, -0.05°)$ (Dawson et al., 2014). The black dashed vertical line marks the position 5.54 km s^{-1}.

我们利用 SPLASH 先导区域观测的连续谱和 OH 四条基态谱线来检验这个方法。因为在一般情况下，我们不知道 OH 分子云是在连续源前方还是后方，所以我们寻找吸收线比较深的速度成分。比较深的吸收表明分子云极有可能是在连续源前方 (沿视线方向)。我们发现在位置 (343.5°, −0.05°, 5.54 km s^{-1}) 上，四条 OH 谱线方程组成的方程组有精确解。这个位置的谱线如图4.6所示，我们计算出的 1612、1665、1667 和 1720 MHz 谱线的精确激发温度分别为 3.24 、7.17、5.66 和 57.82 K，精确的光深分别为 0.023、0.052、0.121 和 0.0013。虽然我们只找到了一组精确解，但这说明我们的方法是有效的。有些速度成分解算失败，原因可能是 Parkes 的空间分辨率不高或者 1720 MHz 谱线信噪比偏低。

4.5.2 解算 CMZ

解算 CMZ 中的 OH 辐射转移，我们主要有两个困难：第一，我们不知道 OH 分子云视线方向背后的连续谱亮温度，导致多出一个未知量；第二，银心分子云大的速度弥散导致两条 OH 主线混合在一起，导致我们失去一个方程。因此，我们需要额外的两个方程来解算 CMZ 中的辐射转移，而这两个方程来自我们的第二条和第三条假设。

在第三条假设中，我们假设两条主线激发温度相等，这提供了一个关于 OH 激发温度的方程。如果沿视线方向上速度弥散过大，则 1667 MHz 线的正速度 (红移) 端跟 1665 MHz 的负速度段 (蓝移) 端混在一起，这种情况下，我们失去了一个主线方程。银心中也有部分区域可以准确观测这两条主线，但是由于大量的区域显示基线不准，我们只能使用这两条主线观测方程中的一个。Crutcher (1977, 1979) 研究发现，OH 两条主线的激发温度的差别在 $1-2$ K 之内。虽然他们发现即使 OH 主线激发温度差别很小也会导致柱密度测量不准，但是在我们的计算中，OH 的柱密度已被 CO 亮温度限制，并且是利用柱密度解算激发温度，因此实际上第三条假设是基本正确的。我们在 §4.6.3会对这个假设导致的误差做详细讨论。

第三条假设的数学表达为：

$$T_{\rm ex1665} = T_{\rm ex1667}, \tag{4.8}$$

其中，$T_{\rm ex1665}$ 和 $T_{\rm ex1667}$ 分别代表 1665 和 1667 MHz 谱线的激发温度。我们对 OH 两条次线不做任何限制，实际上 OH 次线的激发温度跟主线的差别很大。方程4.8可以代替一条 OH 主线的观测方程。因此，对 CMZ 来说，我们仍然有四个比较准确的方程。

对这四条谱线，我们看似需要解算四个连续谱辐射，但实际上由于 OH 分子云背后的连续谱辐射占沿视线方向的总连续谱积分的比例对四条谱线来说是相同的，我们只需要增加一个未知数。为了方便起见，我们以 1665 MHz 谱线背后的连续谱辐射，$T_{\rm c}$，作为未知数。其他波段的连续谱辐射可以根据 1665 MHz 谱线的比例求出。

在第二条假设中，我们假设 CO 柱密度跟 OH 柱密度成正比，这提供了第五个方程。CO 的柱密度可以由光学薄的谱线来示踪。相比于 ^{12}CO $(J=1\rightarrow0)$，^{13}CO $(J=1\rightarrow0)$ 更趋向于光学薄，但是 Mopra 观测的 ^{13}CO $(J=1\rightarrow0)$ 的信噪比不高，而且 ^{12}CO $(J=1\rightarrow0)$ 虽然容易光学厚，但是由于银心大的速度梯度和 Parkes 低的空间分辨率 (∼38 pc)，这种效应会被削弱很多。因此，我们仍然主要使用 ^{12}CO $(J=1\rightarrow0)$，但是会用 ^{13}CO $(J=1\rightarrow0)$ 改正光学厚的区域。光学厚的

区域可以根据 ^{12}CO/^{13}CO 的比值来检测。

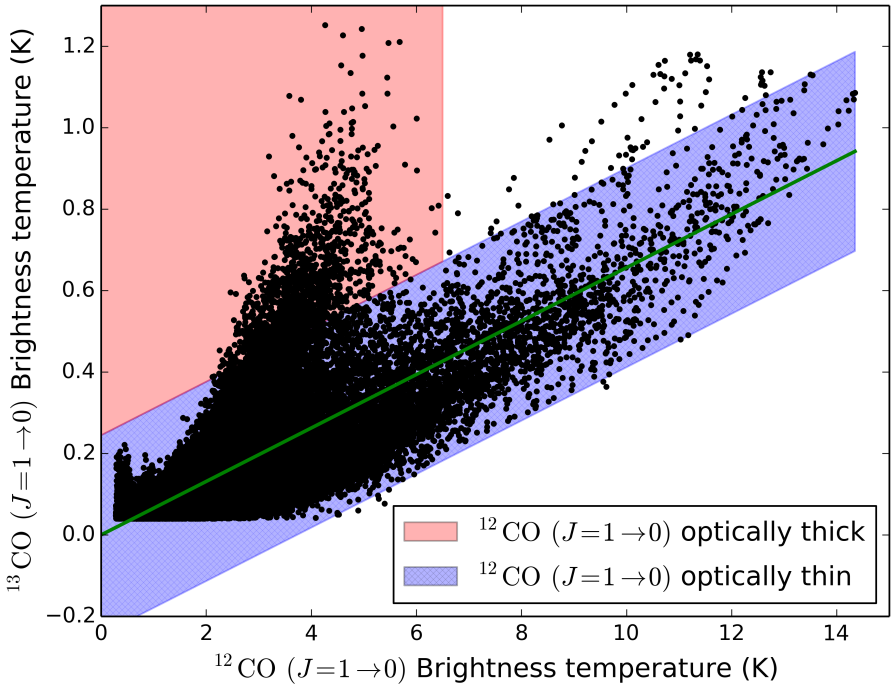

图 4.7: ^{12}CO ($J = 1 \rightarrow 0$) 和 ^{13}CO ($J = 1 \rightarrow 0$) 亮温度对比图。图中过原点的绿色线的斜率为 0.066±0.020，绿色线的拟合只采用大于 6.5 K 的数据。^{12}CO ($J = 1 \rightarrow 0$) 在蓝色区域大部分处于光学薄，而在红色区域，多部分是光学厚。

Figure 4.7. The brightness temperature of ^{12}CO ($J = 1 \rightarrow 0$) versus ^{13}CO ($J = 1 \rightarrow 0$). The green line, which passes through the origin with a slope of 0.066±0.020, was fitted with data whose brightness temperature of ^{12}CO ($J = 1 \rightarrow 0$) is greater than 6.5 K. The blue area is the coverage within 2σ (σ = 0.12 K) of the residual, where ^{12}CO ($J = 1 \rightarrow 0$) emission is mostly optically thin, while beyond this blue area, marked in red, the ^{12}CO ($J = 1 \rightarrow 0$) emission is mostly optically thick.

如图4.7所示，我们通过比较 ^{12}CO ($J = 1 \rightarrow 0$) 和 ^{13}CO ($J = 1 \rightarrow 0$) 的亮温度，来检测 ^{12}CO ($J = 1 \rightarrow 0$) 光学厚的区域。过程中，我们只采用 CO 信号大于 3σ 的值。如果 ^{12}CO/^{13}CO 比值在 CMZ 内是常数，那么在光学薄的情况下，^{12}CO ($J = 1 \rightarrow 0$) 亮温度跟 ^{13}CO ($J = 1 \rightarrow 0$) 的亮温度应该成正比，所以，我们可以通过拟合一条直线来判别光学薄区域。我们发现在 ^{12}CO ($J = 1 \rightarrow 0$) 大于 6.5 K 的情况下，^{12}CO ($J = 1 \rightarrow 0$) 跟 ^{13}CO ($J = 1 \rightarrow 0$) 大体成线性关系，我们认为 ^{12}CO ($J = 1 \rightarrow 0$) 基本上光学薄。而在 ^{12}CO ($J = 1 \rightarrow 0$) 亮温度小于 6.5 K 的区域，有很多光学厚的点。因此，我们的拟合只采用 ^{12}CO ($J = 1 \rightarrow 0$) 亮温度大于 6.5 K 的点。

我们发现 ^{12}CO/^{13}CO 的亮温度比例为 15.2。这跟Oka et al. (1998) 给出的值 (5.19) 有较大差别，但是我们认为这个值跟望远镜的分辨率有很大关系。这是由于 ^{12}CO ($J = 1 \rightarrow 0$) 和 ^{13}CO ($J = 1 \rightarrow 0$) 谱线观测的波束填充因子并不一致，不同的空间分辨率观测到的谱线形状有一定差别。Oka et al. (1998) 观测的空间分辨率为 17′ (100 GHz)，大大高于 CfA ^{12}CO ($J = 1 \rightarrow 0$) 观测的空间分辨率。高分辨率会降低波束平均从而提高 ^{13}CO ($J = 1 \rightarrow 0$) 的亮温度，所以Oka et al. (1998) 给出的 ^{12}CO/^{13}CO 值比较低。

在图4.7中蓝色区域内，由于 ^{12}CO ($J = 1 \rightarrow 0$) 和 ^{13}CO ($J = 1 \rightarrow 0$) 整体上成正比，我们认为 ^{12}CO ($J = 1 \rightarrow 0$) 大多是光学薄的。在红色区域，^{13}CO ($J = 1 \rightarrow 0$) 亮温度比较高，但 ^{12}CO ($J = 1 \rightarrow 0$) 却比较低，说明 ^{12}CO ($J = 1 \rightarrow 0$) 辐射已无法穿透分子核的中心区域，也就是已经光学厚了。我们把红色区域的点改正到绿色线上，这样整体上来说，可以认为改正后 ^{12}CO ($J = 1 \rightarrow 0$) 是光学薄的。从图4.7中可以看出，有一些点不在红色和蓝色区域内，但是由于这些点比较少，我们对这些点不再做任何改正。

图4.7显示，有些光学厚的 ^{12}CO ($J = 1 \rightarrow 0$) 的亮温度低于光学薄的 ^{12}CO ($J = 1 \rightarrow 0$) 亮温度，这是因为在光学厚的情况下，我们只能看到分子云核的表层，而表层的温度比较低。这种现象跟 ^{12}CO ($J = 1 \rightarrow 0$) 自吸收线是类似的，例如H II 区N14 的区域的平均谱线图 (Yan et al., 2016, 图 1)。在 ^{12}CO ($J = 1 \rightarrow 0$) 有自吸收的时候，中间光学厚区域的亮温度会比周围光学薄的区域低，一些分子云核的自吸收线会表现得特别明显 (Yan et al., 2016, 图 29)。

^{12}CO ($J = 1 \rightarrow 0$) 谱线提供的第五个方程的数学表达为：

$$N_1 + N_2 + N_3 + N_4 = f_{1234} \times T_{\rm CO}, \tag{4.9}$$

其中 N_1、N_2、N_3 和 N_4 是 OH 四个基态能级的柱密度，$T_{\rm CO}$ 是改正后的 ^{12}CO ($J = 1 \rightarrow 0$) 亮温度，f_{1234} 是比例系数。我们在 §4.6.2 中会给出确定 f_{1234} 的值的方法。

至此，我们已经有了五个方程来求解五个未知数。这五个方程为 OH 基态的三条谱线加上方程4.9和4.8，五个未知数是 OH 四个基态的柱密度加上其中任意一条跃迁谱线的背景连续辐射温度。

4.5.3 方程组形式

为了明确起见，我们在本小节给出完整的方程组形式。我们选择 1665 MHz 谱线背景连续谱辐射温度为第五个参数，则其他三条 OH 线的背景连续谱辐射为：

$$\begin{cases} T_{\rm c1667} = f_{1667} \times T_{\rm c}, \\ T_{\rm c1612} = f_{1612} \times T_{\rm c}, \\ T_{\rm c1720} = f_{1720} \times T_{\rm c}, \end{cases} \tag{4.10}$$

其中, $T_{\rm c1667}$、$T_{\rm c1612}$ 和 $T_{\rm c1720}$ 是位于分子云背后的连续谱辐射亮温度, 分别对应 1667、1612 和 1720 MHz 谱线，f_{1667}、f_{1612} 和 f_{1720} 分别是三个波段连续谱跟 1665 MHz 波段值的比值。f_{1667}、f_{1612} 和 f_{1720} 可以由观测的总的连续谱值 (沿视线方向从无穷远到太阳位置的积分) 给出，所以是可观测得。公式4.10的隐含意义是，对四个波段的连续谱辐射来说，分子云背后的那部分辐射占总连续谱辐射的比率是相同的。

表 4.3: OH 四条基态跃迁的参数。

Table 4.3. Parameters of the four ground-state transitions of OH.

Line	Rest frequency (MHz)	Einstein-A coefficient (10^{-11} s^{-1})
1612 MHz	1612.231	1.302
1665 MHz	1665.402	7.177
1667 MHz	1667.359	7.778
1720 MHz	1720.530	0.9496

为了简化计算，我们的变量不都采用柱密度，而是采用部分柱密度和部分激发温度的混合形式。根据公式4.8，我们假设两条 OH 主线的激发温度相等，为了方便起见，我们把这个主线温度作为一个未知数——$T_{\rm exm}$。用这个作为未知数的好处是在数值求解的时候可以方便地设定初值。我们用 ν_{1665}、ν_{1667}、ν_{1612} 和 ν_{1720} 表示四条谱线的本地静止频率，具体值见表4.3。四条谱线的速度 v 成分的光深分别用 $\tau_{\rm v1665}$、$\tau_{\rm v1667}$、$\tau_{\rm v1612}$ 和 $\tau_{\rm v1720}$ 表示，谱线的统计权重为 $2F+1$(Barrett, 1964)，爱因斯坦系数 A_{1612}、A_{1665}、A_{1667} 和 A_{1720} 的值见表4.3。

利用主线激发温度，$T_{\rm exm}$，我们可以用 N_3 和 N_4 表示 N_1 和 N_2。相应的，在方程4.9中，我们只需要限制 N_3 和 N_4，所以方程4.9变为:

$$N_3 + N_4 = f \times T_{\rm CO}. \tag{4.11}$$

其中，比例系数 f 的值大约为方程4.9中系数 f_{1234} 的一半。

至此，我们只需要求解四个未知数，$T_{\rm exm}$、$T_{\rm c}$、N_3 和 N_4，因为方程4.8已经被使用过了。用 $T_{1665}({\rm v})$、$T_{1667}({\rm v})$、$T_{1612}({\rm v})$ 和 $T_{1720}({\rm v})$ 来表示四条谱线在速度 v 上

的亮温度，我们的方程组的完整形式为：

$$\begin{cases} \left(T_{\rm exm}-T_{\rm c}-T_{\rm cmb}\right)\left(1-{\rm e}^{-\tau_{\rm vmain}}\right) = & T_{\rm bmain}\left({\rm v}\right) \\ \left(\frac{h\nu_{1612}/k}{\ln(3N_3)-\ln(5N_2)}-f_{1612}T_{\rm c}-T_{\rm cmb}\right)\left(1-{\rm e}^{-\tau_{\rm v1612}}\right) = & T_{\rm b1612}\left({\rm v}\right) \\ \left(\frac{h\nu_{1720}/k}{\ln(5N_4)-\ln(3N_1)}-f_{1720}T_{\rm c}-T_{\rm cmb}\right)\left(1-{\rm e}^{-\tau_{\rm v1720}}\right) = & T_{\rm b1720}\left({\rm v}\right) \\ N_3+N_4 = & f\times T_{\rm CO}, \end{cases} \tag{4.12}$$

其中，

$$\begin{aligned} T_{\rm cmb} &= 2.73\ {\rm K}, \\ N_1 &= N_3\exp\left(-\tfrac{h\nu_{1667}}{kT_{\rm exm}}\right), \\ N_2 &= N_4\exp\left(-\tfrac{h\nu_{1665}}{kT_{\rm exm}}\right), \\ T_{\rm bmain}\left({\rm v}\right) &= T_{\rm b1665}\left({\rm v}\right)\ {\rm or}\ T_{\rm b1667}\left({\rm v}\right), \\ \tau_{\rm vmain} &= \tfrac{c^3}{8\pi\nu_{1665}^3}A_{1665}\left(N_4-N_2\right)\phi_{\rm v}\ {\rm or}\ \tfrac{c^3}{8\pi\nu_{1667}^3}A_{1667}\left(N_3-N_1\right)\phi_{\rm v}, \\ \tau_{\rm v1612} &= \tfrac{c^3}{8\pi\nu_{1612}^3}A_{1612}\left(\tfrac{3}{5}N_3-N_2\right)\phi_{\rm v}, \\ \tau_{\rm v1720} &= \tfrac{c^3}{8\pi\nu_{1720}^3}A_{1720}\left(\tfrac{5}{3}N_4-N_1\right)\phi_{\rm v}. \end{aligned} \tag{4.13}$$

4.5.4 数值求解方程组

显然，方程组4.12是非线性系统，求解析解非常困难，所以我们采用数值方法来求解。在视线方向上，我们对每一个速度值上的观测求解一次方程组，在这种情况下，由于归一化，$\phi_{\rm v}$ 的值退化为速度分辨率的倒数。

为了检验解的唯一性，我们对方程组4.12进行了简化。因为 1720 MHz 谱线的光深一般来说最小 (爱因斯坦 A 系数最小)，所以我们对 1720 MHz 谱线进行线性化。我们进一步假设 $h\nu/(kT_{\rm ex1720})\ll 1$，这在 $T_{\rm ex1720}$ 不低于 1 K 的情况是成立的。线性化后我们有：

$$\begin{cases} T_{\rm ex1720}=\frac{h\nu_{1720}/k}{\ln(5N_4)-\ln(3N_1)} & \approx \frac{h\nu_{1720}}{k}\frac{5N_4}{5N_4-3N_1} \\ 1-{\rm e}^{-\tau_{\rm v1720}} & \approx \tau_{\rm v1720}. \end{cases} \tag{4.14}$$

这样 1720 MHz 谱线的观测方程已经是 N_3 和 N_4 的线性方程组。联合方程4.11，我们可以写出 N_3 和 N_4 的解析表达式——用 $T_{\rm c}$ 和 $T_{\rm exm}$ 表示，然后代入主线和 1612 MHz 谱线方程，这样我们就得到了一个只含有 $T_{\rm c}$ 和 $T_{\rm exm}$ 两个未知数的方程组，这个包含方程组形式非常复杂，但是有利于数值求解，因为这两个值的初值比较容易设置。我们在 $T_{\rm c}$ 和 $T_{\rm exm}$ 的二维坐标网格上搜索方程组的解，发现方程组的解是满足唯一性的。

计算的时候，$T_{\rm exm}$ 的初值我们设置为 7 K，$T_{\rm c}$ 的初值设置为总观测值的一半。利用解算的 $T_{\rm exm}$ 和 $T_{\rm c}$ 值，我们求得 N_3 和 N_4，并进一步以此作为初值，对方程4.12进行解算。

4.6 银心分子云的三维结构

在本小节，我们利用改进后的方法来推导 CMZ 分子云的三维结构。Sawada et al. (2004) 只计算了银道面 ($b = 0°$) 的正向结构，而我们对银纬方向 $b = -0.375°$、$-0.25°$、$-0.125°$、0°、0.125° 和 0.25° 六个切片的正向结构都进行了计算，合并后可以获得 CMZ 分子云的三维结构。

利用方程4.12，解算出分子云背景连续谱辐射的亮温度之后，我们利用建立的连续谱辐射模型来计算分子云相对于银心的位置。计算方法为从无穷远处开始对连续谱模型进行积分，直到积分值跟计算出的背景连续谱相等，此时的位置即为分子云的位置。高分辨率的观测 (Law et al., 2008) 表明连续谱的辐射中心是 Sgr A*，$(l, b) = (-0.06°, -0.05°)$，但是由于 Parkes 的分辨率不足以分辨出 Sgr A*，我们简单认为 $(l, b) = (0.0°, 0.0°)$ 为连续谱辐射中心。

计算中，我们采用Reid et al. (2014) 给出的银心到太阳的距离——8.34 kpc。在此距离上，Parkes 对应的分辨率为 38 pc。

4.6.1 连续谱高斯拟合

连续谱谱线拟合是计算 CMZ 分子云三维模型非常重要的一步，因为连续谱的辐射分布直接决定了分子云的位置。我们发现 CMZ 分子云大部分位于范围 $-0.375° \leqslant b \leqslant 0.25°$ 内，所以我们只对 $b = -0.375°$、$-0.25°$、$-0.125°$、0°、0.125° 和 0.25° 位置的连续谱进行建模。

采用Sawada et al. (2004) 的方法，根据连续谱轴对称假设，我们用三个高斯成分来拟合连续谱。由于 Parkes 的波束不足以分辨 Sgr A*，所以我们把高斯成分的中心设置为 $l = 0°$。需要注意的是，在积分连续谱的时候，我们需要使用 Sgr A*，连续谱中心到视线方向的垂直距离，而不是简单的用银经。但是我们发现，用一个线性转换参数 145.56 pc degree^{-1} 把距离转换为度数后，距离跟银经的值差别小于 0.01°，这个远小于我们的空间分辨率，所以我们认为这个效应对我们的计算影响不大。

沿视线方向，从无穷远处到太阳，连续谱的积分值可以表示为：

$$T_{\rm cont}\,(l) = a_1 \exp\left(-\frac{x^2}{2\sigma_1^2}\right) + a_2 \exp\left(-\frac{x^2}{2\sigma_2^2}\right) + a_3 \exp\left(-\frac{x^2}{2\sigma_3^2}\right) \tag{4.15}$$

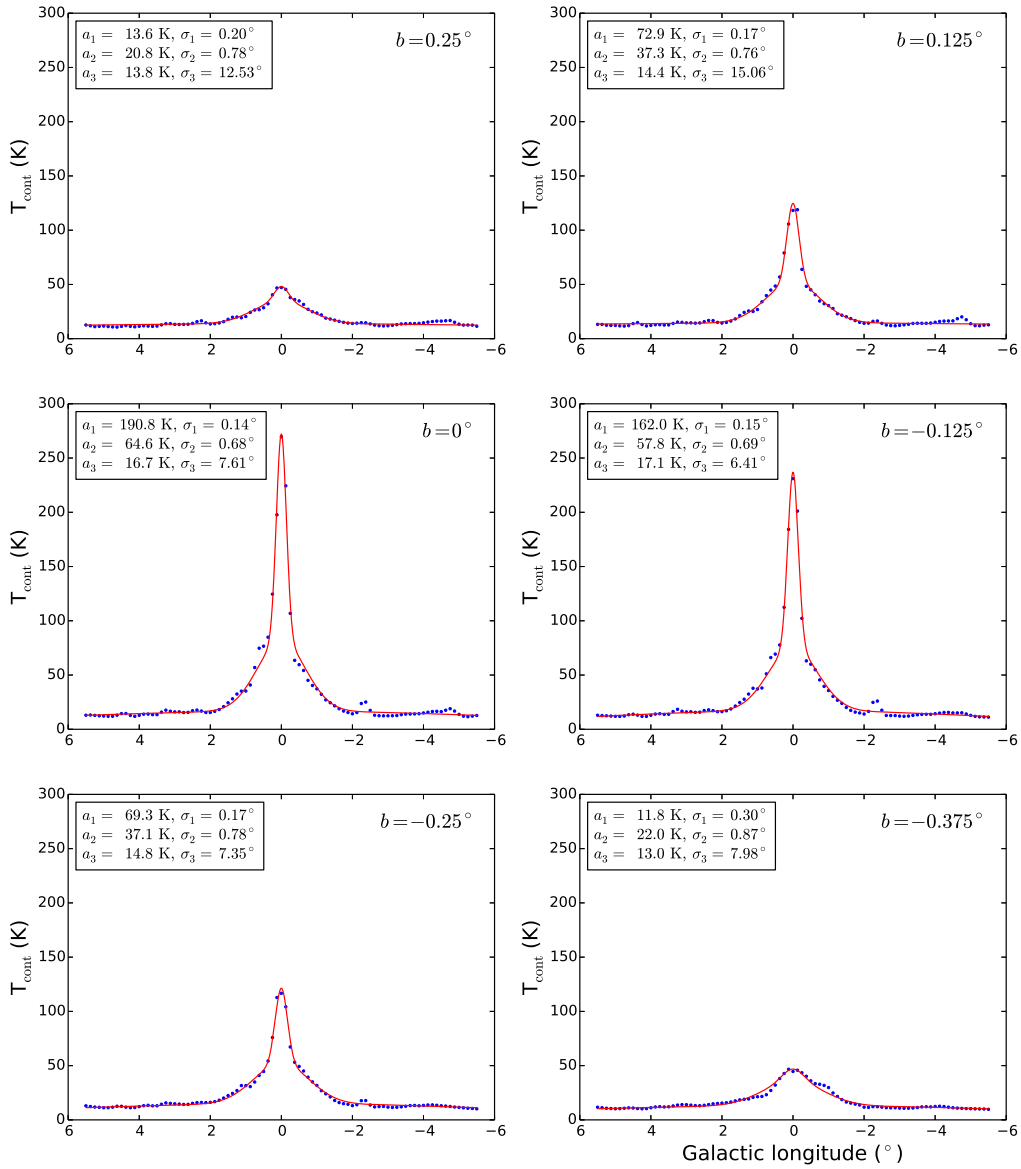

图 4.8: 1612 MHz 波段连续谱高斯成分拟合。我们只对 $b = -0.375°$、$-0.25°$、$-0.125°$、$0°$、$0.125°$ 和 $0.25°$ 进行了计算。红色实线是三个高斯成分相加后的结果，蓝色点为我们观测的连续谱值——沿视线方向从无穷远处积分到太阳位置。

Figure 4.8. Continuum emission fitting at 1612 MHz for $b = -0.375°$, $-0.25°$, $-0.125°$, $0°$, $0.125°$, and $0.25°$. Each red line contains three Gaussian components. The continuum emission data (blue points) is observed by the SPLASH. The parameters of each Gaussian component (see equation (4.15)) are displayed in the upper-left corder of each panel.

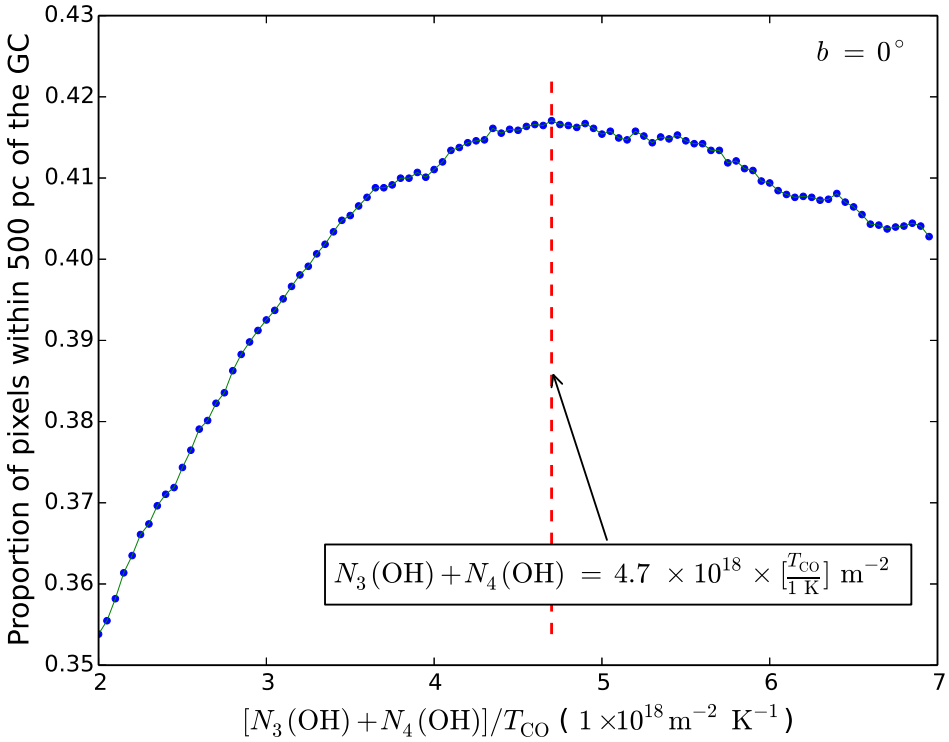

图 4.9: 确定 OH 柱密度和 CO 亮温度比。我们通过调整这个比值，使得位于银心 500 pc 以内的分子云比例达到最大值。图中已标注我们确定的比值

Figure 4.9. Determining the ratio of the OH column density to the brightness temperature of CO according to the proportion of pixels within 500 pc of the GC for the face-on view of $b = 0°$. The red dashed line denotes the ratio corresponding to the maximum proportion.

其中，l 是银经 (单位是度)，$x = 8340 \times \sin(l)/145.56$——根据银经计算的连续谱中心到视线方向的垂直距离 (转换为度数表示)，a 和 σ 分别表示高斯曲线的峰值和标准差。

利用公式4.15，我们对 1612 MHz 连续谱进行高斯成分拟合。总的来说，CMZ 连续谱的拟合残差比较小，但是在恒星形成区方向，由于自由-自由辐射，观测的连续谱值会略高于模型值。这是因为这部分连续谱并非属于高斯成分。拟合结果表明，连续谱的轴对称假设是合理的。

4.6.2 CO 和 OH 柱密度比

至此，我们的方程组4.12中还剩下唯一一个自由参数 f 待定。f 值会影响我们对 OH 分子云背景连续谱温度的估计的准确性，不论 f 值偏大还是偏小，都会导致分子云位于 CMZ 范围以外。因为大部分分子云位于 CMZ 以内，所以我们在一

个合理的范围内搜索 f 的值，使得位于 CMZ 内分子云比例达到最大值。

我们根据银河系其他地方的 OH 观测来确定 f 的搜索范围。Goicoechea et al. (2011) 观测给出猎户座星云中 OH 的柱密度为 1×10^{19} m^{-2}。但是Goicoechea et al. (2011) 给出的值的积分速度范围很大，因此对于我们单个速度通道成分的计算来说，OH 柱密度差不多要低一个量级。因此，我们在 1×10^{18} m^{-2} 附近搜索最佳 f 值。

我们根据沿银道面 ($b = 0°$) 计算的分子云分布在银心 500 pc 以内的比例来确定 f 值。由于大部分分子云分布在银道面上，所以只需要根据 $b = 0°$ 的计算来确定参数 f。

如图4.9所示，我们以步长 0.05×10^{18} m^{-2} K^{-1} 来搜索。根据计算，f 的最优值为 4.7×10^{18} m^{-2} K^{-1}，对应 CMZ 内分子云比例为 42%，说明有一半左右的计算无解或者解不准确——主要发生在 OH 吸收线比较微弱 (低信噪比) 的区域。在最优值附近，CMZ 内的分子云比例变化不大，说明，f 的微小变化，对分子云位置影响不大。

4.6.3 OH 主线激发温度相等假设

尽管 CMZ 中分子云的速度弥散很大，但是仍然有一些天区，我们可以准确的观测四条 OH 基态跃迁。这些天区的计算不需要假设 OH 主线激发温度相等，所以我们可以验证 OH 主线温度假设的准确性。计算过程中，我们把根据方程组4.12计算的值作为初值，代入由四条 OH 观测给出的准确方程组中，进而求得精确解。

我们计算了位于 $(l, b) = (1°, 0°)$ 的分子云位置，结果见图4.10。图4.10中的红色线是不引入假设计算的值，可以看出，这和根据假设计算给出的值差别不大。因为 OH 柱密度已被 CO 亮温度限制 (见方程4.11)，所以在两种情况下，计算给出的柱密度值差别微小。一些速度成分上的 ^{12}CO ($J = 1 \rightarrow 0$) 光学厚改正不是很准确，在这种情况下，计算倾向于无解。

因此，我们引入的 §A.3.3 中的第三条假设是很好的近似。

4.6.4 模型检验

在利用改进后的模型计算 CMZ 分子云三维结构之前，我们对模型进行了检验。我们检验基于两点：第一，计算参数在银纬-速度 (L-V) 图上的分布；第二，对另外一条 OH 主线亮温度的预测情况。

为了检验我们计算出的分子云参数的合理性，我们分析了计算结果在 L-V 图上的分布。如图4.11所示，我们画出了银道面附近 ($b = 0°$) 分子云位置的 Y 轴值、

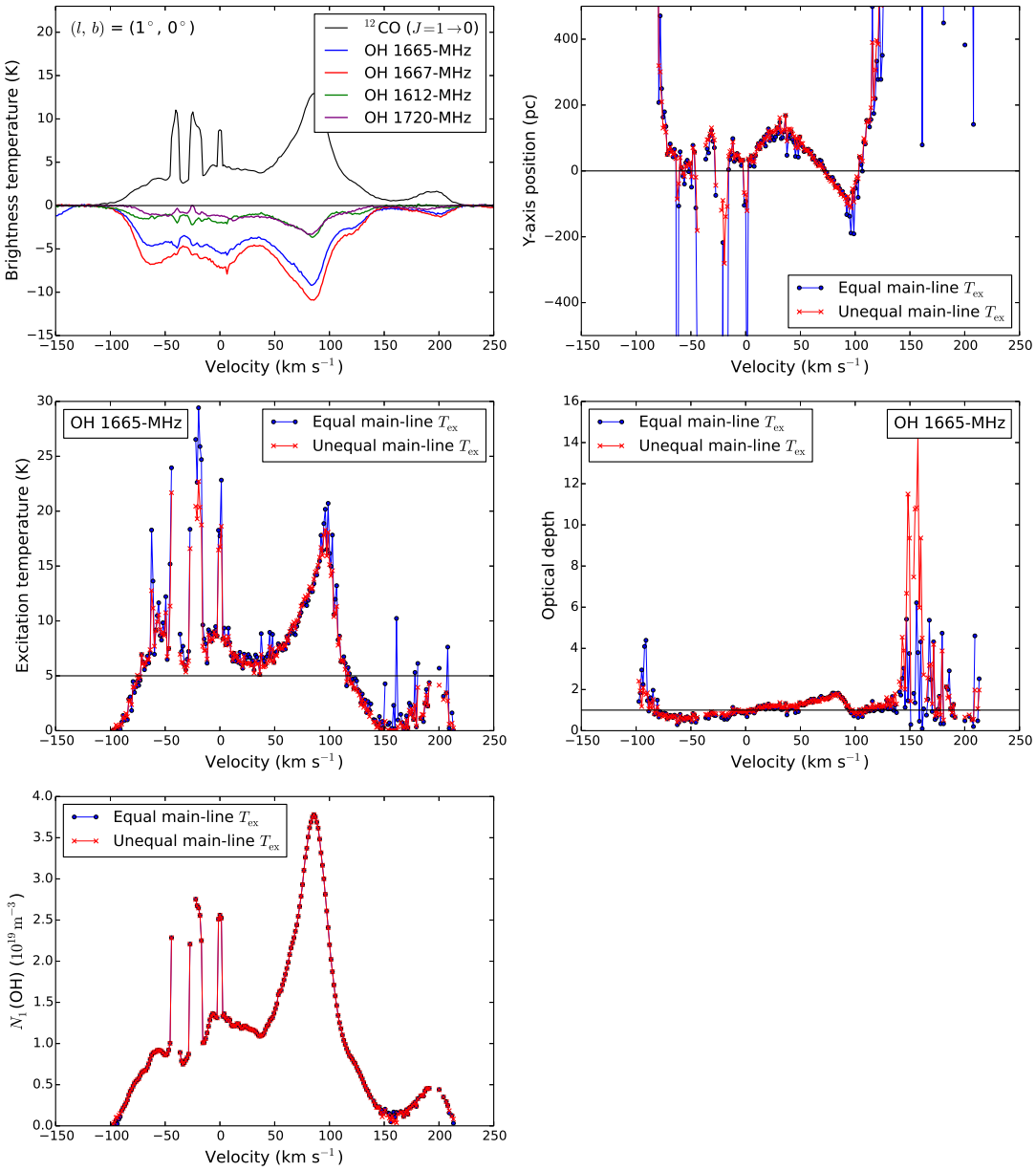

图 4.10: 检验 OH 主线激发温度相等假设。我们比较了假设 OH 主线激发温度相等和不做假设两种情况下的计算结果。计算点在 $(l, b) = (1°, 0°)$。五个图中分别画出的是 CO 和 OH 谱线、沿 Y 轴的距离 (Y 轴的意义见图4.13)、OH 的 1665 MHz 线的激发温度、光深和 N_1(OH) 的值 (N_1 的意义见图4.1)

Figure 4.10. The comparison of results calculated with equal (blue lines) and unequal (red lines) main-line excitation temperature, for $(l, b) = (1°, 0°)$. The top panel displays four OH ground-state lines as well as the ^{12}CO $(J = 1 \rightarrow 0)$ spectrum. The rest four panels compare the results of calculated positions along the Y axis (see Figure 4.13), the excitation temperatures and optical depths of OH 1665-MHz line, and the column densities of N_1(OH) (see Fig. 4.1), respectively.

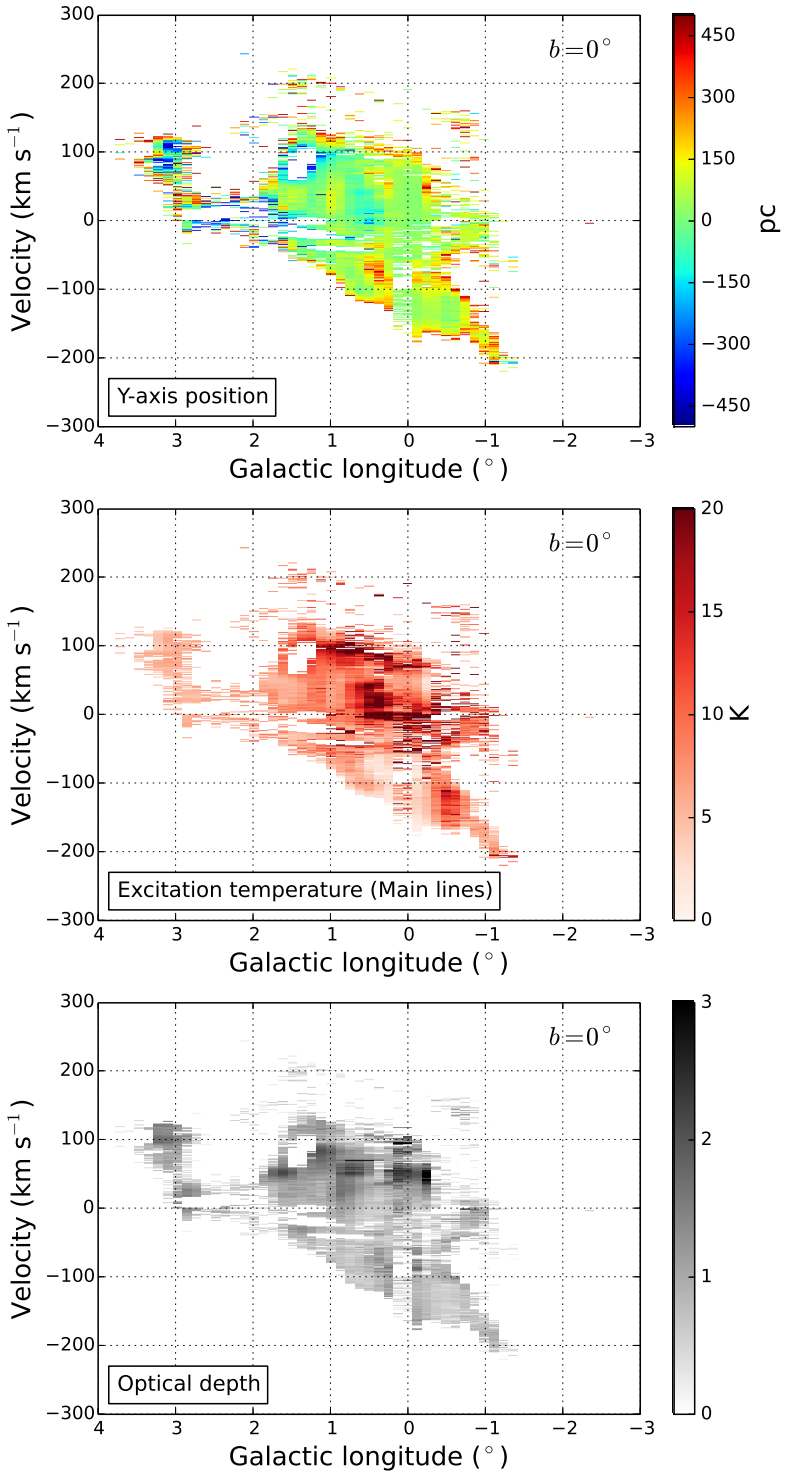

图 4.11: 计算参数在 L-V 图上的分布。图中从上到下展示的参数为 Y 轴位置、主线激发温度和 1662 MHz 主线的光深。

Figure 4.11. The position in Y axis (upper), the excitation temperature for the main lines (middle), and the optical depth of 1667-MHz line (lower) in L-V space for $b = 0°$. Pixels with absolute values of positions in Y axis > 500 pc are masked.

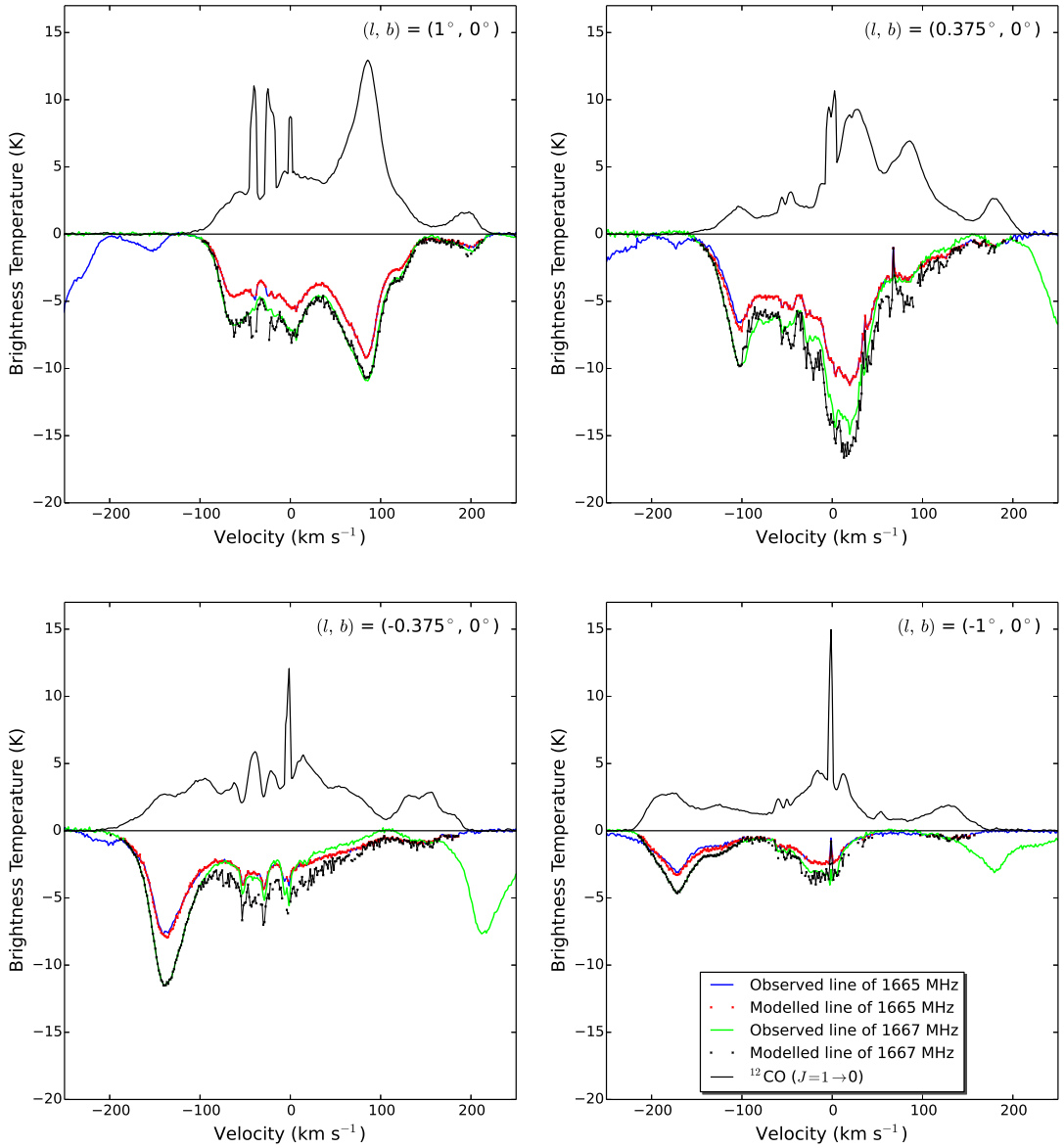

图 4.12: 模型预测 OH 主线亮温度跟观测到的亮温度的比较。比较的位置包括 $(l, b) = (1°, 0°)$、$(0.375°, 0°)$、$(-0.375°, 0°)$ 和 $(-1°, 0°)$。图中蓝色和绿色实线代表观测到的 1665 和 1667 MHz 谱线，而红色和黑色点代表模型预测值。在视线速度小于 -100 km s^{-1} 的区间，我们的计算采用 1667 MHz 谱线，其他区间采用 1665 MHz 谱线。

Figure 4.12. Modelled spectral lines at four positions, $(l, b) = (1°, 0°)$, $(0.375°, 0°)$, $(-0.375°, 0°)$, and $(-1°, 0°)$. Blue and green represent observed 1665- and 1667-MHz lines, while the red and black star markers denote their modelled values, respectively. The black lines are the emission of ^{12}CO $(J = 1 \to 0)$ corrected with ^{13}CO $(J = 1 \to 0)$. For the range where velocities are smaller than -100 km s^{-1}, the 1667-MHz line is used in equation (4.12), while beyond this velocity range, the 1665-MHz line is used.

主线激发温度和光深在 L-V 图上的分布。从分布上来看，这三个值的相关性不大，说明这三个值是独立的。L-V 图上值的分布比较连续，这跟 L-V 图上位置相近的点的参数值也应该相近的预测是一致的。

除了检验计算结果在 L-V 上的分布，我们还可以利用 OH 主线观测来检验模型。在方程组 4.12中，我们只使用了 OH 主线中的一条，而另外一条主线的亮温度可以由方程组计算出的参数来预测。在 CMZ 中有些天区的速度弥散不是太大，两条 OH 主线没有互相干扰，这种情况下，我们可以准确的观测四条 OH 谱线。因此，利用这些天区可以比较模型预测的谱线值跟实际观测到的谱线值，进而检验模型的有效性。

在图4.12中，我们比较了四个位置的模型预测谱线跟观测谱线，四个位置分别为 $(l, b) = (1°, 0°)$，$(0.375°, 0°)$，$(-0.375°\ 0°)$ 和 $(-1°, 0°)$。图中蓝色和绿色实线分别代表观测到的 1665 和 1667 MHz 谱线，而红色和黑色点代表模型预测值。在速度小于 -100 km s^{-1} 的区间，我们采用 1667 MHz 谱线计算，而在其他区间采用 1665 MHz 谱线。但是对于 Sgr B2，由于 1665 MHz 谱线上有大量脉泽发射，我们采用 1667 MHz 线来计算，关于 Sgr B2 的一些计算参数见表4.4。图4.12显示，预测线跟观测线基本重合，说明我们的模型可以很好的预测另外一条谱线。我们的计算显示，在位置 $(0.375°,\ 0°)$ 和 $(-0.375°,\ 0°)$ 上，由于基线不准，见 §4.3 的数据处理，观测给出 1667 MHz 谱线亮温度并不准确。

从上述检验结果来看，我们的模型可以很好地解释观测数据。除了小部分 ^{12}CO $(J = 1 \rightarrow 0)$ 光学厚的速度区间和一些 OH 信号信噪比不高的区域，我们的计算结果是可靠的。

4.6.5 CMZ 分子三维结构

利用新发现的计算 OH 柱密度、激发温度和光深的方法，我们解算了 CMZ 分子云的相对位置，并计算出沿银纬六个切片的正向分布，进而推导出 CMZ 的三维结构。

在计算 CMZ 分子云正向分布 (face-on view) 的过程中，我们对每一条视线方向的谱线计算所有沿视线方向分子云的位置，然后把沿视线方向的位置投影到正向图上。最后我们把正向图重采样为分辨率为 0.125° 的网格。考虑到观测精度，我们在计算中剔除了低于 0.3 K (3σ) 的 CO 和 OH 谱线值。

考虑到数据空间分辨率和 CMZ 分子云沿银纬的分布，我们计算了 CMZ 中六个切片的正向结构——具体结果见图4.13、4.14、4.15、4.16、4.17和4.18。各图中，噪声水平为 1.38 K，所以我们掩盖了低于 4.1 K (3σ) 的点。

如图4.16所示，银道面附近的分子云有明显的棒结构，因此，我们的结果可以证明银心附近的分子云也呈棒旋结构。我们对这个棒结构的倾角做了线性回归分析——忽略值小于 7 K km s^{-1} (5σ) 和距离银心大于 300 pc 的像素，倾角的拟合值为 $67.5 \pm 2.1°$。

图4.16右侧的速度分布显示，在正银经一侧，正速度占主导，也就是说这些分子云正远离我们。而在负银纬区域，负向速度占主导，说明这些分子云正在靠近我们。这样的速度分布说明，分子云在绕 Sgr A* 旋转。

图 4.19展示了六个切片的积分图。可以明显看出分子云的棒结构，但是图中的环形结构并不明显。我们认为这是分子谱线的空间分辨率不高造成的，关于数据空间分辨率的影响在 §4.7.2 中有比较详细地讨论。

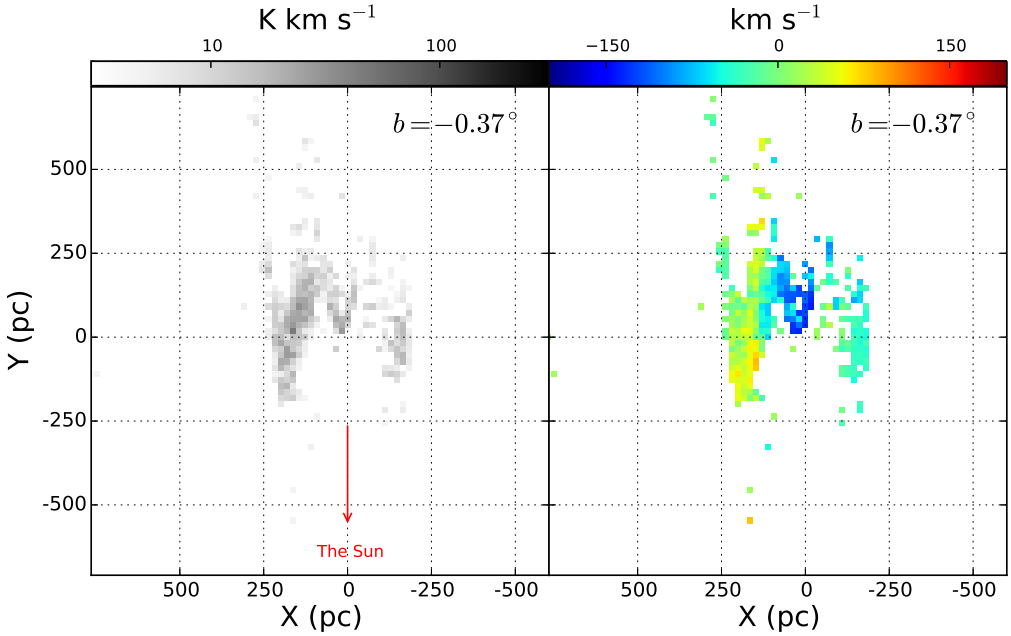

图 4.13: CMZ 分子云三维结构——$b = -0.375°$。左图是积分强度图，右图是速度分布图。图原点位置为 Sgr A*，X 轴对应 $l = 0°$。积分强度低于 4.1 K km s^{-1} (3σ) 的点，已被屏蔽。

Figure 4.13. The face-on view of CO clouds at $b = -0.375°$. The left panels are face-on view of each Galactic latitude, and the right panels are the distributions of velocities which are intensity weighted. The originate of X and Y axes is Sgr A*, and X $= 0$ corresponds to $l = 0°$. We masked the pixels where the integral brightness temperature is less than 4.1 K km s^{-1} (3σ).

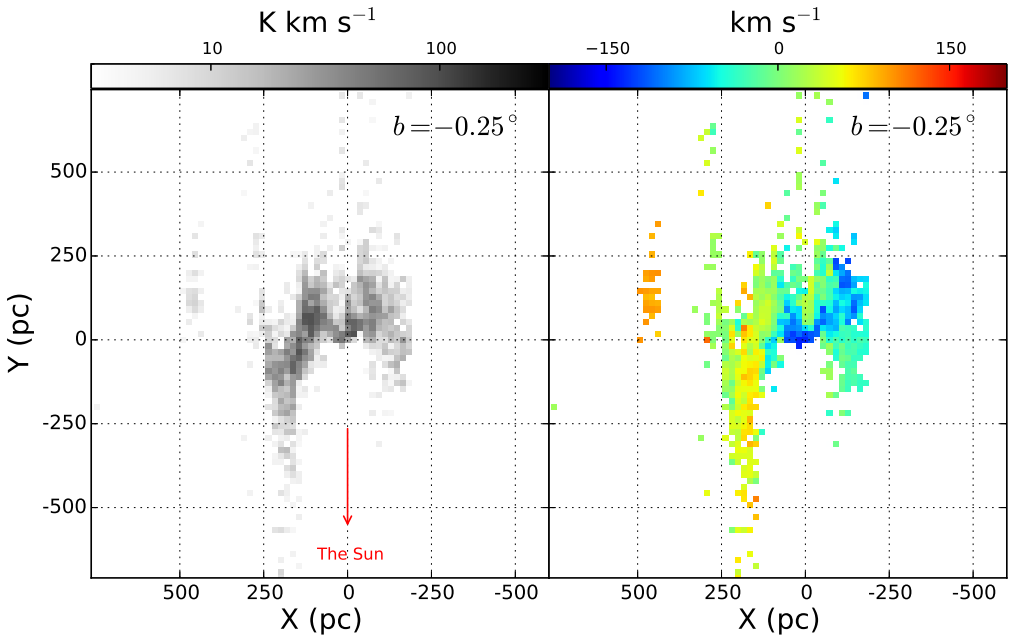

图 4.14: CMZ 分子云三维结构——$b = -0.25°$。图释见4.13。

Figure 4.14. The face-on view of CO clouds at $b = -0.25°$. Please see the caption of Figure 4.13 .

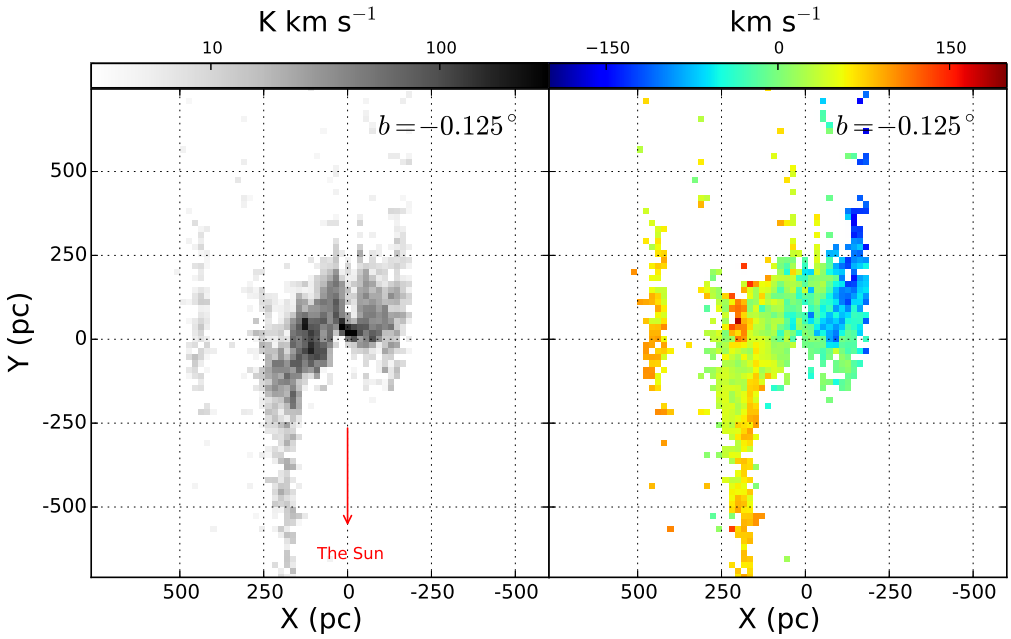

图 4.15: CMZ 分子云三维结构——$b = -0.125°$。图释见4.13。

Figure 4.15. The face-on view of CO clouds at $b = -0.125°$. Please see the caption of Figure 4.13 .

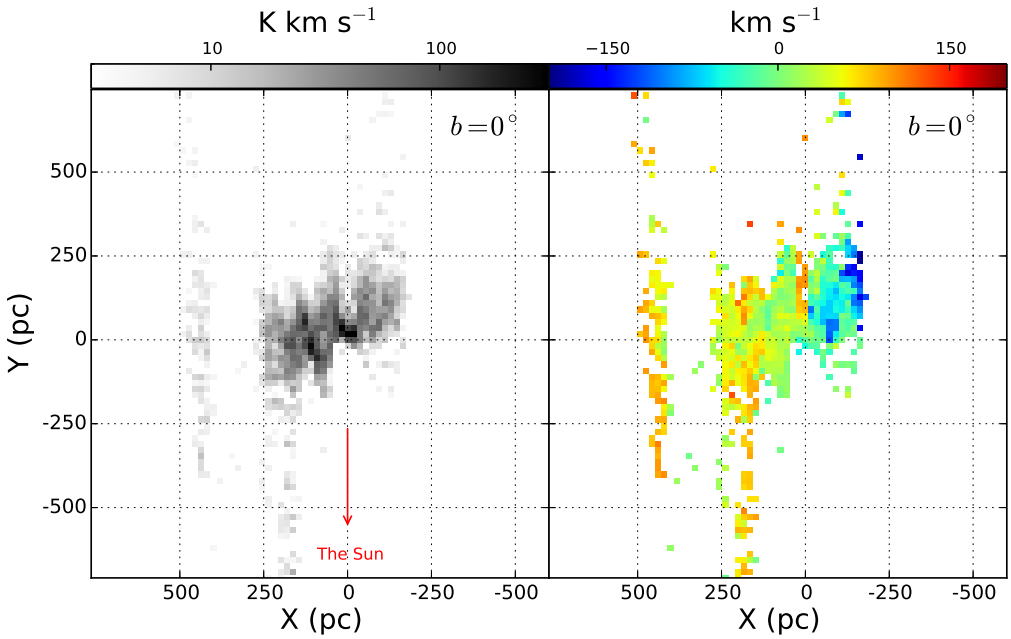

图 4.16: CMZ 分子云三维结构——$b = 0°$。图释见4.13。

Figure 4.16. The face-on view of CO clouds at $b = 0°$. Please see the caption of Figure 4.13 .

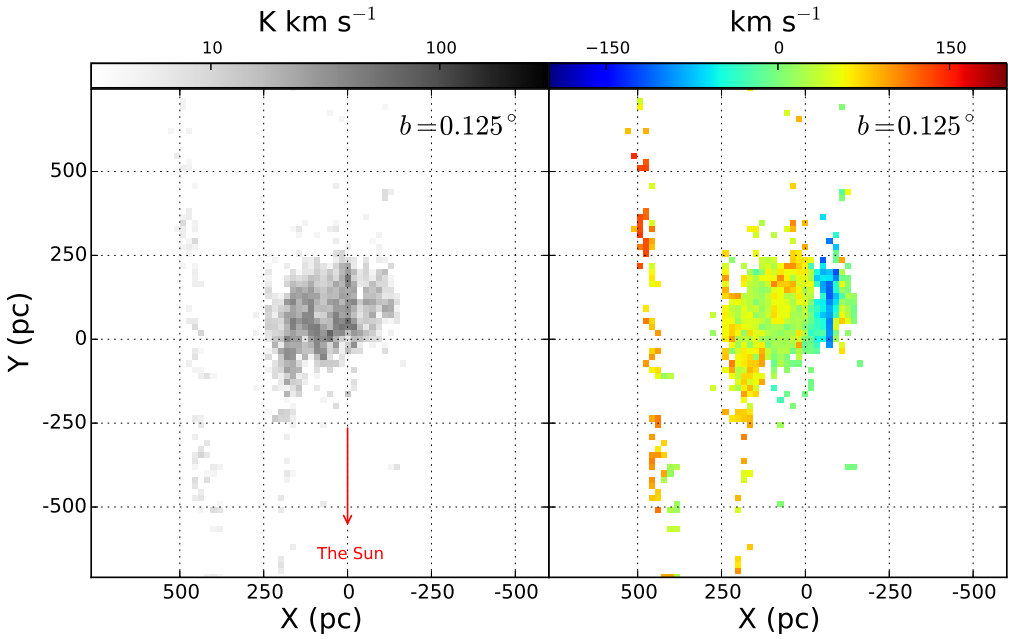

图 4.17: CMZ 分子云三维结构——$b = 0.125°$。图释见4.13。

Figure 4.17. The face-on view of CO clouds at $b = 0.125°$. Please see the caption of Figure 4.13 .

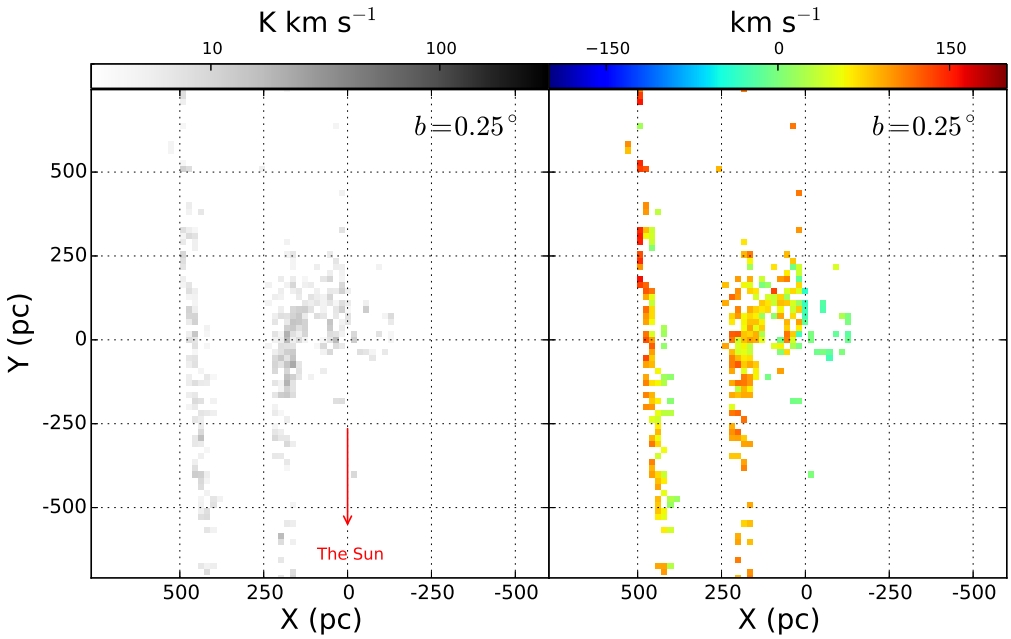

图 4.18: CMZ 分子云三维结构——$b = 0.25°$。图释见4.13。

Figure 4.18. The face-on view of CO clouds at $b = 0.25°$. Please see the caption of Figure 4.13 .

我们顺便计算了 CMZ 内 OH 分子的总质量。因为大部分 OH 分子处于基态，所以基态 OH 分子的质量可以近似代表总的 OH 分子质量。我们只累计银心 500 pc 以内的 OH 分子，发现 OH 分子的质量为 2400 $M_\odot$。这个值是 OH 分子的质量下限，因为有相当一部分数据无解或者解不准确。用 OH 柱密度跟 CO 亮温度的比率，把所有的 CO 辐射都转换为 OH 质量，我们发现 OH 的质量为 5100 $M_\odot$，这个值是我们给出的 OH 质量的上限。

4.7 CMZ 分子云三维结构分析

4.7.1 OH 分子基态激发温度

为了进一步确认计算结果，我们跟前人用其他一些方法计算出的银盘上分子云内的 OH 激发温度。如图4.20所示，我们推导出的 OH 激发温度的值在 $5 - 10$ K 左右，这个跟前人的结果基本一致，说明 CMZ 环境对 OH 分子的激发温度影响不大。

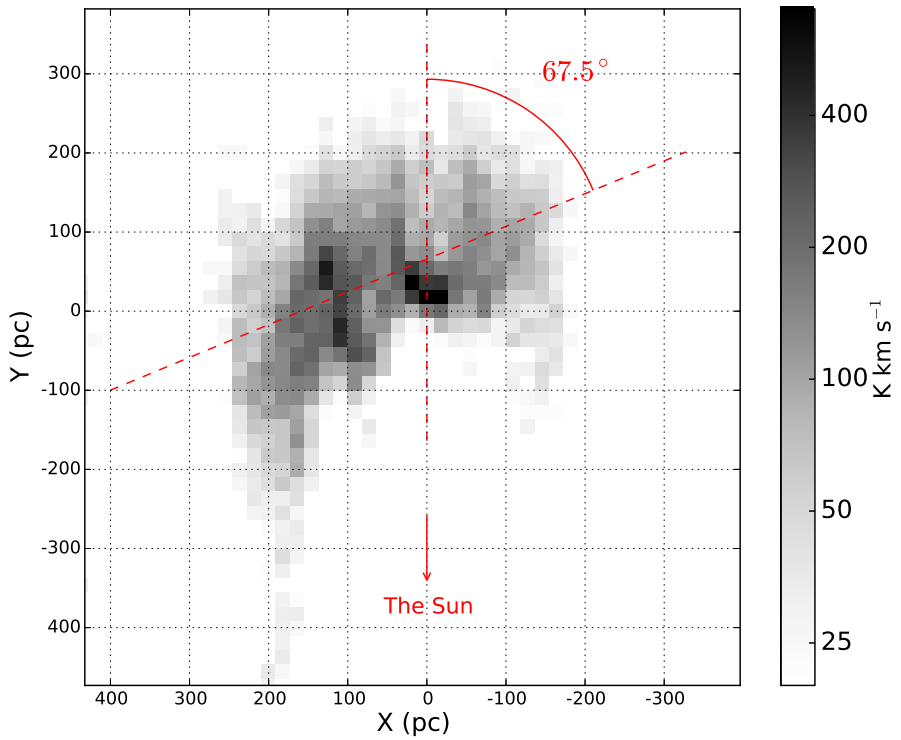

图 4.19: 六个切片相加后，CMZ 分子云的正向分布。倾角是根据图4.16的数据拟合的。

Figure 4.19. The face-on view of all molecular clouds in the GC integrated across six slices. The inclination angle is fitted with the molecular clouds at $b = 0°$, as shown in Fig. 4.16.

Crutcher (1977) 利用 ON 点和 OFF 点 (相对于背景连续源的位置来说) 的观测直接解算了 OH 四条谱线的激发温度。这种方法的原理是 OH 谱线在 ON 点有吸收线，在 OFF 点没有吸收，但是 ON 点和 OFF 点的 OH 激发温度是相等的。因此可以联合 ON 和 OFF 点的观测，组成方程组求解 OH 激发温度和光深。他们的解算结果显示，OH 主线激发温度大约为 6 K，两条主线的激发温度整体比较接近，但差别有时会达 3 K。他们的结果支持我们的第三个假设——OH 主线激发温度相等。

根据 LTE 假设也可以计算 OH 激发温度。这种方法的原理是假设两条 OH 主线激发温度相等且光深比例为 5/9 (Knapp et al., 1973)，在加上两条主线的背景连续辐射温度也相等，利用 OH 两条主线的亮温度比值可以求出两条主线的光深，进而求出激发温度。Li et al. (2003) 的计算显示，利用这个这方法求出的 OH 激发温度范围在 5-9 K。

如图4.20所示，我们的模型给出的 OH 激发温度所在的区间跟前人给出的值基本一致。在 CO 谱线亮温度比较低的区间，有小部分 OH 激发温度比较低。这是因

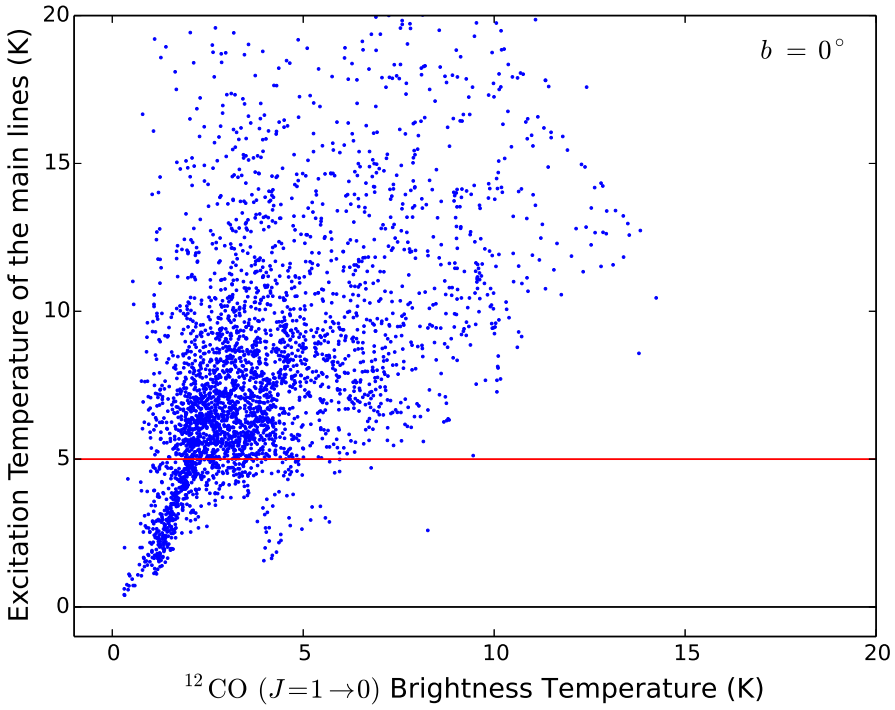

图 4.20: OH 主线激发温度分布图，计算位置为 $b = 0°$。

Figure 4.20. Excitation temperature of the main OH line versus the brightness temperature of ^{12}CO $(J = 1 \rightarrow 0)$ for $b = 0°$. The red horizontal line represent 5 K level.

为，在 CO 亮温度低的时候，四条 OH 吸收线谱线都十分微弱，方程组4.12对光深的约束不强，导致方程组给出低激发温度和高光深的解。总的来说，不正常的 OH 光深值比例很小，说明我们的模型是可靠的。

4.7.2 低分辨率影响

因为我们的计算基于 CO 发射线和 OH 吸收线，所以这些谱线的准确度直接决定了我们结果的可靠性。低分辨率会对谱线造成波束平均，可能会对我们的计算有一定地影响。

首先，由于波束平均，我们的数据无法分辨出 CMZ 中的一些小的结构，例如，我们在谱线中没有找到 G0.253+0.016 的特征。Henshaw et al. (2016) 给出的 G0.253+0.016 的角尺度 (直径) 大约为 4′，而我们的分辨率只有 15.5′，所以，G0.253+0.016 在 35 km s^{-1} 上的信号在 CO 和 OH 谱线上并不明显。因此，我们无法计算这些小结构的相对位置。

如图4.8所示，在 Sgr A* 附近，由于连续谱变化太快，低分辨率无法跟踪谱线变化。Sgr A* 的前景分子云由于背景连续谱辐射很强，吸收线的深度应该比较大，

但是由于波束平均，前景分子云的吸收深度变浅，导致我们计算出的 Y 轴位置大于真实位置。在正向分布图上，这个效应相当于这些前景分子云被推到 SgrA* 附近或者背后。因此，Sgr A* 前方会有一片空白区域，如图4.16所示。

除了 CO 和 OH 谱线，连续谱也可能会对计算有影响。例如对每一个切片来说，我们假设切片的连续谱分布是圆柱形。在一个像素上，如果一个分子云的实际位置靠近银盘的一侧，那么对这个分子云来说，我们低估了连续谱辐射，导致我们计算出的位置更靠近太阳。反之，如果这个分子云的实际位置是在远离银盘的一侧，那么我们计算位置将比真实位置远。

因为我们没有高分辨率的数据来验证分辨率对结果的影响，所以我们对低分辨率造成的影响不再做过多的讨论。可以预期的是，如果使用高分辨率的数据计算，Sgr A* 前方的空白区域会大大减小，而且很可能会探测到 CMZ 中的环形轨道结构。

4.7.3 连续谱辐射超出

如图4.8所示，虽然整体上三个高斯成分可以很好地拟合连续谱，但是有些天区的辐射不能完全用高斯成分来拟合。这些非高斯成分可能会对其前景分子云的位置有一定影响。

例如，在大质量恒星形成区 Sgr B2 的视线方向上，连续谱辐射观测值比高斯模型给出的模型值略高，这是因为大质量恒星形成区会额外辐射自由-自由辐射。沿这些区域的视线方向，区域背后分子云的位置不会受到影响，因为方程组4.12计算出的背景连续谱辐射跟高斯分布模型给出的值仍然一致；但是对大质量恒星形成区前方的分子云来说，虽然方程组4.12给出的值仍然正确，但是有一部分并未归入高斯模型。因此，为了拟补这些额外的背景连续谱输入，前景分子云会被拉近。这种情况下，在沿着 Sgr B2 方向上，我们应该能看到一个断层。但是，我们并没有观测到断层，所以我们认为目前数据的空间分辨率还不足以检测这个效应。

4.7.4 跟其他模型的比较

CMZ 分子云的结构模型一直是研究的热点，关于这些模型的综述，见Henshaw et al. (2016)。由于我们的方法是建立在谱线观测之上，不依赖于动力学模型，所以可以用来检验其他的动力学模型。但是，由于我们数据空间分辨率太低，我们无法验证 $\{l, v_{\rm LSR}\}$ 图上连续气体流的轨道形状。退而求其次，我们计算了 CMZ 中一些子区域的相对位置，并以此来验证一些动力学模型。我们总共计算了五个区域的位置，

表 4.4: CMZ 中五个子区域的参数。

Table 4.4. Parameters of five subregions in the CMZ.

Name	Coordinate (l, b)	Velocity (km s^{-1})	Face-on position (pc, pc)
Sgr A*[a]	($-0.06°$, $-0.05°$)	...	(0, 0)
Sgr B2[b]	($0.68°$, $-0.04°$)	[60, 64]	(90, -45)
Sgr C[c]	($-0.57°$, $-0.09°$)	[-65, -55]	(-93, 147)
20 km s^{-1} cloud[d]	($-0.13°$, $-0.08°$)	[18, 22]	(-18, 17)
50 km s^{-1} cloud[d]	($-0.02°$, $-0.07°$)	[47, 53]	(0, 22)

[a] Petrov et al. (2011)

[b] Reid et al. (2009)

[c] Kendrew et al. (2013)

[d] Pierce-Price et al. (2000)

其中包括 Sgr B2、Sgr C、Sgr A*、20 km s^{-1} 分子云 (the 20 km s^{-1} molecular cloud，20MC), and 50 km s^{-1} 分子云 (the 50 km s^{-1} molecular cloud，50MC)，具体的计算参数和结果见表4.4和图4.21。在表4.4中，从左到右依次列出每个区域的名称、坐标、速度区间和在正向图上的位置。

首先，我们跟Sawada et al. (2004) 给出的结果进行了比较。我们发现Sawada et al. (2004) 给出的 Sgr B2 距离比 Sgr A* 远，而我们的计算显示 Sgr B2 比 Sgr A* 近大约 45 pc。Reid et al. (2009) 的视差测量表明 Sgr B2 比 Sgr A* 近大约 130 pc，所以我们的结果跟视差测量更接近，也比Sawada et al. (2004) 给出的结果准确。从分子云正向分布图上也可以看出，用我们改进后的模型计算的分子云的分布也更清晰。

我们计算的 Sgr B2 和 Sgr A* 位置跟Kruijssen et al. (2015) 提出的模型一致，但是 Sgr C 的位置跟Kruijssen et al. (2015) 给出的值并不相符。如图4.21所示，20MC 和 50MC 都在 Sgr A* 附近，但是 Sgr C 位于 Sgr A* 的背景。高分辨率的观测 (Coil et al., 2000) 显示 20MC 和 50MC 都在 Sgr A* 10 pc 以内，并且 20MC 位于 Sgr A* 的前景而 50MC 位于 Sgr A* 的背景。由于分辨率不够，虽然我们给出的 20MC 和 50MC 都位于 Sgr A* 的背景，但是我们仍然得到 20MC 比 50MC 距离近的结果。我们对 Sgr C 的位置计算应该是比较准确的，因为在负银经区域，前景的分子云很少。所以根据我们的计算，Kruijssen et al. (2015) 模型中 Sgr C 的位置可能不正确。

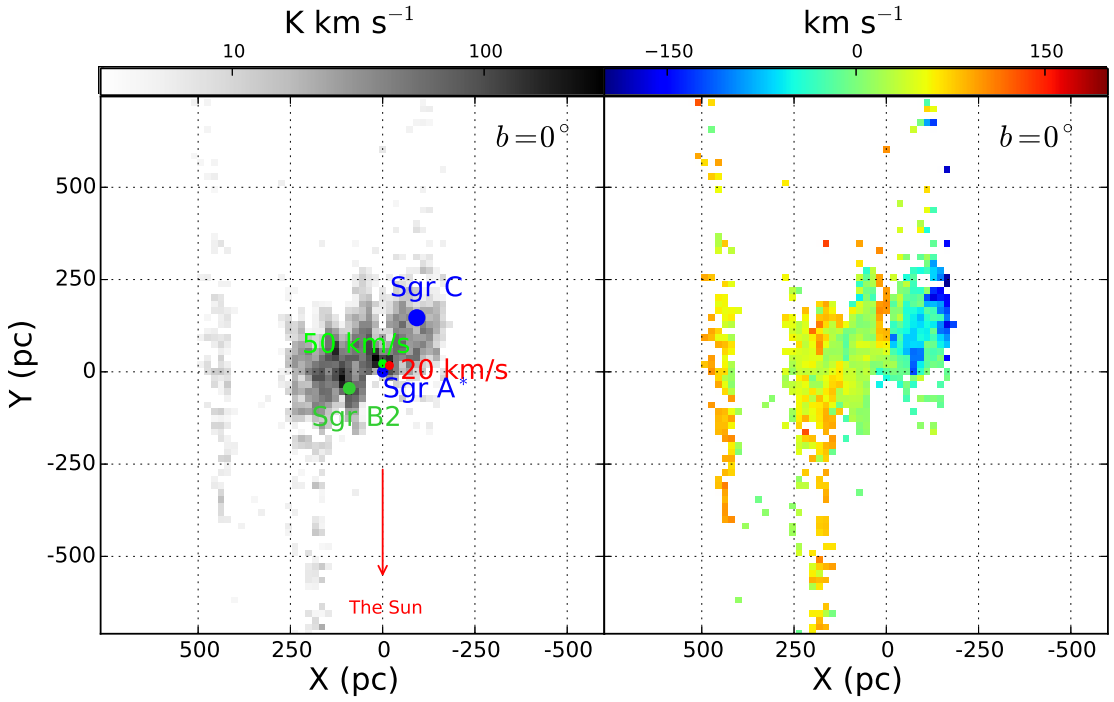

图 4.21: 图中标注了 Sgr B2、Sgr C、Sgr A*、20 km s^{-1} 分子云和 km s^{-1} 分子云在 CMZ 中的相对位置。

Figure 4.21. The left panel is a face-on view for $b = 0°$ with five components marked: Sgr B2, Sgr C, Sgr A*, 20 km s^{-1} molecular cloud, and 50 km s^{-1} molecular cloud, while the right panel is the distribution of velocities which are weighted by the intensity.

最近Sofue (2017) 利用高空间分辨率的 ^{12}CO ($J = 1 \rightarrow 0$) 观测分析了 CMZ 中分子云的三维结构。他们认为 CMZ 中的气体分布可能为圆柱形，这跟图4.13中的结构一致。

我们得到的一个比较有意思的结论是，CMZ 中分子云棒结构的倾角大约为 67.5°，这比前人给出的由恒星导出得倾角大。银心的棒结构包括长棒 (long bar) 和短棒 (short bar) 两部分：短棒的倾角和长度分别为 20° 和 2.5 kpc 左右 (Babusiaux et al., 2005; Binney et al., 1991; Bissantz et al., 2002; Cabrera-Lavers et al., 2008; Dwek et al., 1995)；而长棒的倾角和长度分别为 45° 和 9 kpc 左右 (Benjamin et al., 2005; Cabrera-Lavers et al., 2007, 2008; Nataf et al., 2013; Wegg et al., 2015)。我们结果表明，CMZ 中的分子云分布跟银河系中心的长棒结构一致。

4.8 CMZ 分子云三维结构总结

利用 CO 发射线和 OH 吸收线，我们计算了银河系中心分子云的三维结构。我采用已公开的 CfA 1.2 米望远镜 ^{12}CO ($J = 1 \rightarrow 0$) 巡天数据，并用 Mopra 观测的 ^{13}CO ($J = 1 \rightarrow 0$) 数据来改正 ^{12}CO ($J = 1 \rightarrow 0$) 光学厚的区域。OH 谱线观测则是 SPLASH 巡天的一部分，共包含四条 OH 谱线，分别为 1612、1665、1667 和 1720 MHz 谱线。谱线数据的空间和速度分辨率分别为 15.5′ 和 1.3 km s^{-1}。在银心距离上 (8.34 kpc)，数据的空间分辨率为 38 pc。

我们发现了一个可以同时精确计算 OH 基态柱密度、激发温度和光深的方法。在背景连续源辐射温度已知的情况下，我们可以用四条 OH 基态跃迁精确解算 OH 基态四个能级的柱密度，并进而求得激发温度和光深。对于 CMZ 来说，分子云背后的连续谱辐射是待求量，而且由于大的速度弥散，两条 OH 主线中的一条不准确。为了补足模型，我们引入了两个假设：第一，OH 两条主线的激发温度相等；第二，OH 柱密度跟光学薄的 CO 亮温度成正比。

利用改进后的模型，我们计算了银心六个切片的正向结构，包括 $b = -0.375°$、$-0.25°$、$-0.125°$、$0°$、$0.125°$ 和 $0.25°$，进而获得银心分子云的三维结构。银道面分子云的正向结构表明，分子云在 CMZ 也呈棒结构，分子云棒相对于视线方向的倾角为 $67.5 \pm 2.1°$，这个值比前人得出的倾角偏大。由于低的分辨率，我们无法探测 CMZ 分子云精确的轨道结构。我们的计算显示，CMZ 中 OH 分子的总质量在 2400 $M_\odot$ 到 5100 $M_\odot$ 之间。

高分辨率的观测可以显著提高我们的计算结果。我们已经申请并且利用 JVLA (the Karl G. Jansky Very Large Array) 完成了银心 OH 的干涉测量，再加上 Mopra 观测的 ^{12}CO ($J = 1 \rightarrow 0$) 和 ^{13}CO ($J = 1 \rightarrow 0$) 数据以及 ASKAP (the Australian Square Kilometre Array Pathfinder telescope) 即将观测的 OH 数据 (Dickey et al., 2013)，我们可以极大的提高解算精度并获得银心分子云的轨道信息。

第五章　大熊座分子云 CO 巡天

Although I was hoping that my IMF was roughly right on the average, I expected that it would vary extremely strongly with varying conditions.

— Edwin E. Salpeter

相对于银盘和银心来说，高银纬分子云 ($|b| \geqslant 30°$) 的巡天和研究比较少。一方面，高银纬分子云的柱密度、体密度和温度都很低，导致可供研究高银纬分子云的工具比较少，主要是 CO 谱线和远红外辐射，分别示踪分子气体和尘埃；另一方面，高银纬的分子云谱线微弱，分布面积广，需要大量的望远镜时间观测。在上世纪末和本世纪初，CO 分子巡天观测比较热，带动高银纬分子云研究比较活跃 (Heithausen et al., 1993)，后来随着对分子云研究的细化，高银纬分子云研究由于会占用太多的望远镜时间而逐渐被搁置。但是，近来中远红外观测技术的进步，使得大规模的巡天成为可能，高银纬的分子云研究开始逐步升温。

其实大多数高银纬的分子云的三维空间位置并没有脱离银道面，而仅仅而是因为距离太阳比较近，造成高度角比较大 (McGehee, 2008)。类比而言，距离一个高层建筑比较近的时候，我们会觉得这个建筑很高，实际上从远距离上看，这些高层建筑依然在地球表面上。

高银纬的观测对于分子云形成和演化的研究是很有意义的。高银纬的分子云受视线方向上其他成分的干扰很少，而且距离太阳很近，使得我们可以观测分子云的微小结构。高银纬分子云通常是一些弥散的暂现云 (translucent clouds)，研究这些暂现云的形成和消散，对寻找分子云的形成和演化的线索有重要价值。

McGehee (2008) 对高银纬的分子云和恒星形成做了一些综述。高银纬的分子云有两大主要结构——古德带 (the Gould Belt) 和金牛座小质量恒星形成区 (the Taurus star formation region)，除此之外，还有一些距离太阳比较近的零散分子云 (见Magnani et al. (1985) 给出的 MBM 高银纬分子云星表)。

古德带是位于太阳附近的一个环状恒星形成区在天球上的投影。古德带在天球上的位置及其包含的一些恒星形成区见图5.1。由于其距离优势，针对古德带的研究方兴未艾。例如 JCMT SCUBA-2 的分子谱线巡天 (Hatchell et al., 2013; Mowat et al., 2017; Pattle et al., 2015)，*Spitzer* 的中远红外巡天 (Broekhoven-Fiene et al., 2014; Harvey et al., 2008; Hatchell et al., 2012) 和 *Herschel* 的远红外巡天 (André et al., 2010; Kirk et al., 2013; Könyves et al., 2015)。由于古德带和金牛座恒星形成区不是本文的研究重点，我们不做过多阐述。在本章中，我们把青海站望远镜指向一个纬度更高

的分子云——大熊座分子云 (the Ursa Major Clouds)。

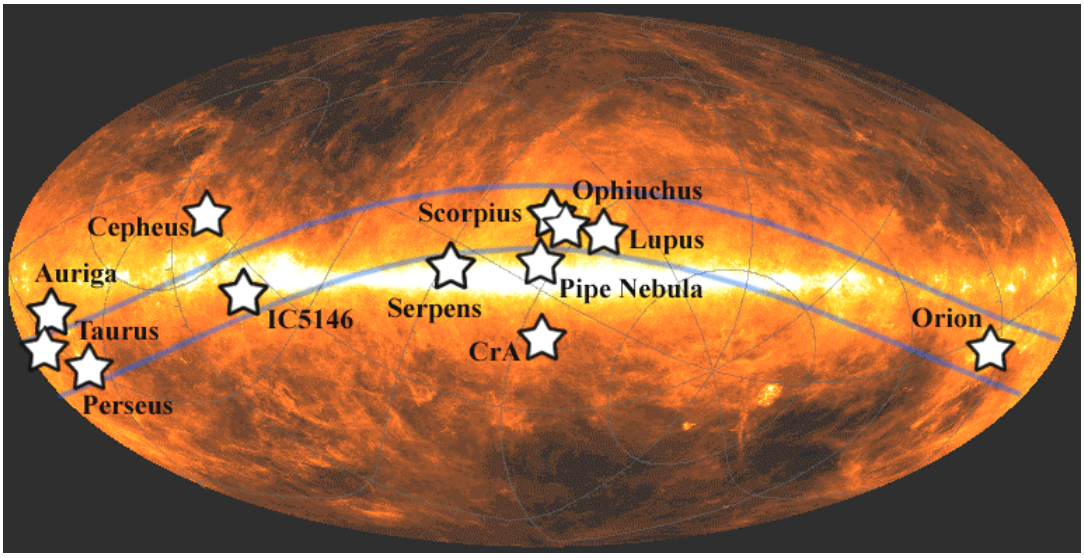

图 5.1: 古德带和其包含的一些恒星形成区在天球上的位置。**版权：Wayne Holland，爱丁堡皇家天文台。**

Figure 5.1. The Gould Belt and star forming regions in it. **Image Courtesy of Wayne Holland, UK ATC, Royal Observatory Edinburgh.**

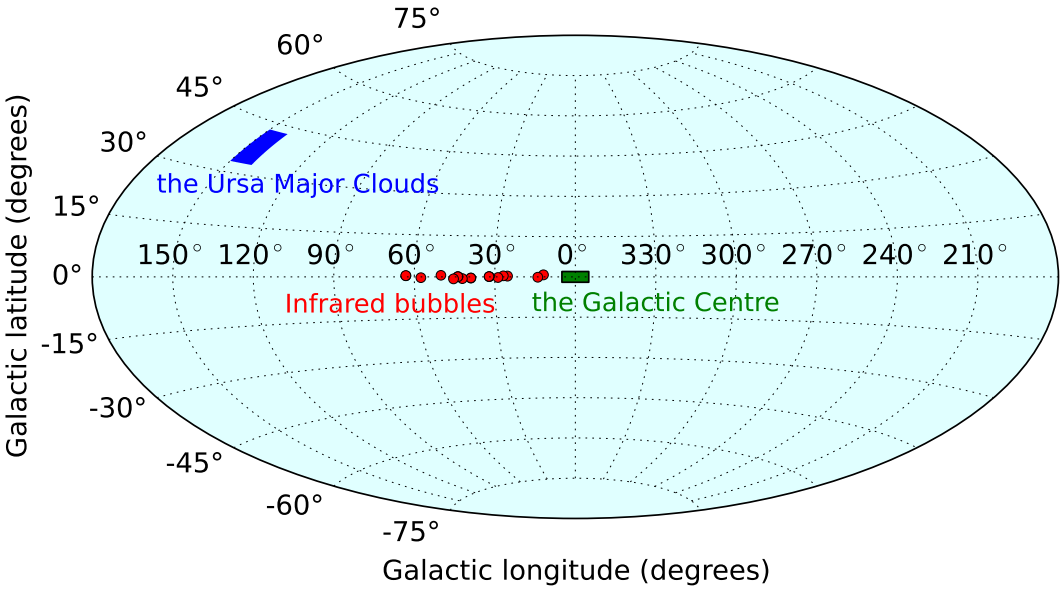

图 5.2: 大熊座分子云 (蓝色)，银心 (绿色) 和红外 Bubble(红色) 的位置示意图。这是本论文研究的银河系中的三个典型区域。

Figure 5.2. Three regions studied in this PhD thesis.

5.1 大熊座分子云

大熊座分子云的中心坐标大约为 $(l, b) = (145°, 39°)$，到太阳的距离约为 110 ± 10 pc (Penprase, 1993)。图5.2中的蓝色区域是大熊座分子云在银道坐标系中的位置，我们在图中还画出了第二章和第四章研究过的红外 Bubble 和 CMZ 的位置。

图5.3展示了Heithausen et al. (1993) 利用 CfA 1.2 米望远镜观测的大熊座分子云 ^{12}CO $(J = 1 \rightarrow 0)$ 谱线积分强度图，空间分辨率仅有 8.7′。低分辨率会掩盖很多分子云的细节，而这些细节很可能可以提供关于分子云的形成和演化的重要线索。

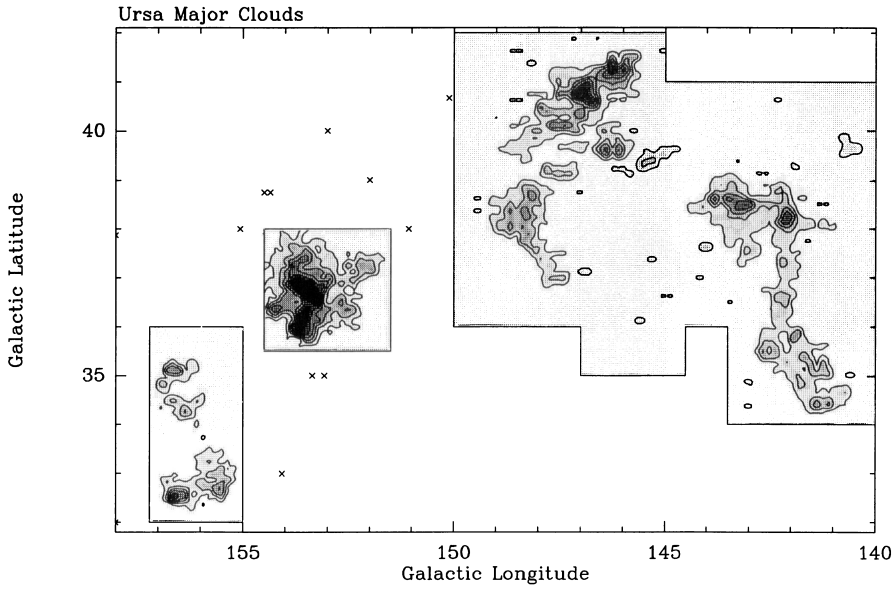

图 5.3: 大熊座分子云 ^{12}CO $(J = 1 \rightarrow 0)$ 积分强度图 (Heithausen et al., 1993)。

Figure 5.3. The integral intensity map of ^{12}CO $(J = 1 \rightarrow 0)$ towards the Ursa Major Clouds (Heithausen et al., 1993).

继Heithausen et al. (1993) 之后，针对大熊座分子云的研究大多都基于一些低分辨率 (Pound et al., 1997) 或者不完全覆盖的观测 (Barriault et al., 2010; Matsuhara et al., 1997; Miville-Deschênes et al., 2002, 2003)，我们将在本章利用青海站望远镜对大熊座分子云做详细的观测。由于观测最近才结束，在本论文中，我们只给出关于大熊座分子云的一些初步结果。

5.2 数据观测和处理

我们观测用的是紫金山天文台青海观测站 13.7 米毫米波射电望远镜，望远镜具体的观测参数和数据处理步骤跟第二章，§2.2，红外 Bubble 的观测基本一致，这

里我们重点介绍针对高银纬的数据做的一些附加处理。

我们总共观测了三条同位素谱线——^{12}CO ($J = 1 \rightarrow 0$)、^{13}CO ($J = 1 \rightarrow 0$) 和 C^{18}O ($J = 1 \rightarrow 0$)。观测采用 OTF 成图模式，每次扫描单个天区，单个天区的银经和银纬的范围为 $(\Delta l, \Delta b) = (0.5°, 0.5°)$，扫描面积大约为 0.2 平方度，总巡天面积大约为 28 平方度。每个天区的扫描时间大约为 10 小时 (扫描 8 次)，总观测时间大约为 1400 小时。

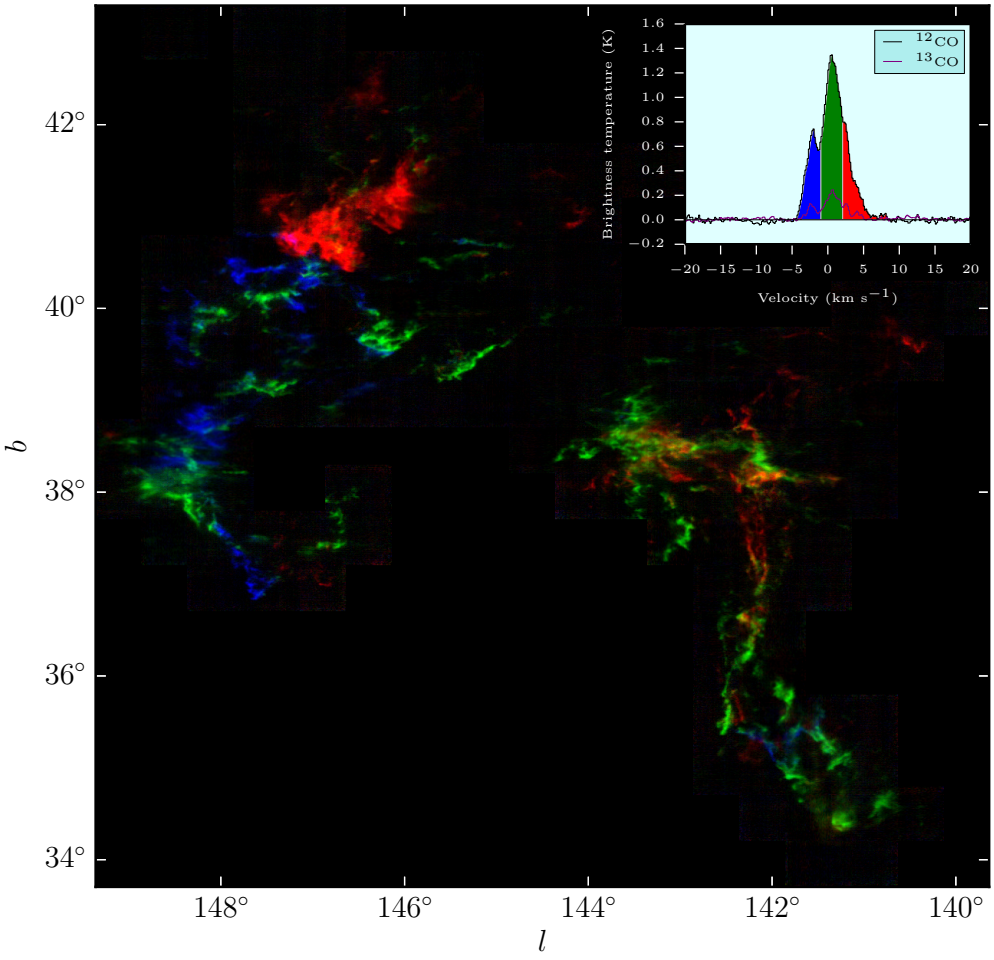

图 5.4: ^{12}CO ($J = 1 \rightarrow 0$) 的积分图，其中蓝色积分区间为 [-7, -1] km s^{-1}，绿色区间为 [-1, 2] km s^{-1}，红色区间为 [2, 9] km s^{-1}。右上角是分子云核峰值点累加并平均后的 ^{12}CO ($J = 1 \rightarrow 0$) 和 ^{13}CO ($J = 1 \rightarrow 0$) 谱线。

Figure 5.4. The integral intensity map of ^{12}CO ($J = 1 \rightarrow 0$). The integral velocity range for the blue, green, and red colors are [-7, -1] km s^{-1}, [-1, 2] km s^{-1}, and [2 , 9] km s^{-1}, respectively. The average spectral of ^{12}CO ($J = 1 \rightarrow 0$) and ^{13}CO ($J = 1 \rightarrow 0$) (only accounting for the peak position of cores) are shown in the upper-left corner.

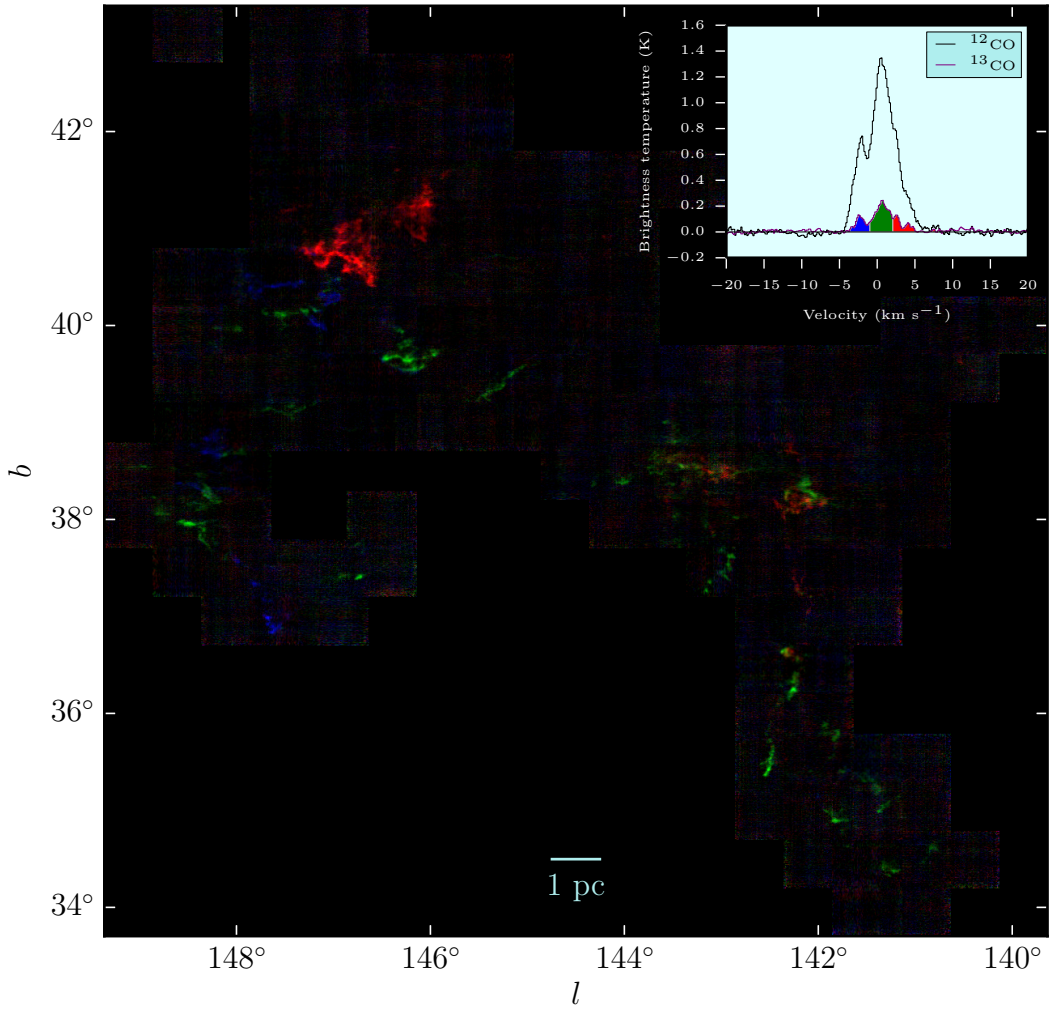

图 5.5: ^{13}CO ($J = 1 \rightarrow 0$) 的积分图，其中蓝色积分区间为 [-7, -1] km s^{-1}，绿色区间为 [-1, 2] km s^{-1}，红色区间为 [2, 9] km s^{-1}。右上角是分子云核峰值点累加并平均后的 ^{12}CO ($J = 1 \rightarrow 0$) 和 ^{13}CO ($J = 1 \rightarrow 0$) 谱线。

Figure 5.5. The integral intensity map of ^{13}CO ($J = 1 \rightarrow 0$). The integral velocity range for the blue, green, and red colors are [-7, -1] km s^{-1}, [-1, 2] km s^{-1}, and [2 , 9] km s^{-1}, respectively. The average spectral of ^{12}CO ($J = 1 \rightarrow 0$) and ^{13}CO ($J = 1 \rightarrow 0$) (only accounting for the peak position of cores) are shown in the upper-left corner.

我们先用GILDAS软件包把每个天区的数据处理成FITS格式，随后利用Montage软件包[1]将所有的 FITS 文件重投影，并合并为一个总的 FITS。^{12}CO ($J = 1 \rightarrow 0$) 谱线的噪声水平为 0.2 K，^{13}CO ($J = 1 \rightarrow 0$) 和 C^{18}O ($J = 1 \rightarrow 0$) 谱线的噪声会平为 0.1 K，谱线的空间和速度分辨率分别为 52″ 和 0.16 km s^{-1}。

[1] http://montage.ipac.caltech.edu/

5.3 大熊座分子云 CO 观测结果和初步分析

在三条 CO 同位素谱线中，我们只探测到 ^{12}CO ($J = 1 \rightarrow 0$) 和 ^{13}CO ($J = 1 \rightarrow 0$) 信号，没有发现 C^{18}O ($J = 1 \rightarrow 0$) 辐射。我们认为 C^{18}O ($J = 1 \rightarrow 0$) 的信号过于微弱，大大低于青海站的望远镜的灵敏度。

5.3.1 ^{12}CO 和 ^{13}CO 积分强度分布

我们对 ^{12}CO ($J = 1 \rightarrow 0$) 和 ^{13}CO ($J = 1 \rightarrow 0$) 三个速度区间进行了积分，并合成三色图，分别见图5.4和图5.5。从图中可以看出，高分辨率和完全采样的 CO 观测揭示了大熊座分子云的诸多细节。由于受到周围星风的影响，高银纬分子云的内部运动也比较复杂。

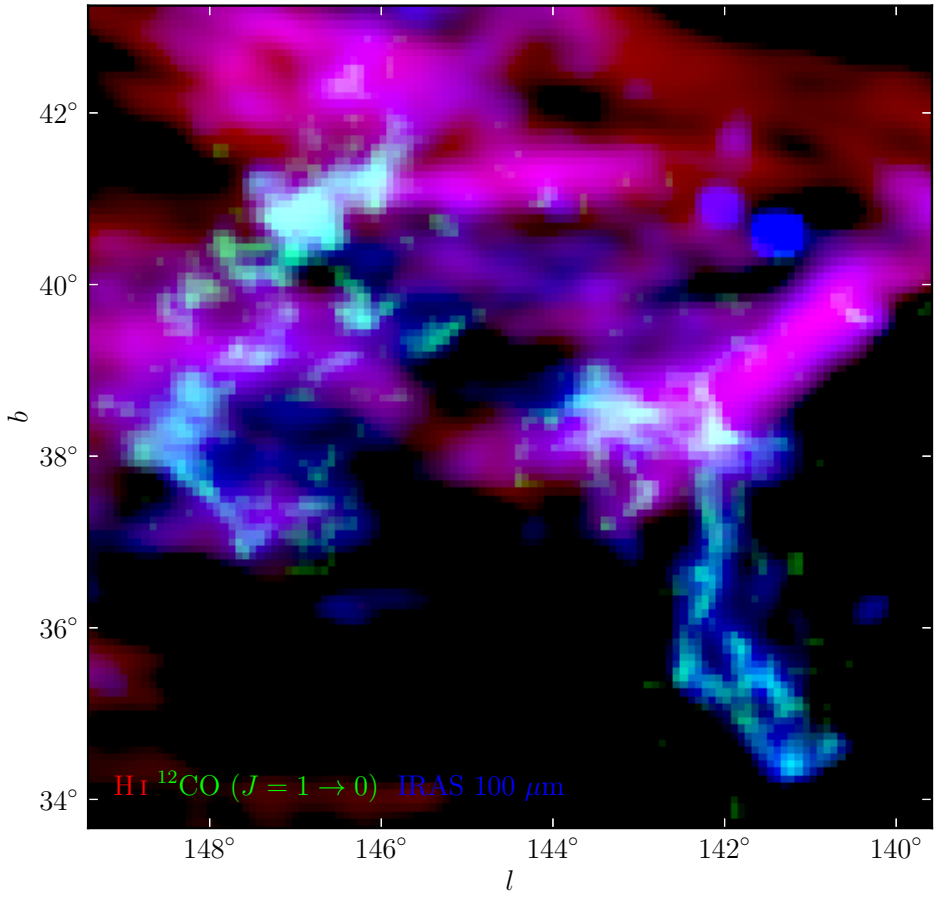

图 5.6: 分子氢 (^{12}CO ($J = 1 \rightarrow 0$))、原子氢 (H I) 以及尘埃 (IRAS 100 μm) 的分布图。

Figure 5.6. The distribution of molecular gas (^{12}CO ($J = 1 \rightarrow 0$)), atomic gas (H I), and dust (IRAS 100 μm)。

5.3.2 H I、^{12}CO、IRAS 100 μm 分布对比

为了比较大熊座天区内分子气体、原子气体和尘埃的分布，我们把有代表性的 ^{12}CO ($J = 1 \rightarrow 0$)、H I和 IRAS 100 μm 辐射，画在了同一张三色图上。由于H I数据 (HI4PI Collaboration et al., 2016) 的空间分辨率最低，大约为 5′，我们把 ^{12}CO ($J = 1 \rightarrow 0$) 和 IRAS 100 μm 的数据进行平滑并重采样为同样的空间分辨率。

分子气体 (绿色, ^{12}CO ($J = 1 \rightarrow 0$))、原子气体 (红色, H I) 和尘埃 (蓝色, IRAS 100 μm) 的分布如图5.6所示。图中的粉色区域是原子气体和尘埃的重合部分，说明分子云周围的尘埃和原子气体成协。在远离分子云的地方有部分天区只有原子气体并没有尘埃辐射，例如右上角的区域。图5.6中的绿色区域基本上和蓝色区域重合，说名分子气体和尘埃是成协的。显然，绿色区域和红色区域的重合部分很少，说明分子气体跟原子气体一般不共存。

5.3.3 分子核

根据 ^{12}CO ($J = 1 \rightarrow 0$) 谱线，我们使用`Duchamp` (见 §4.3.2) 软件来搜索分子核。严格意义上讲，这些不是分子核不是表1.1中定义的“分子核”，只是分子云中密度比较大的成分。高银纬分子核包含的分子云质量达不到一般意义下分子核的定义质量，但是，为了方便起见，我们仍称他们为分子核。在搜索分子核的时候，我们屏蔽亮温度低于 0.28 K (3σ) 的区间，并要求分子核至少要在连续 3 个速度通道内有信号，每个速度通道内分子核像素数目不少与 6 个，总的像素数不低于 39 个。具体的参数见表5.1.

根据表5.1中的参数，我们搜索了整个 ^{12}CO ($J = 1 \rightarrow 0$) FITS 文件，剔除边缘的一些假分子核后，总共证认出 106 个，其分布见图5.7。由`Duchamp` 给出的分子核的谱线和跟 ^{12}CO ($J = 1 \rightarrow 0$) 积分强度的对比来看，分子核的位置是可靠的。

5.3.4 分子核质量函数

恒星的初始质量函数 (the initial mass function, IMF) 是恒星形成的重点问题之一 (Kroupa et al., 1993; Salpeter, 1955)。恒星的初始质量函数，由于其对各种恒星系统的形状不变性 (Bastian et al., 2010)，使得天文学家不得不相信这背后一定有深层次的原因，而这个原因很可能是破解恒星形成各种难题的关键。从应用的角度上讲，初始质量函数的准确性直接关系到河外星系很多重要参数的估计。

Motte et al. (1998) 研究发现，分子核质量函数 (the core mass function, CMF) 在形状上极为相似，因此 CMF 很可能是 IMF 的前身。随着近年来高分辨率射电干

表 5.1: Duchamp 证认分子核的参数设置。

Table 5.1. Parameters of Duchamp for identifying molecular cores.

Parameter	Value
imageFile	CO13_C.fits
logFile	duchamp-Logfile.txt
outFile	duchamp-Results.txt
spectraFile	duchamp-Spectra.ps
momentMap	duchamp-MomentMap.ps
detectionMap	duchamp-DetectionMap.ps
flagXOutput	true
flagOutputMask	false
flagOutputMomentMap	false
flagOutputMomentMask	false
flagOutputBaseline	false
searchType	spatial
flagTrim	false
flagNegative	false
flagBaseline	True
flagSmooth	True
flagATrous	false
flagRobustStats	true
flagFDR	false
threshold	0.28
minPix	6
minChannels	3
minVoxels	39
flagGrowth	false
flagAdjacent	true
threshVelocity	1
flagRejectBeforeMerge	false
flagTwoStageMerging	true
spectralMethod	peak
pixelCentre	centroid

涉阵列 (例如 ALMA) (Reid et al., 2010; Tokuda et al., 2016) 和空间红外望远镜 (例如 *Herschel*) (André et al., 2011; Tremblin et al., 2014b) 技术的发展，CMF 的研究正逐步揭开 IMF 的神秘面纱。

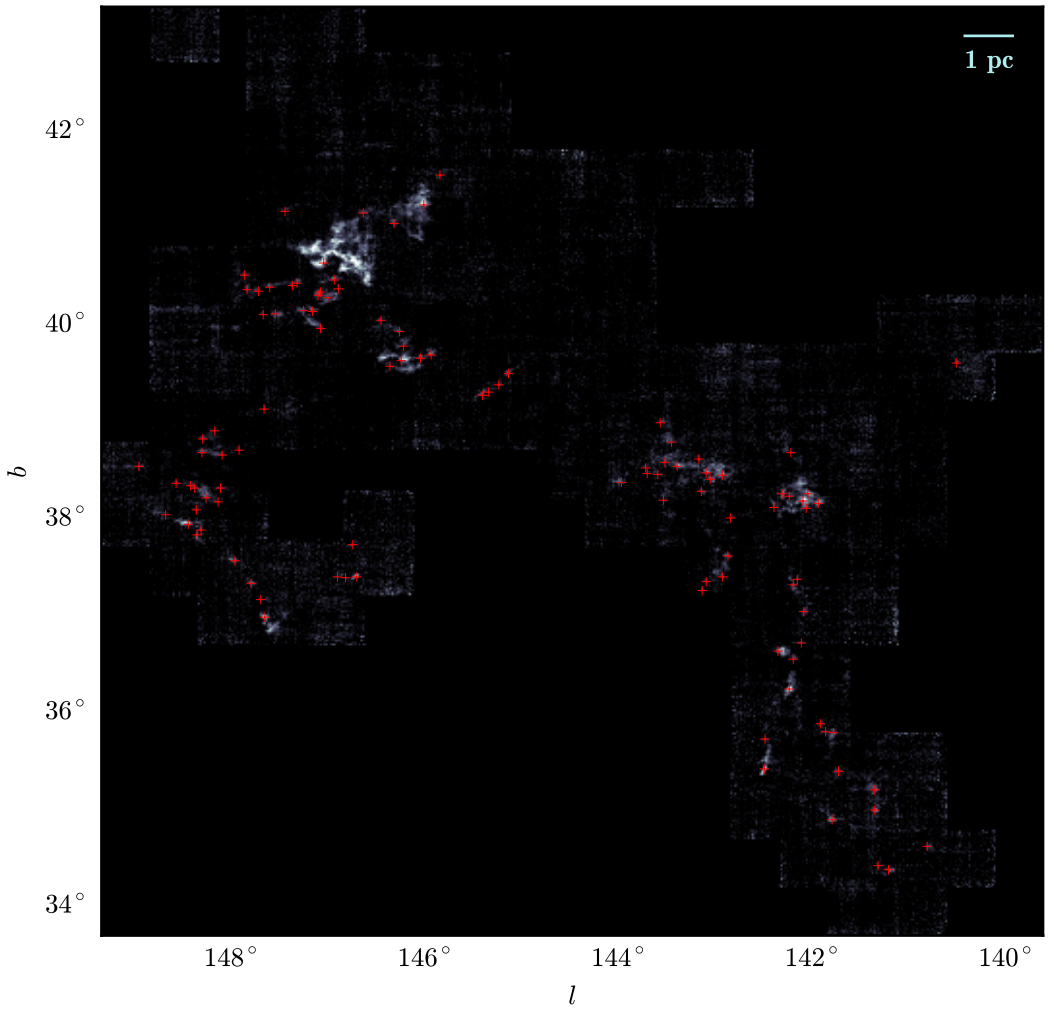

图 5.7: 由 ^{13}CO ($J = 1 \rightarrow 0$) 谱线证认出的分子核分布 (共计 106 个)，红色十字标记峰值点。背景为 ^{13}CO ($J = 1 \rightarrow 0$) 积分图，积分区间 [-6, 8.2] km s^{-1}。图中左上角有一块片白色区域没有分子核标记，是因为这块区域整个地构成一个分子核。

Figure 5.7. Molecular cores identified by `Duchamp` with ^{13}CO ($J = 1 \rightarrow 0$) data. The background is the integral intensity map of ^{13}CO ($J = 1 \rightarrow 0$) from -6 to 8.2 km s^{-1}. Red crosses represent the peak of molecualr cores.

因为高银纬分子云内部的性质和周围的恒星形成活动跟银心附近和银盘上的分子云有很大差别，所以研究高银纬分子云中致密的成分的质量分布，对研究 CMF 和 IMF 的成因有重要价值。在高银纬，利用 ^{12}CO ($J = 1 \rightarrow 0$) 积分强度计算氢分

子柱密度的 X 因子跟银盘上的值差别可能比较大，而且 X 因子本身的不确定性也很大，所以我们暂时不对分子核进行质量估计而仅关注大熊座分子核质量分布函数的形状。

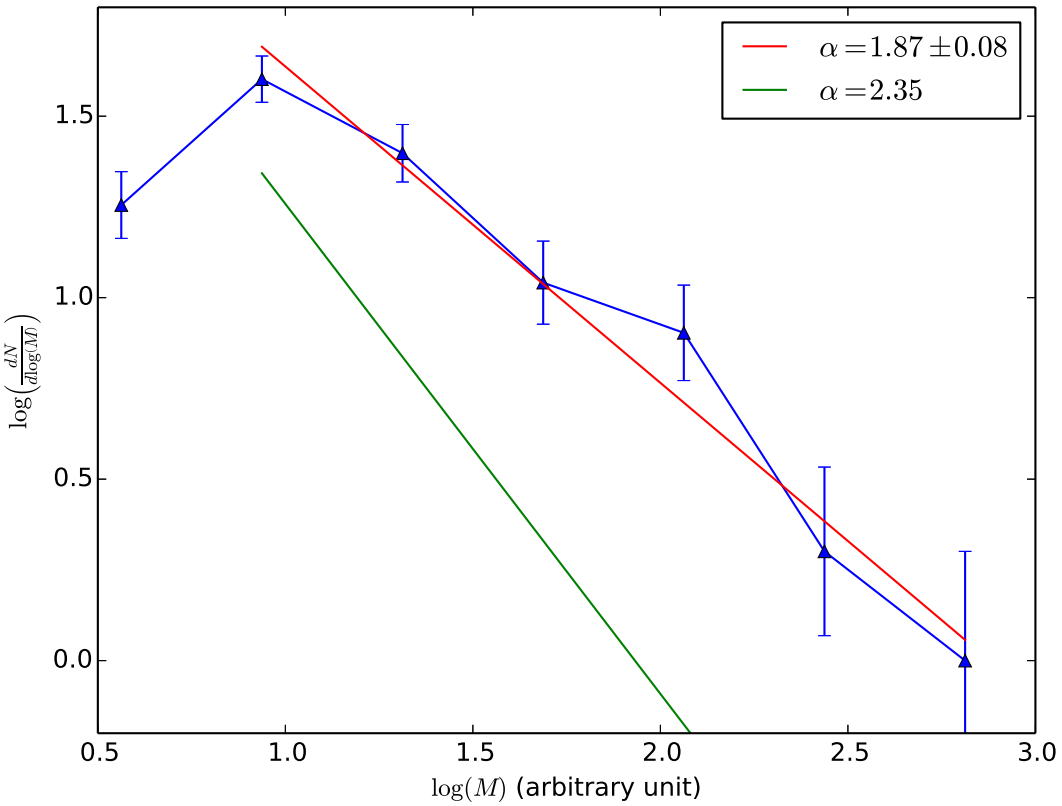

图 5.8: 大熊座分子云 CMF 形式。α 定义为 $\frac{dN}{dM} \propto M^{-\alpha}$。

Figure 5.8. The shap of the CMF in the Ursa Major Clouds. The definiation of CMF is $\frac{dN}{dM} \propto M^{-\alpha}$.

大熊座分子云 CMF 的形状如图5.8所示。图5.8中，横坐标是分子核的 ^{13}CO $(J = 1 \rightarrow 0)$ 积分强度值，单位为 K m s^{-1}。由于 ^{13}CO $(J = 1 \rightarrow 0)$ 积分强度值跟分子云质量大体上线性相关，所以使用 ^{13}CO $(J = 1 \rightarrow 0)$ 积分强度值计算 CMF 并不影响其形状。

CMF 的定义式为：

$$\frac{dN}{dM} \propto M^{-\alpha}, \tag{5.1}$$

其中，α 是指数。如图5.8所示，我们计算出的大熊座分子云中 CMF 的指数为 $\alpha = 1.87 \pm 0.08$，这跟Li et al. (2015) $(\alpha = 1.87 \pm 0.08)$ 和Kramer et al. (1998) $(1.6 < \alpha < 1.8)$ 给出的其他的弥散分子云的指数一致。

5.4 大熊座分子云 CO 观测总结

我们观测了大熊座分子云的三条 CO 同位素谱线——^{12}CO ($J = 1 \rightarrow 0$)、^{13}CO ($J = 1 \rightarrow 0$) 和 C^{18}O ($J = 1 \rightarrow 0$)。以 0.1 K 的探测灵敏度，我们没有探测到 C^{18}O ($J = 1 \rightarrow 0$) 信号。^{12}CO ($J = 1 \rightarrow 0$) 和 ^{13}CO ($J = 1 \rightarrow 0$) 的结果显示，高银纬的弥散分子云内部运动比较复杂，其中尘埃跟分子气体和原子气体都成协，但是分子气体和原子气体的分布基本上是分离的。

利用`Duchamp` 软件包，我们在大熊座分子云中找到 106 个分子核。我们发现大熊座分子云中分子核质量分布函数的指数为 $\alpha = 1.87 \pm 0.08$，这跟前人对弥散分子云的研究结果一致。

第六章　研究总结与展望

The truth is that we don't understand star formation at a fundamental level.

— Abraham Loeb

本论文通过分子谱线观测，研究了银河系中心、银道面和高银纬三个典型区域的分子云和恒星形成。通过这三个区域的研究，我们可以看到多波段观测数据、天文学基础理论的突破和计算机软硬技术的进步对天文研究的推动力。

分子云包含分子气体和尘埃，所以研究分子云的工具一般包括射电波段的分子谱线和红外波段的尘埃辐射。在我们利用青海站的观测数据寻找H II 区附近外流的时候，我们使用了五条分子谱线和多个红外和射电波段的巡天。使用的分子谱线包括 ^{12}CO $(J = 1 \rightarrow 0)$、^{13}CO $(J = 1 \rightarrow 0)$、C^{18}O $(J = 1 \rightarrow 0)$、HCN $(J = 1 \rightarrow 0)$ 和 HCO$^+$ $(J = 1 \rightarrow 0)$，使用的巡天数据波段包括 8 μm，24 μm，0.87 毫米，1.1 毫米和 20 厘米。不论是寻找外向分子流，还是研究H II 区本身的性质，多波段的观测总是可以提供更多的信息，使得我们的结论更加可靠。

在研究银河系中心分子云的过程中，我们提出了一个可以精确解算 OH 柱密度、激发温度和光深的新方法。利用这个方法，我们推导出了银心分子云的三维结构。没有这个方法，即使观测再多的数据，我们的进展仍然会十分缓慢。有了这个方法，再加上 Parkes 望远镜观测的多条 OH 谱线，我们才能清晰的看到银河系中心分子云的棒旋结构。

大质量恒星形成区的样本对大质量恒星形成的研究非常重要。我们在研究如何从 IRAS 中比较准确的挑选H II 区的时候发现监督式机器学习中的 SVM 算法可以很好地解决这类问题。利用 SVM 算法，我们确实提高了筛选H II 区的准确性。我们将在下一步的工作中，利用已公开的巡天数据来确认这些新选出的H II 区。

天文的数据处理是天文研究最基础也是最重要的一环，计算机技术的发展在提高数据处理的效率和准确性上，功不可没。例如在处理大熊座分子云巡天数据的时候，我们使用 *python* 语言搭建了一个可以下载和处理数据的脚本，极大的方便了我们研究。一些天文软件包也可以大大提高我们处理数据的速度，例如`Montage`，`Duchamp`，`GILDAS/CLASS`，*sklearn*，`GRIDZILLA`，`MIRIAD` 和 `ASAP` 等。

由于在研究银河系分子云的过程中，我们的结果受限于 CO 和 OH 谱线的空间分辨率。为了改进我们的结果，我们利用 VLA 观测了银心附近分子云的 OH 谱线，再加上 Mopra 观测的高分辨率 CO 谱线，我们预期可以获得关于银心分子云更清晰的图像。

附录 A Summary in English

With the motivation of studying the molecular clouds and star formation in the Milky Way, we investigated three representative regions, including the Galactic plane, the Galactic Centre (GC), and the high Galactic latitudes.

Primarly, we use newly obtained CO and OH spectral lines with with the Purple Mountain Observatory Delingha (PMODLH) 13.7-m millimeter telescope and the Parkes 64-m telescope to perform our studies, as well as several publicly available radio and infrared surveys.

In §A.1 and §A.2, we introduce our work on triggered star formation near H II regions and new criteria for identifying H II regions from IRAS sources, respectively. We present our results with respect to the three-dimensional structure of the molecular clouds in the GC in §A.3. In §A.4, we display preliminary results of a deep CO survey towards the Ursa Major Clouds, and we summarize our work in §A.5.

A.1 Triggered Star Formation

In order to study high-mass star-forming regions in the Galactic plane, we investigated the physical properties of molecular clouds and star formation processes around infrared bubbles which are essentially expanding H II regions. We performed observations of 13 galactic infrared bubble fields containing 18 bubbles. Five molecular lines, ^{12}CO ($J = 1 \rightarrow 0$), ^{13}CO ($J = 1 \rightarrow 0$), C^{18}O ($J = 1 \rightarrow 0$), HCN ($J = 1 \rightarrow 0$), and HCO$^+$ ($J = 1 \rightarrow 0$), were observed, and several publicly available surveys, GLIMPSE, MIPSGAL, ATLASGAL, BGPS, VGPS, MAGPIS, and NVSS, were used for comparison. We present our results about star formation activities around H II regions in this section and refer the reader to Yan et al. (2016).

A.1.1 Scenarios of Triggered Star Formation

Elmegreen et al. (1977) proposed that star formation can be triggered by the propagation of ionization and shock fronts through a molecular cloud complex. Those processes usually happen near OB associations, because the UV radiation emanated from OB star can ionize surrounding gas and the expansion of ionize gas produces ionization

and shock fronts. Mainly, we have two popular mechanisms for triggered star formation, which are collect-and-collapse (Elmegreen et al., 1977), and radiation-driven implosion (RDI) (Bertoldi, 1989).

Since the discovery of many H II regions by *spitzer* Galactic Legacy Infrared Mid-Plane Survey Extraordinaire (GLIMPSE; Benjamin et al. (2003); Churchwell et al. (2009)), the triggered star formation process have been being intensively studied. Benjamin et al. (2003); Churchwell et al. (2009)) identifies almost 600 bubbles (Churchwell et al., 2006, 2007), extended to 5106 by the Milky Way Project (MWP) (Simpson et al., 2012). Bubbles were defined by the 8.0 micron emission (Leger et al., 1984), which contains 7.7 micron and 8.6 micron polycyclic aromatic hydrocarbon (PAH) features, including the continuum (Everett et al., 2010). Churchwell et al. (2006) claimed that 25% of 322 bubbles outside 10° of the Galactic centre coincide with known radio H II regions, and Deharveng et al. (2010) extended this proportion to 86% based on a sample of 102 bubbles selected from the catalog provided by Churchwell et al. (2006).

However, robust evidence of triggered star formation is rare, because it is difficult to proof the formation of a star or a star cluster is triggered rather than spontaneous. Dale et al. (2015) investigated the most commonly used signposts and found none of them significantly improved the chances of correctly identifying a given star as triggered. They argued that we should be cautious in interpreting observations of star formation near feedback driven structures in terms of triggering.

A better way of studying triggered star formation is using statistics, rather than focusing on individuals. Seventeen candidate regions for the collect-and-collapse process were identified by Deharveng et al. (2005), and a large number of young stellar objects (YSOs) were found in the vicinity of bubbles (Watson et al., 2008, 2009, 2010). Kendrew et al. (2012) found a strong positional correlation between high-mass YSOs (HMYSOs) and H II regions with MWP bubbles at separations of <2 bubble radii. A statistical study of YSOs around 322 *Spitzer* mid-infrared bubbles has been done by Thompson et al. (2012), and they found a significant overdensity of Red MSX-Source Survey (RMS) YSOs around the bubbles. Hou et al. (2014) performed a statistical study of infrared bubbles using GRS ^{13}CO ($J = 1 \rightarrow 0$) data. They found 60 percent of 309 MWP bubbles are associated with molecular clumps. The correlation between bubble morphology and molecular gas distribution make them believe some of these clumps near bubbles are produced by the expansion of bubbles. These results support that expanding H II regions can provide an

effective mechanism to form next generation stars.

However, molecular outflows, which are direct signposts of star formation, are rarely present in current studies. Identifying YSOs is the most commonly used method to study triggered star formation. However, it is difficult to determine the distances, ages, and masses of YSOs. If bubbles can truly trigger star formation, then the characteristics of star formation, i.e., collapse, outflows, or masers, should be found around them. Although these phenomena are not specific for triggered star formation, the more star formation process we find around bubbles, the safer we can say they are triggered or accelerated by expanding H II regions.

In this part of this thesis, we studied 13 infrared bubble regions selected from the bubble catalog of Churchwell et al. (2006), including 18 bubbles. For each bubble, five molecular lines were observed, revealing the dynamic and physical features of molecular clouds around bubbles. Among the five lines, $C^{18}O$ (J=1-0), HCN (J=1-0), and HCO^+(J=1-0) are not widely present in previous observations. Several publicly available surveys are also involved, such as the GLIMPSE (Benjamin et al., 2003; Churchwell et al., 2009), the Multiband Imaging Photometer for *Spitzer* (MIPS) Galactic Plane Survey (MIPSGAL) (Carey et al., 2009; Gutermuth et al., 2015), the APEX Telescope Large Area Survey of the Galaxy (ATLASGAL) (Schuller et al., 2009), the Bolocam Galactic Plane Survey (BGPS) (Aguirre et al., 2011; Rosolowsky et al., 2010), the VLA Galactic Plane Survey (VGPS) (Stil et al., 2006), the Multi-Array Galactic Plane Imaging Survey (MAGPIS) (Helfand et al., 2006), and the NRAO VLA Sky Survey (NVSS) (Condon et al., 1998). Details of these surveys are described in Table 2.2. Combing these surveys, we performed a multi-wavelength analysis of the 18 bubbles, focusing on their physical properties and star formation processes around them.

A.1.2 Observations of five molecular lines

We selected 13 bubble regions from the catalog provided by Churchwell et al. (2006) by checking the 8 μm band image of GLIMPSE surveys visually, and 18 bubbles in total were identified. Three criteria were applied to identify a bubble: (1) Located in the northern sky; (2) With outer major axis larger than 1.5 arcmin; (3) With approximate circular or elliptical shape. For small size bubbles, the dynamic expansion of H II regions and the bipolar motion of outflows are mixed together, which cannot be resolved by the limited resolution (about $52''$) of the Purple Mountain Observatory Delingha (PMODLH) 13.7

m millimeter telescope. We assume that regular shapes of bubbles indicating relatively simple environments, which make it possible to do outflow and bubble structure analysis.

Observations were performed with the PMODLH 13.7 m millimeter telescope at Qinghai station, latitude 37°22′.4, from 30 May to 27 December, 2013, employing a superconducting array receiver (SSAR) with 3×3 beam array running in sideband separation mode (Shan et al., 2012). Spectral analysis was performed using the fast Fourier transform spectrometer (FFTS) with velocity resolution 0.16 km s^{-1}. Details about the telescope are described in the PMODLH status report[1].

Five molecular lines were observed: ^{12}CO ($J = 1 \rightarrow 0$), ^{13}CO ($J = 1 \rightarrow 0$), C^{18}O ($J = 1 \rightarrow 0$), HCN ($J = 1 \rightarrow 0$), and HCO$^+$ ($J = 1 \rightarrow 0$). Observations of these three CO lines were performed simultaneously, separated from observations of HCO$^+$ and HCN. The half power beamwidth (HPBW) of the telescope is approximately 52″ at 110.2 GHz, with pointing and tracking uncertainty approximately 5″ and 1.4″, respectively. The beam efficiency is approximately 46% for ^{12}CO, 51% for ^{13}CO, and 55% for C^{18}O, HCN, and HCO$^+$. The system temperature was approximately 280 K for ^{12}CO, 185 K for ^{13}CO and C^{18}O, and 140 K for HCN and HCO$^+$. The on the fly (OTF) scanning model was used for the observations, with scanning rate of 50″ s^{-1}, and spectra were recorded every 0.3 s. For each bubble, the total observation time for CO was approximately 2 hours, and 5 hours for HCN and HCO$^+$. Further observations were taken for bubble regions with weak emissions.

The typical observed size for bubbles was approximately 10′ × 10′, which is large enough to include the molecular clouds surrounding them. Data reduction was achieved with the Grenoble Image and Line Data Analysis Software (GILDAS) package. After replacing bad channels with adjacent channels in the spectra, the data was regridded to 30″×30″ pixels and mosaicked to a FITS cube file after calibrating. The root mean square (rms) noise is approximately 0.45 K for ^{12}CO at 0.16 km s^{-1} resolution, 0.20 K for ^{13}CO and C^{18}O at 0.17 km s^{-1} resolution, and 0.07 K for HCN and HCO$^+$ at a resolution of 0.18 km s^{-1}.

A.1.3 Molecular Clouds Near H II Regions

Except N89 and N90 where no C^{18}O and only weak HCO$^+$ emission was detected, all the molecular lines were detected for the other bubble regions. Two bubbles, N44 and

[1] http://www.radioast.nsdc.cn/zhuangtaibaogao.php

N123, show relatively low signal to noise ratio (SNR). For all bubbles, the SNR of $C^{18}O$ are generally lower than the other four lines, because of its equal integration time with ^{12}CO and ^{13}CO, but comparable low antenna temperature with HCN and HCO^+.

The physical properties for molecular clouds and clumps associated with these bubbles were calculated using three CO isotopic lines, with the assumption of local thermodynamic equilibrium (LTE). ^{12}CO $(J = 1 \rightarrow 0)$ is assumed to be optically thick, whereas ^{13}CO $(J = 1 \rightarrow 0)$ is generally optical thin, which means we could estimate the excitation temperature (T_{ex}) and optical depth (τ), respectively. The velocities were determined according to ionized gas velocities (Anderson et al., 2014; Lockman, 1989), CO velocities (Beaumont et al., 2010), and were confirmed by the spatial coherence between the ^{13}CO integrated intensity and bubbles. We also searched for outflows around bubbles using the profiles of ^{12}CO and HCO^+.

Following Tremblin et al. (2014a), we estimated the age for each bubble using parameters listed in Table 2.1. Tremblin et al. (2014a) provided a new method to determine the age and size of H II regions using 3D simulations. They included the internal turbulence of molecular clouds surrounding the bubbles, which we believe is more accurate.

Details of the physical parameters of the bubbles and molecular clumps are shown in Table 2.4 and 2.5, respectively. The masses of clouds within bubble squares are in the range of 100 - 19000 solar mass, and their ages are in the range of 0.3 - 3.7 Myr. In total, 23 molecular clumps are found around 18 bubbles, and each bubble contains at least one molecular clump at its border. Since the ^{13}CO lines tend to be optically thick at the peak of clumps, we estimated the mass of molecular clumps using ^{12}CO and $C^{18}O$ lines. N89 and N90 show low SNR for $C^{18}O$, and consequently we used ^{13}CO instead for these two bubbles.

We identified outflows by checking the profiles, integrated intensity maps, and particularly, the position velocity (P-V) diagrams, in which outflows are characterized with protruding structures (Beuther et al., 2004; Smith et al., 1997). However, we must be cautious about interpreting wing profiles near infrared bubbles as outflows, since the interaction between bubbles and molecular clouds can also produce similar structures. Therefore, intensity maps of lobes are also required to be clearly distinguished from background emissions, and, most importantly, the line wings should be significantly wide.

By search for molecular outflows, it is required that along the line of sight, at least one end of the profile is uncontaminated by other components. We found seven bubbles agree

with this condition , which are N14, N37, N55, N74, N105, and N133, and we found four molecular outflows near N14, N55, N105, and N133. However, only N55 shows evident bipolar structure, while the other three bubbles display single wings, mainly due to the contamination of adjacent components with similar velocities.

Following Snell et al. (1984), we calculated the mass, momentum, and energy entrained in the outflowing gas without any projection effect calibrated. The LTE assumption was applied, and we also assumed the optical depth of the ^{12}CO were thin at line wings. We found that two molecular outflows, which are associated with N105 and N55, are probably driven by high-mass stars.

In addition to molecular outflows, there are three bubbles, N55, N49, and N123, display ultra-compact (UC) H II regions at their borders, which are traced by 20 or 6 cm continuum emission. These UC H II regions are mostly tracing high-mass stars which could be triggered by bubbles.

A.1.4 Summary of Infrared Bubble Research

We have presented an investigation of 13 regions containing 18 infrared bubbles, using three CO isotopic lines and two high density molecular lines, HCO^+ and HCN ($J = 1 \rightarrow 0$). Some profiles of bubble regions show broad redshifted ^{12}CO profiles, arc structures, and ^{12}CO velocity gradients, indicating they are probably interacting with the molecular clouds around them. Most of the bubbles are associated with dense molecular gas traced by HCO^+ and HCN, and using C^{18}O, we identified 24 molecular clumps near 18 infrared bubbles, most of which are gravitationally bound. These facts are generally in agreement with either the collect-and-collapse or the RDI model.

A search of outflow was carried out in six bubble regions. Four bubble regions, N14, N37, N55, and N133, show outflow activities, while only N55 shows a bipolar structure. The energy of outflows indicates the driven source of this outflow is probably high-mass, and however, no EGO is found towards these outflow candidates. These outflows are convincing evidence that the star formation processes are occurring around bubbles. Besides outflows, ultra-compact H II regions are found on the border of N55, N49, and N123. Among the 18 selected bubbles, six bubbles possess star formation activities nearby, and the detection ratio of outflows and UC H II regions near bubbles is about 0.3. We speculate that star formation processes might have been triggered around these bubbles. However, higher spatial resolution observations are needed to confirm these star formation activities.

A.2 New Criteria For H II Regions

When we were studying the infrared bubbles, we found that some infrared bubbles have counterparts in IRAS catalogue. This provides an opportunity of studying the distribution of H II regions on two-colour diagram more precisely. With the H II region catalogue provided by Anderson et al. (2014) and machine learning algorithms, we produced new criteria of selecting H II regions from IRAS sources. In addition, we examined the evolution of H II regions on two-colour diagram.

A.2.1 High-mass Stars and H II Regions

High-mass stars, whose masses exceed 8 $M_{\odot}$ (Zinnecker et al., 2007), are OB stars which emit strong UV radiation, thereby ionizing surrounding atomic and molecular gases. Composed mainly of ionized hydrogen, these ionized gases are usually called H II regions. Most H II regions essentially trace high-mass stars, hence the evolution and distribution of H II regions is useful for investigating high-mass stars in the Milky Way.

Although the amount of H II regions forming high-mass stars is an important evolutionary indicator of the Milky Way, their total number is still unclear due to the difficulty in detecting and identifying them due to their large distances and rapid evolution (Zinnecker et al., 2007). In their early stages, when H II regions are compact, high-mass stars are deeply embedded in cold thick molecular clouds, whose typical temperature is about 30 K (Garay et al., 1999; Wolfire et al., 1994). In this phase, high-mass stars are invisible at optical wavelengths due to high extinction caused by dust grains, but they are observable at longer wavelengths, notably in the infrared or radio bands. The infrared output of H II regions is generally due to the thermal emission of their internal or surrounding dust grains (Churchwell, 2002; Garay et al., 1999), whereas the radio output is generated by their internal free-free emission (Kurtz et al., 1994; Walsh et al., 1998). However, the properties of infrared emission vary with temperature, while the optical depth of free-free emission hinges on the frequency (Kurtz et al., 1994).

Wood et al. (1989a, here after WC89) investigated the population and distribution of embedded high-mass stars in the Milky Way using the all-sky Infrared Astronomical Satellite (IRAS) Point Source catalogue (PSC) (Helou et al., 1988; Neugebauer et al., 1984) over four infrared bands at 12 μm, 25 μm, 60 μm and 100 μm. If there is no detection in one band, the flux density quality of this band is marked with an upper limit.

With the help of some ultracompact (UC) H II regions (Wood et al., 1989b), they derived a criterion for embedded high-mass stars: $\log(F_{60}/F_{12}) \leqslant 1.30$ and $\log(F_{25}/F_{12}) \leqslant 0.57$, where F_{12}, F_{25}, and F_{60} represent fluxes at 12 μm, 25 μm, 60 μm, respectively. They further rejected sources whose flux density quality at either 25 or 60 μm is marked by an upper limit. They identified 1717 UC H II region candidates and potentially missed many evolved H II regions.

Using known H II regions, including UC H II regions, Hughes et al. (1989, here after HM89) investigated the H II regions based on a two-colour diagram of IRAS sources. They provided a decision boundary of $\log(F_{25}/F_{12}) \leqslant 0$ and $\log(F_{60}/F_{25}) \leqslant 0$. They also imposed extra constraints on F_{100} and Galactic latitudes. The total number of H II regions identified was 2298. However, the sample of known H II regions they used is far from complete, and therefore the criterion were not well constrained.

Recently, Anderson et al. (2014) created a catalogue of H II regions, providing an opportunity to improve the selection criteria for H II regions. This H II region catalogue is based on the *WISE* (Wright et al., 2010). They created this catalogue by identifying infrared bubbles (Churchwell et al., 2006) manually. Infrared bubbles essentially are H II regions produced by high-mass stars. The 12 μm band emission traces polycyclic aromatic hydrocarbon (PAH) molecules, delineating the edge of H II regions, while the 24 μm band emission mostly traces internal thermal emission from dust grains heated by ionized gases. This is the most complete catalogue of H II regions forming high-mass stars, because the covering area is much larger than that of the *Spitzer*/GLIMPSE survey (Benjamin et al., 2003), and the number (8399) of identified H II regions exceeds that provided by another similar undertaking: the Milky Way Project (MWP) (Simpson et al., 2012).

However, the catalogue of Anderson et al. (2014) can potentially miss those H II regions that have small angular sizes or that are not easily identified visually. In this paper, we investigate possible criteria for selecting H II regions from IRAS sources to obtain a more complete census of H II regions forming high-mass stars in the Milky Way, using publicly available radio and infrared surveys and sophisticated algorithms. Essentially, the criteria are defined by the decision boundary of two samples: the IRAS sources which are associated H II regions and those sources which are non-H II regions. The *WISE* H II region catalogue (Anderson et al., 2014) is used to create the H II region sample by matching the IRAS PSC position, while the IRAS point sources at high Galactic latitudes serve as the non-H II regions. Support vector machines (SVMs) (Vapnik, 1995), which are machine

learning algorithms used to do supervised classification, are applied to derive the decision boundary of the two samples. A 3D simulation of the expansion of H II regions (Tremblin et al., 2014a) enables us to estimate the age of H II regions and to investigate the evolution of H II regions on two-colour diagrams of IRAS sources.

A.2.2 Determining the Criteria

Our analysis is based on the IRAS PSC (Helou et al., 1988), the *WISE* H II region catalogue (Anderson et al., 2014), and three radio continuum source catalogues (Condon et al., 1998; Mauch et al., 2003; Murphy et al., 2007).

The H II region catalogue that we use to extract H II regions from the IRAS PSC is created by Anderson et al. (2014) from *WISE* data. This catalogue contains 8399 H II regions, covering $|b| \leqslant 8°$ and five high-mass star-forming regions at high Galactic latitudes. In this catalogue, 1413 H II regions have their distances determined, and we estimate their ages based on a numerical simulation of the 3D expansion of H II region (Tremblin et al., 2014a).

In their catalogue, Anderson et al. (2014) found that the coexistence of radio continuum and mid-infrared emission can identify H II regions at a 95% confidence level. Therefore, in order to examine the quality of H II region candidates, we use three radio continuum surveys: the NRAO VLA Sky Survey (NVSS) (Condon et al., 1998), the Sydney University Molonglo Sky Survey (SUMSS) (Bock et al., 1999; Mauch et al., 2003), and the second epoch Molonglo Galactic Plane Survey (MGPS-2) (Murphy et al., 2007). NVSS, SUMSS, and MGPS-2 have similar sensitivities and spatial resolutions and collectively cover the whole sky. At frequencies $\nu \leqslant$ 8-15 GHz, radio free-free emission is optically thick (Kurtz et al., 1994; Protheroe et al., 2008) for UC H II regions, rendering UC H II regions undetectable at these frequencies. Nonetheless, the proportion of sources associated with radio continuum emission is still an excellent indicator of the quality of the selection criteria, because only those H II regions at very early stages are missed.

The entire process of creating selection criteria is divided into five main steps, details of which are described in the rest of this subsection. We choose the optimal criterion according to a metric.

The process of producing criteria includes five main steps:

1. Identify the IRAS sources associated with H II regions, which serve as the sample of H II regions.

2. Select the IRAS sources at high Galactic latitudes, which serve as the sample of non-H II regions.

3. Use SVMs to determine the criteria based on the samples of H II regions and non-H II regions for all possible colour combinations.

4. Apply these criteria to the IRAS PSC.

5. Determine the optimal criterion according to their scores.

In the first step, we matched the IRAS PSC to the *WISE* H II region catalogue. Following Anderson et al. (2014), we only adopted *WISE* sources that have small angular sizes (radii $< 4'$) and ignore those lack detected radio continuum emission (the classification "Q"). In total, 1773 IRAS sources are matched with at least one H II region, and these IRAS sources serve as the sample of H II regions. For a particular colour combination, these sources are further filtered with bands required to have good qualities (better than an upper limit).

The second step is to build the sample of non-H II regions, by selecting IRAS sources at high Galactic latitudes. This is because high-mass stars are generally far away from the Sun and are tightly constrained to the Galactic plane (Zinnecker et al., 2007). Furthermore, they are not overlapping with any of the giant molecular clouds (GMCs) in the Milky Way identified by Rice et al. (2016). At high Galactic latitudes (except the Orion nebula, which is a high-mass star forming region at a distance of about 400 pc from the Sun), most IRAS point sources are low-mass stars or extragalactic objects. Although some extragalactic objects possess similar colours to H II regions, there are relatively few, on account of the reddening caused by the intergalactic medium (IGM) (Assef et al., 2013; Wright, 1981).

Because the *WISE* H II region catalogue extends up to a Galactic latitude of 8°, we selected those IRAS sources whose absolute values of Galactic latitude are greater than 8° ($|b| > 8°$), serving as the sample of non-H II regions. We further rejected those sources in three prominent regions: Orion, the Large Magellanic Cloud (LMC), and the Small Magellanic Cloud (SMC). According to a CO survey performed by Wilson et al. (2005), the range of Galactic longitude and latitude for Orion are [200°, 220°] and [-22°, -8°], respectively. Based on the position and size of galaxies provided by Cook et al. (2014), the Galactic longitude ranges of the LMC and the SMC are [275°, 286°] and [300°, 305.5°] and their Galactic latitude ranges are [-38.5°, -27.5°] and [-47°, -41.5°], respectively.

We used the criteria of WC89 and HM89 (no constraints on Galactic latitudes) to check the quality of those sources at high Galactic latitudes. In total, 6204 sources are tested by the inequalities of WC89 or HM89, and we find 121 (2%) sources at high Galactic latitude ($|b| > 8°$) agree with at least one of these two criteria. After eliminating these 121 sources, we have remaining 100614 sources at high Galactic latitudes, which is used to build the sample of non-H II regions. Despite the incompleteness of WC89 and HM89, we estimate that less than 2% of those sources are possibly H II regions.

In the third step, we checked all the possible two-colour combinations of IRAS bands, each of which involves at least three bands. For each colourr, we require that the shorter wavelength is the denominator so that H II regions will be above the decision boundary. For an IRAS point source, if the shorter wavelength band of its colour is marked with an upper limit, the true value will only move this source to the upper right direction on the two-colour diagram. Therefore, we only require that the flux quality at longer wavelengths is better than an upper limit. In total, there are 15 possible two-colour combinations. With the help of SVMs, we determined the decision boundary for each colour combination, and as mentioned above, the penalty parameter (C) is assigned a value of 1, and the effect caused by a small change of C is negligible. Generally, within the range $0.5 < C < 1.5$, the shifts of slopes and y-intercepts of the criteria are less than 0.01. Before we performed the fourth step, we calculated some statistical measures for the criteria, including sensitivity, specificity, and the F_1 score. The true positives (TP) are the H II region samples agreeing with the criteria, while the false negatives (FN) are the H II region samples rejected by the criteria. The true negatives (TN) are the non-H II region samples rejected by the criteria, while the false positives (FP) are the non-H II region samples agreeing with the criteria. The definition of sensitivity, precision, and the F_1 score are

$$\begin{aligned} \text{sensitivity} &= \frac{TP}{(TP+FN)}, \\ \text{precision} &= \frac{TP}{(TP+FP)}, \\ F_1\,\text{score} &= \frac{2}{(1/\text{sensitivity}+1/\text{precision})}, \end{aligned} \tag{A.1}$$

where sensitivity is also called the recall or the true positive rate (TPR), precision is also called the positive predictive value (PPV), and the $F_1\,\text{score}$ is the harmonic mean of precision and sensitivity. In the fourth step, we modify the $F_1\,\text{score}$ to include the proportion of candidates matching to radio sources (radio association).

In the fourth step, we applied all criteria to 234261 IRAS point sources, identifying H II region candidates. After checking the quality of fluxes, we filter the IRAS point

sources with the inequality of each criterion (see Table 3.2), yielding the H II region candidates. In order to check the quality of criteria, we matched the H II region candidates to radio continuum emission within a radius of 1′ (following Walsh et al. (1997)), and the proportions (radio association) are listed in Table 3.2.

Because the radio association is also an important indicator of the quality of the criteria, we modified the F_1 score and adopt a new type of score which is

$$\mathrm{score} = \frac{3}{(1/\mathrm{sensitivity} + 1/\mathrm{precision} + 1/\mathrm{radio\,association})}, \tag{A.2}$$

where score is the harmonic mean of sensitivity, precision, and radio association.

In Table 3.2, we list the parameters of all criteria, and from left to right, the columns are the identity, the criterion, the number of selected candidates, the proportion of candidates associated with radio continuum (radio association), sensitivity, precision, the number of IRAS sources tested by the inequality of the criteria, and the score. We sort the criteria according to their scores.

We display details of the top six criteria of Table 3.2 in Figure 3.1, where the criteria provided by HM89 and WC89 are delineated by green lines. Figure 3.2 shows the distribution of IRAS sources in terms of distances to the decision boundary, with negative values signifying sources rejected by criteria.

In the final step, we determine the optimal criterion. Because criterion 1 possesses the highest score, we adopt criterion 1 as the optimal criterion. Its sensitivity indicates that ∼91% of H II regions have been identified and its specificity (see Figure 3.2) shows that less than 1% of high Galactic latitude sources are H II regions. The radio association of criterion 1 is approximately 2% higher than the proportion (32%) in *WISE* H II region catalogue, which gives us a high confidence in the reliability of H II region candidates.

A.2.3 The properties of H II Regions in IRAS PSC

In this section, we examine the distribution of H II candidates selected from IRAS PSC, the total number of H II regions forming high-mass stars in the Milky Way, and the evolution of H II regions on the two-colour diagram,

We display the all-sky distribution of those sources selected by criterion 1 in Figure 3.4. As illustrated in Figure 3.4, the Galactic plane is clearly delineated by those 3061 H II region candidates, and the sources at high Galactic latitudes are sparse. The discrete

sources at high Galactic latitudes are mostly distant extragalactic objects. The LMC and the SMC are evident, as well as the Orion nebula.

In Figure 3.6a, we plot histograms of these sources along the Galactic latitude and Galactic longitude axes, the bin sizes of which are 1° and 2°, respectively. The distribution of H II region candidates along the Galactic latitude is approximately Gaussian, despite two prominent groups at high Galactic latitudes, associated with the Orion nebula and the LMC. In the left panel of Figure 3.6a, two peaks are evident near 80° and 280 °, corresponding to the Local Arm and Carina Arm (Avedisova, 1985; Hughes et al., 1989; Xu et al., 2013), respectively.

After eliminating the sources in LMC and SMC, we have 2962 H II regions left. 67% of those H II candidates are in the first and fourth Galactic quadrants (within 90°of the Galactic Centre), and 46% are within 60°of the Galactic Centre. Compared with the proportion of *WISE* catalog (85% and 77%), those proportions are smaller. This is because the spatial resolution of the IRAS is not sufficiently good to resolve many small-angular-size H II regions in the inner Galaxy. The asymmetric distribution of H II regions in Galactic latitude are also present in IRAS H II candidates. 53% of IRAS H II candidates are at negative latitudes, and this is close to the value of *WISE* catalog (56%).

We estimate the total number of H II regions that are forming where high-mass stars in the Milky Way by combining the *WISE* H II region catalogue with the H II region candidates identified by criterion 1. Of the 2962 H II region candidates, in which the sources in LMC and SMC have been eliminated, 1450 candidates are positionally associated with the *WISE* H II region catalog (within 1′). Consequently, the total number of H II regions forming high-mass stars in the Milky Way is approximately 9911.

The number of ∼9900 is a lower limit of the high-mass star forming regions. On one hand, the sensitivity of criterion 1 suggests ∼91% of H II regions in the IRAS sources have been identified, missing a small mount of H II regions; on the other hand, due to the lower spatial resolution and sensitivity, the IRAS catalogue cannot resolve many H II regions whose angular sizes are small and may have missed some H IIregions whose infarared emissions are beyond the detectability of IRAS.

In this section, we examined the evolution of H II regions on two-colour diagrams. A three-dimensional simulation of the expansion of H II regions performed by Tremblin et al. (2014a), involving the effect of the internal turbulence in surrounding gases, enables us to determine the age of IRAS point sources that are tracing H II regions.

The age calculation for H II regions requires the value of the distance and radio continuum flux. Anderson et al. (2014) provides distances for 1413 H II region candidates, 627 of which are associated with both IRAS and radio continuum sources. In order to assure the purity of H II regions, we require that the fluxes of all four bands are better than upper limits, and we calculated the ages for the remaining 305 H II regions, based on the results of the 3D simulation of Tremblin et al. (2014a).

Although the timescale of embedded phase of high-mass stars is unlikely to be greater than 5 Myr (Churchwell, 2002; Zinnecker et al., 2007), we only rejected those H II regions with ages greater than 10 Myr, considering the uncertainty of calculation, for instance, caused by the inaccurate assumption of initial densities of surrounding gases or large errors in distances. We selected those sources younger than 0.5 Myr as the young sample and those sources older than 6 Myr as the evolved sample. These divisions make the number of young and old samples approximate.

The infrared colours of IRAS point sources tend to be bluer with the evolution of H II regions. We display the result of the colour combinations of criterion 1 (left) and WC89 (right) in Figure 3.6. For both cases, the colours of old samples are generally bluer than that of young samples. As a comparison, we plotted colours of blackbodies with different temperatures. The difference in the colour of blackbodies and H II regions indicates that a single blackbody cannot model the whole infrared spectral energy distribution (SED) of an H II region, and this agrees with the result of Walsh et al. (1999), suggesting a two-component blackbody model. This is mainly caused by the distribution of dust grain size (MacLeod et al., 1991; Natta et al., 1976; Ochsendorf et al., 2015), accompanied by the silicate absorption and the polycyclic aromatic hydrocarbon (PAH) emssion (Walsh et al., 1999).

Nevertheless, the evolutionary trend is consistent with a black body, whose temperature is increasing with time. The evolutionary trend of IRAS sources is consistent with the result of Xu et al. (2003). Xu et al. (2003) investigated 482 6.7 GHz methanol masers, 361 of which are associated with IRAS sources, and they find that on the two-colour diagram, most of those IRAS sources concentrate in a small area, $0.57 \leqslant \log(F_{25}/F_{12}) \leqslant 1.30$ and $1.30 \leqslant \log(F_{60}/F_{12}) \leqslant 2.5$. They suggest that the infrared colours of UC H II regions move toward blue colours, which is consistent with the trending revealed by our results, as illustrated in the right panel of Figure 3.6.

A.2.4 Summary of the H II Region Research

We have produced new criteria for identifying H II regions from the IRAS PSC, and the criteria are determined by the distribution of two samples. One sample (H II regions) is produced by matching the *WISE* H II region catalogue to the IRAS PSC; the other sample (non-H II regions) is constructed by filtering IRAS sources at high Galactic latitudes ($|b| > 8^{\circ}$). We determined the decision boundary of the two samples using SVMs, which are efficient classifiers of supervised machine learning.

We find that the optimal selection criterion is $\log(F_{60}/F_{12}) \geqslant (-0.18 \times \log(F_{100}/F_{25}) + 1.51)$, $Q_{60} > 1$, and $Q_{100} > 1$, identifying 3061 H II region candidates from IRAS sources. Because the known H II regions is more complete, we have improved the criterion of HM89 significantly. A high proportion of IRAS H II region candidates have radio counterparts, providing a high confidence for those IRAS H II region candidates. Combining with the *WISE* H II region catalogue, we find that the lower limit of H II regions forming high-mass stars in the Milky Way is $\sim$9900.

We estimate the age of some H II regions based on a 3D simulation involving internal turbulence of surrounding gases, and find that on two-colour diagrams, younger H II regions have redder IRAS colours and with the evolution, their infrared colours become bluer.

The SVM is an efficient classifier to identify H II regions from infrared surveys. With our methodology and future sensitive observations, we will be able to improve the accuracy and the completeness of H II regions in the Milky Way.

A.3 The Galactic Centre

The Galactic Centre (GC) is one of the most intensively studied regions in the Milky Way, because of its diversity of star formation activities and unique environments. However, although this region has attracted a large amount of investigations, the three-dimensional structure of the molecular clouds in the regions is still unclear.

The Southern Parkes Large-Area Survey in Hydroxyl (SPLASH) provides an opportunity of improving a method of driving the relative position of molecular clouds in the Galactic Centre significantly, which is proposed by Sawada et al. (2004). This method is independent of dynamical models, but suffered from inaccurate OH excitation temperatures and optical depths.

In this section, we conducted a study of the three-dimensional structure of the molecular clouds in the Galactic Centre. We found a novel method of the calculating the column densities, excitation temperatures, and the optical depth of OH ground states, which allows us to solve the four column densities of OH ground states precisely by combing four OH ground-state transitions. We applied this method to the Galactic Centre, and derived the three-dimensional structure of the molecular clouds.

A.3.1 The CMZ

The Central Molecular Zone (CMZ), within about 500 pc of the Galactic Centre (GC), is a unique region of the Milky Way (Morris et al., 1996). Although the CMZ covers a small range of Galactic longitude, from $l = -1^\circ$ to approximately $+1.5^\circ$, it is a large reservoir of molecular clouds, the total mass of which is about $5.3 \times 10^7 M_\odot$ (Pierce-Price et al., 2000). The densities (Jones et al., 2012, 2013; Longmore et al., 2013), temperatures (Ao et al., 2013; Ginsburg et al., 2016; Mills et al., 2013), and turbulence (Oka et al., 2001; Shetty et al., 2012) of molecular clouds in the CMZ are all higher than in the Galactic disk. This region contains a large diversity of observed molecules, and is characterised by abundant star formation activity (Corby et al., 2015; Kruijssen et al., 2014; Lu et al., 2015; Walsh et al., 2011; Yusef-Zadeh et al., 2009), making the CMZ a valuable place to study molecular clouds and star formation processes in the Milky Way.

However, because of the edge-on view from our Solar System, the structure of molecular clouds in the CMZ is still unclear. The Hi-GAL survey (Molinari et al., 2010b), performed with *Herschel* in the far infrared, suggested that the CMZ consists of a twisted 100 pc ring with a mass of $\sim 3 \times 10^7 M_\odot$ (Molinari et al., 2011), tracing stable x_2 orbits, whose major axes are perpendicular to the bar (Binney et al., 1991; Contopoulos et al., 1980). Recently, however, Kruijssen et al. (2015) suggested that the orbits of clouds in the CMZ are open rather than closed, in contrast to the ring structure proposed by Molinari et al. (2011).

Sawada et al. (2004) proposed a method to calculate the relative position of molecular clouds with respect to the GC involving CO emission and OH absorption lines that, unlike previous studies (e.g. Binney et al., 1991; Kruijssen et al., 2015), is independent of dynamical models. They assumed that the diffuse radio continuum emission in the GC is axisymmetric and used the absorption depth of the OH 1667-MHz line to estimate the background emission, enabling them to derive the relative position of molecular clouds in the GC. This work confirmed the existence of a bar-like structure in the GC. Their model

adopted a uniform value for the OH excitation temperature and a uniform ratio of CO brightness temperatures to OH optical depths. Thus the accuracy of the model may have been impacted if significant variations in excitation temperature exist, or if the some of the ^{12}CO ($J = 1 \rightarrow 0$) features emanate from optically thick regions.

The Southern Parkes Large-Area Survey in Hydroxyl (SPLASH; Dawson et al. (2014) provides an opportunity to improve the model of Sawada et al. (2004) with greatly improved sensitivity. SPLASH, performed with the Parkes 64-m telescope, observed all four OH ground-state transitions, consisting of two main lines (1665- and 1667-MHz) and two satellite lines (1612- and 1720-MHz) over the CMZ region. These four transitions enable us to confine the optical depth and excitation temperature, and hence significantly improve the model of Sawada et al. (2004).

In order to test the orbital model proposed by Kruijssen et al. (2015), we refine the method of Sawada et al. (2004), by using spatial information derived from all four OH ground-state transitions from the SPLASH, combined with ^{12}CO ($J = 1 \rightarrow 0$) data observed by the Harvard-Smithsonian Center for Astrophysics (CfA) 1.2m telescope (Dame et al., 2001) and ^{13}CO ($J = 1 \rightarrow 0$) data observed by the Mopra 22-m telescope.

A.3.2 CO and OH observations

In our calculation, we use two CO isotopologue spectral lines: ^{12}CO ($J = 1 \rightarrow 0$) and ^{13}CO ($J = 1 \rightarrow 0$). The ^{12}CO ($J = 1 \rightarrow 0$) data is part of a complete CO survey of the Milky Way, conducted by Dame et al. (2001). This survey was performed with two similar 1.2-m telescopes: one is at the CfA of Harvard University in America and the other is at Cerro Tololo Inter-American Observatory in Chile. For the GC, the observation was performed by the latter telescope whose full width at half-maximum (FWHM) is 8.8′ at the frequency of ^{12}CO ($J = 1 \rightarrow 0$), approximately 115 GHz (Bitran et al., 1997). The spatial sampling interval within 1° of the Galactic plane was 7.5′, with a velocity resolution of 1.3 km s^{-1}, and the corresponding root mean square (rms, σ) of the spectral noise was 0.10 K. The ^{12}CO ($J = 1 \rightarrow 0$) data was smoothed using a Gaussian kernel with a FWHM of 12.8′, to match the effective resolution (15.5′) of the OH spectra.

The ^{13}CO ($J = 1 \rightarrow 0$) data is part of a new high resolution survey of the Southern Galactic Plane in CO (described in Burton et al. (2013)) performed with the 22-m Mopra telescope. The particular data set used here is part of a sub-project on the CMZ (Blackwell, 2017), which covers $-1.5° \leqslant l \leqslant 3.5°$ and $-0.5° \leqslant b \leqslant 1.0°$, in the three principal

isotopologues of CO (^{12}CO, ^{13}CO, and C^{18}O). The data were obtained at 0.6′ and 0.1 km s^{-1} angular and spectral resolution through the technique of on-the-fly mapping.

For this analysis, a preliminary version of the ^{13}CO $(J = 1 \rightarrow 0)$ data was provided at 3.0′ and 2 km s^{-1} angular and spectral resolution. The ^{13}CO $(J = 1 \rightarrow 0)$ data was smoothed using a Gaussian kernel with a FWHM of 15.2′, and was subsequently regridded to a pixel resolution of 7.5′.

The OH data constitutes part of SPLASH. A study of the pilot region of SPLASH is presented by Dawson et al. (2014) along with a detailed description of the observations. SPLASH, which covers the GC, provides sensitive, unbiased, and fully sampled spectra of four ground-state 18-cm transitions of OH at 1612-, 1665-, 1667-, and 1720-MHz. Here, we present a brief review of the observations and detail our additional efforts to obtain good spectral baselines for the data in the GC region.

SPLASH was performed with the Australia Telescope National Facility (ATNF) 64-m Parkes telescope. Similar to the pilot region, the GC was covered by on-the-fly mapping of $2^\circ \times 2^\circ$ tiles, where each tile was observed 10 times. The interval between scan rows was 4.2′, oversampling the Parkes beam, which has a FWHM of ∼12.2′ at 1720 MHz. The data presented in this paper cover a Galactic Longitude range of $-6^\circ \leqslant l \leqslant 6^\circ$, while the range in Galactic latitude is $-2^\circ \leqslant b \leqslant 2^\circ$.

The data cubes of the four OH spectral lines are produced with the `GRIDZILLA`[2] software package. Data were gridded with a Gaussian kernel of FWHM 20′ with a cutoff radius of 10′, and a pixel size of 3′, resulting in an effective resolution of ∼ 15.5′. At the spatial and spectral resolution of 15.5′ and 0.18 km s^{-1}, the final noise level of the spectra is about 0.1 K. Because the pixel resolution (7.5′) of CO spectra is approximately half of the spatial resolution of OH spectra, we regridded the OH data to match the pixel resolution of ^{12}CO $(J = 1 \rightarrow 0)$ with the `MIRIAD` software package (Sault et al., 1995).

A.3.3 The Model

Sawada et al. (2004) proposed a method to calculate the relative position of molecular clouds along the line of sight to the GC by combining information from CO emission and OH absorption, based on four assumptions. First, they assume that the CO emission and OH absorption features at a particular velocity correspond to the same location in space. Secondly, they assume the optical depth of OH is proportional to the brightness

[2] http://www.atnf.csiro.au/computing/software/livedata/

temperature of CO, which traces the amount of molecular clouds. Thirdly, they assign the excitation temperature of OH at 1667 MHz a uniform value. Their fourth assumption is that the diffuse continuum emission in the GC is optically thin and axisymmetric, which can be modelled by three Gaussian components.

The principle of deriving relative positions of molecular clouds is depicted in Fig. 4.5. The depth of the OH absorption line is determined by the excitation temperature and optical depth of OH and the level of continuum emission behind molecular clouds. As illustrated in Fig. 4.5, two molecular clouds, with equal excitation temperatures and optical depths but different distances, display distinctive absorption lines.

In their calculations, Sawada et al. (2004) adopted a uniform value of 4 K for the OH excitation temperature and estimated the optical depth from CO. However, this uniform excitation temperature only represents the part above the CMB and the actual excitation temperature they used is about 6.7 K. Although this value is within a reasonable range (Crutcher, 1977; Li et al., 2003), a uniform value for the excitation temperature may be inaccurate. The ratio of optical depth of the 1667-MHz line to the ^{12}CO $(J = 1 \rightarrow 0)$ brightness temperature they used is 0.15 K^{-1}, which may have introduced errors, considering ^{12}CO $(J = 1 \rightarrow 0)$ may be optically thick in some regions.

In this work, we improve the model of Sawada et al. (2004) by implementing a new method to solve the OH excitation temperatures and optical depths precisely. Additionally, the OH data we used is more sensitive and we used ^{13}CO $(J = 1 \rightarrow 0)$ to identify regions where ^{12}CO $(J = 1 \rightarrow 0)$ is optically thick.

We retained the first and fourth assumptions of Sawada et al. (2004) and modified their second and third assumptions. For the second one, we used the CO intensity to constrain the column densities of OH, instead of the optical depths, and this is more reasonable, because the CO intensity is roughly proportional to the column density, if CO emission is optically thin. For the third one, we abandoned the assumption of a uniform excitation temperature, and alternatively, we assume that the excitation temperatures of the two main lines are equal and no assumptions about excitation temperatures of the satellite lines are made.

We summarise these four assumptions as

1. The CO emission and OH absorption features at a particular velocity correspond to the same location in space.

2. The column density of OH at ground states, $N(\mathrm{OH})$, is proportional to the brightness temperature of $^{12}\mathrm{CO}$ $(J = 1 \rightarrow 0)$, meaning $N(\mathrm{OH}) = f \times T_{\mathrm{CO}}$, where f is a constant.

3. The excitation temperatures of the two main lines are equal.

4. The diffuse continuum emission in the GC is optically thin and axisymmetric, and it can be modelled by three Gaussian components.

A.3.4 Solving OH Column Densities

We propose a new method to calculate the column densities, excitation temperatures, and optical depths of OH precisely, which significantly improves on the model proposed by Sawada et al. (2004). The kernel of the idea is to express the OH excitation temperatures and optical depths in terms of the four column densities of the OH ground state hyperfine levels, which are solvable provided that all four lines have been observed.

In many cases of practical interest the background emission and brightness temperature of an absorption line are observable. However, the situation is more difficult for the complicated GC region, because the fraction of the observed background emission arising from behind the OH cloud is unknown, and this requires extra effort to model. In the following two subsections, we first discuss the simple case in which the background is known, and then introduce the treatment as applied to the GC region.

As shown in the basic equation of radiative transfer (Equation 4.3), if T_{c} is known, the unknown quantities are T_{ex} and τ_{v}. Because we observed four OH ground-state transitions, we are able to build four equations, each with two unknown quantities, In total, we have eight variables. However, because of the insufficiency of equations, we cannot solve the excitation temperature and optical depth of OH directly.

To solve for the eight variables, we first convert the four excitation temperatures and four optical depths to four column densities. We use $N1$, $N2$, $N3$, and $N4$ to denote the four column densities of the four ground states of OH, from top to bottom as shown in the schematic of the four OH ground-state transitions in Fig. 4.1. With the definition of the excitation temperature (Equation 4.5) and the formula of the optical depth (Equation 4.7), we can express the radiative transfer equation with column densities.

Consequently, we can solve four column densities with four transition lines of OH ground states.

In the special case of the GC, we mainly have two difficulties: the two main lines contaminate each other because the velocity dispersion is large, and the level of background continuum behind OH clouds is unknown. The first problem eliminates one equation, while the second one introduces an extra variable. Therefore, we only have three equations left, needing two more equations.

We solve the two problems according to the second and third assumptions listed in §A.3.3. The assumption about the main-line excitation temperature provides an equation (Equation 4.8), solving the first problem. In the second assumption, we assume the column densities of CO and OH are proportional, providing the fifth equation. Please see Equations 4.12 for the explicit form of equations, which can be solved numerically.

A.3.5 The distribution of the molecular clouds in the GC

With Equations 4.12, we derived a 3D structure of the molecular clouds in the GC by displaying the slices along the Galactic latitude. Sawada et al. (2004) only provided the face-on view (relative to the Galactic disk) of $b = 0°$, while we calculated the face-on views of b = -0.375°, -0.25°, -0.125°, 0°, 0.125°, and 0.25°, constituting a 3D structure of the GC.

The radio of OH to CO is determined by maximising the the proportion of pixels within 500 pc of the GC in the face-on view of $b = 0°$ (see Figure 4.9).

We present slices of the 3D structure along $b = -0.375°$, $-0.25°$, $-0.125°$, $0°$, $0.125°$, and $0.25°$, in Figure 4.13, 4.14, 4.15, 4.16, 4.17, and 4.18, respectively. Beyond this Galactic latitude range, the molecular cloud density drops to a sufficiently low value to not merit modelling.

The face-on view of $b = 0°$ displays a bar-like structure, which may be part of the Galactic bar. We fitted the inclination angle of the bar using equally weighted simple linear regression. In the fitting process, we rejected the pixels beyond 300 pc of the GC and those pixels whose integral bright temperatures are greater than 7 K km s^{-1} (5σ), in order to avoid involving unrelated noise. We find that the inclination angle with respect to the line of sight along $l = 0°$ is $67.5 \pm 2.1°$, as shown in Fig. 4.19.

We calculated the total mass of OH in the GC. Because the majority of OH molecules are in the ground states, their total mass detected in these states roughly represents the total mass of OH. We counted the molecular clouds within 500 pc of the GC, and found the total mass of OH in the GC is 2400 $M_\odot$, which is a lower limit. However, if we convert all the

^{12}CO ($J = 1 \rightarrow 0$) brightness temperatures into OH columndensity using the value of f determined in §4.6.2 and a typical excitation temperature of 7 K, we found the total mass of OH in the GC is 5100 $M_{\odot}$, which is an upper limit.

Due to insufficient spatial resolution, we are unable to examine detailed structure of the molecular clouds in the GC. However, the large-scale structure of relatively clear and accurate. As illustrated in Fig. 4.20, the OH excitation temperature derived by our method is consistent with previous results.

Interestingly, the inclination angle, 67.5°, derived from our model is greater than the previous results of the short bar as well as the long bar. The length and inclination angle of the short bar is about 2.5 kpc and approximately 20°, respectively (Babusiaux et al., 2005; Binney et al., 1991; Bissantz et al., 2002; Cabrera-Lavers et al., 2008; Dwek et al., 1995), while the half length and inclination angle of the long bar is about 4.5 kpc and around 45°, respectively (Benjamin et al., 2005; Cabrera-Lavers et al., 2007, 2008; Nataf et al., 2013; Wegg et al., 2015). In terms of the inclination angle, the bar-like structure in the face-on view of $b = 0°$ is more consistent with the long bar. However, further observations, charactering high spatial resolutions, are needed to confirm this large inclination angle.

A.3.6 Summary of our work on the GC

We have presented a 3D model of the GC, which is independent of dynamics, with the help of CO emission and OH absorption lines. We use ^{13}CO ($J = 1 \rightarrow 0$) data from Mopra to identify regions where ^{12}CO ($J = 1 \rightarrow 0$) emission may be optically thick. The OH data, which are part of SPLASH, include four OH ground-state transitions: 1612-, 1665-, 1667- and 1720-MHz lines. The angular resolution of OH and CO data is 15.5′, and with a distance of 8.34 kpc to the GC, the corresponding physical resolution is about 38 pc.

We developed a novel method to calculate the column densities, excitation temperatures, and optical depths of the OH ground-state transitions precisely. For the regions where the level of continuum emission behind molecular clouds is observable, the four column densities may be solved from the equations constructed from observations of four ground-state transitions. For the GC, where the two main lines contaminate each other and the background continuum level is unknown, we assume that the excitation temperature of the two main lines are equal and the column densities of OH are proportional to the brightness temperature of CO, enabling us to derive the level of background continuum

behind molecular clouds.

Based on a well modelled volume emission coefficient of the diffuse continuum emission in the GC, we derived the face-on view for b = -0.375°, -0.25°, -0.125°, 0°, 0.125°, and 0.25°, forming a 3D structure of the molecular clouds. The face-on view of $b = 0°$ displays a bar-like structure with an inclination angel of $67.5 \pm 2.1°$ with respect to the line of sight along $l = 0°$. This angle is generally greater than the value derived by previous works. Due to the low spatial resolution of the data, we are unable to resolve the structure of molecular clouds near Sgr A* where the continuum emission varies rapidly.

We found the amount of OH in the CMZ is at least 2400 $M_{\odot}$ and could be as much as 5100 $M_{\odot}$.

Obviously, our model hinges on the spatial resolution of the data. We already have interferometric OH data in hand, observed with the Karl G. Jansky Very Large Array (JVLA), which possesses a much higher spatial resolution than the Parkes data. Combining the ^{12}CO $(J = 1 \rightarrow 0)$ and ^{13}CO $(J = 1 \rightarrow 0)$ data obtained with Mopra and the OH data of the Galactic ASKAP (the Australian Square Kilometre Array Pathfinder telescope) Survey (GASKAP) (Dickey et al., 2013), we will be able to improve our results significantly, which we intend to do in a future paper. Under the scrutiny of high angular resolution (better than 2 pc at a distance of 8.34 kpc), the blank area in front of Sgr A* will shrink and we will be able to resolve the Brick, the 20 km s^{-1} molecular clouds and the 50 km s^{-1} molecular clouds. Most importantly, the ring structure near Sgr A* will become clear.

A.4 The Ursa Major Clouds

As the birthplace of stars, the molecular clouds are essential to the study of star formation. However, despite of their importance, some of the properties of molecular clouds are still not clear, for instance, the evolution and formation. Along the line of sight in the Galactic plane, there are frequently contaminations, but towards the high Galactic latitudes, is is relatively clean. Additionally, the molecular clouds at high Galactic latitudes are near and is suitable to investigate detailed structures. However, the difficulty is the signal is faint, and much observation time is required.

In order to obtain an unbiased sample of the molecular clouds towards the high Galactic latitudes, we performed a deep CO Survey towards the Ursa Major Clouds with a 13.7-m millimetre telescope in China.

This work is still ongoing, and consequently, we only display some preliminary results about this CO survey.

A.4.1 Observations

The telescope we are using is a 13.7-m millimetre telescope, the beam size of which is about 52 arcsec at 100 GaHz. We records three CO isotopologue lines simultaneously, which are ^{12}CO $(J = 1 \rightarrow 0)$, ^{13}CO $(J = 1 \rightarrow 0)$, and C^{18}O $(J = 1 \rightarrow 0)$, and no C^{18}O $(J = 1 \rightarrow 0)$ signal is detected. Therefore, we only have two CO isotopolgue lines. The observations are conducted with OTF model, tile by tile, and the size of each tile is $(\Delta l,\ \Delta b) = (0.5^\circ,\ 0.5^\circ)$. The total observation time is approximately 1400 hours and the total survey area is about 28 deg^2.

The process of data reduction is similar to that in §A.1.2. Additionally, we used `Montage`[3] to perform the mosaic and projection. The spectral rms of ^{12}CO $(J = 1 \rightarrow 0)$ and ^{13}CO $(J = 1 \rightarrow 0)$ are 0.2 K and 0.1 K, respectively, and the spatial and resolution is 52″ and 0.16 km s^{-1}.

A.4.2 Preliminary Results

We examined the distribution and structure of the molecular clouds revealed by CO. Compared with previous observations, our survey has revealed many details about diffuse molecular clouds. As shown in Figure 5.4, the structure is also complicated, suggesting diffuse clouds may also be dominated by turbulence.

Based on the observation of ^{13}CO $(J = 1 \rightarrow 0)$, we identified molecular cores in the Ursa Major Clouds with `Duchamp`, which is a software package dedicated to search sources in three-dimensional space. Table 5.1 shows the parameters we used, and in total, we found 106 molecular cores. We examined the shape of the mass function of those cores. The definition of mass function is:

$$\frac{dN}{dM} \propto M^{-\alpha}, \tag{A.3}$$

Where α is the index. As shown in Figure 5.8, we found the index in the Ursa Major Clouds is $\alpha = 1.87 \pm 0.08$, which is consistent with previous studies on diffuse molecular clouds (Kramer et al., 1998; Li et al., 2015).

[3] http://montage.ipac.caltech.edu/

A.5 Summary

We present a study of molecular clouds and star formation towards three representative regions in the Milky Way, primarily using spectral lines. Our work are characterised with the combination of multi-wavelength observations, new breakthrough of basic theories, and the employment of new computer technologies.

The main components of molecular clouds are molecular gas and dust, and consequently, their molecular lines and dust continuum are efficient tools of studying molecular clouds and star formation. In the study of the infrared bubbles, we observed five molecular lines, including ^{12}CO ($J = 1 \rightarrow 0$), ^{13}CO ($J = 1 \rightarrow 0$), C^{18}O ($J = 1 \rightarrow 0$), HCN ($J = 1 \rightarrow 0$), and HCO$^+$ ($J = 1 \rightarrow 0$)and utilized some publicly available surveys at 8 μm, 24 μm, 0.87 mm, 1.1 mm, and 20 cm. In the identification of molecular outflows, we use ^{12}CO ($J = 1 \rightarrow 0$) and HCO$^+$ ($J = 1 \rightarrow 0$) to find the line wings and 24 μm emission provide auxiliary identification of the driven sources, which makes the conclusion more affirmative.

In the study of the distribution of the molecular clouds in the GC, we found a novel method of calculating the column density, the excitation temperature, and the optical depth of OH ground-state transitions precisely. With this method, we derived the three-dimensional structure of the molecular clouds and have independently confirmed the existence of the molecular bar in the GC. Without this new method, even if we have had more observations, we still cloud not make significant progress. However, our results are limited by the low spatial resolution, and we will improve our work in the future with more sophisticated observations.

In the research of new criteria of H II regions, based on IRAS sources, we find that the machine learning is a powerful tool to extract certain kinds of sources from catalogues. We have newly identified approximately 900 H II region candidates form the IRAS catalogue. We suggest that machine learning is an efficient classifier, which could be implemented to other kinds of astronomical objects.

The Astronomical Journal, 152:117 (30pp), 2016 November doi:10.3847/0004-6256/152/5/117

MOLECULAR LINES OF 13 GALACTIC INFRARED BUBBLE REGIONS

Qing-zeng Yan[1,2,3], Ye Xu[2], Bo Zhang[1], Deng-rong Lu[2], Xi Chen[1], and Zheng-hong Tang[1]
[1] Shanghai Astronomical Observatory, Chinese Academy of Sciences, Shanghai 200030, China; qzyan@shao.ac.cn
[2] Purple Mountain Observatory, Chinese Academy of Sciences, Nanjing 210008, China; xuye@pmo.ac.cn
[3] International Center for Radio Astronomy Research, Curtin University, GPO Box U1987, Perth WA 6845, Australia
Received 2015 August 9; revised 2016 August 22; accepted 2016 August 22; published 2016 October 14

ABSTRACT

We investigated the physical properties of molecular clouds and star formation (SF) processes around infrared bubbles, which are essentially expanding H II regions. We performed observations of 13 galactic infrared bubble fields containing 18 bubbles. We observed five molecular lines—^{12}CO ($J = 1 \rightarrow 0$), ^{13}CO ($J = 1 \rightarrow 0$), C^{18}O ($J = 1 \rightarrow 0$), HCN ($J = 1 \rightarrow 0$), and HCO$^+$ ($J = 1 \rightarrow 0$)—and several publicly available surveys were used for comparison: Galactic Legacy Infrared Mid-Plane Survey Extraordinaire, Multiband Imaging Photometer for *Spitzer* Galactic Plane Survey, APEX Telescope Large Area Survey of the Galaxy, Bolocam Galactic Plane Survey, Very Large Array (VLA) Galactic Plane Survey, Multi-Array Galactic Plane Imaging Survey, and NRAO VLA Sky Survey. We find that these bubbles are generally connected with molecular clouds, most of which are giant. Several bubble regions display velocity gradients and broad-shifted profiles, which could be due to the expansion of bubbles. The masses of molecular clouds within bubbles range from 100 to 19,000 $M_\odot$, and their dynamic ages are about 0.3–3.7 Myr, which takes into account the internal turbulence pressure of surrounding molecular clouds. Clumps are found in the vicinity of all 18 bubbles, and molecular clouds near four of these bubbles with larger angular sizes show shell-like morphologies, indicating that either collect-and-collapse or radiation-driven implosion processes may have occurred. Due to the contamination of adjacent molecular clouds, only six bubble regions are appropriate to search for outflows, and we find that four have outflow activities. Three bubbles display ultra-compact H II regions at their borders, and one is probably responsible for its outflow. In total, only six bubbles show SF activities in the vicinity, and we suggest that SF processes might have been triggered.

Key words: ISM: bubbles – ISM: clouds – ISM: jets and outflows – ISM: kinematics and dynamics – ISM: molecules – stars: formation

1. INTRODUCTION

The *Spitzer* Galactic Legacy Infrared Mid-Plane Survey Extraordinaire (GLIMPSE; Benjamin et al. 2003; Churchwell et al. 2009) identifies almost 600 bubbles (Churchwell et al. 2006, 2007), extended to 5106 by the Milky Way Project (MWP; Simpson et al. 2012). Bubbles were defined by the 8.0 μm emission (Leger & Puget 1984), which contains 7.7 and 8.6 μm polycyclic aromatic hydrocarbon features, including the continuum (Everett & Churchwell 2010). Churchwell et al. (2006) claimed that 25% of 322 bubbles outside 10° of the Galactic center coincide with known radio H II regions, and Deharveng et al. (2010) extended this proportion to 86% based on a sample of 102 bubbles selected from the catalog provided by Churchwell et al. (2006).

Most bubbles are Photodissociation Regions (PDRs; Hollenbach & Tielens 1997; Kaufman et al. 1999) produced by high-mass stars ionizing atomic or molecular hydrogen. Deharveng et al. (2010) proposed a simple model for H II region evolution involving two main phases: rapid ionization of the neutral medium followed by a long expansion. During the second phase, shock and ionization fronts form, and neutral material and cold dust collect between them. There are some studies supporting a three-dimensional (3D) expansion of H II regions. Beaumont & Williams (2010) found 3D structures throughout a sample of 43 bubbles, using the observations of CO ($J = 3 \rightarrow 2$) and HCO$^+$ ($J = 4 \rightarrow 3$) from the James Clerk Maxwell Telescope (JCMT). With more sensitive *Herschel* data, Anderson et al. (2012b) detected emission from the "near-side" and "far-side" of bubbles along the line of sight, which also suggests 3D structures.

Molecular lines, usually characterized with particular critical densities, excitation temperatures, and kinematics information, are superb tools for studying molecular clouds, including those around infrared bubbles. Observations of molecular lines contain physical, chemical, and dynamic information, which is essential to the study of molecular clouds. CO, a good tracer of molecular clouds due to its low excitation temperature and low critical density (Dame et al. 2001; Heyer & Dame 2015), has been widely used to study infrared bubbles. For example, the Galactic Ring Survey (GRS) ^{13}CO data (Jackson et al. 2006) are used in many bubble papers (Petriella et al. 2010; Hou & Gao 2014; Sidorin et al. 2014; Xu & Ju 2014). Other molecular lines, such as HCN ($J = 1 \rightarrow 0$) and HCO$^+$ ($J = 1 \rightarrow 0$), which are probes of dense clumps and cores (Christopher et al. 2005; Wu et al. 2010), can also been found throughout bubble studies (Beaumont & Williams 2010; Kendrew et al. 2012). Moreover, HCO$^+$ and ^{12}CO ($J = 1 \rightarrow 0$) are good tracers of bipolar outflows, which are ubiquitous phenomena in star-forming regions (Zhang et al. 2001; Rawlings et al. 2004), and ^{12}CO has also been used to identify outflows around infrared bubbles (Beaumont & Williams 2010).

A number of papers argue that star formation (SF) processes can be triggered by expanding H II regions, and two mechanisms for the triggering have been proposed: collect-and-collapse (Elmegreen & Lada 1977) and radiation-driven implosion (RDI; Bertoldi 1989). Elmegreen & Lada (1977) proposed that SF can be triggered by the propagation of ionization and shock fronts through a molecular cloud complex. Hosokawa & Inutsuka (2005) analyzed the dynamical

Table 1
Observation Parameters of Surveys

Survey	Wavelengths	Resolutions	Facilities	References
GLIMPSE	3.6, 4.5, 5.8, 8.0 μm	$\sim 2''$	*Spitzer*	Benjamin et al. (2003), Churchwell et al. (2009)
MIPSGAL	24 μm	$6''$	*Spitzer*	Carey et al. (2009), Gutermuth & Heyer (2015)
ATLASGAL	0.87 mm	$19''.2$	APEX	Schuller et al. (2009)
BGPS	1.1 mm	$33''$	Bolocam	Aguirre et al. (2011), Rosolowsky et al. (2010)
VGPS	20 cm	$60''$	VLA	Stil et al. (2006)
MAGPIS	20 cm	$6''$	VLA	Helfand et al. (2006)
NVSS	20 cm	$45''$	VLA	Condon et al. (1998)

expansion of H II regions and the outer PDRs around a high-mass star by solving the UV and FUV radiation transfer and the thermal and chemical processes, using time dependent hydrodynamics. They found that a molecular gas shell with a mass in the order of $10^4\,M_\odot$ can be shaped in $\sim$1 Myr, and this triggering process is of great importance for SFs of the next generation. Deharveng et al. (2005) identified 17 candidate regions for the collect-and-collapse process, and a large number of young stellar objects (YSOs) were found in the vicinity of bubbles (Watson et al. 2008, 2009, 2010). Kendrew et al. (2012) found a strong positional correlation between high-mass YSOs (HMYSOs) and H II regions with MWP bubbles at separations of <2 bubble radii. Thompson et al. (2012) performed a statistical study of YSOs around 322 *Spitzer* mid-infrared bubbles, and found a significant overdensity of Red *MSX*-Source Survey (RMS) YSOs around the bubbles. These results support that expanding H II regions can provide an effective mechanism to form next generation stars.

However, this scenario is not universal. Anderson et al. (2012b) found that the cold gas lies in a ring instead of a sphere, indicating flattened molecular clouds that could be not greatly compressed by expanding shock fronts. In this case, the formation of new stars could be hindered. Dale et al. (2015) investigated the most commonly used signposts and found that none significantly improved the chances of correctly identifying a given star as triggered. They argued that we should be cautious in interpreting observations of SF near feedback-driven structures in terms of triggering.

If bubbles can truly trigger SF, then the characteristics of SF (i.e., collapse, outflows, or masers), should be found around them. Although these phenomena are not specific for triggered SF, the more SF processes we find around bubbles, the safer we can say they are triggered or accelerated by expanding H II regions.

Identifying YSOs is the most commonly used method to study triggered SF. However, it is difficult to determine the distances, ages, and masses of YSOs. If we could find outflows or specific masers, such as OH, H_2O, or CLASS II CH_3OH (Caswell et al. 1995), which are direct signposts for SF, we could at least confirm whether SF processes are indeed present around bubbles, although some of these processes are probably spontaneous. Cyganowski et al. (2009) conducted a class I and II CH_3OH masers survey of approximately 20 HMYSO outflow candidates, referred to as Extend Green Objects (EGOs), which are candidates of massive outflows; three of them are associated with bubbles. Beaumont & Williams (2010) proposed 12 eye-based outflow candidates; however, stronger evidence is required to confirm them because moments maps are inadequate to confirm outflows due to the complex environments around bubbles.

We studied 13 infrared bubble regions selected from the bubble catalog of Churchwell et al. (2006), including 18 bubbles. We observed five molecular lines per bubble, revealing the dynamic and physical features of the molecular clouds around the bubbles. Among the five lines, $C^{18}O$ ($J = 1 \rightarrow 0$), HCN ($J = 1 \rightarrow 0$), and HCO^+($J = 1 \rightarrow 0$) are not widely present in previous observations. Several publicly available surveys were also used, such as GLIMPSE (Benjamin et al. 2003; Churchwell et al. 2009), the Multiband Imaging Photometer for *Spitzer* (MIPS) Galactic Plane Survey (MIPSGAL; Carey et al. 2009; Gutermuth & Heyer 2015), the APEX Telescope Large Area Survey of the Galaxy (ATLASGAL; Schuller et al. 2009), the Bolocam Galactic Plane Survey (BGPS; Aguirre et al. 2011; Rosolowsky et al. 2010), the Very Large Array (VLA) Galactic Plane Survey (VGPS; Stil et al. 2006), the Multi-Array Galactic Plane Imaging Survey (MAGPIS; Helfand et al. 2006), and the NRAO VLA Sky Survey (NVSS; Condon et al. 1998). Details of these surveys are described in Table 1. Combing these surveys, we performed a multiwavelength analysis of the 18 bubbles, focusing on their physical properties and SF processes around them.

2. OBSERVATIONS AND DATA REDUCTIONS

We selected 13 bubble regions from the catalog provided by Churchwell et al. (2006) by checking the 8 μm band image of GLIMPSE surveys visually, and identified 18 bubbles in total. Three criteria were applied to identify a bubble: (1) Located in the northern sky; (2) With outer major axis larger than 1.5 arcmin; (3) With approximate circular or elliptical shape. For small size bubbles, the dynamic expansion of H II regions and the bipolar motion of outflows are mixed together, which cannot be resolved by the limited resolution (about $52''$) of the Purple Mountain Observatory Delingha (PMODLH) 13.7 m millimeter telescope. We assumed regular shaped bubbles indicating relatively simple environments, which made it possible to do outflow and bubble structure analysis. Unfortunately, only 3 of the 12 outflow candidates identified by Beaumont & Williams (2010) were included in our samples.

In Table 2, we list the parameters of the observed bubbles. From left to right, the columns are the bubble identity, galactic longitude, galactic latitude, inner X diameter, inner Y diameter, outer X diameter, ellipse position angle (from the Y axis), velocity of ionized gas, flux density at 1.4 GHz, and distance. Bubbles in the same region are bracketed together. The morphological parameters are provided by Simpson et al. (2012). The integrated flux density of the H II regions at 1.4 GHz is provided by Condon et al. (1998). Distances of these bubbles are generally provided by Deharveng et al. (2010), and the near distance, which is more statistically realistic (Sobolev et al. 2005), is adopted when the kinematic distance is ambiguous.

Table 2
Parameters of the Observed Bubbles

Name (a)	l (b) (deg)	b (b) (deg)	iXdiam (b) (arcminutes)	iYdiam (b) (arcminutes)	oXdiam (b) (arcminutes)	PA (b) (deg)	V_{ion} (h) (km s^{-1})	$S_{1.4\,GHz}$ (j) (mJy)	Distance (c) (kpc)
N4	11.895	+0.751	3.5	3.3	5.8	7	25.1	2109.9	3.2
N14	13.992	−0.129	2.7	2.6	4.3	38	36	1462.6	3.7
N37	25.291	+0.294	2.7	3.4	4.0	13	39.6	222.4	12.6
N44	26.822	+0.383	1.8	1.9	2.8	48	82.0	58.4	5.0/10.1
N49	28.828	−0.228	2.3	2.3	3.6	30	90.6	642.7	5.5
MWP1G032057+000783(b)	32.057	+0.078	1.2	1.1	1.9	8	96.3	100.0	8.4
N55	32.099	+0.092	1.0	1.1	1.5	59	93.0	43.4	8.4
MWP1G032158+001306(b)	32.158	+0.131	1.1	1.2	1.8	16	95.0	653.3	8.4
N74	38.907	−0.439	2.4	2.1	3.9	49	42.1	7.3	2.8/10.4
N75	38.928	−0.386	1.2	1.3	2.0	25	42.1	6.2	2.8/10.4
N82	42.104	−0.623	2.7	2.6	4.7	10	66.0	786.4	4.3 (d)
N89	43.734	+0.117	1.8	2.0	2.8	15	73.1	14.1	6.1
N90	43.775	+0.061	2.5	2.5	3.9	9	70.5	168.3	6.1
N95	45.387	−0.715	2.8	2.8	4.0	27	52.5	315.6	8.0
N105	50.078	+0.570	1.3	1.3	2.4	8	−1.1 (g)	101.2	11.2 (i)
N123	57.544	−0.282	2.1	2.0	3.3	37	2.0 (e)	787.6	8.6 (e)
N132	63.121	+0.386	...	...	0.3	...	16.4	9.6	2.1 (f)
N133	63.163	+0.441	3.9	3.7	6.8	22	16.4	2900.4	2.1 (f)

Note. (1) The columns are, from left to right, the bubble identity, galactic longitude, galactic latitude, inner X diameter, inner Y diameter, outer X diameter, ellipse position angle (from the Y axis), velocity of H II region, flux at 1.4 GHz, and distance. Bubbles in the same region are marked with brackets. (2) For the distance, we adopted 5.0 kpc for N44 and 2.8 kpc for N74 and N75.
References. (a) Churchwell et al. (2006), (b) Simpson et al. (2012), (c) Deharveng et al. (2010), (d) Stead & Hoare (2010), (e) Watson et al. (2003), (f) Watson et al. (2010), (g) Anderson et al. (2011), (h) Anderson et al. (2014), (i) Anderson et al. (2012a), and (j) Condon et al. (1998).

Table 3
Observational Parameters of the Molecular Lines

Molecular line ($J = (1 \rightarrow 0)$)	Rest frequency (GHz)	Critical density[a] (10^3 cm^{-3})	HPBW ($''$)	T_{sys} (K)	η_{mb}	δv (km s^{-1})	rms noise (k)
^{12}CO	115.271204	0.0067–0.64[b]	49	220–300	45.9%	0.16	0.5
^{13}CO	110.201353	0.38–1.9[b]	51	140–190	51.1%	0.17	0.2
C^{18}O	109.782183	1.6–1.9[b]	50	140–190	54.6%	0.17	0.2
HCN	88.6318473	68[c]	56	140–190	55.0%	0.18	0.07
HCO$^+$	89.1885260	470[c]	58	140–190	55.7%	0.18	0.07

Notes.
[a] For the kinematic temperature of 10 K.
[b] Yoshida et al. (2010).
[c] Shirley (2015).

Observations were performed with the PMODLH 13.7 m millimeter telescope at Qinghai station, latitude 37°22′.4, from 2013 May 30 to December 27, employing a superconducting array receiver with 3 × 3 beam array running in sideband separation mode (Shan et al. 2012). Spectral analysis was performed using the fast Fourier transform spectrometer with velocity resolution 0.16 km s^{-1}. Details about the telescope are described in the PMODLH status report.[4]

Five molecular lines were observed: ^{12}CO ($J = 1 \rightarrow 0$), ^{13}CO ($J = 1 \rightarrow 0$), C^{18}O ($J = 1 \rightarrow 0$), HCN ($J = 1 \rightarrow 0$), and HCO$^+$ ($J = 1 \rightarrow 0$). Observations of these three CO lines were performed simultaneously, and separated from observations of HCO$^+$ and HCN. The half-power beamwidth (HPBW) of the telescope is approximately 52″ at 110.2 GHz, with pointing and tracking uncertainty approximately 5″ and 1.″4, respectively. The beam efficiency is approximately 46% for ^{12}CO, 51% for ^{13}CO, and 55% for C^{18}O, HCN, and HCO$^+$. The system temperature was approximately 280 K for ^{12}CO, 185 K for ^{13}CO and C^{18}O, and 140 K for HCN and HCO$^+$. The on-the-fly scanning model was used for the observations, with a scanning rate of 50″ s^{-1}, and spectra were recorded every 0.3 s. For each bubble, the total observation time for CO was approximately 2 hr, and 5 hr for HCN and HCO$^+$. Further observations were taken for bubble regions with weak emissions.

The typical observed size for bubbles was approximately 10′ × 10′, which is large enough to include the molecular clouds surrounding them. Data reduction was achieved with the Grenoble Image and Line Data Analysis Software package. After replacing bad channels with adjacent channels in the spectra, the data was regridded to 30″ × 30″ pixels and mosaicked to a FITS cube file after calibrating. The root mean square (rms) noise is approximately 0.45 K for ^{12}CO at 0.16 km s^{-1} resolution, 0.20 K for ^{13}CO and C^{18}O at 0.17 km s^{-1} resolution, and 0.07 K for HCN and HCO$^+$ at a resolution of 0.18 km s^{-1}.

In Table 3, from left to right, the columns are molecular line, rest frequency, critical density, half-power beamwidth

[4] http://www.radioast.nsdc.cn/zhuangtaibaogao.php

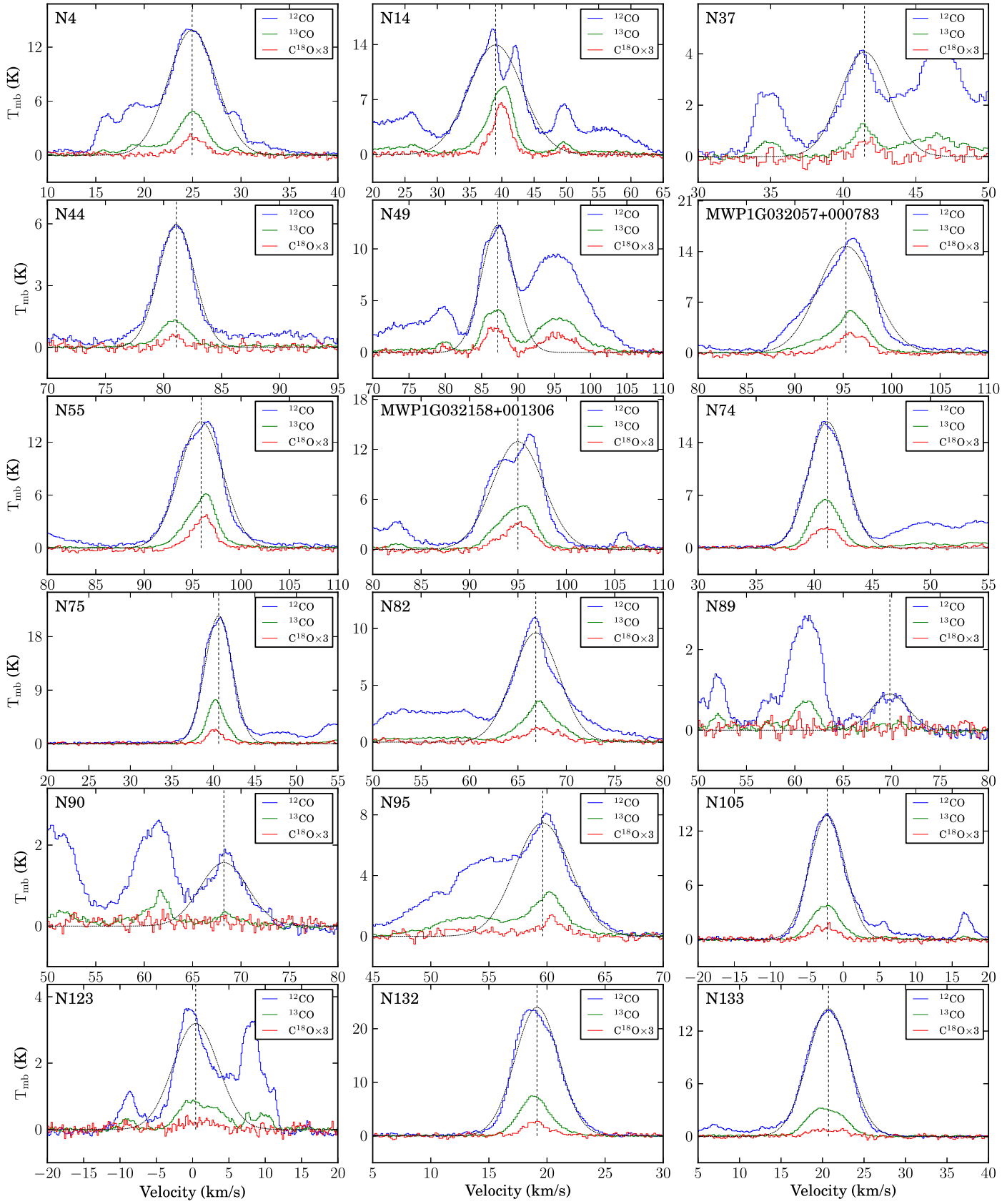

Figure 1. Average spectra for all observed bubbles. The $C^{18}O$ lines are amplified by a factor of 3 for clarity. The black dotted lines delineate the fitted Gaussian curves of ^{12}CO, and the dashed vertical lines mark the center velocities of these Gaussian curves.

(HPBW), system temperature, main beam efficiency, velocity resolution, and the rms of noise. These critical densities are calculated assuming a kinematic temperature of 10 K. The critical densities of three CO lines are given by Yoshida et al. (2010), while the values for HCN and HCO^+ are calculated by Shirley (2015).

3. RESULTS

Except N89 and N90 where no $C^{18}O$ and only weak HCO^+ emission was detected, all the molecular lines were detected for the other bubble regions. Two bubbles, N44 and N123, show a relatively low signal-to-noise ratio (SNR). For all bubbles, the SNR of $C^{18}O$ is generally lower than the other four lines, because of its equal integration time with ^{12}CO and ^{13}CO, but it has comparable low antenna temperature with HCN and HCO^+.

The physical properties for molecular clouds and clumps associated with these bubbles were calculated using three CO isotopic lines. The velocities were determined according to ionized gas velocities (Lockman 1989; Anderson et al. 2014) and CO velocities (Beaumont & Williams 2010), and were confirmed by the spatial coherence between the ^{13}CO integrated intensity and bubbles. We also searched for outflows around bubbles using the profiles of ^{12}CO and HCO^+. The details of these results are presented in this section.

3.1. Physical Properties of Molecular Clouds Around Bubbles

To demonstrate dynamic characteristics of bubbles, we averaged the ^{12}CO and ^{13}CO spectra over the bubble areas, which are squares with the side length equal to the outer major axis provided by Simpson et al. (2012). The spectral profiles are shown in Figure 1. The fitted Gaussian curves of ^{12}CO are plotted in Figure 1. Some average profiles display significant deviation from Gaussian curves. Generally, this could be due to different components with adjacent velocities along the line of sight, which show multi-peaks in the profile. Because ^{13}CO lines are more Gaussian than the ^{12}CO lines, another alternative is that the outer region of clouds is perturbed, which is mainly traced by ^{12}CO.

We estimated the physical properties of each bubble, with the assumption of local thermodynamic equilibrium (LTE). ^{12}CO ($J = 1 \rightarrow 0$) is assumed to be optically thick, whereas ^{13}CO ($J = 1 \rightarrow 0$) is generally optical thin, which means we could estimate the excitation temperature (T_{ex}) and optical depth (τ), respectively (Nagahama et al. 1998; Li et al. 2013)

$$T_{\rm ex} = 5.53\left\{\ln\left[1 + \frac{5.53}{T_R^*(^{12}\mathrm{CO}) + 0.819}\right]\right\}^{-1}, \quad (1)$$

and

$$\tau(\mathrm{C}^{13}\mathrm{O}) = -\ln\left(1 - \frac{T_R^*(^{13}\mathrm{CO})}{\frac{5.29}{\exp(5.29\,/\,T_{\rm ex} - 1)} - 0.89}\right), \quad (2)$$

where $T_R^*(^{12}CO)$ and $T_R^*(^{13}CO)$ are the main beam temperatures of ^{12}CO and ^{13}CO, respectively. The optical depths are generally below 0.5, which indicates that the optical thin assumption is mostly valid.

We determined the molecular cloud angular sizes, A, associated with bubbles from the ellipse centers and outer axes, as given in Simpson et al. (2012). The estimated diameters of the molecular clouds were obtained after deconvolving the telescope beam,

$$l = D\sqrt{4A/\pi - \theta_{\rm MB}^2}, \quad (3)$$

where D is the distance to these bubbles, and $\theta_{\rm MB}$ is the beam size of the telescope.

The second step to deriving the molecular cloud masses was to calculate the averaged H_2 column density, $N(H_2)$, using averaged ^{12}CO and ^{13}CO spectra over the bubble area (Nagahama et al. 1998),

$$N(\mathrm{H_2}) = 1.49 \times 10^{20}\left[1 - \exp\left(\frac{-5.29}{T_{\rm ex}}\right)\right]^{-1} \times \left[\frac{\int T_R^*(^{13}\mathrm{CO})dV}{1\ \mathrm{K\ kms^{-1}}}\right]\mathrm{cm^{-2}}, \quad (4)$$

where $\int T_R^*(^{13}CO)dV$ is the area of the fitted ^{13}CO Gaussian curve. The abundance ratio, $N(H_2)/N(^{13}CO)$, was set to 7×10^5, following Frerking et al. (1982).

Finally, we convert $N(H_2)$ to cloud masses,

$$M = \mu m_{\rm H_2} N(\mathrm{H_2})\pi l^2/4, \quad (5)$$

where m is the mass of the hydrogen molecule, and μ is the ratio of gas to hydrogen by mass, approximately 1.36 (Hildebrand 1983).

Following Tremblin et al. (2014), we estimated the age for each bubble using parameters listed in Table 2. Tremblin et al. (2014) provided a new method to determine the age and size of H II regions using 3D simulations. They included the internal turbulence of molecular clouds surrounding the bubbles, which we believe is more accurate.

Details of the physical parameters of the bubbles are shown in Table 4, where we list the parameters of the fitted Gaussian curve, center velocity, peak temperature, and full width at half maximum (FWHM) of ^{12}CO and ^{13}CO, respectively. We also list the average H_2 column densities, total area of the counted molecular clouds, and the corresponding mass under the assumption of LTE. It should be emphasized that these masses only count the molecular clouds within bubble squares mentioned above, instead of the entire molecular clouds shown in the maps.

From Table 4, we can see that the masses of clouds within the bubble squares are in the range of 100–19,000 solar mass, and their ages are in the range of 0.3–3.7 Myr.

3.2. Molecular Clumps

Following Bergin & Tafalla (2007) and Heyer & Dame (2015), we refer to clumps and cores as substructures of molecular clouds, and their typical sizes are about 0.3–3 and 0.03–0.2 pc, respectively. The PMODLH telescope can only resolve about 0.5 pc for the nearest bubble with a distance of 2.1 kpc, and consequently, the dense parts of the molecular clouds identified by the telescope are generally clumps.

Although HCO^+ and HCN lines possess higher critical densities, they are readily optically thick. $C^{18}O$, however, is always tracing regions with high column densities. Therefore, we used $C^{18}O$ to identify clumps, which were subsequently confirmed by ^{13}CO lines whose SNR were relatively high.

Table 4
Physical Parameters of the Molecular Clouds

Name	$^{12}CO_v$ (km s^{-1})	$^{12}CO_{peak}$ (K)	$^{12}CO_{\Delta V}$ (km s^{-1})	$^{13}CO_v$ (km s^{-1})	$^{13}CO_{peak}$ (K)	$^{13}CO_{\Delta V}$ (km s^{-1})	N_{H_2} (10^{21} cm^{-2})	Area[a] (pc^2)	M_{LTE} (10^3 $M_\odot$)	Age[b] (Myr)
N4	24.9	13.9	5.8	25.0	4.6	3.8	10.1	35	7.7	0.8
N14	39.0	14.0	9.8	39.9	8.4	4.7	22.6	23	11.2	0.6
N37	41.5	4.1	3.9	41.6	1.2	2.3	0.8	406	7.3	3.7
N44	81.1	6.0	3.6	81.0	1.3	2.9	1.3	26	0.8	1.7
N49	87.2	12.3	5.3	87.1	4.3	4.0	8.9	46	8.8	1.2
MWP1G032057+000783	95.3	14.7	6.9	95.7	5.2	4.9	15.0	37	12.1	1.2
N55	95.9	14.3	5.3	96.1	5.7	3.6	12.0	30	7.7	1.7
MWP1G032158+001306	95.0	12.9	6.2	95.0	5.2	4.5	12.7	37	10.3	0.6
N74	41.1	16.8	3.9	41.0	6.5	2.8	11.9	13	3.5	0.8
N75	40.6	21.5	3.9	40.4	7.1	2.7	14.8	5	1.6	0.3
N82	66.8	9.6	5.7	67.3	3.2	4.5	6.4	43	6.0	0.9
N89	69.8	0.9	4.4	70.3	0.2	3.4	0.1	39	0.1	1.8
N90	68.2	1.6	5.8	68.4	0.2	4.6	0.2	64	0.3	2.2
N95	59.6	7.5	5.6	60.0	2.7	4.0	4.1	110	9.8	2.9
N105	−2.2	13.8	5.7	−2.4	3.8	4.6	9.9	96	24.4	1.6
N123	0.4	3.2	7.3	1.0	0.8	6.7	1.5	107	3.4	1.4
N132	19.1	24.0	4.4	19.0	7.3	3.2	19.6	1	0.2	0.3
N133	20.7	14.6	5.9	20.5	3.3	5.1	9.9	30	6.4	0.4

Notes.
[a] The areas are determined using the parameters of bubbles given by Simpson et al. (2012).
[b] The method of estimating ages follows Tremblin et al. (2014).

In total, 23 molecular clumps are found around 18 bubbles, and each bubble contains at least one molecular clump at its border. Because the ^{13}CO lines tend to be optically thick at the peak of clumps, we estimated the mass of molecular clumps using ^{12}CO and C^{18}O lines, with the assumption that they are optically thick and thin, respectively. N89 and N90 show low SNR for C^{18}O, and consequently we used ^{13}CO instead for these two bubbles.

The equations (Scoville et al. 1986; Liu et al. 2014) we used to estimate C^{18}O column density are

$$\tau(\mathrm{C^{18}O}) = -\ln\left(1 - \frac{T_R^*(\mathrm{C^{18}O})}{\frac{5.27}{\exp(5.27/T_{ex})} - 0.89}\right), \quad (6)$$

and

$$\frac{N(\mathrm{C^{18}O})}{\mathrm{cm^{-2}}} = 4.77 \times 10^{13} \frac{T_{ex} + 0.88}{\exp(-5.27/T_{ex})} \times \frac{\tau(\mathrm{C^{18}O})}{1 - \exp(-\tau(\mathrm{C^{18}O}))} \frac{\int T_{mb} dv}{\mathrm{K\ km\ s^{-1}}}, \quad (7)$$

where $\int T_{mb} dv$ is the area under the fitted C^{18}O Gaussian line, and T_{ex} is estimated using Equation (1). The fractional abundance of C^{18}O/H$_2$ is approximately 1.7×10^{-7} (Frerking et al. 1982).

The angular extent of each clump was determined by the contour of the half integrated intensity peak, $A_{1/2}$, and the diameters of the molecular clumps estimated using

$$l_{clump} = D\sqrt{4A_{1/2}/\pi - \theta_{MB}^2}, \quad (8)$$

where D is the distance to clumps, and θ_{MB} is the beam size of the telescope. The clump mass is then given by Equation (5).

The virial masses of clumps are calculated by

$$\frac{M}{(M_\odot)} = k_2 \frac{l_{clump}/2}{(\mathrm{pc})} \left(\frac{\Delta V}{(\mathrm{km\ s^{-1}})}\right)^2 \quad (9)$$

where k_2 is 210 for $\rho(r) =$ constant, and ΔV is the FWHM in unit of km s^{-1} (MacLaren et al. 1988). We assume that molecular cores spread throughout the molecular clumps homogeneously, and consequently, we adopt $\rho(r) =$ constant rather than $\rho(r) = 1/r$, which might be more accurate for single cores. For comparsion, following Rosolowsky et al. (2010), we calculated the dust mass of the corresponding BGPS sources of these clumps, which is displayed in Table 5. The equation we used to estimate the dust mass is

$$M = \frac{d^2 S}{B_\nu(T)_\nu} = 13.1\ M_\odot \left(\frac{d}{1\ \mathrm{kpc}}\right)^2 \left(\frac{S_\nu}{1\ \mathrm{Jy}}\right) \times \left[\frac{\exp(13.0\ K/T_{ex}) - 1}{\exp(13.0/20) - 1}\right]$$

where T_{ex} is estimated using Equation (1), d is the distance, and S_ν is the integrated flux density in the catalog of Rosolowsky et al. (2010).

In Table 5, we summarize the physical properties of molecular clumps. From left to right, the columns are clump name, peak position of integrated intensity, integrated velocity range, center of fitted Gaussian curve, sigma of fitted Gaussian curve, peak value of fitted Gaussian curve, optical depth, column density, clump size, mass with LTE assumption, viral mass of the clump, dust mass of the clump, the line used, and outflow flag. If a clump is associated with an outflow candidate, it is marked by Y. In channel maps, the positions of all these clumps are marked with green crosses.

Table 5
Physical Parameters of the Molecular Clumps

Clumps	Peak position (l, b)	V_{range}[a] (km s^{-1})	V_{center} (km s^{-1})	ΔV (km s^{-1})	Tex (k)	τ	Column density (10^{15} cm^{-2})	Area (pc^2)	M_{LTE} (10^3 $M_\odot$)	M_{vir} (10^3 $M_\odot$)	M_{dust}[b] (10^3 $M_\odot$)	Lines	Outflow[c]
N4A	(11.836, 0.742)	20.1–29.3	24.7	2.7	25.0	0.08	7.4	4.2	4.1	1.8	...	$C^{18}O$	...
N4B	(11.903, 0.717)	21.1–28.7	24.9	2.2	29.5	0.09	9.6	2.7	3.5	1.0	...	$C^{18}O$	...
N14A	(14.009, −0.179)	35.4–45.7	40.5	3.0	24.5	0.20	20.7	5.3	14.7	2.5	0.22	$C^{18}O$	Y
N37A	(25.320, 0.276)	39.1–44.9	42.0	1.7	25.1	0.06	3.6	26.3	12.7	1.8	1.2	$C^{18}O$	...
N44A	(26.844, 0.371)	77.7–83.7	80.7	1.7	16.6	0.08	2.4	2.5	0.8	0.6	0.15	$C^{18}O$	...
N49A	(28.834, −0.253)	82.5–91.5	87.0	2.6	21.4	0.19	13.1	7.6	13.3	2.3	1.8	$C^{18}O$	...
N49B	(28.842, −0.212)	82.2–89.9	86.0	2.3	22.9	0.11	7.3	5.0	4.9	1.4	0.67	$C^{18}O$	...
MWP1G032057+000783A	(32.016, 0.063)	89.5–105.6	97.5	4.7	21.7	0.12	15.6	26.6	55.4	13.7	4.6	$C^{18}O$	...
MWP1G032158+001306A	(32.149, 0.138)	88.4–102.4	95.4	4.1	19.5	0.13	11.4	11.7	17.7	6.9	...	$C^{18}O$	...
N55A	(32.116, 0.088)	92.0–101.0	96.5	2.6	24.3	0.13	11.1	14.7	21.8	3.2	1.9	$C^{18}O$	Y
N75A	(38.925, −0.353)	34.4–43.6	39.0	2.7	32.3	0.06	9.0	2.5	2.9	1.4	0.36	$C^{18}O$	...
N74A	(38.950, −0.462)	37.8–45.9	41.9	2.4	23.7	0.15	11.4	3.3	5.0	1.2	0.23	$C^{18}O$	...
N74B	(38.925, −0.420)	37.0–44.4	40.7	2.2	25.5	0.09	6.9	3.1	2.9	1.0	0.09	$C^{18}O$	...
N82A	(42.120, −0.595)	63.2–72.9	68.0	2.8	21.1	0.09	6.6	5.8	5.1	2.3	...	$C^{18}O$	...
N90A	(43.798, 0.051)	64.6–72.2	68.4	2.3	12.9	0.31	5.1	6.2	0.5	1.5	...	^{13}CO	...
N89A	(43.723, 0.143)	68.2–73.3	70.7	1.5	10.9	0.32	2.4	7.7	0.3	0.7	...	^{13}CO	...
N95A	(45.389, −0.747)	55.2–65.5	60.4	3.0	18.3	0.07	4.2	17.4	9.8	4.5	...	$C^{18}O$	...
N105A	(50.077, 0.561)	−8.9–1.6	−3.6	3.1	21.9	0.06	4.9	24.2	16.0	5.7	...	$C^{18}O$	...
N105B	(50.077, 0.594)	−8.4–4.8	−1.8	3.9	18.6	0.04	3.2	46.4	19.8	12.1	...	$C^{18}O$	Y
N123A	(57.571, −0.288)	−7.7–6.4	−0.6	4.1	14.4	0.04	2.0	19.8	5.3	9.0	1.1	$C^{18}O$	...
N133A	(63.115, 0.406)	15.8–22.9	19.4	2.1	24.7	0.09	6.9	1.6	1.4	0.7	0.06	$C^{18}O$	...
N133B	(63.140, 0.439)	17.1–28.0	22.5	3.2	35.3	0.03	7.1	2.1	2.0	1.8	0.04	$C^{18}O$	Y
N133C	(63.248, 0.431)	13.8–27.3	20.5	4.0	14.7	0.07	3.6	1.0	0.5	1.9	...	$C^{18}O$	...

Notes.
[a] The velocity ranges are the spectral line ranges that are used to fit Gaussian curve and integrate intensities, which are used to determine the areas and masses of clumps.
[b] The dust mass was calculated following Rosolowsky et al. (2010).
[c] If a clump is associated with an outflow candidate, it is marked by Y.

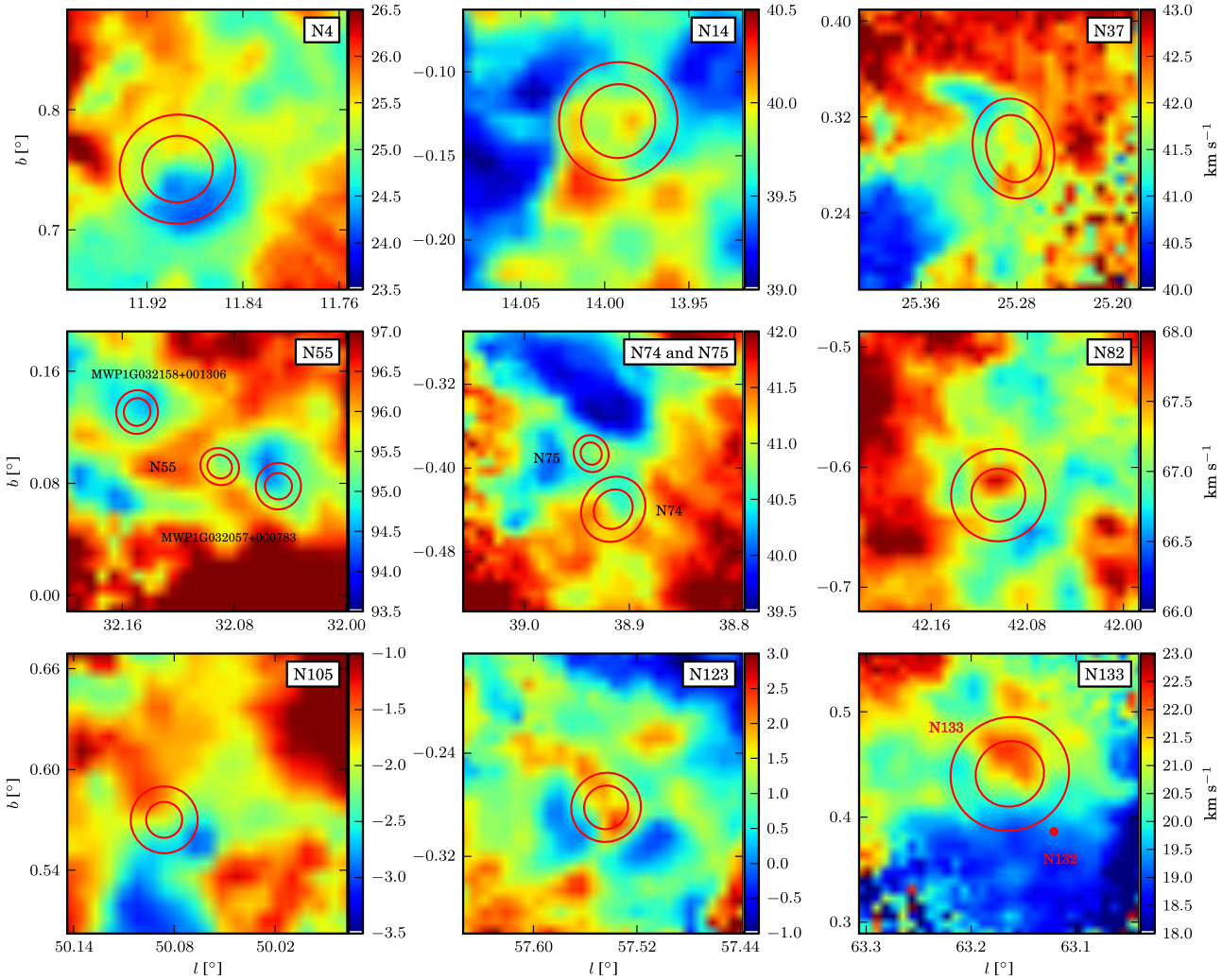

Figure 2. Intensity weighted velocity distribution of ^{12}CO ($J = 1 \rightarrow 0$) for nine bubble regions.

3.3. Expanding H II Regions

To check the velocity field near-infrared bubbles, we calculated the moment 1 (the velocity weighted by intensity) of ^{12}CO ($J = 1 \rightarrow 0$) for all bubbles. ^{12}CO ($J = 1 \rightarrow 0$) possesses the highest SNR, and is more sensitive to the motion of molecular clouds. Nine bubble fields show relatively evident velocity gradients near their borders, as shown in Figure 2. Interestingly, the velocity fields around three bubbles, N14, N74 and N133, display arc-like structures, which are probably tracing the expanding shell of H II regions.

These arc-like structures are similar to bubble N6 studied by Yuan et al. (2014), although their results show larger velocity dispersions. The magnitudes of velocity dispersions are comparable with those of N22 (Ji et al. 2012). These arc-like structures are probably produced by the interaction between bubbles and their surrounding molecular clouds. This speculation is supported by the CO profiles shown in Figure 1. Some CO profiles display significant deviation from Gaussian curves, indicating that the molecular clouds may be interacting with bubbles.

3.4. Individuals

Most of the three-color images of bubbles below are composed of 20 cm continuum MAGPIS data shown in red, 1.1 mm continuum BGPS data shown in green, and 8 μm GLIMPSE data shown in blue. For bubbles N37, N74, and N75, where 20 cm continuum MAGPIS emissions are faint, we used VGPS data instead due to their high sensitivity to extended structures. For regions where BGPS data are unavailable, we adopted 0.87 mm from ATLASGAL data as an alternative. The positions of identified clumps are marked in all integrated intensity maps of five lines by purple crosses and in all channel maps of ^{13}CO ($J = 1 \rightarrow 0$) by green crosses.

3.4.1. N4

Bubble N4 shows a superb ring shape at 8 μm with a 20 cm continuum disk enclosed in it. The radio recombination line (RRL) indicates that the velocity of the local standard of rest is 25.1 km s^{-1} (Lockman 1989; Anderson et al. 2014), which is in good agreement with the CO velocity, 24.9 km s^{-1} (Deharveng et al. 2010; Li et al. 2013). We adopted the near kinematic distance, 3.15 kpc, following Deharveng et al. (2010).

Li et al. (2013) studied three CO isotropic lines using the 13.7 m millimeter telescope at Qinghai Station. They showed that CO emissions were well correlated with an 8 μm structure, which is more likely an inclined ring rather than an expanding spherical shell. They also identified a 15 $M_{\odot}$ star with an age of ~1 Myr, which is probably the energy source of bubble N4. In

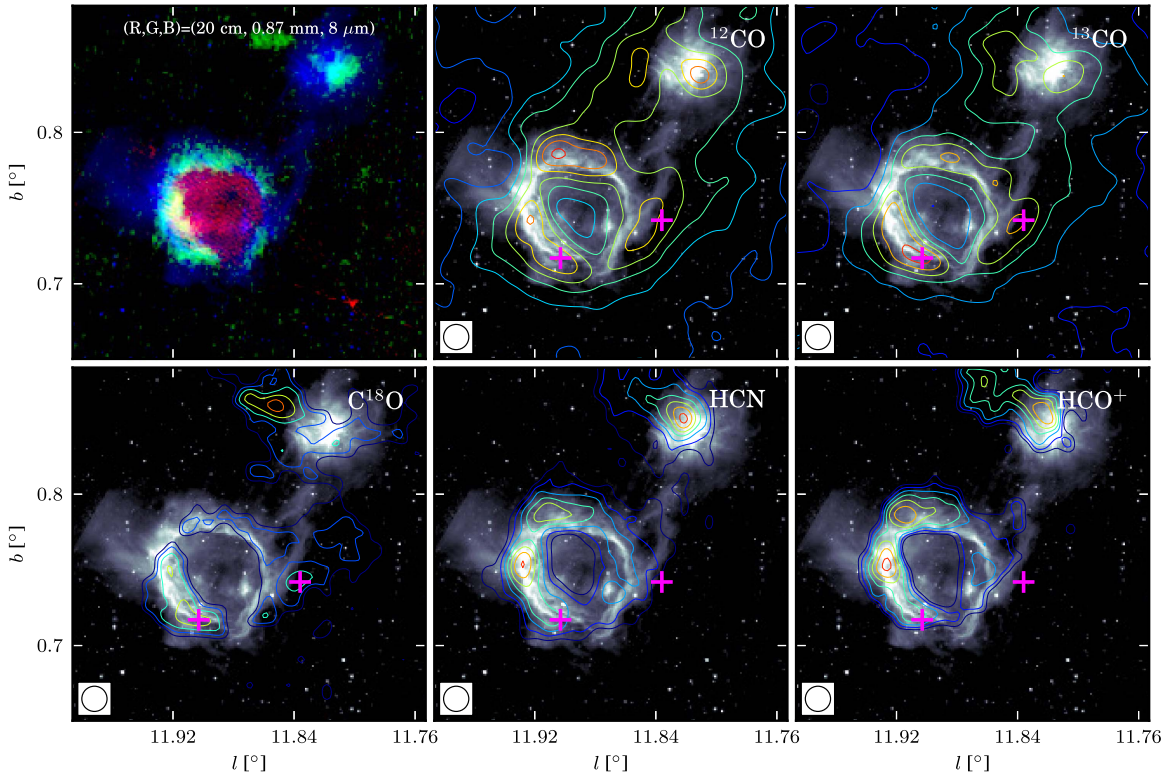

Figure 3. Images of N4. The upper left panel is a three-color image with 20 cm in red, 0.87 mm in green, and 8 μm in blue. The other five panels are contours of five spectral line integrated intensity maps superimposed on the 8 μm image with positions of clumps marked by purple crosses. The contour maps integrate from 21.0 to 29.0 km s^{-1}. The rms (σ) of the five line maps, ^{12}CO, ^{13}CO, C^{18}O, HCN, and HCO$^+$, are 0.54, 0.26, 0.26, 0.08, and 0.09 K km s^{-1}, respectively, and these contours all begin at 8σ, with 29, 21, 4, 5, and 3σ spacing, respectively.

addition, they claimed that they found a possible infall signature, which indicates a triggered SF process may exist at the border of bubble N4.

Our CO observations show similar results to Li et al. (2013). The integrated intensity contour maps of five molecular lines are shown in Figure 3 and the C^{18}O line reveals two molecular clumps, N4A and N4B (shown in Figure 4), at the border of N4. The molecular cloud mass over the region of N4 is approximately $7.7 \times 10^3\,M_\odot$, which is comparable to $7 \times 10^3\,M_\odot$ from Li et al. (2013) using ^{13}CO. The morphology shown by HCN and HCO$^+$ lines is in accordance with 8 μm, which indicates that collect-and-collapse processes may be occurring in this region. However, we did not find any blue asymmetry at the position of the infall candidate identified by Li et al. (2013). Furthermore, both the blue and red ends of the line profiles of CO and HCO$^+$ are contaminated by components with similar velocities, which prevents us from identifying outflows.

3.4.2. N14

This is a large open bubble with strong 8 μm emissions and a diffuse 20 cm continuum enclosed in it. To the south of N14, there is an infrared dark cloud whose position coincides with the 1.1 mm continuum. The RRLs indicate that the velocity of N14 is approximately 36.0 km s^{-1} (Lockman 1989; Anderson et al. 2014), which agrees well with the CO velocity of 40.3 km s^{-1} (Beaumont & Williams 2010). We prefer the near distance of 3.7 kpc due to the strong infrared emission and Hα emission, which is also suggested by Deharveng et al. (2010).

Sherman (2012) observed seven spectral lines and 3 mm continuum in this field. Among their observations, the N_2H^+ emission, which is not exposed to the H II region, shows that N14 is expanding into a very inhomogeneous cloud. They identified 10 compact dust sources in the vicinity of N14 based on 3 mm continuum data and largely correlated with bubble N14; however, no velocity gradient was detected, which is inconsistent with the prediction of the expanding shock. They proposed that triggered SF have occurred, although their findings do not conform to a classic collect-and-collapse model.

Dewangan & Ojha (2013) performed a multiwavelength study of N14. They argued that they found observational signatures of the collected molecular and cold dust material around this bubble. However, they prefer a process of compression of the pre-existing dense clumps by the shock wave and/or small scale Jeans gravitational instabilities in the collected materials because of the disagreement between the ages of the H II region and the fragmentation time of the molecular clouds. A Class II YSO cluster traced by the YSO surface density contours indicates that SF processes might have been triggered by the expansion of the H II region.

Our observations show that CO, HCN, and HCO$^+$ emissions are in good agreement with the 8 μm bubble, as shown in Figure 5 (see Table 3 for the line parameters). We identified a molecular clump near N14, named N14A, which is marked in Figure 6. This clump overlaps with an extended 1.1 mm continuum emission and an infrared dark cloud. Although the CO profiles are seriously contaminated by other components,

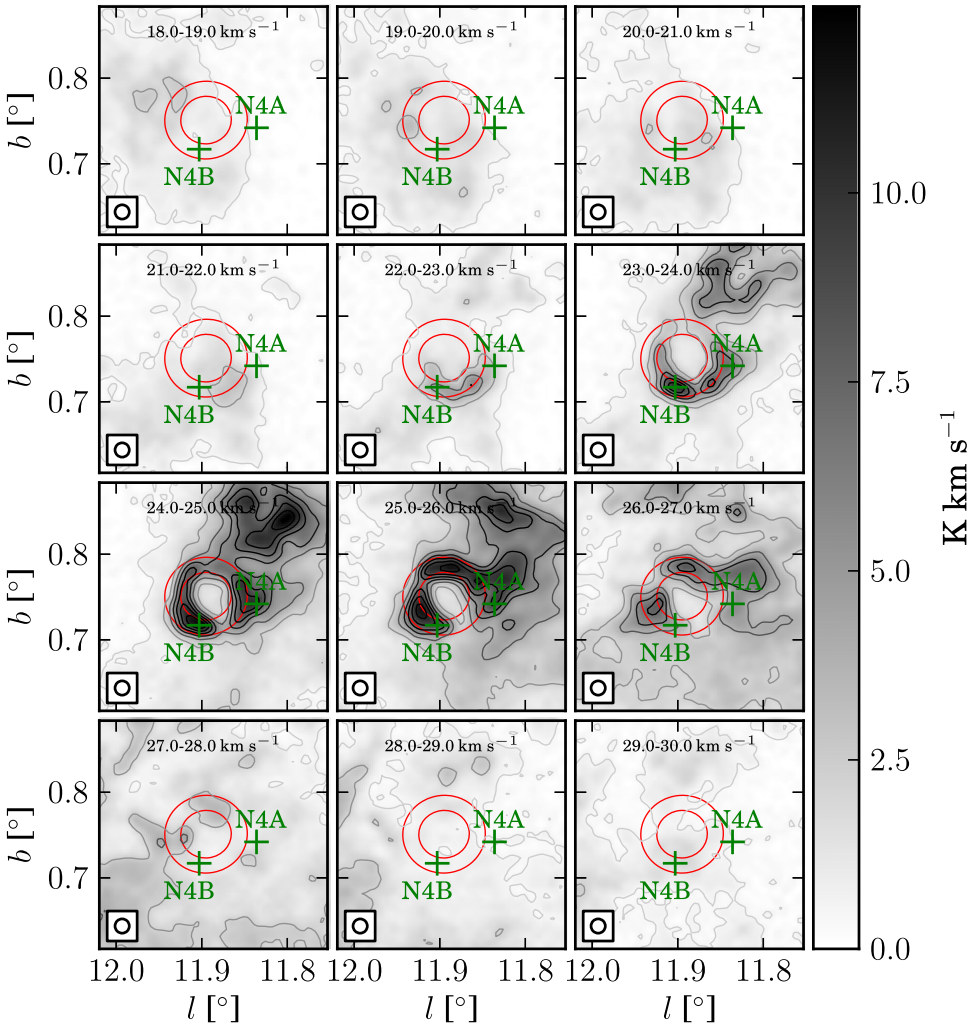

Figure 4. Channel map of ^{13}CO for bubble N4 from 18.0 to 30.0 km s^{-1} with 1.0 km s^{-1} intervals. The red circles mark the position of N4 from Simpson et al. (2012), and the green crosses mark the peak positions of clumps. The RMS (σ) of the image background is about 0.09 K km s^{-1}. The contour levels space linearly from 8.0σ to the peak with a step of 18.1σ.

as shown in Figure 1, we still identified an outflow candidate using the HCO^+ line, which shows a clear red lobe profile. Interestingly, we found a compact 24 μm source near this outflow candidate. A detailed discussion about this outflow is presented in Section 3.5.

3.4.3. N37

N37 is an open bubble with 8 μm emissions encircling weak 20 cm continuum emissions, which are shown in Figure 7 (see Table 3 for the line parameters). The ionized gas velocity of this H II region is 39.6 km s^{-1} (Lockman 1989; Anderson et al. 2014), which is in good accordance with the CO velocity of 40.0 km s^{-1} given by Beaumont & Williams (2010). Although Watson et al. (2010) used a distance of 3.3 kpc, we prefer the far distance of 12.6 kpc, resolved by Anderson & Bania (2009) using two methods: H I emission/absorption (H I E/A) and H I self-absorption (H I SA). This value is identical to the distance adopted by Deharveng et al. (2010).

Based on a visual method, Beaumont & Williams (2010) identified an outflow using CO ($J = 3 \rightarrow 2$) at the position (l, b) = (25.285, 0.266); we did not find evident outflow activity near this position. They suggested that the high and low velocities of this outflow were 30 and 40 km s^{-1}, respectively. However, the ^{12}CO emission is weak and complex in this velocity range, and is not consistent with bubble velocity and morphology. A molecular clump, N37A, was identified at the border of N37, as shown in Figure 8, while the molecular line emission was rather weak at the open part of the bubble.

Although ^{13}CO and HCO^+ display blue wings, no corresponding red wings were found. Furthermore, no 24 μm source was found near the peak of the C^{18}O intensity. Therefore, we suggest the blue wings were either produced by the expansion of the H II regions, or contaminated by other components. Consequently, we did not detect outflows in this region, but considering the limited spatial resolution of PMODLH and the environment traced by ^{12}CO ($J = 1 \rightarrow 0$), we cannot rule out the outflow identified by Beaumont & Williams (2010) using CO ($J = 3 \rightarrow 2$).

3.4.4. N44

N44 is an open bubble with a regular elliptical shape with a weak, diffuse 20 cm continuum enclosed in it. The

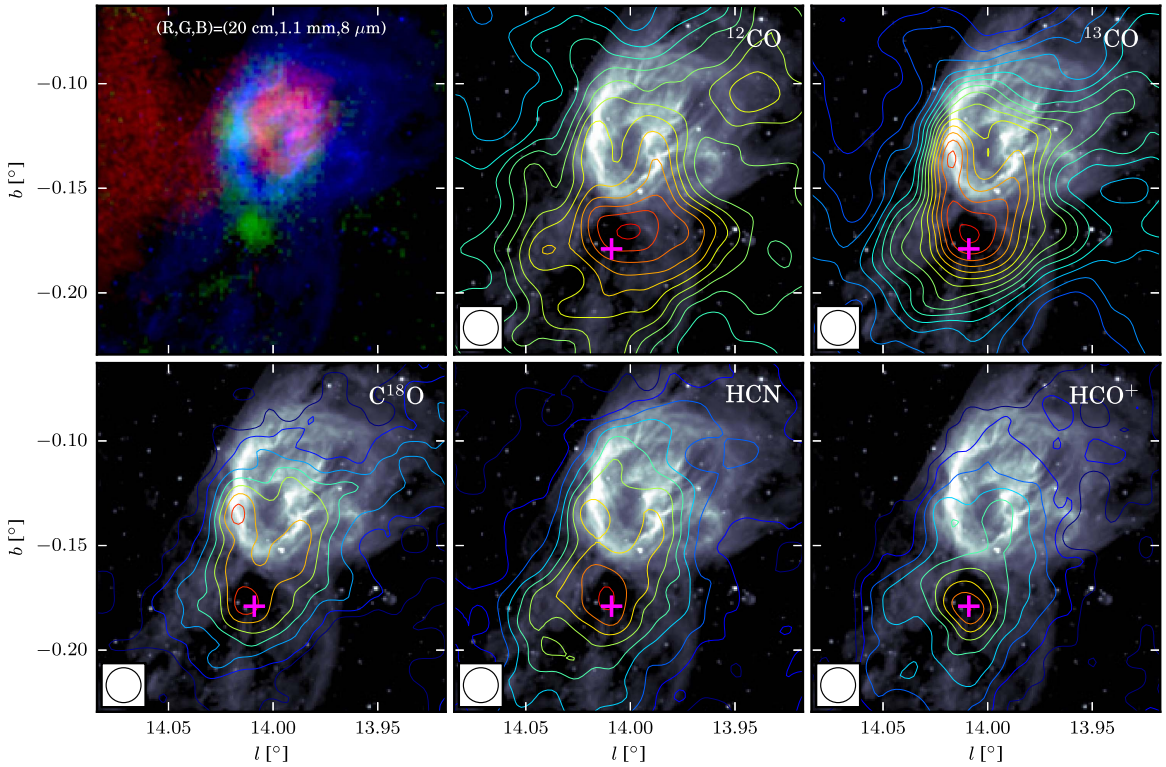

Figure 5. Images of N14. The upper left panel is a three-color image with 20 cm in red, 1.1 mm in green, and 8 μm in blue. The other five panels are contours of five spectral line integrated intensity maps superimposed on the 8 μm image with positions of clumps marked by purple crosses. The contour maps integrate from 36.0 to 44.0 km s^{-1}. The rms (σ) of the five line maps, ^{12}CO, ^{13}CO, C^{18}O, HCN, and HCO$^+$, are 0.57, 0.32, 0.28, 0.07, and 0.08 K km s^{-1}, respectively, and these contours all begin at 8σ, with 14, 11, 6, 6, and 5σ spacing, respectively.

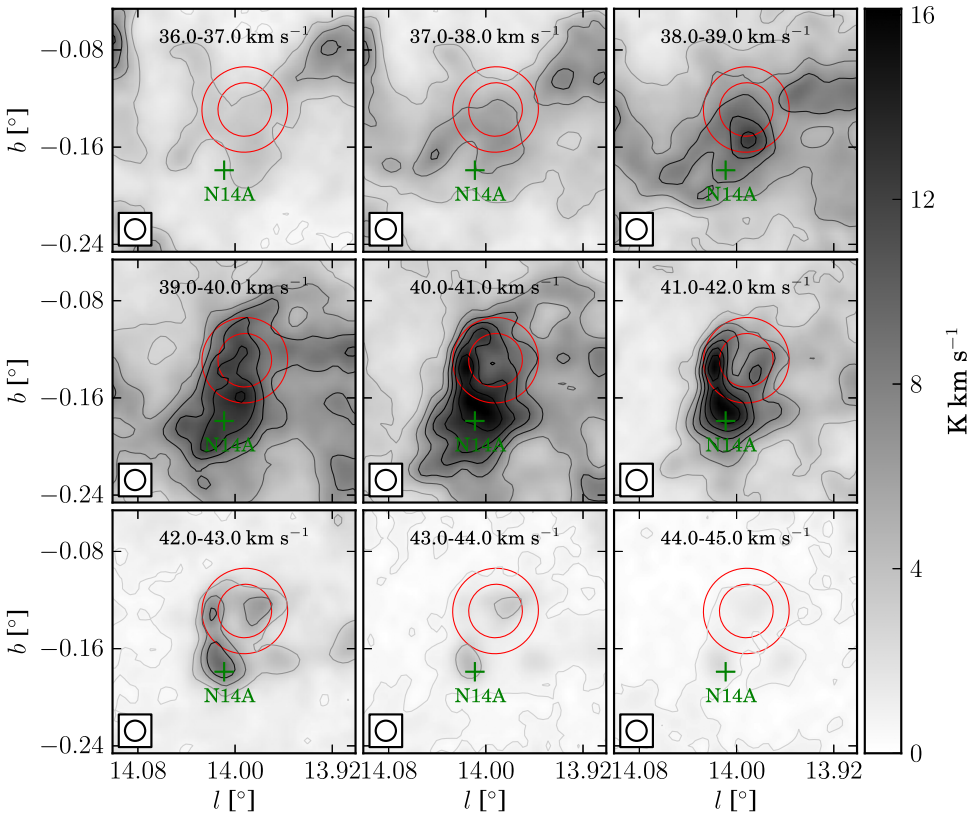

Figure 6. Channel map of ^{13}CO for bubble N14 from 36.0 to 45.0 km s^{-1} with 1.0 km s^{-1} intervals. The red circles mark the position of N14 (Simpson et al. 2012), and the green cross marks the peak position of the clump. The rms (σ) of the image background is about 0.11 K km s^{-1}. The contour levels space linearly from 8σ to the peak with step 19.1σ.

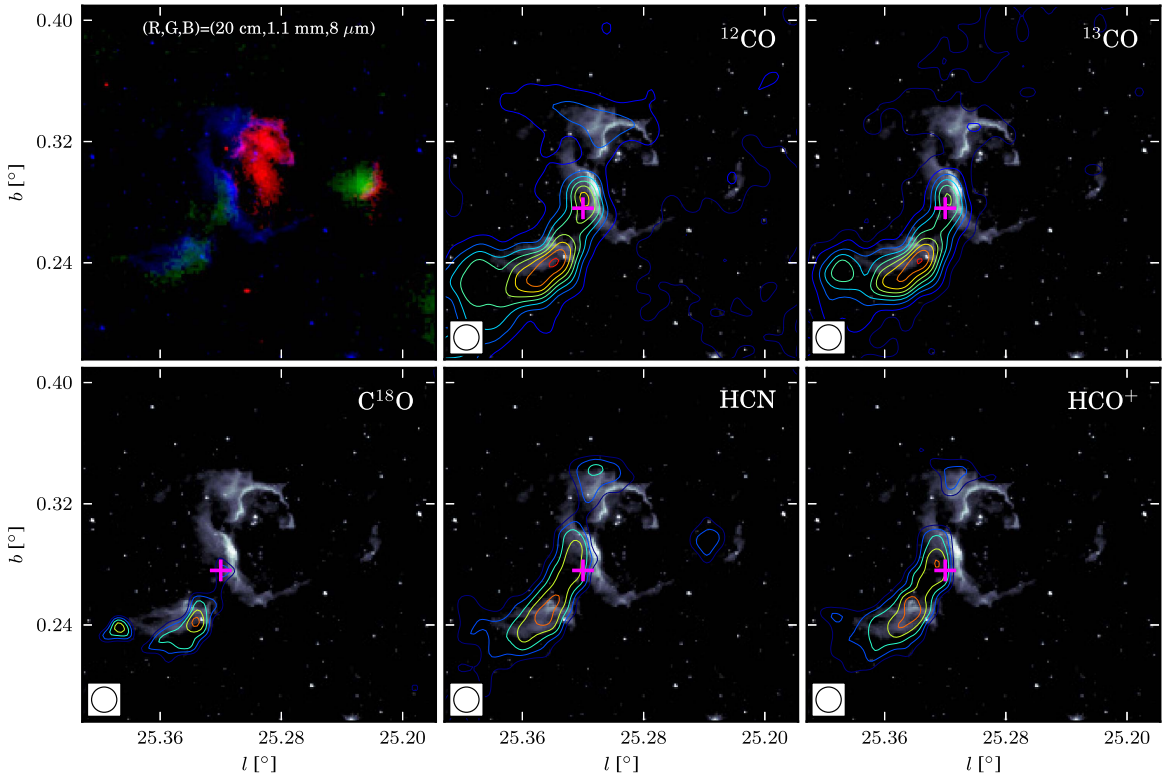

Figure 7. Images of N37. The upper left panel is a three-color image with 20 cm in red, 1.1 mm in green, and 8 μm in blue. The other five panels are contours of five spectral line integrated intensity maps superimposed on the 8 μm image with positions of clumps marked by purple crosses. The contour maps integrate the intensity from 39.0 to 44.0 km s^{-1}. The rms (σ) of the five line maps, ^{12}CO, ^{13}CO, C^{18}O, HCN, and HCO$^+$, are 0.36, 0.21, 0.19, 0.05, and 0.05 K km s^{-1}, respectively, and these contours all begin at 8σ, with 24, 12, 3, 7, and 5σ spacing, respectively.

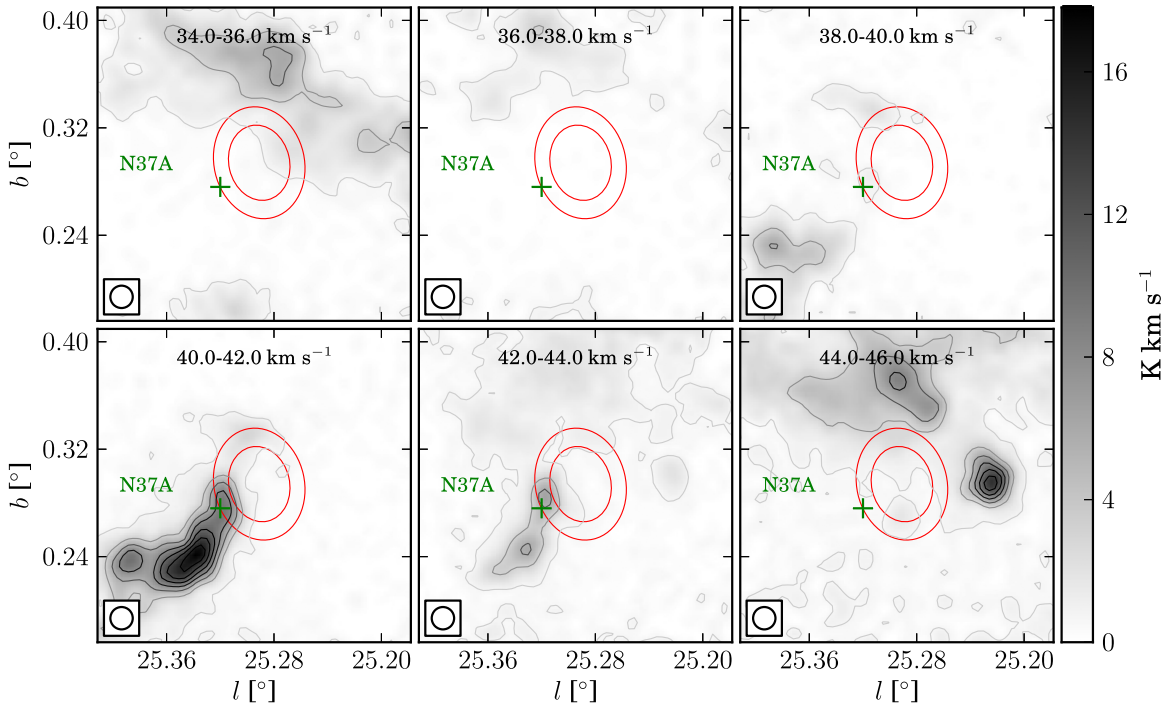

Figure 8. Channel map of ^{13}CO for bubble N37 from 34.0 to 46.0 km s^{-1} with 2.0 km s^{-1} intervals. The red circles mark the position of N37 (Simpson et al. 2012), and the green cross marks the peak position of the clump. The rms (σ) of the image background is about 0.13 K km s^{-1}, and the contour levels space linearly from 5σ to the peak with step 18.3σ.

ionized gas velocity of this bubble is about 82 km s^{-1} (Anderson et al. 2014), which is in good agreement with the CO velocity of 81.1 km s^{-1} (Beaumont & Williams 2010). The kinematic distance of N44 has not been resolved, and we simply adopted a near kinematic distance of 5 kpc.

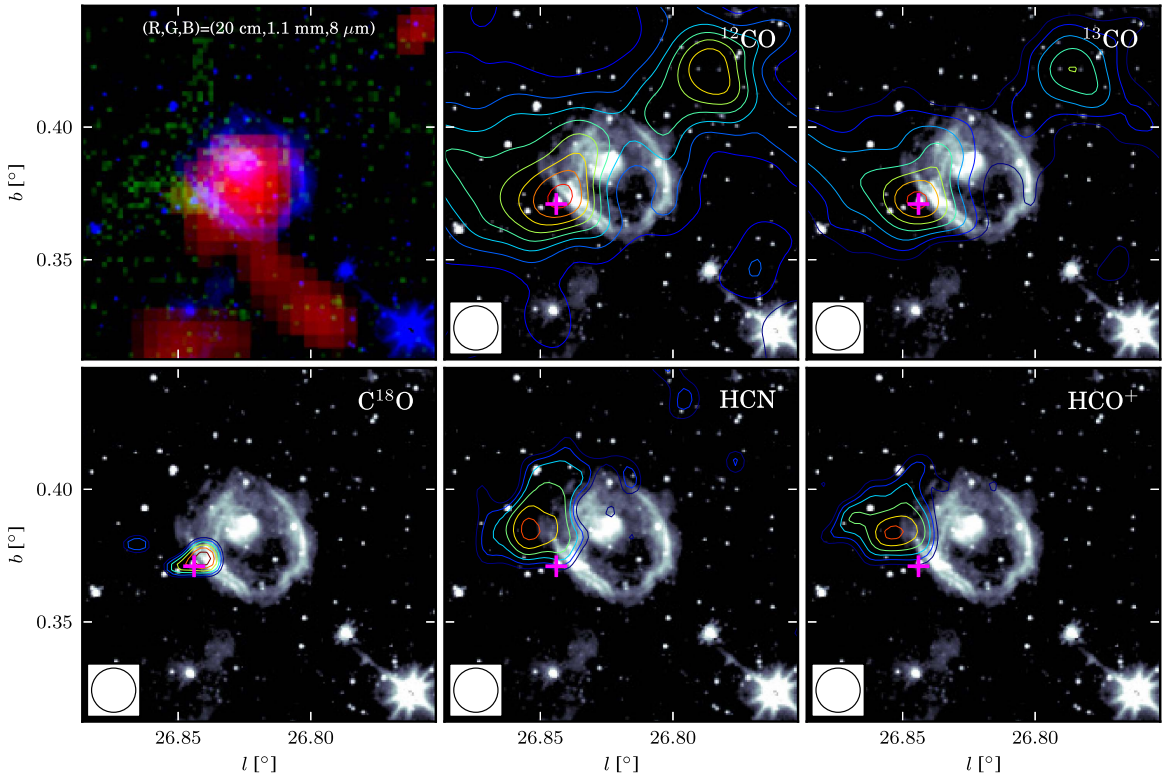

Figure 9. Images of N44. The upper left panel is a three-color image with 20 cm in red, 1.1 mm in green, and 8 μm in blue. The other five panels are contours of five spectral line integrated intensity maps superimposed on the 8 μm image with positions of clumps marked by purple crosses. The contour maps integrate the intensity from 78.0 to 84.0 km s^{-1}. The background rms (σ) of the five line maps, ^{12}CO, ^{13}CO, C^{18}O, HCN, and HCO^{+}, are 0.31, 0.25, 0.16, 0.05, and 0.05 K km s^{-1}, respectively, and these contours all begin at 8σ, with 20, 7, 1, 3, and 3σ spacing, respectively.

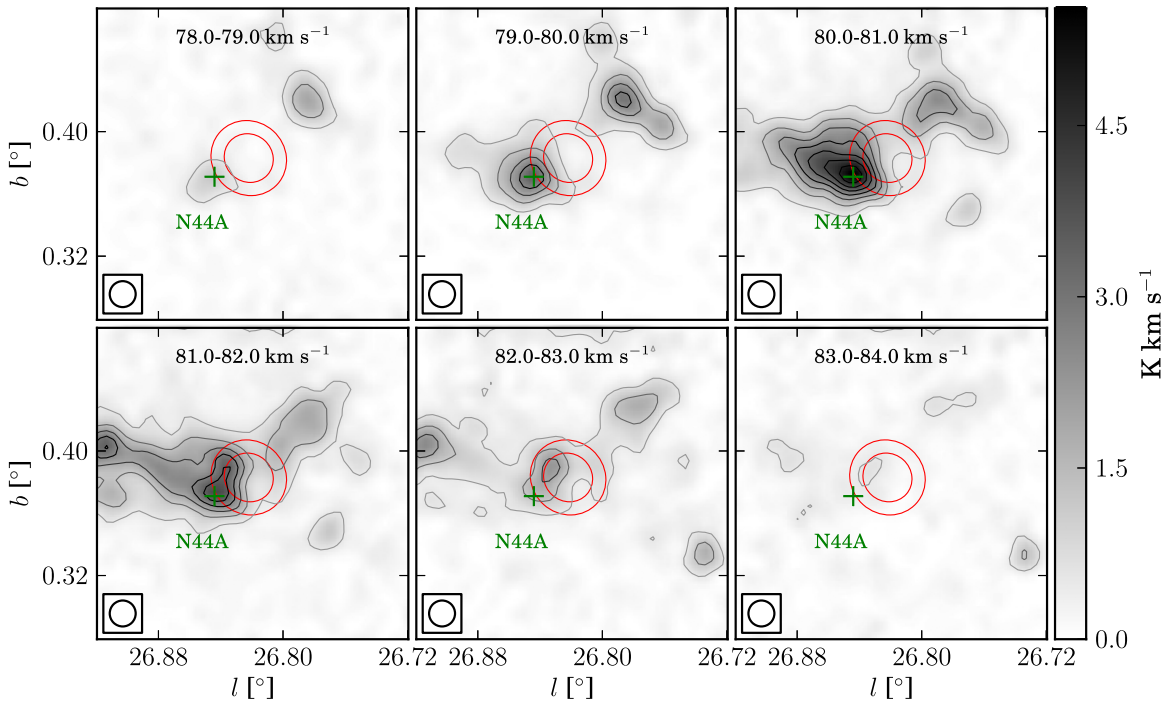

Figure 10. Channel map of ^{13}CO for bubble N44 from 78.0 to 84.0 km s^{-1} with 1.0 km s^{-1} intervals. The two red circles mark the position of N44 (Simpson et al. 2012), and the green cross marks the peak position of the clump. The rms (σ) of the image background is about 0.10 K km s^{-1}, and the contour levels space linearly from 5σ to the peak with step 6.9σ.

Deharveng et al. (2010) found two condensations in this region, and both of which were observed by our CO observations, as shown in Figure 9 (see Table 3 for the line parameters). However, we only consider the one at the edge of N44, which is N44A and marked by a green cross in Figure 10. The CO line wings of this clump are contaminated

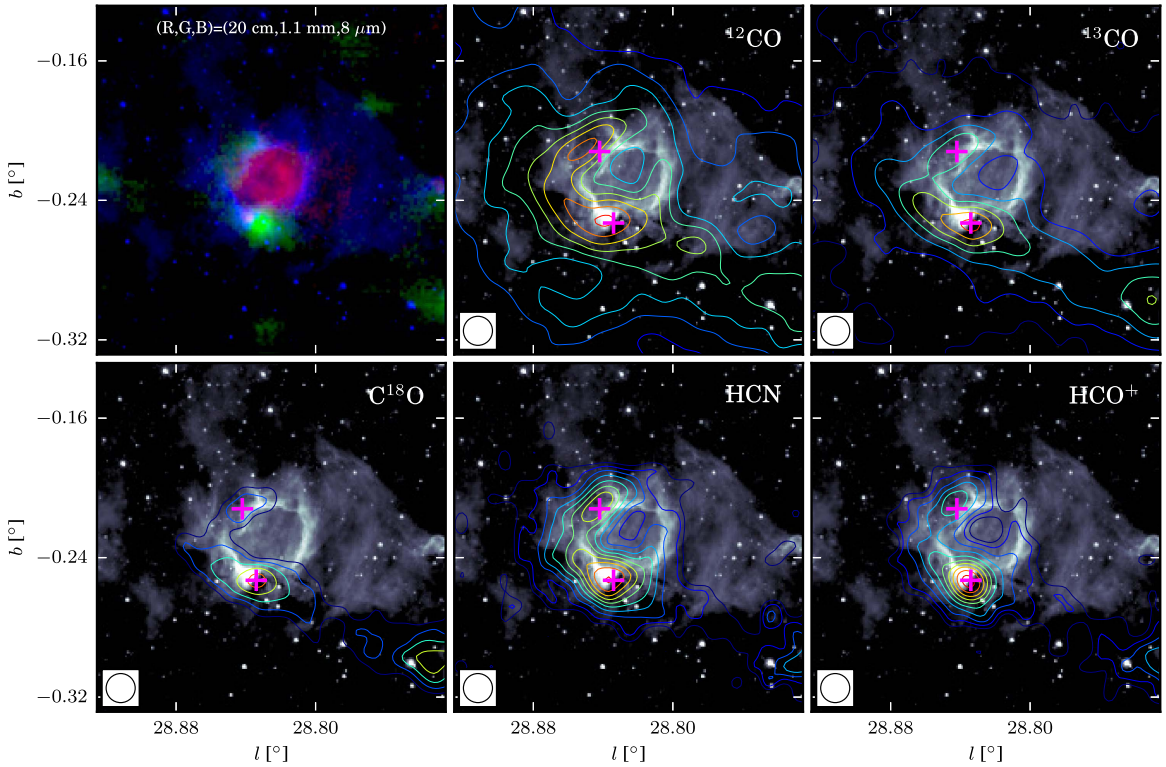

Figure 11. Images of N49. The upper left panel is a three-color image with 20 cm in red, 1.1 mm in green, and 8 μm in blue. The other five panels are contours of five spectral line integrated intensity maps superimposed on the 8 μm image with positions of clumps marked by purple crosses. The contour maps integrate the intensity from 83.0 to 90.0 km s^{-1}. The rms (σ) of five line maps, ^{12}CO, ^{13}CO, C^{18}O, HCN, and HCO$^+$, are 0.44, 0.31, 0.24, 0.06, and 0.07 K km s^{-1}, respectively, and these contours all begin at 8σ, with 25, 19, 7, 4, and 5σ spacing, respectively.

by other adjacent components, which hinders us from searching for outflows.

3.4.5. N49

N49 is a remarkable bubble, and has been investigated by several studies (Watson et al. 2008; Cyganowski et al. 2009; Zavagno et al. 2010). As shown in Figure 11 (see Table 3 for observation parameters), N49 displays a clear typical bubble structure, a ring of 8 μm emission surrounding a disc of 20 cm continuum, and interestingly, an ultra-compact (UC) H II region at the border. The velocity of ionized gas in this field is approximately 90.6 km s^{-1} (given by Lockman 1989; Anderson et al. 2014), and the distance is approximately 5.5 kpc (Deharveng et al. 2010).

Watson et al. (2008) identified seven YSO candidates using the Spectral Energy Distribution (SED) fitting method in this region; two are located at the edge of N49 and possess the largest mass. They proposed that those YSOs were triggered by the expanding shell, because this bubble is being blown by an O5 V star with a dynamical age of $\geqslant 10^5$ yr.

Cyganowski et al. (2009) surveyed class I and II CH_3OH masers toward EGOs using the VLA. One of their samples is situated at the border of N49, and is likely associated with the two YSOs identified by Watson et al. (2008). Both class I and II masers were detected by Cyganowski et al. (2009) in this region. The presence of 6.7 GHz CH_3OH masers indicates that at least one high-mass star is forming here. They suggest the class I 44 GHz CH_3OH masers are tracing an outflow, while the configuration of class II 6.7 GHz CH_3OH masers represents a Keplerian rotation disk. HCO$^+$(3-2), which was also observed by Cyganowski et al. (2009) using the JCMT, shows a similar velocity range to 6.7 GHz methanol masers. However, no H_2O maser was found by Cyganowski et al. (2013) in this region using the Nobeyama Radio Observatory 45 m telescope.

Zavagno et al. (2010) studied SF triggered by the expansion of H II regions using *Herschel* Photoconductor Array Camera and Spectrometer (PACS) and Spectral and Photometric Imaging Receiver (SPRIRE) images from the *Herschel* infrared survey of the Galactic plane (Hi-GAL). The Hi-GAL PACS and SPIRE images reveal a new population of embedded young stars, and five high-mass stars are forming here. They conclude that the high SF efficiency in this region may be caused by the expanding shell.

According to our observations, the CO emission agrees well with the 8 μm band image, and all five lines display arc structures along the edge of N49. The distribution of dense molecular gas traced by HCO$^+$ and HCN suggests that they are probably accumulated by the expanding shell. We identified two clumps, N49A and N49B, at the rim of N49, as shown in Figure 12. Interestingly, the channel map of ^{13}CO of N49 displays a clear shell structure at the velocity range of 85–87 km s^{-1}, which is most likely produced by the expansion of this H II region. The profiles of CO and HCO$^+$ lines are severely contaminated by other components with similar velocities, and therefore we cannot verify the outflow candidate offered by Beaumont & Williams (2010).

3.4.6. N55

Rahman & Murray (2010) suggested that bubble N55 was associated with a star-forming complex (SFC), which is SFCs 18 in their paper, and they classified it as a closed bubble. The

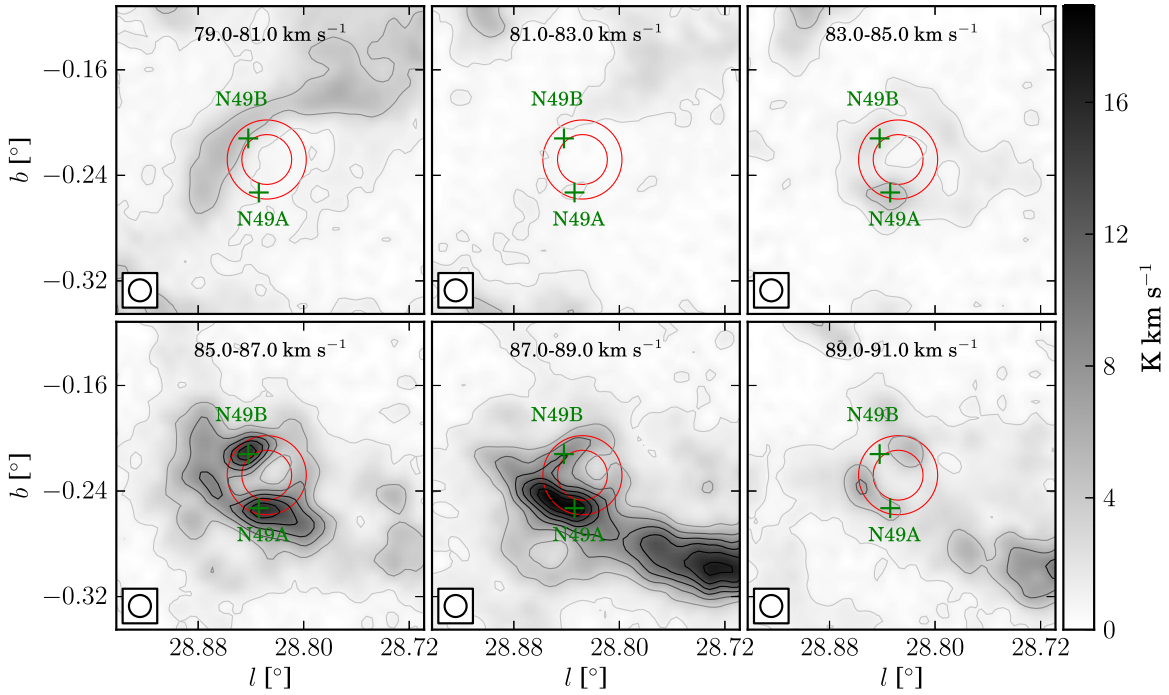

Figure 12. Channel map of ^{13}CO for bubble N49 from 79.0 to 91.0 km s^{-1} with 2.0 km s^{-1} intervals. The red circles mark the position of N49 (Simpson et al. 2012), and the green crosses mark the peak positions of clumps. The rms (σ) of the image background is about 0.17 K km s^{-1}, and the contour levels space linearly from 5σ to the peak with step 15.5σ.

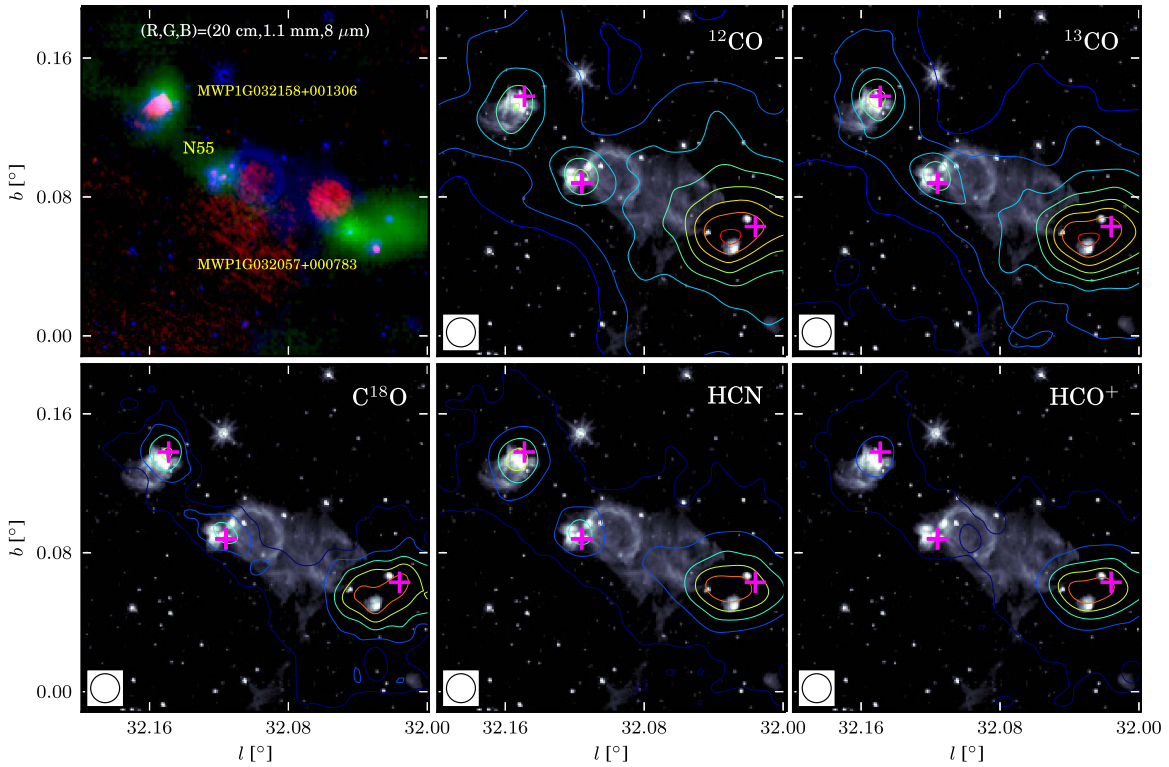

Figure 13. Images of N55. The upper left panel is a three-color image with 20 cm in red, 1.1 mm in green, and 8 μm in blue. The other five panels are contours of five spectral line integrated intensity maps superimposed on the 8 μm image with positions of clumps marked by purple crosses. The contour maps integrate the intensity from 89.0 to 103.0 km s^{-1}. The rms (σ) of five line maps, ^{12}CO, ^{13}CO, C^{18}O, HCN, and HCO$^+$, are 0.49, 0.26, 0.27, 0.10, and 0.10 K km s^{-1}, respectively, and these contours all begin at 8σ, with 47, 29, 7, 19, and 26σ spacing, respectively.

distance and velocity of N55 provided by Deharveng et al. (2010) were 8.4 kpc and 93 km s^{-1}, respectively.

This is a remarkable bubble region, and images of N55 are shown in Figure 13 (the observation parameters are listed in Table 3). There are also two other prominent bubbles in this region: MWPIG032057+000783 and MWPIG032158 +001306 (Simpson et al. 2012). Diffuse and weak emissions of 20 cm continuum spread in and around N55, while each of

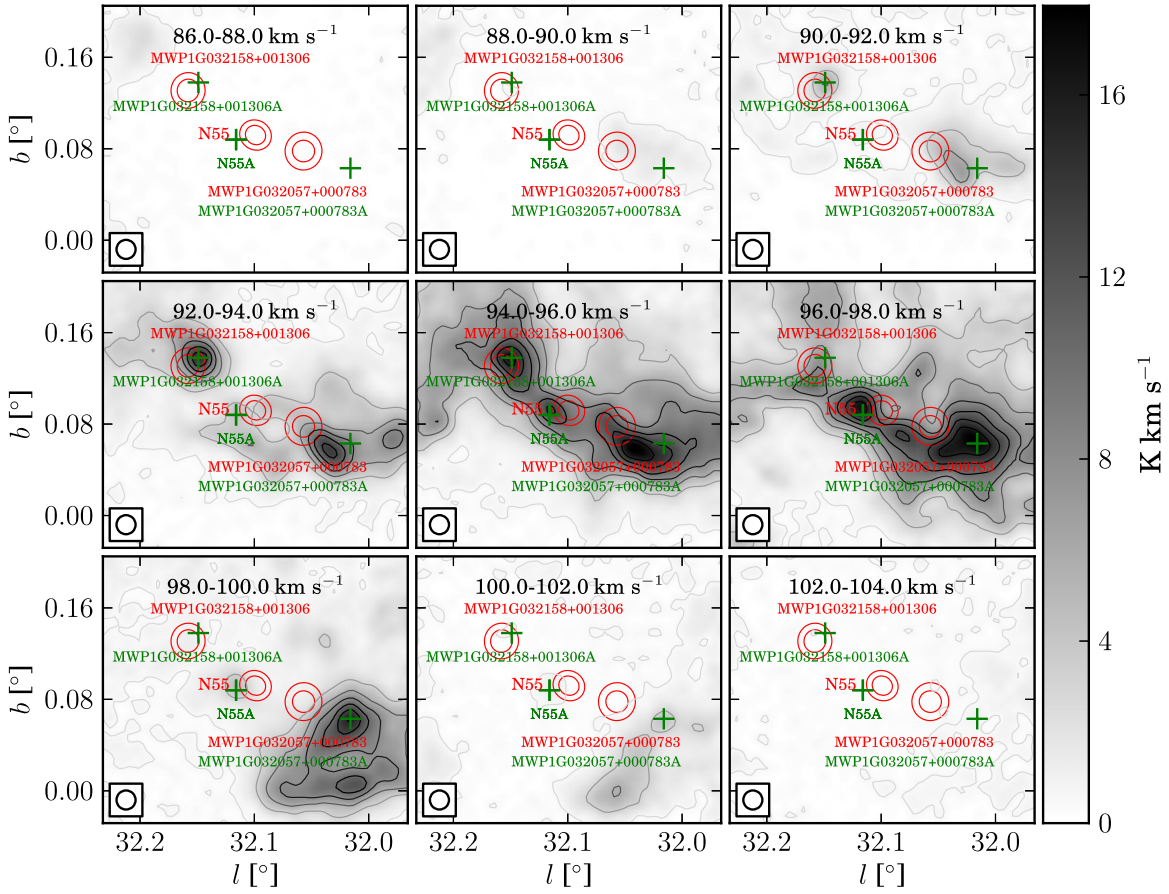

Figure 14. Channel map of ^{13}CO for bubble N55 from 86.0 to 104.0 km s^{-1} with 2.0 km s^{-1} intervals. The red circles delineate the position of N55 from Simpson et al. (2012), and the green crosses mark the peak position of clumps. The rms (σ) of the image background is about 0.10 K km s^{-1}, and the contour levels space linearly from 5σ to the peak with step 25.3σ.

the other two bubbles enclose a 20 cm continuum disk with relatively strong emissions. Several UC H II regions are traced by the 20 cm continuum near N55, which indicates that a cluster of high-mass stars is emerging here. Interestingly, each of the three bubbles harbors a molecular clump traced by the 1.1 mm continuum. Those molecular clumps are confirmed by our C^{18}O lines, and their positions are marked with green crosses in Figure 14.

We found a wide CO line wing at both red and blue ends of profiles of the molecular clump N55A. Because there are at least three UC H II regions near N55A, as shown in Figure 13, it is possible that more than one outflow is occurring here. Because they are not resolved, we simply regard it as one outflow when calculating the outflow parameters. However, we failed to estimate the age for this outflow due to the overlap of peaks of the red and blue lobes, and the outflow parameters are given in Table 6. The CO and HCO$^+$ line profiles of the other two molecular clumps are contaminated with other components, and therefore, it is hard to perform outflow analysis.

3.4.7. N75 and N74

N74 and N75 are two prominent bubbles in SF region G38.9-0.40 (Alexander et al. 2013). N75 is an open bubble with a bright rim and elliptical regular shape, while N74 shows slightly weaker emission at the 8 μm band, as shown in Figure 15 (the observation parameters are shown in Table 3). Unexpectedly, no evident 20 cm emissions were detected within these two bubbles, which is abnormal for such regular bubbles with strong 8 μm band emission. The velocity of the Hydrogen recombination lines (RRLs) in this H II region is about 42.1 km s^{-1} (Anderson et al. 2014), while the velocity of carbon RRLs is about 39.2 km s^{-1} (Wenger et al. 2013). Because the kinematic distance has not been resolved, we simply adopt a near kinematic distance of 2.8 kpc.

Sherman (2012) observed four molecular lines—HCN, HCO$^+$, N_2H^+, and CS—as well as the 3.3 mm continuum emission, using Combined Array for Research in Millimeter-wave Astronomy toward N74. Tentative evidence showed that the molecular clouds on the bubble rims were more fragmented than dark clouds. They suggest that triggered SF may be occurring in this region, although their findings do not indicate a classic collect-and-collapse model.

Alexander et al. (2013) performed a multiwavelength study for this region. They claim that both bubbles are powered by O9.5V stars with star clusters surrounding them. Although they identified 162 YSOs in this region, they did not find feedback-triggered SF, which may be due to the young ages of these bubbles. They found a strong correlation between areal YSO mass surface density and gas mass surface density, which suggests that gas density is a more important factor of SF than stellar feedback.

Our observations show that CO emissions coincide well with these two bubbles, and three molecular cloud clumps were revealed by C^{18}O, which are marked by green crosses in Figure 16. However, at least two components are present at the

Table 6
Outflow Parameters

Name	Distance (kpc)	Lobe	Peak (°, °)	Velocity Range (km s^{-1})	Mass ($M_\odot$)	Momentum ($M_\odot$ km s^{-1})	Energy (10^{45}) (erg)	$\bar{v}$ (km s^{-1})	Scale (pc)	t_{dyn} (10^4) (yr)	$\dot{M}$ (10^{-4}) ($M_\odot$ yr^{-1})	$F_{outflow}$ (10^{-3}) ($M_\odot$ km s^{-1} yr^{-1})	$L_{outflow}$ ($L_\odot$)
N14	3.6	Red	(14.018, −0.171)	44.0–47.0	…	…	…	…	…	…	…	…	…
N55	8.4	Red	(32.116, 0.088)	101.0–106.5	17	103	6.7	…	…	…	…	…	…
N55	8.4	Blue	(32.116, 0.088)	87.4–92.0	24	144	8.8	…	…	…	…	…	…
N105	11.2	Blue	(50.085, 0.611)	−12.3 to −5.8	40.4	231.4	14.0	5.7	2.4	40.6	1.00	0.57	0.28
N133	2.5	Red	(63.148, 0.439)	26.0–32.0	1.4	6.8	0.3	4.9	0.4	7.3	0.19	0.09	0.04

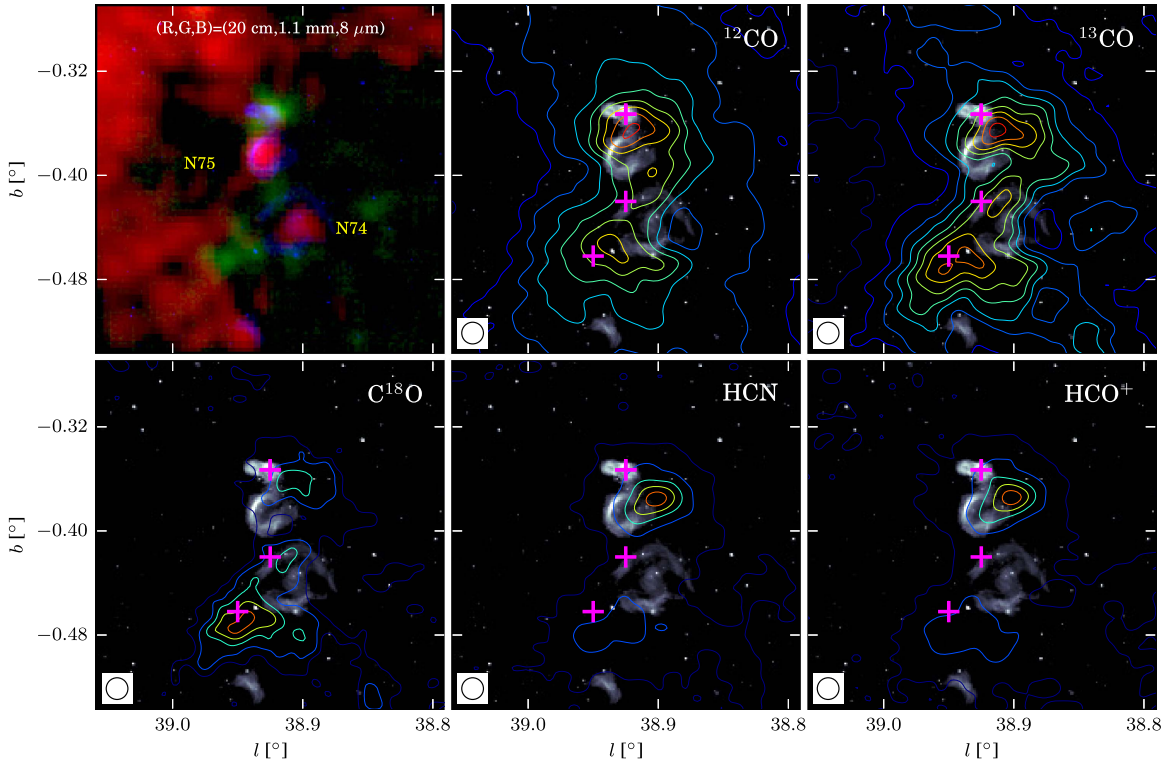

Figure 15. Images of N75 and N74. The upper left panel is a three-color image with 20 cm in red, 1.1 mm in green, and 8 μm in blue. The other five panels are contours of five spectral line integrated intensity maps superimposed on the 8 μm image with positions of clumps marked by purple crosses. The contour maps integrate the intensity from 37.0 to 44.0 km s^{-1}. The rms (σ) of five line maps, ^{12}CO, ^{13}CO, C^{18}O, HCN, and HCO$^+$, are 0.32, 0.18, 0.18, 0.06, and 0.06 K km s^{-1}, respectively, and these contours all begin at 8σ, with 50, 26, 7, 21, and 24σ spacing, respectively.

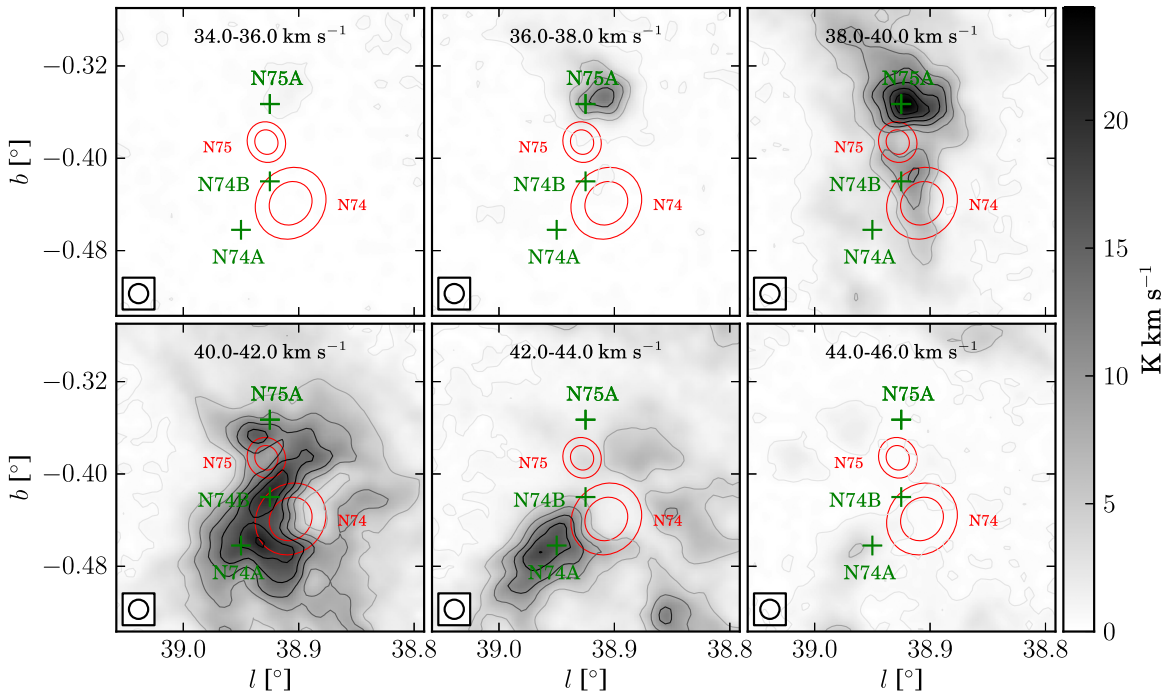

Figure 16. Channel map of ^{13}CO for bubble N75 from 34.0 to 46.0 km s^{-1} with 2.0 km s^{-1} intervals. The two red circles delineate the position of N75 (Simpson et al. 2012), and the green crosses mark the peak position of clumps. The rms (σ) of the image background is about 0.10 K km s^{-1}, and the contour levels space linearly from 5σ to the peak with step 36σ.

border of N75 or N74, which hinders us from identifying outflows from the three clumps, including the one identified by Beaumont & Williams (2010).

3.4.8. N82

N82 is a closed bubble containing a strong 20 cm continuum disk, which is shown in Figure 17 (see Table 3 for the molecular

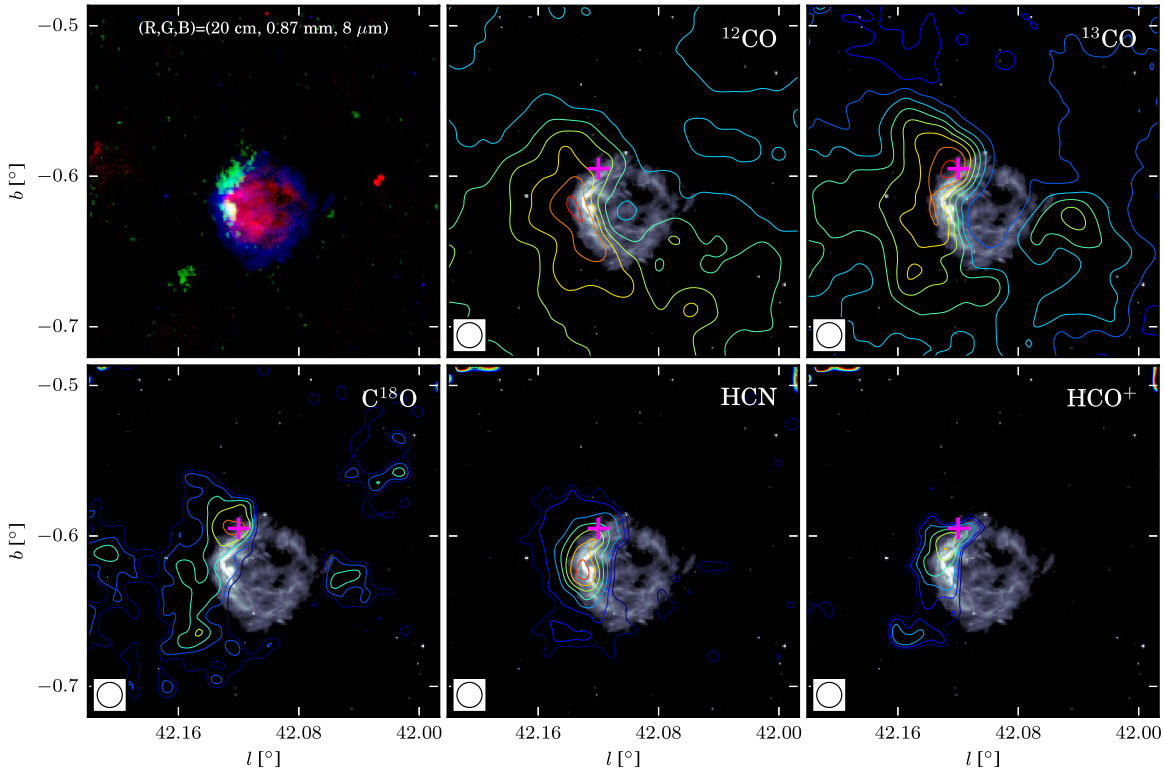

Figure 17. Images of N82. The upper left panel is a three-color image with 20 cm in red, 0.87 mm in green, and 8 μm in blue. The other five panels are contours of five spectral line integrated intensity maps superimposed on the 8 μm image with positions of clumps marked by purple crosses. The contour maps integrate the intensity from 63.0 to 72.0 km s^{-1}. The rms (σ) of five line maps, ^{12}CO, ^{13}CO, C^{18}O, HCN, and HCO^{+}, are 0.38, 0.21, 0.21, 0.08, and 0.08 K km s^{-1}, respectively, and these contours all begin at 8σ, with 28, 17, 3, 4, and 2σ spacing, respectively.

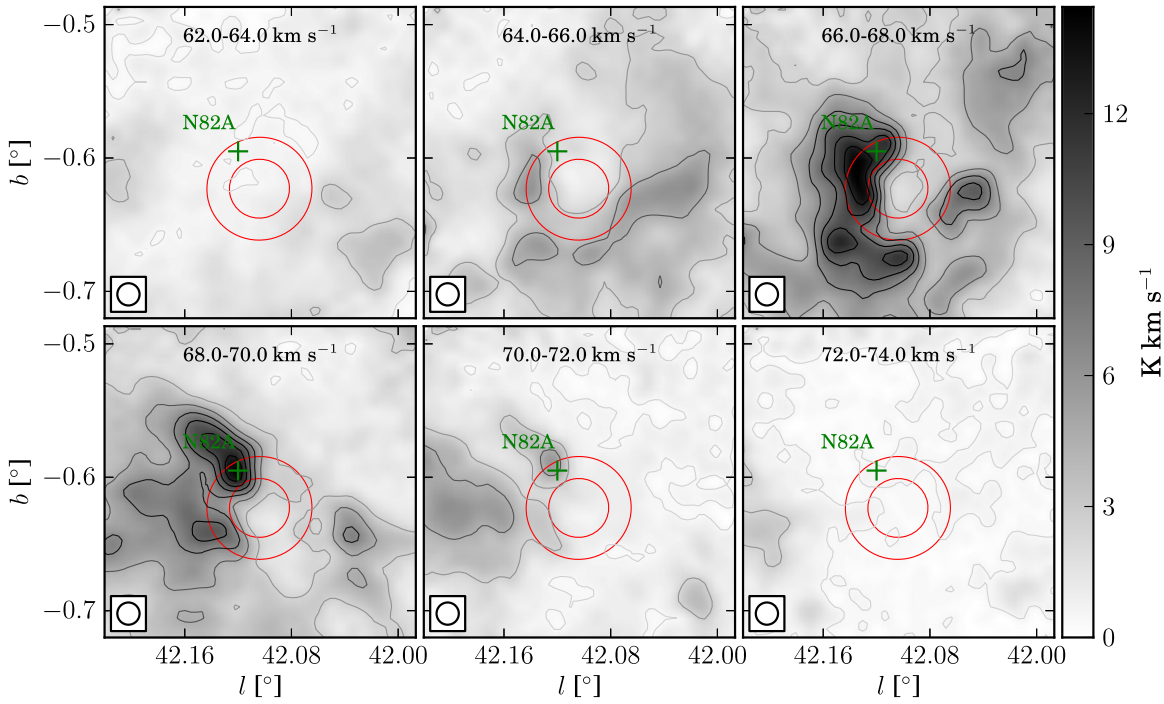

Figure 18. Channel map of ^{13}CO for bubble N82 from 62.0 to 74.0 km s^{-1} with 2.0 km s^{-1} intervals. The red circles delineate the position of N82 provided by Simpson et al. (2012), and the green cross marks the peak position of the clump. The rms (σ) of the image background is about 0.10 K km s^{-1}, and the contour levels space linearly from 3σ to the peak with step 20.6σ.

line parameters). The velocity of Hα is about 66.0 km s^{-1} (Lockman 1989), which is in good agreement with CO velocity, 66.5 km s^{-1}, determined by Beaumont & Williams (2010) using the CO($J = 3 \rightarrow 2$) line. The distance of this molecular cloud was resolved by Stead & Hoare (2010) using infrared extension, which is consistent with the result of Roman-Duval et al. (2009).

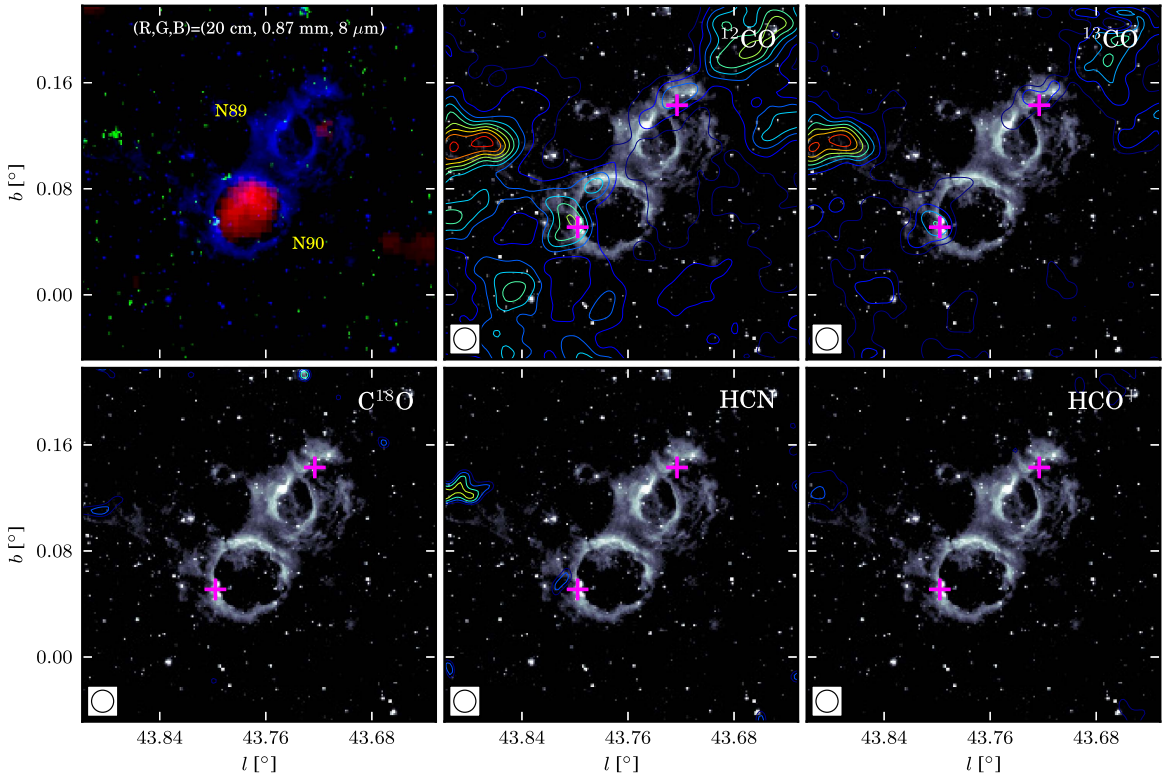

Figure 19. Images of N89 and N90. The upper left panel is a three-color image with 20 cm in red, 0.87 mm in green, and 8 μm in blue. The other five panels are contours of five spectral line integrated intensity maps superimposed on the 8 μm image with positions of clumps marked by purple crosses. The contour maps integrate the intensity from 64.0 to 75.0 km s^{-1}. The rms (σ) of five line maps, ^{12}CO, ^{13}CO, C^{18}O, HCN, and HCO^{+}, are 0.37, 0.18, 0.18, 0.06, and 0.07 K km s^{-1}, respectively, and these contours all begin at 8σ, with 15, 10, 3, 2, and 5σ spacing, respectively.

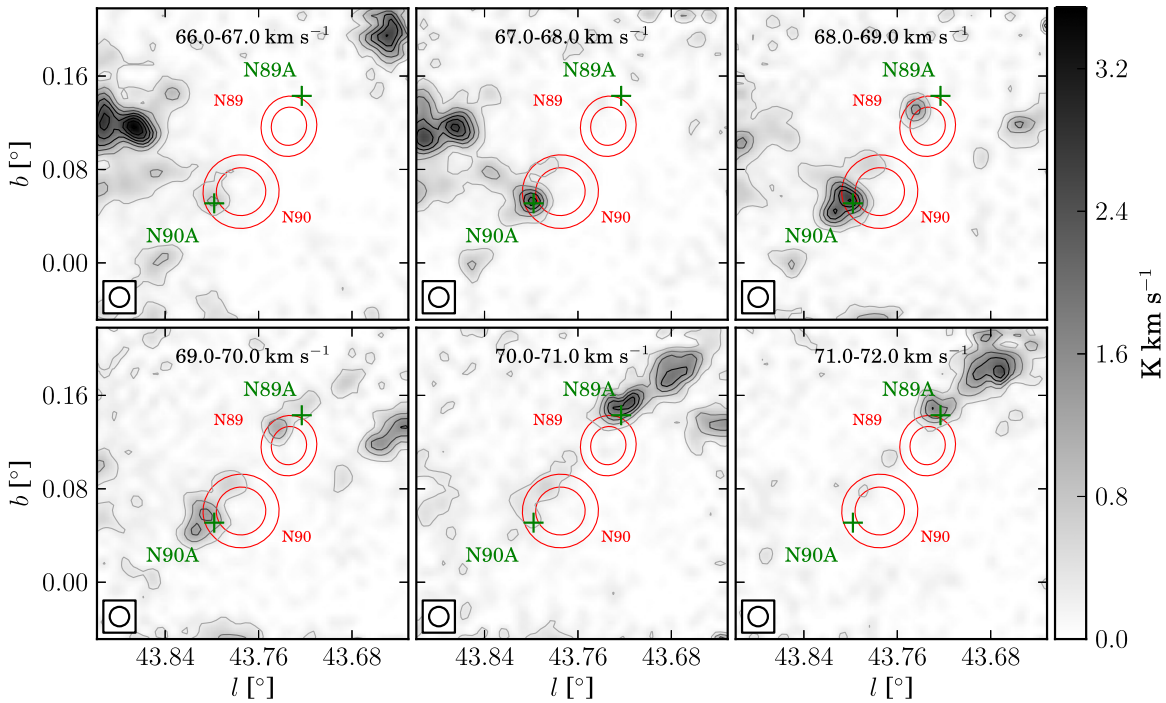

Figure 20. Channel map of ^{13}CO for bubble N89 and N90 from 66.0 to 72.0 km s^{-1} with 1.0 km s^{-1} intervals. The red circles delineate the position of N89 and N90 (Simpson et al. 2012), and green crosses mark the peak position of clumps. The rms (σ) of the image background is about 0.05 K km s^{-1}, and the contour levels space linearly from 5σ to the peak with step 8.6σ.

Consequently, we adopted a distance of 4.3 kpc for N82 following Stead & Hoare (2010), and the far distance suggested by Deharveng et al. (2010) is rejected.

Watson et al. (2010) identified six YSOs from the 8 μm shell of N82, and found a significantly increased YSO density at the 8 μm emission peak. Beaumont & Williams (2010) observed

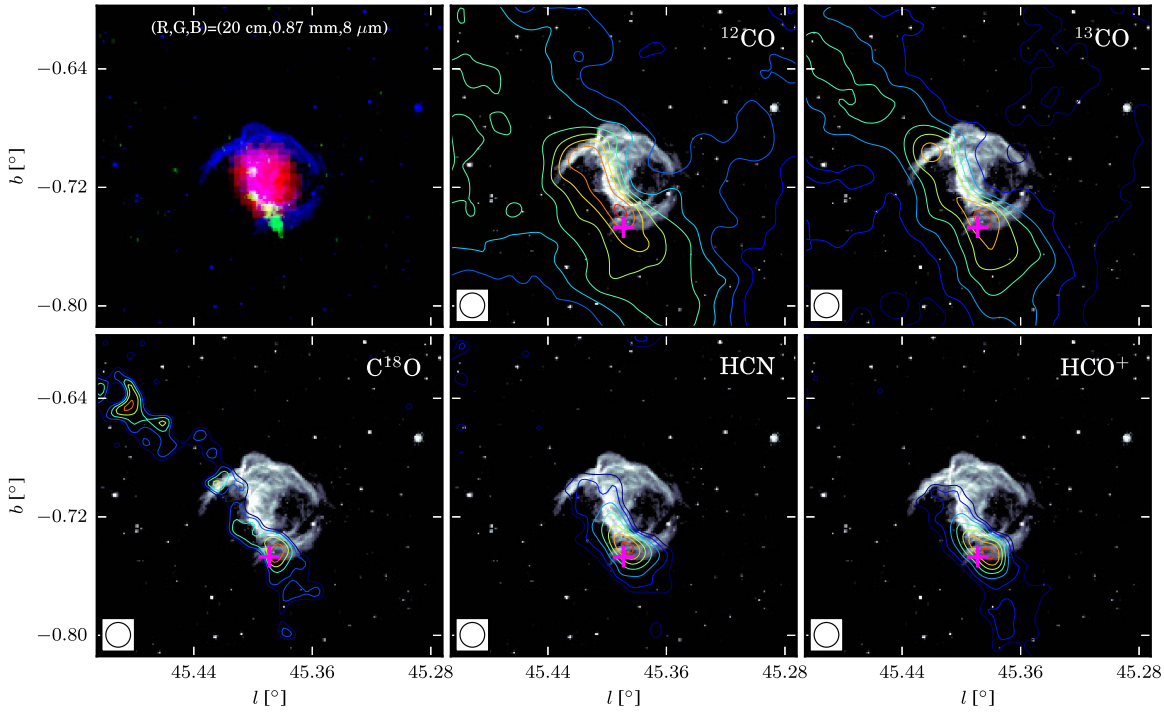

Figure 21. Images of N95. The upper left panel is a three-color image with 20 cm in red, 0.87 mm in green, and 8 μm in blue. The other five panels are contours of five spectral line integrated intensity maps superimposed on the 8 μm image with positions of clumps marked by purple crosses. The contour maps integrate the intensity from 57.0 to 63.0 km s^{-1}. The rms (σ) of five line maps, ^{12}CO, ^{13}CO, C^{18}O, HCN, and HCO$^+$, are 0.32, 0.19, 0.19, 0.05, and 0.05 K km s^{-1}, respectively, and these contours all begin at 8σ, with 22, 18, 2, 5, and 4σ spacing, respectively.

the CO ($J = 3 \rightarrow 2$) line using the JCMT, and suggested that the CO velocity is 66.5 km s^{-1}. Using a new Monte Carlo method, Stead & Hoare (2011) derived an age of approximately 1.8 Myr for clusters in the vicinity of this bubble.

According to our observations, the molecular clouds distribute alongside the bright rim of the bubble, which indicates that the power source of the bubble is probably compressing the molecular clouds. We found a molecular cloud clump near N82, N82A, which is marked in Figure 18. However, the molecular line profiles in this region show that multicomponents are present here, which prevents us from searching for outflows.

3.4.9. N89 and N90

N89 and N90 are two adjacent bubbles with relatively large angle size and weak 8 μm band emissions. N90 contains weak 20 cm continuum emission, which is absent in bubble N89. The velocity of ionized gas from Anderson et al. (2014) is about 70.5 km s^{-1}. Bania et al. (2012) performed a survey of H II regions using the Arecibo radio telescope, and they suggest that velocities for N89 and N90 are 73.1 km s^{-1} and 70.5 km s^{-1}, respectively. The distance of N90 given by Deharveng et al. (2010) is 6.1 kpc.

Profiles of N89 and N90 shown in Figure 1 demonstrate that a strong emission presents at ~60–62 km s^{-1}, but this component is actually a part of Sagittarius Arm (Sawada et al. 2012). Furthermore, no Hα emission is detected at this velocity, and the integrated intensity map over this velocity range is not clearly related to N89 and N90.

According to our CO observation, the molecular cloud at 70.3 and 68.4 km s^{-1} is most likely associated with bubble N89 and N90, respectively, as shown in Figure 19 (set Table 3 for the observation parameters). No C^{18}O signal was detected in this region, and the emission of HCO$^+$ and HCN lines was rather weak. Because C^{18}O emission is absent here, we used the ^{13}CO line to identify clumps, and consequently, these two identified clumps—N89A and N90A, which are marked by green crosses in Figure 20—are not concrete. We could not perform outflow identifications due to the contamination of CO profiles and the poor SNR of HCO$^+$.

3.4.10. N95

N95 is an open bubble, with an approximately round shape split by an arc, containing a strong 20 continuum disk as demonstrated in Figure 21 (see Table 3 for the observations parameters). The velocity and distance offered by Deharveng et al. (2010) are 52.5 km s^{-1} and 8.0 kpc, respectively.

Our observations show that the molecular clouds distribute largely alongside the 8 μm arc, and a molecular clump, N95A, is located at the border of N95, as shown in Figure 22. The profiles of N95 are contaminated by other components with similar velocities, as shown in Figure 1, and consequently, we cannot perform outflow identifications in this region.

3.4.11. N105

N105 is a closed bubble with a small angular size containing weak 20 cm continuum emissions, as shown in Figure 23 (see Table 3 for the observation parameters). Anderson et al. (2012a) suggest a velocity of −1.1 km s^{-1} and a kinematic distance of 11.2 kpc for this H II region. This bubble is not included in the samples of Deharveng et al. (2010).

Our observations show two molecular clumps located at the edge of N105: N105A and N105B, as shown in Figure 24. No clear line wing is found toward 105A, and we found an outflow candidate in N105B. This outflow shows a clear blue wing, while the red end of the profile is slightly contaminated by another molecular component. Details about this outflow are discussed in Section 3.5.

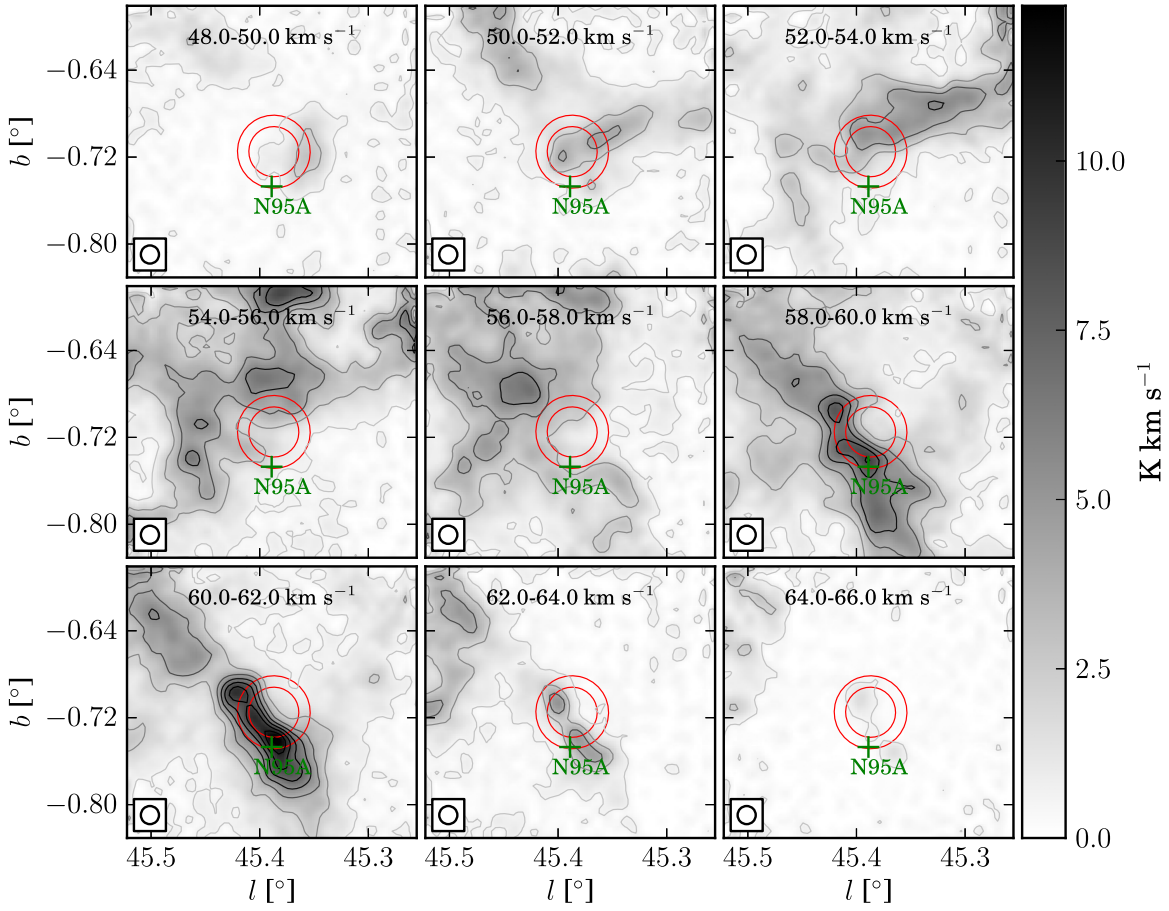

Figure 22. Channel map of ^{13}CO for bubble N95 from 48.0 to 66.0 km s^{-1} with 2.0 km s^{-1} intervals. The red circles delineate the the position of N95 given by Simpson et al. (2012), and the green cross marks the peak position of the clump. The rms (σ) of the image background is about 0.11 K km s^{-1}, and the contour levels space linearly from 5σ to the peak with step 14.9σ.

3.4.12. N123

N123 is a noteworthy bubble with bright compact 20 and 6 cm continuum (White et al. 2005) sources in its rim, as shown in Figure 25 (see Table 3 for the observations parameters), and the flux is saturated at the 24 μm band (Carey et al. 2009; Gutermuth & Heyer 2015). Most likely, they are tracing an UC H II region, which means a high-mass star might have been triggered by the expanding H II shell of N123. Although Watson et al. (2010) suggested a velocity of 25 km s^{-1} for N123, we did not find any consistency between CO and 8 μm emission at this velocity. However, the observations (Watson et al. 2003) of H110α and H_2CO show velocities of 6.3 and 2.0 km s^{-1}, respectively, which are more likely to be associated with N123. Following Watson et al. (2003), we adopted the distance of 8.6 kpc.

According to our results, CO emissions at 2 km s^{-1} are morphologically in good agreement with N123. The dense gas traced by HCN and HCO^+ is present near the border of N123. We identified a molecular clump near N123, which is marked in Figure 26. The profile of N123 is severely contaminated by other components with adjacent velocities, and therefore we failed to perform outflow identification in this region.

3.4.13. N133

N133 is the only optically visible H II region in our sample. The 20 cm continuum emission is prominent, as shown in Figure 27 (see Table 3 for the line parameters). Its velocity and distance are approximately 21.4 km s^{-1} and 2.1 kpc, respectively (Watson et al. 2010), and there is another bubble, N132, with smaller angular size nearby. However, N132 is not resolved by the PMODLH 13.7 m telescope.

Watson et al. (2010) identified six YSOs from this region, with positions that are clearly not coincident with the peaks of the 8 μm emission. Samal et al. (2014) performed a multiwavelength investigation focusing on SF activity in the Sh2-90 H II complex associated with N133. They found 129 low mass YSOs around this bubble, and confirmed the main ionization source as an O8-O9 V star as suggested by Lafon et al. (1983). They proposed that multi-generation SF is present in this complex, and argued that the expanding H II region triggered SF at the borders of Sh2-90.

From our observation, the five molecular line emissions agree well with 8 μm emissions, and three molecular clumps were identified, which are displayed in Figure 28. There is another adjacent component making the blue end of profiles unclean, while the red end is uncontaminated. We identified an outflow near N133, details of which are discussed in Section 3.5.

3.5. Outflows

Outflow is a direct signature of ongoing SF. Although they are hard to detect, especially for bubble regions where high-mass stars are present, we still performed the identification for outflows around bubbles.

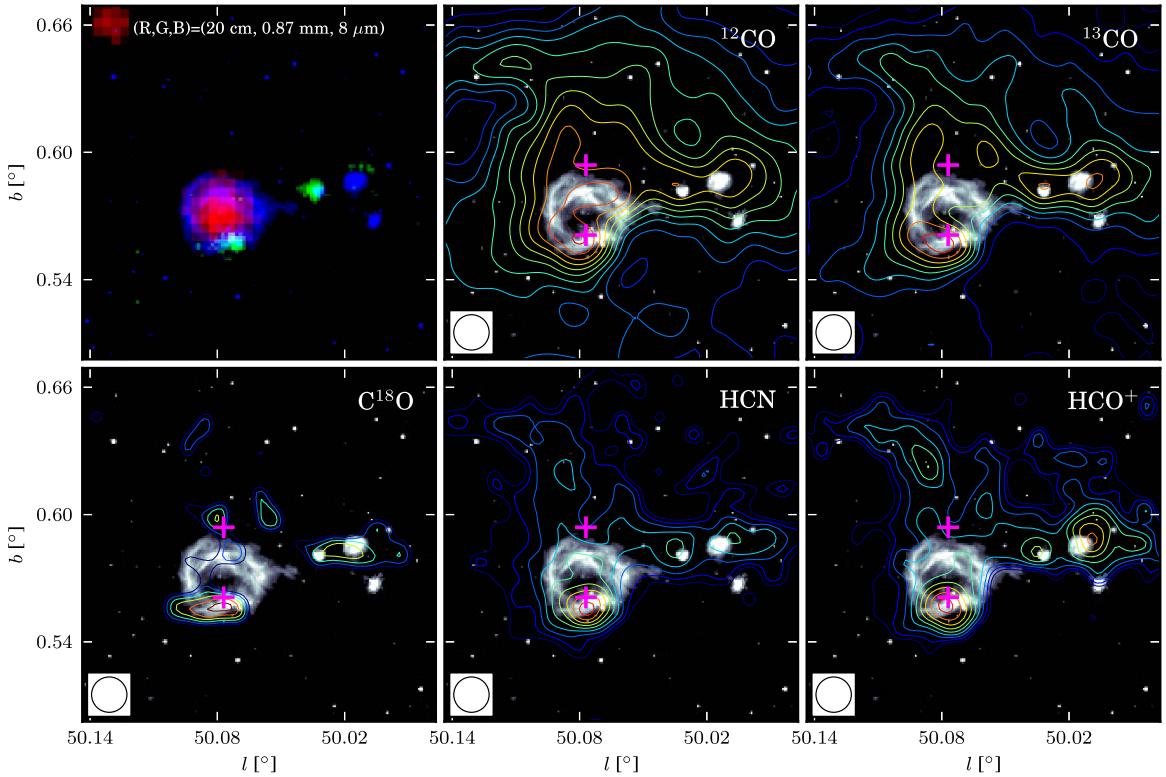

Figure 23. Images of N105. The upper left panel is a three-color image with 20 cm in red, 0.87 mm in green, and 8 μm in blue. The other five panels are contours of five spectral line integrated intensity maps superimposed on the 8 μm image with positions of clumps marked by purple crosses. The contour maps integrate the intensity from -6.0 to 2.0 km s^{-1}. The rms (σ) of five line maps, ^{12}CO, ^{13}CO, C^{18}O, HCN, and HCO$^+$, are 0.40, 0.22, 0.22, 0.06, and 0.06 K km s^{-1}, respectively, and these contours all begin at 8σ, with 21, 14, 2, 3, and 3σ spacing, respectively.

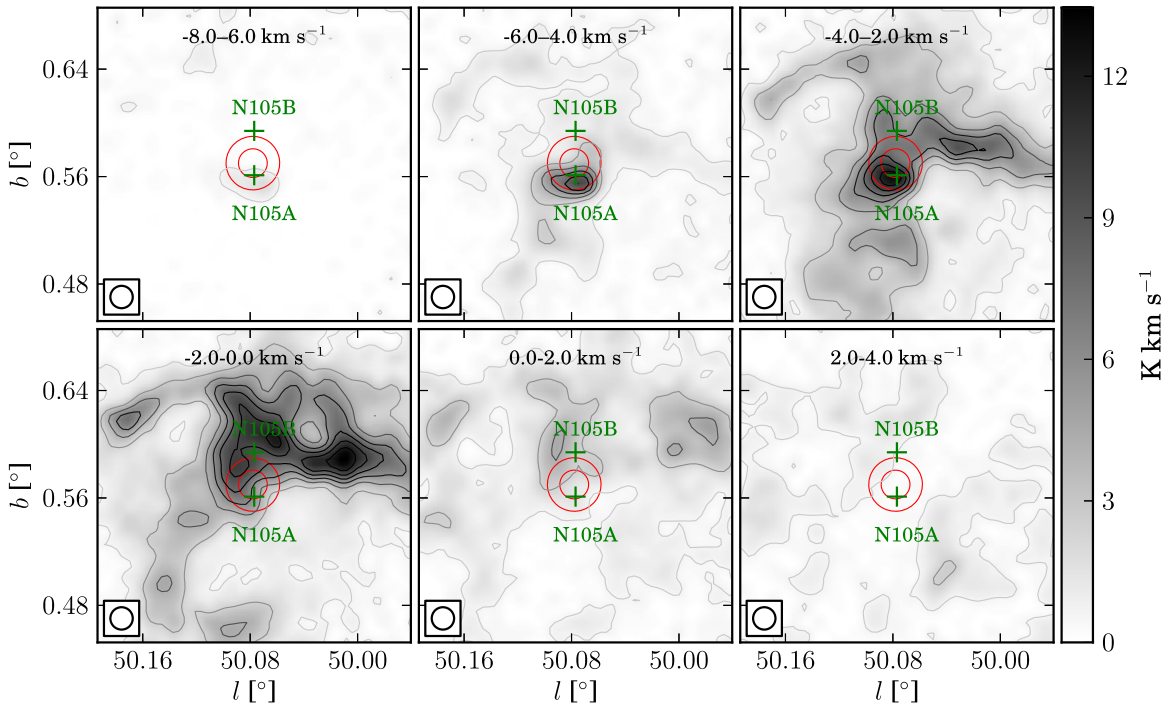

Figure 24. Channel map of ^{13}CO for bubble N105 from -8.0 to 4.0 km s^{-1} with 2.0 km s^{-1} intervals. The red circles delineate the position of N105 provided by Simpson et al. (2012), and the green crosses mark the peak position of clumps. The rms (σ) of the image background is about 0.11 K km s^{-1}, and the contour levels space linearly from 5σ to the peak with step 17σ.

We identified outflows by checking the profiles, integrated intensity maps, and position–velocity (P–V) diagrams, in which outflows are characterized with protruding structures (Smith et al. 1997; Beuther et al. 2004). However, we must be cautious about interpreting wing profiles of near-infrared bubbles as outflows, because the interaction between bubbles and molecular clouds can also produce similar structures. Therefore, the intensity maps of lobes are also required to be clearly

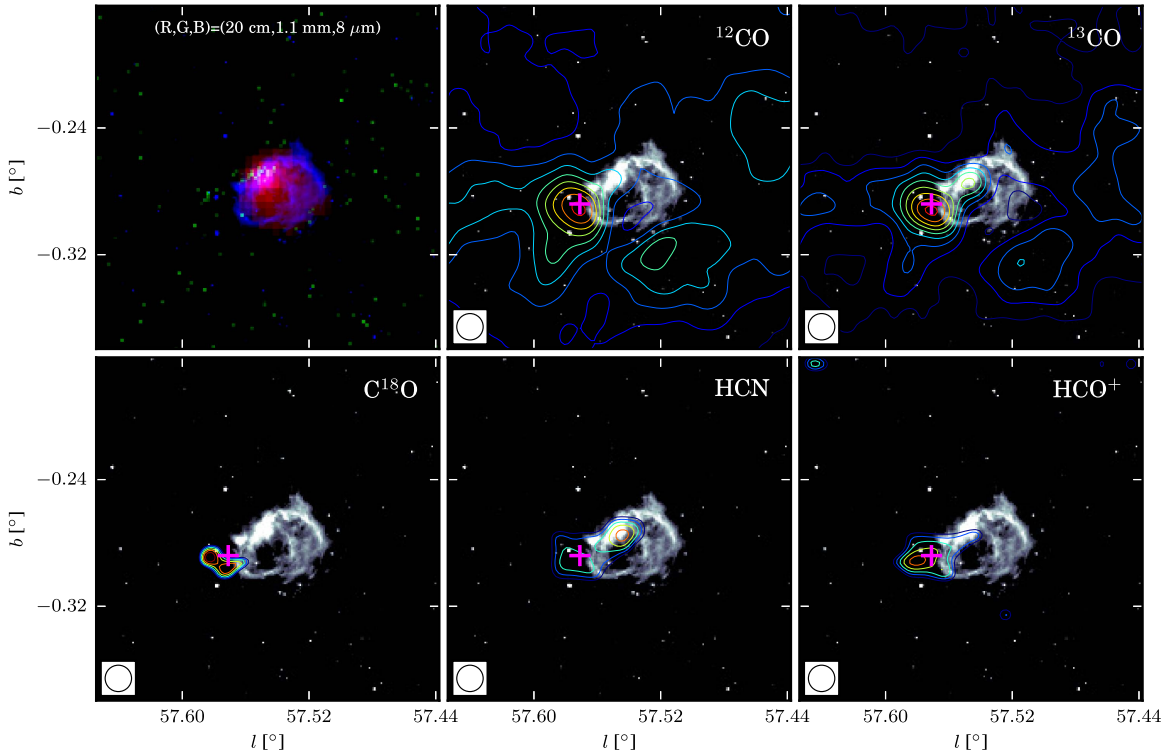

Figure 25. Images of N123. The upper left panel is a three-color image with 20 cm in red, 1.1 mm in green, and 8 μm in blue. The other five panels are contours of five spectral line integrated intensity maps superimposed on 8 μm image with positions of clumps marked by purple crosses. The contour maps integrate the intensity from −4.0 to 6.0 km s^{-1}. The rms (σ) of five line maps, ^{12}CO, ^{13}CO, C^{18}O, HCN, and HCO^{+}, are 0.26, 0.17, 0.16, 0.05, and 0.06 K km s^{-1}, respectively, and these contours all begin at 8σ, with 27, 13, 1, 3, and 3σ spacing, respectively.

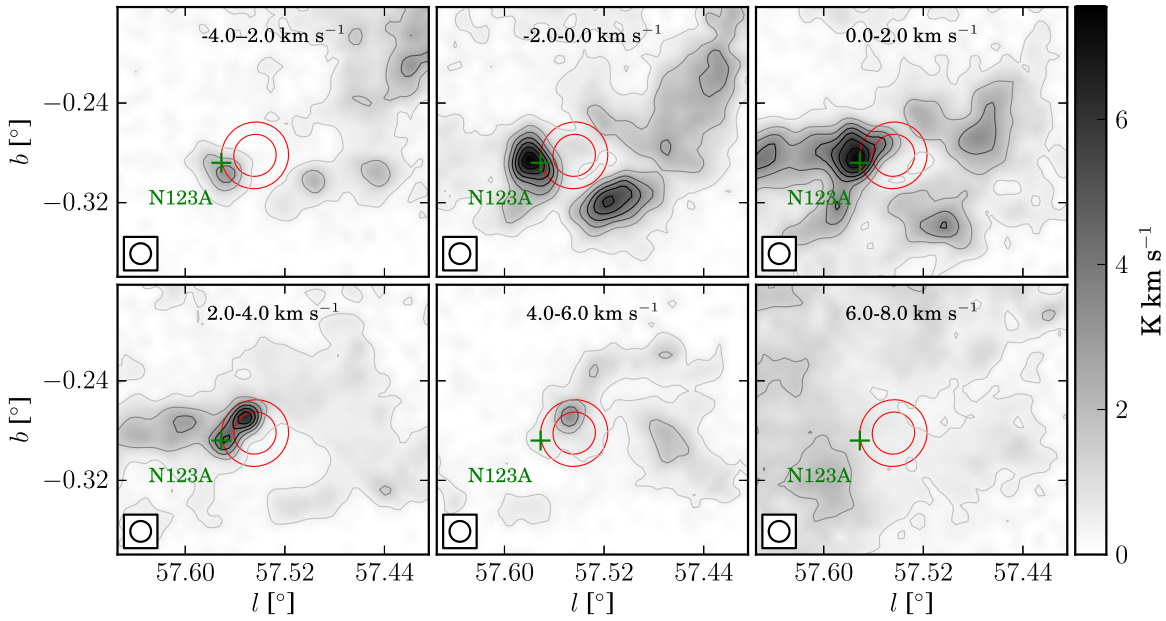

Figure 26. Channel map of ^{13}CO for bubble N123 from −4.0 to 8.0 km s^{-1} with 2.0 km s^{-1} intervals. The red circles delineate the position of N123 provided by Simpson et al. (2012), and the green cross marks the peak position of the clump. The rms (σ) of the image background is about 0.11 K km s^{-1}, and the contour levels space linearly from 5σ to the peak with step 13.7σ.

distinguished from background emissions, and, most importantly, the line wings should be significantly wide.

The specific steps to identify an outflow were:

1. Estimate the center velocity and position of the drive source using C^{18}O line. For a molecular clump in Table 5, we integrated the C^{18}O line over the entire velocity range, and regard the peak of the integrated intensity map of C^{18}O as the possible position of the driven source. Subsequently, we determined the center velocity using the averaged C^{18}O profile over the peak position and its adjacent pixels (within 1 arcmin).
2. To improve SNRs of lines, we smooth the CO and HCO^{+} lines to a velocity resolution of 0.8 km s^{-1}. This is slightly smaller than the value adopted by Zhang et al.

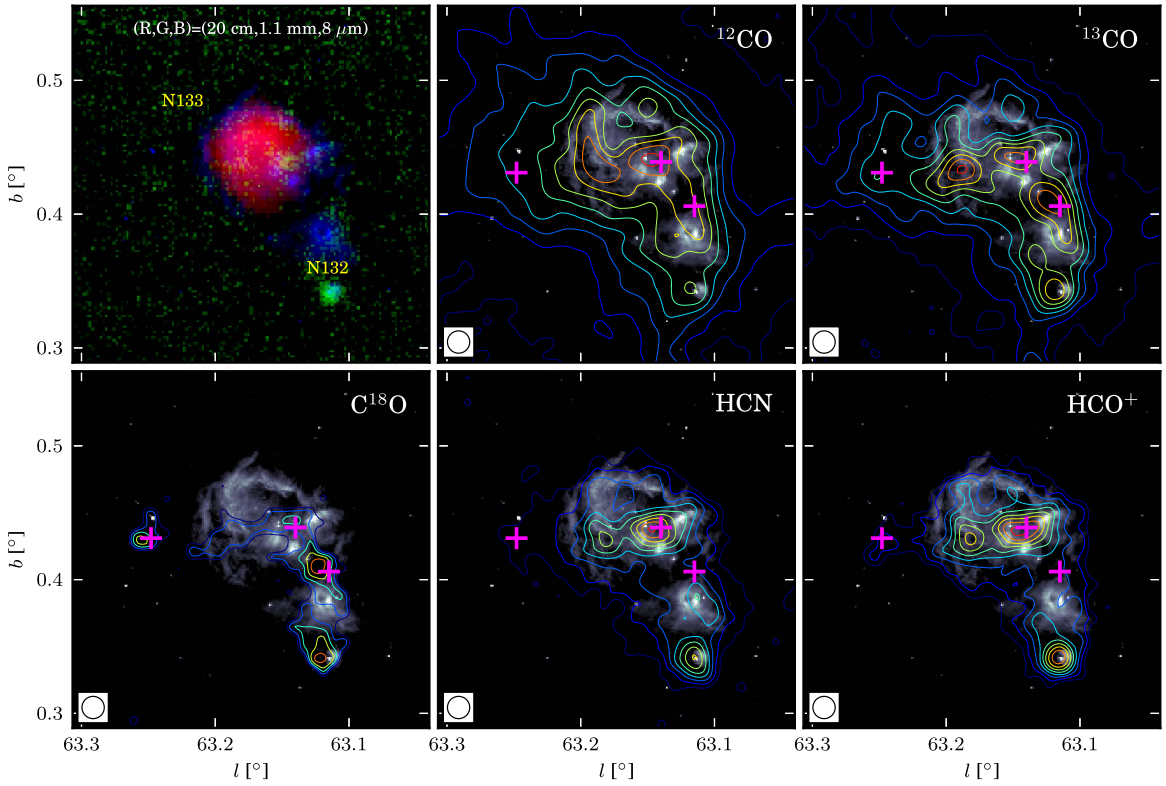

Figure 27. Images of N133. The upper left panel is a three-color image with 20 cm in red, 1.1 mm in green, and 8 μm in blue. The other five panels are contours of five spectral line integrated intensity maps superimposed on the 8 μm image with positions of clumps marked by purple crosses. The contour maps integrate from 15.0 to 25.0 km s^{-1}. The rms (σ) of five line maps, ^{12}CO, ^{13}CO, C^{18}O, HCN, and HCO^{+}, are 0.46, 0.25, 0.24, 0.07, and 0.08 K km s^{-1}, respectively, and these contours all begin at 8σ, with 40, 19, 3, 7, and 5σ spacing, respectively.

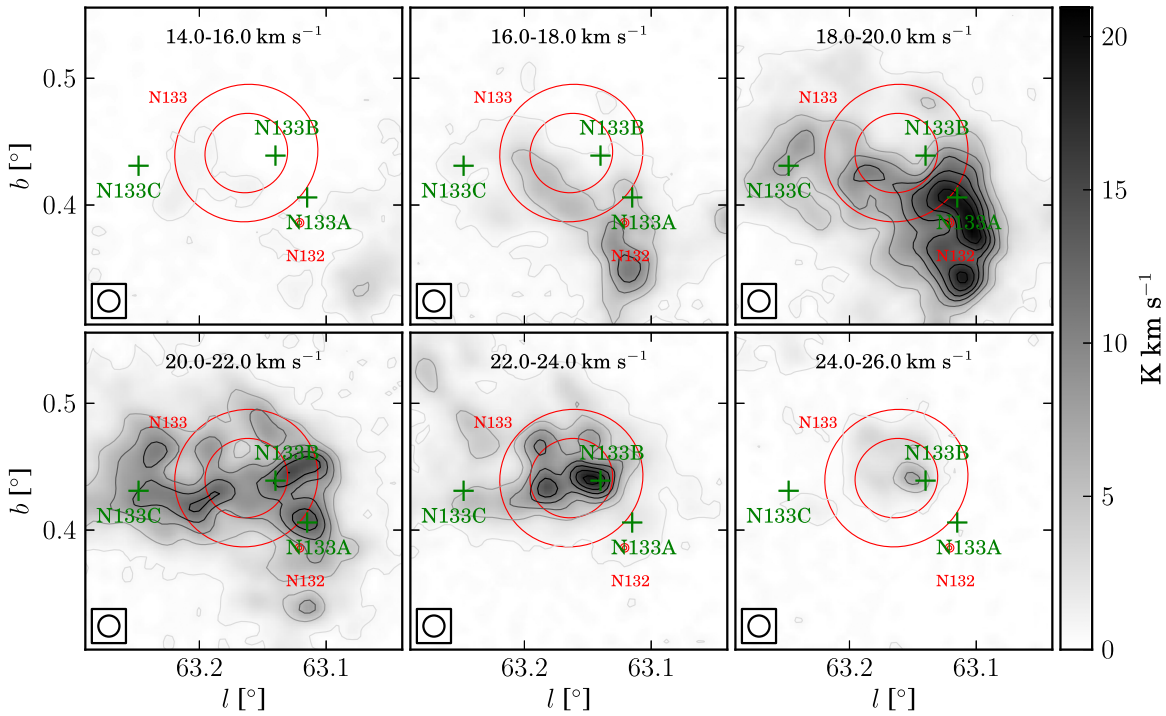

Figure 28. Channel map of ^{13}CO for bubble N133 from 14.0 to 26.0 km s^{-1} with 2.0 km s^{-1} intervals. The red circles delineate the position of N133 offered by Simpson et al. (2012), and the green crosses mark the peak position of clumps. The rms (σ) of the image background is about 0.11 K km s^{-1}, and the contour levels space linearly from 5σ to the peak with step 26.3σ.

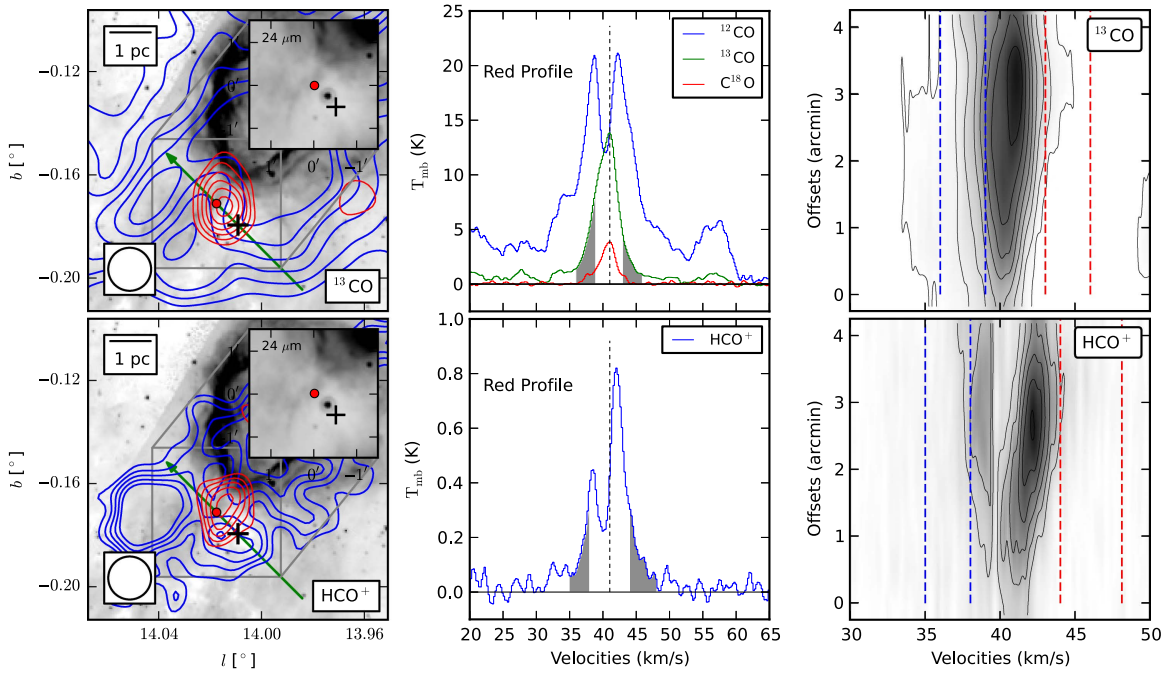

Figure 29. Outflow map of N14. The left map shows the 8 μm background image with the ^{13}CO ($J = 1 \rightarrow 0$) integrated intensity contour map superimposed on it. The inset shows a close section of the MIPSGAL 24 μm image. The integrating ranges for the blue and red lobes are shown in the line profiles and position–velocity (P–V) slice maps. The black cross marks the peak position of the C^{18}O integrated intensity map. The green arrow delineates the origin and direction of the P–V diagram. The ^{12}CO contours start at the 50% level and increase by 10% of the peak value, while the HCO$^+$ contours start at the 60% level and increase by 10% of the peak value.

(2005), about 1 km s^{-1}, which is sufficient to identify outflows with different kinds of masses.

3. Determine the velocity ranges of red and blue wings using the ^{12}CO or HCO$^+$line. We keep the velocity interval between the center velocity and the inner edge of the red and blue lobes equal, and extend the outer end of their velocity ranges to the first zero point of their line profiles. We gradually increased this velocity interval until at least one integrated intensity map of the two lobes was clearly distinguished from the background.
4. Draw the P–V diagram to confirm outflow wings.

We collected samples for searching for outflows by visually investigating the ^{12}CO or HCO$^+$ profiles of the bubble regions. For a bubble, if the red or blue or both ends of the profiles are uncontaminated by other components, it was appended to the sample list. There were six bubbles in this list: N14, N37, N55, N74, N105, and N133. Although the CO profiles of N37 and N14 are complicated, as shown in Figure 1, their HCO$^+$ emissions are relatively strong and uncontaminated, and therefore they are included in our samples. We also used 24 μm (Carey et al. 2009; Gutermuth & Heyer 2015) emissions, which can trace the warmed dust emissions probably heated by protostellars, for confirmation.

Four of these six samples, N14, N55, N105, and N133, are found harboring an outflow candidate. However, only N55 shows evident bipolar structure, while the other three bubbles display single wings that are mainly due to the contamination of adjacent components with similar velocities.

We checked the outflow candidates identified by Beaumont & Williams (2010) using an visual method based on CO ($J = 3 \rightarrow 2$). Three of their candidates, N37, N49, and N74, were included in our bubble observations. For the clumps near N37, the ^{12}CO emissions are quite complex in the velocity range 30–40 km s^{-1}, while no clear line wing is shown by HCO$^+$. Furthermore, no 24 μm source was found in these clumps, indicating that no outflow is present here. For N49, both of the CO and HCO$^+$ profiles are severely contaminated by adjacent components with approximate velocities. Consequently, we cannot perform outflow identification for this region. The outflow candidate near N74 is actually associated with N75; however, there are two components present here, which makes it difficult to identify outflows.

Following Snell et al. (1984), we calculated the mass, momentum, and energy entrained in the outflowing gas without any projection effect calibrated. The LTE assumption was applied, and we also assumed that the optical depth of the ^{12}CO was thin at line wings. ^{12}CO column densities were estimated by

$$N_{^{12}\mathrm{CO}} = \frac{4.2 \times 10^{13} T_{\mathrm{ex}} \int T_R(^{12}\mathrm{CO})\, dV}{\exp(-5.5/T_{\mathrm{ex}})}\ \mathrm{cm}^{-2}, \qquad (10)$$

where T_{ex} is the excitation temperature of ^{12}CO, calculated using the ^{12}CO ($J = 1 \rightarrow 0$) bright temperature at line centers; and $\int T_R(^{12}\mathrm{CO})\, dV$ is the integrated intensity over the velocity range of lobes (Snell et al. 1984). The spectrum was averaged over the area that is determined by the half peak value contour of the integrated intensity over the corresponding velocity range. We adopted a value of $\sim 1 \times 10^4$ for the ratio of the ^{12}CO to H_2 column density, $N(H_2)/N(^{12}\mathrm{CO})$, following Snell et al. (1984).

The momentum, P, is proportional to $\Sigma \int T_R(^{12}\mathrm{CO})\, V dV$, and the energy, E, is proportional to $\Sigma \int T_R(^{12}\mathrm{CO})\, V^2 dV$, where V is the velocity of gas with respect to the driven source. The scale of a single lobe is defined by the the separation between the lobe peaks and the central driven source. The dynamical age,

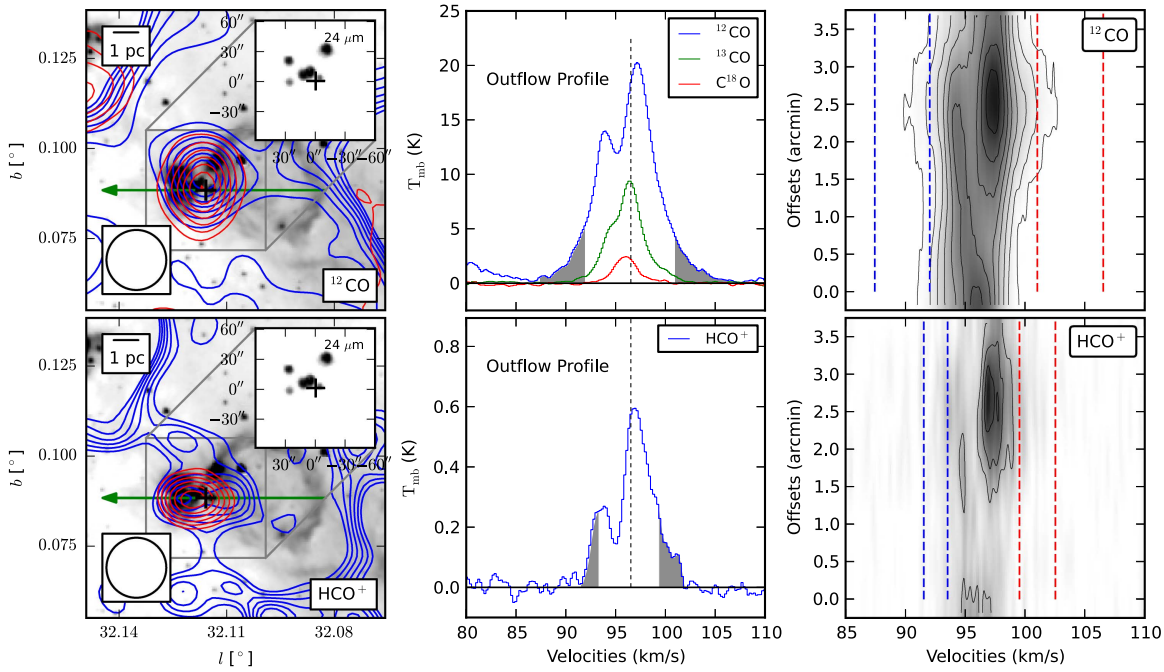

Figure 30. Outflow maps of N55. The left map shows the 8 μm background image with the ^{12}CO ($J = 1 \rightarrow 0$) integrated intensity contour map superimposed on it. The inset shows a close section of the MIPSGAL 24 μm emissions. The integrating ranges for the blue and red lobes are shown in the line profiles and position–velocity (P–V) slice maps. The black cross marks the peak position of the C^{18}O integrated intensity map. The green arrow delineates the origin and direction of the P–V diagram. The ^{12}CO contours start at the 40% level and increase by 10% of the peak, while the HCO$^+$ contours start at 50% and increase by 10% of the peak value.

$t_{\rm dyn}$, was estimated simply by dividing the scale by the mean outflow velocity that is defined as P/M (Cabrit & Bertout 1990). The rate of outflow mass, $\dot{M} = M/t_{\rm dyn}$, the mechanical force, $F_{\rm outflow} = P/t_{\rm dyn}$, and the outflow luminosity $L_{\rm outflow} = E/t_{\rm dyn}$, were also calculated. Details regarding the calculation of outflow parameters can be found in Shepherd & Churchwell (1996) and Zhang et al. (2005). The estimated parameters are summarized in Table 6.

3.5.1. Outflow N14

Although CO profiles provided limited information about this outflow due to their complexities, HCO$^+$ reveals an outflow with a clear red wing near N14, as shown in Figure 29.

The drive source of this outflow is probably located in the clump N14A, toward which we found a 24 μm point source that probably marks a more precise position of the driven source. A clearly protruded structure can be seen in the P–V diagram of the ^{13}CO lines, as demonstrated in Figure 29. However, we cannot calculate the outflow parameters because the CO profiles of this region are exceedingly complicated.

3.5.2. Outflow N55

This is a bipolar outflow, and as shown in Figure 30, the red and blue wings of the CO profiles are wide. There are several UC H II regions traced by the 20 cm continuum in the clump N55A that are associated with this outflow candidate. Consequently, there is probably more than one driven source here, and they are most likely high mass. Because they are not resolved by our observation, we simply treat this candidate as a single outflow when calculating its parameters. However, we cannot estimate the outflow scale, because the blue lobe totally overlaps the red one. Consequently, the time-related parameters cannot be calculated either.

3.5.3. Outflow N105

This single pole outflow candidate was located in the clump N105B, and its ^{12}CO profile displayed a wide clear blue wing, as shown in Figure 31. Unfortunately, the red end of the profile is slightly contaminated by another component. Near the peak of the C^{18}O integrated intensity map, we found a 24 μm continuum source that is probably tracing the driven source. We did not draw HCO$^+$ line maps due to its low SNR. The P–V diagram of ^{12}CO displays a clearly protruded structure, confirming the existence of the outflow.

3.5.4. Outflow N133

The blue profiles in this region are mixed with another component located near N133. However, the ^{12}CO, ^{13}CO, and HCO$^+$ line profiles shows clear red wings, which indicates an outflow may be present here. As shown in Figure 32, there are several 24 μm sources around the C^{18}O clump. Consequently, we could not distinguish which was responsible for this outflow, due to the limited resolution.

4. DISCUSSION

4.1. Molecular Clouds and Clumps Around Bubbles

Our observations show that all 18 bubbles are associated with molecular clouds, and the majority are giant and characterized with complex profiles. All five molecular lines were detected for all bubbles except N89 and N90, where C^{18}O emissions were absent and HCO$^+$ emissions were relatively weak. Clumps present around all 18 bubbles, as well as molecular clouds near four of these bubbles (N4, N14, N49, and N133), display shell morphologies. As shown in Figure 1, some molecular clouds exhibited broad-shifted profiles (e.g., MWP1G032057+000783, N82, and N95). These profiles

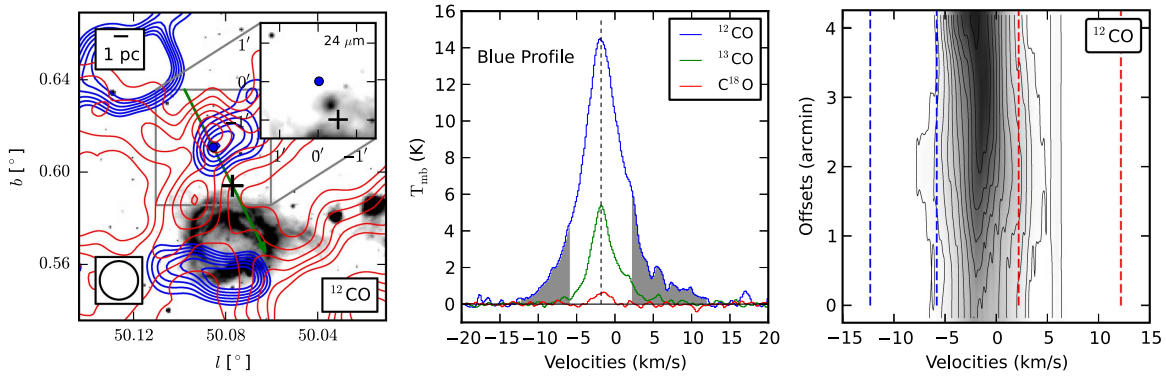

Figure 31. Outflow maps of N105. The left map shows the 8 μm background image with ^{12}CO ($J = 1 \rightarrow 0$) integrated intensity contour map superimposed on it. The inset shows a close section of the MIPSGAL 24 μm background. The integrating ranges for the blue and red lobes are shown in the line profiles and position–velocity (P–V) slice map. The black cross marks the peak position of C^{18}O integrated intensity map. The green arrow delineates the origin and direction of the P–V diagram. The ^{12}CO contour levels start at 50%, and increase by 10% of the peak value.

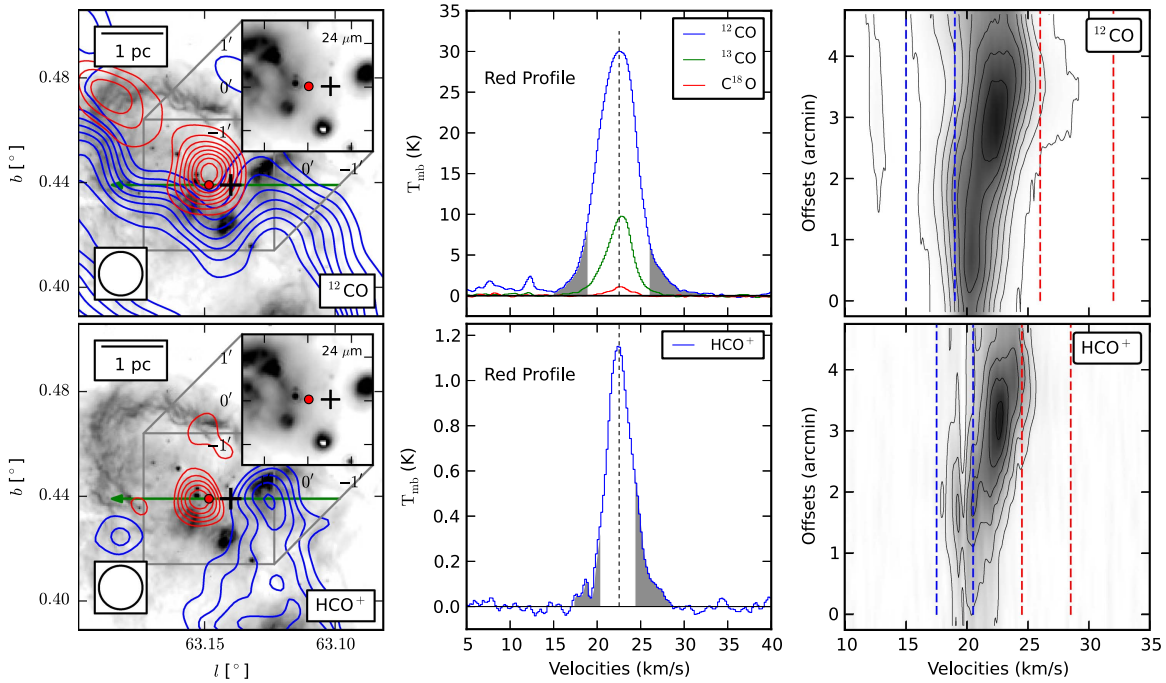

Figure 32. Outflow maps of N133. The left map shows the 8 μm background image with the ^{12}CO ($J = 1 \rightarrow 0$) integrated intensity contour map superimposed on it. The inset shows a close section of the MIPSGAL 24 μm background. The integrating ranges for the blue and red lobes are shown in the line profiles and position–velocity (P–V) slice maps. The black cross marks the peak position of C^{18}O integrated intensity map. The green arrow delineates the origin and direction of the P–V diagram. The ^{12}CO contours start at 30% and increase by 10% of the peak, while the HCO$^+$ contours start at 50% and increase by 10% of the peak.

deviate significantly from the Gaussian curve, which indicates that their environments are greatly affected by the expansion of H II regions. Because these profiles are similar to those displayed by molecular clouds interacting with supernova remnants (SNRs; Su et al. 2014; Zhou et al. 2014), we speculate that these bubbles are probably sweeping the molecular clouds. However, we should be aware that these broad-line features could also be caused by adjacent components and cloud-wide rotation. Because these broad-line features are situated near bubbles, we believe that the interaction between bubbles and their surrounding molecular clouds is the more likely explanation.

We estimated physical properties for the molecular clouds and clumps using three isotopic CO lines, based on LTE assumption. Average spectra were used when calculating the mass for each bubble, and the optical depths calculated from ^{13}CO were generally below 0.5, supporting the assumption of optically thin for the ^{13}CO line. Molecular cloud masses within the bubble regions are of the order 10^3–$10^4\,M_\odot$, which is close to the value of $\sim 10^4\,M_\odot$ calculated by Hosokawa & Inutsuka (2005) for a high-mass star with an age of 1 Myr. According to our calculations, most molecular clumps possess a typical mass of $10^3\,M_\odot$, and the line width of C^{18}O is generally 2 km s^{-1}. However, these masses inevitability include the envelopes around the molecular clumps, and they should be treated as upper limits. Nonetheless, 12 of the 23 identified molecular clumps possess virial masses that are significantly smaller than LTE masses, indicating these clumps are mostly gravitationally bound.

4.2. Outflows and SF Processes

Most of the bubbles display complex profiles due to the complicated environment associated with high-mass stars. We

found that 6 of the 18 bubble regions satisfy the requirements for searching for outflows, which means that at least one end of their profiles is uncontaminated. We identified four outflow candidates from four bubble regions: N14, N55, N105, and N133. However, only N55 displays a bipolar structure, and the other three outflows show single lobes.

The detection ratio of outflows is approximately 67% based on our biased samples. The presence of outflows indicates that SF processes are indeed occurring around the bubbles, which are essentially expanding H II regions. Previous studies of SFs around bubbles mainly focused on YSOs. However, it is hard to determine the masses and ages of those YSOs. In contrast, outflows are reliable tracers of ongoing SF, and are more powerful tools to confirm the existence of SF activity. The estimated dynamical ages for outflows near N105 and N133 are about 0.4 and 0.07 Myr, respectively, while the ages of bubble N105 and N133 are approximately 1.6 and 0.4 Myr, respectively, which are both significantly larger than the ages of outflows. Limited by the spatial resolution of PMODLH, we speculate that the SF processes around these bubbles might be triggered or accelerated by expanding H II regions. However, higher spatial resolution observations are needed to confirm the relationships between bubbles and SF processes around them.

Zhang et al. (2005) carried out an CO ($J = 2 \rightarrow 1$) survey toward 69 high-mass *IRAS* sources, with a resolution of approximately 29″, and found a typical energy of 1×10^{46} erg for the identified outflows. The energy of the blue lobe of the N105 outflow is approximately 1.3×10^{46} erg, and the sum energy of the red and blue lobe of N55 is about 1.6×10^{46} erg. Therefore, the drive sources of these two outflows are probably high mass. We performed a search for EGOs for the clumps that are associated with these four outflows using the method mentioned by Cyganowski et al. (2008). However, we did not find any EGO from these clumps, and no corresponding source was found in their catalog. Two possibilities can be responsible for this result: one is that these two outflows are not high mass, the other is that they are not evolved enough to exhibit excessive 4.5 μm emission, which is mainly tracing shocked molecular gas.

Interestingly, three bubbles, N55, N49, and N123, display UC H II regions at their borders, which are traced by 20 or 6 cm continuum emission. These UC H II regions are mostly tracing high-mass stars that could be triggered by bubbles.

4.3. Compare with Previous Molecular Line Studies on Bubbles

Some investigations of single bubbles using GRS ^{13}CO ($J = 1 \rightarrow 0$) data show that clumps are also present in the vicinity of bubbles beyond our samples. For instance, Petriella et al. (2010) found that some clumps near N65 are probably produced by the fragmentation of their natal molecular clouds, and they speculate that the collect-and-collapse process might be occurring here, which is consistent with what we have found. Furthermore, they identified an EGO in the molecular shell, the mass of which is the same order of magnitude with the clumps identified by us. They identified 22 YSO candidates around N65, and, according to the result of SED fitting for those YSOs, they concluded that the formation of a second generation of stars had occurred. Similar results are found around N107 (Sidorin et al. 2014) and N115 (Xu & Ju 2014). The age of N107 is about 2 Myr, while the age of N115 is about 1.5 Myr. These two values are approximate with the estimated ages of our samples. The molecular mass along the border of N107 is about $4.0 \times 10^4\,M_\odot$, which is comparable with our results.

Hou & Gao (2014) performed a statistical study of infrared bubbles using GRS ^{13}CO ($J = 1 \rightarrow 0$) data. They found that 60 percent of 309 MWP bubbles are associated with molecular clumps. The correlation between bubble morphology and molecular gas distribution made them believe some of the clumps near the bubbles were produced by the expansion of bubbles.

All these studies show that bubbles are likely associated with clumps. According to single bubble studies, the typical age of bubbles is 1 Myr, and the mass of molecular clouds along their borders is approximately $1 \times 10^4\,M_\odot$.

5. CONCLUSIONS

We presented an investigation of 13 regions containing 18 infrared bubbles, using three CO isotopic lines and two high-density molecular lines, HCO^+ and HCN ($J = 1 \rightarrow 0$). Some profiles of bubble regions show broad redshifted ^{12}CO profiles, arc structures, and ^{12}CO velocity gradients, indicating they are probably interacting with the molecular clouds around them. Most of the bubbles are associated with dense molecular gas traced by HCO^+ and HCN; we used $C^{18}O$ to identify 24 molecular clumps near 18 infrared bubbles. Most of these molecular clumps are gravitationally bound. These facts are generally in agreement with either the collect-and-collapse or the RDI model.

A search of the outflow was carried out in six bubble regions. Four bubble regions, N14, N37, N55, and N133, show outflow activities, while only N55 shows a bipolar structure. The energy of outflows indicates that the driven source of this outflow is probably high mass; however, no EGO was found toward these outflow candidates. These outflows are convincing evidence that the SF processes are occurring around bubbles. Aside from outflows, UC H II regions are found on the border of N55, N49, and N123. Among the 18 selected bubbles, 6 bubbles possess SF activities nearby, and the detection ratio of outflows and UC H II regions near bubbles is about 0.3. We speculate that SF processes might have been triggered around these bubbles. However, higher spatial resolution observations are needed to confirm these SF activities.

We are grateful to two anonymous referees for careful readings of the manuscript and constructive comments that made this study complete. Thanks to P. Tremblin for providing a machine-readable data set result of numerical simulation of the expansion of H II regions in turbulent environments. We would also like to thank Sam McSweeney for his helpful report. This work was supported by the National Science Foundation of China (Grants No. 11233007 and 11133008), the National Science Foundation of Shanghai (Grant No. 15ZR1446900), and the Key Laboratory for Radio Astronomy, CAS.

REFERENCES

Aguirre, J. E., Ginsburg, A. G., Dunham, M. K., et al. 2011, ApJS, 192, 4
Alexander, M. J., Kobulnicky, H. A., Kerton, C. R., & Arvidsson, K. 2013, ApJ, 770, 1
Anderson, L. D., & Bania, T. M. 2009, ApJ, 690, 706

Anderson, L. D., Bania, T. M., Balser, D. S., & Rood, R. T. 2011, ApJS, 194, 32
Anderson, L. D., Bania, T. M., Balser, D. S., & Rood, R. T. 2012a, ApJ, 754, 62
Anderson, L. D., Bania, T. M., Balser, D. S., et al. 2014, ApJS, 212, 1
Anderson, L. D., Zavagno, A., Deharveng, L., et al. 2012b, A&A, 542, A10
Bania, T. M., Anderson, L. D., & Balser, D. S. 2012, ApJ, 759, 96
Beaumont, C. N., & Williams, J. P. 2010, ApJ, 709, 791
Benjamin, R. A., Churchwell, E., Babler, B. L., et al. 2003, PASP, 115, 953
Bergin, E. A., & Tafalla, M. 2007, ARA&A, 45, 339
Bertoldi, F. 1989, ApJ, 346, 735
Beuther, H., Schilke, P., & Gueth, F. 2004, ApJ, 608, 330
Cabrit, S., & Bertout, C. 1990, ApJ, 348, 530
Carey, S. J., Noriega-Crespo, A., Mizuno, D. R., et al. 2009, PASP, 121, 76
Caswell, J. L., Vaile, R. A., Ellingsen, S. P., Whiteoak, J. B., & Norris, R. P. 1995, MNRAS, 272, 96
Christopher, M. H., Scoville, N. Z., Stolovy, S. R., & Yun, M. S. 2005, ApJ, 622, 346
Churchwell, E., Babler, B. L., Meade, M. R., et al. 2009, PASP, 121, 213
Churchwell, E., Povich, M. S., Allen, D., et al. 2006, ApJ, 649, 759
Churchwell, E., Watson, D. F., Povich, M. S., et al. 2007, ApJ, 670, 428
Condon, J. J., Cotton, W. D., Greisen, E. W., et al. 1998, AJ, 115, 1693
Cyganowski, C. J., Brogan, C. L., Hunter, T. R., & Churchwell, E. 2009, ApJ, 702, 1615
Cyganowski, C. J., Koda, J., Rosolowsky, E., et al. 2013, ApJ, 764, 61
Cyganowski, C. J., Whitney, B. A., Holden, E., et al. 2008, AJ, 136, 2391
Dale, J. E., Haworth, T. J., & Bressert, E. 2015, MNRAS, 450, 1199
Dame, T. M., Hartmann, D., & Thaddeus, P. 2001, ApJ, 547, 792
Deharveng, L., Schuller, F., Anderson, L. D., et al. 2010, A&A, 523, A6
Deharveng, L., Zavagno, A., & Caplan, J. 2005, A&A, 433, 565
Dewangan, L. K., & Ojha, D. K. 2013, MNRAS, 429, 1386
Elmegreen, B. G., & Lada, C. J. 1977, ApJ, 214, 725
Everett, J. E., & Churchwell, E. 2010, ApJ, 713, 592
Frerking, M. A., Langer, W. D., & Wilson, R. W. 1982, ApJ, 262, 590
Gutermuth, R. A., & Heyer, M. 2015, AJ, 149, 64
Helfand, D. J., Becker, R. H., White, R. L., Fallon, A., & Tuttle, S. 2006, AJ, 131, 2525
Heyer, M., & Dame, T. M. 2015, ARA&A, 53, 583
Hildebrand, R. H. 1983, QJRAS, 24, 267
Hollenbach, D. J., & Tielens, A. G. G. M. 1997, ARA&A, 35, 179
Hosokawa, T., & Inutsuka, S.-i. 2005, ApJ, 623, 917
Hou, L. G., & Gao, X. Y. 2014, MNRAS, 438, 426
Jackson, J. M., Rathborne, J. M., Shah, R. Y., et al. 2006, ApJS, 163, 145
Ji, W.-G., Zhou, J.-J., Esimbek, J., et al. 2012, A&A, 544, A39
Kaufman, M. J., Wolfire, M. G., Hollenbach, D. J., & Luhman, M. L. 1999, ApJ, 527, 795
Kendrew, S., Simpson, R., Bressert, E., et al. 2012, ApJ, 755, 71
Lafon, G., Baudry, A., de La Noe, J., & Deharveng, L. 1983, A&A, 124, 1
Leger, A., & Puget, J. L. 1984, A&A, 137, L5
Li, J.-Y., Jiang, Z.-B., Liu, Y., & Wang, Y. 2013, RAA, 13, 921
Liu, X.-L., Wang, J.-J., & Xu, J.-L. 2014, MNRAS, 443, 2264
Lockman, F. J. 1989, ApJS, 71, 469
MacLaren, I., Richardson, K. M., & Wolfendale, A. W. 1988, ApJ, 333, 821
Nagahama, T., Mizuno, A., Ogawa, H., & Fukui, Y. 1998, AJ, 116, 336
Petriella, A., Paron, S., & Giacani, E. 2010, A&A, 513, A44
Rahman, M., & Murray, N. 2010, ApJ, 719, 1104
Rawlings, J. M. C., Redman, M. P., Keto, E., & Williams, D. A. 2004, MNRAS, 351, 1054
Roman-Duval, J., Jackson, J. M., Heyer, M., et al. 2009, ApJ, 699, 1153
Rosolowsky, E., Dunham, M. K., Ginsburg, A., et al. 2010, ApJS, 188, 123
Samal, M. R., Zavagno, A., Deharveng, L., et al. 2014, A&A, 566, A122
Sawada, T., Hasegawa, T., Sugimoto, M., Koda, J., & Handa, T. 2012, ApJ, 752, 118
Schuller, F., Menten, K. M., Contreras, Y., et al. 2009, A&A, 504, 415
Scoville, N. Z., Sargent, A. I., Sanders, D. B., et al. 1986, ApJ, 303, 416
Shan, W., Yang, J., Shi, S., et al. 2012, IEEE, 2, 593
Shepherd, D. S., & Churchwell, E. 1996, ApJ, 472, 225
Sherman, R. A. 2012, ApJ, 760, 58
Shirley, Y. L. 2015, PASP, 127, 299
Sidorin, V., Douglas, K. A., Palouš, J., Wünsch, R., & Ehlerová, S. 2014, A&A, 565, A6
Simpson, R. J., Povich, M. S., Kendrew, S., et al. 2012, MNRAS, 424, 2442
Smith, M. D., Suttner, G., & Yorke, H. W. 1997, A&A, 323, 223
Snell, R. L., Scoville, N. Z., Sanders, D. B., & Erickson, N. R. 1984, ApJ, 284, 176
Sobolev, A. M., Ostrovskii, A. B., Kirsanova, M. S., et al. 2005, IAUS, 227, 174
Stead, J. J., & Hoare, M. G. 2010, MNRAS, 407, 923
Stead, J. J., & Hoare, M. G. 2011, MNRAS, 418, 2219
Stil, J. M., Taylor, A. R., Dickey, J. M., et al. 2006, AJ, 132, 1158
Su, Y., Yang, J., Zhou, X., Zhou, P., & Chen, Y. 2014, ApJ, 796, 122
Thompson, M. A., Urquhart, J. S., Moore, T. J. T., & Morgan, L. K. 2012, MNRAS, 421, 408
Tremblin, P., Anderson, L. D., Didelon, P., et al. 2014, A&A, 568, A4
Watson, C., Araya, E., Sewilo, M., et al. 2003, ApJ, 587, 714
Watson, C., Corn, T., Churchwell, E. B., et al. 2009, ApJ, 694, 546
Watson, C., Hanspal, U., & Mengistu, A. 2010, ApJ, 716, 1478
Watson, C., Povich, M. S., Churchwell, E. B., et al. 2008, ApJ, 681, 1341
Wenger, T. V., Bania, T. M., Balser, D. S., & Anderson, L. D. 2013, ApJ, 764, 34
White, R. L., Becker, R. H., & Helfand, D. J. 2005, AJ, 130, 586
Wu, J., Evans, N. J., II, Shirley, Y. L., & Knez, C. 2010, ApJS, 188, 313
Xu, J.-L., & Ju, B.-G. 2014, A&A, 569, A36
Yoshida, A., Kitamura, Y., Shimajiri, Y., & Kawabe, R. 2010, ApJ, 718, 1019
Yuan, J.-H., Wu, Y., Li, J. Z., & Liu, H. 2014, ApJ, 797, 40
Zavagno, A., Anderson, L. D., Russeil, D., et al. 2010, A&A, 518, L101
Zhang, Q., Hunter, T. R., Brand, J., et al. 2001, ApJL, 552, L167
Zhang, Q., Hunter, T. R., Brand, J., et al. 2005, ApJ, 625, 864
Zhou, X., Yang, J., Fang, M., & Su, Y. 2014, ApJ, 791, 109

Monthly Notices
of the
ROYAL ASTRONOMICAL SOCIETY

MNRAS **471,** 2523–2536 (2017)
Advance Access publication 2017 July 13

doi:10.1093/mnras/stx1724

Towards a three-dimensional distribution of the molecular clouds in the Galactic Centre

Qing-Zeng Yan,[1,2,3★] A. J. Walsh,[2★] J. R. Dawson,[4,5★] J. P. Macquart,[2] R. Blackwell,[6] M. G. Burton,[7,8] G. P. Rowell,[6] Bo Zhang,[1] Ye Xu,[9] Zheng-Hong Tang[1] and P. J. Hancock[2]

[1]*Shanghai Astronomical Observatory, Chinese Academy of Sciences, Shanghai 200030, China*
[2]*International Centre for Radio Astronomy Research, Curtin University, GPO Box U1987, Perth WA 6845, Australia*
[3]*University of Chinese Academy of Sciences, 19A Yuquanlu, Beijing 100049, China*
[4]*Department of Physics and Astronomy and MQ Research Centre in Astronomy, Astrophysics and Astrophotonics, Macquarie University, NSW 2109, Australia*
[5]*Australia Telescope National Facility, CSIRO Astronomy and Space Science, PO Boc 76, Epping, NSW 1710, Australia*
[6]*School of Physical Sciences, University of Adelaide 5005, South Australia, Australia*
[7]*School of Physics, University of New South Wales 2052, New South Wales, Australia*
[8]*Armagh Observatory & Planetarium, College Hill, Armagh BT61 9DG, Northern Ireland, UK*
[9]*Purple Mountain Observatory, Chinese Academy of Science, Nanjing 210008, China*

Accepted 2017 July 7. Received 2017 June 30; in original form 2017 March 29

ABSTRACT

We present a study of the three-dimensional structure of the molecular clouds in the Galactic Centre (GC) using CO emission and OH absorption lines. Two CO isotopologue lines, ^{12}CO($J = 1 \rightarrow 0$) and ^{13}CO($J = 1 \rightarrow 0$), and four OH ground-state transitions, surveyed by the Southern Parkes Large-Area Survey in Hydroxyl, contribute to this study. We develop a novel method to calculate the OH column density, excitation temperature and optical depth precisely using all four OH lines, and we employ it to derive a three-dimensional model for the distribution of molecular clouds in the GC for six slices in Galactic latitude. The angular resolution of the data is 15.5 arcmin, which at the distance of the GC (8.34 kpc) is equivalent to 38 pc. We find that the total mass of OH in the GC is in the range of 2400–5100 $M_\odot$. The face-on view at a Galactic latitude of $b = 0^\circ$ displays a bar-like structure with an inclination angle of $67.5 \pm 2.1^\circ$ with respect to the line of sight. No ring-like structure in the GC is evident in our data, likely due to the low-spatial resolution of the CO and OH maps.

Key words: ISM: clouds – ISM: kinematics and dynamics – ISM: molecules – ISM: structure – Galaxy: centre – Galaxy: kinematics and dynamics.

1 INTRODUCTION

The central molecular zone (CMZ), within about 500 pc of the Galactic Centre (GC), is a unique region of the Milky Way (Morris & Serabyn 1996). Although the CMZ covers a small range of Galactic longitude, from $l = -1^\circ$ to approximately $+1.5^\circ$, it is a large reservoir of molecular clouds, the total mass of which is about 5.3×10^7 $M_\odot$ (Pierce-Price et al. 2000). The densities (Jones et al. 2012, 2013; Longmore et al. 2013), temperatures (Ao et al. 2013; Mills & Morris 2013; Ginsburg et al. 2016) and turbulence (Oka et al. 2001; Shetty et al. 2012) of molecular clouds in the CMZ are all higher than in the Galactic disc. This region contains a large diversity of observed molecules, and is characterized by abundant star formation activity (Yusef-Zadeh et al. 2009; Walsh et al. 2011; Kruijssen et al. 2014; Corby et al. 2015; Lu et al. 2015), making the CMZ a valuable place to study molecular clouds and star formation processes in the Milky Way.

However, because of the edge-on view from our Solar system, the structure of molecular clouds in the CMZ is still unclear. The Hi-GAL survey (Molinari et al. 2010), performed with *Herschel* in the far-infrared, suggested that the CMZ consists of a twisted 100 pc ring with a mass of $\sim 3 \times 10^7$ $M_\odot$ (Molinari et al. 2011), tracing stable x_2 orbits, whose major axes are perpendicular to the bar (Contopoulos & Papayannopoulos 1980; Binney et al. 1991). Recently, however, Kruijssen, Dale & Longmore (2015) suggested that the orbits of clouds in the CMZ are open rather than closed, in contrast to the ring structure proposed by Molinari et al. (2011).

Sawada et al. (2004) proposed a method to calculate the relative position of molecular clouds with respect to the GC involving CO emission and OH absorption lines that, unlike previous studies

★ E-mail: qzyan@shao.ac.cn (Q-ZY); andrew.walsh@curtin.edu.au (AJW); J.Macquart@curtin.edu.au (JRD)

(e.g. Binney et al. 1991; Kruijssen et al. 2015), is independent of dynamical models. They assumed that the diffuse radio continuum emission in the GC is axisymmetric and used the absorption depth of the OH 1667-MHz line to estimate the background emission, enabling them to derive the relative position of molecular clouds in the GC. This work confirmed the existence of a bar-like structure in the GC. Their model adopted a uniform value for the OH excitation temperature and a uniform ratio of CO brightness temperatures to OH optical depths. Thus, the accuracy of the model may have been impacted if significant variations in excitation temperature exist, or if the some of the ^{12}CO($J = 1 \rightarrow 0$) features emanate from optically thick regions.

The Southern Parkes Large-Area Survey in Hydroxyl (SPLASH; Dawson et al. 2014) provides an opportunity to improve the model of Sawada et al. (2004) with greatly improved sensitivity. SPLASH, performed with the Parkes 64-m telescope, observed all four OH ground-state transitions, consisting of two main lines (1665 and 1667 MHz) and two satellite lines (1612 and 1720 MHz) over the CMZ region. These four transitions enable us to confine the optical depth and excitation temperature, and hence significantly improve the model of Sawada et al. (2004).

In order to test the orbital model proposed by Kruijssen et al. (2015), we refine the method of Sawada et al. (2004), by using spatial information derived from all four OH ground-state transitions from the SPLASH, combined with ^{12}CO($J = 1 \rightarrow 0$) data observed by the Harvard-Smithsonian Center for Astrophysics (CfA) 1.2-m telescope (Dame, Hartmann & Thaddeus 2001) and ^{13}CO($J = 1 \rightarrow 0$) data observed by the Mopra 22-m telescope. Details of our observations are presented in Section 2. We summarize the principle and assumptions of the method in Section 3. In Section 4, we present a method to compute the OH optical depth and excitation temperature precisely, together with a means of estimating the level of background continuum emission and the relative positions of OH clouds along the line of sight. Combining the face-on views of different Galactic latitudes, we investigate the three-dimensional (3D) structure of the molecular clouds in the CMZ in Section 5 and discuss its implications in Section 6. Our conclusions are presented in Section 7.

2 OBSERVATIONS

2.1 Co data

In our calculation, we use two CO isotopologue spectral lines: ^{12}CO($J = 1 \rightarrow 0$) and ^{13}CO($J = 1 \rightarrow 0$). The ^{12}CO($J = 1 \rightarrow 0$) data are part of a complete CO survey of the Milky Way, conducted by Dame et al. (2001). This survey was performed with two similar 1.2-m telescopes: one is at the CfA of Harvard University in America and the other is at Cerro Tololo Inter-American Observatory in Chile. For the GC, the observation was performed by the latter telescope whose full width at half-maximum (FWHM) is 8.8 arcmin at the frequency of ^{12}CO($J = 1 \rightarrow 0$), approximately 115 GHz (Bitran et al. 1997). The spatial sampling interval within 1° of the Galactic plane was 7.5 arcmin, with a velocity resolution of 1.3 km s^{-1}, and the corresponding root mean square (rms, σ) of the spectral noise was 0.10 K. The ^{12}CO($J = 1 \rightarrow 0$) data were smoothed using a Gaussian kernel with an FWHM of 12.8 arcmin to match the effective resolution (15.5 arcmin) of the OH spectra.

The ^{13}CO($J = 1 \rightarrow 0$) data are part of a new high-resolution survey of the Southern Galactic Plane in CO (described in Burton et al. 2013) performed with the 22-m Mopra telescope. The particular data set used here is part of a sub-project on the CMZ (Blackwell in preparation), which covers $-1.5^\circ \leqq l \leqq 3.5^\circ$ and $-0.5^\circ \leqq b \leqq 1.0^\circ$, in the three principal isotopologues of CO (^{12}CO, ^{13}CO and C^{18}O). The data were obtained at 0.6 arcmin and 0.1 km s^{-1} angular and spectral resolution through the technique of on-the-fly mapping.

The methodology of obtaining and reducing the data set is described in Burton et al. (2013), with particular issues relevant to the CMZ further elucidated in Blackwell (in preparation). These issues include (1) refinements to the method of baselining the spectra, given the wide emission lines in the CMZ; (2) the removal of reference beam contamination, a particular issue with the CMZ due to the extended distribution of line emission and (3) a better identification (and removal) of bad data points before processing. The full Mopra CMZ CO data set will be made publicly available following the publication of Blackwell (in preparation), where a full description of these issues is given.

For this analysis, a preliminary version of the ^{13}CO($J = 1 \rightarrow 0$) data was provided at 3.0 arcmin and 2 km s^{-1} angular and spectral resolution. The ^{13}CO($J = 1 \rightarrow 0$) data were smoothed using a Gaussian kernel with an FWHM of 15.2 arcmin and were subsequently regridded to a pixel resolution of 7.5 arcmin.

2.2 OH data

The OH data constitute part of SPLASH. A study of the pilot region of SPLASH is presented by Dawson et al. (2014) along with a detailed description of the observations. SPLASH, which covers the GC, provides sensitive, unbiased and fully sampled spectra of four ground-state 18-cm transitions of OH at 1612, 1665, 1667 and 1720 MHz. Here, we present a brief review of the observations and detail our additional efforts to obtain good spectral baselines for the data in the GC region.

SPLASH was performed with the Australia Telescope National Facility (ATNF) 64-m Parkes telescope. Similar to the pilot region, the GC was covered by on-the-fly mapping of $2^\circ \times 2^\circ$ tiles, where each tile was observed 10 times. The interval between scan rows was 4.2′, oversampling the Parkes beam, which has an FWHM of ∼12.2 arcmin at 1720 MHz. The data presented in this paper cover a Galactic Longitude range of $-6^\circ \leqq l \leqq 6^\circ$, while the range in Galactic latitude is $-2^\circ \leqq b \leqq 2^\circ$.

We used ASAP,[1] a software package to extract both spectral lines and the continuum, in conjunction with the SPLASH data reduction pipeline, which performs bandpass calibration, following Dawson et al. (2014).

We produce the baselines of spectra by blanking out the emission or absorption features in each 4-s, bandpass-calibrated integration, linearly interpolating over the gap, and heavily smoothing. This procedure worked well for SPLASH pilot regions, whereas for the GC, we found the baselines were inaccurate because of the high-continuum level and large velocity dispersion of the lines. In order to produce flat baselines, we improved the procedure for SPLASH pilot regions by performing an iterative process of 3D line detection and masking.

Our processing iterated over the data three times. Each time, we use the data cubes produced by previous process to improve the mask files, which is essential to obtain good spectral baselines.

For the first iteration no mask files were provided, and spectral identification was done by the LINEFINDER of ASAP. Specifically, after masking bright features and interpolating over the masked channels,

[1] http://svn.atnf.csiro.au/trac/asap

we smooth with a Gaussian kernel of $\sigma = 45$ km s^{-1} to obtain the baseline solution, which is then subtracted. This roughly baselined data were then gridded into a data cube (see below for the details on the gridding procedure).

Before computing baseline solutions a second time, we used DUCHAMP (Whiting 2012), which is a 3D source finding software package, to create mask files of all detected voxels in the satellite lines using the data cubes produced in the first iteration. However, for the main lines, due to the spectral overlap caused by close rest frequencies and large velocity dispersions, the baseline modelling is inaccurate. Therefore, we applied the masked velocity ranges of satellite lines to two main lines. With these mask files, we ran the pipeline again, which produced much better baselines.

In the third iteration, we manually unmasked some absorption features above the baselines of the main lines. We found that some absorption features of the main lines were above zero level, and this is due to the large velocity dispersion, which renders the baselines inaccurate. This typically occurred near the velocity range where the two main lines contaminate each other. With the manually modified mask files, we ran the pipeline a third time. The final baselines of the satellite lines are more accurate, while the brightness temperatures of the main lines near manually unmasked channels might be still slightly higher than their true values. However, because any further correction would be model dependent, we decided not to correct for this effect.

The high levels of continuum emission in the immediate vicinity of Sgr A* raised concerns that some of our Parkes observations were affected by saturation. To check this, we observed this small region with a higher attenuation setting. We found that the telescope was indeed saturated within about one beam size of the peak of continuum emission with the normal SPLASH attenuation settings. Therefore, we replaced the spectra where Parkes was saturated with observations taken with the higher attenuation setting.

Both the spectral and continuum emissions are corrected to main-beam brightness temperatures, according to the daily observations of the ATNF standard calibrator source PKS B1934-638.

The data cubes of the four OH spectral lines are produced with the GRIDZILLA[2] software package. Data were gridded with a Gaussian kernel of FWHM 20 arcmin with a cut-off radius of 10 arcmin, and a pixel size of 3 arcmin, resulting in an effective resolution of ∼15.5 arcmin. At the spatial and spectral resolution of 15.5 arcmin and 0.18 km s^{-1}, the final noise level of the spectra is about 0.1 K. Because the pixel resolution (7.5 arcmin) of CO spectra is approximately half of the spatial resolution of OH spectra, we regridded the OH data to match the pixel resolution of ^{12}CO($J = 1 \rightarrow 0$) with the MIRIAD software package (Sault, Teuben & Wright 1995).

2.3 Continuum

Because SPLASH only measures the difference between the ON and OFF positions, we add back the level of continuum emission at OFF positions, which is estimated according to 1.4-GHz continuum map of the H I Parkes All-Sky Survey (HIPASS; Calabretta, Staveley-Smith & Barnes 2014).

The brightness temperature of the OFF positions at 1.4 GHz is about 8 K. After subtracting the cosmic microwave background (CMB), we estimated the brightness temperatures at the frequencies of four OH lines using a spectral index of −2.7 (Platania et al. 2003) and added the brightness temperature of the OFF positions on the continuum emission observed by SPLASH. The levels of continuum emission (not including the CMB) at the OFF positions are 3.7, 3.4, 3.4 and 3.1 K for the 1612-, 1665-, 1667- and 1720-MHz lines, respectively. The fluctuations of observations at different epochs indicate that the uncertainty is less than 10 per cent for the continuum emission.

[2] http://www.atnf.csiro.au/computing/software/livedata/

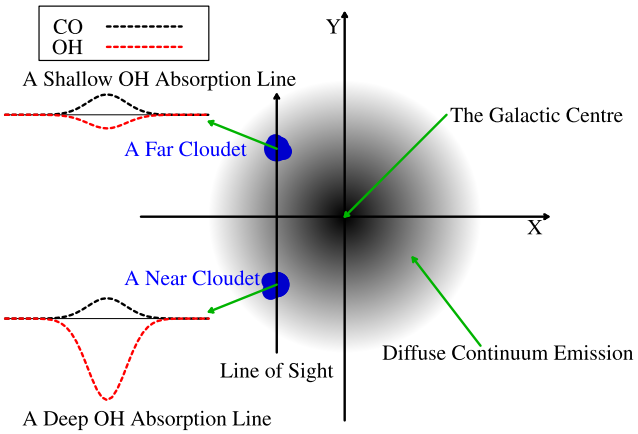

Figure 1. Principles of deriving the relative positions of molecular clouds, which is reproduced from Sawada et al. (2004, fig. 3). The black dashed lines and red lines represent CO emission and OH absorption lines, respectively.

3 THE MODEL

Sawada et al. (2004) proposed a method to calculate the relative position of molecular clouds along the line of sight to the GC by combining information from CO emission and OH absorption, based on four assumptions. First, they assume that the CO emission and OH absorption features at a particular velocity correspond to the same location in space. Secondly, they assume the optical depth of OH is proportional to the brightness temperature of CO, which traces the amount of molecular clouds. Thirdly, they assign the excitation temperature of OH at 1667 MHz, a uniform value. Their fourth assumption is that the diffuse continuum emission in the GC is optically thin and axisymmetric, which can be modelled by three Gaussian components.

The principle of deriving relative positions of molecular clouds is depicted in Fig. 1. The depth of the OH absorption line is determined by the excitation temperature and optical depth of OH and the level of continuum emission behind molecular clouds. As illustrated in Fig. 1, two molecular clouds, with equal excitation temperatures and optical depths but different distances, display distinctive absorption lines.

Details of the expression of the absorption depth (the brightness temperature) in terms of the excitation temperature, the optical depth, and the level of background continuum emission are described in Section 4.1. Similar to higher levels of background continuum emission, larger optical depths also lead to greater absorption depth. Therefore, we need to know the optical depth as well as the excitation temperature before we can derive the level of continuum emission behind molecular clouds. Subsequently, based on a modelled volume emission coefficient of diffuse continuum, we can derive the relative positions of molecular clouds in the GC.

In their calculations, Sawada et al. (2004) adopted a uniform value of 4 K for the OH excitation temperature and estimated the optical depth from CO. However, this uniform excitation temperature only represents the part above the CMB and the actual excitation

temperature they used is about 6.7 K. Although this value is within a reasonable range (Crutcher 1977; Li & Goldsmith 2003), a uniform value for the excitation temperature may be inaccurate. The ratio of optical depth of the 1667-MHz line to the ^{12}CO($J = 1 \rightarrow 0$) brightness temperature they used is 0.15 K^{-1}, which may have introduced errors, considering ^{12}CO($J = 1 \rightarrow 0$) may be optically thick in some regions.

In this work, we improve the model of Sawada et al. (2004) by implementing a new method to solve the OH excitation temperatures and optical depths precisely. Additionally, the OH data we used is more sensitive and we used ^{13}CO($J = 1 \rightarrow 0$) to identify regions where ^{12}CO($J = 1 \rightarrow 0$) is optically thick.

We retained the first and fourth assumptions of Sawada et al. (2004) and modified their second and third assumptions. For the second one, we used the CO intensity to constrain the column densities of OH, instead of the optical depths, and this is more reasonable, because the CO intensity is roughly proportional to the column density, if CO emission is optically thin. For the third one, we abandoned the assumption of a uniform excitation temperature, and alternatively, we assume that the excitation temperatures of the two main lines are equal and no assumptions about excitation temperatures of the satellite lines are made.

We summarize these four assumptions as follows:

(i) The CO emission and OH absorption features at a particular velocity correspond to the same location in space.

(ii) The column density of OH at ground states, N(OH), is proportional to the brightness temperature of ^{12}CO($J = 1 \rightarrow 0$), meaning $N(\mathrm{OH}) = f \times T_{\mathrm{CO}}$, where f is a constant.

(iii) The excitation temperatures of the two main lines are equal.

(iv) The diffuse continuum emission in the GC is optically thin and axisymmetric, and it can be modelled by three Gaussian components.

4 SOLVING OH EXCITATION TEMPERATURES

In this section, we propose a new method to calculate the column densities, excitation temperatures, and optical depths of OH precisely, which significantly improves on the model proposed by Sawada et al. (2004). The kernel of the idea is to express the OH excitation temperatures and optical depths in terms of the four column densities of the OH ground state hyperfine levels, which are solvable provided that all four lines have been observed.

In many cases of practical interest the background emission and brightness temperature of an absorption line are observable. However, the situation is more difficult for the complicated GC region, because the fraction of the observed background emission arising from behind the OH cloud is unknown, and this requires extra effort to model. In the following two subsections, we first discuss the simple case in which the background is known, and then introduce the treatment as applied to the GC region.

4.1 Known background continuum

Before we deal with the GC, we introduce the simple case in which the background continuum emission is known. The basic equation of radiative transfer yields the brightness temperature of the spectral line:

$$T_b\,(\mathrm{v}) = (T_{\mathrm{ex}} - T_{\mathrm{c}} - T_{\mathrm{cmb}})\left(1 - \mathrm{e}^{-\tau_{\mathrm{v}}}\right), \tag{1}$$

where T_{c} and T_{cmb} are the brightness temperatures of the background continuum emission and the CMB (2.73 K), and T_{ex} and τ_{v} are the

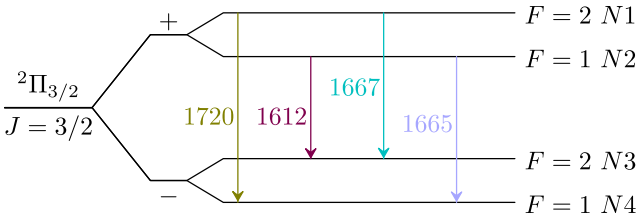

Figure 2. OH ground-state energy levels, reproduced from Dawson et al. (2014, Fig. 1). $N1$, $N2$, $N3$ and $N4$ denote the column densities of their corresponding states, and F represents the total angular momentum.

excitation temperature and optical depth at velocity v, respectively. If $T_{\mathrm{ex}} > T_{\mathrm{cmb}}+T_{\mathrm{c}}$, the spectral line is in emission ($T_b > 0$), while if $T_{\mathrm{ex}} < T_{\mathrm{cmb}}+T_{\mathrm{c}}$, the spectral line is in absorption ($T_b < 0$).

If T_{c} is known, the unknown quantities in equation (1) are T_{ex} and τ_{v}. Because we observed four OH ground-state transitions, we are able to build four equations, each with two unknown quantities, In total, we have eight variables. However, because of the insufficiency of equations, we cannot solve the excitation temperature and optical depth of OH directly.

To solve for the eight variables, we first convert the four excitation temperatures and four optical depths to four column densities. We use $N1$, $N2$, $N3$ and $N4$ to denote the four column densities of the four ground states of OH, from top to bottom as shown in the schematic of the four OH ground-state transitions in Fig. 2.

The excitation temperature, T_{ex}, is defined by

$$\frac{n_{\mathrm{u}}}{n_{\mathrm{l}}} = \frac{g_{\mathrm{u}}}{g_{\mathrm{l}}} \exp\left(-\frac{h\nu_0}{kT_{\mathrm{ex}}}\right), \tag{2}$$

where n_{u} and n_{l} represent the number of molecules in the upper and lower states, g_{u} and g_{l} represent their corresponding statistical weights, h is the Planck constant, k is the Boltzmann constant and ν_0 is the line rest frequency. The excitation temperature is a convenient way to express the ratio of upper to lower states to express the radiative transfer equation as simply as possible (Rybicki & Lightman 1986; Emerson 1996). The excitation temperature has an actual physical meaning only when the upper and lower states are in local thermal equilibrium (LTE), and in most instances, the excitation temperature is simply a proxy for the ratio of upper-to-lower states.

Rearranging for T_{ex} and replacing number densities with column densities, we have

$$T_{\mathrm{ex}} = \frac{h\nu_0/k}{\ln(N_{\mathrm{l}}g_{\mathrm{u}}) - \ln(N_{\mathrm{u}}g_{\mathrm{l}})}, \tag{3}$$

where N_{u} and N_{l} are the upper and lower column densities of the energy states as shown in Fig. 2. Therefore, the excitation temperatures of four ground-state transitions can be calculated with $N1$, $N2$, $N3$ and $N4$.

The optical depth, τ_{v}, is given by

$$\tau_{\mathrm{v}} = \frac{c^3}{8\pi\nu_0^3}\frac{g_{\mathrm{u}}}{g_{\mathrm{l}}}N_{\mathrm{l}}A_{\mathrm{ul}}\left(1 - \mathrm{e}^{-\frac{h\nu_0}{kT_{\mathrm{ex}}}}\right)\phi_{\mathrm{v}}, \tag{4}$$

where N_{l} is the column density of molecules at the lower energy level, A_{ul} is the Einstein-A coefficient and ϕ_{v} is the normalized profile. After substituting equation (3) into equation (4), we have

$$\tau_{\mathrm{v}} = \frac{c^3}{8\pi\nu_0^3}A_{\mathrm{ul}}\left(\frac{g_{\mathrm{u}}}{g_{\mathrm{l}}}N_{\mathrm{l}} - N_{\mathrm{u}}\right)\phi_{\mathrm{v}}. \tag{5}$$

Clearly, the optical depth is also a function of the column density and all four optical depths can be calculated with the column densities of the four ground states.

Mathematically, the independent equations (3) and (5) represent a transformation between the pairs of variables (N_l, N_u) and (T_{ex}, τ_v). Substituting equations (3) and (5) into equation (1), we obtain an equation with only column densities as variables. We hence obtain four equations with only four unknowns, which may be solved. This can be done only because all four OH ground-state transitions share four energy levels, which means the excitation temperatures and optical depths of four OH ground-state transitions are not entirely independent. After obtaining the column densities, the calculation of excitation temperatures and optical depths is trivial.

4.2 The Galactic Centre

In this subsection, we consider the special case of the GC. The difficulties mainly arise from two problems: the two main lines contaminate each other because the velocity dispersion is large, and the level of background continuum behind OH clouds is unknown. The first problem eliminates one equation, while the second one introduces an extra variable. We solve the two problems according to the second and third assumptions listed in Section 3.

The assumption about the main-line excitation temperature provides an equation. Typically, the positive-velocity part of the 1667-MHz line is mixed with the negative-velocity part of the 1665-MHz line over a particular velocity range, meaning one equation is eliminated, and only three equations remain. Crutcher (1977, 1979) found that while the main line T_{ex} are generally within 1–2 K of each other, even small departures from equal main-line T_{ex} can cause significant errors in column density estimates in cases where equal T_{ex} is assumed. However, we are using column densities to estimate excitation temperatures, and the OH column densities are well constrained by the ^{12}CO($J = 1 \rightarrow 0$) brightness temperature. Therefore, the uncertainty caused by this assumption is not significant, and we describe this effect in Section 5.3.

Specifically, the assumption about the main line T_{ex} is expressed as

$$T_{ex1665} = T_{ex1667}, \tag{6}$$

where T_{ex1665} and T_{ex1667} are excitation temperatures of 1665- and 1667-MHz lines, respectively. In contrast, the excitation temperatures of the two satellite lines are in general unequal and significantly different to the excitation temperature of the two main lines. Equation (6) can serve as the fourth equation, and therefore we still have four equations for the GC.

The second problem introduces an extra variable. At first it would seem we have to solve another four parameters, corresponding to the four background continuum levels for the four OH transitions. However, the fraction of continuum emission behind OH clouds for the four OH lines should be equal. Therefore, we only need to add one parameter, T_c, which is the background continuum emission at any given frequency, say at 1665 MHz, and the background continuum levels of the other three lines can then be derived using the ratio between overall continuum emissions measured for each line.

We now have five variables to solve, but only four equations in hand. We supplement this system with data from CO to create the fifth equation, assuming the column densities of CO and OH are proportional. This is possible since the column density of CO in a single velocity channel is roughly proportional to its brightness temperature multiplied by the bandwidth of the channel if the CO spectral line is optically thin.

Compared with ^{12}CO($J = 1 \rightarrow 0$), ^{13}CO($J = 1 \rightarrow 0$) is a better tracer of CO column densities. However, ^{13}CO($J = 1 \rightarrow 0$) is not visible in all positions. Although ^{12}CO($J = 1 \rightarrow 0$) emission is often optically thick, the situation in the GC is not severe due to the large velocity dispersion. The resolution of our data is ∼38 pc, and at this size scale, the optically thick effect is further diminished by beam averaging. Consequently, we use ^{12}CO($J = 1 \rightarrow 0$) and artificially scale it in places where the ^{12}CO/^{13}CO intensity ratio suggests it is optically thick.

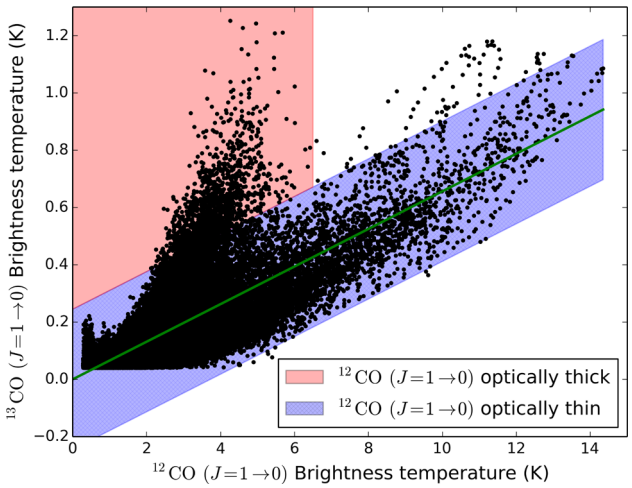

Figure 3. The brightness temperature of ^{12}CO($J = 1 \rightarrow 0$) versus ^{13}CO($J = 1 \rightarrow 0$). The green line, which passes through the origin with a slope of 0.066 ± 0.020, was fitted with data whose brightness temperature of ^{12}CO($J = 1 \rightarrow 0$) is greater than 6.5 K. The blue area is the coverage within 2σ ($\sigma = 0.12$ K) of the residual, where ^{12}CO($J = 1 \rightarrow 0$) emission is mostly optically thin, while beyond this blue area, marked in red, the ^{12}CO($J = 1 \rightarrow 0$) emission is mostly optically thick.

To detect regions where the ^{12}CO($J = 1 \rightarrow 0$) line is optically thick, we compare the brightness temperature of ^{12}CO($J = 1 \rightarrow 0$) versus ^{13}CO($J = 1 \rightarrow 0$), as shown in Fig. 3, where all values less than 3σ are excluded. Assuming a uniform ^{12}CO/^{13}CO abundance ratio, the brightness temperatures of ^{12}CO($J = 1 \rightarrow 0$) should be linearly proportional to the ^{13}CO($J = 1 \rightarrow 0$) emission if they are both optically thin. We therefore fitted a line to the ^{12}CO($J = 1 \rightarrow 0$) to ^{13}CO($J = 1 \rightarrow 0$) relation, restricting the fit to the region with ^{12}CO($J = 1 \rightarrow 0$) brightness temperatures exceeding 6.5 K to avoid the large amount of ^{12}CO($J = 1 \rightarrow 0$) emission that appears to be optically thick in the region <6.5 K.

The fitted line (using linear least squares with y-intercept = 0), delineated in green in Fig. 3, has a slope of 0.066 ± 0.020, yielding a ^{12}CO/^{13}CO intensity ratio of about 15.2. The uncertainty is given by the difference between the fitted slope constrained to pass through the origin and the fitted slope without this constraint. Although Oka et al. (1998) suggests a value of 5.19, this value could change with observations obtained with different beam filling factors. Because ^{12}CO($J = 1 \rightarrow 0$) clouds are more extended than ^{13}CO($J = 1 \rightarrow 0$) clouds, large beam sizes diminish the brightness temperature of ^{13}CO($J = 1 \rightarrow 0$) and increase the value of ^{12}CO/^{13}CO intensity ratio. The Nobeyama Radio Observatory 45-m telescope used by Oka et al. (1998) had a FWHM of about 17 arcsec at 100 GHz, and this angular resolution is much higher than that of Parkes at 1666 MHz. Consequently, the variation of the ^{12}CO/^{13}CO intensity ratio suggests that the beam filling factors of ^{12}CO($J = 1 \rightarrow 0$) and ^{13}CO($J = 1 \rightarrow 0$) are significantly different.

In Fig. 3, the region within 2σ ($\sigma = 0.12$ K) of the residual is marked with blue, where ^{12}CO($J = 1 \rightarrow 0$) emission is roughly optically thin and the optically thick effect if not evident, because

they are linearly correlated with ^{13}CO($J = 1 \rightarrow 0$). Although some points possessing large ^{12}CO($J = 1 \rightarrow 0$) brightness temperatures are also likely optically thick, we keep those points uncorrected, because there are too few such points to significantly affect the outcome. Consequently, we only did the correction for those points in the red region of Fig. 3, where ^{12}CO($J = 1 \rightarrow 0$) brightness temperatures are saturated. For the data in the red region, we replaced the ^{12}CO($J = 1 \rightarrow 0$) brightness temperature with the ^{13}CO($J = 1 \rightarrow 0$) temperatures divided by 0.066 – i.e. the points in the red region were moved horizontally on to the green line.

In Fig. 3, ^{12}CO($J = 1 \rightarrow 0$) brightness temperatures in the optically thick state are lower than some ^{12}CO($J = 1 \rightarrow 0$) brightness temperatures in the optically thin state. This is because when ^{12}CO($J = 1 \rightarrow 0$) is optically thick, the brightness temperature approaches the excitation temperature. The optically thick spectra can only see the outer parts of molecular clouds, and the outer parts of molecular clouds usually have lower excitation temperatures. After the correction, ^{12}CO($J = 1 \rightarrow 0$) data are roughly proportional to ^{13}CO($J = 1 \rightarrow 0$) data.

We use self-absorption spectra of ^{12}CO($J = 1 \rightarrow 0$) to demonstrate this behaviour. The line centres of self-absorption spectra towards molecular cores are lower than their adjacent velocity components. For instance, the average ^{12}CO($J = 1 \rightarrow 0$) spectrum of an H II region N14 (Yan et al. 2016, fig. 1) shows a deep dip in the line centre, and this effect is more evident compared with the single-pixel spectrum (Yan et al. 2016, fig. 29). Consequently, beam averaging can diminish the effect of optically thick regions.

Now, we can replace the column densities of ^{12}CO($J = 1 \rightarrow 0$) with their corrected brightness temperatures. The fifth equation is expressed as

$$N1 + N2 + N3 + N4 = f_{1234} \times T_{\rm CO}, \tag{7}$$

where $N1$, $N2$, $N3$ and $N4$ are column densities of four OH ground states, $T_{\rm CO}$ is the corrected brightness temperature of ^{12}CO($J = 1 \rightarrow 0$), and f_{1234} is the ratio of the sum of column densities of OH ground states to the ^{12}CO($J = 1 \rightarrow 0$) brightness temperature. Although f_{1234} can be estimated from observations towards the Galactic disc, we determine f_{1234} more accurately by a method discussedin Section 5.2.

Now, for the GC, we have five parameters and five equations, and we can solve them simultaneously. In this model, the largest uncertainty comes from equation (7). In the rest of this section, we present the system of equations and its method of solution.

4.3 The system of equations

Here, we write out the system of equations explicitly. We choose the background continuum level of 1665-MHz line, $T_{\rm c}$, as the fifth variable, and the background continuum levels of the other three lines is

$$\begin{aligned} T_{\rm c1667} &= f_{1667} T_{\rm c}, \\ T_{\rm c1612} &= f_{1612} T_{\rm c}, \\ T_{\rm c1720} &= f_{1720} T_{\rm c}, \end{aligned} \tag{8}$$

where $T_{\rm c1667}$, $T_{\rm c1612}$ and $T_{\rm c1720}$ are background continuum emission levels behind molecular clouds at the frequencies of the 1667-, 1612- and 1720-MHz lines and f_{1667}, f_{1612} and f_{1720} are their ratios to the value of 1665-MHz line, respectively. As mentioned above, f_{1667}, f_{1612} and f_{1720} can be calculated from the measured overall continuum emission, because for a particular voxel, the fraction of continuum emission behind molecular clouds is the same for all four lines.

Table 1. Parameters of the four ground-state transitions of OH.

Line	Rest frequency (MHz)	Einstein-A coefficient (10^{-11} s^{-1})
1612 MHz	1612.231	1.302
1665 MHz	1665.402	7.177
1667 MHz	1667.359	7.778
1720 MHz	1720.530	0.9496

In order to simplify our model, we use $T_{\rm exm}$ to denote the excitation temperature of the two main lines. The frequencies of 1665-, 1667-, 1612- and 1720-MHz lines are denoted by ν_{1665}, ν_{1667}, ν_{1612} and ν_{1720}, and their optical depths at a velocity v are denoted by $\tau_{\rm v1665}$, $\tau_{\rm v1667}$, $\tau_{\rm v1612}$ and $\tau_{\rm v1720}$, respectively. The statistical weight of each level can be calculated with their total angular momentums (Barrett 1964). The Einstein-A coefficients of the four lines were calculated by Destombes et al. (1977) and listed in Table 1. We use A_{1612}, A_{1665}, A_{1667} and A_{1720} to denote the Einstein-A coefficients of the four lines. The parameters of the four OH ground-state transitions are summarized in Table 1.

Using the fact that $N1$ and $N2$ can be derived from $T_{\rm exm}$, $N3$ and $N4$, we replaced $N1$ and $N2$ with $T_{\rm exm}$. Equivalently, we only need to constrain the sum of $N3$ and $N4$, and therefore equation (7) is modified to

$$N3 + N4 = f \times T_{\rm CO}. \tag{9}$$

The value of f in equation (9) is roughly half of f_{1234} in equations (7).

Now, we only have to deal with four parameters, which are $T_{\rm exm}$, $T_{\rm c}$, $N3$ and $N4$, because equation (6) has already been used. Denoting the brightness temperatures of the four lines at a velocity v by T_{1665}(v), T_{1667}(v), T_{1612}(v) and T_{1720}(v), we write out the equations as

$$\begin{cases} (T_{\rm exm} - T_{\rm c} - T_{\rm cmb})\,(1 - {\rm e}^{-\tau_{\rm vmain}}) = T_{b\rm main}\,({\rm v}) \\ \left(\frac{h\nu_{1612}/k}{\ln(3N_3) - \ln(5N_2)} - f_{1612} T_{\rm c} - T_{\rm cmb}\right)(1 - {\rm e}^{-\tau_{\rm v1612}}) = T_{b1612}\,({\rm v}) \\ \left(\frac{h\nu_{1720}/k}{\ln(5N_4) - \ln(3N_1)} - f_{1720} T_{\rm c} - T_{\rm cmb}\right)(1 - {\rm e}^{-\tau_{\rm v1720}}) = T_{b1720}\,({\rm v}) \\ N3 + N4 = f \times T_{\rm CO}, \end{cases} \tag{10}$$

where

$$\begin{aligned} T_{\rm cmb} &= 2.73\ {\rm K}, \\ N1 &= N3 \exp\left(-\frac{h\nu_{1667}}{kT_{\rm exm}}\right), \\ N2 &= N4 \exp\left(-\frac{h\nu_{1665}}{kT_{\rm exm}}\right), \\ T_{b\rm main}\,({\rm v}) &= T_{b1665}\,({\rm v}) \ \text{ or } T_{b1667}\,({\rm v}), \\ \tau_{{\rm v}main} &= \frac{c^3}{8\pi\nu_{1665}^3} A_{1665}\,(N_4 - N_2)\,\phi_{\rm v} \\ &\quad \text{or } \frac{c^3}{8\pi\nu_{1667}^3} A_{1667}\,(N_3 - N_1)\,\phi_{\rm v}, \\ \tau_{\rm v1612} &= \frac{c^3}{8\pi\nu_{1612}^3} A_{1612}\left(\frac{3}{5}N_3 - N_2\right)\phi_{\rm v}, \\ \tau_{\rm v1720} &= \frac{c^3}{8\pi\nu_{1720}^3} A_{1720}\left(\frac{5}{3}N_4 - N_1\right)\phi_{\rm v}. \end{aligned} \tag{11}$$

4.4 Solving the system of equations

The non-linear system of equations (10) was solved numerically. Because we solve the system of equation (10) channel by channel, ϕ_v, the line profile becomes approximately constant over a single channel. Due to normalization, the value of ϕ_v equals the reciprocal of the velocity interval between channels.

In order to examine the uniqueness and acquire an approximate initial solution, we simplified equation (10) by linearizing the equation of 1720-MHz line, because this line possesses the smallest Einstein-A coefficient and has the smallest optical depth. We further assume $h\nu/(kT_{\rm ex1720}) \ll 1$, which is generally satisfied if the excitation temperature of the 1720-MHz line, $T_{\rm ex1720}$, is not exceedingly low. Therefore, we have

$$T_{\rm ex1720} = \frac{h\nu_{1720}/k}{\ln(5N_4)-\ln(3N_1)} \approx \frac{h\nu_{1720}}{k}\frac{5N_4}{5N_4-3N_1} \quad (12)$$

and

$$1 - {\rm e}^{-\tau_{\rm v1720}} \approx \tau_{\rm v1720}. \quad (13)$$

Now, the equation of 1720-MHz line is linear with respect to $N3$ and $N4$. Combining with $N3 + N4 = f \times T_{\rm CO}$, we can solve $N3$ and $N4$ with respect to $T_{\rm c}$ and $T_{\rm exm}$. Substituting the expression of $N3$ and $N4$ to the main line and 1612-MHz equations, we acquire two equations with respect to $T_{\rm c}$ and $T_{\rm exm}$, which is much easier to solve numerically. For this two-equation system, we searched the solution over a grid of the possible solutions space and found that uniqueness is satisfied.

We adopted an initial value of 7 K for $T_{\rm exm}$, and the initial value of $T_{\rm c}$ is set to be half of the observed total continuum emission. After solving $T_{\rm c}$ and $T_{\rm exm}$, we calculated the value of $N3$ and $N4$, and equation (10) can be solved numerically based on these initial solutions.

5 RESULTS

In this section, we present a 3D structure of the molecular clouds in the GC by displaying the slices along the Galactic latitude. Sawada et al. (2004) only provided the face-on view (relative to the Galactic disc) of $b = 0^\circ$, while we calculated the face-on views of $b = -0.375^\circ$, -0.25°, -0.125°, 0°, 0.125° and 0.25°, constituting a 3D structure of the GC.

Based on the background continuum level solved by equation (10) and the modelled volume emission coefficient of the continuum emission in the GC, we calculated the position of the molecular clouds along the line of sight. The position was determined by integrating the modelled volume emission coefficient from negative infinity to the position of molecular clouds, making the integration equal the background continuum level. Although 20 cm continuum observations (Law et al. 2008), which have a higher spatial resolution than the Parkes data, suggest that the centre of the continuum emission is Sgr A*, whose Galactic coordinate is about $(l, b) = (-0.06^\circ, -0.05^\circ)$, we set $l = 0^\circ$ as the centre of the continuum emission, because Sgr A* is not far from $(l, b) = (0^\circ, 0^\circ)$.

In our calculation, we adopt a distance to the GC of 8.34 kpc (Reid et al. 2014), resulting in a physical resolution of 38 pc for the CMZ.

5.1 Fitting diffuse continuum emission

The fitting of the diffuse continuum emission in the GC is important, because locations of molecular clouds along the line of sight hinge on the distribution of the continuum volume emission coefficient.

Because we found that only at the range of $-0.375^\circ \le b \le 0.25^\circ$, the number of molecular clouds is significant, we focused on the calculation of the pixels within this range, including $b = -0.375^\circ$, -0.25°, -0.125°, 0°, 0.125° and 0.25°.

Following Sawada et al. (2004), we fitted the diffuse continuum emission along the Galactic longitude using three Gaussian components. Because the spatial resolution of our data is unable to resolve Sgr A*, which is the centre of the diffuse continuum emission, we simply assigned the mean position of Gaussian components $l = 0^\circ$. The integration of observed continuum emission is carried out using the distance from Sgr A* to the line of sight instead of Galactic longitude. We express this distance with degrees using a linear conversion factor of 145.56 pc deg^{-1}, and its difference with Galactic longitude is less than 0.01° for $l = 5^\circ$.

The observed continuum emission, which is integrated all over the line of sight, can be expressed as

$$T_{\rm cont}(l) = a_1 \exp\left(-\frac{x^2}{2\sigma_1^2}\right) + a_2 \exp\left(-\frac{x^2}{2\sigma_2^2}\right) + a_3 \exp\left(-\frac{x^2}{2\sigma_3^2}\right), \quad (14)$$

where l is the Galactic longitude in degrees, $x = 8340 \times \sin(l)/145.56$, and a and σ represent the height of the curve's peak and the standard deviation, respectively.

We display the parameters of all Gaussian components at 1612 MHz in Fig. 4. Generally, the diffuse continuum emission in the CMZ is well fitted by three Gaussian components, indicating the axisymmetric assumption of the continuum emission is reasonable.

5.2 Determining the column density ratio of OH to CO

So far, the value of f, the only free parameter in equation (10), remains undetermined. f affects the estimate of continuum emission levels behind OH clouds, thereby altering positions of molecular clouds in the CMZ. Because most of the molecular clouds are in the CMZ (within 500 pc of the GC), it is reasonable to assign f a value that maximizes the proportion of pixels within the CMZ.

Before we searched for this value, we estimated f according to the observations towards other regions of the Milky Way. Goicoechea et al. (2011) estimated the column densities of OH in the Orion Bar photodissociation region to be greater than 1×10^{19} m^{-2}. However, this value is the result of integration over a large velocity range, and therefore, we consider column densities of OH integrated over one single channel of about 1×10^{18} m^{-2}, around which we searched the optimum value for f.

We used the proportion of pixels within 500 pc of the GC in the face-on view of $b = 0^\circ$ to determine f, because $b = 0^\circ$ contains most of the molecular clouds. We searched the value of f in equation (9) with a step of 0.05×10^{18} m^{-2} K^{-1}. As shown in Fig. 5, near the maximum point, the ratio changes slowly, indicating that the effect caused by small shift of value f is not significant. At the maximum point, we have $f = 4.7 \times 10^{18}$ m^{-2} K^{-1}. The proportion of pixels within 500 pc of the GC is approximately 42 per cent, meaning about half of the voxels have no solutions or their solutions are inaccurate, which usually happens where the OH absorption lines are faint.

5.3 The equal main-line excitation temperature assumption

Although the velocity dispersion in the GC is generally large, in some particular regions, the main lines are not contaminated with

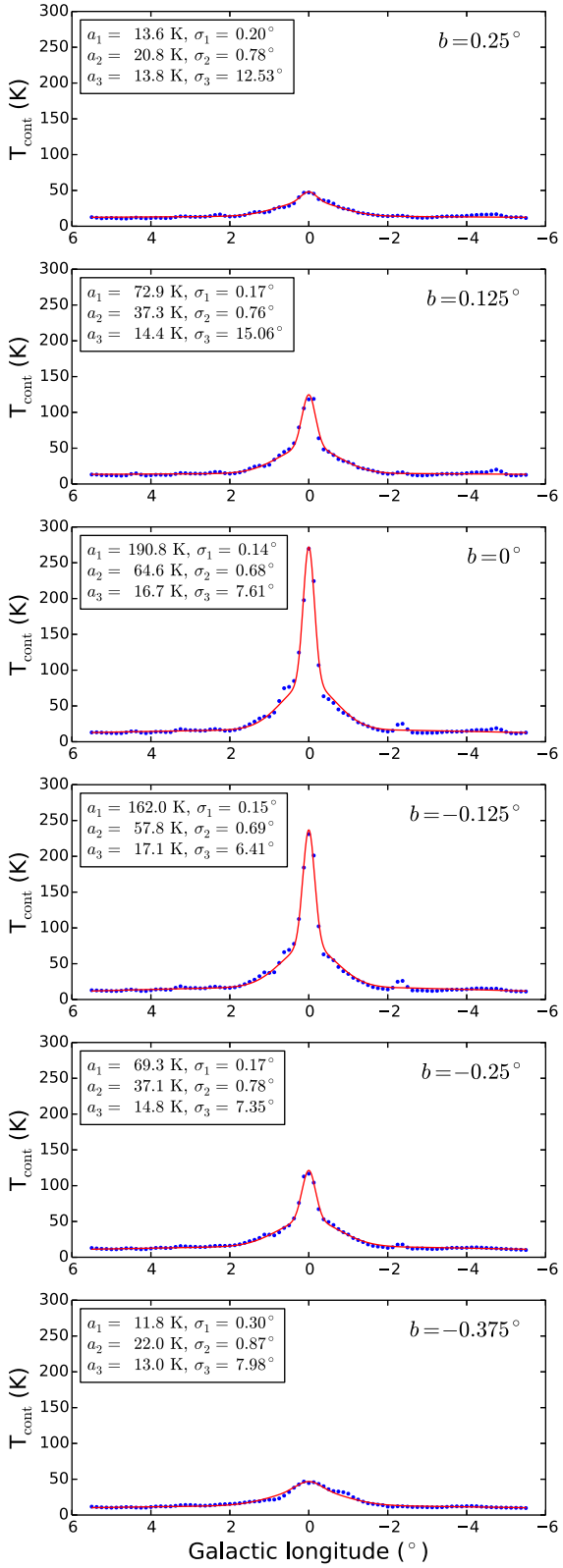

Figure 4. Continuum emission fitting at 1612 MHz for $b = -0.375°$, $-0.25°$, $-0.125°$, $0°$, $0.125°$ and $0.25°$. Each red line contains three Gaussian components. The continuum emission data (blue points) is observed by the SPLASH. The parameters of each Gaussian component (see equation 14) are displayed in the upper-left corner of each panel.

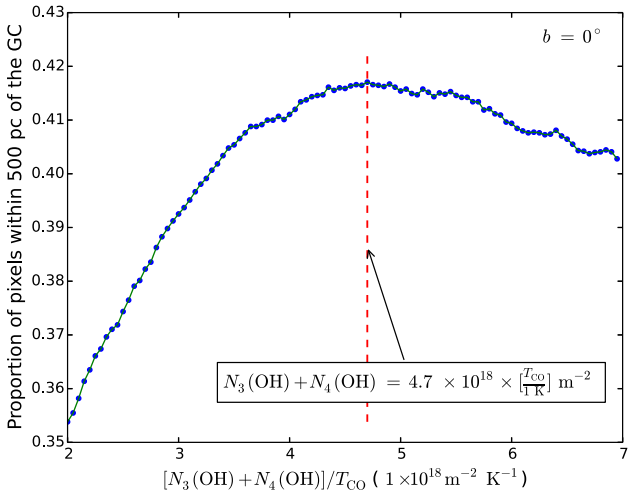

Figure 5. Determining the ratio of the OH column density to the brightness temperature of CO according to the proportion of pixels within 500 pc of the GC for the face-on view of $b = 0°$. The red dashed line denotes the ratio corresponding to the maximum proportion.

each other, which makes us able to check the equal main-line T_{ex} assumption.

For those regions, where we can measure all four ground-state transitions correctly, we can perform calculations without assuming the excitation temperatures of the main lines are equal. For those calculations, we possess five equations, built from four OH ground-state lines and CO observations, which are expressed with four column densities, $N1$, $N2$, $N3$ and $N4$, and the level of continuum emission behind OH clouds at 1665 MHz, T_{c}. The solution of equation (10) serves as the initial solution.

We chose $(l, b) = (1°, 0°)$, where all four OH lines were measured correctly, to check the third assumption listed in Section 3. In Fig. 6, we compare the results calculated with the assumption (blue lines) with that calculated with all four lines (red lines), including the calculated positions along the y-axis, the excitation temperature and optical depth of 1665-MHz line, and the column densities of $N1$ (see Fig. 2). As expected, the column densities of OH derived from both cases are almost identical, because the column densities of OH are constrained by the brightness temperature of ^{12}CO($J = 1 \rightarrow 0$) (see equation 9). Except for some velocity ranges, where the OH absorption lines are faint or optically thick, or ^{12}CO($J = 1 \rightarrow 0$) may not be accurately corrected, the calculated positions, excitation temperatures and optical depths derived under the assumption are generally close to the results calculated with all four lines.

Consequently, the third assumption in Section 3 is a good approximation to derive the relative positions of molecular clouds in the GC.

5.4 Testing the model

Before deriving a 3D structure with our model, it is important to verify its correctness. We examine our model on two points: the distribution of derived parameters in longitude-velocity (L–V) space, and the ability to predict the other main line.

In order to examine the derived parameters, we display the position along the y-axis, the excitation temperature of the main lines, and the optical depth in L–V diagram for $b = 0°$ in Fig. 7. No strong correlation is found between these three parameters, which means the position, excitation temperature and the optical depth are

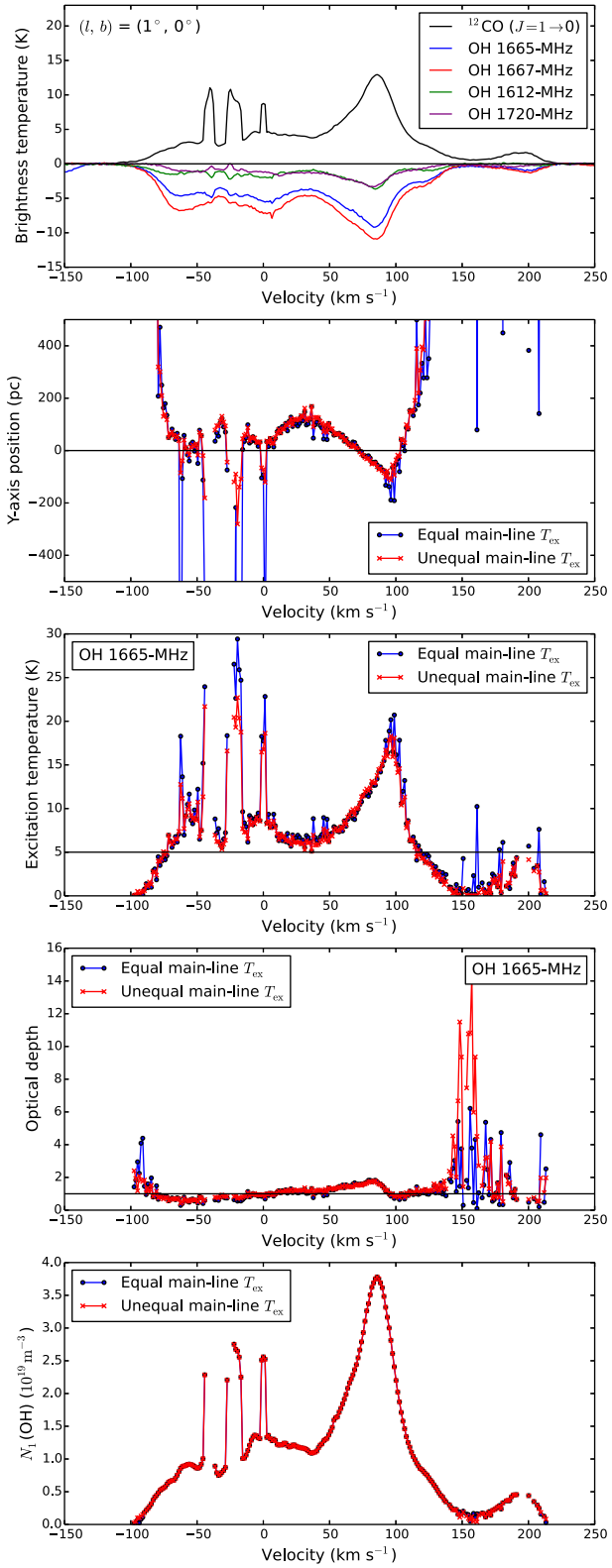

Figure 6. The comparison of results calculated with equal (blue lines) and unequal (red lines) main-line excitation temperature, for $(l, b) = (1^\circ, 0^\circ)$. The top panel displays four OH ground-state lines as well as the ^{12}CO($J = 1 \rightarrow 0$) spectrum. The rest four panels compare the results of calculated positions along the y-axis (see Fig. 9), the excitation temperatures and optical depths of OH 1665-MHz line, and the column densities of N_1(OH) (see Fig. 2), respectively.

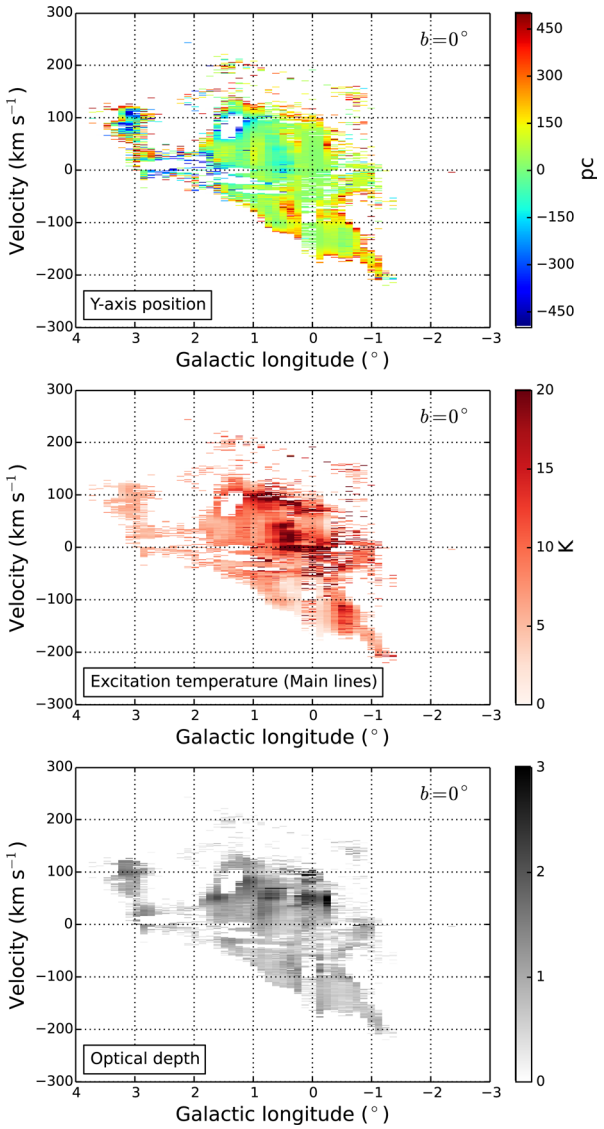

Figure 7. The position in y-axis (upper), the excitation temperature for the main lines (middle), and the optical depth (lower) in $L - V$ space for $b = 0^\circ$. Pixels with absolute values of positions in y-axis >500 pc are masked.

generally independent. Along the line of sight, the derived parameters are roughly continuous, and this continuity also exist along the velocity axis. This result is consistent with the expectation that molecular clouds, which are close in L–V space, should have adjacent positions.

In our calculation, we use only one of the two main lines (see equation 10), and the brightness temperature of the other main line can be calculated by our model according to the column densities. Therefore, how well can we reproduce the other main line is a vital indicator of the correctness of our model. The regions where the two main lines are not contaminated by each other provide the opportunity to check the prediction of the other main line.

We display the modelled main line in Fig. 8 and present the spectra at four positions: $(l, b) = (1^\circ, 0^\circ)$, $(0.375^\circ, 0^\circ)$, $(-0.375^\circ, 0^\circ)$ and $(-1^\circ, 0^\circ)$. We found that, for velocities larger than -100 km s^{-1}, the brightness temperature of 1665-MHz line is more accurate than 1667-MHz line, and accordingly, for voxels whose velocities are greater than -100 km s^{-1}, we used the 1665-MHz line in our calculations. Beyond this velocity range, we adopted 1667-MHz

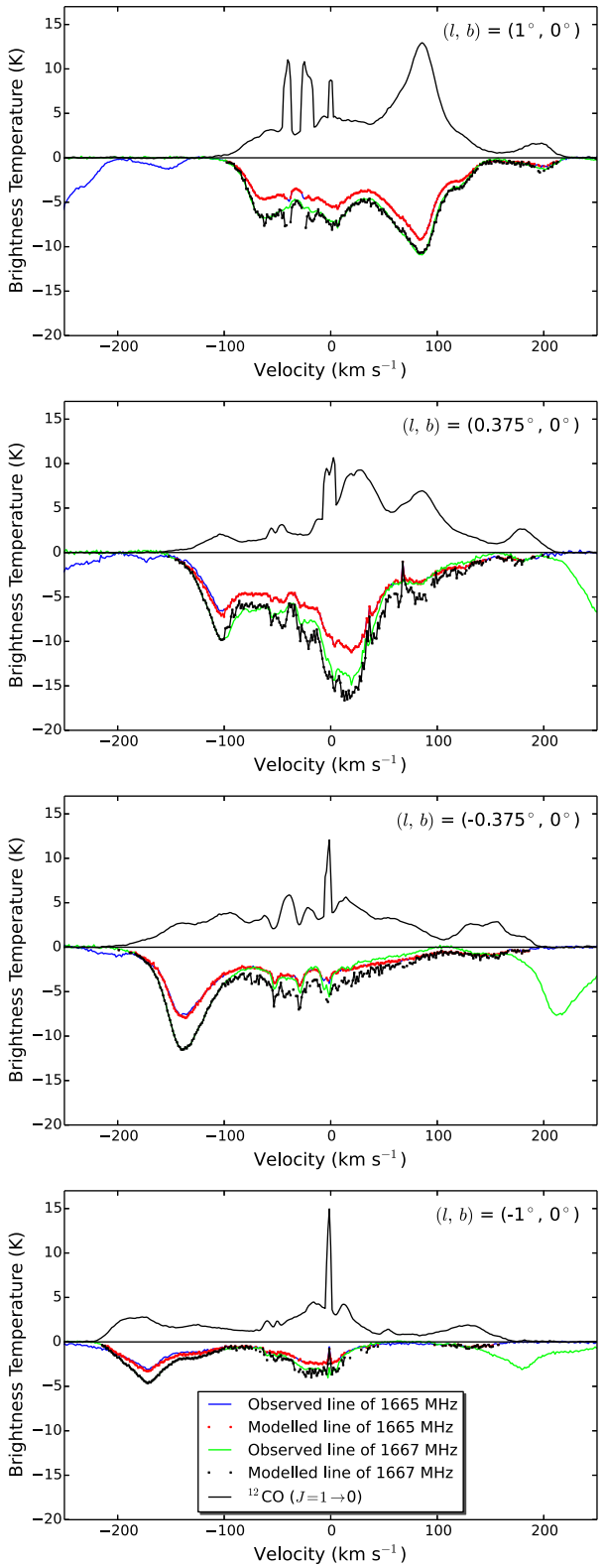

Figure 8. Modelled spectral lines at four positions, $(l, b) = (1°, 0°)$, $(0.375°, 0°)$, $(-0.375°, 0°)$ and $(-1°, 0°)$. Blue and green represent observed 1665- and 1667-MHz lines, while the red and black star markers denote their modelled values, respectively. The black lines are the emission of ^{12}CO($J = 1 \rightarrow 0$) corrected with ^{13}CO($J = 1 \rightarrow 0$). For the range where velocities are smaller than -100 km s^{-1}, the 1667-MHz line is used in equation (10), while beyond this velocity range, the 1665-MHz line is used.

Table 2. Parameters of five subregions in the GC.

Name	Coordinate (l, b)	Velocity (km s^{-1})	Face-on position (pc, pc)
Sgr A*[a]	$(-0.06°, -0.05°)$	...	(0, 0)
Sgr B2[b]	$(0.68°, -0.04°)$	[60, 64]	(90, −45)
Sgr C[c]	$(-0.57°, -0.09°)$	[−65, −55]	(−93, 147)
20 km s^{-1} cloud[d]	$(-0.13°, -0.08°)$	[18, 22]	(−18, 17)
50 km s^{-1} cloud[d]	$(-0.02°, -0.07°)$	[47, 53]	(0, 22)

Notes. [a]Petrov et al. (2011).
[b]Reid et al. (2009).
[c]Kendrew et al. (2013).
[d]Pierce-Price et al. (2000).

line. However, for Sgr B2, due to the presence of masers, we adopted the 1667-MHz line. Details about the velocity range of Sgr B2 are displayed in Table 2.

In Fig. 8, the main lines at $(l, b) = (1°, 0°)$ are not contaminated; therefore, the observed lines are accurate; these are plotted as green and blue lines in this figure. The modelled values are plotted with black and red stars. As shown in the top panel of Fig. 8, both of the modelled lines generally overlap with the observed lines, except for a couple of small intervals where ^{12}CO($J = 1 \rightarrow 0$) emission is optically thick. For the other three Galactic coordinates, the brightness temperature of 1667-MHz line is inaccurate near manually unmasked ranges mentioned in Section 2, whereas the modelled line is more reasonable.

Therefore, our model reproduces the other main line quite well, except in a small fraction of velocity ranges where optically thick ^{12}CO($J = 1 \rightarrow 0$) emission is not accurately corrected.

5.5 3D structure of the GC

Here, we derive the CO face-on view of the 3D GC structure for $b = -0.375°$, $-0.25°$, $-0.125°$, $0°$, $0.125°$and $0.25°$.

The procedure of deriving a face-on view of CO clouds for a particular Galactic latitude is to take each spectrum, calculate the position channel by channel, and project positions on to a face-on view map. The pixel map was generated by interpolating the brightness temperatures across a face-on grid with a resolution of $0.125°$. The chosen interpolation algorithm ensures that the integrated CO bright temperature of the original data equals that of the face-on view map. In the calculation, we masked the values where the brightness temperatures of the main line and CO are less than 0.3 K, which is approximately three times the spectrum noise level.

We present slices of the 3D structure along $b = -0.375°$, $-0.25°$, $-0.125°$, $0°$, $0.125°$ and $0.25°$ in Fig. 9. Beyond this Galactic latitude range, the molecular cloud density drops to a sufficiently low value to not merit modelling. Because of the background noise level of face-on view maps is about 1.38 K, we masked the pixels where the ^{12}CO($J = 1 \rightarrow 0$) brightness temperatures is less than 4.1 K.

The face-on view of $b = 0°$ displays a bar-like structure, which may be part of the Galactic bar. We fitted the inclination angle of the bar using equally weighted simple linear regression. In the fitting process, we rejected the pixels beyond 300 pc of the GC and those pixels whose integral bright temperatures are greater than 7 K km s^{-1} (5σ), in order to avoid involving unrelated noise. We find that the inclination angle with respect to the line of sight along $l = 0°$ is $67.5 \pm 2.1°$, as shown in Fig. 9.

In the right-hand panels of Fig. 9, positive velocities dominate the positive Galactic longitudes, while negative velocities dominate

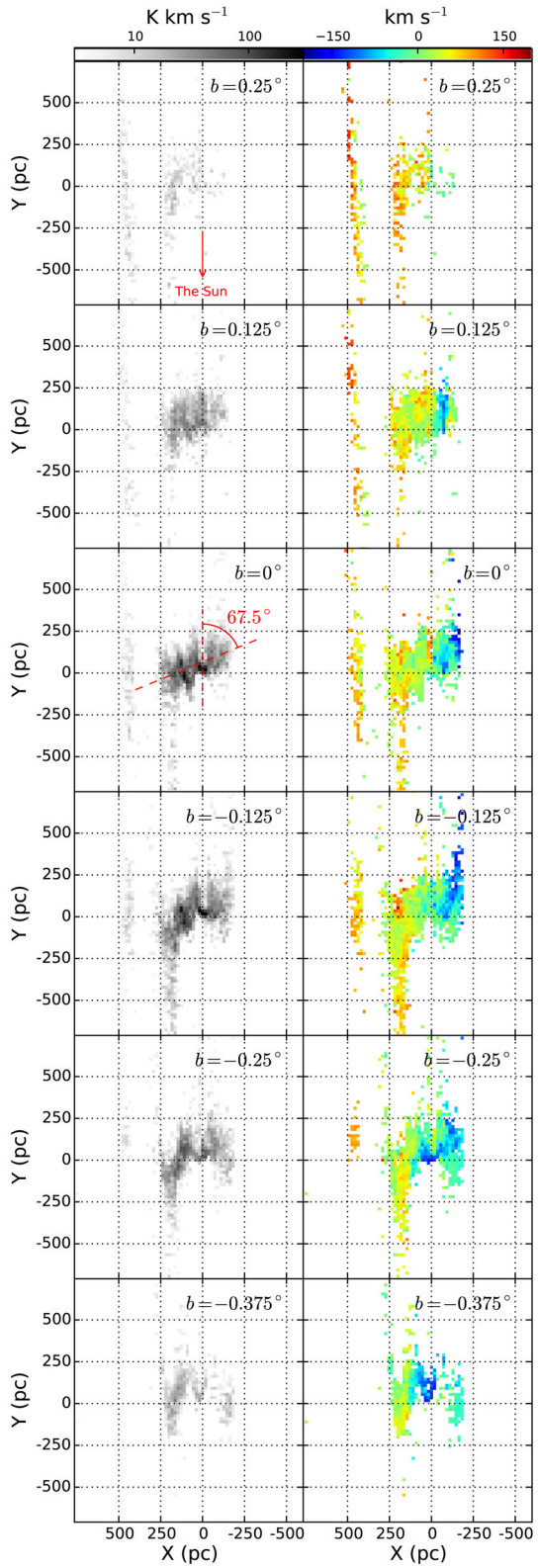

Figure 9. Face-on views of CO clouds for $b = -0.375°$, $-0.25°$, $-0.125°$, $0°$, $0.125°$ and $0.25°$. The left panels are face-on view of each Galactic latitude, and the right panels are the distributions of velocities which are intensity weighted. The originate of x- and y-axes is Sgr A*, and $X = 0$ corresponds to $l = 0°$. We masked the pixels where the integral brightness temperature is less than 4.1 K km s^{-1} (3σ).

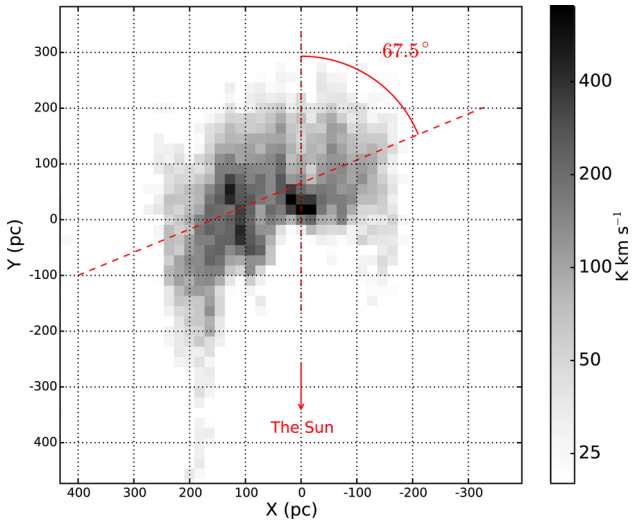

Figure 10. The face-on view of all molecular clouds in the GC integrated across six slices. The inclination angle is fitted with the molecular clouds at $b = 0°$, as shown in Fig. 9.

the negative Galactic longitudes, indicating the molecular clouds are rotating around Sgr A*.

Fig. 10 displays the distribution of all of the molecular clouds integrated over all Galactic latitudes. A bar-like structure is evident from the distribution, but the data do not reveal any strong evidence for a ring-like structure.

We calculated the total mass of OH in the GC. Because the majority of OH molecules are in the ground states, their total mass detected in these states roughly represents the total mass of OH. We counted the molecular clouds within 500 pc of the GC and found the total mass of OH in the GC is 2400 $M_\odot$, which is a lower limit. However, if we convert all the ^{12}CO($J = 1 \rightarrow 0$) brightness temperatures into OH column density using the value of f determined in Section 5.2 and a typical excitation temperature of 7 K, we found the total mass of OH in the GC is 5100 $M_\odot$, which is an upper limit.

6 DISCUSSION

6.1 OH excitation temperatures

In order to further check the reliability of our model, we compare the excitation temperature derived by our model with the values determined by previous work, although most of the previous observations were performed towards the Galactic disc instead of the GC. We display the main line excitation temperature calculated by our model for $b = 0°$ in Fig. 11.

Crutcher (1977) solved excitation temperatures directly by constructing equations from the observations towards ON and OFF positions of two radio continuum sources W40 and 3C 123. Their solutions suggest that the excitation temperatures of the main lines are both close to 6 K, although the difference of the excitation temperatures between main lines can occasionally reach 3 K. Their results support the assumption that the excitation temperatures of the main lines are approximately equal.

The OH excitation temperature can also be determined using *on* and *off* spectra of a single OH line towards compact background continuum sources. However, this method requires high-spatial resolution. Using the Nançay radio telescope, whose FWHM is about

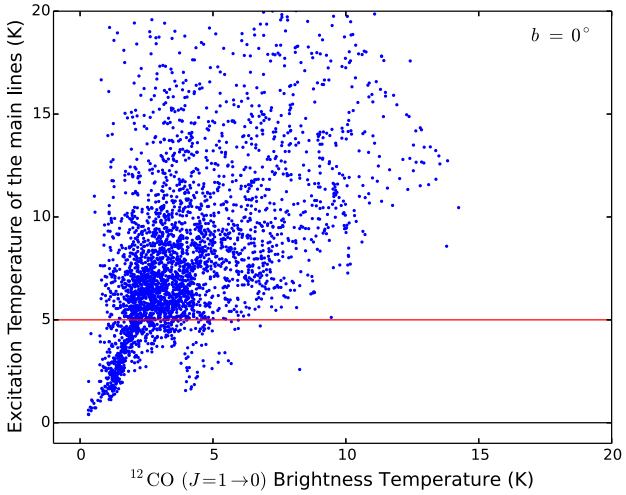

Figure 11. Excitation temperature of the main OH line versus the brightness temperature of ^{12}CO($J = 1 \rightarrow 0$) for $b = 0°$. The red horizontal line represents 5 K level.

3.5 arcmin at 1666 MHz, Dickey, Crovisier & Kazes (1981) performed an OH survey of 58 H I absorption regions against extragalactic background continuum sources and found that 16 regions show OH absorption or emission. These 16 regions show a large dispersion in Galactic longitude but are generally located within 15° of the Galactic plane. They derived the OH excitation temperature using OH absorption lines *on* the background continuum sources and OH emission lines *off* the background continuum sources. They found that the OH excitation temperature is in the range of 4–8 K. Colgan, Salpeter & Terzian (1989) performed a similar study using the Arecibo telescope and found the averaged main-line excitation temperature is in the range of 4–13 K.

Another way to estimate the excitation temperature of OH is based on LTE, assuming the excitation temperature of the two main lines is equal and the ratio of optical depths of 1665- to 1667-MHz lines is 5/9 (Knapp & Kerr 1973). Li & Goldsmith (2003) performed a OH and H I survey of 31 dark clouds, and with the LTE assumption, they found that the excitation temperature of OH is generally greater than 5 K and less than 9 K.

Instead of assuming LTE, Crutcher (1979) solved the excitation temperatures for both the main lines using observations obtained with the Arecibo and Vermilion River Observatory (VRO) telescopes. They found that the excitation temperature of the two main lines is in the range of 3–8 K and the anomaly of the main-line excitation temperatures is 1–2 K.

As illustrated in Fig. 11, most of the excitation temperatures of OH main lines calculated by our model are in a reasonable range. A small number of low values are present in the bottom left, where both CO emission and OH absorption lines are faint. The reason is that when OH absorption lines are faint, equation (6) may be unable to impose sufficient constraints on the optical depth, leading to higher optical depths and lower excitation temperatures.

6.2 Effect of low-spatial resolution

Because our model is based on CO and OH spectral information, the impact of spatial resolution may be significant.

The spectral features of small-scale components can be diminished due to beam averaging. For instance, we failed to identify the feature of the Brick (G0.253+0.016) feature, which is a high-mass molecular clump lacking star formation activity (Longmore et al. 2012). The size of the Brick is approximately 4 arcmin (Henshaw et al. 2016), and its 35 km s^{-1} component is not evident in either CO or OH spectra. Consequently, we cannot determine the position of the Brick on the face-on view map.

The low-spatial resolution of the data can fail to trace the structure near Sgr A*, where the brightness of the continuum emission varies rapidly. For molecular clouds in front of Sgr A*, the absorption depth of OH should be deep, because the background continuum level is high. However, due to the low-spatial resolution, the absorption depth is diminished, which makes the calculated background continuum level lower than true values. Consequently, on the face-on map, the molecular clouds are moved backward along the line of sight to match a lower level of continuum emission, thereby leaving a blank area in front of Sgr A*, as shown in the face-on view of $b = 0°$ in Fig. 9.

As an example, we examined the y-axis positions of Arms I and II, as defined in Sofue (1995), at $(l, b) = (0.5°, 0°)$. The velocities of Arms I and II are ∼30 and ∼87 km s^{-1}(Sofue 2017), respectively, and their y-axis positions are −52 pc (averaged over the velocity range of 25–35 km s^{-1}) and 50 pc (averaged over the velocity range of 85–90 km s^{-1}), respectively. Although they are already well separated, the true distance between Arms I and II may be larger than 102 pc.

In addition to the OH and CO spectra, the insufficient resolution of the continuum can also affect our result. We assume a cylindrical continuum for each slice. However, if an unresolved molecular cloud is closer to the Galactic plane, we have underestimated the continuum level when deriving its position. On the contrary, if the cloud is further from the Galactic plane, then we have overestimated the continuum level.

In order to illustrate this effect, we examined two slices, $b = -0.125°$ and $b = -0.25°$. Considering a cloud (y-axis position = 0 pc) at $(l, b) = (0.5°, -0.125°)$, if the continuum at $(l, b) = (0.5°, -0.25°)$ is used to derive the position, its corresponding y-axis position is ∼−73 pc. Those clouds with negative y-axis positions (<−100 pc) are pushed beyond the CMZ (y-axis position <−1000 pc). Conversely, if the continuum level at $(l, b) = (0.5°, -0.125°)$ is used to derived the position, clouds with a y-axis position of 0 pc at coordinates $(l, b) = (0.5°, -0.25°)$ would be found to have a measured y-axis position of ∼44 pc. Clouds with negative y-axis positions are measured to have much smaller absolute values. In both cases, if a molecular cloud has positive y-axis position (further away from Sgr A*), the uncertainty of its position is not large (generally less than 38 pc). However, these uncertainties are upper limits, and because the spectra and continuum have been averaged simultaneously, the real uncertainty is smaller.

If high-spatial resolution data are used, the blank area (see Fig. 9) in front of Sgr A* will shrink and more details about the structure in the CMZ will emerge.

6.3 Effect of extra continuum emission

Overall, the diffuse continuum emission is well fitted by three Gaussian components, but small fluctuations are present, as shown in Fig. 4. Those fluctuations might be able to affect the apparent positions of molecular clouds calculated by our model.

Towards high-mass star-forming regions, for instance, Sgr B2, the observed continuum emission is slightly higher than the modelled values due to extra free–free emission from H II regions. For those molecular clouds behind a high-mass star-forming region, the

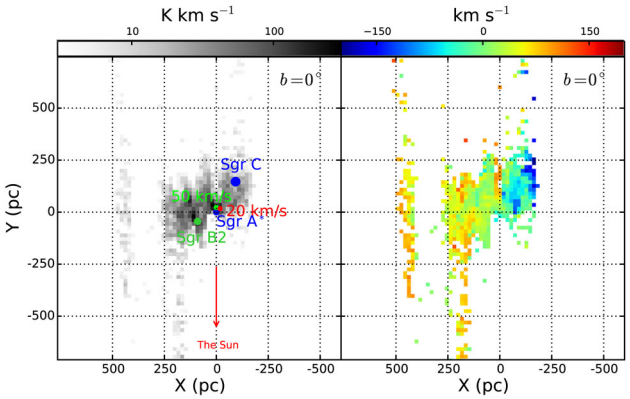

Figure 12. The left-hand panel is a face-on view for $b = 0°$ with five components marked: Sgr B2, Sgr C, Sgr A*, 20 km s^{-1} molecular cloud, and 50 km s^{-1} molecular cloud, while the right-hand panel is the distribution of velocities that are weighted by the intensity.

apparent positions are not affected, because the background emission level derived from equation (10) is still correct.

For the molecular clouds in front of high-mass star-forming regions, although the background continuum level derived from equation (10) is still correct, this continuum level contains free–free emission, which cannot be modelled by Gaussian components. Consequently, the molecular clouds may be artificially moved forward along the line of sight, in order to match a slightly higher background continuum level, generating a gap between the star-forming regions and the molecular clouds in front of it.

However, we did not identify this gap along the line of sight of Sgr B2. Therefore, we suppose this gap is not large and our data are inadequate to resolve this gap due to the insufficient spatial resolution.

6.4 Comparing with other models

Many models have been proposed to explain the 3D structure of molecular clouds in the GC. Three main types of models are competitive (see Henshaw et al. 2016, for a review). One model characterizes the GC with a pattern of two spiral arms (Scoville, Solomon & Jefferts 1974; Sofue 1995; Sawada et al. 2004), while another interprets the molecular clouds as a being distributed on a closed elliptical orbit (Binney et al. 1991; Molinari et al. 2011). Yet another explanation, proposed by Kruijssen et al. (2015), suggests that the orbits of the gas streams in the CMZ are open rather than closed.

Because of the dynamical independence, our model provides a valuable comparison for other dynamical models. Unfortunately, due to the insufficient spatial resolution, we are unable to provide an accurate orbit for the gas streams in $\{l, v_{\rm LSR}\}$ space. However, we derived the position of five prominent subregions, Sgr B2, Sgr C, Sgr A*, 20 km s^{-1} molecular cloud (20MC) and 50 km s^{-1} molecular cloud (50MC), which are marked by coloured dots in Fig. 12. The parameters of the five subregions are listed in Table 2, the columns of which are the name, the Galactic coordinate, the velocity and the mean position over the velocity.

Compared with Sawada et al. (2004), the position of molecular clouds derived from our model is more accurate, because we calculated the excitation temperature and optical depth more precisely, and the morphology of the bar-like structure is clearer. The positions of Sgr A* and Sgr C are consistent with their results.

We find that Sgr B2 is 45 pc nearer than Sgr A*; this result is smaller than the value, 130 pc, found by Reid et al. (2009) using parallax measurements. However, this discrepancy is mostly due to the low-spatial resolution, as discussed in Section 6.2.

The positions of Sgr B2 and Sgr A* are consistent with the model of Kruijssen et al. (2015), while the position of Sgr C is inconsistent with the same model. As shown in Fig. 12, the 20MC and 50MC gather around Sgr A*, while Sgr C is located farther than Sgr A*. Interferometric observations (Coil & Ho 2000) suggest that both the 20MC and 50MC are within 10 pc of Sgr A*, with the 20MC closer to us than Sgr A* and the 50MC farther. Although our calculations put both molecular clouds farther than Sgr A*, the 20MC is still nearer to us than the 50MC. However, the positions of the 20MC and 50MC may be severely affected by the low-spatial resolution, as discussed in Section 6.2. The position of Sgr C should be accurate because few molecular clouds are located nearer than Sgr A* at negative Galactic longitudes. Therefore, there is only one inconsistency between our model and that of Kruijssen et al. (2015).

Recently, Sofue (2017) analysed the 3D structure of the expanding molecular ring (EMR; Scoville 1972) in the CMZ with the help of high-spatial resolution observations of ^{12}CO($J = 1 \rightarrow 0$). In the face-on view of $b = -0.375°$ in Fig. 9, the molecular clouds display a round ring structure with a radius of ∼200 pc. This is consistent with the vertical cylinder model proposed by Sofue (2017) for the EMR.

Interestingly, the inclination angle, 67.5°, derived from our model is greater than the previous results of the short bar as well as the long bar. The length and inclination angle of the short bar is about 2.5 kpc and approximately 20°, respectively (Binney et al. 1991; Dwek et al. 1995; Bissantz & Gerhard 2002; Babusiaux & Gilmore 2005; Cabrera-Lavers et al. 2008), while the half length and inclination angle of the long bar is about 4.5 kpc and around 45°, respectively (Benjamin et al. 2005; Cabrera-Lavers et al. 2007, 2008; Nataf et al. 2013; Wegg, Gerhard & Portail 2015). In terms of the inclination angle, the bar-like structure in the face-on view of $b = 0°$ is more consistent with the long bar. However, further observations, charactering high-spatial resolutions, are needed to confirm this large inclination angle.

6.5 Future improvements in our model

Obviously, our model hinges on the spatial resolution of the data. We already have interferometric OH data in hand, observed with the Karl G. Jansky Very Large Array, which possesses a much higher spatial resolution than the Parkes data. Combining the ^{12}CO($J = 1 \rightarrow 0$) and ^{13}CO($J = 1 \rightarrow 0$) data obtained with Mopra and the OH data of the Galactic ASKAP (the Australian Square Kilometre Array Pathfinder telescope) Survey (GASKAP; Dickey et al. 2013), we will be able to improve our results significantly, which we intend to do in a future paper. Under the scrutiny of high-angular resolution (better than 2 pc at a distance of 8.34 kpc), the blank area in front of Sgr A* will shrink and we will be able to resolve the Brick, the 20MC and the 50MC. Most importantly, the ring structure near Sgr A* will become clear.

7 CONCLUSIONS

We have presented a 3D model of the GC, which is independent of dynamics, with the help of CO emission and OH absorption lines. We use ^{13}CO($J = 1 \rightarrow 0$) data from Mopra to identify regions, where ^{12}CO($J = 1 \rightarrow 0$) emission may be optically thick. The OH data, which are part of SPLASH, include four OH ground-state

transitions: 1612-, 1665-, 1667- and 1720-MHz lines. The angular resolution of OH and CO data is 15.5 arcmin, and with a distance of 8.34 kpc to the GC, the corresponding physical resolution is about 38 pc.

We developed a novel method to calculate the column densities, excitation temperatures and optical depths of the OH ground-state transitions precisely. For the regions where the level of continuum emission behind molecular clouds is observable, the four column densities may be solved from the equations constructed from observations of four ground-state transitions. For the GC, where the two main lines contaminate each other and the background continuum level is unknown, we assume that the excitation temperature of the two main lines are equal and the column densities of OH are proportional to the brightness temperature of CO, enabling us to derive the level of background continuum behind molecular clouds.

Based on a well-modelled volume emission coefficient of the diffuse continuum emission in the GC, we derived the face-on view for $b = -0.375^\circ$, -0.25°, -0.125°, 0°, 0.125° and 0.25°, forming a 3D structure of the molecular clouds. The face-on view of $b = 0^\circ$ displays a bar-like structure with an inclination angel of $67.5 \pm 2.1^\circ$ with respect to the line of sight along $l = 0^\circ$. This angle is generally greater than the value derived by previous works. Due to the low-spatial resolution of the data, we are unable to resolve the structure of molecular clouds near Sgr A* where the continuum emission varies rapidly.

We found the amount of OH in the CMZ is at least 2400 $M_\odot$ and could be as much as 5100 $M_\odot$.

ACKNOWLEDGEMENTS

We would like to thank Sam McSweeney for his helpful report. This work was partly sponsored by the 100 Talents Project of the Chinese Academy of Sciences, the National Science Foundation of China (grant nos 11673066, 11673051 and 11233007) and the Natural Science Foundation of Shanghai under grant no. 15ZR1446900.

REFERENCES

Ao Y. et al., 2013, A&A, 550, A135
Babusiaux C., Gilmore G., 2005, MNRAS, 358, 1309
Barrett A. H., 1964, IEEE Trans. Mil. Electron., 8, 156
Benjamin R. A. et al., 2005, ApJ, 630, L149
Binney J., Gerhard O. E., Stark A. A., Bally J., Uchida K. I., 1991, MNRAS, 252, 210
Bissantz N., Gerhard O., 2002, MNRAS, 330, 591
Bitran M., Alvarez H., Bronfman L., May J., Thaddeus P., 1997, AAPS, 125
Burton M. G. et al., 2013, PASA, 30, e044
Cabrera-Lavers A., Hammersley P. L., González-Fernández C., López-Corredoira M., Garzón F., Mahoney T. J., 2007, A&A, 465, 825
Cabrera-Lavers A., González-Fernández C., Garzón F., Hammersley P. L., López-Corredoira M., 2008, A&A, 491, 781
Calabretta M. R., Staveley-Smith L., Barnes D. G., 2014, PASA, 31, e007
Coil A. L., Ho P. T. P., 2000, ApJ, 533, 245
Colgan S. W. J., Salpeter E. E., Terzian Y., 1989, ApJ, 336, 231
Contopoulos G., Papayannopoulos T., 1980, A&A, 92, 33
Corby J. F. et al., 2015, MNRAS, 452, 3969
Crutcher R. M., 1977, ApJ, 216, 308
Crutcher R. M., 1979, ApJ, 234, 881
Dame T. M., Hartmann D., Thaddeus P., 2001, ApJ, 547, 792
Dawson J. R. et al., 2014, MNRAS, 439, 1596
Destombes J. L., Marliere C., Baudry A., Brillet J., 1977, A&A, 60, 55
Dickey J. M., Crovisier J., Kazes I., 1981, A&A, 98, 271
Dickey J. M. et al., 2013, PASA, 30, e003
Dwek E. et al., 1995, ApJ, 445, 716
Emerson D., 1996, Interpreting Astronomical Spectra. Wiley-VCH, Weinheim, Germany
Ginsburg A. et al., 2016, A&A, 586, A50
Goicoechea J. R. et al., 2011, A&A, 530, L16
Henshaw J. D. et al., 2016, MNRAS, 457, 2675
Jones P. A. et al., 2012, MNRAS, 419, 2961
Jones P. A., Burton M. G., Cunningham M. R., Tothill N. F. H., Walsh A. J., 2013, MNRAS, 433, 221
Kendrew S., Ginsburg A., Johnston K., Beuther H., Bally J., Cyganowski C. J., Battersby C., 2013, ApJ, 775, L50
Knapp G. R., Kerr F. J., 1973, AJ, 78, 453
Kruijssen J. M. D., Longmore S. N., Elmegreen B. G., Murray N., Bally J., Testi L., Kennicutt R. C., 2014, MNRAS, 440, 3370
Kruijssen J. M. D., Dale J. E., Longmore S. N., 2015, MNRAS, 447, 1059
Law C. J., Yusef-Zadeh F., Cotton W. D., Maddalena R. J., 2008, ApJS, 177, 255
Li D., Goldsmith P. F., 2003, ApJ, 585, 823
Longmore S. N. et al., 2012, ApJ, 746, 117
Longmore S. N. et al., 2013, MNRAS, 429, 987
Lu X., Zhang Q., Kauffmann J., Pillai T., Longmore S. N., Kruijssen J. M. D., Battersby C., Gu Q., 2015, ApJ, 814, L18
Mills E. A. C., Morris M. R., 2013, ApJ, 772, 105
Molinari S. et al., 2010, PASP, 122, 314
Molinari S. et al., 2011, ApJ, 735, L33
Morris M., Serabyn E., 1996, ARA&A, 34, 645
Nataf D. M. et al., 2013, ApJ, 769, 88
Oka T., Hasegawa T., Sato F., Tsuboi M., Miyazaki A., 1998, ApJS, 118, 455
Oka T., Hasegawa T., Sato F., Tsuboi M., Miyazaki A., Sugimoto M., 2001, ApJ, 562, 348
Petrov L., Kovalev Y. Y., Fomalont E. B., Gordon D., 2011, AJ, 142, 35
Pierce-Price D. et al., 2000, ApJ, 545, L121
Platania P., Burigana C., Maino D., Caserini E., Bersanelli M., Cappellini B., Mennella A., 2003, A&A, 410, 847
Reid M. J., Menten K. M., Zheng X. W., Brunthaler A., Xu Y., 2009, ApJ, 705, 1548
Reid M. J. et al., 2014, ApJ, 783, 130
Rybicki G. B., Lightman A. P., 1986, Radiative Processes in Astrophysics. Wiley-VCH
Sault R. J., Teuben P. J., Wright M. C. H., 1995, in Shaw R. A., Payne H. E., Hayes J. J. E., eds, ASP Conf. Ser. Vol. 77, Astronomical Data Analysis Software and Systems IV. Astron. Soc. Pac., San Francisco, p. 433
Sawada T., Hasegawa T., Handa T., Cohen R. J., 2004, MNRAS, 349, 1167
Scoville N. Z., 1972, ApJ, 175, L127
Scoville N. Z., Solomon P. M., Jefferts K. B., 1974, ApJ, 187, L63
Shetty R., Beaumont C. N., Burton M. G., Kelly B. C., Klessen R. S., 2012, MNRAS, 425, 720
Sofue Y., 1995, PASJ, 47, 527
Sofue Y., 2017, preprint (arXiv:1706.00157)
Walsh A. J. et al., 2011, MNRAS, 416, 1764
Wegg C., Gerhard O., Portail M., 2015, MNRAS, 450, 4050
Whiting M. T., 2012, MNRAS, 421, 3242
Yan Q.-z., Xu Y., Zhang B., Lu D.-r., Chen X., Tang Z.-h., 2016, AJ, 152, 117
Yusef-Zadeh F. et al., 2009, ApJ, 702, 178

This paper has been typeset from a TEX/LATEX file prepared by the author.

参考文献

Aguirre J E, Ginsburg A G, Dunham M K, et al. The Bolocam Galactic Plane Survey: Survey Description and Data Reduction[J]. ApJS. January 2011, 192: 4. DOI: 10.1088/0067-0049/192/1/4.

Alexander M J, Kobulnicky H A, Kerton C R, et al. The Interstellar Bubbles of G38.9-0.4 and the Impact of Stellar Feedback on Star Formation[J]. ApJ. June 2013, 770: 1. DOI: 10.1088/0004-637X/770/1/1.

Allen R J, Ivette Rodríguez M, Black J H, et al. Faint Extended OH Emission from the Local Interstellar Medium in the Direction l ≈ 108°, b ≈ 5°[J]. AJ. April 2012, 143: 97. DOI: 10.1088/0004-6256/143/4/97.

Allen R J, Ivette Rodríguez M, Black J H, et al. Erratum: ”Faint Extended OH Emission from the Local Interstellar Medium in the Direction l ≈ 108°, b ≈ 5°” <A href=”/abs/2012AJ....143...97A”>(2012, AJ, 143, 97)</A>[J]. AJ. March 2013, 145: 85. DOI: 10.1088/0004-6256/145/3/85.

Allen R J, Hogg D E, Engelke P D. The Structure of Dark Molecular Gas in the Galaxy. I. A Pilot Survey for 18 cm OH Emission Toward l≈ 105°, b≈ +1°[J]. AJ. April 2015, 149: 123. DOI: 10.1088/0004-6256/149/4/123.

An D, Ramírez S V, Sellgren K, et al. Massive Young Stellar Objects in the Galactic Center. I. Spectroscopic Identification from Spitzer Infrared Spectrograph Observations[J]. ApJ. August 2011, 736: 133. DOI: 10.1088/0004-637X/736/2/133.

Anderson L D, Bania T M. Resolution of the Distance Ambiguity for Galactic H II Regions[J]. ApJ. January 2009, 690: 706-719. DOI: 10.1088/0004-637X/690/1/706.

Anderson L D, Bania T M, Balser D S, et al. The Green Bank Telescope H II Region Discovery Survey. II. The Source Catalog[J]. ApJS. June 2011, 194: 32. DOI: 10.1088/0067-0049/194/2/32.

Anderson L D, Bania T M, Balser D S, et al. The Green Bank Telescope H II Region Discovery Survey. III. Kinematic Distances[J]. ApJ. July 2012a, 754: 62. DOI: 10.1088/0004-637X/754/1/62.

Anderson L D, Zavagno A, Deharveng L, et al. The dust properties of bubble H II regions as seen by Herschel[J]. A&A. June 2012b, 542: A10. DOI: 10.1051/0004-6361/201117283.

Anderson L D, Bania T M, Balser D S, et al. The WISE Catalog of Galactic H II Regions[J]. ApJS. May 2014, 212: 1. DOI: 10.1088/0067-0049/212/1/1.

André P, Men'shchikov A, Bontemps S, et al. From filamentary clouds to prestellar cores to the stellar IMF: Initial highlights from the Herschel Gould Belt Survey[J]. A&A. July 2010, 518: L102. DOI: 10.1051/0004-6361/201014666.

André P, Men'shchikov A, Könyves V, et al. Origin of the prestellar core mass function and link to the IMF - Herschel first results[C]//Alves J, Elmegreen B G, Girart J M, et al., Computational Star Formation: volume 270. [S.l.], April 2011: 255-262. DOI: 10.1017/S1743921311000470.

Ao Y, Henkel C, Menten K M, et al. The thermal state of molecular clouds in the Galactic center: evidence for non-photon-driven heating[J]. A&A. February 2013, 550: A135. DOI: 10.1051/0004-6361/201220096.

Argon A L, Reid M J, Menten K M. Interstellar Hydroxyl Masers in the Galaxy. I. The VLA Survey[J]. ApJS. July 2000, 129: 159-227. DOI: 10.1086/313406.

Arzoumanian D, André P, Didelon P, et al. Characterizing interstellar filaments with Herschel in IC 5146[J]. A&A. May 2011, 529: L6. DOI: 10.1051/0004-6361/201116596.

Assef R J, Stern D, Kochanek C S, et al. Mid-infrared Selection of Active Galactic Nuclei with the Wide-field Infrared Survey Explorer. II. Properties of WISE-selected Active Galactic Nuclei in the NDWFS Boötes Field[J]. ApJ. July 2013, 772: 26. DOI: 10.1088/0004-637X/772/1/26.

Avedisova V S. Galactic Spiral Structure Outlined by Diffuse Nebulae in the Solar Neighborhood[J]. Soviet Astronomy Letters. June 1985, 11: 185-188.

Babusiaux C, Gilmore G. The structure of the Galactic bar[J]. MNRAS. April 2005, 358: 1309-1319. DOI: 10.1111/j.1365-2966.2005.08828.x.

Bai Y, Zou H, Liu J, et al. An Updated Ultraviolet Catalog of GALEX Nearby Galaxies[J]. ApJS. September 2015, 220: 6. DOI: 10.1088/0067-0049/220/1/6.

Bally J, Aguirre J, Battersby C, et al. The Bolocam Galactic Plane Survey: λ = 1.1 and 0.35 mm Dust Continuum Emission in the Galactic Center Region[J]. ApJ. September 2010, 721: 137-163. DOI: 10.1088/0004-637X/721/1/137.

Bania T M, Anderson L D, Balser D S. The Arecibo H II Region Discovery Survey[J]. ApJ. November 2012, 759: 96. DOI: 10.1088/0004-637X/759/2/96.

Barrett A H. The Detection of the OH and Other Molecular Lines in the Radio Spectrum of the Interstellar Medium[J]. IEEE Transactions on Military Electronics. July 1964, 8: 156-165. DOI: 10.1109/TME.1964.4323141.

BARRETT A H. The detection of the oh and other molecular lines in the radio spectrum of the interstellar medium[J]. Military Electronics, IEEE Transactions on. 1964, 8 (3): 156–165.

Barriault L, Joncas G, Falgarone E, et al. Multiwavelength observations of cirrus clouds in the North Celestial Loop: the transition from atomic to molecular gas[J]. MNRAS. August 2010, 406: 2713-2731. DOI: 10.1111/j.1365-2966.2010.16871.x.

Bastian N, Covey K R, Meyer M R. A Universal Stellar Initial Mass Function? A Critical Look at Variations[J]. ARA&A. September 2010, 48: 339-389. DOI: 10.1146/annurev-astro-082708-101642.

Battersby C, Ginsburg A, Bally J, et al. The Onset of Massive Star Formation: The Evolution of Temperature and Density Structure in an Infrared Dark Cloud[J]. ApJ. June 2014, 787: 113. DOI: 10.1088/0004-637X/787/2/113.

Beaumont C N, Williams J P. Molecular Rings Around Interstellar Bubbles and the Thickness of Star-Forming Clouds[J]. ApJ. February 2010, 709: 791-800. DOI: 10.1088/0004-637X/709/2/791.

Benjamin R A, GLIMPSE360 Team. GLIMPSE360: Completing the Mid-Infrared View of the Galactic Disk[C]//American Astronomical Society Meeting Abstracts: volume 222. [S.l.], June 2013: 303.03.

Benjamin R A, Churchwell E, Babler B L, et al. GLIMPSE. I. An SIRTF Legacy Project to Map the Inner Galaxy[J]. PASP. August 2003, 115: 953-964. DOI: 10.1086/376696.

Benjamin R A, Churchwell E, Babler B L, et al. First GLIMPSE Results on the Stellar Structure of the Galaxy[J]. ApJ. September 2005, 630: L149-L152. DOI: 10.1086/491785.

Bergin E A, Tafalla M. Cold Dark Clouds: The Initial Conditions for Star Formation[J]. ARA&A. September 2007, 45: 339-396. DOI: 10.1146/annurev.astro.45.071206.100404.

Bertoldi F. The photoevaporation of interstellar clouds. I - Radiation-driven implosion[J]. ApJ. November 1989, 346: 735-755. DOI: 10.1086/168055.

Beuther H, Schilke P, Gueth F. Massive Molecular Outflows at High Spatial Resolution[J]. ApJ. June 2004, 608: 330-340. DOI: 10.1086/386543.

Binney J, Gerhard O E, Stark A A, et al. Understanding the kinematics of Galactic centre gas[J]. MNRAS. September 1991, 252: 210-218. DOI: 10.1093/mnras/252.2.210.

Bissantz N, Gerhard O. Spiral arms, bar shape and bulge microlensing in the Milky

Way[J]. MNRAS. March 2002, 330: 591-608. DOI: 10.1046/j.1365-8711.2002.05116.x.

Bitran M, Alvarez H, Bronfman L, et al. A large scale CO survey of the Galactic center region[J]. AAPS. October 1997, 125. DOI: 10.1051/aas:1997214.

Blaauw A. The O Associations in the Solar Neighborhood[J]. ARA&A. 1964, 2: 213. DOI: 10.1146/annurev.aa.02.090164.001241.

Blackwell R. In preparation, 2017.

Bock D C J, Large M I, Sadler E M. SUMSS: A Wide-Field Radio Imaging Survey of the Southern Sky. I. Science Goals, Survey Design, and Instrumentation[J]. AJ. March 1999, 117: 1578-1593. DOI: 10.1086/300786.

Boyce P J, Cohen R J. A large-scale survey of OH in the galactic centre.[J]. A&AS. November 1994, 107.

Broekhoven-Fiene H, Matthews B C, Harvey P M, et al. The Spitzer Survey of Interstellar Clouds in the Gould Belt. VI. The Auriga-California Molecular Cloud Observed with IRAC and MIPS[J]. ApJ. May 2014, 786: 37. DOI: 10.1088/0004-637X/786/1/37.

Burton M G, Braiding C, Glueck C, et al. The Mopra Southern Galactic Plane CO Survey[J]. PASA. August 2013, 30: e044. DOI: 10.1017/pasa.2013.22.

Cabrera-Lavers A, Hammersley P L, González-Fernández C, et al. Tracing the long bar with red-clump giants[J]. A&A. April 2007, 465: 825-838. DOI: 10.1051/0004-6361:20066185.

Cabrera-Lavers A, González-Fernández C, Garzón F, et al. The long Galactic bar as seen by UKIDSS Galactic plane survey[J]. A&A. December 2008, 491: 781-787. DOI: 10.1051/0004-6361:200810720.

Cabrit S, Bertout C. CO line formation in bipolar flows. II - Decelerated outflow case and summary of results[J]. ApJ. January 1990, 348: 530-541. DOI: 10.1086/168261.

Calabretta M R, Staveley-Smith L, Barnes D G. A New 1.4 GHz Radio Continuum Map of the Sky South of Declination +25°[J]. PASA. January 2014, 31: e007. DOI: 10.1017/pasa.2013.36.

Calzetti D, Wu S Y, Hong S, et al. The Calibration of Monochromatic Far-Infrared Star Formation Rate Indicators[J]. ApJ. May 2010, 714: 1256-1279. DOI: 10.1088/0004-637X/714/2/1256.

Carey S J, Noriega-Crespo A, Mizuno D R, et al. MIPSGAL: A Survey of the Inner Galactic Plane at 24 and 70 μm[J]. PASP. January 2009, 121: 76-97. DOI: 10.1086/596581.

Caswell J L. Positions of hydroxyl masers at 1665 and 1667 MHz[J]. MNRAS. June 1998, 297: 215-235. DOI: 10.1046/j.1365-8711.1998.01468.x.

Caswell J L. OH masers at 1612 and 1720MHz in star-forming regions[J]. MNRAS. September 1999, 308: 683-690. DOI: 10.1046/j.1365-8711.1999.02778.x.

Caswell J L, Haynes R F. Survey of OH masers at 1665 MHz. II - Galactic longitude 340 deg to the galactic centre[J]. Australian Journal of Physics. 1983, 36: 361-399.

Caswell J L, Haynes R F. Survey of OH masers at 1665 MHz. III - Galactic longitudes 233 to 326 deg[J]. Australian Journal of Physics. 1987, 40: 215-238.

Caswell J L, Haynes R F, Goss W M. Survey of OH masers at 1665 and 1667 MHz. I - Galactic longitudes 326 deg to 340 deg[J]. Australian Journal of Physics. September 1980, 33: 639-669.

Caswell J L, Vaile R A, Ellingsen S P, et al. Galactic methanol masers at 6.6 GHz[J]. MNRAS. January 1995, 272: 96-138.

CASWELL J. OH 1720-MHz masers in southern star-forming regions[J]. \mnras. mar 2004, 349: 99–114. DOI: 10.1111/j.1365-2966.2004.07472.x.

CHAISSON E, MCMILLAN S. Astronomy today[M]. [S.l.]: Pearson/Prentice Hall, 2005.

Christopher M H, Scoville N Z, Stolovy S R, et al. HCN and HCO^+ Observations of the Galactic Circumnuclear Disk[J]. ApJ. March 2005, 622: 346-365. DOI: 10.1086/427911.

Churchwell E. Ultra-Compact HII Regions and Massive Star Formation[J]. ARA&A. 2002, 40: 27-62. DOI: 10.1146/annurev.astro.40.060401.093845.

Churchwell E, Povich M S, Allen D, et al. The Bubbling Galactic Disk[J]. ApJ. October 2006, 649: 759-778. DOI: 10.1086/507015.

Churchwell E, Watson D F, Povich M S, et al. The Bubbling Galactic Disk. II. The Inner 20°[J]. ApJ. November 2007, 670: 428-441. DOI: 10.1086/521646.

Churchwell E, Babler B L, Meade M R, et al. The Spitzer/GLIMPSE Surveys: A New View of the Milky Way[J]. PASP. March 2009, 121: 213-230. DOI: 10.1086/597811.

Coil A L, Ho P T P. The Dynamics of Molecular Material within 15 PARSECS of the Galactic Center[J]. ApJ. April 2000, 533: 245-259. DOI: 10.1086/308650.

Condon J J, Cotton W D, Greisen E W, et al. The NRAO VLA Sky Survey[J]. AJ. May 1998, 115: 1693-1716. DOI: 10.1086/300337.

Contopoulos G, Papayannopoulos T. Orbits in weak and strong bars[J]. A&A. December 1980, 92: 33-46.

Cook D O, Dale D A, Johnson B D, et al. The Spitzer Local Volume Legacy (LVL) global optical photometry[J]. MNRAS. November 2014, 445: 881-889. DOI: 10.1093/mnras/stu1580.

Corby J F, Jones P A, Cunningham M R, et al. An ATCA survey of Sagittarius B2 at 7 mm: chemical complexity meets broad-band interferometry[J]. MNRAS. October 2015, 452: 3969-3993. DOI: 10.1093/mnras/stv1494.

Crutcher R M. Excitation of OH toward interstellar dust clouds[J]. ApJ. August 1977, 216: 308-319. DOI: 10.1086/155472.

Crutcher R M. Nonthermal OH main lines and the abundance of OH in interstellar dust clouds[J]. ApJ. December 1979, 234: 881-890. DOI: 10.1086/157570.

Crutcher R M. Magnetic Fields in Molecular Clouds[J]. ARA&A. September 2012, 50: 29-63. DOI: 10.1146/annurev-astro-081811-125514.

Cyganowski C J, Whitney B A, Holden E, et al. A Catalog of Extended Green Objects in the GLIMPSE Survey: A New Sample of Massive Young Stellar Object Outflow Candidates[J]. AJ. December 2008, 136: 2391-2412. DOI: 10.1088/0004-6256/136/6/2391.

Cyganowski C J, Brogan C L, Hunter T R, et al. A Class I and Class II CH_3OH Maser Survey of EGOs from the GLIMPSE Survey[J]. ApJ. September 2009, 702: 1615-1647. DOI: 10.1088/0004-637X/702/2/1615.

Cyganowski C J, Koda J, Rosolowsky E, et al. A Water Maser and NH_3 Survey of GLIMPSE Extended Green Objects[J]. ApJ. February 2013, 764: 61. DOI: 10.1088/0004-637X/764/1/61.

Dahmen G, Huettemeister S, Wilson T L, et al. Molecular gas in the Galactic center region. I. Data from a large scale $C^{18}O(J = 1 \rightarrow 0)$ survey[J]. A&AS. December 1997, 126. DOI: 10.1051/aas:1997389.

Dale J E, Haworth T J, Bressert E. The dangers of being trigger-happy[J]. MNRAS. June 2015, 450: 1199-1211. DOI: 10.1093/mnras/stv396.

Dame T M, Hartmann D, Thaddeus P. The Milky Way in Molecular Clouds: A New Complete CO Survey[J]. ApJ. February 2001, 547: 792-813. DOI: 10.1086/318388.

Danby G, Flower D R, Valiron P, et al. A recalibration of the interstellar ammonia thermometer[J]. MNRAS. November 1988, 235: 229-238. DOI: 10.1093/mnras/235.1.229.

Dawson J R, Walsh A J, Jones P A, et al. SPLASH: the Southern Parkes Large-Area Survey in Hydroxyl - first science from the pilot region[J]. MNRAS. April 2014, 439: 1596-1614. DOI: 10.1093/mnras/stu032.

DAWSON J R, WALSH A J, JONES P A, et al. SPLASH: The southern parkes large-area survey in hydroxyl-first science from the pilot region[J]. Monthly Notices of the Royal Astronomical Society. 2014, 439: 1596–1614. DOI: 10.1093/mnras/stu032.

Deharveng L, Zavagno A, Caplan J. Triggered massive-star formation on the borders of Galactic H II regions. I. A search for "collect and collapse" candidates[J]. A&A. April 2005, 433: 565-577. DOI: 10.1051/0004-6361:20041946.

Deharveng L, Lefloch B, Massi F, et al. Triggered massive-star formation on the borders of Galactic H II regions. III. Star formation at the periphery of Sh2-219[J]. A&A. October 2006, 458: 191-201. DOI: 10.1051/0004-6361:20054641.

Deharveng L, Lefloch B, Kurtz S, et al. Triggered massive-star formation on the borders of Galactic H II regions. IV. Star formation at the periphery of Sh2-212[J]. A&A. May 2008, 482: 585-596. DOI: 10.1051/0004-6361:20079233.

Deharveng L, Schuller F, Anderson L D, et al. A gallery of bubbles. The nature of the bubbles observed by Spitzer and what ATLASGAL tells us about the surrounding neutral material[J]. A&A. November 2010, 523: A6. DOI: 10.1051/0004-6361/201014422.

Dewangan L K, Ojha D K. Multi-wavelength study of triggered star formation around the mid-infrared bubble N14[J]. MNRAS. February 2013, 429: 1386-1397. DOI: 10.1093/mnras/sts430.

Dickey J M, McClure-Griffiths N, Gibson S J, et al. GASKAP-The Galactic ASKAP Survey[J]. PASA. January 2013, 30: e003. DOI: 10.1017/pasa.2012.003.

Dwek E, Arendt R G, Hauser M G, et al. Morphology, near-infrared luminosity, and mass of the Galactic bulge from COBE DIRBE observations[J]. ApJ. June 1995, 445: 716-730. DOI: 10.1086/175734.

Eder J, Lewis B M, Terzian Y. New OH/IR stars from color-selected IRAS sources - 1612 MHz observations[J]. ApJS. February 1988, 66: 183-207. DOI: 10.1086/191252.

Elitzur M. Inversion of the OH 1720-MHz Line[J]. ApJ. January 1976, 203: 124-131. DOI: 10.1086/154054.

Elitzur M, Goldreich P, Scoville N. OH-IR stars. II. A model for the 1612 MHz masers.[J]. ApJ. April 1976, 205: 384-396. DOI: 10.1086/154289.

Elmegreen B G, Lada C J. Sequential formation of subgroups in OB associations[J]. ApJ. June 1977, 214: 725-741. DOI: 10.1086/155302.

Elmegreen B G, Scalo J. Interstellar Turbulence I: Observations and Processes[J]. ARA&A. September 2004, 42: 211-273. DOI: 10.1146/annurev.astro.41.011802.094859.

Emerson D. Interpreting Astronomical Spectra. Wiley-VCH[M]. [S.l.]: [s.n.], June 1996: 472.

Evans N J, II. Physical Conditions in Regions of Star Formation[J]. ARA&A. 1999, 37: 311-362. DOI: 10.1146/annurev.astro.37.1.311.

Everett J E, Churchwell E. Dusty Wind-blown Bubbles[J]. ApJ. April 2010, 713: 592-602. DOI: 10.1088/0004-637X/713/1/592.

Fish V L, Reid M J, Argon A L, et al. Interstellar Hydroxyl Masers in the Galaxy. II. Zeeman Pairs and the Galactic Magnetic Field[J]. ApJ. October 2003, 596: 328-343. DOI: 10.1086/377081.

Forster J R, Caswell J L. The spatial relationship of OH and H2O masers[J]. A&A. April 1989, 213: 339-350.

Frerking M A, Langer W D, Wilson R W. The relationship between carbon monoxide abundance and visual extinction in interstellar clouds[J]. ApJ. November 1982, 262: 590-605. DOI: 10.1086/160451.

Frew D J, Bojičić I S, Parker Q A. A catalogue of integrated Hα fluxes for 1258 Galactic planetary nebulae[J]. MNRAS. May 2013, 431: 2-26. DOI: 10.1093/mnras/sts393.

Fukui Y, Kawamura A. Molecular Clouds in Nearby Galaxies[J]. ARA&A. September 2010, 48: 547-580. DOI: 10.1146/annurev-astro-081309-130854.

Fullmer L, Lonsdale C J. Cataloged galaxies and quasars observed in the IRAS survey. Version 2.[J]. JPL D-1932, Version 2, part no 3, 0 (1989). 1989.

Garay G, Lizano S. Massive Stars: Their Environment and Formation[J]. PASP. September 1999, 111: 1049-1087. DOI: 10.1086/316416.

Ginsburg A, Henkel C, Ao Y, et al. Dense gas in the Galactic central molecular zone is warm and heated by turbulence[J]. A&A. February 2016, 586: A50. DOI: 10.1051/0004-6361/201526100.

Goicoechea J R, Joblin C, Contursi A, et al. OH emission from warm and dense gas in the Orion Bar PDR[J]. A&A. June 2011, 530: L16. DOI: 10.1051/0004-6361/201116977.

Green A J, Frail D A, Goss W M, et al. Continuation of a survey of OH (1720 MHz) Maser Emission Towards Supernova Remnants[J]. AJ. November 1997, 114: 2058. DOI: 10.1086/118626.

Gutermuth R A, Heyer M. A 24 μm Point Source Catalog of the Galactic Plane from Spitzer/MIPSGAL[J]. AJ. February 2015, 149: 64. DOI: 10.1088/0004-6256/149/2/64.

Hacar A, Tafalla M, Kauffmann J, et al. Cores, filaments, and bundles: hierarchical core

formation in the L1495/B213 Taurus region[J]. A&A. June 2013, 554: A55. DOI: 10.1051/0004-6361/201220090.

Harvey P M, Huard T L, Jørgensen J K, et al. The Spitzer Survey of Interstellar Clouds in the Gould Belt. I. IC 5146 Observed With IRAC and MIPS[J]. ApJ. June 2008, 680: 495-516. DOI: 10.1086/587687.

Hatchell J, Terebey S, Huard T, et al. The Spitzer Survey of Interstellar Clouds in the Gould Belt. V. Ophiuchus North Observed with IRAC and MIPS[J]. ApJ. August 2012, 754: 104. DOI: 10.1088/0004-637X/754/2/104.

Hatchell J, Wilson T, Drabek E, et al. The JCMT Gould Belt Survey: SCUBA-2 observations of radiative feedback in NGC 1333[J]. MNRAS. February 2013, 429: L10-L14. DOI: 10.1093/mnrasl/sls015.

Haynes R F, Caswell J L. An OH survey on the 1720-MHz transition and comparisons with 1612, 1665 and 1667-MHz observations[J]. MNRAS. January 1977, 178: 219-230. DOI: 10.1093/mnras/178.2.219.

Heithausen A, Stacy J G, de Vries H W, et al. A composite large-scale CO survey at high galactic latitudes in the second quadrant[J]. A&A. February 1993, 268: 265-275.

Helfand D J, Becker R H, White R L, et al. MAGPIS: A Multi-Array Galactic Plane Imaging Survey[J]. AJ. May 2006, 131: 2525-2537. DOI: 10.1086/503253.

Helou G, Walker D W. Infrared astronomical satellite (IRAS) catalogs and atlases. Volume 7: The small scale structure catalog: volume 7[C]. [S.l.], 1988: 1-265.

Henshaw J D, Longmore S N, Kruijssen J M D, et al. Molecular gas kinematics within the central 250 pc of the Milky Way[J]. MNRAS. April 2016, 457: 2675-2702. DOI: 10.1093/mnras/stw121.

HERBST E. Chemistry in the interstellar medium[J]. Annual Review of Physical Chemistry. 1995, 46 (1): 27–54.

Heyer M, Dame T M. Molecular Clouds in the Milky Way[J]. ARA&A. August 2015, 53: 583-629. DOI: 10.1146/annurev-astro-082214-122324.

HI4PI Collaboration, Ben Bekhti N, Flöer L, et al. HI4PI: A full-sky H I survey based on EBHIS and GASS[J]. A&A. October 2016, 594: A116. DOI: 10.1051/0004-6361/201629178.

Hildebrand R H. The Determination of Cloud Masses and Dust Characteristics from Submillimetre Thermal Emission[J]. QJRAS. September 1983, 24: 267.

Hosokawa T, Inutsuka S I. Dynamical Expansion of Ionization and Dissociation Fronts

around a Massive Star. I. A Mode of Triggered Star Formation[J]. ApJ. April 2005, 623: 917-921. DOI: 10.1086/428648.

Hosokawa T, Inutsuka S I. Dynamical Expansion of Ionization and Dissociation Front around a Massive Star. II. On the Generality of Triggered Star Formation[J]. ApJ. July 2006, 646: 240-257. DOI: 10.1086/504789.

Hou L G, Gao X Y. A statistical study of gaseous environment of Spitzer interstellar bubbles[J]. MNRAS. February 2014, 438: 426-437. DOI: 10.1093/mnras/stt2212.

Hughes V A, MacLeod G C. The use of IRAS data to define H II regions[J]. AJ. March 1989, 97: 786-800. DOI: 10.1086/115024.

Immer K, Brunthaler A, Reid M J, et al. The VLBA Calibrator Search for the BeSSeL Survey[J]. ApJS. June 2011, 194: 25. DOI: 10.1088/0067-0049/194/2/25.

Jackson J M, Rathborne J M, Shah R Y, et al. The Boston University-Five College Radio Astronomy Observatory Galactic Ring Survey[J]. ApJS. March 2006, 163: 145-159. DOI: 10.1086/500091.

Ji W G, Zhou J J, Esimbek J, et al. The infrared dust bubble N22: an expanding H ii region and the star formation around it[J]. A&A. August 2012, 544: A39. DOI: 10.1051/0004-6361/201218861.

Jones P A, Burton M G, Cunningham M R, et al. Spectral imaging of the Central Molecular Zone in multiple 3-mm molecular lines[J]. MNRAS. February 2012, 419: 2961-2986. DOI: 10.1111/j.1365-2966.2011.19941.x.

Jones P A, Burton M G, Cunningham M R, et al. Spectral imaging of the central molecular zone in multiple 7-mm molecular lines[J]. MNRAS. July 2013, 433: 221-234. DOI: 10.1093/mnras/stt717.

Karachentsev I D, Makarov D I, Kaisina E I. Updated Nearby Galaxy Catalog[J]. AJ. April 2013, 145: 101. DOI: 10.1088/0004-6256/145/4/101.

Karlsson R, Sandqvist A, Fathi K, et al. The OH-streamer in Sagittarius A revisited: analysis of hydroxyl absorption within 10 pc from the Galactic centre[J]. A&A. October 2015, 582: A118. DOI: 10.1051/0004-6361/201424426.

Kauffmann J, Pillai T, Zhang Q, et al. The Galactic Center Molecular Cloud Survey. I. A steep linewidth-size relation and suppression of star formation[J]. A&A. July 2017, 603: A89. DOI: 10.1051/0004-6361/201628088.

Kendrew S, Simpson R, Bressert E, et al. The Milky Way Project: A Statistical Study of Massive Star Formation Associated with Infrared Bubbles[J]. ApJ. August 2012, 755: 71. DOI: 10.1088/0004-637X/755/1/71.

Kendrew S, Ginsburg A, Johnston K, et al. Early-stage Massive Star Formation near the Galactic Center: Sgr C[J]. ApJ. October 2013, 775: L50. DOI: 10.1088/2041-8205/775/2/L50.

Kennicutt R C, Jr., Calzetti D, Walter F, et al. Star Formation in NGC 5194 (M51a). II. The Spatially Resolved Star Formation Law[J]. ApJ. December 2007, 671: 333-348. DOI: 10.1086/522300.

Kirk J M, Ward-Thompson D, Palmeirim P, et al. First results from the Herschel Gould Belt Survey in Taurus[J]. MNRAS. June 2013, 432: 1424-1433. DOI: 10.1093/mnras/stt561.

Knapp G R, Kerr F J. OH observations of 16 interstellar dust clouds[J]. AJ. August 1973, 78: 453-457. DOI: 10.1086/111439.

Könyves V, André P, Men'shchikov A, et al. A census of dense cores in the Aquila cloud complex: SPIRE/PACS observations from the Herschel Gould Belt survey[J]. A&A. December 2015, 584: A91. DOI: 10.1051/0004-6361/201525861.

Kraan-Korteweg R C. A catalog of 2810 nearby galaxies - The effect of the Virgocentric flow model on their observed velocities[J]. A&AS. December 1986, 66: 255-279.

Kramer C, Stutzki J, Rohrig R, et al. Clump mass spectra of molecular clouds[J]. A&A. January 1998, 329: 249-264.

Kroupa P, Tout C A, Gilmore G. The distribution of low-mass stars in the Galactic disc[J]. MNRAS. June 1993, 262: 545-587. DOI: 10.1093/mnras/262.3.545.

Kruijssen J M D, Longmore S N, Elmegreen B G, et al. What controls star formation in the central 500 pc of the Galaxy?[J]. MNRAS. June 2014, 440: 3370-3391. DOI: 10.1093/mnras/stu494.

Kruijssen J M D, Dale J E, Longmore S N. The dynamical evolution of molecular clouds near the Galactic Centre - I. Orbital structure and evolutionary timeline[J]. MNRAS. February 2015, 447: 1059-1079. DOI: 10.1093/mnras/stu2526.

Kurtz S, Churchwell E, Wood D O S. Ultracompact H II regions. 2: New high-resolution radio images[J]. ApJS. April 1994, 91: 659-712. DOI: 10.1086/191952.

Lafon G, Baudry A, de La Noe J, et al. The molecular cloud-H II region complexes associated with SH 90 and SH 235[J]. A&A. July 1983, 124: 1-10.

Larson R B. Turbulence and star formation in molecular clouds[J]. MNRAS. March 1981, 194: 809-826. DOI: 10.1093/mnras/194.4.809.

Law C J, Yusef-Zadeh F, Cotton W D, et al. Green Bank Telescope Multiwavelength

Survey of the Galactic Center Region[J]. ApJS. July 2008, 177: 255-274. DOI: 10.1086/533587.

Leger A, Puget J L. Identification of the 'unidentified' IR emission features of interstellar dust?[J]. A&A. August 1984, 137: L5-L8.

Leroy A K, Walter F, Brinks E, et al. The Star Formation Efficiency in Nearby Galaxies: Measuring Where Gas Forms Stars Effectively[J]. AJ. December 2008, 136: 2782-2845. DOI: 10.1088/0004-6256/136/6/2782.

Li D, Goldsmith P F. H I Narrow Self-Absorption in Dark Clouds[J]. ApJ. March 2003, 585: 823-839. DOI: 10.1086/346227.

Li F C, Xu Y, Wu Y W, et al. Ammonia and CO Outflow around 6.7 GHz Methanol Masers[J]. AJ. October 2016, 152: 92. DOI: 10.3847/0004-6256/152/4/92.

Li J Y, Jiang Z B, Liu Y, et al. CO observations of the Galactic bubble N4[J]. Research in Astronomy and Astrophysics. August 2013, 13: 921-934. DOI: 10.1088/1674-4527/13/8/004.

Li Y, Xu Y, Yang J, et al. CO Core Candidates in the Gemini Molecular Cloud[J]. AJ. August 2015, 150: 60. DOI: 10.1088/0004-6256/150/2/60.

Lis D C, Carlstrom J E. Submillimeter continuum survey of the Galactic center[J]. APJ. March 1994, 424: 189-199. DOI: 10.1086/173882.

Lis D C, Menten K M. Infrared Space Observatory Long Wavelength Spectrometer Observations of a Cold Giant Molecular Cloud Core near the Galactic Center[J]. APJ. November 1998, 507: 794-804. DOI: 10.1086/306366.

Liu X L, Wang J J, Xu J L. Physical properties, kinematics and mass function of 12 northern infrared dark clouds[J]. MNRAS. September 2014, 443: 2264-2284. DOI: 10.1093/mnras/stu1268.

Lockman F J. A survey of radio H II regions in the northern sky[J]. ApJS. November 1989, 71: 469-479. DOI: 10.1086/191383.

Longmore S N, Bally J, Testi L, et al. Variations in the Galactic star formation rate and density thresholds for star formation[J]. MNRAS. February 2013, 429: 987-1000. DOI: 10.1093/mnras/sts376.

Longmore S N, Walsh A J, Purcell C R, et al. H_2O Southern Galactic Plane Survey (HOPS): Paper III - properties of dense molecular gas across the inner Milky Way[J]. MNRAS. September 2017, 470: 1462-1490. DOI: 10.1093/mnras/stx1226.

Lu X, Zhang Q, Kauffmann J, et al. Deeply Embedded Protostellar Population in the 20

km s$^{?}$ Cloud of the Central Molecular Zone[J]. ApJ. December 2015, 814: L18. DOI: 10.1088/2041-8205/814/2/L18.

MacLaren I, Richardson K M, Wolfendale A W. Corrections to virial estimates of molecular cloud masses[J]. ApJ. October 1988, 333: 821-825. DOI: 10.1086/166791.

MacLeod G C, Hughes V A. Optically thin dust models for IRAS point sources[J]. AJ. August 1991, 102: 658-665. DOI: 10.1086/115899.

Magnani L, Blitz L, Mundy L. Molecular gas at high Galactic latitudes[J]. ApJ. August 1985, 295: 402-421. DOI: 10.1086/163385.

Martin C L, Walsh W M, Xiao K, et al. The AST/RO Survey of the Galactic Center Region. I. The Inner 3 Degrees[J]. ApJS. January 2004, 150: 239-262. DOI: 10.1086/379661.

Matsuhara H, Tanaka M, Yonekura Y, et al. Observations of [C II] 158 Micron Line and Far-Infrared Continuum Emission toward the High-Latitude Molecular Clouds in Ursa Major[J]. ApJ. December 1997, 490: 744-751. DOI: 10.1086/304895.

Mauch T, Murphy T, Buttery H J, et al. SUMSS: a wide-field radio imaging survey of the southern sky - II. The source catalogue[J]. MNRAS. July 2003, 342: 1117-1130. DOI: 10.1046/j.1365-8711.2003.06605.x.

McClure-Griffiths N M, Dickey J M, Gaensler B M, et al. The Australia Telescope Compact Array H I Survey of the Galactic Center[J]. ApJS. March 2012, 199: 12. DOI: 10.1088/0067-0049/199/1/12.

McGehee P M. Star Formation and Molecular Clouds at High Galactic Latitude[M]. [S.l.]: [s.n.], December 2008: 813.

Menten K M. The discovery of a new, very strong, and widespread interstellar methanol maser line[J]. ApJ. October 1991, 380: L75-L78. DOI: 10.1086/186177.

Mills E A C, Morris M R. Detection of Widespread Hot Ammonia in the Galactic Center[J]. ApJ. August 2013, 772: 105. DOI: 10.1088/0004-637X/772/2/105.

Miville-Deschênes M A, Boulanger F, Joncas G, et al. ISOCAM observations of the Ursa Major cirrus:. Evidence for large abundance variations of small dust grains[J]. A&A. January 2002, 381: 209-218. DOI: 10.1051/0004-6361:20011074.

Miville-Deschênes M A, Joncas G, Falgarone E, et al. High resolution 21 cm mapping of the Ursa Major Galactic cirrus: Power spectra of the high-latitude H I gas[J]. A&A. November 2003, 411: 109-121. DOI: 10.1051/0004-6361:20031297.

Miyazaki A, Tsuboi M. Dense Molecular Clouds in the Galactic Center Region. II. Statistical Properties of the Galactic Center Molecular Clouds[J]. ApJ. June 2000, 536: 357-367. DOI: 10.1086/308899.

Molinari S, Swinyard B, Bally J, et al. Clouds, filaments, and protostars: The Herschel Hi-GAL Milky Way[J]. A&A. July 2010a, 518: L100. DOI: 10.1051/0004-6361/201014659.

Molinari S, Swinyard B, Bally J, et al. Hi-GAL: The Herschel Infrared Galactic Plane Survey[J]. PASP. March 2010b, 122: 314-325. DOI: 10.1086/651314.

Molinari S, Bally J, Noriega-Crespo A, et al. A 100 pc Elliptical and Twisted Ring of Cold and Dense Molecular Clouds Revealed by Herschel Around the Galactic Center[J]. ApJ. July 2011, 735: L33. DOI: 10.1088/2041-8205/735/2/L33.

Morris M, Serabyn E. The Galactic Center Environment[J]. ARA&A. 1996, 34: 645-702. DOI: 10.1146/annurev.astro.34.1.645.

Motte F, Andre P, Neri R. The initial conditions of star formation in the rho Ophiuchi main cloud: wide-field millimeter continuum mapping[J]. A&A. August 1998, 336: 150-172.

Mowat C, Hatchell J, Rumble D, et al. The JCMT Gould Belt Survey: A First Look at SCUBA-2 Observations of the Lupus I Molecular Cloud[J]. MNRAS. May 2017, 467: 812-835. DOI: 10.1093/mnras/stx042.

Murphy T, Mauch T, Green A, et al. The second epoch Molonglo Galactic Plane Survey: compact source catalogue[J]. MNRAS. November 2007, 382: 382-392. DOI: 10.1111/j.1365-2966.2007.12379.x.

Murray N. Star Formation Efficiencies and Lifetimes of Giant Molecular Clouds in the Milky Way[J]. ApJ. March 2011, 729: 133. DOI: 10.1088/0004-637X/729/2/133.

Nagahama T, Mizuno A, Ogawa H, et al. A Spatially Complete ˆ13CO J = 1-0 Survey of the Orion A Cloud[J]. AJ. July 1998, 116: 336-348. DOI: 10.1086/300392.

Narayanan G, Heyer M H, Brunt C, et al. The Five College Radio Astronomy Observatory CO Mapping Survey of the Taurus Molecular Cloud[J]. ApJS. July 2008, 177: 341-361. DOI: 10.1086/587786.

Nataf D M, Gould A, Fouqué P, et al. Reddening and Extinction toward the Galactic Bulge from OGLE-III: The Inner Milky Way's R_V ˜ 2.5 Extinction Curve[J]. ApJ. June 2013, 769: 88. DOI: 10.1088/0004-637X/769/2/88.

Natta A, Panagia N. Model calculations of dusty H II regions[J]. A&A. July 1976, 50: 191-211.

Neugebauer G, Habing H J, van Duinen R, et al. The Infrared Astronomical Satellite (IRAS) mission[J]. ApJ. March 1984, 278: L1-L6. DOI: 10.1086/184209.

Ochsendorf B B, Tielens A G G M. A bimodal dust grain distribution in the IC 434 H ii region[J]. A&A. April 2015, 576: A2. DOI: 10.1051/0004-6361/201424799.

Oka T, Hasegawa T, Sato F, et al. A Large-Scale CO Survey of the Galactic Center[J]. ApJS. October 1998, 118: 455-515. DOI: 10.1086/313138.

Oka T, Hasegawa T, Sato F, et al. Statistical Properties of Molecular Clouds in the Galactic Center[J]. ApJ. November 2001, 562: 348-362. DOI: 10.1086/322976.

Oka T, Geballe T R, Goto M, et al. Hot and Diffuse Clouds near the Galactic Center Probed by Metastable $H^{+}_{3}1$,[J]. ApJ. October 2005, 632: 882-893. DOI: 10.1086/432679.

Ott J, Weiß A, Staveley-Smith L, et al. ATCA Survey of Ammonia in the Galactic Center: The Temperatures of Dense Gas Clumps between Sgr A* and Sgr B2[J]. ApJ. April 2014, 785: 55. DOI: 10.1088/0004-637X/785/1/55.

Padoan P, Nordlund Å. The Star Formation Rate of Supersonic Magnetohydrodynamic Turbulence[J]. ApJ. March 2011, 730: 40. DOI: 10.1088/0004-637X/730/1/40.

Pattle K, Ward-Thompson D, Kirk J M, et al. The JCMT Gould Belt Survey: first results from the SCUBA-2 observations of the Ophiuchus molecular cloud and a virial analysis of its prestellar core population[J]. MNRAS. June 2015, 450: 1094-1122. DOI: 10.1093/mnras/stv376.

Peeters E, Spoon H W W, Tielens A G G M. Polycyclic Aromatic Hydrocarbons as a Tracer of Star Formation?[J]. ApJ. October 2004, 613: 986-1003. DOI: 10.1086/423237.

Penprase B E. Photometric and spectroscopic analysis of high galactic latitude molecular clouds. II - High-resolution spectroscopic observations of NA I, CA II, CA I, CH, and CH(+1)[J]. ApJS. October 1993, 88: 433-475. DOI: 10.1086/191829.

Petriella A, Paron S, Giacani E. The environment of the infrared dust bubble N65: a multiwavelength study[J]. A&A. April 2010, 513: A44. DOI: 10.1051/0004-6361/200913617.

Petrov L, Kovalev Y Y, Fomalont E B, et al. The Very Long Baseline Array Galactic Plane Survey VGaPS[J]. AJ. August 2011, 142: 35. DOI: 10.1088/0004-6256/142/2/35.

Pierce-Price D, Richer J S, Greaves J S, et al. A Deep Submillimeter Survey of the Galactic Center[J]. ApJ. December 2000, 545: L121-L125. DOI: 10.1086/317884.

Platania P, Burigana C, Maino D, et al. Full sky study of diffuse Galactic emission at decimeter wavelengths[J]. A&A. November 2003, 410: 847-863. DOI: 10.1051/0004-6361:20031125.

Pomarès M, Zavagno A, Deharveng L, et al. Triggered star formation on the borders of

the Galactic Hii region RCW 82[J]. A&A. February 2009, 494: 987-1003. DOI: 10.1051/0004-6361:200811050.

Pound M W, Goodman A A. Kinematics of the Ursa Major Molecular Clouds[J]. ApJ. June 1997, 482: 334-354. DOI: 10.1086/304136.

Prisinzano L, Damiani F, Micela G, et al. The star formation region NGC 6530: Distance, ages and initial mass function[J]. A&A. February 2005, 430: 941-957. DOI: 10.1051/0004-6361:20040432.

Protheroe R J, Ott J, Ekers R D, et al. Interpretation of radio continuum and molecular line observations of Sgr B2: free-free and synchrotron emission, and implications for cosmic rays[J]. MNRAS. October 2008, 390: 683-692. DOI: 10.1111/j.1365-2966.2008.13752.x.

Purcell C R, Longmore S N, Walsh A J, et al. The H_2O Southern Galactic Plane Survey: NH_3 (1,1) and (2,2) catalogues[J]. MNRAS. November 2012, 426: 1972-1991. DOI: 10.1111/j.1365-2966.2012.21800.x.

Qiao H H, Walsh A J, Green J A, et al. Accurate OH Maser Positions from the SPLASH Pilot Region[J]. ApJS. December 2016, 227: 26. DOI: 10.3847/1538-4365/227/2/26.

Rahman M, Murray N. A New Sample of Very Massive Star Forming Complexes in the Spitzer Glimpse Survey[J]. ApJ. August 2010, 719: 1104-1122. DOI: 10.1088/0004-637X/719/2/1104.

Rathborne J M, Longmore S N, Jackson J M, et al. Turbulence Sets the Initial Conditions for Star Formation in High-pressure Environments[J]. ApJ. November 2014, 795: L25. DOI: 10.1088/2041-8205/795/2/L25.

Rawlings J M C, Redman M P, Keto E, et al. HCO^+ emission excess in bipolar outflows[J]. MNRAS. July 2004, 351: 1054-1062. DOI: 10.1111/j.1365-2966.2004.07855.x.

Reid M A, Wadsley J, Petitclerc N, et al. Measuring the Clump Mass Function in the Age of SCUBA2, Herschel, and ALMA[J]. ApJ. August 2010, 719: 561-575. DOI: 10.1088/0004-637X/719/1/561.

Reid M J, Menten K M, Zheng X W, et al. A Trigonometric Parallax of Sgr B2[J]. ApJ. November 2009, 705: 1548-1553. DOI: 10.1088/0004-637X/705/2/1548.

Reid M J, Menten K M, Brunthaler A, et al. Trigonometric Parallaxes of High Mass Star Forming Regions: The Structure and Kinematics of the Milky Way[J]. ApJ. March 2014, 783: 130. DOI: 10.1088/0004-637X/783/2/130.

Reiners A, Basri G. On the magnetic topology of partially and fully convective stars[J]. A&A. March 2009, 496: 787-790. DOI: 10.1051/0004-6361:200811450.

Rice T S, Goodman A A, Bergin E A, et al. A Uniform Catalog of Molecular Clouds in the Milky Way[J]. ApJ. May 2016, 822: 52. DOI: 10.3847/0004-637X/822/1/52.

Robinson B J, McGee R X. OH Molecules in the Interstellar Medium[J]. ARA&A. 1967, 5: 183. DOI: 10.1146/annurev.aa.05.090167.001151.

Roman-Duval J, Jackson J M, Heyer M, et al. Kinematic Distances to Molecular Clouds Identified in the Galactic Ring Survey[J]. ApJ. July 2009, 699: 1153-1170. DOI: 10.1088/0004-637X/699/2/1153.

Rosolowsky E, Dunham M K, Ginsburg A, et al. The Bolocam Galactic Plane Survey. II. Catalog of the Image Data[J]. ApJS. May 2010, 188: 123-138. DOI: 10.1088/0067-0049/188/1/123.

Rybicki G B, Lightman A P. Radiative Processes in Astrophysics. Wiley-VCH[M]. [S.l.]: [s.n.], June 1986: 400.

Salpeter E E. The Luminosity Function and Stellar Evolution.[J]. ApJ. January 1955, 121: 161. DOI: 10.1086/145971.

Samal M R, Zavagno A, Deharveng L, et al. The molecular complex associated with the Galactic H II region Sh2-90: a possible site of triggered star formation[J]. A&A. June 2014, 566: A122. DOI: 10.1051/0004-6361/201321794.

Sault R J, Teuben P J, Wright M C H. A Retrospective View of MIRIAD[C]//Shaw R A, Payne H E, Hayes J J E, Astronomical Data Analysis Software and Systems IV: volume 77. [S.l.], 1995: 433.

Sawada T, Hasegawa T, Handa T, et al. A molecular face-on view of the Galactic Centre region[J]. MNRAS. April 2004, 349: 1167-1178. DOI: 10.1111/j.1365-2966.2004.07603.x.

Sawada T, Hasegawa T, Sugimoto M, et al. Structural Variation of Molecular Gas in the Sagittarius Arm and Interarm Regions[J]. ApJ. June 2012, 752: 118. DOI: 10.1088/0004-637X/752/2/118.

SAWADA T, HASEGAWA T, HANDA T, et al. A molecular face-on view of the Galactic Centre region[J/OL]. Monthly Notices of the Royal Astronomical Society. 2004, 349 (4): 1167–1178. http://mnras.oxfordjournals.org/cgi/doi/10.1111/j.1365-2966.2004.07603.x. DOI: 10.1111/j.1365-2966.2004.07603.x.

Scalo J, Elmegreen B G. Interstellar Turbulence II: Implications and Effects[J]. ARA&A. September 2004, 42: 275-316. DOI: 10.1146/annurev.astro.42.120403.143327.

Schneider N, Csengeri T, Hennemann M, et al. Cluster-formation in the Rosette molecular

cloud at the junctions of filaments[J]. A&A. April 2012, 540: L11. DOI: 10.1051/0004-6361/201118566.

Schuller F, Menten K M, Contreras Y, et al. ATLASGAL - The APEX telescope large area survey of the galaxy at 870 μm[J]. A&A. September 2009, 504: 415-427. DOI: 10.1051/0004-6361/200811568.

Scoville N Z, Sargent A I, Sanders D B, et al. High-resolution mapping of molecular outflows in NGC 2071, W49, and NGC 7538[J]. ApJ. April 1986, 303: 416-432. DOI: 10.1086/164086.

Sevenster M N, Chapman J M, Habing H J, et al. The ATCA/VLA OH 1612 MHz survey. I. Observations of the galactic bulge Region[J]. A&AS. April 1997a, 122. DOI: 10.1051/aas:1997294.

Sevenster M N, Chapman J M, Habing H J, et al. The ATCA/VLA OH 1612 MHz survey. II. Observations of the galactic Disk region[J]. A&AS. September 1997b, 124. DOI: 10.1051/aas:1997365.

Sevenster M N, van Langevelde H J, Moody R A, et al. The ATCA/VLA OH 1612 MHz survey. III. Observations of the Northern Galactic Plane[J]. A&A. February 2001, 366: 481-489. DOI: 10.1051/0004-6361:20000354.

SHAN W, YANG J, SHI S, et al. Development of superconducting spectroscopic array receiver: A multibeam 2sb sis receiver for millimeter-wave radio astronomy[J]. IEEE. 2012, 2: 593.

Shepherd D S, Churchwell E. Bipolar Molecular Outflows in Massive Star Formation Regions[J]. ApJ. November 1996, 472: 225. DOI: 10.1086/178057.

Sherman R A. Investigation of Molecular Cloud Structure around Infrared Bubbles: CARMA Observations of N14, N22, and N74[J]. ApJ. November 2012, 760: 58. DOI: 10.1088/0004-637X/760/1/58.

Shetty R, Beaumont C N, Burton M G, et al. The linewidth-size relationship in the dense interstellar medium of the Central Molecular Zone[J]. MNRAS. September 2012, 425: 720-729. DOI: 10.1111/j.1365-2966.2012.21588.x.

Shirley Y L. The Critical Density and the Effective Excitation Density of Commonly Observed Molecular Dense Gas Tracers[J]. PASP. March 2015, 127: 299-310. DOI: 10.1086/680342.

Shu F H, Adams F C, Lizano S. Star formation in molecular clouds - Observation and theory[J]. ARA&A. 1987, 25: 23-81. DOI: 10.1146/annurev.aa.25.090187.000323.

Sidorin V, Douglas K A, Palouš J, et al. Exploring GLIMPSE bubble N107. Multi-wavelength observations and simulations[J]. A&A. May 2014, 565: A6. DOI: 10.1051/0004-6361/201322687.

Simpson R J, Povich M S, Kendrew S, et al. The Milky Way Project First Data Release: a bubblier Galactic disc[J]. MNRAS. August 2012, 424: 2442-2460. DOI: 10.1111/j.1365-2966.2012.20770.x.

Smith M D, Suttner G, Yorke H W. Numerical hydrodynamic simulations of jet-driven bipolar outflows.[J]. A&A. July 1997, 323: 223-230.

Snell R L, Scoville N Z, Sanders D B, et al. High-velocity molecular jets[J]. ApJ. September 1984, 284: 176-193. DOI: 10.1086/162397.

Snow T P, McCall B J. Diffuse Atomic and Molecular Clouds[J]. ARA&A. September 2006, 44: 367-414. DOI: 10.1146/annurev.astro.43.072103.150624.

Sodroski T J, Bennett C, Boggess N, et al. Large-scale characteristics of interstellar dust from COBE DIRBE observations[J]. ApJ. June 1994, 428: 638-646. DOI: 10.1086/174274.

Sofue Y. Galactic-Center Molecular Arms, Ring, and Expanding Shell. I. Kinematical Structures in Longitude–Velocity Diagrams[J]. PASJ. October 1995, 47: 527-549.

Sofue Y. The 200-pc molecular cylinder in the Galactic Centre[J]. MNRAS. September 2017, 470: 1982-1990. DOI: 10.1093/mnras/stx1389.

Stead J J, Hoare M G. Molecular cloud distance determination from deep NIR survey extinction measurements[J]. MNRAS. September 2010, 407: 923-936. DOI: 10.1111/j.1365-2966.2010.17014.x.

Stead J J, Hoare M G. Determining the age of young embedded clusters[J]. MNRAS. December 2011, 418: 2219-2233. DOI: 10.1111/j.1365-2966.2011.19522.x.

Stil J M, Taylor A R, Dickey J M, et al. The VLA Galactic Plane Survey[J]. AJ. September 2006, 132: 1158-1176. DOI: 10.1086/505940.

Su Y, Yang J, Zhou X, et al. Interaction between Supernova Remnant G22.7-0.2 and the Ambient Molecular Clouds[J]. ApJ. December 2014, 796: 122. DOI: 10.1088/0004-637X/796/2/122.

Sugitani K, Ogura K. A catalog of bright-rimmed clouds with IRAS point sources: Candidates for star formation by radiation-driven implosion. 2: The southern hemisphere[J]. ApJS. May 1994, 92: 163-172. DOI: 10.1086/191964.

Sugitani K, Fukui Y, Ogura K. A catalog of bright-rimmed clouds with IRAS point

sources: Candidates for star formation by radiation-driven implosion. I - The Northern Hemisphere[J]. ApJS. September 1991, 77: 59-66. DOI: 10.1086/191597.

Szymczak M, Kus A J, Hrynek G, et al. 6.7 GHz methanol masers at sites of star formation. A blind survey of the Galactic plane between 20 degr ⩽⩽= 40 degr and |b| ⩽= 0\fdg52[J]. A&A. September 2002, 392: 277-286. DOI: 10.1051/0004-6361: 20020907.

te Lintel Hekkert P, Caswell J L, Habing H J, et al. 1612 MHz OH survey of IRAS point sources. I - Observations made at Dwingeloo, Effelsberg and Parkes[J]. A&AS. October 1991, 90: 327-353.

Thompson M A, Urquhart J S, Moore T J T, et al. The statistics of triggered star formation: an overdensity of massive young stellar objects around Spitzer bubbles[J]. MNRAS. March 2012, 421: 408-418. DOI: 10.1111/j.1365-2966.2011.20315.x.

Tokuda K, Onishi T, Matsumoto T, et al. Revealing a Detailed Mass Distribution of a High-density Core MC27/L1521F in Taurus with ALMA[J]. ApJ. July 2016, 826: 26. DOI: 10.3847/0004-637X/826/1/26.

Tothill N F H, Gagné M, Stecklum B, et al. The Lagoon Nebula and its Vicinity[M]. [S.l.]: [s.n.], December 2008: 533.

Tremblin P, Anderson L D, Didelon P, et al. Age, size, and position of H ii regions in the Galaxy. Expansion of ionized gas in turbulent molecular clouds[J]. A&A. August 2014a, 568: A4. DOI: 10.1051/0004-6361/201423959.

Tremblin P, Schneider N, Minier V, et al. Ionization compression impact on dense gas distribution and star formation. Probability density functions around H II regions as seen by Herschel[J]. A&A. April 2014b, 564: A106. DOI: 10.1051/0004-6361/201322700.

Tsuboi M, Handa T, Ukita N. Dense Molecular Clouds in the Galactic Center Region. I. Observations and Data[J]. ApJS. January 1999, 120: 1-39. DOI: 10.1086/313165.

VAPNIK V N. The nature of statistical learning theory[M]//[S.l.]: Springer-Verlag New York, Inc., 1995.

Walmsley C M, Ungerechts H. Ammonia as a molecular cloud thermometer[J]. A&A. June 1983, 122: 164-170.

Walsh A, Voronkov M, Lo N, et al. HOPS - the H2O southern galactic Plane Survey[M]. [S.l.]: [s.n.], April 2010.

Walsh A J, Hyland A R, Robinson G, et al. Studies of ultracompact HII regions - I. Methanol maser survey of IRAS-selected sources[J]. MNRAS. October 1997, 291: 261-278. DOI: 10.1093/mnras/291.2.261.

Walsh A J, Burton M G, Hyland A R, et al. Studies of ultracompact HII regions - II. High-resolution radio continuum and methanol maser survey[J]. MNRAS. December 1998, 301: 640-698. DOI: 10.1046/j.1365-8711.1998.02014.x.

Walsh A J, Burton M G, Hyland A R, et al. Studies of ultracompact HII regions - III. Near-infrared survey of selected regions[J]. MNRAS. November 1999, 309: 905-922. DOI: 10.1046/j.1365-8711.1999.02890.x.

Walsh A J, Breen S L, Britton T, et al. The H_2O Southern Galactic Plane Survey (HOPS) - I. Techniques and H_2O maser data[J]. MNRAS. September 2011, 416: 1764-1821. DOI: 10.1111/j.1365-2966.2011.19115.x.

Walsh A J, Purcell C R, Longmore S N, et al. Accurate water maser positions from HOPS[J]. MNRAS. August 2014, 442: 2240-2252. DOI: 10.1093/mnras/stu989.

Watson C, Araya E, Sewilo M, et al. Resolution of Distance Ambiguities of Inner Galaxy Massive Star Formation Regions. I.[J]. ApJ. April 2003, 587: 714-726. DOI: 10.1086/368286.

Watson C, Povich M S, Churchwell E B, et al. Infrared Dust Bubbles: Probing the Detailed Structure and Young Massive Stellar Populations of Galactic H II Regions[J]. ApJ. July 2008, 681: 1341-1355. DOI: 10.1086/588005.

Watson C, Corn T, Churchwell E B, et al. IR Dust Bubbles. II. Probing the Detailed Structure and Young Massive Stellar Populations of Galactic H II Regions[J]. ApJ. March 2009, 694: 546-555. DOI: 10.1088/0004-637X/694/1/546.

Watson C, Hanspal U, Mengistu A. Triggered Star Formation and Dust Around Mid-infrared-identified Bubbles[J]. ApJ. June 2010, 716: 1478-1492. DOI: 10.1088/0004-637X/716/2/1478.

Wegg C, Gerhard O, Portail M. The structure of the Milky Way's bar outside the bulge[J]. MNRAS. July 2015, 450: 4050-4069. DOI: 10.1093/mnras/stv745.

Weinreb S, Barrett A H, Meeks M L, et al. Radio Observations of OH in the Interstellar Medium[J]. Nature. November 1963, 200: 829-831. DOI: 10.1038/200829a0.

Wenger T V, Bania T M, Balser D S, et al. The Green Bank Telescope H II Region Discovery Survey. IV. Helium and Carbon Recombination Lines[J]. ApJ. February 2013, 764: 34. DOI: 10.1088/0004-637X/764/1/34.

White R L, Becker R H, Helfand D J. New Catalogs of Compact Radio Sources in the Galactic Plane[J]. AJ. August 2005, 130: 586-596. DOI: 10.1086/431249.

Whiting M T. DUCHAMP: a 3D source finder for spectral-line data[J]. MNRAS. April 2012, 421: 3242-3256. DOI: 10.1111/j.1365-2966.2012.20548.x.

Wilson B A, Dame T M, Masheder M R W, et al. A uniform CO survey of the molecular clouds in Orion and Monoceros[J]. A&A. February 2005, 430: 523-539. DOI: 10.1051/0004-6361:20035943.

Wilson R W, Jefferts K B, Penzias A A. Carbon Monoxide in the Orion Nebula[J]. ApJ. July 1970, 161: L43. DOI: 10.1086/180567.

Wolfire M G, Churchwell E. Circumstellar dust emission models[J]. ApJ. June 1994, 427: 889-897. DOI: 10.1086/174194.

Wood D O S, Churchwell E. Massive stars embedded in molecular clouds - Their population and distribution in the galaxy[J]. ApJ. May 1989a, 340: 265-272. DOI: 10.1086/167390.

Wood D O S, Churchwell E. The morphologies and physical properties of ultracompact H II regions[J]. ApJS. April 1989b, 69: 831-895. DOI: 10.1086/191329.

Wood P R, Whiteoak J B, Hughes S M G, et al. OH/IR stars in the Magellanic Clouds[J]. ApJ. October 1992, 397: 552-569. DOI: 10.1086/171812.

Wootten A, Sargent A, Knapp G, et al. The structure of bright-rimmed molecular clouds[J]. ApJ. June 1983, 269: 147-163. DOI: 10.1086/161026.

Wright E L. Quasar reddening, intergalactic dust, and the microwave background[J]. ApJ. November 1981, 250: 1-6. DOI: 10.1086/159342.

Wright E L, Eisenhardt P R M, Mainzer A K, et al. The Wide-field Infrared Survey Explorer (WISE): Mission Description and Initial On-orbit Performance[J]. AJ. December 2010, 140: 1868-1881. DOI: 10.1088/0004-6256/140/6/1868.

Wu J, Evans N J, II, Shirley Y L, et al. The Properties of Massive, Dense Clumps: Mapping Surveys of HCN and CS[J]. ApJS. June 2010, 188: 313-357. DOI: 10.1088/0067-0049/188/2/313.

Wynn-Williams C G, Becklin E E, Neugebauer G. Infrared studies of H II regions and OH sources.[J]. ApJ. February 1974, 187: 473-485. DOI: 10.1086/152656.

Xu J L, Ju B G. Star formation associated with a large-scale infrared bubble[J]. A&A. September 2014, 569: A36. DOI: 10.1051/0004-6361/201423952.

Xu Y, Zheng X W, Jiang D R. Statistical Properties of 6.7 GHz Methanol Maser Sources[J]. ChJAA (Chin. J. Astron. Astrophys.). February 2003, 3: 49-68.

Xu Y, Reid M J, Menten K M, et al. Search for Compact Extragalactic Radio Sources near Massive Star-forming Regions[J]. ApJS. October 2006, 166: 526-533. DOI: 10.1086/507112.

Xu Y, Li J J, Reid M J, et al. On the Nature of the Local Spiral Arm of the Milky Way[J]. ApJ. May 2013, 769: 15. DOI: 10.1088/0004-637X/769/1/15.

Yan Q Z, Xu Y, Zhang B, et al. Molecular Lines of 13 Galactic Infrared Bubble Regions[J]. AJ. November 2016, 152: 117. DOI: 10.3847/0004-6256/152/5/117.

Yoshida A, Kitamura Y, Shimajiri Y, et al. Dependence of the Turbulent Velocity Field on Gas Density in L1551[J]. ApJ. August 2010, 718: 1019-1035. DOI: 10.1088/0004-637X/718/2/1019.

Yuan J H, Wu Y, Li J Z, et al. Expanding Shell and Star Formation in the Infrared Dust Bubble N6[J]. ApJ. December 2014, 797: 40. DOI: 10.1088/0004-637X/797/1/40.

Yusef-Zadeh F, Roberts D A, Goss W M, et al. High-Resolution Observations of OH (1720 MHZ) Masers toward the Galactic Center[J]. ApJ. February 1999, 512: 230-236. DOI: 10.1086/306769.

Yusef-Zadeh F, Hewitt J W, Cotton W. A 20 Centimeter Survey of the Galactic Center Region. I. Detection of Numerous Linear Filaments[J]. ApJS. December 2004, 155: 421-550. DOI: 10.1086/425257.

Yusef-Zadeh F, Hewitt J W, Arendt R G, et al. Star Formation in the Central 400 pc of the Milky Way: Evidence for a Population of Massive Young Stellar Objects[J]. ApJ. September 2009, 702: 178-225. DOI: 10.1088/0004-637X/702/1/178.

YUSEF-ZADEH F, HEWITT J W, ARENDT R G, et al. Star Formation in the Central 400 Pc of the Milky Way: Evidence for a Population of Massive Young Stellar Objects[J/OL]. The Astrophysical Journal. 2009, 702 (1): 178–225. http://adsabs.harvard.edu/abs/2009ApJ...702..178Y. DOI: 10.1088/0004-637X/702/1/178.

Zavagno A, Deharveng L, Comerón F, et al. Triggered massive-star formation on the borders of Galactic H II regions. II. Evidence for the collect and collapse process around RCW 79[J]. A&A. January 2006, 446: 171-184. DOI: 10.1051/0004-6361:20053952.

Zavagno A, Anderson L D, Russeil D, et al. Star formation triggered by H II regions in our Galaxy. First results for N49 from the Herschel infrared survey of the Galactic plane[J]. A&A. July 2010, 518: L101. DOI: 10.1051/0004-6361/201014587.

Zhang Q, Hunter T R, Brand J, et al. Search for CO Outflows toward a Sample of 69 High-Mass Protostellar Candidates: Frequency of Occurrence[J]. ApJ. May 2001, 552: L167-L170. DOI: 10.1086/320345.

Zhang Q, Hunter T R, Brand J, et al. Search for CO Outflows toward a Sample of 69 High-Mass Protostellar Candidates. II. Outflow Properties[J]. ApJ. June 2005, 625: 864-882. DOI: 10.1086/429660.

Zhou X, Yang J, Fang M, et al. Discovery of a Pre-existing Molecular Filament Associated with Supernova Remnant G127.1+0.5[J]. ApJ. August 2014, 791: 109. DOI: 10.1088/0004-637X/791/2/109.

Zinnecker H, Yorke H W. Toward Understanding Massive Star Formation[J]. ARA&A. September 2007, 45: 481-563. DOI: 10.1146/annurev.astro.44.051905.092549.

作者简历

基本情况

闫庆增，男，1986 年 10 月出生于山东省，中国科学院上海天文台博士研究生

教育状况

2004 年 9 月至 2008 年 7 月，华东师范大学软件学院，本科——软件工程。

2009 年 9 月至 2012 年 12 月，中国科学院上海天文台，硕士——天体测量与天体力学。

2013 年 9 月至 2015 年 11 月，中国科学院上海天文台 & 紫金山天文台，博士联合培养——天体测量与天体力学。

2015 年 11 月至 2017 年，中国科学院上海天文台 & 科廷大学 (Curtin University)，博士联合培养——天体测量与天体力学。

指导老师

中国科学院上海天天文台：唐正宏、张波研究员

紫金山天文台：徐烨研究员

科廷大学：Dr. Jean-Pierre Macquart、Dr. Andrew J. Walsh、Dr. Paul J. Hancock

联系方式

通讯地址：上海市南丹路 80 号上海天文台

邮编：200030

E-mail: qzyan@shao.ac.cn　　yqz206@gmail.com

研究兴趣

分子云与大质量恒星形成，分子外向流

H II 区

银河系中心与银河系结构

博士期间发表论文

[1] **Yan, Q.-Z.** and Xu, Y. and Zhang, B. and Lu, D.-R. and Chen, X. and Tang, Z.-H. *Molecular Lines of 13 Galactic Infrared Bubble Regions*. 2016. **The Astronomical Journal**, Volume 152, Issue 5, article id. 117, 30 pp. (2016). **ADS Link**.

[2] **Qing-Zeng Yan**, A. J. Walsh, J. R. Dawson, J. P. Macquart, R. Blackwell, M. G. Burton, G. Rowell, Bo Zhang, Ye Xu, Zheng-Hong Tang, P. J. Hancock. 2017. , *Towards a Three-Dimensional Distribution of Molecular Clouds in the Galactic Centre*, **Monthly Notices of the Royal Astronomical Society**, Volume 471, Issue 3, 1 November 2017 **ADS Link**.

[3] **Qing-Zeng Yan**, Ye Xu, A. J. Walsh, J. P. Macquart, G.C. MacLeod, Bo Zhang, P. J. Hancock, Xi Chen, Zheng-Hong Tang. *Improved Selection Criteria For H* II *Regions, Based on IRAS Sources*. 2017. **Submitted to MNRAS**.

致　谢

We are all in the gutter, but some of us are looking at the stars.

— Oscar Wilde

谨以此博士论文，献给我的导师、家人、同学和朋友。

感谢我的导师唐正宏研究员。从硕士研究生开始，唐老师就是我的导师，时至今日，已八年有余。第一次见到唐老师，是在硕士研究生面试的时候，隐约记得唐老师问我，关于天文你都知道哪些内容，我说我知道 CCD。其实，我只是知道 CCD 三个字母而已。从那时的一无所知，到现在完成博士工作，唐老师功不可没。唐老师知道我的天文基础不好，所以二次送我去南京大学学习基础课，实际上，在南大的学习对我的科研工作意义深远。我理解一些问题有时比较缓慢，有时连我自己都会对自己失去信心；但是，唐老师却一直耐心地指导我，直到我完成学业。在以后的科研，我会谨记唐老师的教导，不畏困难，毅然前行。

感谢我的导师徐烨研究员。在我还没硕士入学之前，唐老师就跟我介绍徐老师关于英仙臂视差测量的工作，一直令我神往。其实过了很久，我才真正地理解视差。去了紫金山天文台以后，跟着徐老师做分子外流的工作，发现徐老师对天文和科研的理解的确很深。徐老师做事不拘小节，处理数据却非常仔细。从徐老师身上，我能感受到一个科学家对数据的珍惜，这也许是徐老师能做出好的成果的原因吧。我在 2015 年夏天跟同学一起去青海站观测的时候，徐老师对我们的生活十分关心和照顾，令我十分感动。在以后的数据处理中，我要像徐老师一样，认真仔细。

感谢我的导师张波研究员。张老师也是我硕士工作的指导老师。我在科研过程中，遇到不理解的事情会请教张老师。张老师总是细心地回复我的问题和仔细地修改我的文章草稿，这对我工作的进展有重要意义。张老师还经常教我一些做科研的方法，使我受益非浅。记得在收到银心文章的审稿人的意见后，我发现审稿人误解了我的工作，非常失望；但是张老师跟我说，即使如此，也要认真回复。这让我重新打起精神，后来这个文章很快就发表了。有张老师的指导，我一定会在科研这条路上走的更远。

感谢我在科廷大学的导师 Jean-Pierre Macquart、Andew J. Walsh 和 Paul J. Hancock。Andew 是我在澳洲的第一个导师，后来 Andrew 工作到期，我导师换为 J-P。Andrew 是一个很正直的人，他跟徐老师一样，处理数据也很仔细。刚到澳洲的时候，我的英语口语差到不忍卒听，但是 Andrew 却没有嫌弃我，还细心的帮我改英文。我一直很欣赏 Andrew 的为人，我能看到一个天文学家对天文的热爱，我希望

他以后能重新回到天文工作上来。在澳洲的最后一年，一直是 J-P 在帮我修改文章和工作申请。虽然 J-P 没有做过分子谱线方面的工作，但是他能很快地理解我的工作，并还能提出修改意见，让我十分佩服。J-P 和 Andrew 是我的学习目标和榜样。

感谢紫金山天文台的同学和老师们。在紫金山天文台两年多，我学到了很多东西。刚去紫台的时候，由于对单天线还不是很了解，一直是李发成同学 (以下简称发哥) 带我学习GILDAS/CLASS。我们平时也会探讨一些科研的问题，虽然发哥没有在他的博士论文致谢中感谢我 (至少得感谢我陪他打乒乓球锻炼身体，我觉得)，但是我还是得感谢一下发哥。感谢紫金山天文台的老师们，你们严谨治学的作风，对我影响颇深。感谢青海观测站的老师们对我观测的帮助，这对我工作的完成有重要意义。

感谢我在澳大利亚的同学和朋友，是你们陪我一起走过在国外求学的两年。我想特别感谢一下 Joanne Dawson。Jo 对我银心的工作帮助很大，尤其是在数据处理和文章修改上，算是半个导师。Jo 是我见过最负责任的合作者之一，另外一个是 Gordon MacLeod。Gordon 对我 IRAS/H II 区判据的工作提出了很多宝贵意见，收益良多。感谢 Angela 和 Chris 对我的关心和帮助。Angela 和 Chris 每周会带我去吃中餐，对向我这样不会做饭又没有驾照，行动不便的学生来说，这是对我学习的最大帮助！感谢 Sammy McSweeney 每星期给我们上英语课，耐心的给我们讲解一些常识。Sam 辛苦了！感谢 Mira Jiang 对我生活的照顾，刚来澳洲的时候，对这里的环境和生活一无所知，是 Mira 教会我怎么在澳洲生活，怎么练习英语。没有 Mira，我很难想象我能否完成澳洲的学业。

最后，我想感谢一下一直在背后默默支持我的家人。